ANALYSIS OF WELLBORE STABILITY

by

Michael Richard McLean, MSc, DIC

88

A thesis submitted to the University of London for the degree of Doctor of Philosophy in the Faculty of Engineering.

Rock Mechanics Section
Dept. of Mineral Resources Engineering
Royal School of Mines
Imperial college
LONDON SW7 2BP

ACKNOWLEDGEMENTS

20528113

There are many people I could name who have helped me through the rigors of carrying out this PhD to its fruition, but it is not practical to name them all, so it is necessary to restrict the list of acknowledgments to those who have had the greatest impact on helping me to complete this, my first major exploit into the world of being a researcher.

First, I must thank the financiers of the project who are the SERC and The British Petroleum Company, in particular Dr. Matt Barr who initiated the research.

My supervisor for this project has been Professor Ted Brown. Not only has Ted been friendly and supportive, but during some difficult times has helped me beyond the call of duty. I made a good choice to carry out this research under his supervision.

In addition to having Ted Brown as my supervisor, I was lucky enough to have two other leaders in their respective fields to help and advise me, namely Dr. John Bray and Dr. John Watson. I believe I would have had difficulty in finding anywhere else where I could surround myself with such a prestigious and helpful line up of support. They have both had a tremendous influence on my career and general attitude.

Possibly one of the most important events to influence my research was the introduction of a joint cooperation program between this research and research carried out by Dr. Fred Santarelli on behalf of Elf Aquataine. Fred is not only a brilliant researcher but has become a close friend. I have benefited considerably from working alongside him.

Lastly, I must thank Bob Klein of The British Petroleum Company. Bob has done much to put my research firmly in its place and point out weaknesses and strengths in the research when taken to its ultimate conclusion of applying it to the field.

ABSTRACT

This research was carried out under a research contract between The British Petroleum Company and Imperial College, London. In addition the research was the subject of a CASE award financed by the SERC. The aim of the research was to develop a numerical model that could be applied to circular openings in rock with particular reference to stress related behaviour of wells drilled in the Petroleum Industry.

Preliminary work was carried out on this research project at Imperial College by Professor E.T.Brown and Dr J.W.Bray.[1] This work set broad requirements for the numerical model. The three most important requirements were, (i) to handle deviated wells in addition to vertical wells, (ii) to be able to follow the complete stress-strain characteristics of typical sedimentary rocks (the problem being the inclusion of strain softening behaviour) and (iii) to allow for the effect of pore pressure gradients on the stress-strain behaviour around the well. The first two requirements have been implemented in the computer coding, but pore pressure gradient effects have not been included. However, the effects of pore pressure gradients have been studied using simpler linear elastic techniques in Chapter 2.

Although not an original requirement of the computer code, the numerical model has allowed for the inclusion of stress dependent elastic properties as opposed to simple linear elasticity. The existence

and marked influence of stress dependent elasticity in dry sedimentary rocks was noted by Dr F.Santarelli while carrying out research at Imperial College in parallel with this work. Its inclusion in analyses allowed significant improvements in the prediction failure around model wellbores (hollow cylinders) tested under laboratory conditions. Thus, this behaviour is catered for in the numerical model developed here.

In addition to development of the numerical model, linear elasticity is used as a basis for presenting and developing closed form solutions for the analysis of wellbore stability. These solutions are used in a parametric study to gain insight into the relative effects of a variety of parameters on wellbore stability (e.g. temperature, time, mud cake efficiency).

CONVENTIONS AND UNITS

* Throughout the text compression is taken to be positive and tension negative.

* In cases where a three dimensional stress state is considered a right-hand coordinate system is used.

* The thesis is directed at the Petroleum Industry where an assortment of units are used (primarily Imperial). Thus, in certain instances both the conventional Petroleum Industry unit and its SI equivalent are given.

TOTAL AND EFFECTIVE STRESSES

In Chapter 2 the effective stress principal is used and distinction is made between total and effective stresses. In the finite element modelling and behaviour law developments in Chapters 3 to 6 no reference is made to pore pressures and it is assumed that the pore pressure is zero and effective and total stresses are therefore equivalent. However, in cases where the pore pressure takes on non-zero values the behaviour laws and yield functions given in Chapters 3 to 6 must be taken to be in terms of effective stresses rather than total stresses. Thus, the pore pressure component is taken as a datum and its value subtracted from all pressures and normal stresses. Naturally this can only be done in cases where there is no fluid flow and the pore pressure is uniform within the bounds of the problem under consideration.

NOMENCLATURE

a	Tunnel/wellbore radius
$[a]$	Associated flow vector (see Page 240)
b_x, b_y, b_z	Body force components (see Page 124)
$[B_i]$	Matrix of shape function derivatives (see Page 135)
c	Mohr-Coulomb cohesion strength parameter
$[d]$	Displacement vector (see Pages 132 and 156)
$[\bar{d}]$	Vector of virtual displacements (see Page 127)
$[D]$	Matrix of stress-strain stiffnesses (see Page 241)
$[D]^*$	As above but without the axial components (see Page 136)
E	Youngs Modulus
E_0	Young's Modulus for uniaxial compression (see Page 336)
E'	Variation of E with confining pressure (see Page 336)
F	Associated flow potential function (see Page 192)
$[f]$	Non-accosiated flow vector (see Page 222)
f_1	Plastic flow component in the maximum principal stress direction (see Page 242)
G	Shear stiffness modulus
H'	Hardening/softening parameter (see Page 249)
I_1, I_2, I_3	Stress invariants (see Page 237)
$[J]$	Jacobian matrix (see Page 135)
J_1, J_2, J_3	Stress deviatoric invariants (see Page 237)
k	Rock coefficient of absolute permeability (see Page 82)
m	Hoek-Brown strength parameter (see Page 200)
m_I, m_R	Initial and residual values of m (see Page 290)
N_i	Shape function for node 'i' (see Page 130)
n	Porosity
P_{xj}, P_{yj}, P_{zj}	Nodal load components for node 'j' (see Pages 151 & 157)

NOMENCLATURE - con'd

P_a	Support pressure applied to a circular opening (see Page 272)
P_C	Pore pressure at the mud cake/wellbore wall interface (see Figure 2.3)
P_F	Formation pressure
p_f	Pore pressure
P_W	Wellbore pressure
Q	Flow rule potential function (see Page 221)
r	Radius
R	Radius for uniform temperature or pore pressure (see Figures 2.2 - 2.5)
s	Hoek-Brown strength parameter (see Page 200)
s_I, s_R	Initial and residual values of s (see Page 290)
T	Temperature
T_F	Original formation temperature
T_W	Well temperature
t	Time
[t]	Traction vector (see Page 122)
u, v, w	Displacement components (see Page 155)
$\mathbb{V}$	Virtual work (see Page 126)
$\mathbb{V}_T$, $\mathbb{V}_B$, $\mathbb{V}_{SE}$	Surface tractions, body force and strain energy virtual work components (see Pages 126 & 127)
α_r	Thermal coefficient of linear expansion of the formation
β_f	Thermal coefficient of volume expansion of the pore fluid
β_r	Thermal coefficient of volume expansion of the formation
ε_v	Volumetric strain
ε_r, ε_θ, ε_z	Normal strains referenced in terms of polar coordinates
ε_1, ε_2, ε_3	Maximum, intermediate and minimum principal strains

NOMENCLATURE - con'd

$(\varepsilon_1^p)_P$	Maximum principal plastic strain at peak strength (see Figure 4.10)
$(\varepsilon_1^p)_R$	As above but at residual strength (see Figure 4.10)
ε^e, ε^p	Elastic and Plastic strain components
ϕ	Mohr-Coulomb friction angle
$\gamma_{r\theta}$, $\gamma_{\theta z}$, γ_{zr}	Shear strains referenced in terms of polar coordinates
κ	Diffusivity coefficient (see Page 83)
λ	Plastic multiplier (see Page 214)
ν	Poisson's ratio
μ	Fluid kinematic viscosity
$[\psi]$	Load vector (see Page 142)
σ_r, σ_θ, σ_z	Total normal stresses referenced in terms of polar coordinates
σ'_r, σ'_θ, σ'_z	Effective normal stresses referenced in terms of polar coordinates (see Page 50)
σ_r, σ_θ, σ_z	Deviatoric stress components (see Page 237)
σ_1, σ_2, σ_3	Maximum, intermediate and minimum principal stresses
$[\sigma]$	Stress vector
$[\sigma]^*$	As above but without the axial component (see Page 160)
σ_c	Uniaxial compressive strength
σ_{LE}	Predicted applied loading for failure of a circular opening in rock assuming linear elasticity (see Page 398)
σ_{NL}	As above but assuming a PDS elastic and plastic behaviour (see Page 401)
σ_{PDS}	As above but assuming PDS elasticity only (see Page 398)
σ_Y	Yield strength
$\tau_{r\theta}$, $\tau_{\theta z}$, τ_{zr}	Shear stresses referenced in terms of polar coordinates

CONTENTS

TITLE..... i

AKNOWLEDGEMENTS..... ii

ASTRACT..... iv

CONVENTIONS..... vi

CONTENTS..... vii

INDEX OF FIGURES..... xiii

INDEX OF TABLES..... xxiv

CHAPTER 1
BACKGROUND TO THE PROBLEM 1

1.1 PETROLEUM DRILLING OPERATIONS 1
1.1.1 Well Deviation 1
1.1.2 The Drilling Mud and Casing Design 2
1.2 TYPES OF WELLBORE INSTABILITY 9
1.2.1 Chemically Induced Instability 9
1.2.2 Mechanically Induced Instabilities 10
1.3 CASE HISTORIES OF WELLBORE INSTABILITIES 13
1.4 NUMERICAL MODELING OF WELLBORE STABILITY 14
1.4.1 Factors Influencing Wellbore Stability Modelling ... 15
1.4.2 Requirements of Numerical Modelling 31
1.4.3 Controllable parameters 32
1.5 CURRENT WELLBORE STABILITY MODELS 35
1.7 CONTENT OF THE THESIS 41
1.6 CONCLUDING REMARKS 40

CHAPTER 2
ELASTIC SOLUTIONS FOR ANALTYIS OF WELLBORE STABILITY 43

2.1 INTRODUCTION 43
2.1.1 General Conditions 44
2.1.2 Assumptions 45
2.2 REDISTRIBUTION OF THE IN-SITU STRESSES - DRAINED CONDITIONS 46
2.3 INDUCED PORE PRESSURES FOR UNDRAINED STRESS REDISTRIBUTION 49
2.4 STRESSES AND PORE FLUID PRESSURES RESULTING FROM FLUID FLOW 58
2.5 THERMAL STRESSES IN PERMEABLE FORMATIONS 65
2.5.1 Conditions of Zero Fluid Invasion/Influx 68
2.5.2 Condition of Fluid Invasion/Inflow 71
2.6 THERMAL STRESSES AND PORE PRESSURES IN LOW PERMEABILITY FORMATIONS 73
2.7 TRANSIENT PORE FLUID PRESSURES IN LOW PERMEABILITY FORMATIONS 79
2.8 PARAMETRIC STUDY - STEADY STATE CONDITIONS 90
2.8.1 Problem Definition 90
2.8.1.1 Material Behaviour 90

2.8.1.2 In-Situ Stress State 92
2.8.1.3 Well Azimuth 92
2.8.1.4 Remaining Parameters 92
2.8.1.5 Failure Mechanisms 93
2.8.2 Relevant Equations 95
2.8.3 Results 96
2.8.3.1 Effect of Well Azimuth 96
2.8.3.2 Effect of Temperature on Stability 102
2.8.3.3 Effect of Poisson's Ratio on Stability 105
2.8.3.4 Effect of the Mud Cake on Stability 105
2.8.3.5 Effect on Leak Off Interpretation 107
2.9 TIME DEPENDANT STABILITY - TRANSIENT SOLUTION 110
2.9.1 Failure Conditions 111
2.9.2 Input Parameters 112
2.9.3 Relevent Equations 113
2.9.4 Results 113
2.10 CONCLUDING REMARKS 118

CHAPTER 3
APPLICATION OF THE FEM TO 2-DIMENSIONAL LINEAR ELASTIC PROBLEMS 121

3.1 INTRODUCTION 121
3.2 THE VIRTUAL WORK EXPRESSION 121
3.3 FINITE ELEMENTS - PLANE STRAIN CONDITIONS 128
3.3.1 The Shape Functions 130
3.3.2 Strain-Displacement relationships 134
3.3.3 The Jacobian 135
3.3.4 Stress-Strain Relationship 136
3.3.5 Local and Global Node Numbering 137
3.3.6 Virtual Work Applied to Finite Elements 137
3.3.7 The Stiffness Matrix 141
3.3.8 Numerical Integration of the Strain Energy Term 145
3.3.9 The Load Vector 149
3.4 COMPLETE PLANE STRAIN CONDITIONS 151
3.4.1 Method of Loading 151
3.4.2 Strain-Displacement Relationships 153
3.4.3 The FEM Applied to Complete Plane Strain 156
3.5 THE FEM IN TERMS OF POLAR COORDINATES 158
3.5.1 Strain-Displacement Relationships 158
3.5.2 The Jacobian 160
3.5.3 Stress-Strain Relationship 160
3.5.4 Integration of the Strain Energy Term 160
3.5.5 Surface Traction Term 161
3.6 EQUATION SOLUTION 161
3.7 POST PROCESSING 163
3.8 PROBLEM DEFINITION 164
3.8.1 Location of the Outer Boundary 164
3.8.2 Rigid Body Displacement 166
3.8.3 Infinite Elements 167
3.8.4 Symmetry Conditions 170
3.8.5 Mesh Generation 175
3.9 PROGRAMME VALIDATION FOR LINEAR ELASTIC BEHAVIOUR 177
3.9.1 The Axisymmetric Wellbore 178
3.9.2 Plane Strain Conditions 181

3.9.3 Complete Plane Strain Conditions 184
3.10 CONCLUDING REMARKS 186

CHAPTER 4
PLASTICITY AS A MEANS OF MODELLING MATERIAL BEHAVIOUR 187

4.1 INTRODUCTION 187
4.2 TYPES OF NONLINEAR PROBLEMS 187
4.2.1 Geometric Nonlinearity 189
4.2.2 Material Nonlinearity 189
4.3 PLASITICITY THEORY 190
4.3.1 Behaviour Law Requirements 191
4.4 THE STRENGTH CRITERION 192
4.4.1 Uniaxial Loading 193
4.4.2 2-Dimensional Stress State 195
4.4.3 Triaxial Stress State 198
4.4.4 Other Yield Criteria 200
4.5 EXPANSION/CONTRACTION OF THE YIELD SURFACE 203
4.5.1 Measurement of the Maximum Principal Plastic Strain 204
4.5.2 Strength Parameter-Plastic Strain Relationships 208
4.5.3 Variation of Plastic Strain with Confining Pressure 210
4.6 THE FLOW RULE 211
4.6.1 Associated Flow 213
4.6.2 Measurement of Plastic Flow Ratios 218
4.6.3 Non-Associated Flow 219
4.7 APPLICATION OF MODEL TO CARBONIFEROUS SANDSTONE TRIAXIAL RESULTS 222
4.7.1 Mohr-Coulomb Criterion 222
4.7.2 Hoek-Brown Criterion 225
4.7.3 Conclusions on Model Behaviour 227

CHAPTER 5
THE FEM APPLIED TO ELASTO-PLASTIC MATERIAL BEHAVIOUR 229

5.1 ITERATIVE TECHNIQUES 229
5.1.1 Initial Stiffness Method 230
5.1.2 Tangential Stiffness Method 233
5.1.3 Mixed Algorithm 235
5.2 STRESS INVARIANTS APPLIED TO YIELD CRITERIA 236
5.2.1 Principal Stresses in Terms of Stress Invariants ... 236
5.3 RETURNING STRESS POINTS TO THE YIELD SURFACE 239
5.3.1 Determination of the Plastic Multiplier 239
5.3.2 Determination of the Vector of Yield Function Derivatives, [a] 243
5.3.3 Determination of the Flow Vector, [f] 245
5.3.4 Singularities on the yield surface 246
5.3.5 Determination of the 'Hardening Parameter' 249
5.3.6 Returning Stress Points to the Yield Surface 250
5.3.7 The Elasto-Plastic Stress-Strain Compliances 255
5.4 ADDITIONAL NUMERICAL REQUIREMENTS FOR ANALYSIS OF STRAIN SOFTENING 257
5.4.1 Adapted Algorithm for Strain Softening Materials ... 261
5.4.2 Fictitious Support Applied to Wellbore Analysis 265

5.4.3 Potential Sources of Instability in the Plastic Multiplier 267
5.5 VALIDATION OF THE FEM PROGRAM FOR PLASTIC BEHAVIOUR 271
5.5.1 Validation of FEM using Galin's Solution 272
5.5.2 Validation of the FEM using Detournay's Solution ... 280
5.5.3 Finite Difference Analysis of Strain Softening 285
5.5.3.1 Dependence of Strength Parameters on Plastic Strain 285
5.5.3.2 Axial Plastic Strain Components 288
5.5.3.3 FEM Validation for Strain Softening Axisymmetric Conditions 289
5.5.4 Conclusions on FEM validation 292
5.6 PARAMETRIC ANALYSIS 292
5.6.1 Material Models 294
5.6.1.1 Model Material A - 'Strong Sandstone Formation' 296
5.6.1.2 Model Material B - 'Weak/Medium Strength Sandstone Formation' 297
5.6.2 Plastic Behaviour Law Study 299
5.6.2.1 In-situ Stress Conditions 300
5.6.2.2 Wellbore Pressure 300
5.6.2.3 Results 301
5.6.3 Keyseating or Stress Induced Failure? 309
5.6.4 Effect of a Weak Zone around a Circular Opening under Axisymmetric Loading 313
5.6.4.1 Case of a Vertical Wellbore 315
5.6.4.2 Case of a Hollow Cylinder 315
5.6.4.3 Conclusions 319
5.6.5 Plastic Regions Developed around Deviated Wells 320
5.6.5.1 Problem Definition 321
5.6.5.2 FEM Mesh and Loading Parameters 323
5.6.5.3 Results 323
5.6.5.4 Computer Time Consumption 327
5.7 CONCLUDING REMARKS 328

CHAPTER 6
ANALYSIS USING A PRESSURE DEPENDENT STIFFNESS..... 331

6.1 BACKGROUND AND DEFINITION OF PRESSURE DEPENDENT STIFFNESS (PDS) 331
6.1.1 Triaxial Testing 331
6.1.2 Application to Hollow Cylinder Analysis 334
6.2 BEHAVIOUR LAWS 336
6.2.1 Linear Behaviour Law 336
6.2.2 Comparison Between Behaviour Law Predictions 337
6.2.2.1 Radial and Circumferential Stress State 338
6.2.2.2 Radial Closure 340
6.2.3 Comparison Between Model Predictions and Measured Displacements 342
6.2.4 Prediction of Axial Stress State 345
6.2.5 Conclusions on the Linear Behaviour Law 345
6.3 APPLICATION OF THE FEM TO PDS BEHAVIOUR 347
6.3.1 PDS Nonlinearity 348
6.3.2 Iterative Method Adopted for PDS Behaviour 349
6.3.3 PDS Elastic Tangent Stiffness 351
6.3.3.1 Determination of the Stress-Strain Compliance Matrix, [S'] 353

6.3.3.2 Singularities in the Determination of [S'] 355
6.3.3.3 Inversion of [S'] 357
6.3.4 Correction of Stress State 357
6.3.4.1 Disadvantage of the PDS Power Law Behaviour 360
6.3.5 Factors Effecting the Accuracy of the Results 361
6.3.6 Points at which the Tangent Stiffness is Redetermined..... 362
6.3.7 Irregularities in Material Response 364
6.4 APPLICATION OF THE FEM TO COUPLED PDS AND PLASTICITY BEHAVIOUR 365
6.4.1 Returning Stress Points to the Yield Surface 366
6.4.2 The PDS Elasto-Plastic Stress-Strain Stiffness Matrix 368
6.4.3 Numerical Instabilities 369
6.5 PROGRAM VALIDATION FOR PDS BEHAVIOUR 373
6.5.1 Axisymmetric Loading 373
6.5.1.1 PDS Elastic Behaviour 374
6.5.1.2 PDS Elastic-Perfectly Plastic Behaviour 376
6.5.1.3 PDS Elasticity followed by Strain Softening 378
6.5.2 Anisotropic Loading under Plane Strain Conditions .. 385
6.6 QUANTITATIVE ASSESSMENT OF FAILURE PREDICTION 389
6.6.1 Tensile Failure 392
6.7 PARAMETRIC ANALYSIS 396
6.7.1 Influence of PDS Elasticity in Anisotropic In-Situ Stress Regimes 397
6.7.2 Failure of the Carboniferous Sandstone under Anisotropic Loading 401
6.7.3 Mud Weights Required for Deviated Wells 402
6.8 CONCLUDING REMARKS..... 407

CHAPTER 7
SUMMARY OF WORK AND FUTURE RESEARCH REQUIREMENTS..... 409

7.1 SUMMARY OF WORK PRESENTED 409
7.2 MAIN CONCLUSIONS 412
7.3 RESTRICTIONS AND POTENTIAL AREAS FOR IMPROVEMENT 415
7.3.1 Restrictions of this Research 415
7.3.2 Scope for Improvement 418

REFERENCES..... 425

APPENDIX A
COMPARISON OF VARIOUS MODEL ROCK BEHAVIOUR LAWS WITH A SET OF TRIAXIAL TESTS CARRIED OUR ON A CARBONIFEROUS SANDSTONE..... 437

APPENDIX B
GALIN'S SOLUTION FOR THE ELASTO-PLASTIC STRESS DISTRIBUTION AROUND A CIRCULAR OPENING IN A MATERIAL OBEYING THE TRESCA YIELD CRITERION..... 469

APPENDIX C
APPROXIMATE SOLUTION FOR THE CONTOUR DEFINING THE ELASTO-PLASTIC BOUNDARY AROUND A CIRCULAR OPENING IN A PERFECTLY PLASTIC MHR-COULOMB MATERIAL SUBJECTED TO A NON-HYDROSTATIC STRESS FIELD IN PLANE STRAIN..... 475

APPENDIX D
FINITE DIFFERENCE ANALYSIS OF STRAIN SOFTENING BEHAVIOUR AROUND A CIRCULAR OPENING IN A HYDROSTATIC IN-SITU STRESS FIELD..... 479

APPENDIX E
SEMI-CLOSED FORM SOLUTION FOR THE ANALYSIS OF STRESSES AROUND A CIRCULAR OPENING SUBJECTED TO AXISYMMETRIC LOADING ASSUMING A PRESSURE DEPENDENT STIFFNESS (PDS)..... 491

APPENDIX F
INPUT, OUTPUT AND PROGRAM OPERATION..... 503

INDEX OF FIGURES

Figure 1.1 Offshore drilling. 3

Figure 1.2 Directional drilling. 4

Figure 1.3 Increased length of hole open to reservoir for horizontal wells. 5

Figure 1.4 Typical vertical well profiles. 5

Figure 1.5 Selection of casing seat points. 8

Figure 1.6 Types of mechanical instability. 11

Figure 1.7 Key seating due to rubbing of drill string on wellbore wall. 12

Figure 1.8 Homogeneity scale dependence. 16

Figure 1.9 Casing collapse. 19

Figure 1.10 Perforated production casing. 19

Figure 1.11 Formation of the mud cake. 20

Figure 1.12 Radial fluid flow in overbalance conditions. 20

Figure 1.13 Pore pressure profile during DST's. 22

Figure 1.14 Damaged zone around wellbore due to drilling fluid invasion. 22

Figure 1.15 Reduced radial effective stress due to formation damage. 23

Figure 1.16 Triaxial tests carried out on sandstone. 23

Figure 1.17 Nonlinear elastic modelling of a circular excavation in rock. 26

Figure 1.18 Reduction of load bearing area after fracture. 28

Figure 1.19 'True' and nominal uniaxial stress-strain curves. 28

Figure 2.1 Transformation of the in-situ stress tensor. 47

Figure 2.2 Pore pressure profile for steady-state fluid flow. 60

Figure 2.3 Pore pressure profile when mud cake is present. 60

Figure 2.4 Steady-state temperature distribution. 67

Figure 2.5 Temperature distribution for fluid injection well. 67

Figure 2.6 Transient radial fluid flow. 81

Figure 2.7 Pore pressure profiles as a function of distance and time. 87

Figure 2.8 Section through deviated wellbore. 94

Figure 2.9 Variation of failure initiation gradients with well deviation. Well deviated // to σ_H in 'sandstone' formation. 98

Figure 2.10 Variation of failure initiation gradients with well deviation. Well deviated // to σ_h in 'sandstone' formation. 98

Figure 2.11 Variation of failure initiation gradients with well deviation. Well deviated // to σ_H in 'shale' formation - undrained response. 100

Figure 2.12 Variation of failure initiation gradients with well deviation. Well deviated // to σ_h in 'shale' formation - undrained response. 100

Figure 2.13 Variation of failure initiation gradients with well deviation. Well deviated // to σ_H in 'shale' formation - drained response. 100

Figure 2.14 Variation of failure initiation gradients with well deviation. Well deviated // to σ_h in 'shale' formation - drained response. 100

Figure 2.15 Stresses acting in a plane perpendicular to the well axis for wells deviated in a direction perpendicular to σ_H. 101

Figure 2.16 Variation of failure initiation gradients with mud temperature. 'Sandstone' formation. 103

Figure 2.17 Variation of failure initiation gradients with mud temperature. 'Shale' formation - undrained response. 103

Figure 2.18 Variation of failure initiation gradients with mud temperature. 'Shale' formation - drained response. 103

Figure 2.19 Effect of rock elastic and expansion properties on fracture gradients. 'Sandstone' formation. 104

Figure 2.20 Effect of rock elastic and expansion properties on fracture gradients. 'Shale' formation - undrained response. 104

Figure 2.21 Effect of rock elastic and expansion properties on fracture gradients. 'Shale' formation - drained response. 104

Figure 2.22 Variation of failure initiation gradients with Poisson's ratio. 'Sandstone' formation. 106

Figure 2.23 Variation of failure initiation gradients with Poisson's ratio. 'Shale' formation - undrained response. 106

Figure 2.24 Variation of failure initiation gradients with Poisson's ratio. 'Shale' formation - drained response. 106

Figure 2.25 Variation of failure initiation gradients with mud cake parameter (h). 'Sandstone' and drained 'shale' behaviour. 108

Figure 2.26 Typical leak off test plot. 108

Figure 2.27 Change in fracture pressure from short term to long term conditions. Well deviated // to σ_H. 108

Figure 2.28 Stress/Pressure profile for 'shale' of permeability 10^{-7} Darcys during overbalance conditions. 114

Figure 2.29 Stress/Pressure profile for 'shale' of permeability 10^{-7} Darcys during underbalance conditions. 114

Figure 2.30 Variation of failure initiation gradients with time. 117

Figure 3.1 Virtual displacements applied to a circular excavation in rock. 123

Figure 3.2 Stress and virtual displacements imposed on element. 125

Figure 3.3 Structure divided into finite elements. 129

Figure 3.4 Transferring elements from cartesian to intrinsic space. 131

Figure 3.5 Local and global node numbering. 138

Figure 3.6 Symmetry in the global stiffness matrix about the leading diagonal. 144

Figure 3.7 Portion of element mapped from intrinsic to cartesian space. 146

Figure 3.8 Element edge with distributed loading. 146

Figure 3.9 Combination of original and induced loading to give resultant stress state. 152

Figure 3.10 Antiplane shear loading. 154

Figure 3.11 Circular excavation defined in terms of polar coordinates. 159

Figure 3.12 Prevention of rigid body displacement. 165

Figure 3.13 Mapping of infinite elements. 168

Figure 3.14 Relevant boundary condition for utilization of symmetry. 171

Figure 3.15 Gradation of the element mesh. 174

Figure 3.16 Element numbering. 174

Figure 3.17 Various FEM meshes for analysis of axisymmetric loading. 176

Figure 3.18 FEM mesh for validation under plane strain conditions. 180

Figure 3.19 FEM mesh for validation under complete plane strain conditions. 183

Figure 4.1 Various plastic responses to loading. 188

Figure 4.2 Irrecoverable strain and variation of secant stiffness. 188

Figure 4.3 Variation of yield strength with deformation. 194

Figure 4.4 Mohr-Coulomb yield surfaces resulting from triaxial data. 197

Figure 4.5 3-D interpretation of the Mohr-Coulomb and Drucker-Prager yield criteria. 199

Figure 4.6 3-D interpretation of the Tresca and Von Mises yield criteria. 199

Figure 4.7 The Hoek-Brown criterion. 202

Figure 4.8 Measurement of major principal plastic strain for triaxial data. 205

Figure 4.9 Idealized representation of rock stress-strain behaviour. 207

Figure 4.10 Idealized representation of a triaxial test using Mohr-Coulomb strength parameters. 207

Figure 4.11 Idealized model representation of triaxial test results showing no increase in ductility with increased confining pressure. 209

Figure 4.12 Variation of ε_1^p at peak and residual as a function of confining pressure. 209

Figure 4.13 Radial response to loading in a triaxial test. 212

Figure 4.14 Measurment of ε_3^p from triaxial test data. 217

Figure 4.15 Plot of interpreted flow ratio ($\partial\varepsilon_3^p/\partial\varepsilon_1^p$) against confining pressure. 220

Figure 4.16 Mohr-Coulomb criterion fitted to yield, peak and residual strength for a Carboniferous sandstone. 223

Figure 4.17 Hoek-Brown criterion fitted to yield, peak and residual strength for a Carboniferous sandstone. 223

Figure 5.1 Initial stiffness method applied to simple uniaxial loading case. 231

Figure 5.2 Tangent stiffness method. 234

Figure 5.3 Mixed algorithm approach. 234

Figure 5.4 Flow at singular points on the yield surface. 247

Figure 5.5 Returning stress point to yield surface with respect to the Hoek-Brown criterion. 254

Figure 5.6 Iterative techniques applied to a strain softening material. 258

Figure 5.7 Prediction of localized failure in a uniaxially loaded sample undergoing strain softening (or perfect plasticity). 260

Figure 5.8 Localized failure in a steel bar loaded uniaxially. 260

Figure 5.9 Adapted algorithm for the tangent stiffness method applied to strain softening materials. 262

Figure 5.10 FEM analysis of strain softening behaviour around a wellbore using a fictitious liner. 266

Figure 5.11 Class I, Class II and transitional material behaviour. 270

Figure 5.12 FEM mesh for analysis of a circular excavation in an anisotropic stress field under plane strain conditions. 270

Figure 5.13 FEM definition of the elasto-plastic contour around a circular opening compared with Galin's solution. 276

Figure 5.14 FEM definition of the elasto-plastic contour around a circular opening in a frictional material compared with Detournay's approximate solution. 283

Figure 5.15 Idealized model behaviour inferred by Brown et al.[49] 283

Figure 5.16 Stress state around a circular opening subjected to axi-symmetric loading and plane strain constraints. 291

Figure 5.17 Induced displacements at excavation boundary with reduction in support pressure. 291

Figure 5.18 Triaxial interpretation of material Model A - 'strong sandstone formation'. 295

Figure 5.19 Triaxial interpretation of material Model B - 'weak-medium strength sandstone formation'. 298

Figure 5.20 Applied loading in terms of effective stresses and overbalance pressure for material model behaviour law study. 302

Figure 5.21 Plastic zones around a wellbore subjected to loading defined as per Figure 5.20, using material Model A1. 303

Figure 5.22 Plastic zones around a wellbore subjected to loading defined as per Figure 5.20, using material Model A2. 303

Figure 5.23 Plastic zones around a wellbore subjected to loading defined as per Figure 5.20, using material Model A3. 304

Figure 5.24 Plastic zones around a wellbore subjected to loading defined as per Figure 5.20, using material Model A4. 304

Figure 5.25 Variation of radial displacements as a function of overbalance pressure and material model type. 307

Figure 5.26 Loading conditions and FEM mesh for analysis of the effect of a weak zone on the plastic region around a wellbore in an anisotropic stress field. 310

Figure 5.27 Triaxial interpretations of model material behaviour used to simulate a weak zone at the wellbore wall. 311

Figure 5.28 Plastic regions developed around a wellbore in an anisotropic stress field, with the presence of a weak zone. 312

Figure 5.29 Elliptical failure around circular cavity in a sample of Red Wildmoor sandstone subjected to axisymmetric loading. 314

Figure 5.30 Variation of plastic zones around a vertical wellbore in an isotropic horizontal stress field with the presence of a weak zone. 316

Figure 5.31 Variation of plastic zones around a hollow cylinder with the presence of a weak zone for various boundary ratios (R/a). 318

Figure 5.32 FEM mesh for analysis of plastic regions around deviated wellbores. 322

Figure 5.33 Plastic regions developed around a vertical well and wells deviated at angles of 20° and 40°. 324

Figure 5.34 Plastic regions developed around wells deviated at angles of 60° and 80° and a horizontal well. 325

Figure 5.35 Projection of NW onto inclined wellbore section for a well deviated in a Northerly direction. 326

Figure 6.1 Test results and behaviour law defining the variation of Young's modulus with confining pressure for a Carboniferous sandstone. 333

Figure 6.2 Loading conditions applied to a hollow cylinder rock sample. 335

Figure 6.3 Comparison of predicted stress states within a hollow cylinder using linear and power PDS behaviour laws. 339

Figure 6.4 Comparison between predicted and actual radial closure for a hollow cylinder sample of the Carboniferous sandstone. 343

Figure 6.5 Variation of the axial stress, σ_z, within a hollow cylinder sample assuming PDS elasticity and uniform strain conditions. 346

Figure 6.6 Classification of borehole failure mechanisms. 346

Figure 6.7 Iterative algorithms applied to analysis of a hollow cylinder sample with PDS elastic response. 350

Figure 6.8 Algorithm for determining the percentage of load applied before yield occurs. 363

Figure 6.9 Limiting condition for instability of the numerical algorithm for analysis of PDS elasticity coupled with perfect plasticity. 372

Figure 6.10 Predicted axial, radial and circumferential stresses around a circular opening in a hydrostatic stress field assuming a PDS elastic response. 375

Figure 6.11 Elastic and plastic regions around a circular opening in an isotropic in-situ stress field. 375

Figure 6.12 Predicted stress around a circular opening in a hydrostatic stress field, assuming a PDS elastic-perfectly plastic behaviour. 379

Figure 6.13 Predicted load-displacement response for a circular opening in a hydrostatic in-situ stress field, assuming a PDS elastic - perfectly plastic behaviour. 380

Figure 6.14 Predicted stresses around a circular opening in a hydrostatic stress field assuming a PDS elastic - strain softening plastic behaviour. 383

Figure 6.15 Elasto-plastic contour around a circular opening in an anisotropic in-plane in-situ stress field, where the material is defined by PDS elastic - perfectly plastic behaviour. 387

Figure 6.16 Comparison between hollow cylinder test results on a Carboniferous sandstone and model predictions. 391

Figure 6.17 Predicted circumferential stress at the internal wall of a hollow cylinder of the Carboniferous sandstone with a high internal pressure. 393

Figure 6.18 Predicted variation of radial and circumferential stress within a hollow cylinder of the Carboniferous sandstone with external and internal pressures of 50 and 150 MPa respectively. 395

Figure 6.19 Assumed loading conditions at infinity for study of PDS behaviour under anisotropic loading. 399

Figure 6.20 Ratio of σ_{PDS}/σ_{LE} as a function of in-situ stress anisotropy. 400

Figure 6.21 Variation of FEM predicted failure loads relative to linear elastic failure loads as a function of in-situ stress anisotropy for the Carboniferous sandstone. 403

Figure 6.22 Variation of mud weight requirements with deviation and PDS response. 406

INDEX OF TABLES

Table 1 Tabulated values of $\left(\frac{P_f - P_F}{P_W - P_F}\right)$ for varying values of time and radius. 86

Table 2 Tabulated values of Q for varying values of time and radius. 89

Table 3 Gauss weights and sampling points for numerical integration. 148

Table 4 Cases of symmetry conditions for analysis of stresses around a wellbore. 173

Table 5 Results of an elastic analysis of a wellbore in a hydrostatic stress field. 179

Table 6 Results of an elastic analysis of a vertical wellbore in an anisotropic stress field. 182

Table 7 Results of a complete plane strain elastic analysis of a deviated wellbore in an anisotropic stress field. 185

Table 8 Strain ratios found from the application of the associated flow rule. 216

Table 9 Results of an elastic-perfectly plastic analysis with ASSOCIATED flow of a vertical wellbore subjected to an anisotropic horizontal in-situ stress field. 275

Table 10 Results of an elastic-perfectly plastic analysis with NON-ASSOCIATED flow of a vertical wellbore subjected to an anisotropic horizontal in-situ stress field. 278

Table 11 Comparisons of Associated and Non-associated flow models on the radial closure around a hole subjected to non-hydrostatic loading under plane strain conditions. 279

Table 12 Variation of predicted coordinates of the elasto-plastic interface around a circular opening with number of terms taken from the truncated series used in Detournay's solution. 281

Table 13 Comparison between FEM and exact solutions for the stress state in the plastic zone around a circular excavation in an elasto-plastic Mohr-Coulomb material. Number of plastic load steps = 5. 284

Table 14 Comparison between FEM and exact solutions for the stress state in the plastic zone around a circular excavation in an elasto-plastic Mohr-Coulomb material. Number of plastic load steps = 20. 286

Table 15 Comparisons of PDS Power and Linear behaviour Law predictions of displacement-load response for Carboniferous sandstone hollow cylinder samples. 341

Table 16 Comparison of FEM and exact solution for the stress state in the plastic region for a material exhibiting a PDS elastic-Tresca perfectly plastic response. 388

CHAPTER 1

BACKGROUND TO THE PROBLEM

This chapter introduces the problems encountered during drilling wellbores that can be assigned to stress induced instability and their impact on the whole drilling operation. The chapter then goes on to review published methods of assessing these problems and their relative usefulness.

1.1 PETROLEUM DRILLING OPERATIONS

For completeness, this section describes some of the factors involved in drilling operations that have a bearing on wellbore instability. Firstly, the deviation of the wellbore from the vertical is discussed followed by the role of the drilling fluid and its effect on casing design.

1.1.1 Well Deviation

Present petroleum operations are often categorized into exploration and development drilling. Exploration is the process of finding petroleum reservoirs and development the process of drilling to extract oil in economically viable reservoirs. A further important distinction must be made between land based and offshore based drilling operations. In general, exploration wells will be vertical, and providing site location is not a problem, land based wells will be vertical. In the case of offshore development drilling one platform will be stationed over an oil field so that it can cover a large portion of the reservoir

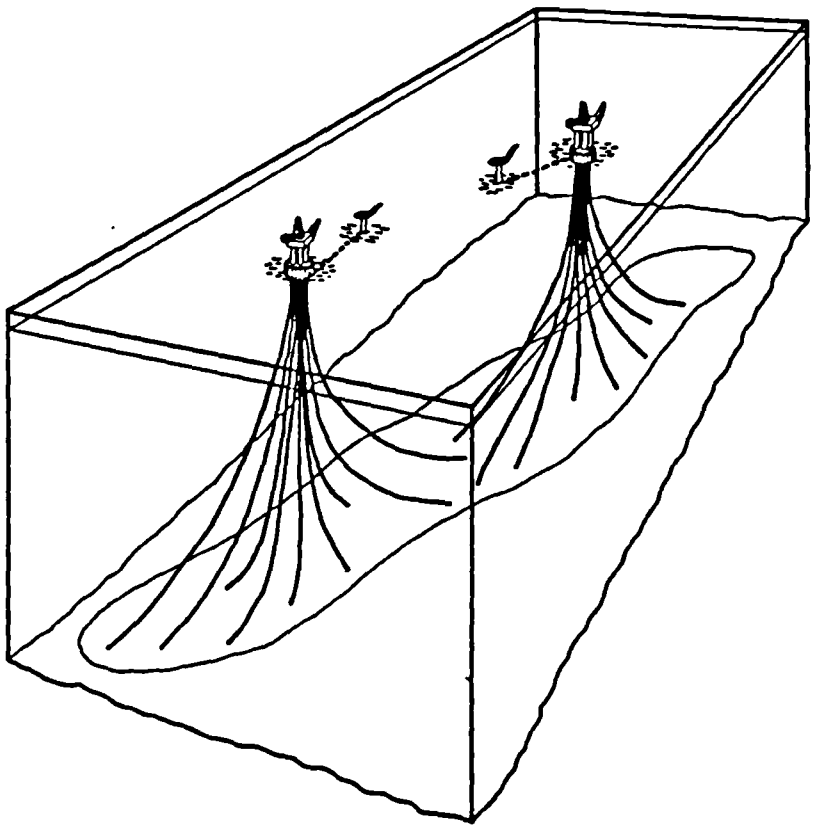
from one location (Figure 1.1). The wells drilled from such a platform will, in general be deviated (examples of the Forties Platforms are are reported by Kock[2]). Offshore deviated wells can build to angles as great as 60° from the vertical (e.g. Holder[3]). In cases where access to a position above the reservoir is restricted (Figure 1.2a) or a potential hazard, such as drilling through a salt dome, is to be avoided (Figure 1.2b), then land based wells may also involve the drilling of deviated wells. Recent advances in drilling techniques have meant that horizontal drilling may become common practice in the future, due to the potential of gaining much larger drainage areas (hence increased production) from a single well (Figure 1.3). Horizontal drilling has been reported by a number of operators, for example Hardman.[4]

1.1.2 The Drilling Mud and Casing Design

A time consuming and expensive part of any petroleum based drilling operation is the casing of the wellbore. Both exploration and production wells are normally cased in stages. At each setting of a casing string a smaller size drill bit is used so that it can pass through the newly set casing, hence hole sizes will reduce in diameter with depth. Typical U.K. land based and North Sea offshore well sizes are shown in Figure 1.4.

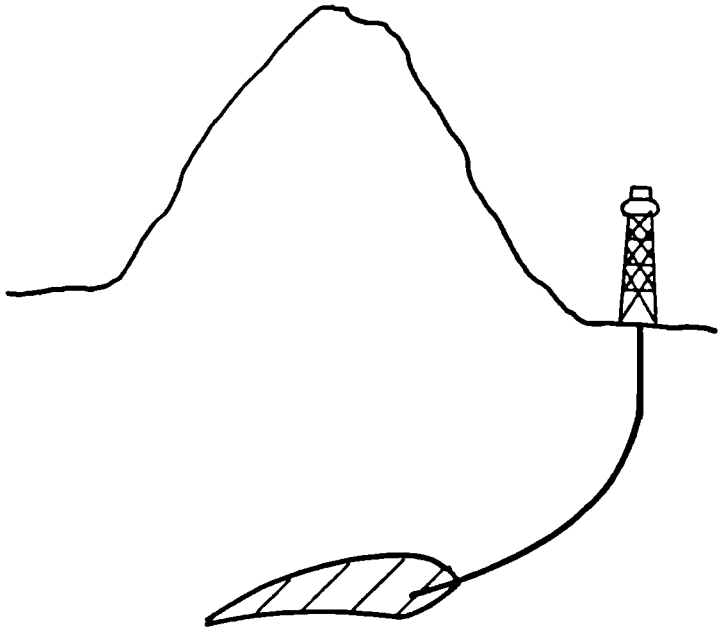
A number of factors dictate the frequency and position of casing strings. Two of the most important are the formation pore pressure and the fracture gradient. To understand the effect that these factors have on casing design it is necessary to appreciate the role of the drilling fluid.

The drilling fluid (or drilling mud) has a number of functions, one



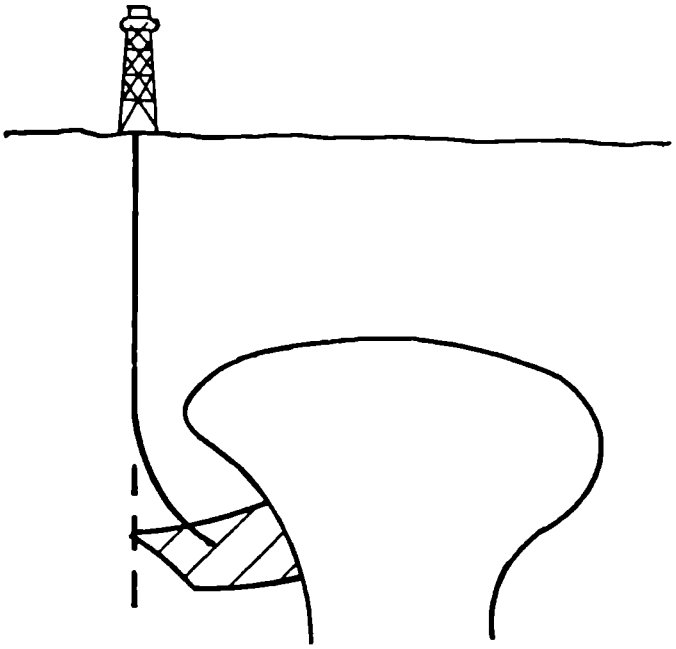
Offshore drilling.

Figure 1.1



Inaccessible locations.

(a)

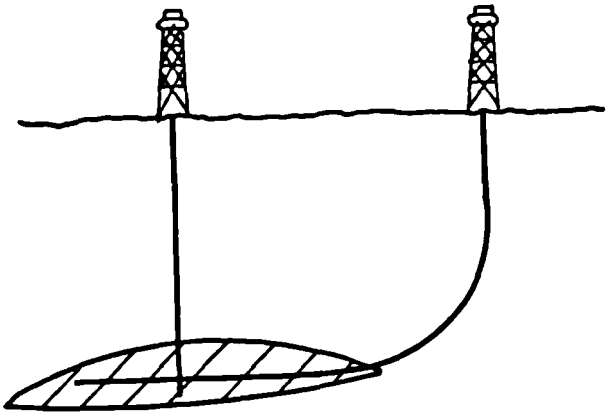


Salt dome drilling.

(b)

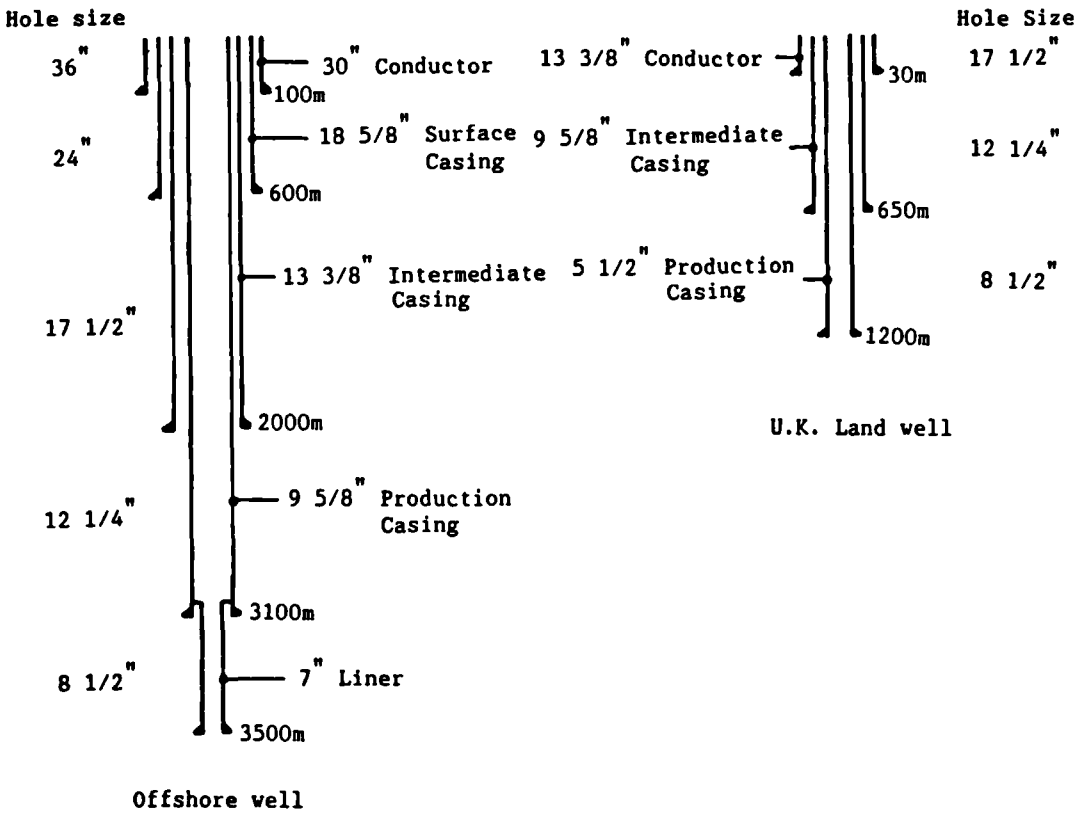
Directional drilling.

Figure 1.2



Increased length of hole open to reservoir for horizontal wells.

Figure 1.3



Typical vertical well profiles.

Figure 1.4

of which is to prevent 'kicks' or 'blow outs'. A 'kick' will occur when the pore fluid pressure is greater than the pressure exerted by the drilling fluid on the wellbore wall and the well receives an influx of the pore fluid. Influx from the formation to the well may simply contaminate the drilling fluid, in the case of water influx, or be potentially dangerous in the case of gas influx.

A potential hazard with the drilling fluid is loss of the fluid into the formation due to hydraulic fracture. Hydraulic fracture of the formation is brought about when the mud pressure is so great that it induces tensile stresses in the wellbore wall which eventually leads to a fracture which may extend well into the formation (see Figure 1.6a). Hydraulic fracture can result in expensive losses of fluid and time and can be potentially dangerous if a kick were to occur elsewhere in the wellbore, since the fracture would prevent any increase in mud pressure necessary to control the kick.

In addition to the above factors, the rate of penetration (ROP) of the drill bit can be affected by the mud pressure (e.g. Eckel[5]). It is believed that the mud exerts a hold down pressure on the cuttings which impedes the removal of the cuttings away from the drill bit. The greater the mud overbalance pressure (mud pressure less formation pore pressure) the greater the hold down pressure and hence the lower the ROP. Another factor maybe that the strength of the rock being drilled is increased by structural support applied by the overbalance, resulting in reduced drillability, but whatever the process involved, reduction of ROP with increased mud weight is commonly observed in the field.

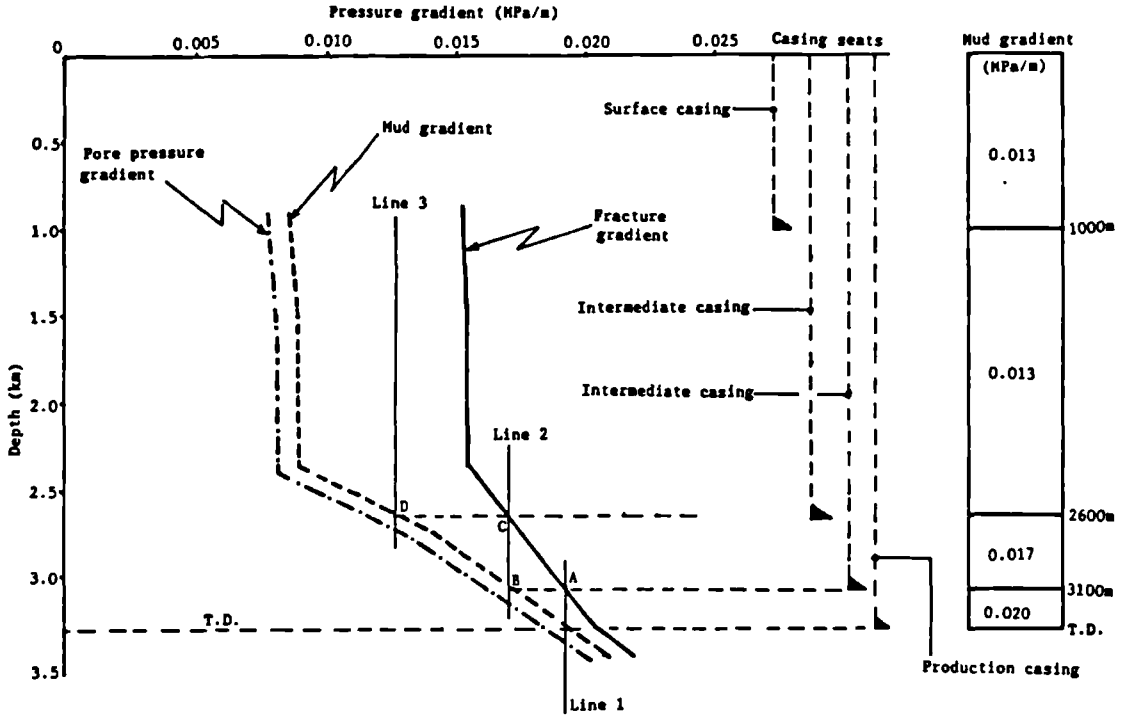
It can be seen that the three factors above will determine what

range of mud pressures are acceptable while drilling a certain section of the wellbore. The mud pressure must be kept greater that the formation pore pressure for kick prevention. The mud overbalance pressure at the hole bottom should be kept to a minimum to enhance ROP (the overbalance pressure is usually around 1.4 MPa (200 psi)). The mud density should not exceed the fracture gradient so as to prevent unintentional fracture.

The following example shows how casing design is made based on the above considerations (adapted from Rabia[6]).

Assume that Figure 1.5 represents the pore pressure gradient, the mud pressure gradient and the fracture gradient variations with depth for a wellbore. A pressure/fracture gradient is calculated by dividing the formation/fracture pressure at a certain position in the well by the depth at that position. The change in pore pressure gradient around 2400 m (8000 ft) in Figure 1.5 can be attributed to an overpressurised zone. It is assumed that a desirable mud pressure would be slightly in excess of the pore pressure.

For a certain density of drilling fluid, the mud pressure gradient will be constant all the way up the wellbore (neglecting pressure losses when circulating the mud - Moore[7]), so at certain stages in the drilling operation the mud weight must be changed to suit the formation conditions. Starting at the mud weight suitable at the bottom of the wellbore (TD), then the line of constant mud pressure gradient (line 1) intersects the fracture gradient at point A. In effect, this means that the mud weight required for drilling operations at TD would fracture the formation at A. Therefore a casing seat must be cemented in at, or below, point A to prevent fracture when the mud weight is increased.



Selection of casing seat points.

Figure 1.5 (adapted from Rabia[6])

Moving horizontally across from A to intersect at B gives the mud density (pressure gradient) suitable for drilling at B (line 2). Continuing this process up the wellbore will give all the casing points as shown in Figure 1.5.

1.2 TYPES OF WELLBORE INSTABILITY

In the context of this thesis wellbore instability is defined as any reaction of the rock surrounding the wellbore due to the introduction of the hole, and subsequent operations, that will have an adverse effect on drilling and casing costs. Wellbore instability can be categorized into two groups, namely Chemically induced instability and Mechanically induced instability, although in many instances occurrences of instability may be due to a combination of both.

1.2.1 Chemically Induced Instability

The most common chemically induced instabilities are water absorption in argillaceous formations (e.g. shales) and leaching of salt formations by the water phase in the drilling fluid. Water absorption in shales can lead to swelling and loss of strength in the formation which may cause hole size enlargement by caving in, or reduction of hole size if the rock remains intact. Leaching of salt formations may create large cavities around the wellbore and contaminate the drilling fluid to the extent that it must be completely replaced. These instabilities are tackled by changing the chemical composition of the drilling fluid (Kelly et al,[8] Chenevert,[9] Jokancsik and Grieve[10]). This research does not attempt to investigate chemically induced instabilities.

1.2.2 Mechanically Induced Instabilities

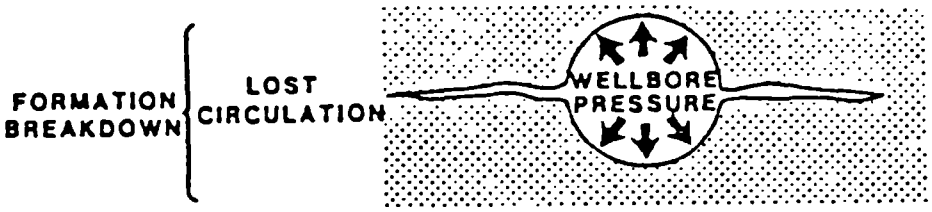
Bradley[11] categorized the three main types of stress-induced wellbore instabilities (Figure 1.6):

1. Hole-size reduction due to the plastic flow of rock into the wellbore (e.g. flowing shale or salt). Symptoms of this are repeated requirements of reaming the hole to get back to gauge and, in extreme conditions, stuck pipe, or stuck casing string.

2. Hole enlargement due to rock failing in a brittle manner and falling into the wellbore (e.g. sloughing shales). Problems resulting from the wellbore enlargement include fill on trips, poor directional control, increased costs of cementing materials and poor bonding of the cement with the wellbore wall.

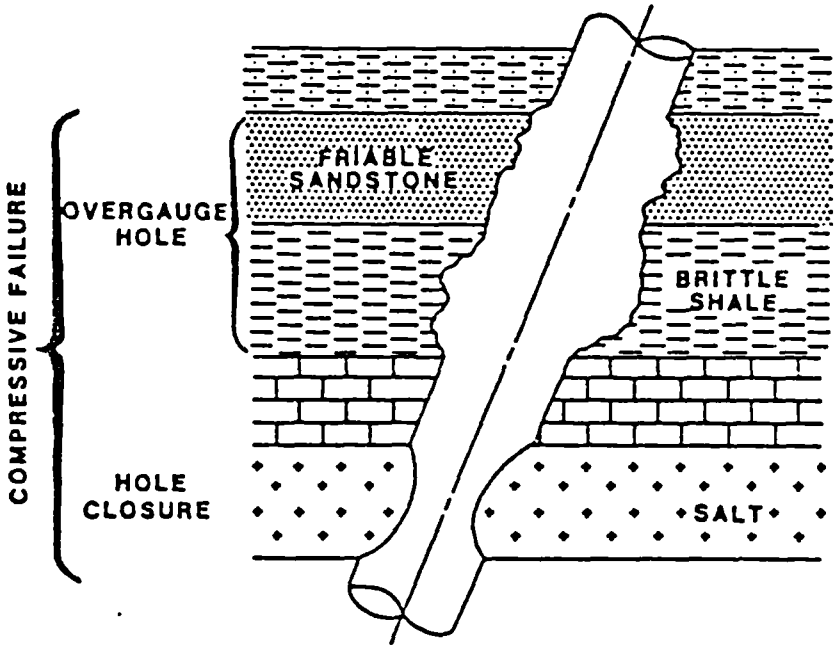
3. Unintentional fracturing of the wellbore due to tensile splitting of the rock from excessive mud pressure. Severe loss of drilling fluid to the formation from fracturing causes lost time as well as increased mud costs and may result in well control problems as discussed in Section 1.1.2.

In addition to the three instabilities mentioned above, hole erosion due to the flow of drilling fluid (Gaylord[12]) and wear of the wellbore wall due to rubbing of the drill string, often called 'key seating' (see Figure 1.7), could be included in the grouping of mechanically induced wellbore instabilities, but these are not considered in this research, and only the three instabilities related to stress redistribution around the wellbore are dealt with.



Tensile failure

(a)

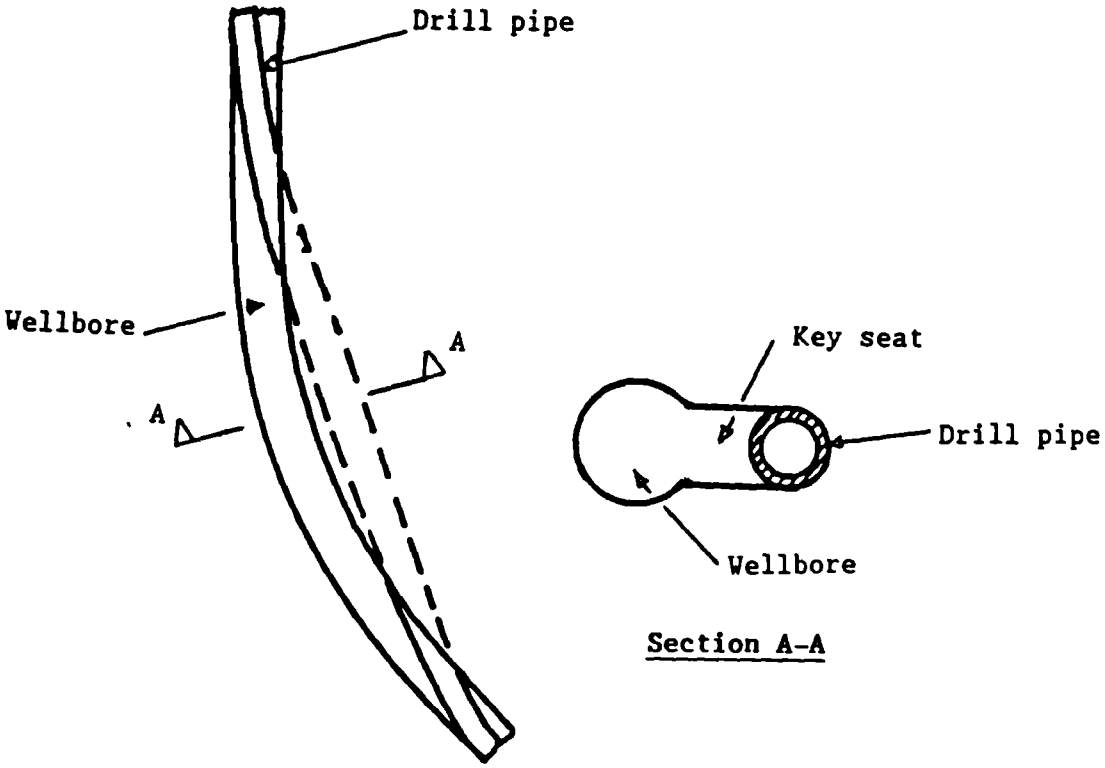


Compressive failure

(b)

Types of mechanical instability.

Figure 1.6



Key seating due to rubbing of drill string on wellbore wall.

Figure 1.7

1.3 CASE HISTORIES OF WELLBORE INSTABILITIES

A number of papers have been published on stress related wellbore instability which make reference to the high costs that these instabilities have cost the Petroleum Industry each year (e.g. Bradley[11]), but unfortunately few actually quote case histories and try and apply mechanical principles to back analyse them. The reason for this sparsity of published data is possibly due to the high degree of confidentiality Petroleum Companies attach to drilling information. Some of the few case histories that have been published are work by Kalof & Shennawy[13] (hole size reduction), Infante & Chenevert[14] (hole size reduction), Mauray & Sauzay[15] (hole size reduction and unintentional fracture) and Hottman et al[16] (hole size enlargement). Both Kalof & Shennawy and Infante & Chenevert refer to hole reduction with respect to plastic and viscous behaviour in salt formations and Infante & Chenevert attempt to apply theory to calculate mud weights required to alleviate these problems. Hottman et al back analyse wellbore instability to make assessments of the in-situ stress field. In addition, a number of papers use hole enlargement (breakout) as a method for determining the direction of the maximum and minimum horizontal, principal in-situ stresses (e.g. Klein & Barr[17]).

Apart from the lack of published data on field cases of wellbore instability, there are problems in applying mechanical theory to field cases for a number of reasons, most notably the lack of knowledge and understanding of the in-situ stress field. Attention is already being drawn to this problem, and there is currently a research drive in this area as exemplified by the International Symposium on Rock Stress and

Rock Stress Measurements, held in Stockholm in September 1986. Other problems in applying theory to the field are lack of information on material properties (since coring is particularly expensive in petroleum drilling operations, any core taken is usually restricted to the reservoir formation), variability of rock formations, inaccessibility to view the instabilities and the complexity of rock behaviour. The problem of how applicable a mechanical behaviour law is to real rock behaviour is one that is often overlooked in theoretically based research, and the importance of this aspect is made clear by the laboratory and numerical research carried out by Santarelli.[18] Other laboratory based research has been done on wellbore stability (e.g. Gay,[19] Darley[20]), but few researchers developed a numerical model that could accurately predict the recorded model wellbore response.

1.4 NUMERICAL MODELING OF WELLBORE STABILITY

In contrast to the scarcity of published data on case histories of wellbore instability there are numerous papers on the theoretical aspect. A great number of these publications attempt to explain the deformation process around the wellbore using plasticity in various forms and complexity (e.g. Horsrud et al,[21] Medlin & Masse,[22] Kojic & Cheatham[23]), but these models may prove of little use in quantitative prediction, if put to the test of predicting the behaviour of the relatively simple case of a hollow cylinder test, where applied loads and material properties can be accurately measured and monitored.

1.4.1 Factors Influencing Wellbore Stability Modelling

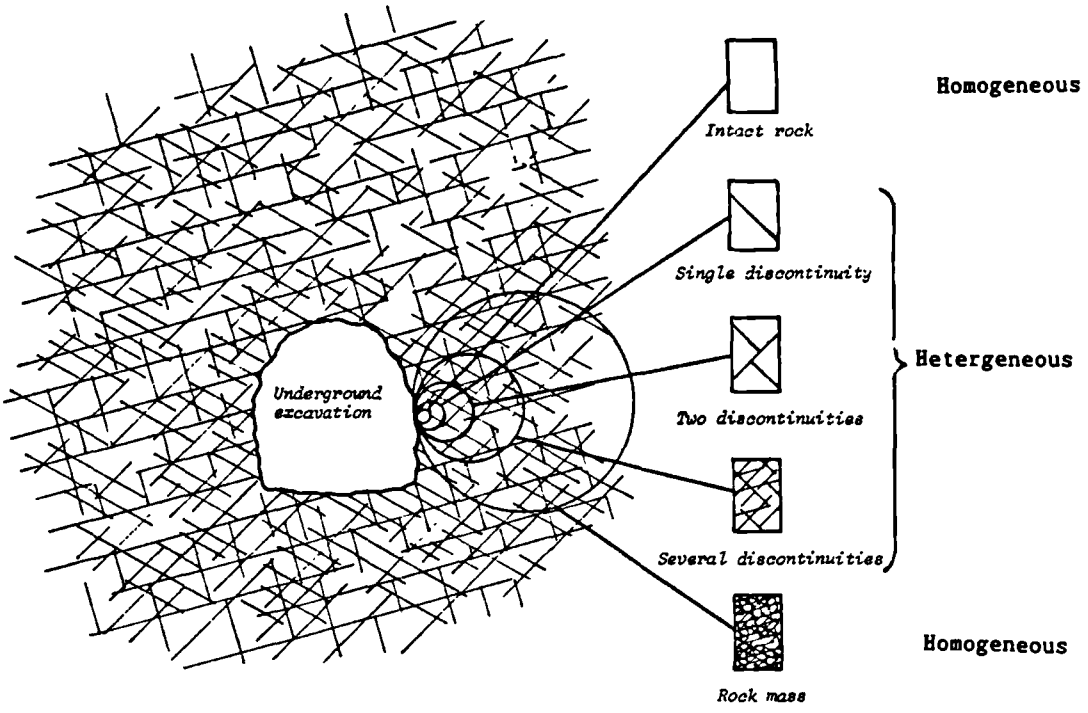
To decide on the suitability of a numerical model for analysing wellbore stability it is necessary to take a closer look at the parameters and conditions encountered during wellbore instability. A comprehensive list of the factors that may influence wellbore instability is given and discussed below.

A. Wellbore axis relative to the in-situ stress field

There is substantial evidence that in the horizontal plane the in-situ stress field is anisotropic (i.e. there exists two unequal horizontal principal stresses, e.g. Klein & Barr[17]), so even for vertical wells an axial symmetric condition could not apply. As already mentioned in Section 1.1.1, wells are often non-vertical, in which case simple plane strain (well axis parallel to a principal stress direction) is no longer applicable.

B. Material strength and deformation anisotropy

In sedimentary rocks both rock strength and elastic stress-strain response are likely to be transversely isotropic (i.e. the strength and elastic constants along the plane of bedding will differ to the properties perpendicular to the bedding). Material behaviour within the plane of bedding may also be anisotropic if the formation has been subjected to high shear stresses due to differences in the horizontal principal stress magnitudes.



Homogeneity scale dependence.

Figure 1.8 (adapted from Hoek and Brown[24])

C. Fracture Frequency

Figure 1.8 shows the classical scale dependence of material homogeneity relative to fracture frequency as given in a number of rock mechanics text books (e.g. Hoek and Brown[24]). On the smallest scale the rock is intact and can be considered as homogeneous. As the problem size increases the rock under consideration will contain discrete discontinuities and the rock mass can no longer be considered as homogeneous. On continuing to increase the problem size the individual behaviour of the intact rock and discontinuities can be combined into a homogeneous rock mass response, but in this case there would be problems in testing a sample large enough to be representative of the rock mass response. Thus, the applicability of homogeneity depends on the wellbore size relative to the natural fracture frequency.

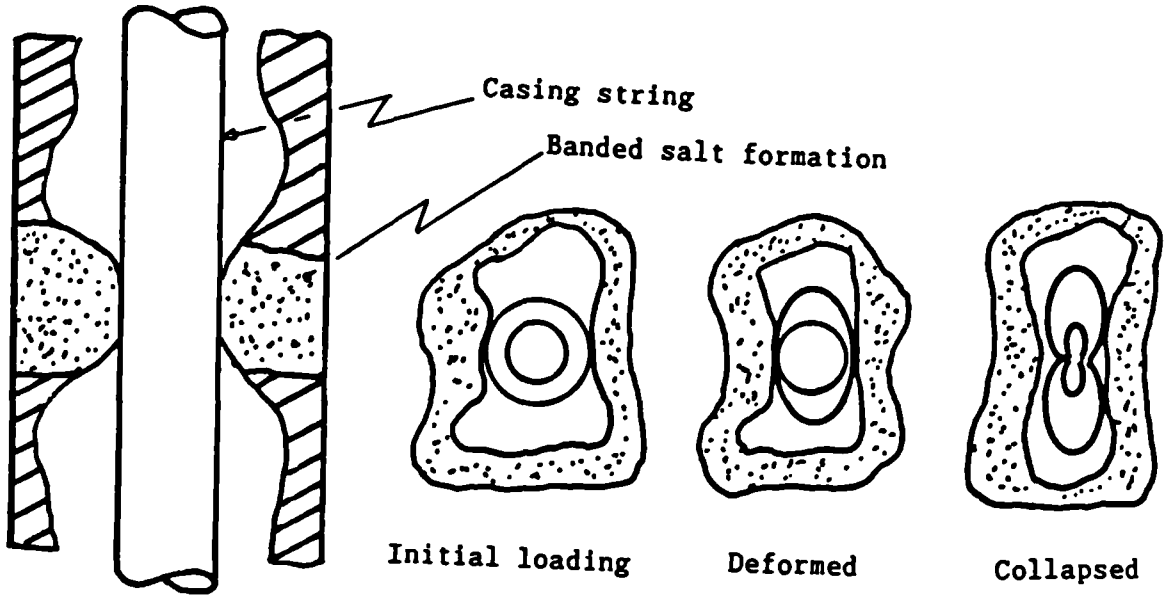
D. Viscous behaviour

Viscous behaviour can be considered as due to rock creep behaviour (e.g. salt creep) or due to pore pressure redistribution in low permeability rocks (e.g. shales and siltstones). Formations that do not exhibit significant creep response and are relatively permeable in nature, such as sandstones and limestones, may be considered as non-viscous. A number of papers make reference to hole closure as a result of creep in salt formations (e.g. Infante and Chenevert[14]), but time dependent response as a result of pore pressure redistribution is not so well documented. Before a well is drilled the pore fluid pressure within a formation will be uniform within the horizontal plane. Once the well has been drilled the stresses around the well are redistributed due to the removal of the support offered by the now excavated rock, which is

replaced by a drilling fluid pressure. In low permeable rocks viscous effects can materialize through two processes; (i) through fluid flow/migration due to an imbalance between the drilling fluid pressure and the formation pressure, and (ii) due to the pore fluid being unable to flow freely to adapt to any volume changes imposed on the rock elements due to the stress redistibution (Detournay et al[25]), or thermal expansion/contraction. Thus, pore pressure gradients will be set up around the wellbore, and due to the low permeability of the formation it will be some time before the pressure gradient approaches a steady state condition. The reaction to stresses imposed on an element of rock is made up of a pore pressure response and a rock matrix stress response. Thus, as the pore fluid migrates the rock matrix stresses will compensate for any changes in the pore fluid pressure. Such behaviour introduces the concept of short and long term stability similar to clay in soil mechanics (refer to any good text book on soil mechanics, e.g. Terzaghi and Peck[26]).

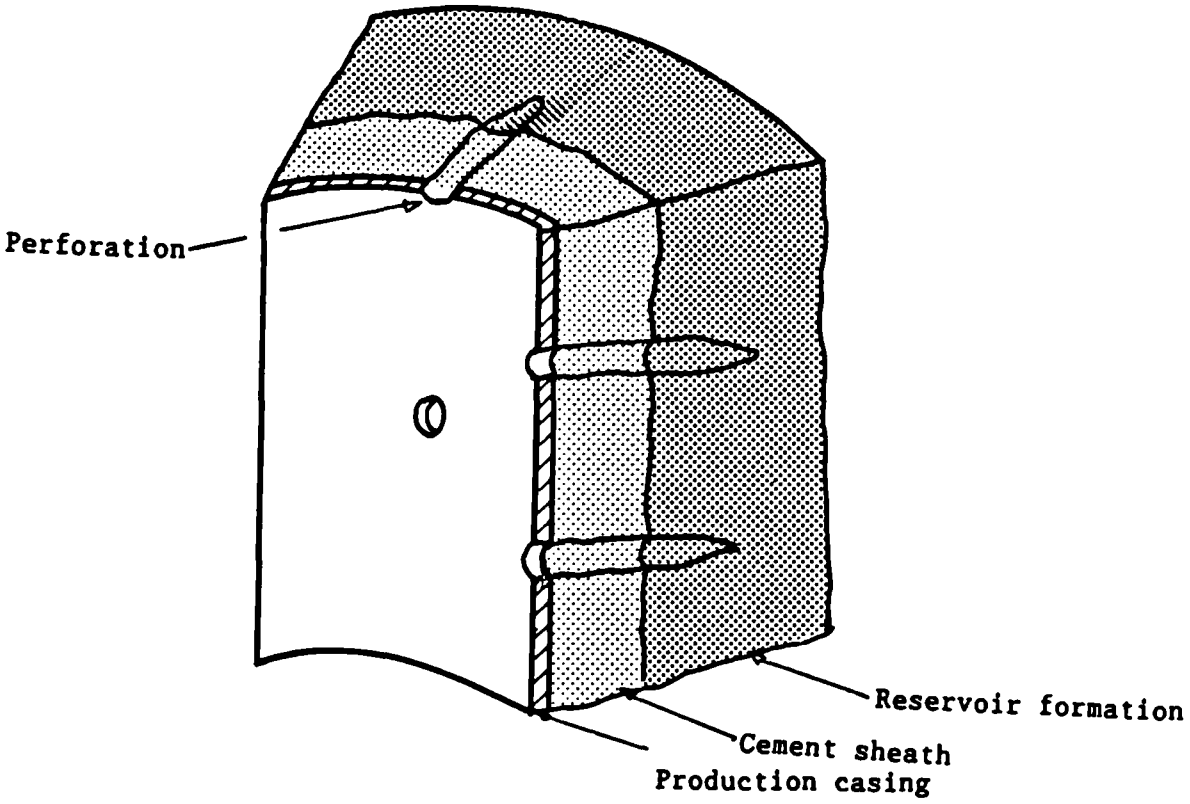
E. Rock-support interaction

Wellbore stability may not be confined to open hole conditions (i.e. before the hole is cased). Casing collapse can be assigned to wellbore instabilities through excessive or unequal loading from salt flow as displayed in Figure 1.9 (e.g. Clegg[27]). Also sand influx through perforations in the production casing (see Figure 1.10) can be attributed to stress redistribution around the well (e.g. Bratli & Risnes[28]). To analyse these forms of instability the interaction between the surrounding rock and the cemented casing must be taken into account.



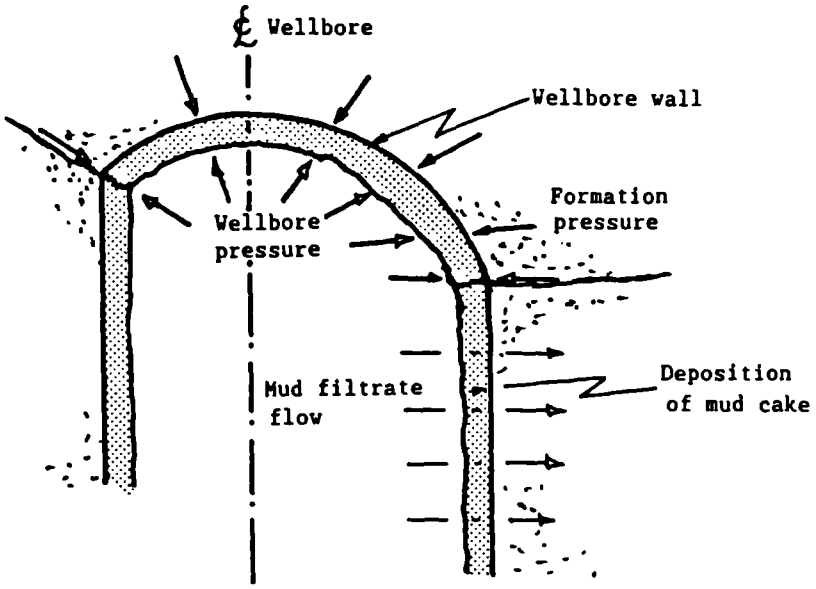
Casing Collapse.

Figure 1.9



Perforated production casing.

Figure 1.10



Formation of the mud cake.

Figure 1.11

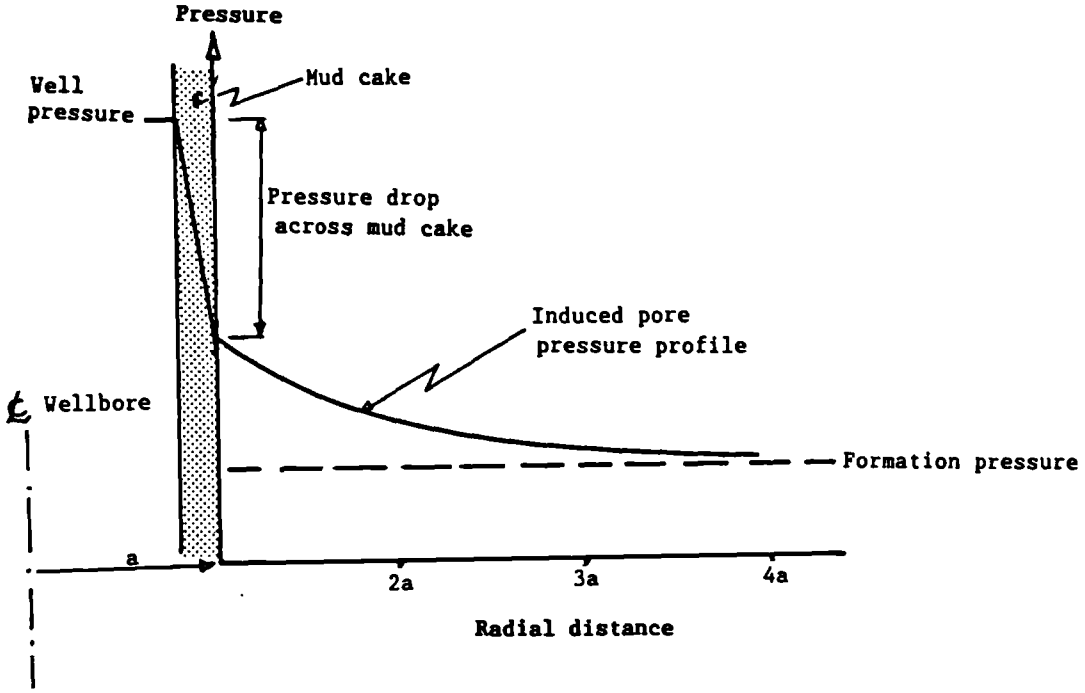


Figure 1.12 Radial fluid flow in overbalance conditions.

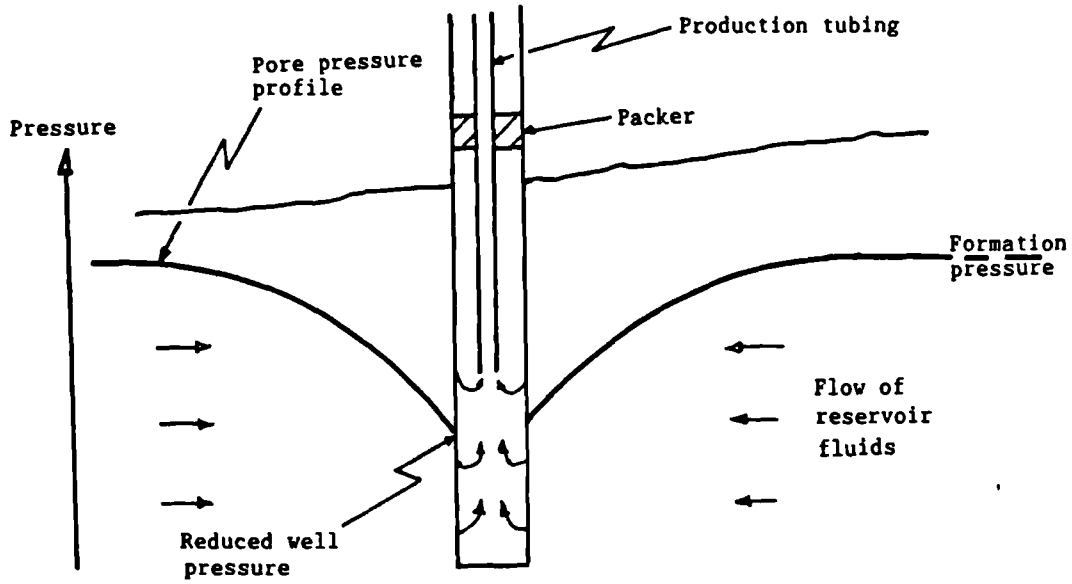
F. Flow of fluids from and to the formation

In general, the drilling fluid used will contain solids that filter out in high permeability materials to form a mud cake (see Figure 1.11). The mud cake created will be of lower permeability than the rock, which will result in a pressure loss across the mud cake. The resulting pressure drop applies a mechanical support to the wellbore wall provided the mud pressure remains greater than the pore fluid pressure. Depending on the filter cake characteristics relative to the formation permeability, fluid loss into the formation can take place, setting up a pore pressure gradient around the wellbore (see Figure 1.12).

In addition to mud fluid losses to the formation, the reverse can happen when tripping the drill string out of the hole causing swabbing pressures which create an underbalance pressure, although care is usually taken to minimise swabbing effects by pulling the drill string out slowly. A more common occurrence of pore fluid flow in open holes is during open hole drill stem tests (DST's). This takes place when the last casing set is immediately above the reservoir formation and the well pressure is reduced to test the production of the well before the production casing is set (see Figure 1.13). Land wells are often tested in open hole conditions.

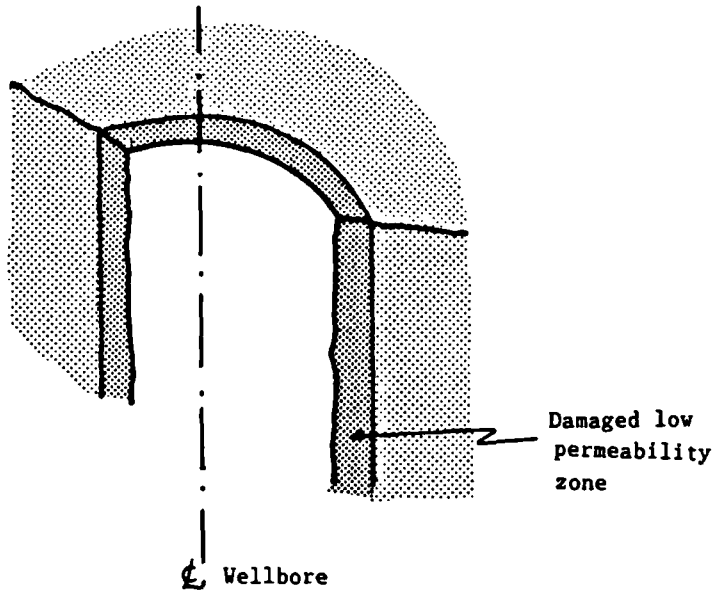
G. Formation damage

Formation damage is a term used in the Petroleum Industry to describe the adverse effects that drilling and completion operations can have on the flow of hydrocarbons into the well. A common occurrence of formation damage will be the reduction of permeability of the rock



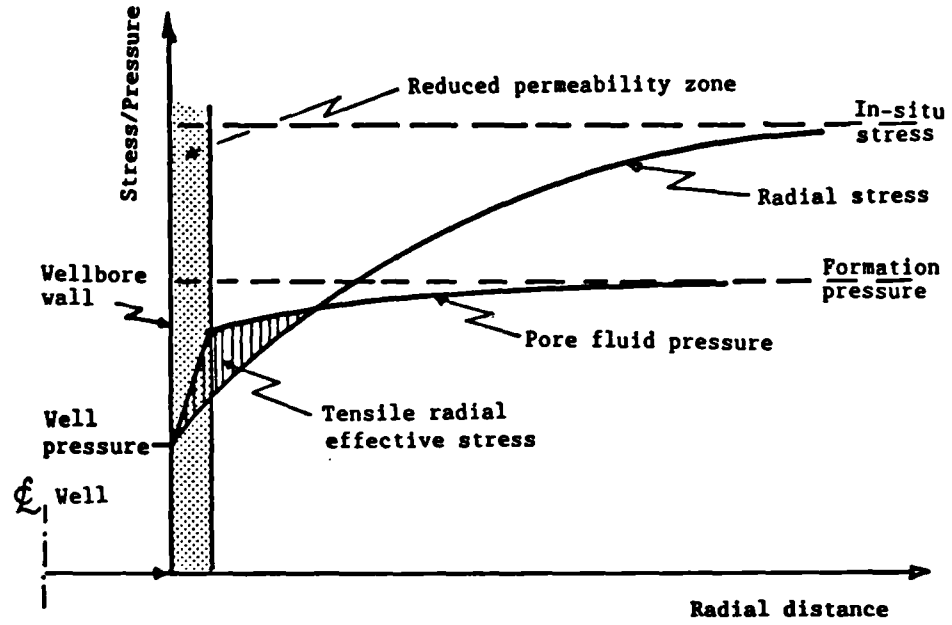
Pore pressure profile during DST's.

Figure 1.13



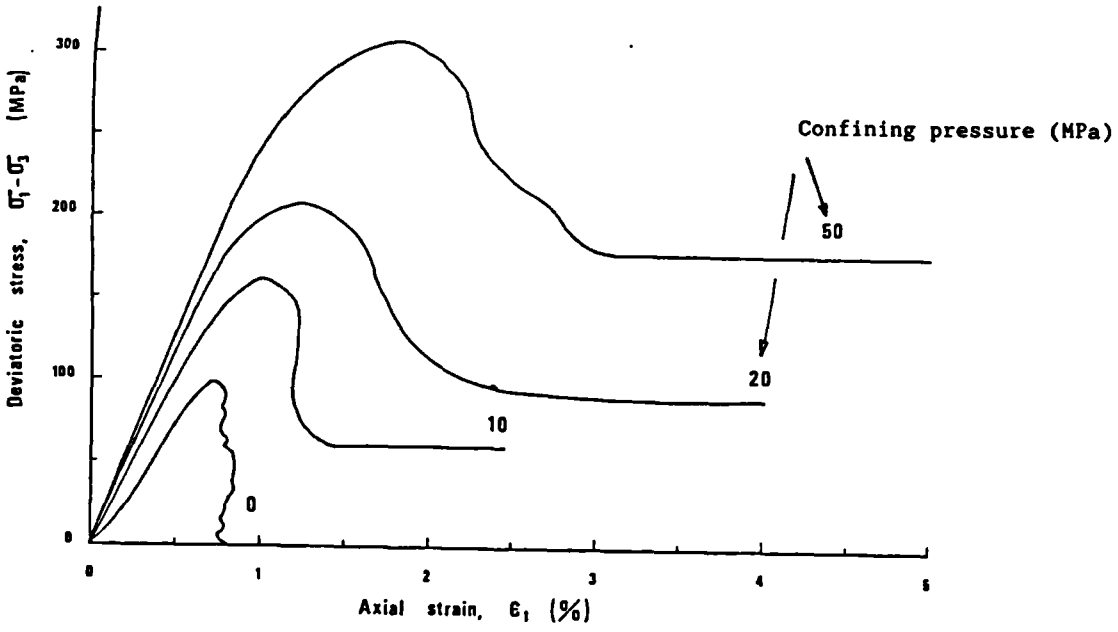
Damaged zone around wellbore due to drilling fluid invasion.

Figure 1.14



Reduced radial effective stress due to formation damage.

Figure 1.15



Triaxial tests carried out on Sandstone.

Figure 1.16 (after Santarelli[18])

immediately surrounding the wellbore due to invasion of the mud filtrate into the formation (see Figure 1.14). In addition to the production problems that this may cause, the reduction of permeability can reduce the wellbore stability. An example of the type of problem that may occur in open hole drill stem testing is shown in Figure 1.15. Here the effective radial stress near the wellbore has been reduced due to the high pore pressure gradients set up in the damaged zone. In certain conditions the pore pressure may be high enough to induce tensile effective radial stresses. Paslay and Cheatham[29] developed a numerical treatment for the case of formation damage, but only considered the possibility of compressive shear failure.

H. Wellbore pressures

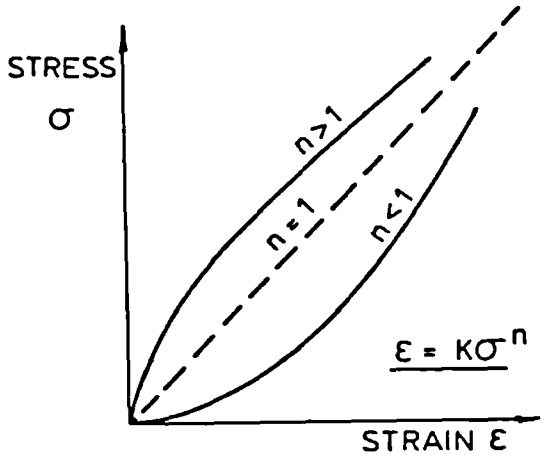
As already stated in Section 1.1.2 the present day strategy for well pressures is to keep it slightly above the formation pore pressure to prevent kicks and blow outs. The overbalance pressure exerted on the formation will vary depending on whether the drilling mud is circulating or not. When the drilling fluid is static the overbalance can be determined from the difference between the hydrostatic mud pressure and the formation pore fluid pressure, but during drilling the mud is circulating and the down hole pressures will be greater than the mud hydrostatic pressure in order to overcome the drilling fluid viscous forces. In addition, the well pressure will vary due to swab and surge pressures during tripping (Klein and McLean[30]). Any occurrence of instabilites may be influenced by these variations in well pressures.

I. Rock material behaviour

Even for permeable, isotropic, homogeneous rock formations the material's response to loading is far from simple. Often the response to loading is neither linear elastic nor elastic-perfectly plastic. Typical curves for Sandstones tested at Imperial College (Santarelli[18]) are shown in Figure 1.16. Tests carried out in uniaxial compression and at low confining pressures exhibit an increase in stiffness at low deviatoric stresses (Morita and Gray[31]). The slope of the linear portion of the curve tends to increase with confining pressure (King,[32] Kulhawy[33]). Before peak strength is reached the material appears to and undergo strain hardening, the greater the confinement the more marked the hardening portion. Upon reaching peak strength the sample loses strength and undergoes a portion of strain softening, the greater the confinement the less rapid the drop in strength with deformation. Eventually the sample reaches a residual strength and continues to deform without loss or gain in strength.

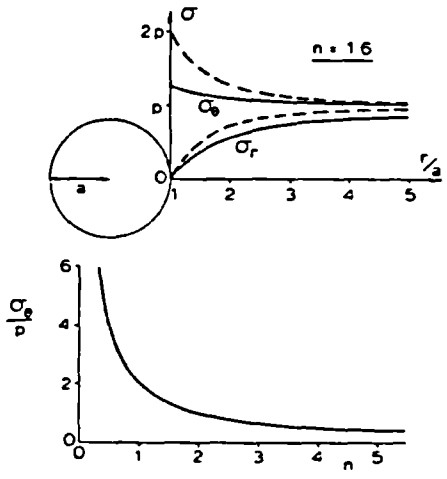
The importance of plasticity in relation to stress redistribution was noted by Westergaard[34] in 1940, where he proposed an elastic-perfectly plastic solution. Since then solutions have been proposed for elastic strain hardening models (although not specifically related to Rock Mechanics problems, e.g. Owen and Hinton[35]), and elastic strain softening models (e.g. Brown and Bray[36]). However, there are few papers that consider nonlinear elastic response and its importance with respect to analysis of circular openings in rock. There are a few notable exceptions to this and they are mentioned below.

1. Bray[37] assumes the stiffness to be a function of the deviator stress as shown in Figure 1.17a. This relationship effectively allows for the



Non-linear elasticity

(a)



Non-linear elasticity: circular excavation in hydrostatic stress field

(b)

Non linear elastic modelling of a circular excavation in rock.

Figure 1.17 (after Bray[37])

micro crack closure ('bedding in') portion of the stress-strain curve. The resultant effect is a considerable increase in the hoop stress (Figure 1.17b).

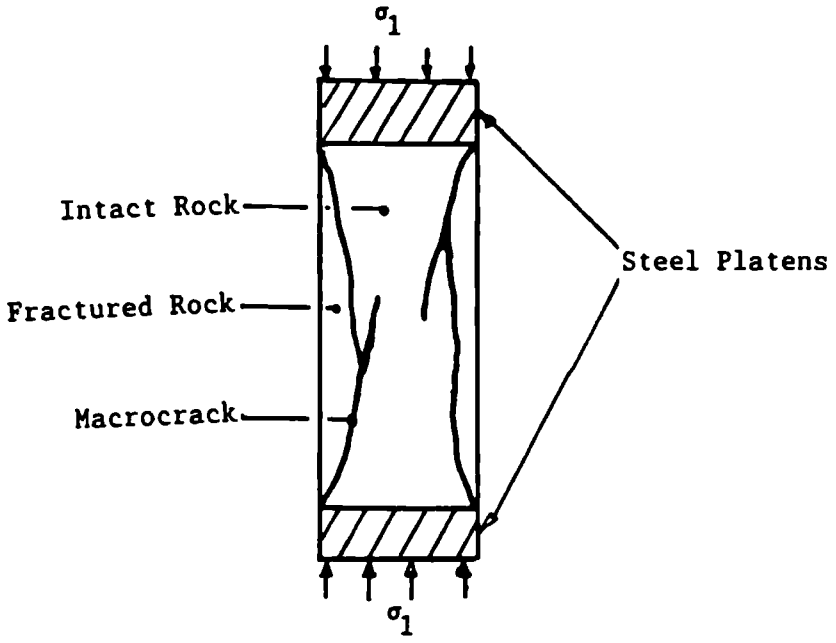
2. Probably the most complex and advanced nonlinear elastic behaviour model to be published is given by Morita & Gray.[31] The model is not discussed here since it is covered in detail in Section 1.5.

3. Finally work done by Santarelli[18] could prove to be a break through in changing researchers approach to material behaviour modelling. Again this model is discussed in more detail in Section 1.5.

J. Strain softening behaviour

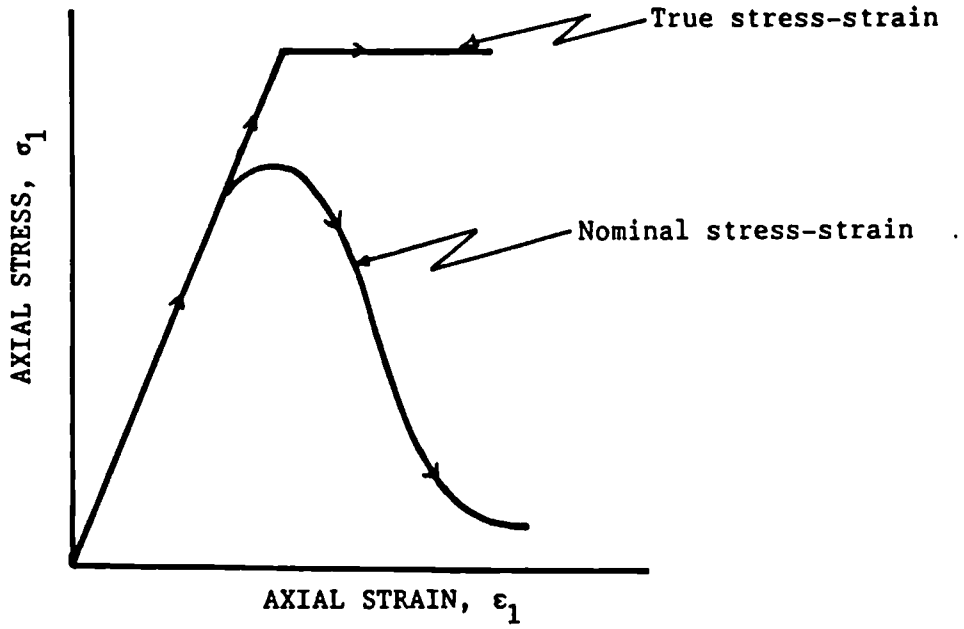
A separate section has been devoted to strain softening since it is one of the most controversial of rock material behaviour characteristics and is still as yet unresolved.

A number of researchers believe that strain softening behaviour is not a real material property as represented in many triaxial test data carried out on 'stiff' or servo-controlled testing rigs. Undoubtedly materials lose strength when subjected to continued plastic deformation, but the question posed is whether current methods of determining the post peak behaviour of rocks is representative of the true rock properties. Read and Hegemier[38] give convincing arguments to suggest that the present day approach to strain softening is incorrect. During uniaxial testing (and to a lesser extent triaxial testing) the inhomogeneous and anisotropic nature of the rock on the micro level induces local tensile stresses which produce microcracks that grow and



Reduction of load bearing area bearing area after fracture.

Figure 1.18 (adapted from Read & Hemegier[38])



'True' and nominal uniaxial stress-strain curves.

Figure 1.19 (adapted from Read & Hemegier[38])

become aligned with the loading axis. As loading increases so does the density of microcracks leading to a vertically aligned macrocrack which results in gross slabbing of the material from the specimens lateral surfaces. Due to lateral restraint from end effects, slabbing is concentrated in the central portion of the sample (see Figure 1.18). The gross slabbing of the sample continuously reduces the cross-sectional area of the remaining intact material, and to find the true stress at some cross-section, the current (true) area of the intact material should be used, instead of the original area as used in standard rock testing interpretation. Read and Hemegier conclude that the falling branch of the stress-strain curve is actually not a material property, but the result of the propagation of a macroscopic fracture plane through the specimen. Beyond the peak of the stress-strain curve the specimens were in the process of splitting and could not be treated as homogeneous continua. Therefore, what appears to be a strain-softening behaviour may only reflect the reduction in diameter of the load bearing rock. Read and Hegemier suggest that materials that are believed to be undergoing strain softening may in fact be behaving in an elastic-perfectly plastic manner (see Figure 1.19).

Pariseau[39] carried out finite element modelling of triaxial testing assuming a no slip condition between the end platens and the rock sample. He assumed the rock behaviour could be characterized by a sudden drop in elastic modulus on reaching a critical stress state, defined by a yield function. Using the material behaviour and boundary conditions described, he was able to give qualitative predictions of the change in failure mechanisms and load-displacement response, with change in sample length to diameter ratios. A conclusion of the work was that the rock may be of greater strength than given by triaxial testing due to the

reduction in the diameter of the load bearing rock.

A further problem when applying numerical treatment to strain softening is that it is normally assumed that the material is a continuum, which is not the case in post peak conditions in uniaxial and triaxial testing where the sample becomes a combination of intact rock and discrete macroscopic fractures. It could be argued that provided induced fractures are small compared with the structure and rock mass being analysed the material may still be considered to be a continuum (as discussed in Section 1.4.1, Item C). However, Klein and Barr[17] give examples of rock chips from wellbore breakout which are 1/2" thick by 5" long from an 8 1/2" well, so it would be incorrect to treat such a case as a continuum.

K. Thermal effects

The temperature gradient with depth may vary considerably from region to region, but typically for North Sea drilling the reservoir temperatures at around 3000 m (10000 ft) depth may be around 150°C. Although the drilling mud will warm up due to heating by the formation, in general at the depths of interest to the Petroleum Industry the drilling fluid will be cooler than the surrounding formation. A cooling of the formation around the wellbore should reduce the compressive hoop stresses and thus reduce the wells susceptibility to compressive shear failure. Further up the wellbore the drilling fluid, having been heated at the bottom of the well, may be heating up the formation and having the reverse effect.

1.4.2 Requirements of Numerical Modelling

An ideal numerical model would take account, both qualitatively and quantitatively, of all the imposed boundary conditions and the relavant material behaviour. However, such a numerical analysis would be extremely complex and far in advance of present day modelling of circular openings in rock. Also, the accuracy of any numerical model will be limited by the quality of the input parameters, which can be extremely uncertain in cases such as the in-situ stress field. Another limitation to development of numerical models is the ability to validate them under laboratory controlled conditions. Often the conditions modelled numerically cannot be simulated satisfactorily in the laboratory, so that it is not possible to determine whether the complexity of a model is justified by its increased accuracy. However, an advanced numerical model based on sound mechanical theory, may show the relative importance of various parameters on stability, but all numerical modelling should really be considered as hypotheses until proven under laboratory controlled conditions.

In addition to the above considerations a numerical model should be developed in relation to the area of the well under consideration. For example, it is pointless to incorporate viscous effects when analysing permeable reservoir formations of sandstone or limestone. In salt formations it is believed that hydrostatic stress conditions are present before the well is drilled (Infante and Chenevert[14]), since salt creep over long periods of time will tend to dissipate any deviatoric stresses that may have been imposed. In such conditions the problem can be greatly simplified by considering conditions to comply with axial symmetry. In shale formations there is no point in considering formation

damage, since no significant filtrate invasion is likely to take place.

Finally, consideration should be given to the relative importance of the parameters involved. If, for example, strength anisotropy has little bearing on predictions relative to, say, nonlinear elasticity, then the direction of any advanced numerical model should be towards better elastic modelling rather than anisotropic effects. The various parameters should first be assessed using simple analytical techniques where possible, and the numerical model tackled according to the relative impact the parameters have on the stress distribution and failure mechanism. Naturally some parameters (e.g. viscous effects created by pore fluid migration) can only be assessed by complex numerical models.

1.4.3 Controllable parameters

An important consideration when developing such a numerical model are the parameters that can be controlled by the operator, either during drilling and completion operations (e.g. mud weight and tripping speeds) or when planning the development of a field (e.g. well directions and casing setting depths). It is important for those financing such research to believe that actions can be taken on the basis of future numerical and laboratory studies which may lead to a reduction of the occurrences of instability, or that advantage can be taken of prior knowledge of a material's impending instability. If the operator has no control over the parameters that influence a well's resistance to instability, then the exercise becomes of academic interest only. The following are areas where planning and operational decisions could be influenced by wellbore stability analyses.

A. Naturally, in-situ stress conditions cannot be controlled, but the well's direction relative to these stresses could be controlled in certain circumstances. Despite this being a common consideration in Mining and Civil Engineering tunnel design, little note of it is taken in the Petroleum Industry. Notable exceptions to this are Bradley[40] and Maury & Sauzay,[15] who consider a well's direction relative to the disturbed stress around salt domes, and Bradley[41] who considers change in stress concentration with change in well azimuth in an 'undisturbed' stress field.

B. It may prove possible and desirable to control the temperature effects by lowering the temperature of the drilling fluid before it is circulated down the drill string in order to reduce the compressive hoop stresses. Again Mauray and Sauzay make reference to a well drilled with the drilling fluid being cooled at the well head. Unfortunately they make no firm assessment as to the success, or otherwise of the technique.

C. There may be some flexibility in the mud weight used, although due to the reduction in ROP with increase in overbalance (see Section 1.1.2) there would have to be convincing increases in wellbore stability before operators would make significant increases in mud weight. An example of this is given by Bradley[41] who sets down a procedure for selecting mud weights to prevent wellbore instability, based on linear elasticity.

D. Operators would like to trip the drill string in and out of the well as quickly as possible due to the high time related costs involved. Tripping speeds are already curtailed to prevent formation fracture during tripping in, and formation fluid influx during tripping out. A

wellbore stability analysis, coupled with a swab/surge prediction model, could provide the drilling operation with a safe range of tripping speeds.

E. Stability of a well during open hole drill stem testing may be a source of concern for the operator (e.g. Klein and McLean[30]) and a wellbore stability analysis could provide a safe range of well pressures and rate of draw down.

F. A design consideration that could be influenced by prior knowledge of wellbore instability are the number and frequency of casing settings. The prediction of formation fracture has been an important consideration of the Petroleum Industry for many years, but present methods of prediction (e.g. Eaton,[42] Daines[43]) are at best semi-empirical, since unsubstantiated and quite dubious assumptions are made in relation to the in-situ stress state. Better predictions and understanding of fracture relative to in-situ stress conditions, formation type and well deviation and direction could lead to more efficient and cost effective casing designs. However, the key to better prediction of fracture initiation is in prior knowledge of the in-situ stresses, rather than wellbore stability modelling.

G. Drilling through salt formations can be a hazardous condition in some areas (e.g. Unger and Howard[44]). Salt creep can lead to continual reaming and in the worst cases stuck drill string. A mud weight sufficient to prevent hole closure would have to be close to the overburden stress (approximately 0.023 MPa/m (1 psi/ft) - Infante and Chenevert[14]). Such a mud weight would be so great that it is likely to cause hydraulic fracture further up the wellbore, or fracture any banded

layers within the salt formation. In such cases a wellbore stability analysis able to predict rates of closure with respect to the mud weight could provide operators with safe drill times before it became necessary to ream back up the hole. In such cases it obviously becomes important to quantify response with time.

1.5 CURRENT WELLBORE STABILITY MODELS

As mentioned in Section 1.3 there is an abundance of numerical models developed for analysing stresses around circular openings. Brown et al[49] carried out an extensive review of models used in previous analyses of rock-support interaction around tunnels, an analogous problem to the wellbore response to drilling. The review concentrated on the deficiencies of the models with respect to strength criterion, plastic behaviour and applied loading conditions. The main criticisms of past analyses were that few models took account of strain softening, and those that did, suffered from poor predictions of plastic volumetric strains, and secondly, that models were invariably considered to be under plane strain conditions and often in a hydrostatic stress field.

Below is a selected list of the more notable numerical models to be published and an assessment of their suitability.

1. Bradley[11] presents a set of equations for the stresses around a circular opening using equations that he attributes to Fairhurst.[45] Both these solutions allow for the 'complete plane strain' conditions as defined by Brady and Bray,[46] rather than simply the plane strain condition. This solution allows for the general case of the well not being parallel to a principal stress direction, i.e. deviated wells. The

equations (presented in Section 2.2, Chapter 2) are for simple linear elasticity only, and do not consider plastic or nonlinear elastic behaviour, so can only be considered as a qualitative rather than quantitative numerical tool. In addition, the solutions take no account of temperature or pore pressure gradients, mud cake effectiveness, material anisotropy or time effects. Despite the limitations of the solutions, they are a useful base from which to expand, and as discussed in Chapter 2, they give an assessment of the relative stability of wells with direction and deviation. Bradleys publication made considerable progress in drawing the attention of the Petroleum Industry to the possibility of mechanical instability.

2. Paslay and Cheatham[29] present a set of closed form equations based on linear elasticity to describe the stress state around a circular opening in plane strain, axisymmetric conditions, with radial fluid flow into the wellbore during draw down conditions. The authors extend the analysis to allow for a region of reduced permeability surrounding the wellbore due to mud filtrate invasion into the formation during drilling operations. The equations presented are useful in determining the influence of fluid flow on instability, although the authors fail to consider the possibility of tensile effective radial stresses during rapid draw down (as dealt with in Section 2.9, Chapter 2). Again, due to the idealised behaviour, the model cannot be regarded as quantitative in its predictions. On its own the model is restricted to an isotropic stress state, and takes no account of temperature effects.

3. Deily and Owens[47] superimpose a steady state radial flow condition of the type given above, with the solution for stress redistribution given by the Kirsch equations.[48] In addition, they introduce the concept of a

mud cake efficiency as discussed in more detail in Section 2.4, Chapter 2. The model is useful in considering the effect of mud cake on stress distribution, and is an improvement on Paslay and Cheatham's model in that an anisotropic in-situ stress field is allowed, although still only in plane strain. As before the model suffers from idealised material behaviour and could not be considered quantitative.

4. Brown et al[49] present an elasto-plastic (strain softening) model for analysis of rock-support interaction in circular underground tunnels. The model is for plane strain axisymmetric loading conditions. Brown and Bray[36] also published an extended version of this model to incorporate pore pressure gradients in the case of fluid flow, and allowed for variation of permeability in the broken or plastic zone. The solution is limited by its idealised boundary conditions to a vertical well with an isotropic horizontal stress field, but attempts to better model the rock material behaviour. However, the inclusion of strain softening behaviour is a controversial point as noted in Section 1.3, and, as discussed later in Section 5.4.3.1, Chapter 5, what at first sight seems a realistic model for strain softening behaviour, becomes unrealistic when applied to analysis of circular openings due to the stress path followed.

5. Infante and Chenevert[14] apply an elasto-plastic model to the analysis of hole closure in salt formations. Although the model is only for the axisymmetric wellbore, this is probably sufficient in salt formations, since the in-situ stress field is likely to be close to hydrostatic. However, although creep is discussed, the model makes no attempt at modeling a viscous response, and deformation is considered instantaneous.

6. Aadnoy and Chenevert[50] use a simple linear elastic model of the type presented by Bradley[11] and extend the solution to allow for strength anisotropy when considering well deviation with respect to bedding planes in shales. Although the model does not make use of real stress-strain behaviour, and pore pressure and temperature gradients, it is a useful qualitative tool in providing insight into the effect of anisotropy on wellbore stability.

7. Perkins and Gonzalez[51] are unique in their application of temperature effects to the study of stresses around a wellbore. Maury and Sauzay[15] pay some attention to temperature effects, but not nearly to the same analytical extent that Perkins and Gonzalez approach the problem. However, the model they present was concerned with fracture extension in a reservoir rather than near wellbore stresses and consequently the wellbore radius was considered to be zero.

8. Morita and Gray[31] attempt to apply real material stress-strain behaviour to the prediction of stresses around the axisymmetric wellbore. The material behaviour quoted is possibly the most advanced yet published. However, the model uses the FEM analysis technique, and as such is not open to scrutiny. The model allows for bedding in, pressure dependent elasticity, anisotropy with respect to bedding planes and a pre-peak plastic portion. The analysis published was for the case of tensile fracturing of hollow cylinders. Unfortunately, the fracture initiation prediction for the model only differs by around 17% from simple elastic analysis, which cannot be considered as notable in rock mechanics terms. If the model had been used to estimate compressive shear failure the authors may have discovered that it had far reaching implications on predictions. Although the published work only considered

isotropic boundary conditions, since it is an FEM analysis, it must be assumed that the case of unequal principal stresses is within its capabilities. The only criticism that could be made of the material modelling is that it may be too complex, given that laboratory validation of the model predictions was not carried out. It is not easy to establish the limitations of such a model, since, to the reader at least, the analysis is carried out by a 'black box', in the form of a FEM analysis. However, it is likely that the program only worked in plane strain (i.e. vertical wells only), and no account of temperature and pore pressure gradients was possible.

9. Santarelli and Brown[52] present a numerical model that also attempts to use more appropriate material behaviour modelling for a better predictive model. Santarelli[18] carried out a series of triaxial tests on sandstone and noted the material's tendency to increase in stiffness with increase in confining pressure. When the same material was tested in hollow cylinders the load-displacement curve and failure loads could not be explained by linear elasticity without the introduction of commonly used, unquantifiable 'fudge factors' such as size effects. When allowance was made for 'real' material behaviour (pressure dependent elasticity and pre-peak plasticity) the model was able to predict the load-displacement curve and shear failure initiation to within 15% for the Carboniferous sandstone, and as such can be regarded as one of the very few models that is quantitative in its predictions. The model behaviour is not as advanced as that published by Morita and Gray, but has the advantage of laboratory support, and due to its simplicity can be used in closed form solution. Limitations of the model are that it only deals with the axisymmetric wellbore and does not attempt to allow for pore pressure or temperature gradients.

1.6 CONCLUDING REMARKS

Mechanical wellbore instability can cost the Petroleum Industry large sums of money each year through lost time, lost equipment down hole, and lost wells, although the extent of the sums involved have either not been properly quantified, or more likely not published.

Treatment of mechanical wellbore instability has been restricted to a number of closed form solutions which concentrate on using simple elastic, or elasto-plastic behaviour. Two published solutions (Morita and Gray,[31] and Santarelli[18]) attempt to provide better quantitative models by allowing for more realistic material behaviour modelling. However, there are still many problems in quantifying the important parameters such as the in-situ stress field.

Apart from field work done by Elf (Maury and Sauzay[15]) and analytical modelling by Perkins and Gonzalez[51] little or no attempt has been made to investigate the importance of temperature gradients on wellbore stability.

A few models (e.g. Infante and Chenevert[14]) have looked at viscous behaviour with respect to creep in salt formations, but little or no modelling work has been published on viscous behaviour due to pore fluid migration in low permeability formations.

Where ever possible, numerical models should be compared with model wellbore behaviour (e.g. hollow cylinder tests) to test their quantitative as well as qualitative predictions under controlled conditions. A numerical model that is capable of allowing for all the

factors involved in mechanical wellbore stability, as set out in Section 1.4.1, is unreasonable at this stage, and unjustified until laboratory capabilities are improved, to test the validity of advanced numerical models, and better knowledge of the input parameters (e.g. in-situ stresses) can be gained.

1.7 CONTENT OF THE THESIS

The following chapters consider two different aspects of numerical modelling, namely a qualitative approach and a quantitative approach. The purpose of the research was to develop a nonlinear computer code for analysis of wellbore stability. However, it is unreasonable to include in such a computer code the effect of all the important physical conditions such as temperature gradients, viscous behaviour, stress induced pore pressures, etc. Thus, in Chapter 2, closed form solutions based on linear elasticity are used to assess the influence on wellbore stability of many of the parameters discussed in this chapter. Although linear behaviour will not provide quantitative predictions, it still has an important role in developing understanding. Therefore, a large portion of the work effort was directed to presenting, and in certain cases developing these solutions and assessing their implications.

The second part of the thesis concentrates on the development of a nonlinear wellbore stability model using the finite element method (FEM). The model concentrates on attempting to use more realistic rock behaviour with particular reference to plasticity and pressure dependent elasticity (Santarelli and Brown[51]). However, the numerical model does not consider a wide variety of physical conditions. No attempt is made

to account for temperature gradients. Pore pressure gradients are not considered, either as a result of fluid flow, or as a result of applied loading in low permeable formations. However, the process by which steady state fluid flow can be incorporated into the computer code is discussed in Chapter 7. Since hollow cylinder testing (Santarelli[18]) was performed at Imperial College at the same time as this study, it was possible to check the validity of the numerical model under axisymmetric conditions against laboratory predictions, in addition to checking the numerical validity of the computer code. The foundation of the FEM for linear elastic behaviour in plane strain and complete plane strain (Brady and Bray[46]) is given in Chapter 3. Classical plasticity is extended to allow for strain-softening behaviour and non-associated flow rules in Chapter 4, with an assessment of the model elasto-plastic behaviour when applied to a set of triaxial tests carried out on a Carboniferous sandstone. Chapter 5 discusses and develops the techniques necessary for analyzing elasto-plastic behaviour using the FEM, and presents a number of analytical/numerical solutions for validation purposes. Chapter 6 continues the development of the FEM to allow for pressure dependent elasticity, and presents a simpler solution for the case of an isotropic stress field, which only requires numerical integration. This solution is used to help validate the computer code in the context of pressure dependent elasticity. Parametric studies in reference to wellbore instability problems are carried out with respect to plastic and pressure dependent elastic nonlinearities at the end of Chapters 5 and 6 respectively. Finally, in Chapter 7, the applicability of the computer model and its shortfalls in modelling wellbore behaviour are discussed, conclusions of the work are presented and recommendations for further research are made.

CHAPTER 2

ELASTIC SOLUTIONS FOR ANALYSIS OF WELLBORE STABILITY

2.1 INTRODUCTION

There are many parameters, of varying degrees of importance that may effect the stresses around a wellbore, and therefore the mechanical stability. A powerful and reasonably simple approach that can often be applied to help understand mechanical behaviour is linear elasticity. Although the results of a linear elastic analysis cannot be considered to be quantitatively accurate due to the complicated behaviour of rocks, they can give engineers a 'first approximation' to solving the problem at hand, and may give a far better physical understanding of the problem than could be attained from using 'black box' numerical tools such as finite elements or boundary elements. This chapter sets out a number of solutions, based on linear elasticity, that may be used to appreciate the influence of the following factors on wellbore stability,

- in-situ stress magnitudes,
- well direction relative to the in-situ stress field,
- formation pressure,
- well pressure,
- pore pressures induced by fluid flow from/to the formation,
- thermal gradients due to differences between mud and formation temperatures,
- time dependent pore fluid pressure variations,
- mud cake effectiveness,
- rock properties (strength, permeability, Youngs Modulus, Poisson's ratio).

2.1.1 General Conditions

Six different solutions are presented which consider the effect of a particular parameter or condition on the stress state around a wellbore. These are:

1. Redistribution of the in-situ stress state around a wellbore for the case of balanced well and formation pressures, balanced temperatures and assuming drained conditions.

2. Induced pore pressures and stresses additional to those in case (1) above, for the case of undrained conditions.

3. Pore pressures and stresses induced from pore fluid flow into the well in the case of a negative overbalance (underbalance), or drill fluid influx in the case of a positive overbalance, and assuming steady state conditions. For the case of drill fluid influx, the mud cake effectiveness can be tailored to represent a zero, finite or infinite cake permeability relative to the formation permeability.

4. Thermally induced stresses resulting from a difference between mud and formation temperature in a permeable formation.

5. Thermally induced stresses and pore pressures resulting from a difference between mud and formation temperatures in an impermeable formation.

6. Pore pressures and stresses as a result of transient fluid influx/outflow in low permeability formations for an isotropic stress field. This solution is developed to quantify the importance of time.

Since these solutions assume linear elasticity and assume that the rock permeability and heat conduction and expansion coefficients are independent of pressure and temperature, a number of the solutions obey the laws of superposition. Thus, solutions 1, 2 and 5 could be combined to give the total stress conditions shortly after the well is drilled allowing for stress redistribution and temperature effects in a low permeable formation.

Certain combinations of the above solutions must be avoided, since they would relate to non-existent situations. For example, a combination of 1, 2 and 4 would relate to thermal stresses induced in high permeability formations (case 4), but pore pressures related to low permeability formations (case 2). The equations derived in Section 2.7 (item 6 above) cannot be combined with any of the other solutions, since they are based on radial, transient fluid flow in low permeability formations, requiring a uniform pore fluid pressure within the formation immediately after drilling a section. This condition can only be achieved if the stress state perpendicular to the well axis is isotropic, and no thermally induced pore pressures have been set up.

2.1.2 Assumptions

The application of the solutions that are presented are restricted by the following assumptions:

- The rock is homogeneous, isotropic and linear elastic.
- Temperature and fluid flow are considered to be steady state in

cases 3, 4 and 5 (Section 2.1.1 above).

- Biots constant[53] as defined below, is equal to 1.

  Biots Constant $\beta = 1 - C_{ma}/C_b$

  where C_{ma} is the compressibility of the rock matrix

  and C_b is the bulk compressibility.

- The permeability of the rock surrounding the wellbore is unaffected by drilling fluid invasion.
- Complete plane strain conditions apply.
- Permeability, thermal conduction and expansion coefficients are independent of pressure and temperature.
- Rock elastic properties are independent of temperature.
- The self weight of the rock mass is negligible compared with the in-situ stress field loading.

2.2 REDISTRIBUTION OF THE IN-SITU STRESSES - DRAINED CONDITIONS

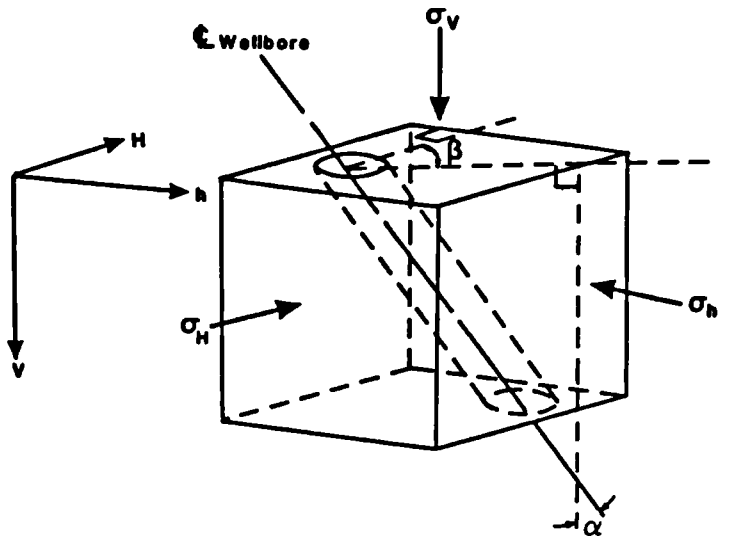
The resultant stresses after drilling a well can be found in a number of papers (e.g. Bradley[11]), so they will not be derived here.

Before the equations of stresses are presented it is necessary to transpose the in-situ stress tensor relative to a coordinate system with one of its axes parallel to the wellbore axis and another which lies in the horizontal plane (see Figure 2.1). Since it is assumed that one of the principal in-situ stresses is vertical, the general 3D stress transformation equations can be simplified to the set of equations given below,

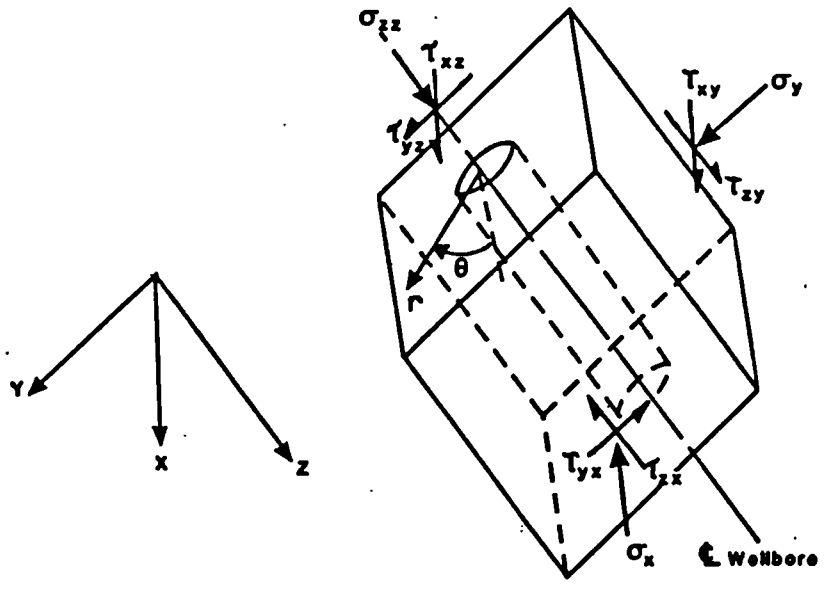
$$\sigma_x = \sigma_H \sin^2\beta + \sigma_h \cos^2\beta \qquad (1)$$

$$\sigma_y = \cos^2\alpha \, (\sigma_H \cos^2\beta + \sigma_h \sin^2\beta) + \sigma_v \sin^2\alpha \qquad (2)$$

HORIZONTAL AND VERTICAL CO-ORDINATE SYSTEM



CO-ORDINATE SYSTEM ROTATED TO ALIGN WITH WELLBORE.
X-AXIS LIES IN THE HORIZONTAL PLANE



Transformation of the in-situ stress tensor.

Figure 2.1

$$\sigma_{zz} = \sin^2\alpha\,(\sigma_H\cos^2\beta + \sigma_h\sin^2\beta) + \sigma_v\cos^2\alpha \qquad (3)$$

$$\tau_{xy} = \cos\alpha\,\sin\beta\,\cos\beta\,(\sigma_H - \sigma_h) \qquad (4)$$

$$\tau_{yz} = \sin\alpha\,\cos\alpha\,(\sigma_v - \sigma_H\cos^2\beta - \sigma_h\sin^2\beta) \qquad (5)$$

$$\tau_{zx} = \sin\alpha\,\sin\beta\,\cos\beta\,(\sigma_h - \sigma_H) \qquad (6)$$

where σ_v is the vertical (overburden) stress,

σ_H & σ_h are the maximum and minimum horizontal principal stresses respectively,

α is the well deviation angle (measured from the vertical),

β is the well direction relative to the maximum horizontal principal stress direction.

and σ_x, σ_y, σ_{zz}, τ_{xy}, τ_{yz} and τ_{zx} represent the new in-situ stress tensor as defined in Figure 2.1.

[Note: When considering 3-dimensional stress analysis problems, as for the case of deviated wells, it is important to have consistency in the coordinate systems. In this chapter, and throughout the thesis, right-hand coordinate systems are used.]

The stresses around the wellbore can now be written in terms of the transposed stress system defined by equations (1) to (6). The redistributed stresses are given by equations (7) to (12) below, and it is assumed that the well is in a balanced condition, i.e. the well pressure (P_W) is equal to the formation pressure (P_F). Thus,

$$\sigma_r = P_F + \tfrac{1}{2}(\sigma_x + \sigma_y - 2P_F)(1 - {}^{a^2}/_{r^2}) + \left[\tfrac{1}{2}(\sigma_x - \sigma_y)\cos 2\theta + \tau_{xy}\sin 2\theta\right](1 + {}^{3a^4}/_{r^4} - {}^{4a^2}/_{r^2}) \qquad (7)$$

$$\sigma_\theta = P_F + \tfrac{1}{2}(\sigma_x + \sigma_y - 2P_F)(1 + {}^{a^2}/_{r^2}) - \left[\tfrac{1}{2}(\sigma_x - \sigma_y)\cos 2\theta + \tau_{xy}\sin 2\theta\right](1 + {}^{3a^4}/_{r^4}) \qquad (8)$$

$$\sigma_z = \sigma_{zz} + \nu(\sigma_r + \sigma_\theta - \sigma_y - \sigma_x) \tag{9}$$

$$\tau_{r\theta} = \left[\frac{1}{2}(\sigma_y - \sigma_x)\sin 2\theta + \tau_{xy}\cos 2\theta\right](1 - {}^{3a^4}/_{r^4} + {}^{2a^2}/_{r^2}) \tag{10}$$

$$\tau_{\theta z} = (\tau_{yz}\cos\theta - \tau_{zx}\sin\theta)(1 + {}^{a^2}/_{r^2}) \tag{11}$$

$$\tau_{zr} = (\tau_{yz}\sin\theta + \tau_{zx}\cos\theta)(1 - {}^{a^2}/_{r^2}) \tag{12}$$

and the pore fluid pressure is constant and given by

$$p_f = P_F \tag{13}$$

The stress conditions at the wellbore wall (r = a) reduce to

$$\sigma_r = P_F \qquad (\text{note: } P_W = P_F) \tag{14}$$

$$\sigma_\theta = (\sigma_x + \sigma_y - P_F) - 2(\sigma_x - \sigma_y)\cos 2\theta - 4\tau_{xy}\sin 2\theta \tag{15}$$

$$\sigma_z = \sigma_{zz} - 2\nu[(\sigma_x - \sigma_y)\cos 2\theta + 2\tau_{xy}\sin 2\theta)] \tag{16}$$

$$\tau_{\theta z} = 2(\tau_{yz}\cos\theta - \tau_{zx}\sin\theta) \tag{17}$$

and $\tau_{r\theta} = \tau_{zr} = 0$.

Equations (7) to (13) can be considered as the base equations for all problem cases. Any effects due to fluid flow, low permeability, or temperature gradients derived in the following sections must be added to the stresses calculated from these equations to give the total stress state for the problem being considered.

2.3 INDUCED PORE PRESSURES FOR UNDRAINED STRESS REDISTRIBUTION

Initially, taking the particular case of a well drilled parallel to a principal stress the problem reduces to plane strain and in (7), (8) and (10) the shear stress τ_{xy} is zero and σ_x and σ_y represent principal stresses, and the antiplane shear stresses $\tau_{\theta z}$ and τ_{zr} are zero.

The total stress acting on an element of rock is made up of a pore pressure and the rock matrix stress, or effective stress. Here the effective stress relationship presented by Terzaghi[54] shall be assumed, as defined by (18),

$$\sigma = \sigma' + p_f \tag{18}$$

where σ is the total normal stress on an element or rock,

σ' is the rock matrix or effective stress,

and p_f is the pore fluid pressure.

The relationship between stress and strain when considering pore pressures is assumed to take the following form,

$$\varepsilon_r = \frac{\sigma'_r - \nu(\sigma'_\theta + \sigma'_z)}{E} \tag{19}$$

where ε_r is the radial strain.

Note that Biot's constant is taken to be unity. The circumferential strain (ε_θ) and the axial strain (ε_z) relationships are obtained by rotating the subscripts θ, r and z in equation (19).

The shear strain ($\gamma_{r\theta}$) v shear stress relationship is unaffected by pore pressures and the standard expression given below is assumed to hold,

$$\gamma_{r\theta} = \frac{2(1+\nu)\tau_{r\theta}}{E}$$

The total radial strain (ε_r) and circumferential strain (ε_θ) for plane strain conditions are given by,

$$\varepsilon_r = \frac{(1 - \nu^2)\sigma'_r - \nu(1 + \nu)\sigma'_\theta}{E} \tag{20}$$

and

$$\varepsilon_\theta = \frac{(1 - \nu^2)\sigma'_\theta - \nu(1 + \nu)\sigma'_r}{E} \tag{21}$$

and the volumetric strain (ε_v) is given by,

$$\varepsilon_v = \varepsilon_r + \varepsilon_\theta + \varepsilon_z$$

Since for plane strain $\varepsilon_z = 0$ (ε_z is in fact constant and non zero, but the problem is simplified, without introducing any errors, by ignoring the initial or pre-existing axial stress and strain) then from (20) and (21) we get,

$$\varepsilon_v = \frac{(1 - 2\nu)(1 + \nu)(\sigma'_r + \sigma'_\theta)}{E} \tag{22}$$

The induced volumetric strain (i.e. the difference in the volumetric strain before and after drilling the well) is given by,

$$\Delta\varepsilon_v = \frac{(1 - 2\nu)(1 + \nu)(\sigma'_r + \sigma'_\theta - \sigma'_x - \sigma'_y)}{E}$$

Since at this stage it is assumed that the pore pressure within the formation is the same before and after drilling the well the equation above is of the same form in total stresses as effective stresses,

$$\therefore \quad \Delta\varepsilon_v = \frac{(1 - 2\nu)(1 + \nu)(\sigma_r + \sigma_\theta - \sigma_x - \sigma_y)}{E} \tag{23}$$

Let $\sigma = \frac{1}{2}(\sigma_x - \sigma_y)$, then by substituting for σ_r and σ_θ into (23) using (7) and (8) we get,

$$\Delta\varepsilon_v = -\frac{4(1 - 2\nu)(1 + \nu)\sigma}{E}\cdot\frac{a^2}{r^2}\cos 2\theta \tag{24}$$

The induced volumetric strain given in equation (24) will take place provided the conditions are drained. For the case of undrained conditions in low permeable formations, the pore fluid will develop positive pressures in the case of an element that is attempting to reduce in volume, or negative pressures in the case of an element that is attempting to dilate. If it is assumed that the pore fluid and rock matrix are incompressible (i.e. only closure of pore spaces result in a net volumetric strain), then for undrained conditions the pore fluid will prevent any volumetric strain.

It can be assumed that the loading for undrained redistribution of

the in-situ stress field takes place in two stages. Firstly, the rock around the wellbore is allowed to redistribute in drained conditions (i.e. volumetric strain is allowed to take place), and secondly a stress and pore pressure state is applied to produce a volumetric strain equal and opposite to the drained volumetric strain. The first loading stage is given by equations (7) to (13), so only the second stage will be considered here.

In order to reduce the amount of mathematical notation that follows, pore pressures and stresses in the r, θ coordinate system shall now be assumed to be stresses additional to the stress state given by the base equations (7) to (13), given in Section 2.2. Thus, when reference is made to σ_r, it refers to the radial stress additional to that given by (7) for the case of undrained redistribution of the in-situ stress state.

The volumteric strain resulting from the second stage loading (the additional stresses due to undrained redistribution of the in-situ stress state) is given by (22). By letting the sum of the induced volumetric strain ($\Delta\varepsilon_v$) given in (24) and the volumetric strain given in (22) be zero we obtain undrained conditions. Thus, from (22) and (24) we have for volumetric constraint,

$$\sigma'_r + \sigma'_\theta = 4\sigma \frac{a^2}{r^2}\cos 2\theta \qquad (25)$$

Neglecting body forces the equilibrium equations in polar coordinates are,

$$\frac{\partial \sigma_r}{\partial r} + \frac{1}{r}\frac{\partial \tau_{r\theta}}{\partial \theta} + \frac{\sigma_r - \sigma_\theta}{r} = 0 \qquad (26)$$

and

$$\frac{1}{r}\frac{\partial \sigma_\theta}{\partial \theta} + \frac{\partial \tau_{r\theta}}{\partial r} + \frac{2\tau_{r\theta}}{r} = 0 \qquad (27)$$

Using the effective stress relationship given in (18) the equilibrium equations can be rewritten in terms of effective stresses as,

$$\frac{\partial \sigma'_r}{\partial r} + \frac{\partial p_f}{\partial r} + \frac{1}{r}\frac{\partial \tau_{r\theta}}{\partial \theta} + \frac{\sigma'_r - \sigma'_\theta}{r} = 0 \qquad (28)$$

and $$\frac{1}{r}\frac{\partial \sigma'_\theta}{\partial \theta} + \frac{1}{r}\frac{\partial p_f}{\partial \theta} + \frac{\partial \tau_{r\theta}}{\partial r} + \frac{2\tau_{r\theta}}{r} = 0 \qquad (29)$$

The compatibility equation in terms of stress and polar coordinates can be found in most Mechanical Engineering text books on stress analysis (e.g. Timoshenko and Goodier[55]). The equation is,

$$\left(\frac{\partial^2}{\partial r^2} + \frac{1}{r}\frac{\partial}{\partial r} + \frac{1}{r^2}\frac{\partial^2}{\partial \theta^2}\right)(\sigma_r + \sigma_\theta) = 0$$

This compatibility equation will not hold when pore fluid pressures are present. If the compatibility equations are developed from first principles using the relationships given by (18) and (19), it can be shown that in terms of effective stress and pore pressure the compatibility equation becomes,

$$\left(\frac{\partial^2}{\partial r^2} + \frac{1}{r}\frac{\partial}{\partial r} + \frac{1}{r^2}\frac{\partial^2}{\partial \theta^2}\right)[(1 - \nu)(\sigma'_r + \sigma'_\theta) + p_f] = 0 \qquad (30)$$

The partial differential equations for volume constraint, equilibrium and compatibility as given above ((25), (28), (29) and (30)) with boundary conditions must be solved to give the relationships for stress and pore pressure as a function of radius and angle. The solution to the four differential equations is simply a relationship for pore pressure with all total normal and shear stresses being unaffected by the introduction of undrained conditions. However, this result will be shown from first principles in the following analysis.

Assuming that the variables r and θ can be separated, then as with the Kirsch solutions, from inspection of symmetry conditions the

stresses and pore pressure can be written in the following general terms,

$$\sigma'_r = F_1 \cos 2\theta$$

$$\sigma'_\theta = F_2 \cos 2\theta$$

$$\tau_{r\theta} = F_3 \sin 2\theta$$

$$p_f = F_4 \cos 2\theta$$

where F_1, F_2, F_3 and F_4 are all functions of r.

Expressing (25) in terms of the general equations for σ'_r and σ'_θ given above results in,

$$F_1 + F_2 = 4\sigma \frac{a^2}{r^2} \qquad (31)$$

Using (25) to eliminate σ'_r and σ'_θ from (30), differentiating and rearranging then,

$$F_4'' + \frac{1}{r} F_4' - \frac{4}{r^2} F_4 = 0 \qquad \text{where } F'' = \frac{d^2F}{dr^2} \quad \text{and } F' = \frac{dF}{dr}$$

Multiplying by r^3 then,

$$r^3 F_4'' + r^2 F_4' - 4rF_4 = 0$$

giving after integration,

$$r^3 F_4' - 2r^2 F_4 = A$$

where A is a constant of integration

Multiplying by r^{-5} and integrating again and rearranging gives,

$$F_4 = -\frac{A}{4r^2} + Br^2$$

where B is a constant of integration

As $r \to \infty$, $p_f \to 0$, thus $F_4 \to 0$, and so $B = 0$, in which case

$$F_4 = -\frac{A}{4r^2} \qquad (32)$$

Substituting the stress and pore fluid general relationships into (28) and differentiating gives,

$$F_1' + F_4' + \frac{2}{r} F_3 + \frac{1}{r} F_1 - \frac{1}{r} F_2 = 0$$

Eliminating F_4' in the above by differentiating (32) gives, after rearranging,

$$F_3 = - \frac{r}{2} F_1' - \frac{1}{2} F_1 + \frac{1}{2} F_2 - \frac{A}{4r^2} \tag{33}$$

Substituting the pore pressure and stress general relationships into (29) gives,

$$- \frac{2}{r} F_2 - \frac{2}{r} F_4 + F_3' + \frac{2}{r} F_3 = 0$$

Using (32) to eliminate F_4 from the above gives,

$$- \frac{2}{r} F_2 + \frac{A}{2r^3} + F_3' + \frac{2}{r} F_3 = 0 \tag{34}$$

Using (33) to eliminate F_3 and F_3' from (34) gives,

$$- \frac{r}{2} F_1'' - 2F_1' - \frac{1}{r} F_1 + \frac{1}{2} F_2' - \frac{1}{r} F_2 + \frac{A}{2r^3} = 0$$

Using (31) to elimate F_2 and F_2' from the above gives,

$$r F_1'' + 5F_1' + \frac{(16a^2\sigma - A)}{r^3} = 0$$

Multiplying by r^4 and integrating gives,

$$r^5 F_1' + \frac{(16a^2\sigma - A)r^2}{2} + C = 0$$

where C is a constant of integration.

Dividing by r^5 and integrating gives,

$$F_1 = \frac{16a^2\sigma - A}{4r^2} + \frac{C}{4r^4} + D$$

where D is a constant of integration.

Since σ_r' (and therefore F_1) tends to zero as $r \to \infty$, then $D = 0$, and so

$$F_1 = \frac{16a^2\sigma - A}{4r^2} + \frac{C}{4r^4} \tag{35}$$

From the boundary conditions, we have at $r = a$,

$$\sigma_r = \sigma_r' + p_f = 0$$

$$\therefore \quad F_1(a) + F_4(a) = 0$$

$\therefore$ from (32) and (35),

$$\frac{16a^2\sigma - A}{4a^2} + \frac{C}{4a^4} - \frac{A}{4a^2} = 0$$

$$\therefore \quad C = 2a^2(A - 8a^2\sigma) \tag{36}$$

Eliminating F_1 from (31) using (35) gives,

$$F_2 = \frac{A}{4r^2} - \frac{C}{4r^4} \tag{37}$$

Using (35) and (37) to eliminate F_1, F_1' and F_2 from (33) gives,

$$F_3 = \frac{8a^2\sigma - A}{4r^2} + \frac{C}{4r^4} \tag{38}$$

For the boundary condition at $r = a$, $\tau_{r\theta} = 0$,

$$\therefore \quad 8a^2\sigma - A + \frac{C}{a^2} = 0$$

$$\therefore \quad C = a^2(A - 8a^2\sigma) \tag{39}$$

From inspection of (36) and (39) it can be seen that C must be equal to zero for the conditions to be satisified and $A = 8a^2\sigma$.

By substituting the constants into the relevant equations ((32),(35), (37) and (38)) and using equation (18) to convert effective stresses to total stresses we can arrive at the additional stresses and pore pressures (over and above the stress state for drained conditions in

plane strain, as defined by the Kirsch equations[48]), when the formation is considered to be undrained. The resulting substitution shows that the additional total radial stress (σ_r), circumferential stress (σ_θ) and shear stress ($\tau_{r\theta}$) are all zero and therefore unaffected by imposing undrained conditions. However, the pore fluid pressure does produce a non zero relationship and is given in equation (40). To distinguish the additional pore pressure due to undrained conditions, from the base equation (13) given in Section 2.2, it has been prefixed by 'Δ' in equation (40). Thus, for plane strain conditions

$$\Delta p_f = -(\sigma_x - \sigma_y)\frac{a^2}{r^2}\cos 2\theta \qquad (40)$$

and $\Delta\sigma_r$, $\Delta\sigma_\theta$ and $\Delta\tau_{r\theta}$ are zero for all r and θ.

and from plane strain considerations,

$$\Delta\sigma_z = -(1-2\nu)(\sigma_x - \sigma_y)\frac{a^2}{r^2}\cos 2\theta \qquad (41)$$

The solution can be extended to the condition of complete plane strain from consideration of the major and minor normal stresses in the plane normal to the wellbore axis. The additional pore pressure due to undrained conditions for complete plane strain is given by

$$\Delta p_f = -2\rho\frac{a^2}{r^2}\cos 2(\theta-\omega) \qquad (42)$$

where $\omega = \frac{1}{2}\tan^{-1}\frac{2\tau_{xy}}{\sigma_x - \sigma_y}$

and $\rho = \frac{1}{2}(\sigma_x - \sigma_y)\cos 2\omega + \tau_{xy}\sin 2\omega$

and as before $\Delta\sigma_r$, $\Delta\sigma_\theta$ and $\Delta\tau_{r\theta}$ are zero for all r and θ and the axial stress is given by

$$\Delta\sigma_z = -2(1-2\nu)\rho\frac{a^2}{r^2}\cos 2(\theta-\omega) \qquad (43)$$

At the wellbore wall (r=a) the pore pressure Δp_f for plane strain and complete plane strain reduce to (44) and (45) respectively, with $\Delta\sigma_z$ for both conditions given by (46). Thus,

$$\Delta p_f = -(\sigma_x - \sigma_y)\cos 2\theta \qquad \text{(plane strain)} \qquad (44)$$

$$\Delta p_f = -2\rho \cos 2(\theta-\omega) \qquad \text{(complete plane strain)} \qquad (45)$$

$$\Delta\sigma_z = (1-2\nu)\Delta p_f \qquad (46)$$

Although the wellbore wall is theoretically the surface of the maximum and minimum pore pressures, in practice the maximum and minimum will lie on a circle a finite distance beyond the wellbore wall, since the infinite pressure gradient between the pore fluids and the drilling fluid will be alleviated by contact at the wellbore wall.

2.4 STRESSES AND PORE FLUID PRESSURES RESULTING FROM FLUID FLOW

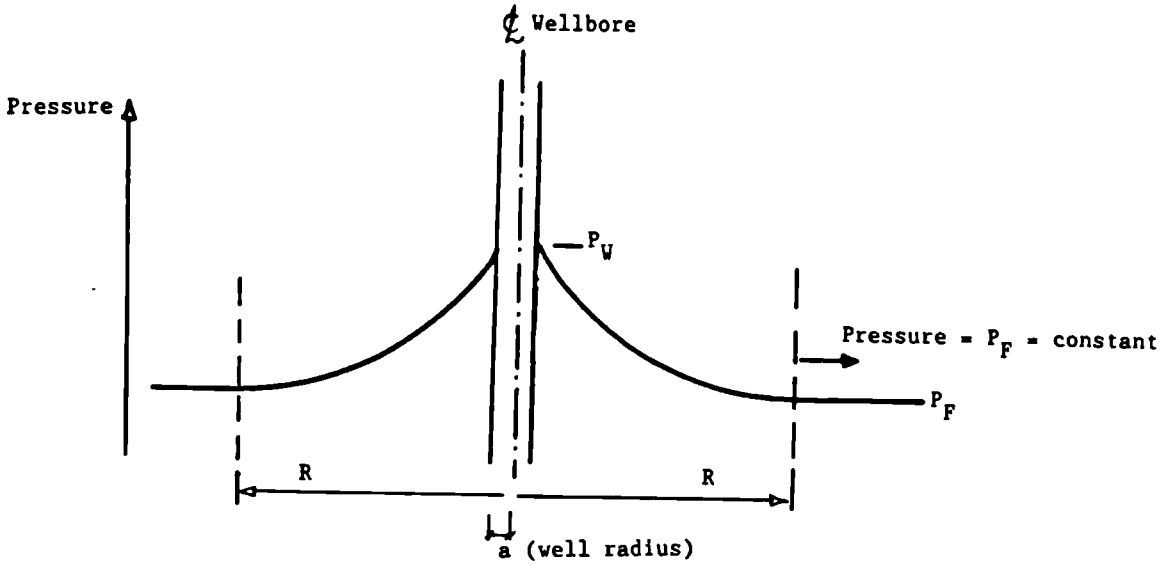
When the drilling fluid invades the formation in the case of overbalance, or the pore fluids flow into the wellbore due to underbalance, a pore pressure gradient is induced. This pore pressure gradient will result in a change to both the total and effective stress regimes. In this section only the stresses and pore pressures induced by the fluid flow will be considered, and the resultant stress regime and pore fluid pressures must be found by combining the base stress regime given in Section 2.2 with the stresses derived in this section.

The well is considered to be in an infinite medium, and for such conditions fluid flow (whether influx or outflow) will be transient (i.e. changing continually with time). A true transient solution is dealt with later in this chapter, but for the present a pseudo-steady state solution will be considered. In order to calculate the pore

pressure distribution for steady state conditions it is necessary to know the radial distance (R) at which the formation pressure is unaffected by the flow of fluid from or to the wellbore (see Figure 2.2). With increase in time this radial distance will increase. For large R, say ten times the wellbore radius (a), the near wellbore stresses become relatively unaffected by further increases in R, and therefore further increases in time. Since it is only the near wellbore stresses that are of interest in wellbore stability, a pseudo-steady state solution is acceptable for drilling through permeable formations (e.g. sandstones), where R is large almost immediately after drilling a section. For low permeability formations where R may be small for a significant time, and wellbore stresses will be sensitive to changes in R, a steady state solution is not acceptable.

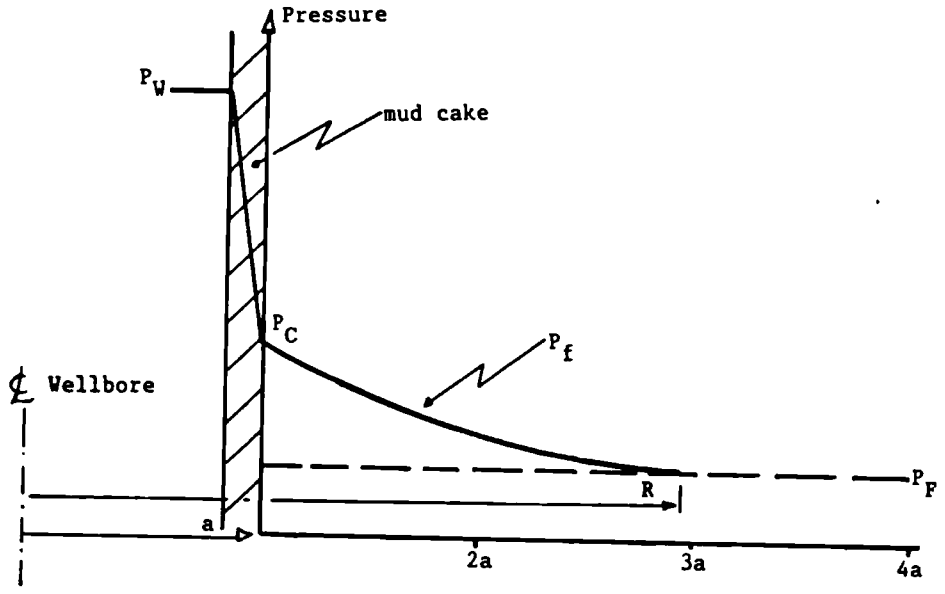
The conditions that are considered here are depicted in Figure 2.3. The in-situ stress regime is ignored since it has been accounted for in the base equations derived in Section 2.2. Since a constant pore pressure regime of P_p due to balanced drilling conditions has also been accounted for in the base equations, the pore pressures in this section shall be considered relative to a datum of P_p as in Section 2.3.

Figure 2.3 shows a typical pore pressure distribution for the case of drilling with an overbalance, with a mud cake of finite permeability. The pressure applied to the outside of the mud cake is the well pressure, P_w. A pressure drop takes place across the mud cake, so that the pressure on the inside of the mud cake is given by P_c. A futher drop in pressure occurs from the inside of the wellbore through the formation, till at a radius R, the pore pressure equals the formation pressure. Fluid flow is considered to be radial (i.e. one dimensional).



Pore pressure profile for steady-state fluid flow.

Figure 2.2



Pore pressure profile when mud cake is present.

Figure 2.3

The equations presented at the end of this section are based on the conditions shown in Figure 2.3. Although they are for a specific case, other drilling conditions can be simulated using the same set of equations by simply altering the values of P_W and P_C. The following are all the cases that can be simulated,

1. Drilling with overbalance and an impermeable mud cake:-

$$P_W > P_F \quad \text{and} \quad P_C = P_F$$

2. Drilling with overbalance and no mud cake:-

$$P_W > P_F \quad \text{and} \quad P_C = P_W$$

3. Drilling with an underbalance:-

$$P_W < P_F \quad \text{and} \quad P_C = P_W$$

Note: In the case of an underbalance it is considered that any mud cake has been washed away by the flow of formation fluids into the wellbore. No allowance is made for formation damage (reduction in the permeability of the near wellbore region due to 'plugging' from drilling fluid particle invasion).

From integration of Darcys law for steady state flow (see any good text book on fluid flow, e.g. Dake[56]) we get,

$$\text{total pore pressure} = P_F + \frac{P_C - P_F}{\ln\frac{a}{R}}.\ln\frac{r}{R}$$

Since the datum is being taken as P_F the formation pressure must be subtracted from the total pressure to give the additional pore pressure due to drilling with an imbalance.

$$\therefore \quad p_f = \frac{P_C - P_F}{\ln\frac{a}{R}}.\ln\frac{r}{R} \tag{47}$$

Since only radial flow is considered, the equilibrium equations (26) and (27) reduce to one non trivial relationship, given by

$$\frac{d\sigma_r}{dr} + \frac{\sigma_r - \sigma_\theta}{r} = 0 \tag{48}$$

and in terms of effective stress (28) and (29) reduce to the single expression given by

$$\frac{d\sigma'_r}{dr} + \frac{dp_f}{dr} + \frac{\sigma'_r - \sigma'_\theta}{r} = 0 \tag{49}$$

The strain-displacement relationships for axial symmetry are,

$$\varepsilon_r = -\frac{du}{dr}, \quad \text{and} \quad \varepsilon_\theta = -\frac{u}{r}, \tag{50}$$

where u is the radial displacement.

Using the stress-strain relationships defined by (19) in Section 2.3, and converting strain to displacement, we arrive at

$$\sigma'_r = -\frac{2G}{1-2\nu}\left[(1-\nu)\frac{du}{dr} + \nu\frac{u}{r}\right] \tag{51}$$

$$\sigma'_\theta = -\frac{2G}{1-2\nu}\left[(1-\nu)\frac{u}{r} + \nu\frac{du}{dr}\right] \tag{52}$$

where G is the shear modulus given by

$$G = \frac{E}{2(1+\nu)}$$

Using equations (51) and (52) to express (49) in terms of displacement we get after rearranging,

$$-\frac{2G(1-\nu)}{1-2\nu}\left[\frac{d^2u}{dr^2} + \frac{1}{r}\frac{du}{dr} - \frac{u}{r^2}\right] + \frac{dp_f}{dr} = 0 \tag{53}$$

Integrating (53) gives,

$$-\frac{2G(1-\nu)}{1-2\nu}\left[\frac{du}{dr} + \frac{u}{r}\right] + p_f = A$$

where A is a constant of integration.

Multiplying by r and integrating gives,

$$-\frac{2G(1-\nu)}{1-2\nu}ur + \int p_f r dr = \frac{Ar^2}{2} + B$$

where B is a constant of integration.

Rearranging we get,

$$u = -\frac{1-2\nu}{2G(1-\nu)}\left[\frac{Ar}{2} + \frac{B}{r} - \frac{1}{r}\int p_f r dr\right] \tag{54}$$

Using (54) to eliminate $\frac{u}{r}$ and $\frac{du}{dr}$ in (51) we get,

$$\sigma_r = \sigma'_r + p_f = \frac{1}{1-\nu}\left[\frac{A}{2} - \frac{(1-2\nu)}{r^2}\int p_f r dr\right] \tag{55}$$

From (47) we get

$$\frac{1}{r^2}\int p_f r dr = \frac{1}{r^2}\int \frac{(P_C-P_F)}{\ln\frac{a}{R}} \ln\frac{r}{R}.r dr = \frac{P_C-P_F}{4\ln\frac{a}{R}}\left(2\ln\frac{r}{R} - 1\right)$$

$$\text{let } C(r) = \frac{P_C-P_F}{4\ln\frac{a}{R}}\left(2\ln\frac{r}{R} - 1\right) \tag{56}$$

then (55) can be expressed as

$$\sigma_r = \frac{1}{1-\nu}\left[\frac{A}{2} - (1-2\nu)\frac{B}{r^2} + (1-2\nu)C(r)\right] \tag{57}$$

and (54) can be expressed as

$$u = -\frac{1-2\nu}{2G(1-\nu)}\left[\frac{Ar}{2} + \frac{B}{r} - rC(r)\right] \tag{58}$$

From consideration of boundary conditions ($\sigma_r = P_W - P_F$ at $r = a$, and continuity of u at $r = R$), it can be shown that

$$A = 0$$

$$\text{and} \quad B = a^2\left[C(a) - \frac{1-\nu}{1-2\nu}(P_W-P_F)\right] \tag{59}$$

$$\text{where } C(a) = \frac{1}{4}\left[2 - \frac{1}{\ln\frac{a}{R}}\right](P_C-P_F)$$

Using (57) to substitute for σ_r and $\frac{d\sigma_r}{dr}$ into the equilibrium equation in total stresses (48) we get for σ_θ,

$$\sigma_\theta = \frac{1-2\nu}{1-\nu}\left[\frac{B}{r^2} + C(r) + \frac{1}{2}\frac{P_C-P_F}{\ln\frac{a}{R}}\right] \tag{60}$$

Let $h = \frac{P_C - P_F}{P_W - P_F}$, where $0 \leq h \leq 1$ (61)

Thus, for no mud cake, h = 1. For an impermeable mud cake (relative to the formation permeability), h = 0 and values in between represent a partially effective mud cake.

Then by substituting the relationships for A, B and C(r) into (57) and (60) and rearranging, the induced stresses due to drilling with an imbalance are as given below. As in the summary equations in Section 2.3 the stresses and pore pressures are prefixed by Δ to distinguish them from the base equations given in Section 2.2.

For $a \leq r \leq R$

$$\Delta\sigma_r = (P_W - P_F)\left\{\frac{a^2}{r^2} - \frac{(1-2\nu)h}{4(1-\nu)\ln\frac{a}{R}}\left[\left(2\ln\frac{a}{R}-1\right)\frac{a^2}{r^2} - 2\ln\frac{r}{R} + 1\right]\right\} \quad (62)$$

$$\Delta\sigma_\theta = -(P_W - P_F)\left\{\frac{a^2}{r^2} - \frac{(1-2\nu)h}{4(1-\nu)\ln\frac{a}{R}}\left[\left(2\ln\frac{a}{R}-1\right)\frac{a^2}{r^2} + 2\ln\frac{r}{R} + 1\right]\right\} \quad (63)$$

with the induced pore fluid pressure distribution given by prefixing p_f in (47) by 'Δ'. Thus,

$$\Delta p_f = \frac{P_C - P_F}{\ln\frac{a}{R}} \cdot \ln\frac{r}{R} \quad (64)$$

From plane strain considerations it can be shown that the induced axial stress ($\Delta\sigma_z$) is given by

$$\Delta\sigma_z = \nu(\Delta\sigma_r + \Delta\sigma_\theta) + (1-2\nu)\Delta p_f \quad (65)$$

For the condition $r \geq R$, $\Delta\sigma_z$ and Δp_f are zero, but $\Delta\sigma_r$ and $\Delta\sigma_\theta$ are given by

$$\Delta\sigma_r = \frac{R^2}{r^2} \cdot \Delta\sigma_R \quad (66)$$

$$\Delta\sigma_\theta = -\frac{R^2}{r^2} \cdot \Delta\sigma_R \quad (67)$$

where $\Delta\sigma_R$ is the value of $\Delta\sigma_r$ in equation (62) for r = R.

The induced stresses at the wellbore wall are found by putting r = a, giving,

$$\Delta p_f = h(P_W - P_F) \qquad \text{(note: above the datum of } P_F\text{)} \qquad (68)$$

$$\Delta\sigma_r = P_W - P_F \qquad (69)$$

$$\Delta\sigma_\theta = -(P_W - P_F)\left[1 - \frac{(1-2\nu)h}{1-\nu}\right] \qquad (70)$$

$$\Delta\sigma_z = \frac{h(1-2\nu)(P_W - P_F)}{1-\nu} \qquad (71)$$

2.5 THERMAL STRESSES IN PERMEABLE FORMATIONS

There are three possible temperature conditions,

1. Drilling fluid temperature = Formation temperature
2. Drilling fluid temperature > Formation temperature
3. Drilling fluid temperature < Formation temperature

The first condition is unlikely to be common in practice, but the temperature difference may be sufficiently small that any temperature induced stresses will be insignificant. The second condition is likely to occur in the first few hundred meters of the wellbore. As depth increases so does the formation temperature, and the most common situation will be the third case in which the drilling fluid is cooler than the formation. However, in long open hole sections the drilling fluid having been heated at the hole bottom could be warmer than the formation still exposed further up the well.

It is assumed that the formation is sufficiently permeable, so that any induced volumetric strains will be able to take place in fully drained conditions, i.e. no thermally induced pore pressures. Two cases

are dealt with here:

(i) No fluid invasion into the formation.

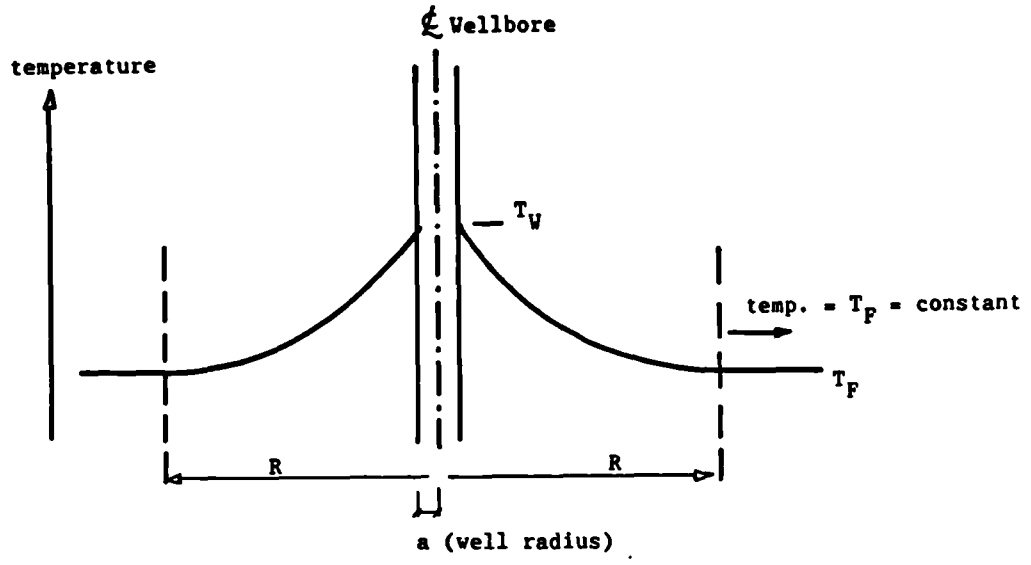
(ii) Fluid invasion due to only partial plugging by the mud cake, or flow in an injection well.

In the case of no fluid flow the heat flow from the formation to the well is transient and as with fluid flow (Section 2.4) a pseudo-steady state condition shall be assumed, with the radial distance R increasing with time (see Figure 2.4).

For the case of fluid flow into the well, the temperature variation with radius will be distorted by the cooling medium (drilling fluid) flowing into the warmer medium (formation). The real variation of temperature with radius (Figure 2.5) will be complex, and not amenable to simple closed form analysis, so the idealised relationship as used by Perkins and Gonzalez,[51] and shown in Figure 2.5 is used.

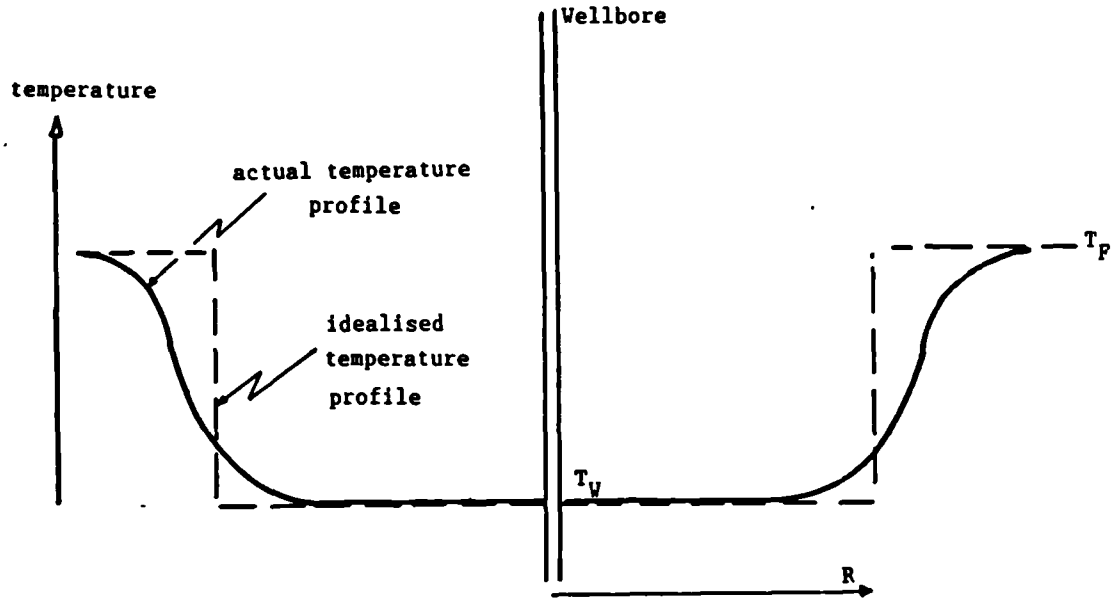
There is the possibility of having fluid flow from the formation into the well in conjunction with a temperature difference, but unless the fluid flow is extremely small (low permeable formation), the flow of the pore fluid into the well will prevent any temperature gradient being induced. The problem of pore fluid pressures set up by temperature gradients in low permeability formations is dealt with in Section 2.6.

As with the previous two sections the radial and circumferential stresses derived here will be additional to the stresses due to the redistribution of the in-situ stress state; the stresses refer only to the increment in the stress state due to thermal gradient effects.



Steady-state temperature distribution.

Figure 2.4



Temperature distribution for fluid injection well.

Figure 2.5

2.5.1 Conditions of Zero Fluid Invasion/Influx

The temperature flow, as with fluid flow in Section 2.4, is considered to take place in a radial direction in an infinite medium and under steady state conditions (see Figure 2.4). The analysis is analogous to fluid flow resulting in the temperature variation defined below (the derivation of the temperature variation equation given below can be found in many Mechanical Engineering text books, e.g. Timosenko and Goodier[55]),

$$T = T_F - \frac{T_F - T_W}{\ln\frac{a}{R}} \ln\frac{r}{R}$$

Therefore the temperature decrease is given by,

$$\Delta T = T_F - T = \frac{T_F - T_W}{\ln\frac{a}{R}} \ln\frac{r}{R} \qquad (72)$$

where a is the wellbore radius,

T is the temperaure at a radius r,

T_F is the formation temperature,

T_W is the well temperature,

and R is the radius at which the formation temperature is unaffected by the introduction of the well.

Beyond R (i.e. $r > R$) $\Delta T = 0$.

For the condition $a \leq r \leq R$ the stress-strain relationships are given by,

$$\varepsilon_r = \frac{\sigma_r - \nu(\sigma_\theta + \sigma_z)}{E} + \alpha_r \Delta T$$

$$\varepsilon_\theta = \frac{\sigma_\theta - \nu(\sigma_r + \sigma_z)}{E} + \alpha_r \Delta T$$

and $$\varepsilon_z = \frac{\sigma_z - \nu(\sigma_\theta + \sigma_r)}{E} + \alpha_r \Delta T = 0 \qquad \text{(plane strain conditions)}$$

where α_r is the linear coefficient of thermal expansion for the

formation.

[Note: Since it is assumed that the pore fluid pressure is constant in this analysis, it is not necessary to express the stress-strain relationships in terms of effective stresses as given in (19).]

By rearranging the above equations and using the strain-displacement relationships (50), we get,

$$\sigma_r = -\frac{2G}{1-2\nu}\left[(1-\nu)\frac{du}{dr} + \nu\frac{u}{r} + (1+\nu)\alpha_r\Delta T\right] \tag{73}$$

and $$\sigma_\theta = -\frac{2G}{1-2\nu}\left[(1-\nu)\frac{u}{r} + \nu\frac{du}{dr} + (1+\nu)\alpha_r\Delta T\right] \tag{74}$$

Using (73) and (74) to eliminate σ_r, σ_θ and $\frac{d\sigma_r}{dr}$ from the equilibrium equation (48) we get,

$$\frac{d^2u}{dr^2} + \frac{1}{r}\frac{du}{dr} - \frac{u}{r^2} + \frac{(1+\nu)}{(1-\nu)}\alpha_r\frac{d(\Delta T)}{dr} = 0$$

By intergrating twice we get,

$$u = \frac{Ar}{2} + \frac{B}{r} - \frac{(1+\nu)\alpha_r}{(1-\nu)r}\int r\Delta T dr \tag{75}$$

where A and B are constants of integration.

Using (75) to substitute for u and $\frac{du}{dr}$ into (73) gives,

$$\sigma_r = -\frac{2G}{1-2\nu}\left[\frac{A}{2} - (1-2\nu)\frac{B}{r^2} + \frac{(1-2\nu)(1+\nu)}{(1-\nu)r^2}\alpha_r\int r\Delta T dr\right] \tag{76}$$

Using (72) to substitute for ΔT in (76) gives,

$$\frac{1+\nu}{(1-\nu)r^2}\cdot\alpha_r\int r\Delta T dr = \frac{1+\nu}{(1-\nu)r^2}\cdot\alpha_r\int\frac{(T_F-T_W)}{\ln\frac{a}{R}}\ln\frac{r}{R}.rdr$$

$$= \frac{(1+\nu)\alpha_r(T_F-T_W)}{4(1-\nu)\ln\frac{a}{R}}\left(2\ln\frac{r}{R} - 1\right)$$

$$\text{let}\quad C(r) = \frac{(1+\nu)\alpha_r(T_F-T_W)}{4(1-\nu)\ln\frac{a}{R}}\left(2\ln\frac{r}{R} - 1\right)$$

$$\text{Then} \quad \sigma_r = -\frac{2G}{1-2\nu}\left[\frac{A}{2} - (1-2\nu)\left(\frac{B}{r^2} + C(r)\right)\right] \tag{77}$$

$$\text{and} \quad u = \frac{Ar}{2} + \frac{B}{r} - rC(r) \tag{78}$$

From consideration of the boundary conditions,

1. at $r = R$, continuity of u,
2. at $r = a$, $\sigma_r = 0$,

it can be shown that $A = 0$

$$\text{and} \quad B = a^2C(a)$$

$$\text{where } C(a) = \frac{(1+\nu)\alpha_r(T_F-T_W)}{4(1-\nu)}\left(2 - \frac{1}{\ln\frac{a}{R}}\right)$$

As with the summary equations in Sections 2.3 and 2.4 the radial and circumferential stresses have been prefixed by Δ to signify that they are additional to those given by the base equations given in Section 2.2. Therefore by substituting for A, B and C(r) into (77) it can be shown that for the condition $a \leq r \leq R$,

$$\Delta\sigma_r = \frac{(T_F-T_W)E\ \alpha_r}{4(1-\nu)\ln\frac{a}{R}}\left[\left(2\ln\frac{a}{R}-1\right)\frac{a^2}{r^2} - 2\ln\frac{r}{R} + 1\right] \tag{79}$$

Similarly it can be shown that

$$\Delta\sigma_\theta = -\frac{(T_F-T_W)E\ \alpha_r}{4(1-\nu)\ln\frac{a}{R}}\left[\left(2\ln\frac{a}{R}-1\right)\frac{a^2}{r^2} + 2\ln\frac{r}{R} + 1\right] \tag{80}$$

and from plane strain considerations it can be shown that $\Delta\sigma_z$ is given by,

$$\Delta\sigma_z = -\frac{\nu(T_F-T_W)E\ \alpha_r\ \ln\frac{r}{R}}{(1-\nu)\ln\frac{a}{R}} \tag{81}$$

(It can be seen that there are similarities between (79) and (80) and the fluid flow equations (63) and (64)).

The pore pressure p_f remains unaffected by the thermal gradient under

these circumstances (i.e. $\Delta p_f = 0$), where the formation is permeable. For the condition $r \geq R$, $\Delta\sigma_z$ becomes zero and $\Delta\sigma_r$ and $\Delta\sigma_\theta$ are given by

$$\Delta\sigma_r = \frac{R^2}{r^2}.\Delta\sigma_R \tag{82}$$

and $$\Delta\sigma_\theta = -\frac{R^2}{r^2}.\Delta\sigma_R \tag{83}$$

where $\Delta\sigma_R$ is the value of $\Delta\sigma_r$ given by equation (79) for $r = R$.

At the wellbore wall the stresses are obtained by putting $r = a$ in equations (79) to (81) giving

$$\Delta\sigma_r = 0$$

$$\Delta\sigma_\theta = -\frac{(T_F - T_W)E\ \alpha_r}{1-\nu} \tag{84}$$

and $$\Delta\sigma_z = -\frac{\nu(T_F - T_W)E\ \alpha_r}{1-\nu} \tag{85}$$

2.5.2 Condition of Fluid Invasion/Inflow

The idealised temperature variation for this condition is given in Figure 2.5. The radial distance R, progresses out with time (e.g. the example given by Perkins and Gonzalez[51] for an injection well is 60 m (200 ft) in 3 years). Again axial symmetry and plane strain conditions are assumed, and temperature and fluid flow are considered to be in the radial direction only. These assumptions will not hold true as the radius of influence, R, increases (Perkins and Gonzalez[51]). For example, in an injection well, radial heat flow and plane strain conditions will be a function of the ratio of h/R where h is the reservoir height. As h/R becomes small the heat flow will have a greater component in the axial direction, and the structure will tend towards a 'thin plate', and plane stress rather than plane strain conditions will hold. But, in the

field of open hole wellbore stability (injection wells are cased), where the fluid flow will be over a much shorter time scale, the assumptions are fair provided there is no significant anisotropy within the plane perpendicular to the wellbore.

As with Section 2.5.1 only the stresses induced by the temperature gradient are considered here, and the stress state due to the redistribution of the in-situ stress field (Section 2.2) are not dealt with. Also, although there will be a pore fluid gradient and associated induced stresses, these will not be considered here. Stress and pore fluid components associated with the fluid flow are dealt with in Section 2.4.

For this case the temperature decrease is

$$\text{for } r \leq R \qquad \Delta T = T_F - T_W \tag{86}$$

and for $r \geq R$, $\Delta T = 0$.

Proceding as in Section 2.5.1, the equation for σ_r is again given by (76), but in this instance we have,

$$\frac{1+\nu}{(1-\nu)r^2}\cdot\alpha_r\int r\Delta T dr = \frac{1+\nu}{(1-\nu)r^2}\cdot\alpha_r\int r(T_F-T_W)dr$$

$$= \frac{(1+\nu)}{(1-\nu)}\alpha_r(T_F-T_W)$$

Therefore from (76),

$$\sigma_r = -\frac{2G}{1-2\nu}\left[\frac{A}{2} - (1-2\nu)\frac{B}{r^2} + \frac{(1-2\nu)(1+\nu)}{(1-\nu)}\alpha_r(T_F-T_W)\right] \tag{87}$$

From consideration of the same boundary conditions as used in Section 2.5.1 it can be shown that

$$A = -\frac{(1+\nu)\alpha_r(T_W-T_F)}{(1-\nu)}$$

and $$B = \frac{a^2(1+\nu)\alpha_r(T_F-T_W)}{2(1-\nu)}$$

Rewriting σ_r as $\Delta\sigma_r$ to distinguish it from the base equations given in Section 2.2 and inserting the expressions for the constants into (87), then within the region $a \leq r \leq R$

$$\Delta\sigma_r = - \frac{E}{2(1-\nu)}\left[1 - \frac{a^2}{r^2}\right]\alpha_r(T_F-T_W) \tag{88}$$

Similarly it can be shown that within the same boundary $\Delta\sigma_\theta$ is given by

$$\Delta\sigma_\theta = - \frac{E}{2(1-\nu)}\left[1 + \frac{a^2}{r^2}\right]\alpha_r(T_F-T_W) \tag{89}$$

and from plane strain conditions $\Delta\sigma_z$ is given by,

$$\Delta\sigma_z = - \frac{\nu(T_F-T_W)E\ \alpha_r}{1-\nu} \tag{90}$$

From thick walled cylinder theory it can be shown that in the region $R \leq r$, $\Delta\sigma_z = 0$ and $\Delta\sigma_r$ and $\Delta\sigma_\theta$ are given by,

$$\Delta\sigma_r = - \frac{E}{2(1-\nu)}\left[\frac{R^2-a^2}{r^2}\right]\alpha_r(T_F-T_W) \tag{91}$$

and $$\Delta\sigma_\theta = \frac{E}{2(1-\nu)}\left[\frac{R^2-a^2}{r^2}\right]\alpha_r(T_F-T_W) \tag{92}$$

At the wellbore wall the radial induced stress is zero, the circumferential induced stress is given, as before, by (84) in Section 2.5.1, and the axial induced stress is still given by (90) since it is independent of radius in the region $a \leq r \leq R$.

2.6 THERMAL STRESSES AND PORE PRESSURES IN LOW PERMEABILITY FORMATIONS

For low permeable formations it is considered here that all loading and volumetric strain occurs under undrained conditions, and the pore fluid is incompressible. The problem is complicated by the pore fluid and rock structure not having the same volumetric expansions. Typical

volumetric coefficients of thermal expansion are

Pore Fluid (water) $\simeq$ 2×10^{-4} /°C

and Rock $\simeq$ 3×10^{-5} /°C

From these coefficients it can be seen that typically the pore fluid expansion may be greater than the pore space expansion. It shall be assumed that the rock porosity remains unaltered by heating or cooling. Thus, if a unit volume of dry rock of porosity, n, undergoes a thermal expansion of $\times$ then the respective volume changes are given by,

pore space:-	n	$\rightarrow$	$n(1+\times)$
rock structure:-	$1-n$	$\rightarrow$	$(1-n)(1+\times)$
total volume:-	1	$\rightarrow$	$1+\times$

Assume that a saturated low permeability rock is heated, then the pore fluid will expand much more than the pore volume. Since the rock has a low permeability, then the pore fluid cannot migrate easily from the pore space it occupies, and consequently a pore fluid pressure is set up as the rock attempts to restrict the expansion of the pore fluid. For thermal contraction the reverse is the case, and a negative pore fluid pressure is set up, since the rock attempts to restict the contraction of the pore fluid. As the pore fluid is being treated as incompressible, the stresses in the rock must adjust to allow the pore spaces to expand/contract to accommodate the thermal expansion/ contraction of the pore fluid. Thus, the imposed volumetric change due to the thermal expansion/contraction of the pore fluid is given as,

$$\varepsilon_v = n\beta_f \Delta T \tag{93}$$

where n is the rock porosity,

β_f is the volumetric coefficient of thermal expansion of the

pore fluid,

and ΔT is the temperature decrease

In addition to the thermal effects on the pore fluid, the expansion or contraction of the rock matrix must be considered. In this case the volumetric strain of the rock matrix due to temperature changes is given by

$$\varepsilon_v = (1-n)\beta_r \Delta T \tag{94}$$

where β_r is the bulk volumetric coefficient of thermal expansion of the rock.

It is assumed that thermal expansion is isotropic and the coefficient of linear expansion (α_r) is related to the volumetric expansion by

$$\alpha_r = \frac{\beta_r}{3}$$

The effects of the two volumetric strain components given by (93) and (94) will be combined, but it is worth pointing out the differences between the two to help with physical interpretation. In simple physical terms the expansion of the pore fluid in low permeability rocks (equation (93)) will result in pore pressures and rock matrix stresses on a free standing sample of rock, whereas the expansion of the rock matrix (equation (94)) will only induce stresses and pore pressures if the sample of rock is restricted as it attempts to undergo expansion or contraction. On combining the two components of volumetric strain we get,

$$\varepsilon_v = [n\beta_f + 3(1-n)\alpha_r]\Delta T \tag{95}$$

The stress-strain relationships in this case must be expressed in terms of effective stress because the conditions are undrained and therefore

induced pore pressures are set up. Thus the stress-strain relationships for the bulk response are,

$$\varepsilon_r = \frac{\sigma'_r - \nu(\sigma'_\theta + \sigma'_z)}{E} + \alpha_r \Delta T \tag{96}$$

$$\varepsilon_\theta = \frac{\sigma'_\theta - \nu(\sigma'_z + \sigma'_r)}{E} + \alpha_r \Delta T \tag{97}$$

and $$\varepsilon_z = \frac{\sigma'_z - \nu(\sigma'_r + \sigma'_\theta)}{E} + \alpha_r \Delta T \qquad (= 0 \text{ for plane strain}) \tag{98}$$

Heat flow is considered to be steady state and in a radial direction only as in Section 2.5.1. The variation of temperature with radius is as shown in Figure 2.4. As in Section 2.5 the equation relating temperature decrease with radius is given by (72).

Now $\varepsilon_r = -\frac{du}{dr}$, $\varepsilon_\theta = -\frac{u}{r}$ and $\varepsilon_z = 0$ for plane strain,

$$\therefore \quad \varepsilon_v = \varepsilon_r + \varepsilon_\theta + \varepsilon_z = -\frac{du}{dr} - \frac{u}{r}$$

Therefore from (95) and (72),

$$\frac{du}{dr} + \frac{u}{r} = -A_1 \ln\frac{r}{R} \tag{99}$$

where $$A_1 = [n\beta_f + 3(1-n)\alpha_r]\frac{T_F - T_W}{\ln\frac{a}{R}}$$

Multiplying (99) by r and integrating gives,

$$u = -\frac{A_1 r}{4}(2\ln\frac{r}{R} - 1) + \frac{B}{r} \tag{100}$$

where B is a constant of integration.

Equations (96) to (98) can be used to get an expression for σ'_r in terms of ε_r and ε_θ, and by substituting for ΔT using (72) it can be shown that,

$$\sigma'_r = \frac{2G}{1-2\nu}\left[(1-\nu)\varepsilon_r + \nu\varepsilon_\theta - (1+\nu)A_2 \ln\frac{r}{R}\right]$$

and by substituting the strain-displacement relationships (50) we get,

$$\sigma'_r = -\frac{2G}{1-2\nu}\left[(1-\nu)\frac{du}{dr} + \nu\frac{u}{r} + (1+\nu)A_2\ln\frac{r}{R}\right] \tag{101}$$

where $A_2 = \dfrac{\alpha_r(T_F-T_W)}{\ln\frac{a}{R}}$

Using (100) to substitute for u and $\frac{du}{dr}$ into (101) gives,

$$\sigma'_r = \frac{2G}{1-2\nu}\left[\left(\frac{A_1}{4}+\frac{B}{r^2}\right)(1-2\nu) + \frac{A_1}{2}\ln\frac{r}{R} - (1+\nu)A_2\ln\frac{r}{R}\right] \tag{102}$$

Similarly it can be shown that σ'_θ is given by,

$$\sigma'_\theta = -\frac{2G}{1-2\nu}\left[\left(\frac{A_1}{4}+\frac{B}{r^2}\right)(1-2\nu) - \frac{A_1}{2}\ln\frac{r}{R} + (1+\nu)A_2\ln\frac{r}{R}\right] \tag{103}$$

Using (102) and (103) to substitute for σ'_r, $\frac{d\sigma'_r}{dr}$ and σ'_θ into the equilibrium equation in terms of effective stress (49), gives,

$$\frac{dp_f}{dr} = -\frac{2G}{1-2\nu}\left[\frac{A_1}{r}(1-\nu) - \frac{A_2}{r}(1+\nu)\right]$$

which on integration and consideration of the condition $p_f = 0$ at $r = R$, gives,

$$p_f = -\frac{2G}{1-2\nu}\left[(1-\nu)A_1 - (1+\nu)A_2\right]\ln\frac{r}{R} \tag{104}$$

From (102) and (104) we get,

$$\sigma_r = \sigma'_r + p_f = 2G\left[\frac{A_1}{4} + \frac{B}{r^2} - \frac{A_1}{2}\ln\frac{r}{R}\right] \tag{105}$$

Using the condition that at $r = a$, $\sigma_r = 0$, allows B to be determined as

$$B = \frac{a^2A_1}{4}\left[2\ln\frac{a}{R} - 1\right]$$

Having found the unknown constant B, the stresses and pore pressure can now be summarised. As in Sections 2.3 to 2.5, the stresses and pore fluid pressure are prefixed by Δ, to show that they represent induced

stresses additional to the stress and pore pressure state given in Section 2.2.

Thus, for the condition $a \leq r \leq R$,

$$\Delta\sigma_r = \frac{G}{2}[n\beta_f + 3(1-n)\alpha_r]\frac{T_F-T_W}{\ln\frac{a}{R}}\left[\left(2\ln\frac{a}{R}-1\right)\frac{a^2}{r^2} - 2\ln\frac{r}{R} + 1\right] \quad (106)$$

$$\Delta\sigma_\theta = -\frac{G}{2}[n\beta_f + 3(1-n)\alpha_r]\frac{T_F-T_W}{\ln\frac{a}{R}}\left[\left(2\ln\frac{a}{R}-1\right)\frac{a^2}{r^2} + 2\ln\frac{r}{R} + 1\right] \quad (107)$$

$$\Delta p_f = -\frac{2G}{1-2\nu}\left[(1-\nu)n(\beta_f-3\alpha_r) + 2(1-2\nu)\alpha_r\right]\frac{T_F-T_W}{\ln\frac{a}{R}}\ln\frac{r}{R} \quad (108)$$

and from plane strain considerations it can be shown that $\Delta\sigma_z$ is given by

$$\Delta\sigma_z = -2G(1+\nu)\left[n(\beta_f-3\alpha_r) + 2\alpha_r\right]\frac{T_F-T_W}{\ln\frac{a}{R}}\ln\frac{r}{R} \quad (109)$$

For the condition $r \geq R$, $\Delta\sigma_z = 0$ and $\Delta p_f = 0$, and $\Delta\sigma_r$ and $\Delta\sigma_\theta$ are given by

$$\Delta\sigma_r = \frac{R^2}{r^2}.\Delta\sigma_R \quad (110)$$

$$\Delta\sigma_\theta = -\frac{R^2}{r^2}.\Delta\sigma_R \quad (111)$$

where $\Delta\sigma_R$ is the value of $\Delta\sigma_r$ in equation (106) for $r = R$.

At the wellbore wall (r=a) we get,

$$\Delta\sigma_r = 0 \quad (112)$$

$$\Delta\sigma_\theta = -2G\left[n\beta_f + 3(1-n)\alpha_r\right](T_F-T_W) \quad (113)$$

$$\Delta p_f = -\frac{2G}{1-2\nu}\left[(1-\nu)n(\beta_f-3\alpha_r) + 2(1-2\nu)\alpha_r\right](T_F-T_W) \quad (114)$$

and $$\Delta\sigma_z = -2G(1+\nu)[n(\beta_f-3\alpha_r) + 2\alpha_r](T_F-T_W) \quad (115)$$

2.7 TRANSIENT PORE FLUID PRESSURES IN LOW PERMEABILITY FORMATIONS

So far all solutions relating to fluid and heat flow have been obtained assuming a pseudo-steady state solution, and only the variation of distance R (defined in Figure 2.2 for fluid flow and Figure 2.4 for heat flow) can be related to time. However, the solutions may be inadequate for short times when the ratio R/a approaches 1 and secondly, the solution gives no quantitiative relation with time, and although it is known that R increases with time, the magnitude of time is unknown. This section sets out to provide a solution for the case of radial flow of pore fluid in low permeable formations, where it may be important to have a better understanding of the influence of time and its magnitude.

A limitation of this solution is that it cannot be coupled with any of the previous solutions by superposition. The redistribution of the in-situ stress state given in Sections 2.2 and 2.3 are too general for the transient solution presented here. Drained redistribution of the in-situ stress state would not be applicable since the transient solution given here is applicable to low permeability formations. Only if the formation were allowed to stand for a long period of time in balanced conditions, so that the pore pressure could equalize before the application of the imbalance, could these two solutions be superimposed; such a situation is unrealistic. The undrained in-situ stress and pore pressure redistribution given in Section 2.3 is applicable for the initial conditions, but since the pore pressure distibution varies with angle, as well as with radius, the fluid migration/flow will not be simply radial. Thus, the solution presented here is only applicable to the case of an isotropic in-situ stress field in the plane perpendicular to the well axis.

Since this transient solution cannot be superimposed onto solutions presented earlier, the pore pressures and stresses given are for both the in-situ stress state redistribution and the pore pressures and stresses induced by fluid flow.

For the case of axial symmetry the equilibrium equation in terms of effective stress and pore pressure is given by (49) in Section 2.4.

The two general 2-dimensional compatibility equation in terms of effective stress and pore pressure was presented in (30). For the case of axial symmetry the strain compatibility equation is given by

$$\frac{\partial \varepsilon_\theta}{\partial r} = \frac{\varepsilon_r - \varepsilon_\theta}{r}$$

Using the effective stress versions of the stress-strain equations, (20) and (21), and the axial symmetry equilibrium equation (49), strain compatibility is converted to the effective stress compatibility for axial symmetry given below,

$$\frac{\partial}{\partial r}\left[(1-\nu)(\sigma'_r + \sigma'_\theta) + p_f\right] = 0 \qquad (116)$$

The third and final differential equation leads to the diffusivity equation and is derived from considering flow in and out of an element (see Figure 2.6).

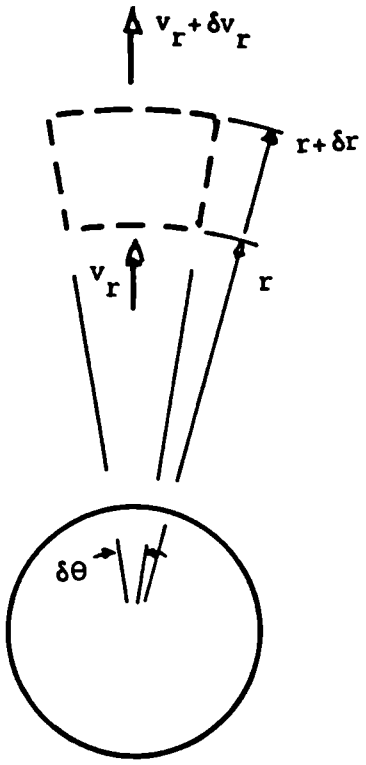
Assuming the element of rock to be of unit thickness, then the volume flow into the sample (Q_1) and the volume flow out of the sample (Q_2) are given by

$$Q_1 = v_r r.\delta\theta.\delta t$$

$$Q_2 = (v_r+\delta v_r)(r+\delta r)\delta\theta.\delta t$$

where v_r is the radial flow velocity,

and δt is an increment of time.



Transient radial fluid flow.

Figure 2.6

If it is assumed that both rock matrix and pore fluid are incompressible and the pore volume is saturated, then any volume change must be equal to the net fluid inflow/outflow. Thus, the reduction in volume (δV) of the element of rock is given by

$$\delta V = Q_2 - Q_1 = (\delta v_r r + v_r \delta r)\delta\theta . \delta t$$

The original volume of the element (V) is given by,

$$V = r . \delta r . \delta\theta$$

Therefore the increment of volumetric strain ($\delta\varepsilon_v$) is given by,

$$\delta\varepsilon_v = \frac{\delta V}{V} = \left[\frac{\delta v_r}{\delta r} + \frac{v_r}{r}\right]\delta t$$

which, in the limit, gives

$$\frac{\partial \varepsilon_v}{\partial t} = \frac{\partial v_r}{\partial r} + \frac{v_r}{r} \qquad (117)$$

From Darcy's Law,

$$v_r = - \frac{k}{\mu} \frac{\partial p_f}{\partial r}$$

where k is the absolute coefficient of permeability,

and μ is the viscosity of the fluid.

Therefore on substituting v_r in (117) we get

$$\frac{\partial \varepsilon_v}{\partial t} = - \frac{k}{\mu} \left(\frac{\partial^2 p_f}{\partial r^2} + \frac{1}{r} \frac{\partial p_f}{\partial r}\right) \qquad (118)$$

The relationship between stress and volumetric strain under plane strain conditions is given by (22) in Section 2.3. Using (118) to substitute for ε_v in (22) gives

$$\frac{\partial}{\partial t}(\sigma'_r + \sigma'_\theta) = - \frac{E\, k}{(1-2\nu)(1+\nu)\mu} \left(\frac{\partial^2 p_f}{\partial r^2} + \frac{1}{r} \frac{\partial p_f}{\partial r}\right) \qquad (119)$$

Integrating (116) gives,

$$(1-\nu)(\sigma'_r + \sigma'_\theta) + p_f = C(t) \tag{120}$$

where C is unknown function of t.

From the condition at $r \to \infty$ we have,

$$p_f = P_F, \quad \sigma'_r = \sigma_h - P_F \quad \text{and} \quad \sigma'_\theta = \sigma_h - P_F.$$

where σ_h is the isotropic in-situ stress field in the plane perpendicular to the well axis. (In general σ_h will be the horizontal stress.)

Therefore C is independent of time, and reduces to a constant and (120) becomes,

$$\sigma'_r + \sigma'_\theta = - \frac{p_f}{1-\nu} + 2\sigma_h - \frac{1-2\nu}{1-\nu} P_F \tag{121}$$

Using (121), σ'_r and σ'_θ can be eliminated from (119) giving the diffusivity equation,

$$\frac{\partial p_f}{\partial t} = \kappa \left(\frac{\partial^2 p_f}{\partial r^2} + \frac{1}{r} \frac{\partial p_f}{\partial r} \right) \tag{122}$$

where $\kappa = \frac{(1-\nu)E\ k}{(1-2\nu)(1+\nu)\mu}$

and κ is referred to as the diffusion coefficient.

The solution for p_f will be a function of r and t,

i.e. $p_f = p_f(r,t)$

The boundary conditions are,

$$p_f(r=a,\ t) = P_W$$

$$p_f(r>a,\ 0) = P_F$$

$$p_f(r,\ t=\infty) = P_W$$

and $$P_f(r=\infty,\ t) = P_F$$

The solution to (122) together with the imposed boundary conditions can be found in Carslaw and Jaeger[57] for the analagous problem of heat flow

in a hollow cylinder of infinite height and outer radius. The solution is

$$p_f = P_W + \frac{2(P_W-P_F)}{\pi}\int_0^{\infty} e^{-\kappa u^2 t}.\frac{J_0(ur)Y_0(ua) - Y_0(ur)J_0(ua)}{J_0^2(ua) + Y_0^2(ua)}.\frac{du}{u}.dr \qquad (123)$$

where J_0 is the Bessel function of the first order and the first kind, given by,

$$J_0(x) = \sum_{m=0}^{\infty}\frac{(-1)^{m-1}x^{2m}}{2^{2m}(m!)^2}$$

and Y_0 is the Bessel function of the first order and the second kind, and given by,

$$Y_0(x) = \frac{2}{\pi}\left[J_0(x)(\ln\frac{x}{2} + \gamma) + \sum_{m=1}^{\infty}\frac{(-1)^{m-1}h_m x^{2m}}{2^{2m}(m!)^2}\right]$$

and $h_m = \sum_{n=1}^{m}\frac{1}{n}$

The form of (123) is not readily usable and it would require a rigorous computer code to calculate p_f by numerical integration, since the Bessel functions oscillate and can be extremely slow in converging. Carslaw and Jaeger give the following approximate solution of (123) suitable for small times (small being defined as $\kappa t/a^2 < 0.02$),

$$p_f = P_F + (P_W-P_F)\frac{\sqrt{a}}{\sqrt{r}}\text{erfc}\frac{r-a}{2\sqrt{(\kappa t)}} + (P_W-P_F)\frac{(r-a)\sqrt{(\kappa t)}}{4\sqrt{(ar^3)}}\text{ierfc}\frac{r-a}{2\sqrt{(\kappa t)}} +$$

$$+ (P_W-P_F)\frac{(9a^2-2ar-7r^2)\kappa t}{32\sqrt{(a^3r^5)}}i^2\text{erfc}\frac{r-a}{2\sqrt{(\kappa t)}} + \ldots. \qquad (124)$$

where erfc is the converse of the error function erf, so that

$$\text{erfc}(x) = 1 - \text{erf}(x) = \frac{2}{\sqrt{\pi}}\int_x^{\infty} e^{-\xi^2}d\xi$$

and $$i^n\text{erfc}(x) = \int_x^{\infty} i^{n-1}\text{erfc}(\xi)d\xi \quad n = 1,2,3\ldots$$

with $$i^0\text{erfc}(x) = \text{erfc}(x)$$

Although the small time solution is more readily usable, since many main frame computers have the calculation of the error function and its derivatives available as standard routines, few engineers would welcome the prospect of handling such a solution. Probably the easiest approach is to use published dimensionless results tabulated for the solution of (123) (e.g. Jaeger[58]). The table produced by Jaeger is presented in Table 1; the parameter τ is given by Kt/a^2. A graphical representation of Table 1 is shown in Figure 2.7.

Once the pore pressure distribution has been established for a specified time, it remains to find expressions for the radial and circumferential stresses.

Using (121) to substitute for σ'_θ into the equilibrium equation (49), then

$$\frac{\partial \sigma'_r}{\partial r} + \frac{2\sigma'_r}{r} = -\frac{\partial p_f}{\partial r} - \frac{p_f}{(1-\nu)r} - \frac{1-2\nu}{(1-\nu)r} P_F + \frac{2\sigma_h}{r}$$

From integration and rearranging we get,

$$\sigma'_r = -p_f + \frac{1-2\nu}{(1-\nu)r^2}\int_0^r p_f r \, dr + \sigma_h - \frac{1-2\nu}{2(1-\nu)}P_F + \frac{C_3(t)}{r^2}$$

and by adding the pore fluid pressure in accordance with the effective stress relationship (18) in Section 2.3, we get,

$$\sigma_r = \frac{1-2\nu}{(1-\nu)r^2}\int_0^r p_f r \, dr + \sigma_h - \frac{1-2\nu}{2(1-\nu)}P_F + \frac{C_3(t)}{r^2} \qquad (125)$$

where $C_3(t)$ is an unknown function of t.

From the boundary condition we have at $r = a$, $\sigma_r = P_W$.

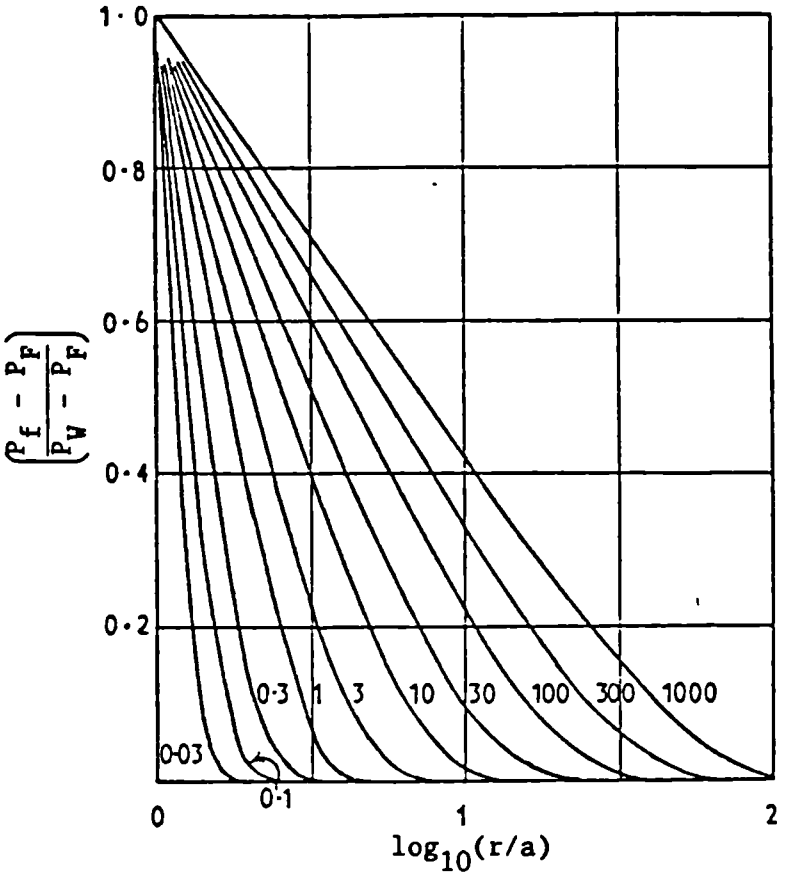
Since the boundary condition is independent of t, C_3 reduces to a constant, and is given by

$$C_3 = a^2 P_W - \frac{1-2\nu}{1-\nu}\int_0^a p_f r \, dr - a^2\sigma_h + \frac{1-2\nu}{2(1-\nu)}a^2 P_F$$

τ	r/a													
	1.0	1.1	1.2	1.3	1.4	1.5	1.6	1.7	1.8	1.9	2.0	3.0	4.0	5.0
0.001	1.000	0.024												
0.002	1.000	0.109	0.001											
0.003	1.000	0.188	0.009											
0.004	1.000	0.251	0.023	0.001										
0.005	1.000	0.303	0.042	0.002										
0.006	1.000	0.345	0.062	0.005										
0.007	1.000	0.380	0.083	0.010	0.001									
0.008	1.000	0.410	0.104	0.016	0.001									
0.009	1.000	0.435	0.124	0.022	0.002									
0.01	1.000	0.458	0.144	0.030	0.004									
0.02	1.000	0.589	0.290	0.117	0.039	0.010	0.002							
0.03	1.000	0.652	0.379	0.194	0.087	0.034	0.011	0.003	0.001					
0.04	1.000	0.691	0.439	0.254	0.133	0.063	0.027	0.010	0.004	0.001				
0.05	1.000	0.718	0.483	0.302	0.175	0.093	0.046	0.021	0.009	0.003	0.001			
0.06	1.000	0.739	0.517	0.341	0.211	0.122	0.066	0.033	0.016	0.007	0.003			
0.07	1.000	0.754	0.544	0.373	0.242	0.149	0.087	0.047	0.024	0.012	0.005			
0.08	1.000	0.767	0.566	0.400	0.270	0.174	0.106	0.062	0.034	0.018	0.009			
0.09	1.000	0.779	0.585	0.423	0.294	0.196	0.125	0.077	0.045	0.025	0.013			
0.1	1.000	0.787	0.601	0.443	0.316	0.217	0.143	0.091	0.055	0.032	0.018			
0.2	1.000	0.837	0.691	0.562	0.450	0.355	0.275	0.209	0.156	0.114	0.082	0.001		
0.3	1.000	0.860	0.733	0.620	0.519	0.430	0.352	0.286	0.229	0.181	0.142	0.006		
0.4	1.000	0.873	0.758	0.655	0.562	0.479	0.405	0.339	0.282	0.233	0.191	0.015		
0.5	1.000	0.883	0.776	0.680	0.592	0.514	0.443	0.380	0.323	0.274	0.230	0.027	0.001	
0.6	1.000	0.890	0.789	0.698	0.615	0.540	0.472	0.411	0.356	0.307	0.263	0.040	0.003	
0.7	1.000	0.895	0.800	0.713	0.634	0.562	0.496	0.436	0.382	0.334	0.290	0.054	0.006	
0.8	1.000	0.899	0.808	0.725	0.649	0.579	0.515	0.457	0.405	0.357	0.313	0.068	0.009	0.001
0.9	1.000	0.903	0.815	0.735	0.661	0.594	0.532	0.475	0.424	0.377	0.334	0.082	0.013	0.001
1	1.000	0.906	0.821	0.743	0.672	0.606	0.546	0.491	0.440	0.394	0.351	0.095	0.018	0.002
2	1.000	0.924	0.854	0.790	0.732	0.677	0.627	0.580	0.536	0.496	0.458	0.194	0.071	0.022
3	1.000	0.932	0.870	0.812	0.760	0.711	0.665	0.623	0.583	0.546	0.511	0.256	0.119	0.049
4	1.000	0.937	0.879	0.826	0.777	0.731	0.689	0.649	0.612	0.577	0.544	0.300	0.157	0.076
5	1.000	0.940	0.886	0.835	0.789	0.746	0.706	0.668	0.633	0.599	0.568	0.332	0.188	0.101
6	1.000	0.943	0.890	0.842	0.798	0.757	0.718	0.682	0.648	0.616	0.586	0.357	0.214	0.123
7	1.000	0.945	0.894	0.805	0.848	0.765	0.728	0.693	0.661	0.630	0.601	0.378	0.235	0.142
8	1.000	0.946	0.898	0.853	0.811	0.773	0.737	0.703	0.671	0.641	0.613	0.395	0.254	0.159
9	1.000	0.948	0.900	0.857	0.816	0.779	0.743	0.711	0.680	0.650	0.623	0.409	0.270	0.175
10	1.000	0.949	0.903	0.860	0.820	0.784	0.749	0.717	0.687	0.658	0.631	0.422	0.284	0.189
20	1.000	0.956	0.916	0.879	0.845	0.813	0.783	0.756	0.729	0.704	0.681	0.497	0.370	0.277
30	1.000	0.959	0.922	0.888	0.856	0.827	0.800	0.774	0.750	0.726	0.705	0.534	0.415	0.325
40	1.000	0.962	0.926	0.894	0.864	0.836	0.810	0.786	0.762	0.741	0.720	0.558	0.444	0.358
50	1.000	0.963	0.929	0.898	0.869	0.843	0.818	0.794	0.772	0.751	0.731	0.574	0.464	0.381
60	1.000	0.964	0.931	0.901	0.874	0.848	0.823	0.800	0.779	0.759	0.739	0.588	0.481	0.399
70	1.000	0.965	0.933	0.904	0.877	0.851	0.823	0.806	0.785	0.765	0.746	0.598	0.494	0.414
80	1.000	0.966	0.935	0.906	0.879	0.855	0.832	0.810	0.789	0.770	0.752	0.607	0.505	0.427
90	1.000	0.966	0.936	0.908	0.882	0.857	0.835	0.813	0.793	0.774	0.756	0.614	0.514	0.437
100	1.000	0.967	0.937	0.909	0.884	0.860	0.838	0.817	0.797	0.778	0.760	0.621	0.522	0.446
200	1.000	0.970	0.943	0.919	0.895	0.874	0.854	0.835	0.817	0.800	0.784	0.658	0.569	0.500
300	1.000	0.972	0.946	0.923	0.901	0.881	0.862	0.844	0.827	0.811	0.796	0.677	0.593	0.529
400	1.000	0.973	0.948	0.926	0.905	0.886	0.867	0.850	0.834	0.819	0.804	0.690	0.609	0.546
500	1.000	0.974	0.950	0.928	0.908	0.889	0.871	0.855	0.839	0.824	0.810	0.699	0.620	0.559
600	1.000	0.974	0.951	0.930	0.910	0.891	0.874	0.858	0.842	0.828	0.814	0.706	0.629	0.569
700	1.000	0.975	0.952	0.931	0.912	0.893	0.877	0.861	0.846	0.831	0.818	0.712	0.636	0.578
800	1.000	0.975	0.953	0.932	0.913	0.895	0.879	0.863	0.848	0.834	0.821	0.716	0.642	0.585
900	1.000	0.976	0.954	0.933	0.914	0.897	0.880	0.865	0.850	0.837	0.824	0.720	0.647	0.591
1000	1.000	0.976	0.954	0.934	0.915	0.898	0.882	0.867	0.852	0.839	0.826	0.724	0.652	0.596

Tabulated values of $\left(\frac{P_f - P_F}{P_W - P_F}\right)$ for varying values of time and radius.

TABLE 1 (after Jaeger[58])



Pore fluid pressure profiles as a function of distance and time. The numbers on the curves are the values of τ (= Kt/a^2).

Figure 2.7 (after Jaeger[58])

Thus, (125) becomes

$$\sigma_r = \sigma_h - \frac{a^2}{r^2}(\sigma_h - P_W) + \frac{1-2\nu}{(1-\nu)r^2}\int_a^r r(p_f-P_F)dr \qquad (126)$$

Simililarly, it can be shown that σ_θ is given by

$$\sigma_\theta = \sigma_h + \frac{a^2}{r^2}(\sigma_h - P_W) + \frac{1-2\nu}{1-\nu}(p_f - P_F) - \frac{(1-2\nu)}{r^2}\int_a^r r(p_f-P_F)dr \qquad (127)$$

and from plane strain considerations that σ_z is given by

$$\sigma_z = \sigma_{zz} + \nu(\sigma_r+\sigma_\theta-2\sigma_h) + (p_f-P_F)(1-2\nu) \qquad (128)$$

where σ_{zz} is the pre-existing axial in-situ stress (which in practice will be the overburden, or vertical stress σ_v).

Although the intergrand in (126) and (127) can be integrated by parts, the resulting derivatives of the Bessel functions are not readily usable, and it is simpler to integrate the product $(r.p_f)$ numerically using the results for p_f given in Table 1. Thus, rewriting the intergrand in (126) and (127) as

$$\Omega = \frac{1}{(P_W-P_F)r^2}\int_a^r r(p_f-P_F)dr \qquad (129)$$

where values for Ω have been calculated numerically and given in Table 2, σ_r and σ_θ can be expressed as

$$\sigma_r = \sigma_h - \frac{a^2}{r^2}(\sigma_h-P_W) + \frac{1-2\nu}{1-\nu}(P_W-P_F)\Omega \qquad (130)$$

$$\sigma_\theta = \sigma_h + \frac{a^2}{r^2}(\sigma_h-P_W) + \frac{1-2\nu}{1-\nu}(p_f-P_F) - \frac{1-2\nu}{1-\nu}(P_W-P_F)\Omega \qquad (131)$$

In conclusion the pore pressures for the transient state fluid migration/ flow is given in (123), or for small times relavent to low

τ	r/a													
	1.0	1.1	1.2	1.3	1.4	1.5	1.6	1.7	1.8	1.9	2.0	3.0	4.0	5.0
0.001	0.000	0.043	0.037	0.032	0.027	0.024	0.021	0.019	0.017	0.015	0.013	0.012	0.011	0.010
0.002	0.000	0.047	0.044	0.037	0.032	0.028	0.025	0.022	0.019	0.017	0.016	0.014	0.013	0.012
0.003	0.000	0.050	0.050	0.043	0.037	0.032	0.028	0.025	0.022	0.020	0.018	0.016	0.015	0.014
0.004	0.000	0.053	0.055	0.048	0.041	0.036	0.032	0.028	0.025	0.023	0.020	0.018	0.017	0.015
0.005	0.000	0.056	0.060	0.053	0.046	0.040	0.035	0.031	0.028	0.025	0.022	0.020	0.018	0.017
0.006	0.000	0.057	0.064	0.057	0.049	0.043	0.038	0.034	0.030	0.027	0.024	0.022	0.020	0.018
0.007	0.000	0.059	0.068	0.061	0.053	0.046	0.041	0.036	0.032	0.029	0.026	0.024	0.021	0.020
0.008	0.000	0.060	0.071	0.065	0.056	0.049	0.043	0.038	0.034	0.031	0.028	0.025	0.023	0.021
0.009	0.000	0.061	0.074	0.068	0.059	0.052	0.046	0.040	0.036	0.032	0.029	0.026	0.024	0.022
0.01	0.000	0.063	0.076	0.071	0.063	0.055	0.048	0.043	0.038	0.034	0.031	0.028	0.025	0.023
0.02	0.000	0.068	0.092	0.093	0.086	0.076	0.067	0.060	0.053	0.048	0.043	0.039	0.036	0.033
0.03	0.000	0.071	0.101	0.107	0.102	0.092	0.083	0.074	0.066	0.059	0.053	0.048	0.044	0.040
0.04	0.000	0.073	0.106	0.116	0.113	0.105	0.095	0.085	0.076	0.069	0.062	0.056	0.051	0.047
0.05	0.000	0.074	0.110	0.123	0.122	0.115	0.105	0.095	0.086	0.077	0.070	0.063	0.058	0.053
0.06	0.000	0.075	0.113	0.128	0.129	0.123	0.114	0.104	0.094	0.085	0.077	0.070	0.063	0.058
0.07	0.000	0.076	0.115	0.132	0.135	0.130	0.121	0.111	0.101	0.092	0.083	0.076	0.069	0.063
0.08	0.000	0.076	0.117	0.135	0.140	0.136	0.128	0.118	0.108	0.098	0.089	0.081	0.074	0.068
0.09	0.000	0.077	0.119	0.138	0.144	0.141	0.134	0.124	0.114	0.104	0.095	0.086	0.079	0.072
0.1	0.000	0.077	0.120	0.141	0.147	0.146	0.139	0.130	0.119	0.109	0.100	0.091	0.083	0.076
0.2	0.000	0.079	0.128	0.155	0.168	0.173	0.171	0.165	0.157	0.148	0.138	0.127	0.116	0.106
0.3	0.000	0.081	0.131	0.162	0.179	0.186	0.187	0.184	0.178	0.170	0.161	0.150	0.137	0.125
0.4	0.000	0.081	0.133	0.166	0.185	0.194	0.197	0.195	0.192	0.185	0.177	0.166	0.151	0.138
0.5	0.000	0.082	0.135	0.168	0.189	0.200	0.205	0.205	0.202	0.196	0.189	0.178	0.163	0.149
0.6	0.000	0.082	0.136	0.171	0.192	0.205	0.210	0.212	0.209	0.205	0.199	0.187	0.172	0.157
0.7	0.000	0.082	0.137	0.172	0.195	0.208	0.215	0.217	0.216	0.212	0.206	0.195	0.179	0.164
0.8	0.000	0.082	0.137	0.173	0.197	0.211	0.219	0.221	0.221	0.218	0.213	0.202	0.185	0.170
0.9	0.000	0.082	0.138	0.175	0.199	0.213	0.222	0.225	0.225	0.222	0.218	0.207	0.191	0.175
1	0.000	0.083	0.138	0.176	0.200	0.215	0.224	0.228	0.229	0.227	0.223	0.212	0.196	0.180
2	0.000	0.083	0.141	0.181	0.208	0.227	0.239	0.246	0.250	0.250	0.249	0.241	0.225	0.208
3	0.000	0.084	0.142	0.183	0.212	0.232	0.246	0.254	0.259	0.262	0.262	0.255	0.241	0.224
4	0.000	0.084	0.143	0.185	0.215	0.235	0.250	0.260	0.266	0.269	0.270	0.264	0.251	0.235
5	0.000	0.084	0.144	0.186	0.216	0.238	0.253	0.263	0.270	0.274	0.276	0.271	0.258	0.242
6	0.000	0.084	0.144	0.187	0.217	0.239	0.255	0.266	0.273	0.277	0.280	0.276	0.264	0.248
7	0.000	0.084	0.144	0.186	0.217	0.241	0.257	0.268	0.276	0.281	0.283	0.280	0.268	0.253
8	0.000	0.084	0.144	0.188	0.219	0.242	0.258	0.270	0.278	0.283	0.286	0.283	0.272	0.258
9	0.000	0.084	0.145	0.188	0.220	0.243	0.260	0.271	0.280	0.285	0.288	0.285	0.275	0.261
10	0.000	0.084	0.145	0.189	0.220	0.244	0.261	0.273	0.281	0.287	0.290	0.288	0.278	0.264
20	0.000	0.085	0.146	0.191	0.224	0.248	0.267	0.280	0.290	0.297	0.302	0.301	0.293	0.282
30	0.000	0.085	0.146	0.192	0.225	0.250	0.269	0.284	0.294	0.302	0.307	0.307	0.301	0.291
40	0.000	0.085	0.147	0.192	0.226	0.252	0.271	0.286	0.297	0.305	0.311	0.311	0.306	0.297
50	0.000	0.085	0.147	0.193	0.227	0.253	0.273	0.287	0.299	0.307	0.313	0.314	0.310	0.301
60	0.000	0.085	0.147	0.193	0.228	0.254	0.274	0.289	0.300	0.309	0.315	0.317	0.312	0.304
70	0.000	0.085	0.147	0.193	0.228	0.254	0.274	0.289	0.301	0.310	0.317	0.318	0.314	0.307
80	0.000	0.085	0.148	0.194	0.229	0.255	0.275	0.291	0.302	0.311	0.318	0.320	0.316	0.309
90	0.000	0.085	0.148	0.194	0.229	0.255	0.276	0.291	0.303	0.312	0.319	0.321	0.318	0.311
100	0.000	0.085	0.148	0.194	0.229	0.256	0.276	0.292	0.304	0.313	0.320	0.322	0.319	0.312
200	0.000	0.085	0.148	0.195	0.231	0.258	0.279	0.295	0.308	0.318	0.325	0.329	0.327	0.322
300	0.000	0.086	0.148	0.196	0.231	0.259	0.280	0.297	0.310	0.320	0.328	0.332	0.331	0.326
400	0.000	0.086	0.149	0.196	0.232	0.260	0.281	0.298	0.311	0.322	0.330	0.334	0.333	0.329
500	0.000	0.086	0.149	0.196	0.232	0.260	0.282	0.299	0.313	0.323	0.331	0.336	0.335	0.332
600	0.000	0.086	0.149	0.196	0.233	0.261	0.283	0.300	0.313	0.324	0.332	0.337	0.336	0.333
700	0.000	0.086	0.149	0.196	0.233	0.261	0.283	0.300	0.314	0.325	0.333	0.338	0.338	0.335
800	0.000	0.086	0.149	0.197	0.233	0.261	0.283	0.301	0.314	0.325	0.334	0.339	0.339	0.336
900	0.000	0.086	0.149	0.197	0.233	0.262	0.284	0.301	0.315	0.326	0.335	0.339	0.339	0.337
1000	0.000	0.086	0.149	0.197	0.233	0.262	0.284	0.301	0.315	0.326	0.335	0.340	0.340	0.338

Tabulated values of Q for varying values of time and radius.

Q as defined by equation (129).

TABLE 2

permeability formations by equation (124). More realistically, the pore pressure can be obtained using Figure 2.7, or Table 1 by converting the variables to the relavent dimensionless parameters. The stresses σ_r and σ_θ can be found using (130) and (131) by again using Table 1 to find p_f, and using Table 2 to find the dimesionless parameter Ω.

2.8 PARAMETRIC STUDY - STEADY STATE CONDITIONS

Using the equations presented in Sections 2.2 to 2.6, this section studies the influence of the various parameters on wellbore stability and discusses the implications. A quantitative example is used to examine the parameters. Section 2.8.1 sets out the problem definition, and Section 2.8.3 discusses the results obtained.

2.8.1 Problem Definition

2.8.1.1 Material Behaviour

To use the solutions to their full potential two material types are considered. The first material represents a permeable formation and shall be referred to as a sandstone. The second material represents a low permeability material and shall be referred to as a shale formation.

The sandstone is considered sufficiently permeable that drained conditions apply. Also, due to its permeable nature, the drilling fluid is capable of froming an effective mud cake at the wellbore wall. It shall be assumed that the mud cake parameter (h), as defined in equation (61), is equal to 0.2.

The permeability of the shale is considered to be sufficiently small that the two extreme conditions of undrained (short term) and fully drained (long term) must be analysed. In the undrained case no fluid flow takes place across the boundary of the wellbore wall, which is equivalent to having the mud cake parameter equal to zero. For the fully drained case it is considered that, due to the low permeability of the formation, only a poor mud cake is formed; in this case the mud cake parameter is taken to be equal to 0.9. For the undrained behaviour of the shale formation it is also necessary to know the porosity of the rock (n), (see Section 2.6); in this study the porosity is taken as 0.05.

The remaining material properties are taken to apply for both the sandstone and the shale formations

- Compressive shear failure is defined by the Mohr-Coulomb criterion given by,

  $$\sigma_1' = \frac{1 + \sin\phi}{1 - \sin\phi} \cdot \sigma_3' + \frac{2c \cos\phi}{1 - \sin\phi}$$

  where σ_1' is the maximum principal effective stress at failure,

  σ_3' is the minimum principal effective stress at failure,

  c is the rock cohesion and equal to 4.8 MPa (700 psi),

  and ϕ is the angle of friction and equal to 30°.

- Tensile strength, σ_t is 1.7 MPa (250 psi).
- Youngs Modulus, E is 6.9 GPa (10^6 psi).
- Poissons Ratio, ν is 0.25.
- Thermal coefficient of linear expansion, α_r is 10^{-5} /°C.

2.8.1.2 In-Situ Stress State

The in-situ stress field will be one of the most difficult set of parameters to quantify (Klein and McLean[30]), here it shall be assumed that the stress field consists of a vertical and two unequal horizontal principal stresses, with the maximum horizontal principal stress (σ_H) direction taken as 135°/315°, i.e. NW/SE (this conforms roughly with the North Sea regional trend given by Klein and Barr[17]). The vertical principal stress, σ_v, is assumed to be equivalent to the overburden, taken to be 0.023 MPa/m (1.0 psi/ft). The stress gradient of the minimum horizontal principal stress, σ_h, is taken to be 0.016 MPa/m (0.7 psi/ft) (Klein and McLean[30] quote values between 0.014 and 0.018 MPa/m (0.6 and 0.8 psi/ft) for a U.K. land well), and σ_H is given a gradient of 0.019 MPa/m (0.85 psi/ft) (i.e. between σ_v and σ_h).

2.8.1.3 Well Azimuth

The effect of well deviation is studied by considering the two extreme conditions of a well deviated parallel to σ_H and then deviated parallel to σ_h. For analysis of the effect of other parameters on stability (e.g. temperature gradients) the well is considered to be vertical.

2.8.1.4 Remaining Parameters

The following are the values taken for the depth, drilling fluid and formation temperatures, and the volume coefficient of expansion of the pore fluid (undrained response of shale only).

- depth = 1820 m (6000 ft),
- formation temperature, T_F = 70°C,
- formation pressure gradient = 0.011 MPa/m (0.45 psi/ft),
- mud temperature, T_W = 30°C,
- pore fluid volumetric coefficient of thermal expansion, $\beta_f = 2 \times 10^{-4}$ /°C.

2.8.1.5 Failure Mechanisms

Normally the only parameter that can be feasibly adjusted during drilling operations is the mud density. Thus, in the following analysis the mud densities (S.G.) required to prevent compressive and tensile failures are calculated and plotted against variations in the other parameters.

As stated in Section 1.2.2, mechanical instability can occur in three distinct modes (tensile fracture, brittle compressive failure and ductile compressive failure). In the following study only tensile and compressive failure shall be considered, and no distincton shall be made between ductile and brittle failure.

It is considered here that the most critical condition for failure initiation will be at the wellbore wall. For simple linear elasticity with no induced pore pressure gradients this will be the case. However, for low permeability materials that suffer sudden reductions in well pressure this may not apply. This aspect of wellbore instability is covered in more detail in Section 2.9.4.

In the case of the well axis being parallel to a principal stress

SECTION THROUGH DEVIATED WELLBORE

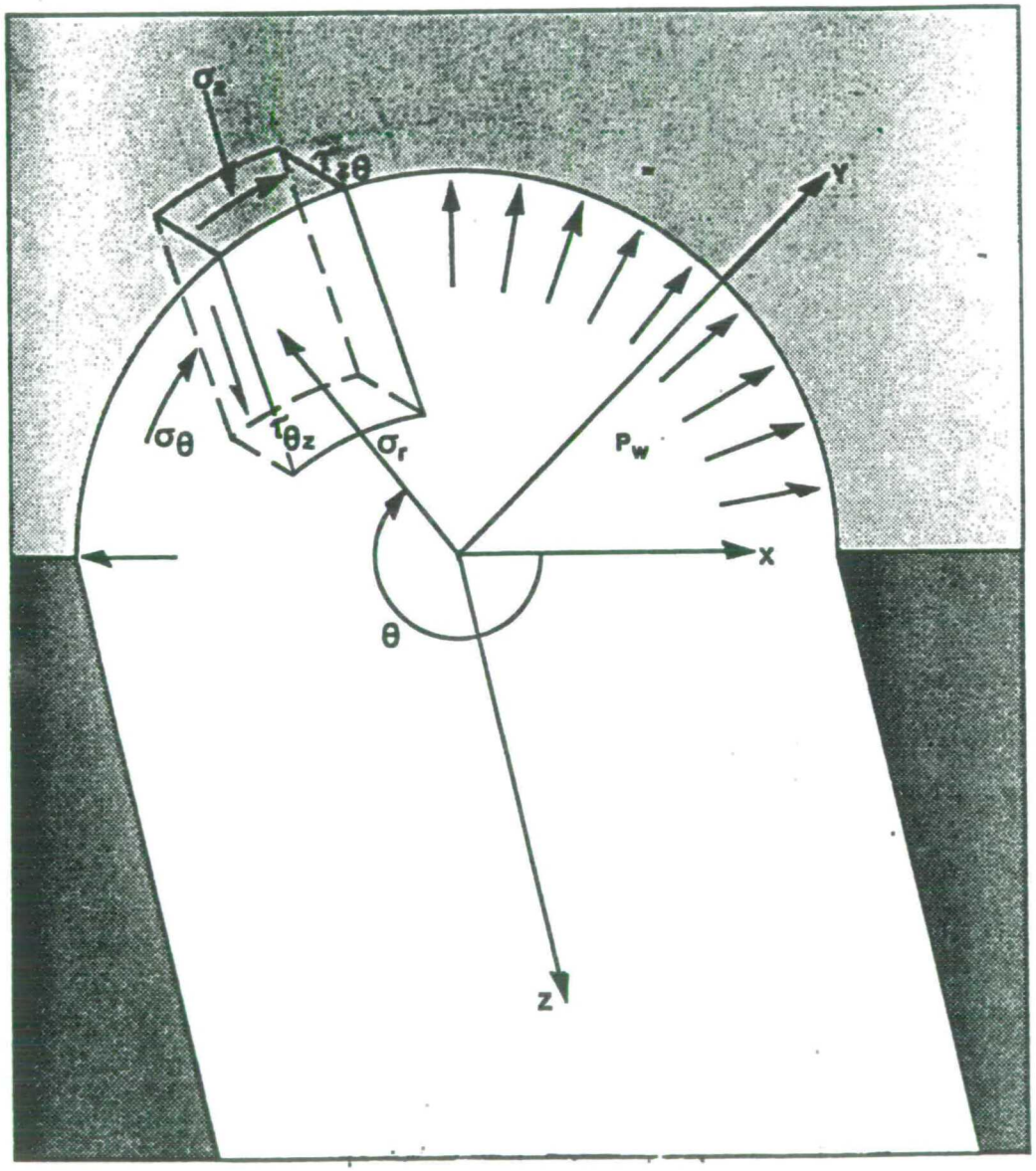


Figure 2.8

direction, compressive failure can be found by considering either the axial stress (σ'_z) or the circumferential stress (σ'_θ) to be the maximum principal effective stress, and the radial stress (σ'_r) to be the minimum. Tensile failure will normally be due to σ'_θ becoming less than the tensile strength of the rock due to excessive mud pressure. For the case of a perfect mud cake (h=0) tensile fracture could not be initiated in a plane perpendicular to σ_z, since increasing the well pressure (P_w) would have no influence on σ_z (refer to equation (71)), nor on the pore fluid pressure (refer to equation (68)). However, if h > 0 (influx of drilling fluid into the formation), then there is a possibility that the axial effective stress, σ'_z, may become tensile, so this form of tensile failure must be considered.

For the general case of a deviated well the influence of the shear stress $\tau_{\theta z}$ (see Figure 2.8) on the maximum and minimum principal stresses at failure must be considered according to the relationship

$$\sigma_1, \sigma_3 = \frac{\sigma_\theta + \sigma_z}{2} \pm \left[\left(\frac{\sigma_\theta - \sigma_z}{2}\right)^2 + \tau_{\theta z}^2\right]^{\frac{1}{2}}$$

2.8.2 Relevant Equations

The resultant values of the stresses and pore pressures for the three material responses (i.e 'Sandstone', 'Shale' - undrained response, and 'Shale' - drained response) are made up of the various contributions due to fluid flow, temperature etc. These values are calculated from the equation numbers given below (the numbers in brackets represent the relevant equation number). The only difference between the behaviour of the sandstone and the drained shale response is in the mud cake parameter (h).

	Section 2.2	Section 2.3	Section 2.4	Section 2.5	Section 2.6

Sandstone (h=0.2) and Drained Shale (h=0.9) Response

$$\sigma_r = \sigma_r(14) + \Delta\sigma_r(69)$$

$$\sigma_\theta = \sigma_\theta(15) + \Delta\sigma_\theta(70) + \Delta\sigma_\theta(84)$$

$$\sigma_z = \sigma_z(16) + \Delta\sigma_z(71) + \Delta\sigma_z(85)$$

$$\tau_{\theta z} = \tau_{\theta z}(17)$$

$$p_f = p_f(13) + \Delta p_f(68)$$

Undrained Shale (h=0) Response

$$\sigma_r = \sigma_r(14) + \Delta\sigma_r(69)$$

$$\sigma_\theta = \sigma_\theta(15) + \Delta\sigma_\theta(70) + \Delta\sigma_\theta(113)$$

$$\sigma_z = \sigma_z(16) + \Delta\sigma_z(46) + \Delta\sigma_z(71) + \Delta\sigma_z(115)$$

$$\tau_{\theta z} = \tau_{\theta z}(17)$$

$$p_f = p_f(13) + \Delta p_f(45) + \Delta p_f(68) + \Delta p_f(114)$$

Using these equations with the input parameters, failure criteria and failure mechanisms given in Sections 2.8.1.1 - 2.8.1.5, the mud weights required to prevent failure were analysed using a simple computer program. The results are presented and discussed below.

2.8.3 Results

2.8.3.1 Effect of Well Azimuth

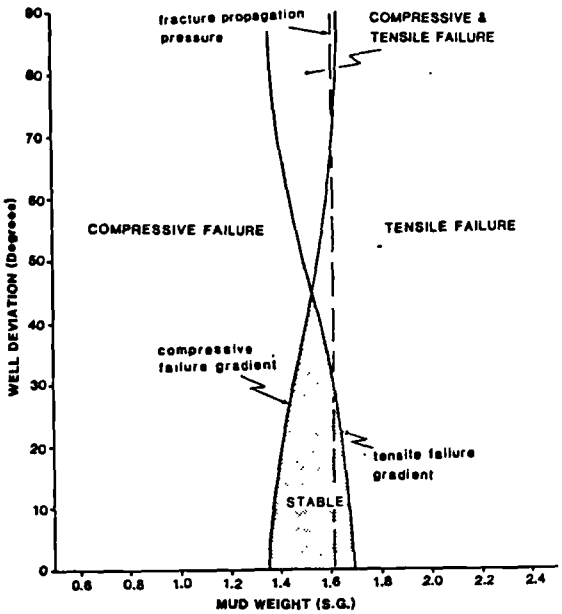
The effect of well azimuth on stability is analysed by varying well direction and deviation while the remaining input parameters are kept constant. Two well directions are considered (i) the well deviated in a NW/SE (135°/315°) direction , i.e. in the same direction as the assumed maximum horizontal principal stress, and (ii) deviation in a NE/SW

(45°/225°) direction, i.e. parallel to the minimum principal stress direction. The results are shown in Figures 2.9 - 2.14.

The tensile failure gradient is the mud weight at which a tensile fracture at the wellbore wall will just be initiated; higher mud weights may cause instability through unintentional hydraulic fracture. The fracture propagation pressure is the mud weight required to overcome the minimum principal in-situ stress, and is therefore independent of well deviation or direction. Where the tensile fracture gradient is greater than the fracture propagation pressure (e.g. Figure 2.10), then if the initiation pressure is exceeded the fracture may extend far into the formation. Where the tensile fracture gradient is less than the fracture propagation pressure (e.g. Figure 2.13), then even if the fracture initiation pressure is exceeded, instability may not occur until the mud weight exceeds the propagation pressure.

The compressive failure gradient is the mud weight required to support the well and prevent the compressive axial or hoop stresses from exceeding the compressive strength of the rock at the wall. At mud weights less than the compressive gradient, then compressive instability may occur causing hole enlargment or hole closure.

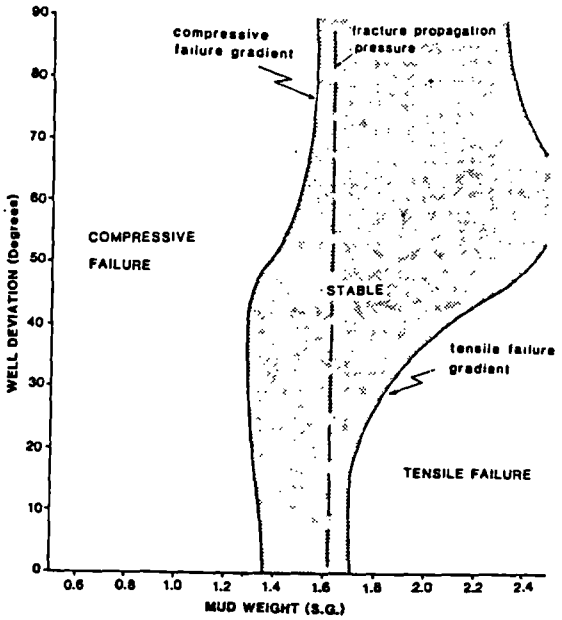
Provided the tensile failure gradient is greater than the compressive failure gradient, there will exist a region of 'safe' mud weights over which the well will be stable and neither compressive nor tensile failure will occur (e.g. Figures 2.9, 2.10). However, if the tensile failure gradient is less than the compressive failure gradient, there will be no range of safe mud weights (e.g. Figure 2.13).



Material :- 'Sandstone' - Well deviated // to σ_H

Variation of failure initiation gradients with well deviation

Figure 2.9



Material :- 'Sandstone' - Well deviated // to σ_h

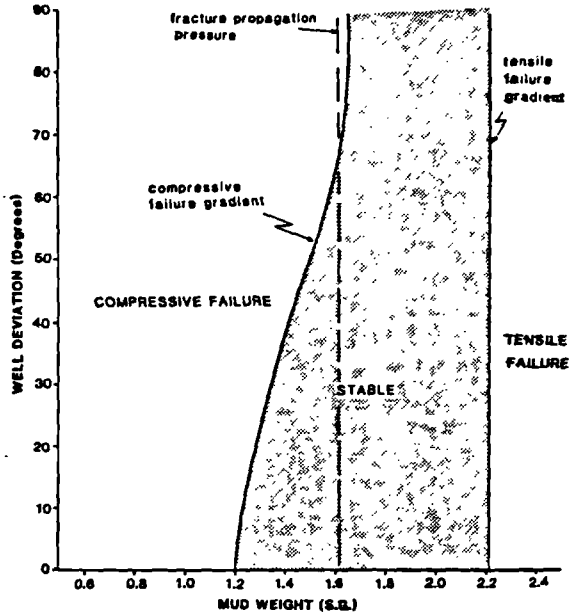
Variation of failure initiation gradients with well deviation

Figure 2.10

For the sandstone it can be seen from Figure 2.9 that there exists a safe range of mud weights for low deviations when drilling in a direction parallel to σ_H, but at higher deviations the well becomes more prone to both tensile and compressive failure, until at around 45° deviation the failure gradients cross, making the well potentially unstable for all mud weights. However, a well deviated parallel to σ_h, becomes less prone to compressive failure as it is deviated up to around 50° and for tensile failure the vertical well is the least stable case.

From Figures 2.11 - 2.14, it can be seen that the shale behaviour in both drained and undrained conditions, has the same tendency as the sandstone in that wells deviated in a direction parallel to σ_h are more stable than those parallel to σ_H. However, from Figures 2.13 and 2.14 it can be seen that for the drained shale response, apart from a small area in Figure 2.14, the well will be unstable for all well azimuths, whatever the mud weight.

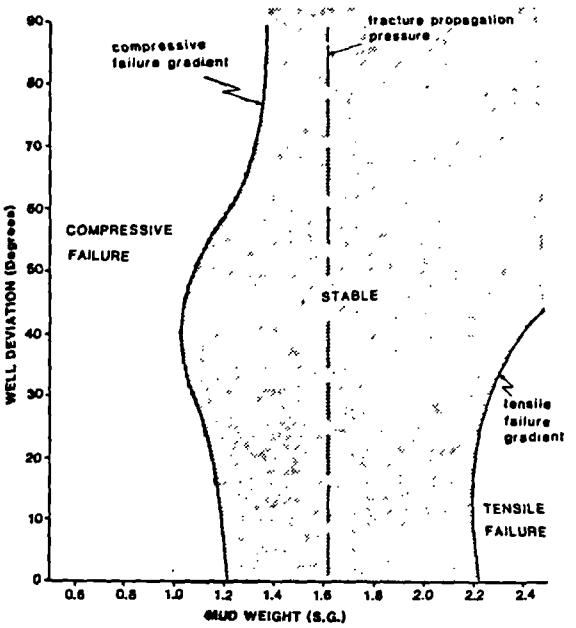
An interesting feature of Figures 2.10, 2.12 and 2.14, is that when deviating in a direction parallel to σ_h, the most stable angle is somewhere between the vertical and horizontal azimuths. The reason for this behaviour is depicted in Figure 2.15. The vertical well has σ_H and σ_h (0.019 and 0.016 MPa/m) acting in a plane perpendicular to its axis. The horizontal well has σ_H and σ_v (0.019 and 0.023 MPa/m) acting in the plane of interest. For wells of intermediate deviation σ_H will continue to act in a plane perpendicular to the well axis, and the normal component of the other stress will lie somewhere between σ_h and σ_v. Thus, there will be some point between the vertical and the horizontal, where the stress regime in the plane perpendicular to the well axis is



Material :- 'Shale' / Undrained response - Well deviated // to σ_H

Variation of failure initiation gradients with well deviation

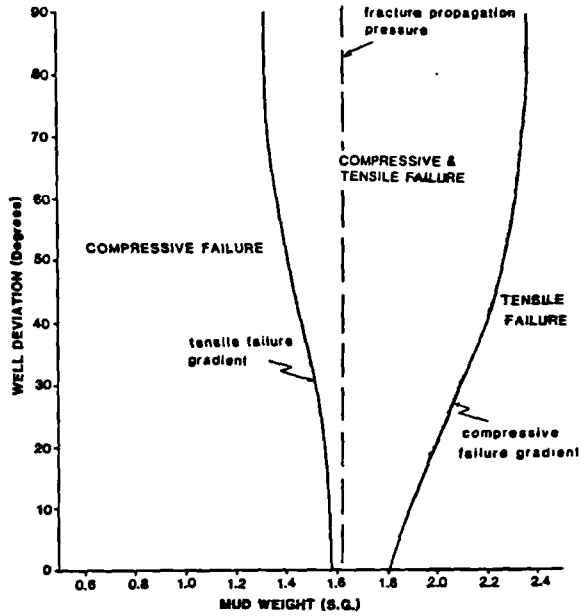
Figure 2.11



Material :- 'Shale' / Undramed response - Well deviated // to σ_h

Variation of failure initiation gradients with well deviation

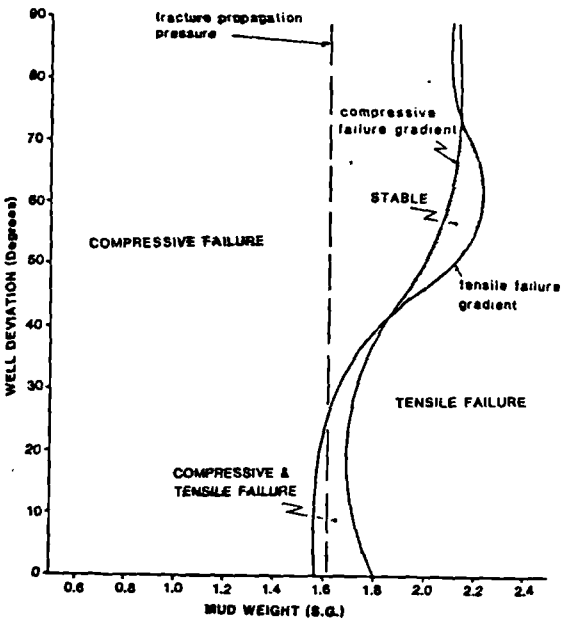
Figure 2.12



Material :- 'Shale' / Drained response - Well deviated // to σ_H

Variation of failure initiation gradients with well deviation

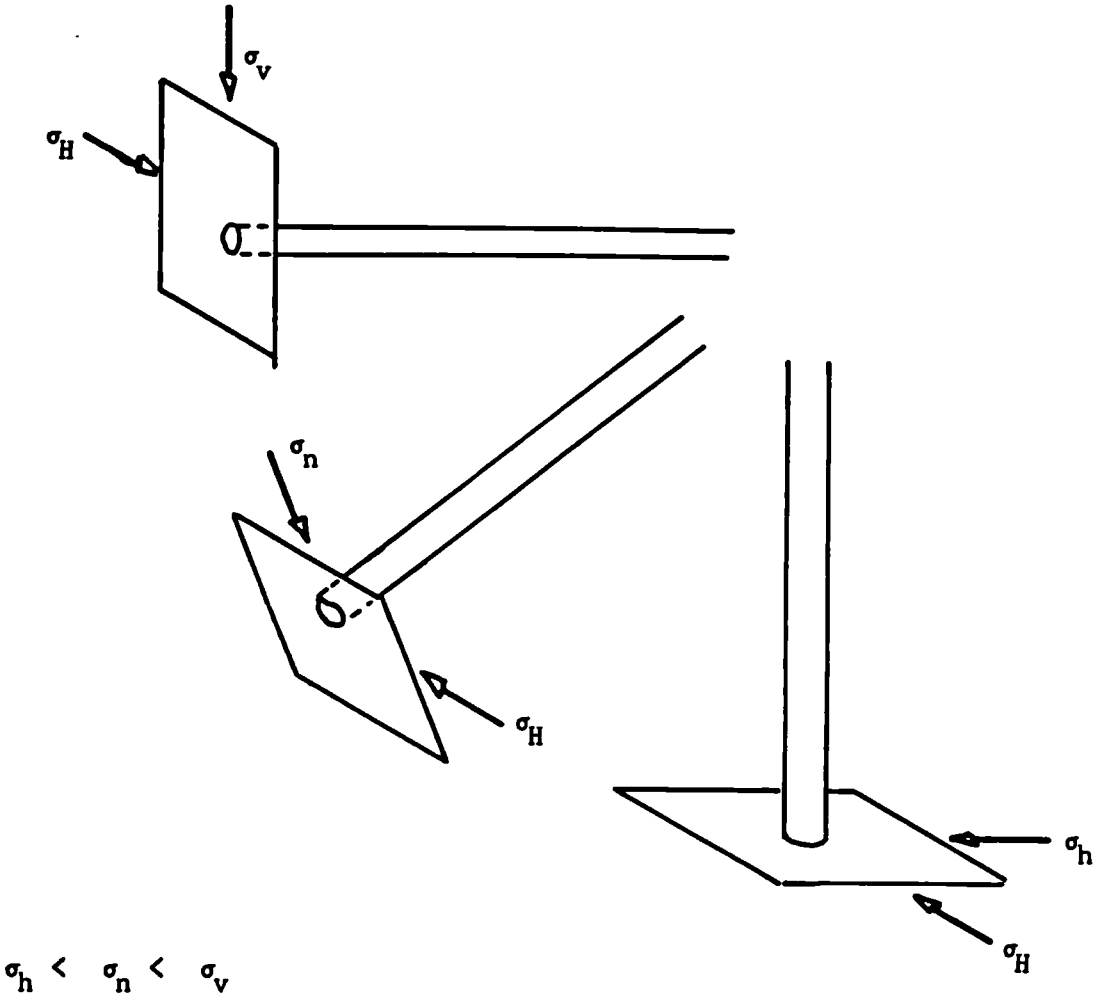
Figure 2.13



Material :- 'Shale' / Drained response - Well deviated // to σ_h

Variation of failure initiation gradients with well deviation

Figure 2.14



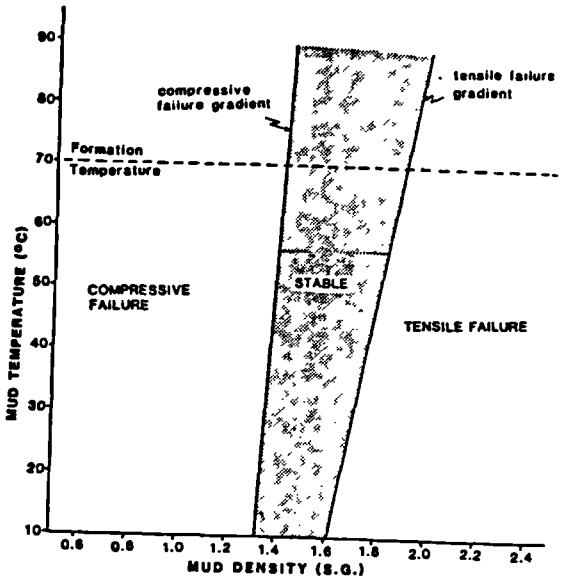
Stresses acting on a plane perpendicular to the well axis for wells deviated in a direction perpendicular to σ_H.

Figure 2.15

the least anisotropic, therefore reducing the stress concentrations, hence increasing the well stability. The same is not true of wells directed parallel to σ_H, for which the greater the deviation angle the less the stability.

2.8.3.2 Effect of Temperature on Stability

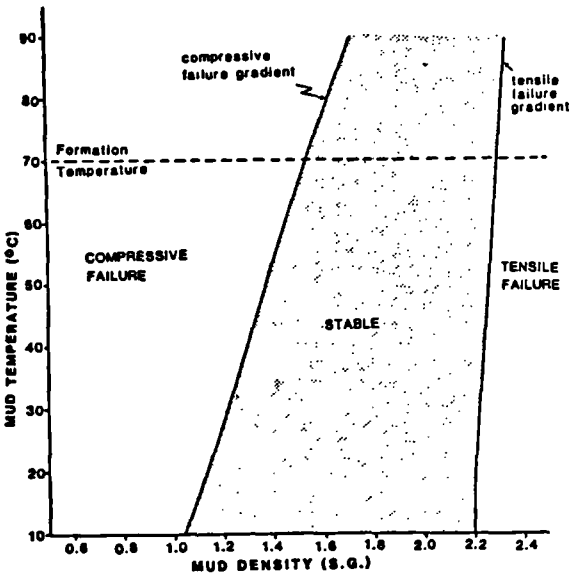
The effect of temperature on the failure initiation gradient for the sandstone, the undrained shale and the drained shale behaviour is shown in Figures 2.16, 2.17 and 2.18, respectively. For these plots the well is considered vertical, the formation temperature is kept constant at 70°C and the drilling fluid temperature is varied. All three material responses show an increase in resistance to compressive failure with reduction in mud temperature and a decrease in resistance to tensile failure with decrease in mud temperature. Although Figures 2.16 - 2.18 show definite trends, the variation in mud weight with temperature is only significant in the case of tensile failure in the sandstone and compressive failure in the undrained shale. However, it can be seen from inspection of equations (84), (85), (113), (114) and (115) that the relative importance of temperature on stability may be strongly influenced by the rock's elastic and thermal expansion properties. Figures 2.16 - 2.18 have been plotted on the basis of a Young's Modulus, E, value of 6.9 GPa (10^6 psi) and coefficient of linear expansion, α_r, of 10^{-5} /°C, giving the product of $E.\alpha_r$ equal to 69 kPa/°C (10 psi/°C). In Figures 2.19 - 2.21 the variation of the failure initiation gradients are given for $E.\alpha_r$ values of 69 kPa/°C (10 psi/°C), 155 kPa/°C (22.5 psi/°C) (i.e. taking E = 10.4 GPa ($1.5x10^6$ psi) and $\alpha_r = 1.5x10^{-5}$/°C) and 276 kPa/°C (40 psi/°C) (i.e. taking E = 13.8 GPa ($2x10^6$ psi) and $\alpha_r = 2x10^{-5}$/°C). It can be seen that for all three material responses the greater the stiffness and the thermal expansion



Material :- 'Sandstone'

Variation of failure initiation gradients with mud temperature.
(E_{α_f}=10 psi/oC).

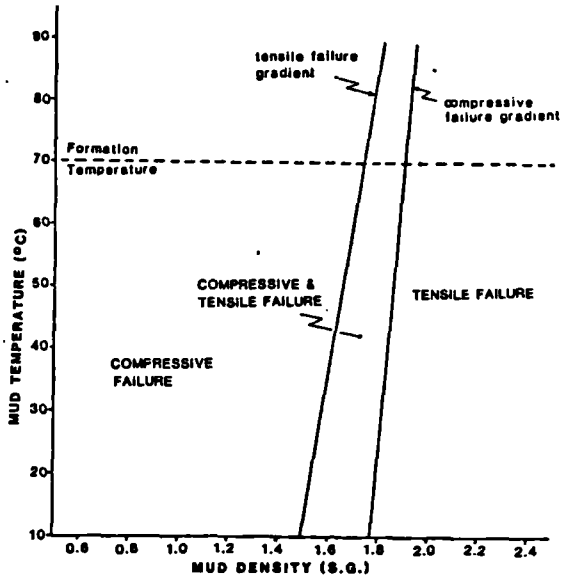
Figure 2.16



Material :- 'Shale' / Undrained response

Variation of failure initiation gradients with mud temperature.
(E_{α_f}=10 psi/oC).

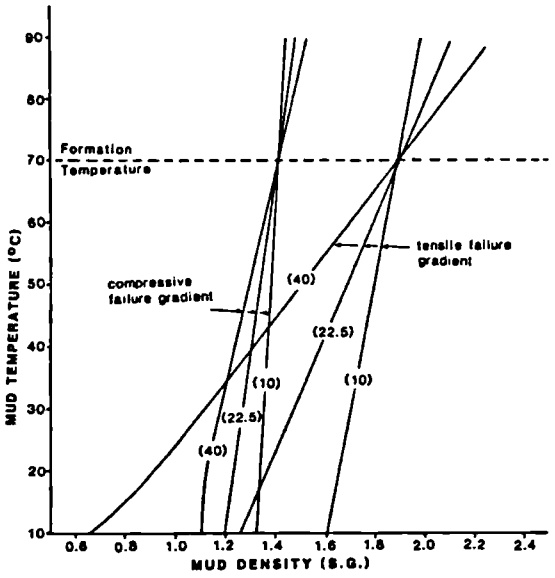
Figure 2.17



Material :- 'Shale' / Drained response

Variation of failure initiation gradients with mud temperature.
(E_{α_f}=10 psi/oC).

Figure 2.18

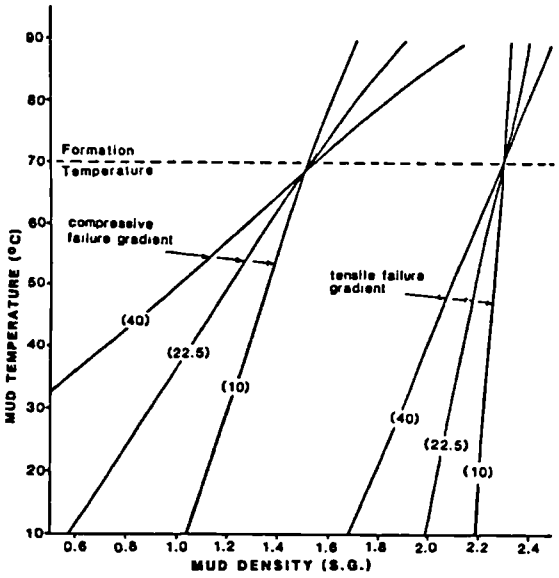


Material :- 'Sandstone'

Effect of rock elastic and expansion properties on fracture gradients.

Bracketted figures indicate value of $E\alpha_r$ in psi/°C.

Figure 2.19

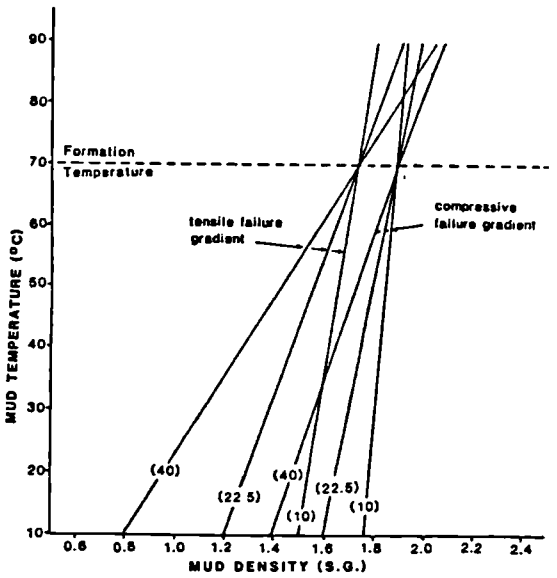


Material :- 'Shale' / Undrained response.

Effect of rock elastic and expansion properties on fracture gradients.

Bracketted figures indicate value of $E\alpha_r$ in psi/°C.

Figure 2.20



Material :- 'Shale' / Drained response.

Effect of rock elastic and expansion properties on fracture gradients.

Bracketted figures indicate value of $E\alpha_r$ in psi/°C.

Figure 2.21

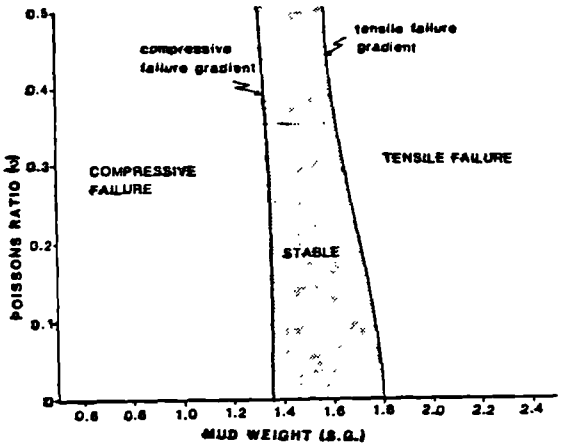
coefficient the greater the influence that temperature may have on wellbore stability.

2.8.3.3 Effect of Poisson's Ratio on Stability

The effect of Poisson's Ratio (ν) was considered by analysing the case of a vertical well with elastic and thermal properties as given in Section 2.8.1 and with formation and well temperatures of 70°C and 30°C, respectively. Figures 2.22, 2.23 and 2.24 give the variation in stability with ν for the sandstone, undrained shale, and drained shale responses respectively. For the sandstone and undrained shale responses ν appears to have only a minor influence on stability, except for very high (and unlikely) values in the case of the undrained shale behaviour. However, for the drained shale response ν may be an important parameter when assessing a well's stability. The reason for the strong influence of ν in the drained shale response and not the sandstone, is due to the poor mud cake effectiveness for long term shale behaviour. From inspection of equations (68) to (71) it can be seen that as the mud cake parameter (h) approaches zero (no filtrate loss) the terms containing ν disappear, whereas, when h approaches unity (no mud cake) the stresses may be strongly influenced by ν.

2.8.3.4 Effect of the Mud Cake on Stability

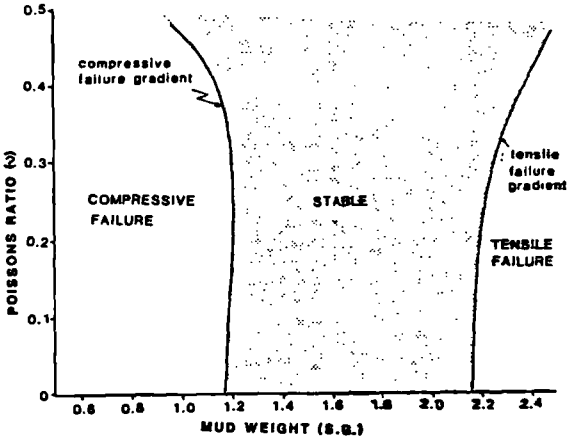
Figure 2.25 shows the effect of varying the drilling fluid filtrate loss characteristics for a drained response. The graph is applicable to sandstone behaviour where it may be possible to cover virtually the whole range of mud cake parameter values. It is unlikely that any mud cake is formed in low permeable formations (e.g. shales), but it may be



Material :- 'Sandstone'

Variation of failure initiation gradients with Poissons Ratio.

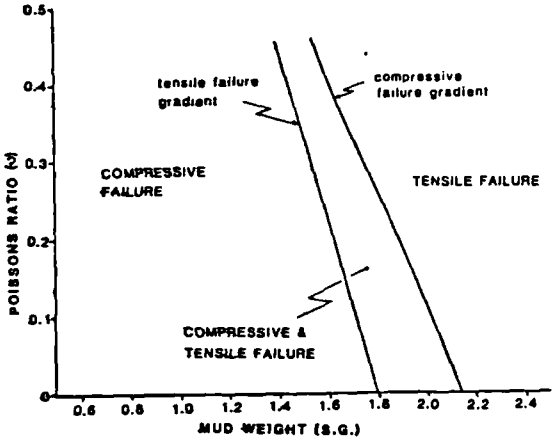
Figure 2.22



Material :- 'Shale' / Undrained response

Variation of failure initiation gradients with Poissons Ratio.

Figure 2.23



Material :- 'Shale' / Drained response

Variation of failure initiation gradients with Poissons Ratio.

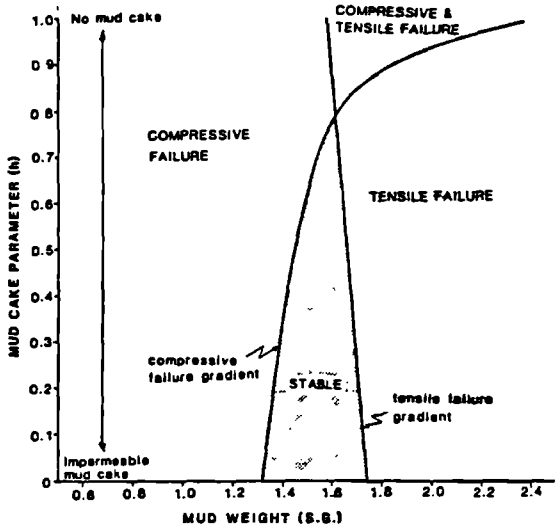
Figure 2.24

possible to reduce the permeability of a portion of the shale around the well and create an 'internal' mud cake. In any case, whatever the process involved in forming a mud cake, Figure 2.25 shows the great importance that structural support supplied by a pressure drop over a reduced permeability zone can have on resistance to compressive instability. For 'h' values between 0 and 0.6 the change in stability is only marginal, but for values over 0.7 the stability drops off dramatically.

From Figure 2.25 it can be seen that the fracture initiation pressure decreases steadily with increased values of 'h' (increased fluid loss to the formation). Thus, the formation's resistance to both tensile and compressive failure reduces as 'h' tends to unity. However, the influence of fluid loss on tensile failure may not be as significant as it's effect on compressive failure.

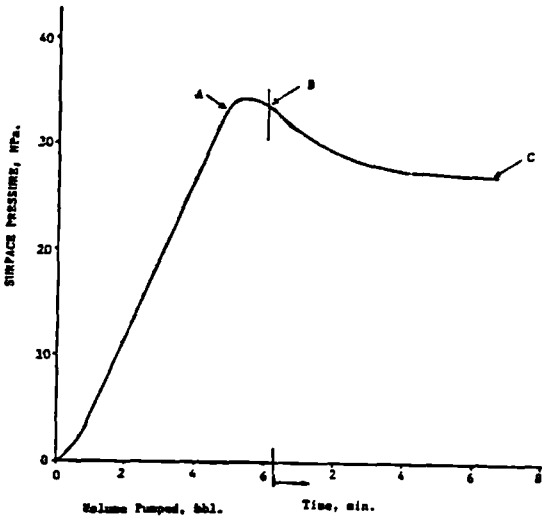
2.8.3.5 Effect on Leak Off Interpretation

Under normal drilling conditions, as soon as a casing shoe has been set, then about 5 metres of hole are drilled beyond the shoe and a leak off test is carried out. A leak off test consists of pressurising the bottom of the well using the drilling fluid and monitoring the pressure increase against volume of drilling fluid pumped (Chenevert and McClure[59]). The object of the test is to discover the resistance of the formation below the shoe to fracture initiation, and also to test the competence of the cemented casing shoe. The point at which the plot of pressure v volume pumped departs from linearity, is taken to be the leak off point (see Figure 2.26), the leak off pressure being the sum of the surface pressure plus the hydrostatic head of the column of mud. Since



Variation of failure initiation gradients with mud cake parameter (h).
Applicable to 'Sandstone' and drained 'Shale' behaviour.

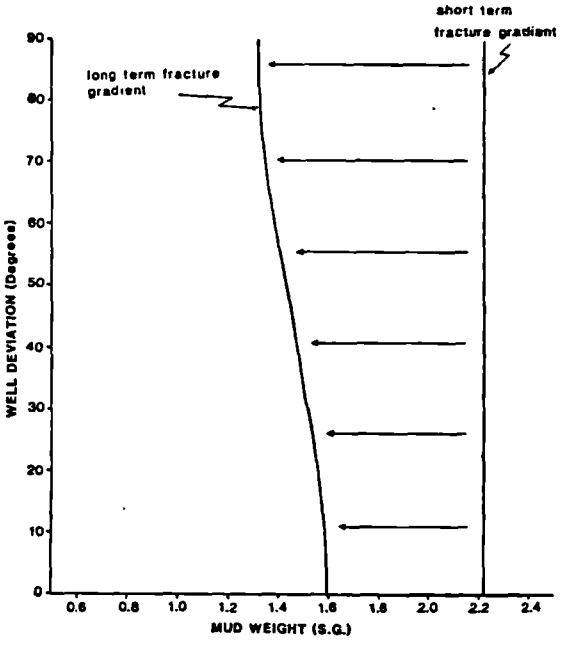
Figure 2.25



A - Leak off pressure
B - Pumping stopped
C - Pressure decline (indication of filtration rate)

Typical Leak off test plot.

Figure 2.26



Material :- 'Shale'
Change in fracture gradient from short term to long term conditions.
Well deviated // to σ_H.

Figure 2.27

it is undesirable to damage the formation by inducing a large fracture, pumping is stopped as soon as leak off occurs. Although it is not certain exactly what physical process is occurring at the hole bottom during leak off, it is probable that the leak off point is close to the fracture initiation point. So it may be possible to infer in-situ stress magnitudes from one or more leak off tests.

To infer the stress magnitudes from leak off test data is similar to interpreting in-situ stresses from hydraulic fracturing as set out by Hubbert and Wills.[60] Hubbert and Willis assume that the peak pressure in a hydraulic fracture test is given by

$$\text{Peak Pressure} = 3\sigma_{min} - \sigma_{max} + |\sigma_t| - P_F$$

where σ_{min} and σ_{max} are the minimum and maximum principal stresses in a plane perpendicular to the well axis,

σ_t is the rock tensile strength,

and P_F is the formation pressure.

The above relationship may be suitable for the drained response of a material with no temperature gradients. However, from Figure 2.27 it can be seen that there may be a considerable difference between the drained and the undrained fracture gradients. Since leak off is invariably carried out in low permeable formations shortly after a 5 metre section of hole is drilled, short term response may have a considerable influence on the leak off value. Ignoring temperature effects and assuming no fluid penetration into the well, from inspection of equations (13), (15) and (44), it can be shown that the minimum

effective hoop stress at the wellbore wall for a vertical well is given by

$$\sigma'_{\theta min} = 3\sigma_h - \sigma_H - P_W - P_F \qquad \text{drained conditions}$$

$$\sigma'_{\theta min} = 2(\sigma_h - P_F) - P_W \qquad \text{undrained conditions}$$

where P_W is the well pressure.

It can be seen from the above relationships that for drained conditions the minimum effective hoop stress, σ'_θ, is dependent on both σ_h and σ_H, whereas for undrained conditions σ'_θ is dependent on only σ_h. Thus, for a well deviated in a direction parallel to σ_H, where σ_h remains perpendicular to the well axis for all deviation angles, the fracture initiation pressure becomes independent of well deviation for the case of undrained response. Therefore, it may be found that leak off values from a number of wells in the same formation do not vary significantly despite large variations in well azimuth.

2.9 TIME DEPENDANT STABILITY - TRANSIENT SOLUTION

From the analyses carried out in the previous section it can be seen that there may be a considerable difference between the short and long term stability of low permeability formations such as shales, and that one of the most important factors in deciding whether or not a well will be stable may be time. The steady state solutions given in Sections 2.2 to 2.6 do not directly quantify time and only the extreme conditions of stability at time zero and time infinity are considered. The solution presented in Section 2.7 does take account of time, although only for the case of an isotropic stress field, and no account of temperature effects is considered.

2.9.1 Failure Conditions

In attempting to assess the importance of time on stability, a number of further assumptions must be made regarding the failure conditions. There is a flaw when using simple linear elasticity to assess stability at the wellbore wall. Ignoring temperature induced pore fluid pressures, then due to the difference in well and formation pressures, at time zero there will be an infinite pressure gradient at the well wall. The infinite pore pressure gradient results in points on the wellbore wall equilibrating to the well pressure immediately, and it is impossible to quantify time behaviour. It will be shown by using the equations developed in Section 2.7 that the stress and pore pressure conditions at the wellbore wall are independent of time, and only at points within the formation are conditions time dependent.

According to linear elasticity, the most severe stress conditions will invariably be at the wellbore wall. Thus, a failure criterion that is based on the most critically stressed point would show that a wells stability is independent of time, as a result of the reasoning given in the previous paragraph. However, a more realistic numerical model would account for plasticity, and possibly nonlinear elasticity (as discussed in Section 1.4.1, Chapter 1). In plasticity modelling, although yield would initiate at the wellbore wall the plastic region of critically stressed material would extend into the formation (e.g. Brown & Bray[36]) and stability of the well becomes dependent on the response of the rock within the formation, and not only on conditions at the wellbore wall. Nonlinear elastic modelling has been reported for the case of dry rock behaviour in permeable formations (e.g. Santarelli[18]), but little or no work has been published on the applicability of pressure dependent

elasticity in saturated low permeability materials. However, if this characteristic is applicable to shales, then the stress conditions at the wellbore wall will be dependent on the stiffness of material within the formation, which will be continually changing with time as drilling fluid invades the formation and alters the confining stress on the elements of rock.

From the above reasoning it can be concluded that instability in low permeable formations will be function of time, although a simple linear elastic solution based on failure being initiated by the peak stresses at the wellbore wall is not capable of modelling this time response. To get any useful data from the solution presented in Section 2.7 it is necessary to assume that failure will be initiated at some finite distance away from the wellbore wall and to ignore the more critically stressed state at the wellbore wall. The results of studies presented in Section 2.9.4 assume that failure is initiated at a radial distance of 1.1 times the well radius, 'a'.

2.9.2 Input Parameters

The in-situ stress field is assumed to consist of a vertical stress (σ_v) equivalent to the overburden of 0.023 MPa/m (1.0 psi/ft), and an isotropic horizontal stress state represented by a single stress (σ_h) equivalent to 0.016 MPa/m (0.7 psi/ft). The formation pressure (P_F) is considered to be equivalent to a gradient of 0.010 MPa/m (0.45 psi/ft). The well is taken to be vertical and the depth chosen is 1820 m (6000 ft). The tensile and compressive strengths and criteria are the same as given in Section 2.8.1.1. The elastic parameters are taken to be $E = 6.9$ GPa (10^6 psi) and $\nu = 0.25$. No temperature effects are considered, hence there is no need to specify the well and formation

temperatures, nor the thermal properties of the formation. However, the diffusion coefficient (κ) used in equations (123) and (124), is dependent on the rock permeability (k) and the pore fluid viscosity (μ) (see equation (122)), and the parameter τ used in Tables 1 and 2 is defined as,

$$\tau = \kappa t/a^2$$

where 't' is time and 'a' is the wellbore radius.
Thus, it is also necessary to define the wellbore radius, which is taken to be 310 mm (12 1/4 inch dia. hole). The drilling fluid filtrate and pore fluid are both assumed to have a viscosity of 10^{-3} kg/m.sec (1 centipoise). The rock permeability will be specified later.

Assuming the parametric values given above and that rock permeability is measured in Darcys then,

$\kappa = 2.99\times10^{4}k \quad m^2/hr \quad (4.67\times10^{7}k \quad in^2/hr)$

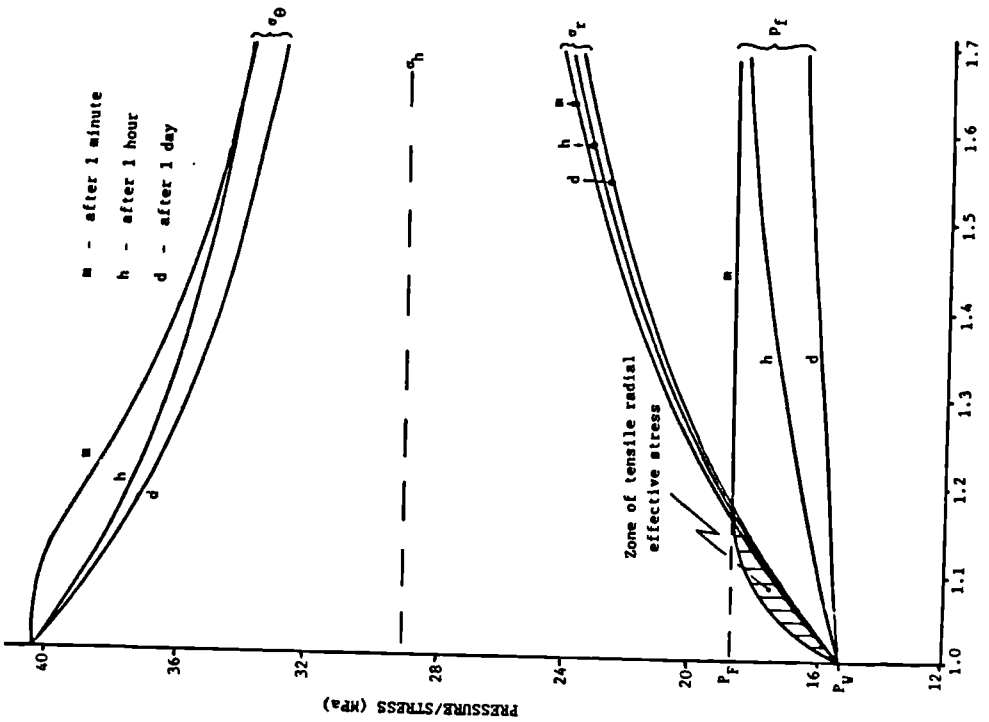
and $\tau = 1.24\times10^{6}k.t$ - dimensionless (where t is in hours)

2.9.3 Relevent Equations

Table 1 is used in conjunction with the expressions for τ given above to determine the pore pressure. Once the pore pressure has been determined equations (130) and (131) are used to determine the total radial and circumferential stresses, respectively. The value of the variable Ω in (130) and (131) is determined from Table 2.

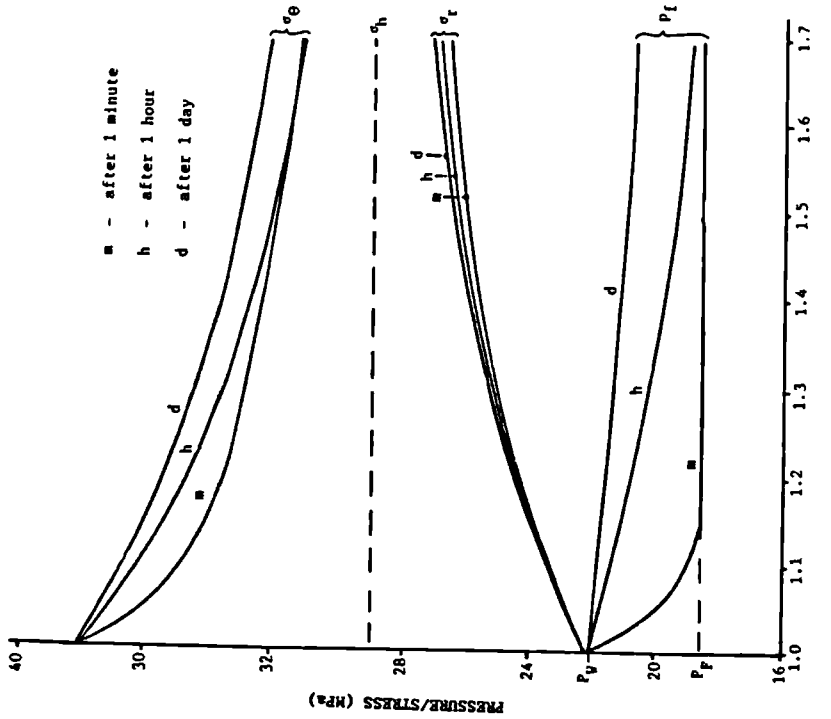
2.9.4 Results

Figure 2.28 shows the radial and circumferential stresses and pore pressure variations, when a 3.4 MPa (500 psi) overbalance is applied, for three time intervals (one minute, one hour and one day) after



Stress/Pressure profile for 'Shale' of permeability 10^{-7} Darcys during Underbalance Conditions.

Figure 2.29



Stress/Pressure profile for 'Shale' of permeability 10^{-7} Darcys during Overbalance Conditions.

Figure 2.28

drilling the hole section. Shale permeabilities are reported to lie in the range 10^{-4} to 10^{-8} Darcys (Haldorsen and Lake[60]). However, previous unpublished work has recorded permeabilities as low as 10^{-9} Darcys (personal communication - W.B.Bradley, Standard Oil of Ohio, SOPC). The permeability chosen for this analysis is 10^{-7} Darcys. It can be seen that there is little variation in the total radial stress (σ_r) with time. However, the pore fluid pressure distribution (p_f) is time dependent and consequently the radial effective stress (σ'_r, given by $\sigma'_r = \sigma_r - p_f$) becomes time dependent and since p_f increases with time, σ'_r reduces with time. The circumferential stress (σ_θ) increases with time. However, since p_f is also increasing with time, σ'_θ will not necessarily increase with time. The resistance of the wellbore to compressive failure will also reduce with time, since it is heavily dependent on the minimum effective stress (σ'_r).

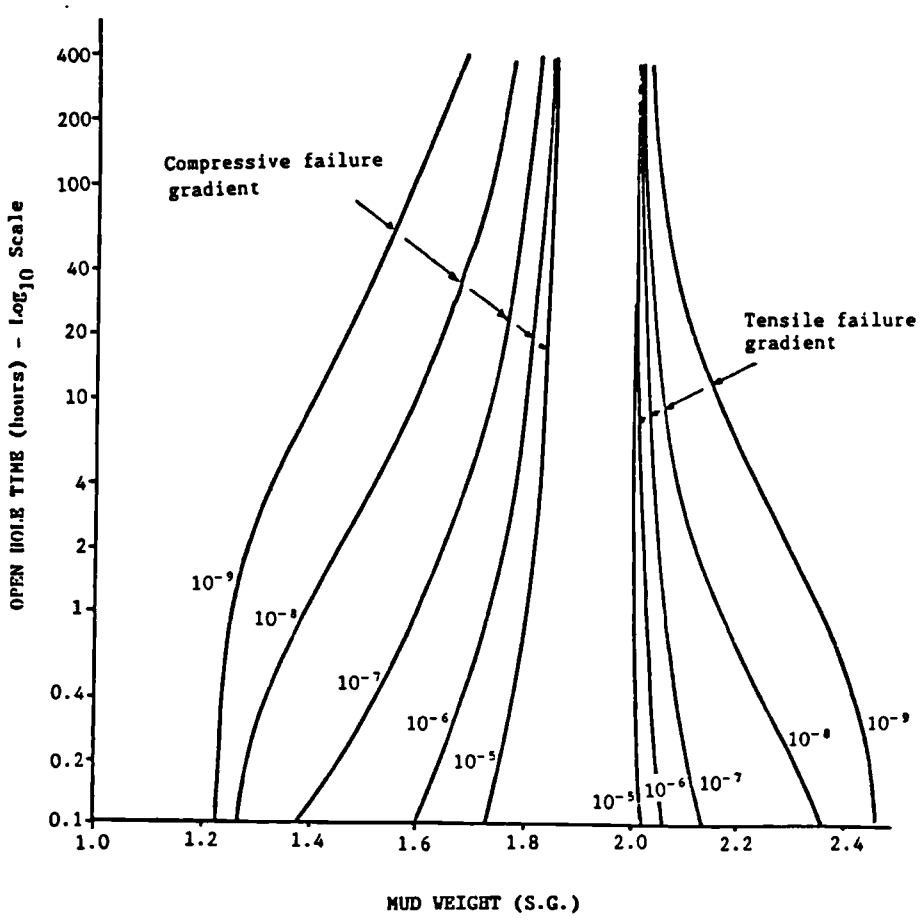
Figure 2.29 shows the stress and pore fluid variation with time and radial distance for the case in which the well pressure has been reduced to give a 3.4 MPa (500 psi) underbalance. Again the rock permeability is taken to be 10^{-7} darcys. In this case the radial effective stress will increase with time and hence the well will become more stable with time. The important point to notice is that in the very early stages after drilling (one minute) the radial effective stress in the near wellbore region (approximately the first 20mm for the 310 mm radius (12 1/4 inch dia.) wellbore considered here) has a tensile effective radial stress, and hence could fail in tension or a combination of tension and shear. The most critically stressed point for this case is no longer at the wellbore wall, but at some finite distance inside the formation.

As noted previously, and shown in Figures 2.28 and 2.29, the only

point at which conditions are independent of time is at the wellbore wall.

The mud weights required to prevent compressive and tensile failure (as defined in Section 2.9.1) are calculated for various times and permeabilities and shown in Figure 2.30. It can be seen that at higher permeabilities ($k = 10^{-5}$ Darcys) the conditions approach the long term stability case for compressive failure soon after the well is drilled, and the tensile failure gradient at 0.1 hours (6 minutes) after the well is drilled is only marginally more stable than in the long term. As permeability reduces, the stability of the wellbore increases due to the reduction of filtrate invasion. For a permeability of 10^{-9} Darcys the compressive and tensile failure gradients show little variation in the early stages of open hole time. This is because no fluid invasion has reached the point at which failure is monitored (1.1 times well radius, 'a'), and it is only after around 1 hour that the pore pressure at this point becomes affected by invasion.

It can be seen that the less permeable formations require less support from the drilling fluid, and are likely to remain stable for longer periods. However, it will be the same less permeable formations which will be susceptible to failure induced by radial tension as shown in Figure 2.29 and described above, since the more permeable formations will react quicker to alleviate the high pore pressure gradients set up. Thus, although the relatively impermeable shales will be more stable in overbalance conditions, they will be more susceptible to failure in underbalance (during tripping out the well for example).



Variations of failure initiation gradients with time.

Figures on the curves represent permeability values in Darcys.

Figure 2.30

2.10 CONCLUDING REMARKS

A number of linear elastic solutions were presented in Sections 2.2 to 2.6 for the analysis of drained and undrained wellbore response to formation stresses and pressures, temperature gradients, and drilling fluid loading and filtration invasion. The solutions cannot be considered as quantitative in their predictive capabilities. However, they are useful for assessing the effects of various parameters on wellbore stability. The conclusions from this study are discussed below.

Temperature gradients caused by a difference between the drilling fluid and the formation temperature may enhance or reduce stability. In the case of wellbore cooling, compressive stability will be increased and tensile stability reduced. The reverse effect will occur when the drilling fluid is of a greater temperature than the formation. The impact of wellbore cooling on the short term stability of shales may be considerable. The influence of temperature on the stress state for a drained response (permable formations and long term shale response) may only be significant for the stiffer rocks. However, the stiffer formations may be of less interest, since an increase in stiffness is often accompanied by an increase in strength, and therefore these rock types may not be susceptible to wellbore instability in the first place.

The drilling fluid fitrate loss characteristics (ability to form an effective mud cake) is likely to have a significant influence on wellbore compressive stability. Unfortunately, the troublesome formations such as shales may not accommodate the forming of a mud cake due to their low permabilities.

It was shown in the case of shale behaviour, from a comparison of short and long term conditions in Section 2.8, that one of the most important parameters is time. A transient solution for analysis of radial fluid migration, due to a difference between the formation and drilling fluid pressures, was presented in Section 2.7. Although the solution helps in appreciating in what range of time period short and long term conditions exist, the solution is lacking in that no account of temperature induced pore pressures and stresses are considered, and only an isotropic stress regime may be considered, otherwise pore fluid migration would have a component in the circumferential direction and not simply be radial. To better appreciate the stability of shale formations it is important to extend this solution to allow for these deficiencies. A step towards this extended solution may be found by following work done by Carslaw and Jaeger[57] who present a solution for the diffusivity equation (122) where the initial conditions in the infinite hollow cylinder consists of a varying temperature distribution in the radial direction.

CHAPTER 3

APPLICATION OF THE FEM TO 2-DIMENSIONAL LINEAR ELASTIC PROBLEMS

3.1 INTRODUCTION

There are a number of good text books that explain the finite element method (FEM) of analysis (e.g. Zienkiewicz,[62] Hinton and and Owen[63]). However, for completeness, certain aspects of the procedure for development of the FEM equations with respect to linear elasticity are included in this chapter. In Chapters 5 and 6 the FEM method is extended to account for plasticity (Chapter 5) and pressure dependent elasticity (Chapter 6). In this chapter the FEM is developed from the theory of virtual work. Relationships are first given for plane strain conditions and then extended to allow for complete plane strain (as defined by Brady and Bray[46]). Next, infinite elements are introduced to reduce the extent of the finite element mesh. Finally, results of test runs using the developed program are given to validate the correctness of the method and the computer coding. (Much of the computer coding used is based on work and listings presented by Owen and Hinton.[35] However, many of the routines are rewritten, mainly for the benefit of this authors understanding.)

3.2 THE VIRTUAL WORK EXPRESSION

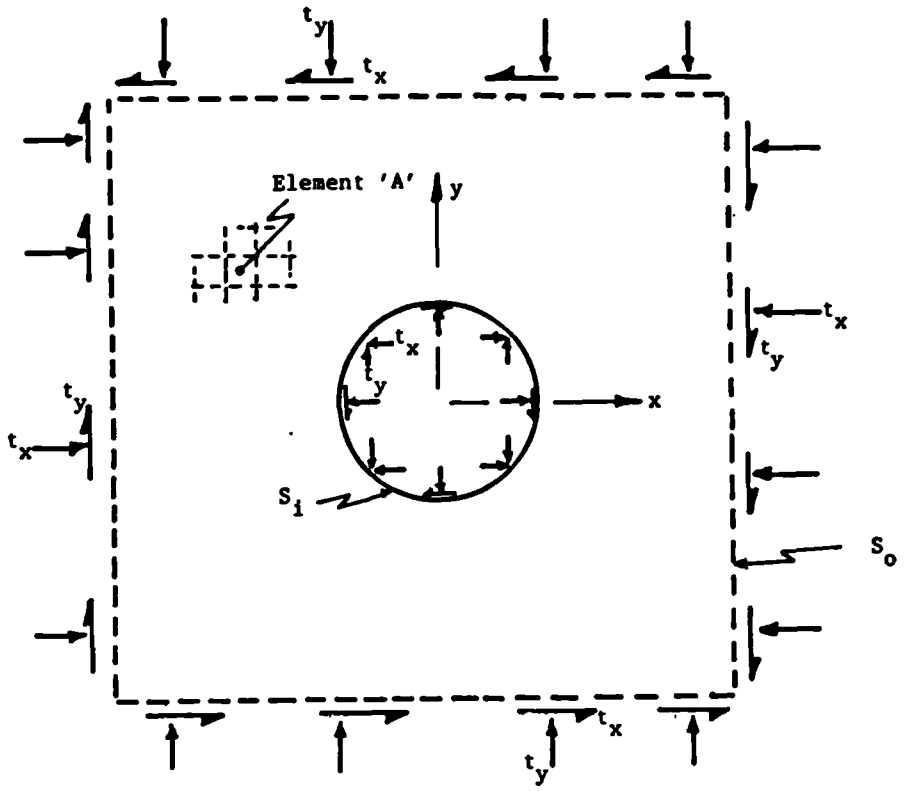
Two possible development procedures can be followed to find expressions that can be utilized by the FEM. One method is to minimize the total potential energy of the structure. The other method, which is adopted here, is through application of the virtual work theorem. Text

books will refer to virtual work using a completely arbitrary structural shape. However, in the following text all formulations are made with reference to the problem at hand, i.e. circular excavations in rock.

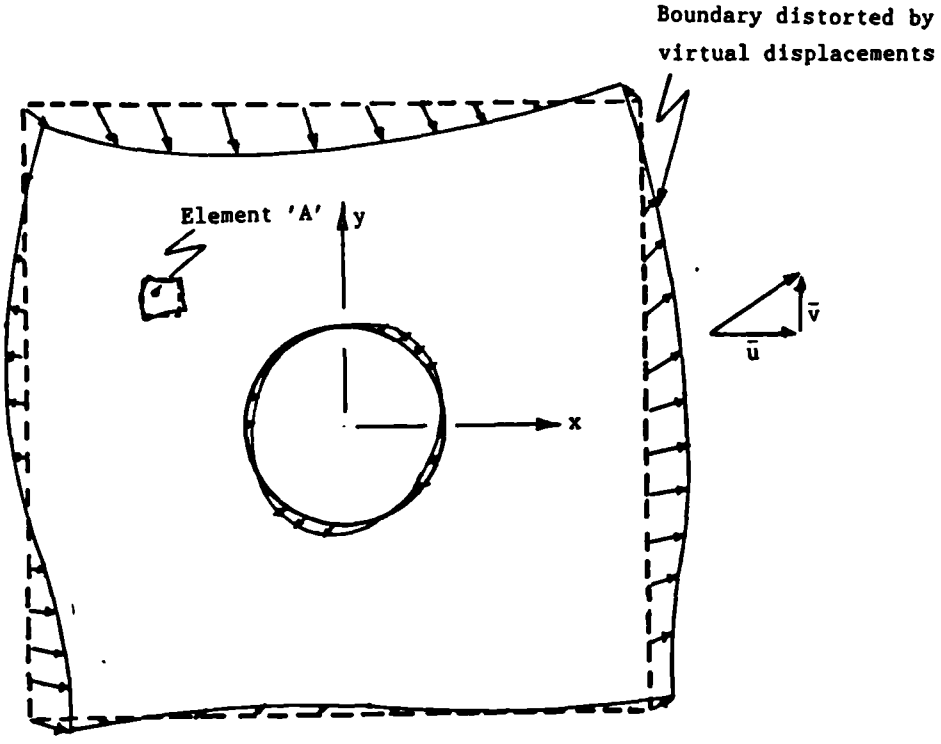
Take the case of a vertical or horizontal excavation in a rock body as shown in Figure 3.1a. The section under examination is assumed to be of unit thickness. The tunnel direction is parallel to a principal stress and the tunnel is of sufficient length (length measured in the axial direction orthogonal to the x-y plane) such that plane strain conditions can be applied. At some far field outer boundary (S_o) it is assumed that the stress conditions are known, such that they can be considered as boundary tractions applied to a surface at some finite distance from the centre of the excavation. On the surface of the excavation (S_i) another set of tractions are applied, either from structural support in the case of a tunnel, or a mud pressure in the case of a wellbore. The boundary tractions on the surfaces S_o and S_i are represented by tractions in the x-direction, t_x, and the y-direction, t_y, which combine to form the vector [t]. Thus,

$$[t] = \begin{bmatrix} t_x \\ t_y \end{bmatrix} \tag{1}$$

Now assume that the inner and outer boundaries of the structure defined in Figure 3.1a undergo a set of very small but finite imaginary or virtual displacements in the x-y plane, which have been exaggerated for sake of clarity in Figure 3.1b. Provided the displacements are small, then the boundary tractions ([t]) and the internal state of stress ([σ]) at any point within the structure remain relatively unchanged. For plane



(a)



(b)

Figure 3.1 Virtual displacements applied to a circular excavation in rock.

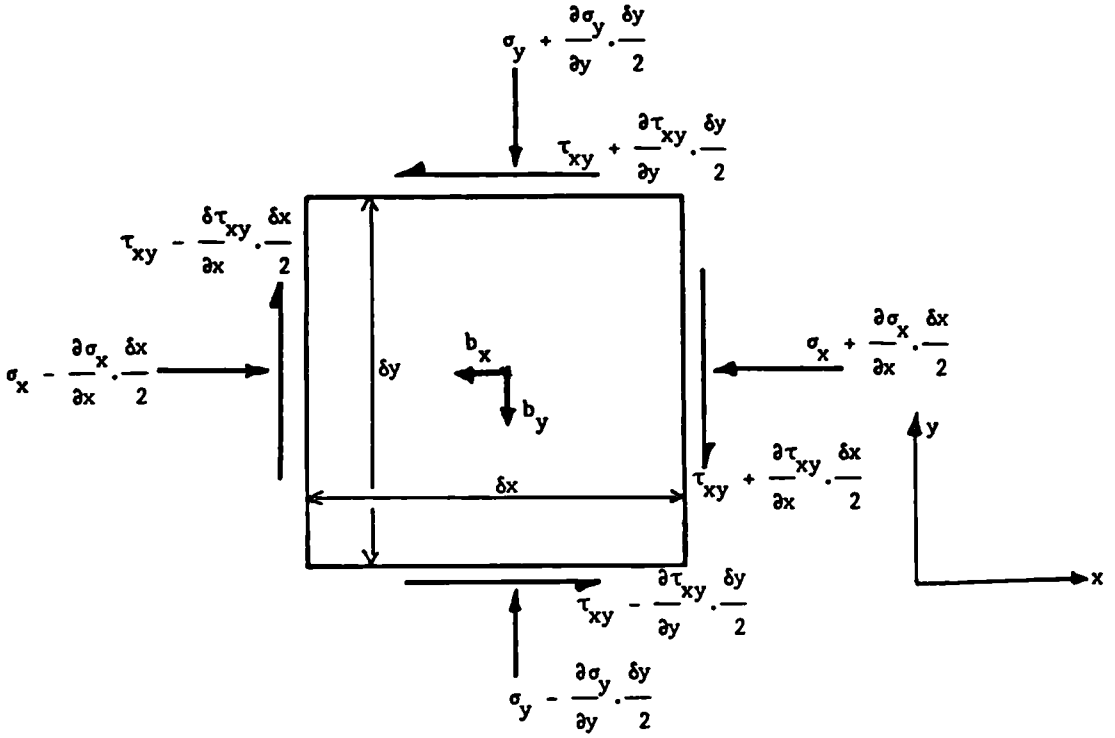
strain conditions the stress vector, $[\sigma]^*$, at any point can be defined by

$$[\sigma]^* = \begin{bmatrix} \sigma_x \\ \sigma_y \\ \tau_{xy} \end{bmatrix} \qquad (2)$$

where σ_x, σ_y, τ_{xy} are the in plane stress components with respect to the x-y cartesian coordinate system.

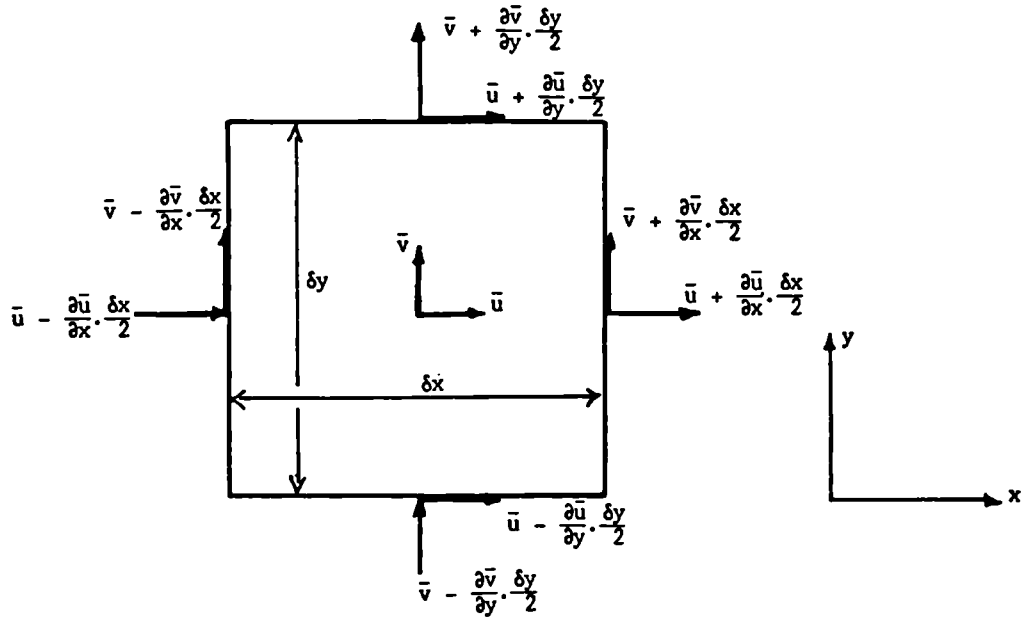
The antiplane shear stresses τ_{yz} and τ_{zx} are zero for plane strain conditions, and therefore need not be included in the stress vector. The stress vector, $[\sigma]$, is superscripted with '*' to indicate that axial components of stress, σ_z, are not included in the vector. In general σ_z is non-zero, however, it need not be included in this analysis since, for plane strain conditions, no virtual displacements occur in the axial direction. This convention is continued throughout the text to distinguish between certain vectors/matrices which do or do not contain the axial components. In Chapters 5 and 6 it is seen that inclusion of axial components becomes necessary when analyizing nonlinear behaviour.

Consider a small element defined by 'A' in Figures 3.1a and 3.1b, which is enlarged in Figure 3.2. Figure 3.2a shows the stresses and body forces acting on the element, where b_x and b_y have units of force per unit volume. In general, the body forces represent gravitational loading. Figure 3.2b represents the virtual displacements imposed on the element, caused by subjecting the boundaries of the structure to virtual displacements, where $\bar{u}$ and $\bar{v}$ are the virtual displacements in the x & y directions respectively. As mentioned before, the virtual displacements are so small that the stresses on the element can be considered to be relatively unchanged. Now consider the net virtual work done on the element as a result of the sum of the edge loading (or surface



Element stress state

(a)



Virtual displacements imposed on element

(b)

Figure 3.2 Stress and virtual displacements imposed on element.

tractions) and the body forces. The surface loading is calculated by summing the work done on each individual edge. Thus, taking the top edge of the element for example, the work done by the applied tractions on this edge is given by

$$-\left(\sigma_y + \frac{\partial \sigma_y}{\partial y}.\frac{\delta y}{2}\right)\delta x.\left(\bar{v} + \frac{\partial \bar{v}}{\partial y}.\frac{\delta y}{2}\right) \quad - \quad \left(\tau_{xy} + \frac{\partial \tau_{xy}}{\partial y}.\frac{\delta y}{2}\right)\delta x.\left(\bar{u} + \frac{\partial \bar{u}}{\partial y}.\frac{\delta y}{2}\right)$$

normal force x y-displacement + shear force x x-displacement

(Note: Work done by applied tractions is negative since on this face the load and displacement directions shown in Figure 3.2 are opposite). Summing the work on all the element edges, ignoring small terms and rearranging, we arrive at the virtual work done by the surface tractions, $\delta\bar{W}_T$, for the element concerned. Thus

$$\delta\bar{W}_T = \left(\sigma_x\bar{\varepsilon}_x + \sigma_y\bar{\varepsilon}_y + \tau_{xy}\bar{\gamma}_{xy} - \frac{\partial \sigma_x}{\partial x}.\bar{u} - \frac{\partial \sigma_y}{\partial y}.\bar{v} - \frac{\partial \tau_{xy}}{\partial x}.\bar{v} - \frac{\partial \tau_{xy}}{\partial y}.\bar{u}\right)\delta x.\delta y$$

where $\bar{\varepsilon}_x$, $\bar{\varepsilon}_y$ and $\bar{\gamma}_{xy}$ are the virtual normal and shear strains and given by

$$\bar{\varepsilon}_x = -\frac{\partial \bar{u}}{\partial x}, \qquad \bar{\varepsilon}_y = -\frac{\partial \bar{v}}{\partial y} \qquad \text{and} \qquad \bar{\gamma}_{xy} = -\frac{\partial \bar{u}}{\partial y} - \frac{\partial \bar{v}}{\partial x}$$

The work done by the body forces for the element, $\delta\bar{W}_B$, is given by

$$\delta\bar{W}_B = -(b_x.\bar{u} + b_y.\bar{v})\delta x.\delta y$$

By summing $\delta\bar{W}_T$ and $\delta\bar{W}_B$ we arrive at the total virtual work, $\delta\bar{W}$, for the element concerned. Thus, after rearranging

$$\delta\bar{W} = \delta\bar{W}_T + \delta\bar{W}_B = \left[\sigma_x\bar{\varepsilon}_x + \sigma_y\bar{\varepsilon}_y + \tau_{xy}\bar{\gamma}_{xy} - \left(\frac{\partial \sigma_x}{\partial x} + \frac{\partial \tau_{xy}}{\partial y} + b_x\right)\bar{u} - \left(\frac{\partial \sigma_y}{\partial y} + \frac{\partial \tau_{xy}}{\partial x} + b_y\right)\bar{v}\right]\delta x.\delta y \qquad (3)$$

From equilibrium conditions we have

$$\frac{\partial \sigma_x}{\partial x} + \frac{\partial \tau_{xy}}{\partial y} + b_x = 0$$

and $$\frac{\partial \sigma_y}{\partial y} + \frac{\partial \tau_{xy}}{\partial x} + b_y = 0$$

Thus, equation (3) reduces to

$$\delta \bar{W}_T + \delta \bar{W}_B = \delta \bar{W}_{SE} \tag{4}$$

where $\bar{W}_{SE}$ is known as the strain energy term, and for the element concerned given by

$$\delta \bar{W}_{SE} = (\sigma_x \bar{\varepsilon}_x + \sigma_y \bar{\varepsilon}_y + \tau_{xy} \bar{\gamma}_{xy}) \delta x . \delta y$$

Now it is necessary to sum (integrate) the elemental virtual work terms over the whole area of the structure. The element considered is completely bounded by the structure, and therefore all its edges are shared by other elements. The work done by the surface tractions on a shared edge will be equal and opposite for the adjacent elements. Thus, for all internal edges the sum of the boundary tractions over the structure is zero. However, the work done on element edges that define the boundary of the whole structure does not cancel out and has some finite value. Thus, on integration of equation (4) we can write

$$\int d\bar{W} = \int [t]^T [\bar{d}] . dS + \int [b]^T [\bar{d}] . dA = \int [\sigma]^T [\bar{\varepsilon}]^* . dA \tag{5}$$

where $[\bar{d}]$ is the virtual displacement vector and defined as

$$[\bar{d}] = \begin{bmatrix} \bar{u} \\ \bar{v} \end{bmatrix}$$

$[\bar{\varepsilon}]^*$ is the virtual strain vector for plane strain and defined as

$$[\bar{\varepsilon}]^* = \begin{bmatrix} \bar{\varepsilon}_x \\ \bar{\varepsilon}_y \\ \bar{\gamma}_{xy} \end{bmatrix}$$

(note: $\bar{\varepsilon}_z$ is zero for plane strain)

and [b] is the body force vector and defined as

$$[b] = \begin{bmatrix} b_x \\ b_y \end{bmatrix}$$

dS represents integration over the boundary surfaces of the structure (i.e. S_i and S_o defined in Figure 3.1),

and dA represents integration over the whole area of the structure.

The suffix T applied to a vector represents the transpose of a column vector to a row vector, e.g. $[\sigma]^{*T} = [\sigma_x, \sigma_y, \tau_{xy}]$

Equation (5) is the virtual work expression applied to a plane continuum. In its present form it may not appear to be a particularly useful relationship, but when applied to a set of finite elements it provides a very powerful numerical tool.

3.3 FINITE ELEMENTS - PLANE STRAIN CONDITIONS

The FEM is based on dividing the structure under consideration into a number of finite elements. For example the structure defined in Figure 3.1 has been divided up into a number of elements as shown in Figure 3.3. The elements shown are all four sided, but the element boundaries need not necessarily be straight lines (e.g. the elements which are adjacent to the excavation boundary).

A typical element from Figure 3.3 is enlarged and shown in Figure 3.4a. Nodes are placed at the corner of the element and at points roughly mid way along the edges. The element shown is known as an 8-node Serendipity element. There are numerous other elements used in FEM analysis, ranging from a 1-D linear element to 3-D cubic elements. However, the 8-noded quadratic element is one of the most efficient elements for 2-D applications (Naylor et el[64]).

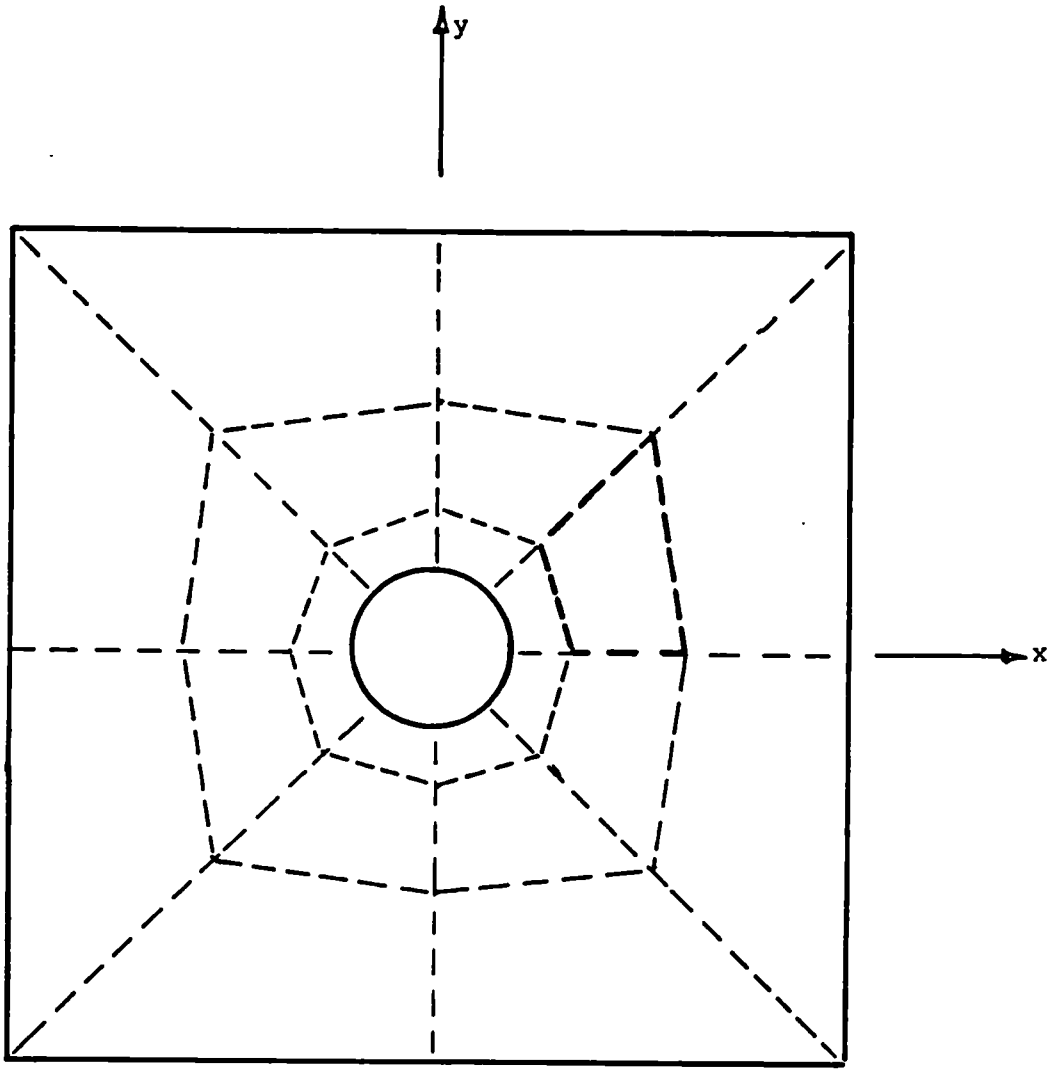


Figure 3.3 Structure divided into finite elements.

3.3.1 The Shape Functions

The geometry of the element in Figure 3.4a is defined in terms of cartesian coordinates. However, the same element can be defined in terms of intrinsic coordinates. In Figure 3.4b the element is mapped on to an intrinsic coordinate system. The cartesian coordinates of a point on the mapped element in Figure 3.4b are only known at the nodes. Therefore, it is necessary to define a set of relationships between the intrinsic coordinate system and the cartesian coordinate system, such that the two systems are continuously related throughout the element. The set of relationships are known as the shape functions. For the node numbering defined in Figure 3.4 the shape functions for 8-node Serendipity elements are

for corner nodes (i=1,3,5,7)

$$N_i = \frac{1}{4}(1 + \xi\xi_i)(1 + \eta\eta_i)(\xi\xi_i + \eta\eta_i - 1) \tag{6}$$

and for midside nodes (i=2,4,6,8)

$$N_i = \frac{\xi_i^2}{2}(1 + \xi\xi_i)(1 - \eta^2) + \frac{\eta_i^2}{2}(1 + \eta\eta_i)(1 - \xi^2) \tag{7}$$

where N_i is the shape function for node i,

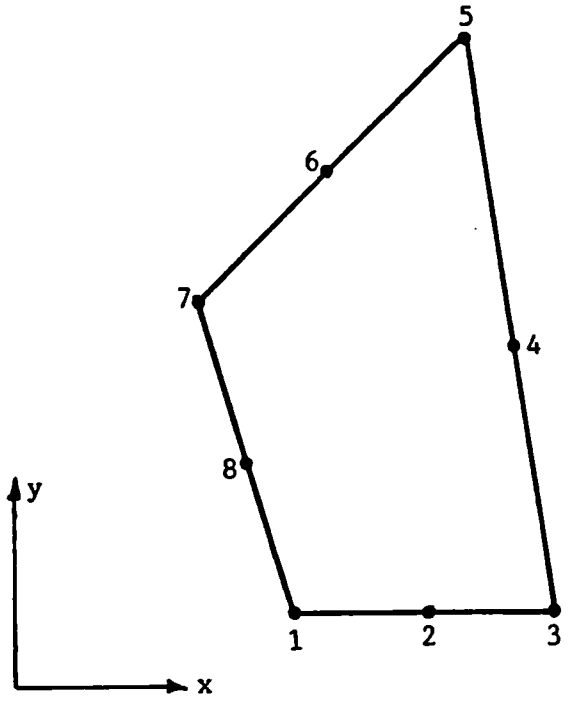
and ξ_i and η_i are the intrinsic coordinates at node i.

The cartesian coordinates of a point within the element defined by the intrinsic coordinates (ξ,η) can now be written as

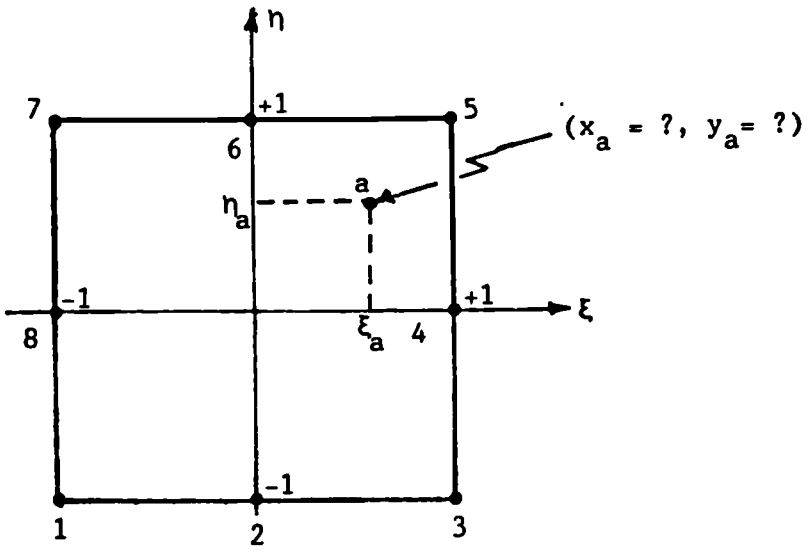
$$x(\xi,\eta) = \sum_{i=1}^{8} N_i(\xi,\eta)x_i \tag{8}$$

$$y(\xi,\eta) = \sum_{i=1}^{8} N_i(\xi,\eta)y_i \tag{9}$$

where x_i and y_i are the known cartesian coordinates at node i.



(a)



(b)

Figure 3.4 Transfering elements from cartesian to intrinsic space.

Thus, the cartesian coordinates of any point within the element can be considered as a weighted sum of all the nodal values, where N_i represents the weighting for node i.

In addition to mapping the geometry from intrinsic coordinates to cartesian (or polar) coordinates, the same shape functions are often used to describe the variation of the basic unknown. In stress analysis the basic unknown is displacement. Assuming for now that the displacement vector is known at the 8 nodes of the element shown in Figure 3.4, then the variation of the displacement throughout the element can be described by replacing x and y in equations (8) and (9) by the components of displacement (u and v). Thus, for plane conditions we have

$$u(\xi,\eta) = \sum_{i=1}^{8} N_i(\xi,\eta)u_i \tag{10}$$

$$v(\xi,\eta) = \sum_{i=1}^{8} N_i(\xi,\eta)v_i \tag{11}$$

Or in vector form

$$[d(\xi,\eta)] = \sum_{i=1}^{8} N_i(\xi,\eta)[d_i] \tag{12}$$

Elements are called isoparametric if the element geometry and the variation of the basic unknown are mapped using the same shape functions. Not all elements are isoparametric; sub and super-parametric elements exist (Zienkiewicz[62]). However, only 8-node Serendipity isoparametric elements are used here.

There is not always a derivation process for establishing the shape function relationships. The Serendipity shape functions, for example, were found by chance and thus named after the famous princes of Serendip noted for their chance discoveries. However, the shape functions whether

derived rigorously or by trial and error, must satisfy a number of conditions to ensure that certain physical discrepancies are not inherent in the functions. These conditions are as follows:

1. $N_i(\xi_i,\eta_i)=1$ for all i, and $N_i(\xi_j,\eta_j)=0$ for $j\neq i$. The reason for this condition is easily apparent. Assume, for example, the nodal value of the displacement vector at node 3, $[d_3]$, is constant and known, and the displacement vector at node 5, $[d_5]$, is variable and unknown. It is invalid that any variation in $[d_5]$ should influence $[d_3]$ which remains constant. Thus, the value of $N_3(\xi_3,\eta_3)$ must be unity and $N_5(\xi_3,\eta_3)$ must be zero, and likewise for the shape functions of nodes 1, 2, 4, 6, 7 and 8 at point (ξ_3,η_3).

2. The sum $\sum N_i(\xi,\eta)=1$ (i=1 to 8), for $-1 \leq \xi \leq 1$ and $-1 \leq \eta \leq 1$. The need for this condition can be appreciated by considering an element that is undergoing rigid body displacement. For rigid body displacement to be conformed to, the displacement vector throughout the element, [d], (including the nodes) must be constant. Thus, $[d_i]=[d]$ for all nodes, and we can write

$$[d(\xi,\eta)] = [d] = \sum_{i=1}^{8} N_i(\xi,\eta)[d_i] = \sum_{i=1}^{8} N_i(\xi,\eta)[d]$$

for the above to hold then $\sum_{i=1}^{8} N_i(\xi,\eta)$ must be unity.

3. Only nodes which define a particular element edge have non zero shape function values along that edge. For example, along the edge defined by $\eta = -1$, the shape functions for nodes 4, 5, 6, 7 and 8 are all zero. Again this can be shown to be a necessary condition by taking a simple example. Assume the edge defined by $\eta = -1$ is a straight line with nodal cartesian coordinates of (0,0), (2,0) and (4,0) for nodes 1, 2 and 3 respectively. Thus, the y-coordinate should remain zero along

the element edge. However, the y-coordinate of the other element nodes have non zero values. Now from condition 1 above it is assured that y values computed at the nodal points along the edge will remain zero. However, to ensure that y remains zero along the intermediate points along the edge, it is necessary that the shape functions for nodes 4, 5, 6, 7 and 8 are all zero for the condition $\eta = -1$.

It may be seen from inspection of equations (6) and (7) that the above 3 conditions are all satisfied.

3.3.2 Strain-Displacement relationships

The strain-displacement relationships for plane conditions are given by

$$\varepsilon_x = -\frac{\partial u}{\partial x}, \quad \varepsilon_y = -\frac{\partial v}{\partial y} \quad \text{and} \quad \gamma_{xy} = -\frac{\partial u}{\partial y} - \frac{\partial v}{\partial x}$$

Thus, by substituting for u and v using the finite element relationships given in equations (10) and (11) we get

$$\varepsilon_x(\xi,\eta) = -\sum_{i=1}^{8} \frac{\partial N_i}{\partial x} u_i \tag{13}$$

$$\varepsilon_y(\xi,\eta) = -\sum_{i=1}^{8} \frac{\partial N_i}{\partial y} v_i \tag{14}$$

and $$\gamma_{xy}(\xi,\eta) = -\sum_{i=1}^{8} \left[\frac{\partial N_i}{\partial y} u_i + \frac{\partial N_i}{\partial x} v_i\right] \tag{15}$$

Combining equations (13), (14) and (15), then in matrix notation we have

$$[\varepsilon]^* = \sum_{i=1}^{8} [B_i][d_i] \tag{16}$$

where $$[\varepsilon]^{*T} = [\varepsilon_x, \ \varepsilon_y, \ \gamma_{xy}] \tag{17}$$

and the B matrix for node i is given by

$$[B_i] = -\begin{bmatrix} \frac{\partial N_i}{\partial x} & 0 \\ 0 & \frac{\partial N_i}{\partial y} \\ \frac{\partial N_i}{\partial y} & \frac{\partial N_i}{\partial x} \end{bmatrix} \tag{18}$$

From equations (6) and (7) it can be seen that N_i cannot be readily differentiated with respect to x and y. However, these derivatives can be determined from matrix manipulation, as described in Section 3.3.3.

3.3.3 The Jacobian

Using rules of partial differentiation the derivatives of N in terms of ξ and η can be expressed as follows

$$\frac{\partial N_i}{\partial \xi} = \frac{\partial N_i}{\partial x}\frac{\partial x}{\partial \xi} + \frac{\partial N_i}{\partial y}\frac{\partial y}{\partial \xi}$$

and $$\frac{\partial N_i}{\partial \eta} = \frac{\partial N_i}{\partial x}\frac{\partial x}{\partial \eta} + \frac{\partial N_i}{\partial y}\frac{\partial y}{\partial \eta}$$

or in matrix notation

$$\begin{bmatrix} \frac{\partial N_i}{\partial \xi} \\ \frac{\partial N_i}{\partial \eta} \end{bmatrix} = [J] \begin{bmatrix} \frac{\partial N_i}{\partial x} \\ \frac{\partial N_i}{\partial y} \end{bmatrix} \tag{19}$$

where [J] is known as the Jacobian matrix for the element concerned and given by

$$[J] = \begin{bmatrix} \frac{\partial x}{\partial \xi} & \frac{\partial y}{\partial \xi} \\ \frac{\partial x}{\partial \eta} & \frac{\partial y}{\partial \eta} \end{bmatrix} = \sum_{i=1}^{8} \left\{ \begin{bmatrix} \frac{\partial N_i}{\partial \xi} \\ \frac{\partial N_i}{\partial \eta} \end{bmatrix} \begin{bmatrix} x_i & y_i \end{bmatrix} \right\} \tag{20}$$

The derivatives of N in terms of x and y can now be found by inverting

equation (19). Thus

$$\begin{bmatrix} \frac{\partial N_i}{\partial x} \\ \frac{\partial N_i}{\partial y} \end{bmatrix} = [J]^{-1} \begin{bmatrix} \frac{\partial N_i}{\partial \xi} \\ \frac{\partial N_i}{\partial \eta} \end{bmatrix} \tag{21}$$

where $[J]^{-1}$ is given by

$$[J]^{-1} = \frac{1}{|J|} \begin{bmatrix} \frac{\partial y}{\partial \eta} & -\frac{\partial y}{\partial \xi} \\ -\frac{\partial x}{\partial \eta} & \frac{\partial x}{\partial \xi} \end{bmatrix} \tag{22}$$

and $|J|$ is the determinant of the Jacobian matrix

All the terms on the right hand side of (22) can be readily determined for a particular point (ξ,η) by differentiating equations (8) and (9). Then from equation (21) the $[B_i]$ matrix (18) can be determined.

3.3.4 Stress-Strain Relationship

The stress-strain relationships for plane strain can be expressed as

$$[\sigma]^* = [D]^*[\varepsilon]^* \tag{23}$$

where the vectors $[\sigma]^*$ and $[\varepsilon]^*$ are defined in (2) and (17) respectively and $[D]^*$ is the matrix of stiffness compliances relating stress to strain, which, for plane strain is given by

$$[D]^* = \frac{E}{(1+\nu)(1-2\nu)} \begin{bmatrix} 1-\nu & \nu & 0 \\ \nu & 1-\nu & 0 \\ 0 & 0 & \frac{1-2\nu}{2} \end{bmatrix} \tag{24}$$

The problems considered here are assumed to be for a circular excavation in a homogeneous, isotropic rock mass, so that in the case of linear elasticity, the matrix of stiffness compliances, $[D]^*$, does not vary throughout the structure considered. Thus, $[D]^*$ is element independent.

However, when the cases of plasticity and pressure dependent elasticity are considered in Chapters 5 and 6, it is found that the instantaneous stress-strain compliances do not only vary from element to element, but from point to point within an element.

3.3.5 Local and Global Node Numbering

The node numbering defined in Figure 3.4 is only relevant on an elemental or local scale. When a Finite Element grid is defined for the whole structure each node must be uniquely numbered on a global scale. Thus, in the simple example in Figure 3.5 we have defined 4 elements and a total of 20 nodes. Taking the global node number 19 for example, then it can be seen that this node is shared by elements 3 and 4. In element 3, node 19 has a local node number of 7, and in element 4, node 19 has a local node number of 5. It is important to distinguish between the two node numbering systems before introducing the Virtual Work expression into finite elements in the next section.

3.3.6 Virtual Work Applied to Finite Elements

Using the rules of matrices and rearranging the virtual work expression given in equation (5) we can arrive at the following

$$\int[\bar{d}]^T[t]dS + \int[\bar{d}]^T[b]dA - \int[\bar{\varepsilon}]^{*T}[\sigma]^* dA = 0 \qquad (25)$$

The finite element expression relating displacement variation given in equation (12) only applies on an elemental scale. Thus, a different set of global node numbers will apply depending in which element the integration point lies. However, this relationship can be made more

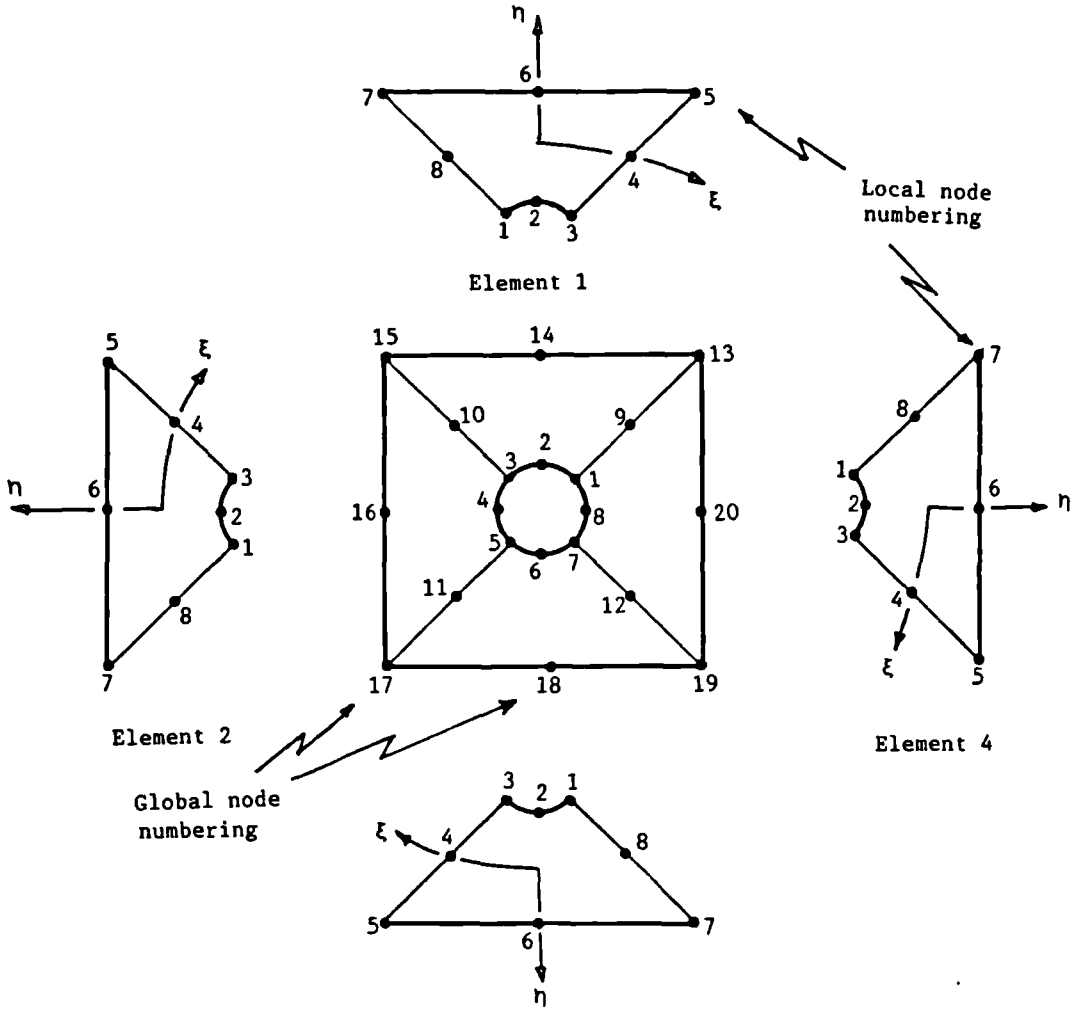


Figure 3.5 Local and global node numbering.

general if the following conditions are stipulated.

1. Values of shape functions and their derivatives are zero for any of the following conditions:- $\xi > 1$, $\xi < -1$, $\eta > 1$ or $\eta < -1$.

2. The origin of the intrinsic coordinate system shifts to a new element as the integration point crosses over an element boundary.

Now equation (12) can be written

$$[d] = \sum_{j=1}^{n} N_j [d_j]$$

or
$$[d]^T = \sum_{j=1}^{n} [d_j]^T N_j \qquad (26)$$

Expression (26) holds true over the entire structure being examined. The counter j now refers to global node numbers, and n is the total number of nodes defining the structure (e.g. for Figure 3.5, n = 20). Similarly the strain-displacement expression (16) can be rewritten as

$$[\varepsilon]^{*T} = \sum_{j=1}^{n} [d_j]^T [B_j]^T \qquad (27)$$

Substituting for $[\bar{d}]$ and $[\bar{\varepsilon}]^*$ into (25) using expressions (26) and (27) gives

$$\int \sum_{j=1}^{n} [\bar{d}_j]^T [t] dS + \int \sum_{j=1}^{n} [\bar{d}_j]^T [b] dA - \int \sum_{j=1}^{n} [\bar{d}_j]^T [B_j]^T [\sigma]^* dA = 0 \qquad (28)$$

From inspection it can be seen that for all three terms in equation (28) the following equivalence is true

$$\int \Sigma \bullet \Sigma \int$$

Also the nodal virtual displacement vector is independent of position and therefore need not remain behind the integral sign. Thus, equation

(28) can be rearranged to give

$$\sum_{j=1}^{n}[\bar{d}_j]\int N_j[t]dS + \sum_{j=1}^{n}[\bar{d}_j]\int N_j[b]dA - \sum_{j=1}^{n}[\bar{d}_j]\int[B_j]^T[\sigma]^*dA = 0$$

or
$$\sum_{j=1}^{n}[\bar{d}_j]\left\{\int N_j[t]dS + \int N_j[b]dA - \int[B_j]^T[\sigma]^*dA\right\} = 0 \qquad (29)$$

The expression within the curly brackets is independent of the nodal virtual displacement vector $[d_j]$. Apart from having stipulated that the virtual displacements must be small in magnitude, no other restrictions have been imposed. Thus, for equation (29) to hold for all sets of imposed virtual displacements the expression within the curly brackets must be zero.

$$\therefore \quad \int N_j[t]dS + \int N_j[b]dA - \int[B_j]^T[\sigma]^*dA = 0$$

or
$$\int N_j[t]dS + \int N_j[b]dA - \int[B_j]^T[D]^*[\varepsilon]^*dA = 0 \qquad (30)$$

where $[D]^*$ and $[\varepsilon]^*$ are given in (24) and (16) respectively.

Equation (30) is the governing equation for finite element analyses. Since equation (30) is derived for node j, and j can take on values of 1 to n, then there will be n versions of (30), one for each node. In the derivation of (30) it was assumed that plane conditions prevail. Thus, the displacement vector has only two non-zero components (x-displacement and y-displacement). From matrix multiplication it can be shown that equation (30) leads to two simultaneous equations per node. Thus, the total number of simultaneous equations for the whole structure will be 2 x n. For simplicity, it is assumed that at each node the displacement is unknown and the imposed loads are known (for internal nodes the imposed loads are zero), and since the strain vector, $[\varepsilon]^*$, is a function of the

nodal displacements, the total number of unknowns will be 2 x n. Therefore, the number of unknowns and the number of equations match and by solving the set of simultaneous equations the unknowns can be found. (This is not necessarily true, since at some exterior nodes it may be the case that the displacement is known and the imposed traction is unknown).

3.3.7 The Stiffness Matrix

As stated in Section 3.3.6, equation (30) leads to a set of simultaneous equations of the form

$$[K_{11}][d_1] + [K_{12}][d_2] + \ldots [K_{1j}][d_j] + \ldots + [K_{1n}][d_n] = [\psi_1]$$
$$[K_{21}][d_1] + [K_{22}][d_2] + \ldots [K_{2j}][d_j] + \ldots + [K_{2n}][d_n] = [\psi_2]$$
$$\ldots\ldots$$
$$\ldots\ldots$$
$$[K_{j1}][d_1] + [K_{j2}][d_2] + \ldots [K_{jj}][d_j] + \ldots + [K_{jn}][d_n] = [\psi_j]$$
$$\ldots\ldots$$
$$\ldots\ldots$$
$$[K_{n1}][d_1] + [K_{n2}][d_2] + \ldots [K_{nj}][d_j] + \ldots + [K_{nn}][d_n] = [\psi_n]$$

i.e. n vector relationships, or 2n scalar simultaneous equations.

Or in matrix notation

$$[K][u] = [\psi] \qquad (31)$$

where [K] is a 2nx2n matrix of known coefficients developed from integration of the strain energy term in equation (30), called the global stiffness matrix,

[u] represents the global displacement vector and is given by

$$[u]^T = [u_1, v_1, u_2, v_2, \ldots u_j, v_j, \ldots u_n, v_n]$$

and $[\psi]$ is known as the load vector, and given by

$$[\psi]^T = [P_{x1}, P_{y1}, P_{x2}, P_{y2}, \ldots P_{xj}, P_{yj}, \ldots P_{xn}, P_{yn}] \qquad (32)$$

where P_{xj} and P_{yj} are nodal loads developed from integration of the boundary traction and body force terms in equation (30).

The formation of the matrix [K] is best illustrated with reference to Figure 3.5. First, substituting for $[\varepsilon]^*$ into the strain energy term using equation (16) and considering the integral over the whole structure as the sum of each element area then we can write the strain energy term as

$$\int [B_j]^T [D]^* [\varepsilon]^* dA = \sum_{e=1}^{m} \int [B_j]^T [D]^* \left[\sum_{i=1}^{8^e} [B_i][d_i] \right] dA_e \qquad (33)$$

where $\sum^e$ signifies that the summation is for element 'e' within which the integration point lies,

m is the number of elements defining the problem (in this case 4),

and dA_e signifies integration over the element e.

By considering that the nodal displacement vector $[d_i]$ is independent of the integrand (dA_e), and taking the $[B_j]$ and $[D]^*$ matrices within the integral sign, then (33) can be rearranged to give

$$\int [B_j]^T [D]^* [\varepsilon]^* dA = \sum_{e=1}^{m} \sum_{i=1}^{8} \left\{ \int [B_j]^T [D]^* [B_i] dA_e \right\} [d_i] \qquad (34)$$

The integral term in the curly brackets in equation (34) represents a 2x2 matrix of stiffness coefficients (since there are two degrees of

freedom per node for plane strain) as a result of integrating over element 'e'. Thus, we can write that the contribution to the global stiffness coefficient sub-matrix, $[K_{jk}]$, from element 'e' is represented by $[K_{jk}]^e$ and expressed as

$$[K_{jk}]^e = \int [B_j]^T [D]^e [B_i] dA_e \qquad (35)$$

where the counter 'k' is the global node number for local node 'i'.

Consider the evaluation of equation (30) for the global node number 9 in Figure 3.5 (i.e. counter j = 9). This node is shared by elements 1 and 4. In element 1 it occupies the local node number 4 and in element 4 it occupies local node number 8. However, node 9 does not exist in elements 2 and 3 and therefore $[B_j]$ is a zero matrix and consequently $[K_{jk}]^e$ in (35) is also a zero matrix for e = 2 and 3. Thus, the set of global sub-matrices, $[K_{jk}]$, for j = 9 and k = 1 to 20, can be found by summing the contributions from only elements 1 and 4. This results in the following

$$[K_{9,k}] = [K_{9,k}]^1 + [K_{9,k}]^4 \qquad \text{for } k = 1,2,3,7,8,9,10,12,13,14,15,19 \text{ \& } 20$$

$$[K_{9,k}] = 0 \qquad \text{for } k = 4,5,6,11,16,17 \text{ \& } 18$$

If node number 14 had been considered, for example, a greater proportion of the stiffness coefficients would have been zero, since node 14 only appears in one element (Element 1). Thus, it can be seen that a large number of the stiffness coefficients are zero, and in a more realistic finite element mesh, where hundreds of elements may be used to define the problem, vast areas of the global stiffness matrix, [K], are occupied by zeros.

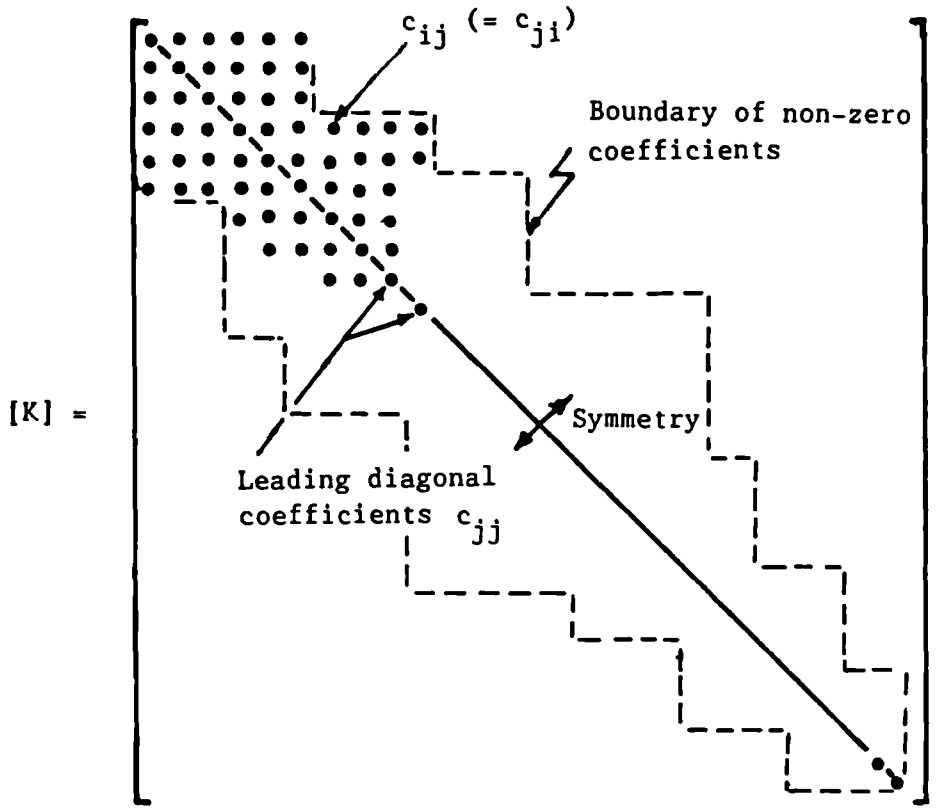


Figure 3.6 Symmetry in the global stiffness matrix about the leading diagonal.

Another property of the stiffness matrix is that it is symmetrical about the leading diagonal (see Figure 3.6) for linear elastic problems and certain cases of nonlinear behaviour. This can be shown by interchanging the counters j and k in equation (35). Thus,

$$[K_{jk}] = [K_{kj}]$$

3.3.8 Numerical Integration of the Strain Energy Term

In order to evaluate the elemental stiffness coefficients given in equation (35) it is necessary to perform the integration over the element with respect to dA_e. The integrand dA_e represents a double integral in terms of linear cartesian coordinates. Thus,

$$\int dA_e = \iint dx_e . dy_e \qquad (36)$$

The matrices $[B_i]$ and $[B_j]$ in equation (35) are evaluated at points defined by intrinsic coordinates, so in order to perform the integration the integrand must be transformed from cartesian to intrinsic space.

Figure 3.7 shows a portion of an element defined in intrinsic coordinates mapped onto a cartesian coordinate grid. Assuming all dimensions are small the area of the shaded portion can be found using simply coordinate geometry. Thus,

$$\delta A = (a+c)(b+d) - 2ad - dc - ab$$
$$= bc - ad$$

The cartesian length of the dimensions a,b,c and d are given by

$$a = \frac{\partial x}{\partial \eta}\delta\eta, \qquad b = \frac{\partial y}{\partial \eta}\delta\eta, \qquad c = \frac{\partial x}{\partial \xi}\delta\xi \quad \text{and} \quad d = \frac{\partial y}{\partial \xi}\delta\xi$$

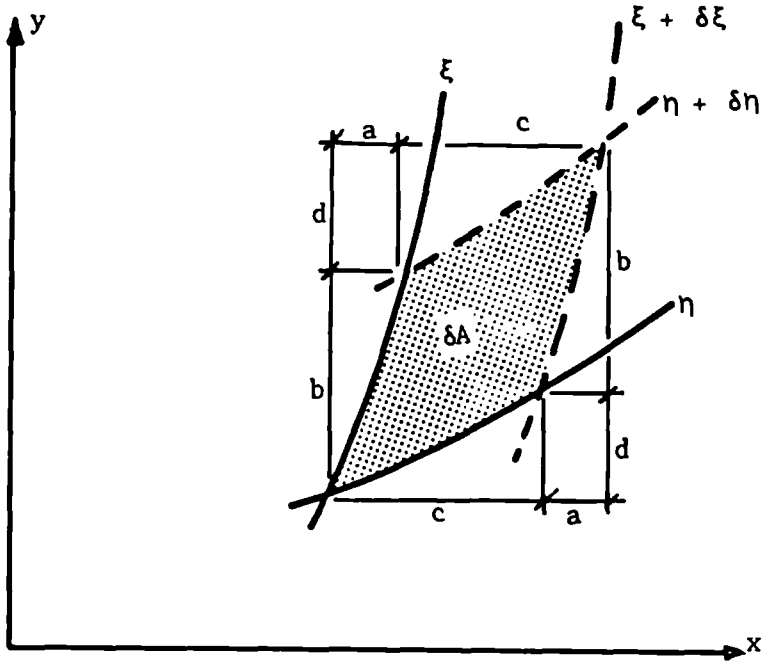


Figure 3.7 Portion of element mapped from intrinsic to cartesian space.

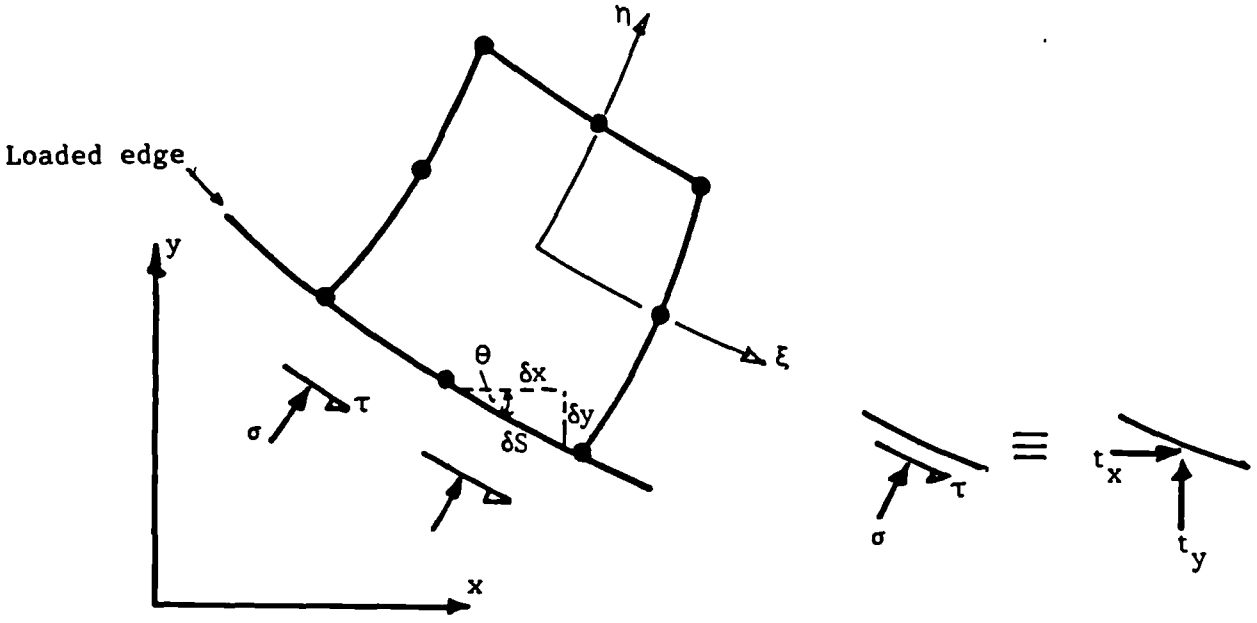


Figure 3.8 Element edge with distributed loading.

$$\therefore \quad \delta A = \left(\frac{\partial y}{\partial \eta}.\frac{\partial x}{\partial \xi} - \frac{\partial x}{\partial \eta}.\frac{\partial y}{\partial \xi}\right)\delta\xi.\delta\eta$$

Or in the limit

$$dA = |J|d\xi.d\eta$$

where $|J|$ is the determinant of the Jacobian matrix given in equation (20). Thus, expression (35) can be written as

$$[K_{jk}]^{\bullet} = \int_{-1}^{+1}\int_{-1}^{+1}[T_{jk}]^{\bullet}d\xi_{\bullet}.d\eta_{\bullet} \qquad (37)$$

where $[T_{jk}]^{\bullet} = [B_j]^{T}[D]^{\bullet}[B_i]|J^{\bullet}|$

Equation (37) cannot be integrated into a closed form solution, therefore it is necessary to turn to numerical methods for integration of (37). There are a number of numerical integration methods available, but the one which is favoured most in FEM techniques is Gauss quadrature integration. This technique is described in some detail in numerous mathematical text books and a number of FEM text books (e.g. Zienkiewicz[62]), but only details on its application are given here.

The Gaussian integration method involves selecting a number of points (Gauss points) at specific intrinsic coordinates within the element as sampling points. The value of the variable ($[T_{jk}]^{\bullet}$ in this case) at the sampling points is then multiplied by a weighting factor (Gauss weight). The number of points that can be used to integrate over an element is virtually unlimited. However, the most common are the 2x2 and 3x3 Gauss point rules for 2-dimensional problems. If we assume that the numerical integration is carried out using a gxg Gauss quadrature rule then $[K_{jk}]^{\bullet}$ can be expressed as

$$[K_{jk}]^{\bullet} = \sum_{p=1}^{g}\sum_{q=1}^{g}[T(\xi_p,\eta_q)_{jk}]W_pW_q$$

where ξ_p and η_q are the sampling point coordinates,

and W_p and W_q are the gauss weights.

Counters		Sampling Point		Gauss Weight	
p	q	ξ_p	η_q	W_p	W_q
2 x 2 Gauss point integration					
1	1	-0.5773503	-0.5773503	1.0	1.0
1	2	-0.5773503	0.5773503	1.0	1.0
2	1	0.5773503	-0.5773503	1.0	1.0
2	2	0.5773503	0.5773503	1.0	1.0
3 x 3 Gauss point integration					
1	1	-0.7745967	-0.7745967	0.5555556	0.5555556
1	2	-0.7745967	0.0	0.5555556	0.8888889
1	3	-0.7745967	0.7745967	0.5555556	0.5555556
2	1	0.0	-0.7745967	0.8888889	0.5555556
2	2	0.0	0.0	0.8888889	0.8888889
2	3	0.0	0.7745967	0.8888889	0.5555556
3	1	0.7756967	-0.7745967	0.5555556	0.5555556
3	2	0.7756967	0.0	0.5555556	0.8888889
3	3	0.7756967	0.7756967	0.5555556	0.5555556

Gauss weights and sampling points for numerical integration.

TABLE 3

The sampling points and weights for the 2x2 and 3x3 point rules are given in Table 3.

3.3.9 The Load Vector

The load vector $[\psi]$ defined in (32) is a result of integration of the body force and surface traction terms in equation (30). However, the body force term shall not be dealt with here, since it is a reasonable assumption for wellbore stress analysis that the self weight of the rock at depth is insignificant compared with the in-situ stress loading. Thus, only the surface loading term shall be considered and the FEM expression given in (30), reduces to

$$\int [B_j]^T [D]^* [\varepsilon]^* dA = \int N_j [t] dS \quad \left(\equiv [\psi_j] \right) \tag{38}$$

where $[\psi_j]^T = [P_{xj}, P_{yj}]$

In general the surface loading can be made up of distributed loads and point loads. However, for the study of stresses around a wellbore only distributed surface loading need be considered, therefore application of point loads is not covered here.

Assume that the surface loads are input as tractions normal (σ) and parallel (τ) to the problem boundaries as per the convention shown in Figure 3.8. The element shown in Figure 3.8 has the loaded edge defined by $\eta = -1$. However, this is not a requirement and any of the four element edges could be subjected to external loading.

Consider a small length along the loaded boundary. Its length in intrinsic space is given by $\delta\xi$, and in cartesian space by δS. Since η is

constant along the loaded edge the length of the x and y components of δS are given by

$$\delta x = \frac{\partial x}{\partial \xi}\delta\xi \qquad \text{and} \quad \delta y = \frac{\partial y}{\partial \xi}\delta\xi$$

Therefore the angle θ, as defined in Figure 3.8, is given by

$$\sin\theta = -\frac{\delta y}{\delta S} = -\frac{\partial y}{\partial \xi}\cdot\frac{\delta \xi}{\delta S} = -\frac{\partial y}{\partial \xi}\cdot\frac{d\xi}{dS} \quad \text{(in the limit)} \tag{39}$$

$$\cos\theta = \frac{\delta x}{\delta S} = \frac{\partial x}{\partial \xi}\cdot\frac{\delta \xi}{\delta S} = \frac{\partial x}{\partial \xi}\cdot\frac{d\xi}{dS} \quad \text{(in the limit)} \tag{40}$$

From consideration of force equilibrium it can be seen that the tractions t_x and t_y are related to σ and τ by the following

$$t_x = \sigma.\sin\theta + \tau.\cos\theta$$

and $$t_y = \sigma.\cos\theta - \tau.\sin\theta$$

Thus, by substituting for $\sin\theta$ and $\cos\theta$ using (39) and (40) respectively, we get

$$t_x = \left(\tau\frac{\partial x}{\partial \xi} - \sigma\frac{\partial y}{\partial \xi}\right)\frac{d\xi}{dS}$$

and $$t_y = \left(\sigma\frac{\partial x}{\partial \xi} + \tau\frac{\partial y}{\partial \xi}\right)\frac{d\xi}{dS}$$

Thus, the components of the nodal load vector $[\psi_j]$, defined in (38), for a node lying on the element edge as shown in Figure 3.8 are given by

$$P_{xj} = \int N_j\left(\tau\frac{\partial x}{\partial \xi} - \sigma\frac{\partial y}{\partial \xi}\right)\frac{d\xi}{dS}dS = \int N_j\left(\tau\frac{\partial x}{\delta \xi} - \sigma\frac{\partial y}{\partial \xi}\right)d\xi \qquad (\eta = -1) \tag{41}$$

$$P_{yj} = \int N_j\left(\sigma\frac{\partial x}{\partial \xi} + \tau\frac{\partial y}{\partial \xi}\right)\frac{d\xi}{dS}dS = \int N_j\left(\sigma\frac{\partial x}{\partial \xi} + \tau\frac{\partial y}{\partial \xi}\right)d\xi \qquad (\eta = -1) \tag{42}$$

The derivatives of x and y with respect to ξ are determined in the same manner as the Jacobian matrix in Section 3.3.3.

Similar expressions can be found for loading on the other three element edges.

As with the strain energy term in equation (34) the boundary traction

term is considered as a sum of integrations over individual elements. Thus, equations (41) and (42) can be written as

$$P_{xj} = \sum_{e=1}^{m} \int N_j \left(\tau\frac{\partial x}{\partial \xi} - \sigma\frac{\partial y}{\partial \xi}\right)[t_n]^e d\xi^e \qquad (\eta = -1) \qquad (43)$$

$$P_{yj} = \sum_{e=1}^{m} \int N_j \left(\sigma\frac{\partial x}{\partial \xi} + \tau\frac{\partial y}{\partial \xi}\right)[t_n]^e d\xi^e \qquad (\eta = -1) \qquad (44)$$

Although the summation is shown to be over all 'm' elements, in practice summation will only be over one element when j represents a mid node, and two elements when j represents a corner node.

Equations (43) and (44) cannot be integrated using calculus, so integration has to be performed numerically. Again this is performed using the Gauss quadrature formula (see Section 3.3.8). Taking equation (43) for example, we can write

$$P_{xj} = \sum_{e=1}^{m} \sum_{p=1}^{g} N_j(\eta_p) \left[\tau(\xi_p)\left(\frac{\partial x}{\partial \xi}\right)_{\xi_p} - \sigma(\xi_p)\left(\frac{\partial y}{\partial \xi}\right)_{\xi_p}\right] W_p \qquad (\eta = -1) \qquad (45)$$

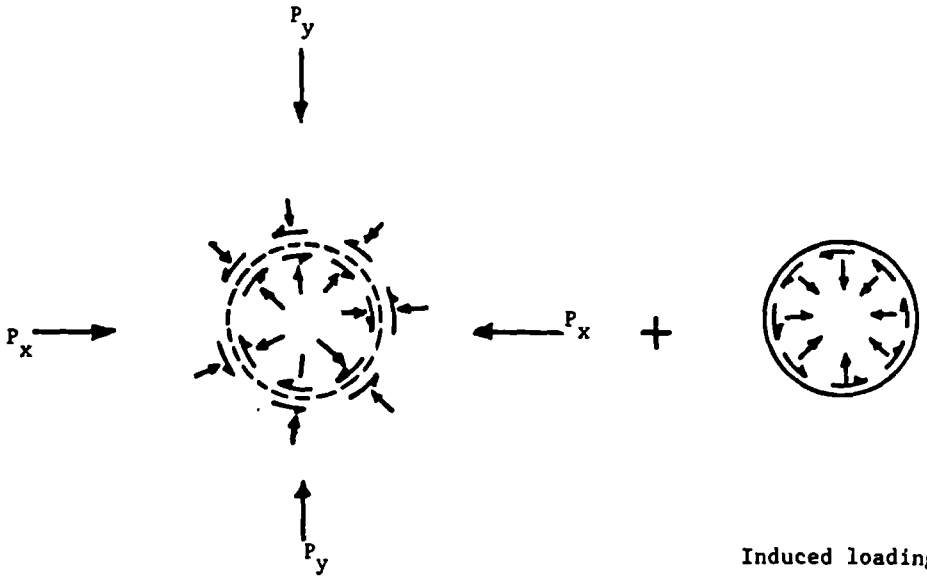
Equation (45) results in a nodal load which is equivalent to the imposed x-component of the boundary loading. A similar expression can be found for the y-component. The components of the load vector thus found are known as the equivalent nodal loads.

3.4 COMPLETE PLANE STRAIN CONDITIONS

3.4.1 Method of Loading

The stress state around an excavation in rock can be calculated by two methods of loading:

1. Determination of the resultant stress distribution directly taking

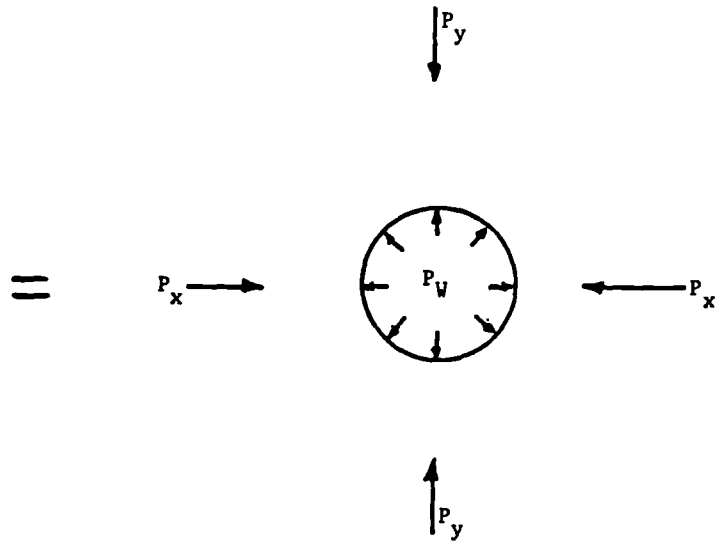


Original loading

(a)

Induced loading due to forming opening

(b)



Resultant loading

(c)

Figure 3.9 Combination of original and induced loading to give resultant stress state.

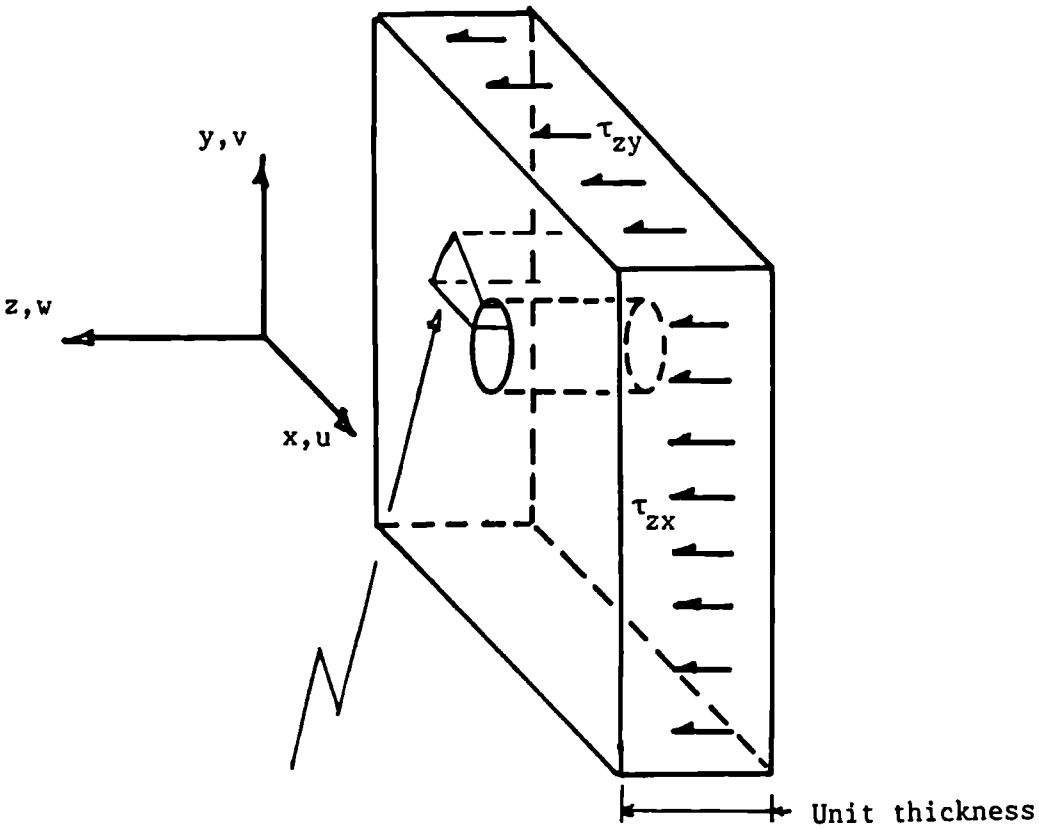
into account the far field stress conditions (in-situ stress state) and the boundary conditions at the hole (Figure 3.9c).

2. Determination of the stresses induced by the excavation allowing for the change in tractions, at the boundary of the hole (Figure 3.9b). The induced stresses are then added to the original stress state (Figure 3.9a), using superposition, to get the resultant stress distribution (Figure 3.9c).

In the context of this thesis Method 2 is used in preference to Method 1. Both methods are equally accurate, but Method 2 does have some advantages. Firstly, the displacements of interest to the engineer are those due to the formation of the excavation (i.e. induced displacements). Using Method 1, displacements would contain a component related to the deposition of the rock mass. Secondly, the definition of plane strain is mathematically neater if applied to the induced stresses rather than the resultant stress distribution. Considering stresses and strains to be induced, then it can be said that for plane strain the axial strain is zero, whereas, for the resultant stresses and strains this is not true, and the axial strain is constant, but not necessarily zero.

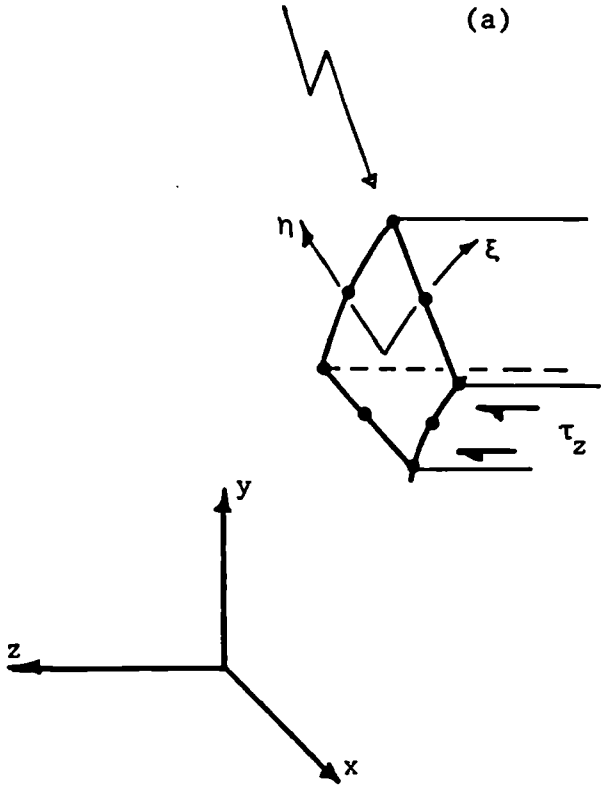
3.4.2 Strain-Displacement Relationships

Considering only the induced loading stress state, as discussed in Section 3.4.1, then the definition of plane strain is that there is no variation in conditions in the axial direction and the axial displacement is zero. Assume a coordinate system relative to the excavation defined by the x, y and z axes, with z as the axial direction



Typical element

(a)



(b)

Figure 3.10 Antiplane shear loading.

(e.g. Figure 3.10a), and the respective displacement components are u, v and w. Then, for plane strain we can write

$$w = 0, \quad \frac{\partial w}{\partial x} = 0, \quad \frac{\partial w}{\partial y} = 0, \quad \frac{\partial w}{\partial z} = 0, \quad \frac{\partial u}{\partial z} = 0 \quad \text{and} \quad \frac{\partial v}{\partial z} = 0$$

Using the above conditions the general 3-dimensional strain-displacement relationships reduce to

$$\varepsilon_x = -\frac{\partial u}{\partial x}, \qquad \varepsilon_y = -\frac{\partial v}{\partial y}, \qquad \varepsilon_z = 0,$$

$$\gamma_{xy} = -\frac{\partial u}{\partial y} - \frac{\partial v}{\partial x}, \qquad \gamma_{yz} = 0 \quad \text{and} \quad \gamma_{zx} = 0$$

These relationships were used to define the [B] matrices used in the FEM development in Section 3.3.2.

The definition of plane strain given above restricts its use to conditions where the axial direction of the excavation is parallel to a principal in-situ stress direction. If this were not the case then antiplane shear stresses ($\tau_{\theta z}$ and/or τ_{zr}) would be set up, and the condition that the axial displacement is zero would not hold throughout the section. However, the condition of zero axial displacement is an unreasonable restriction on plane strain. Brady and Bray[46] proposed a more general definition of plane strain. They proposed that plane strain requirements are met when conditions (i.e. loading, geometry and displacement) are independent of the axial direction, but did not impose the further restriction that axial displacements are zero. In order to differentiate their definition of plane strain from the more popular definition, Brady and Bray called it 'complete plane strain'. Thus, for complete plane strain the following differential equations apply,

$$\frac{\partial u}{\partial z} = 0, \quad \frac{\partial v}{\partial z} = 0 \quad \text{and} \quad \frac{\partial w}{\partial z} = 0$$

and in general $\frac{\partial w}{\partial x} \neq 0$ and $\frac{\partial w}{\partial y} \neq 0$

The 3-dimensional strain-displacement relationships are now given by

$$\varepsilon_x = -\frac{\partial u}{\partial x}, \qquad \varepsilon_y = -\frac{\partial v}{\partial y}, \qquad \varepsilon_z = 0,$$

$$\gamma_{zy} = -\frac{\partial u}{\partial y} - \frac{\partial v}{\partial x}, \qquad \gamma_{yz} = -\frac{\partial w}{\partial z}, \qquad \text{and} \qquad \gamma_{zx} = -\frac{\partial w}{\partial x}$$

3.4.3 The FEM Applied to Complete Plane Strain

If the same development procedure followed in Section 3.2 is applied to complete plane strain it can be shown that the general form of the virtual work expression is the same. However, a number of changes occur in the FEM relationships, as detailed below.

In the strain-displacement relationship given by equation (16) we now have

$$[\varepsilon]^{*T} = [\varepsilon_x, \varepsilon_y, \gamma_{xy}, \gamma_{yz}, \gamma_{zx}]$$

$$[d]^T = [u, v, w]$$

and

$$[B_i]^T = -\begin{bmatrix} \frac{\partial N_i}{\partial x} & 0 & \frac{\partial N_i}{\partial y} & 0 & 0 \\ 0 & \frac{\partial N_i}{\partial y} & \frac{\partial N_i}{\partial x} & 0 & 0 \\ 0 & 0 & 0 & \frac{\partial N_i}{\partial y} & \frac{\partial N_i}{\partial x} \end{bmatrix}.$$

In the case of the stress-strain relationships given by equation (23) we now have

$$[\sigma]^{*T} = [\sigma_x, \sigma_y, \tau_{xy}, \tau_{yz}, \tau_{zx}]$$

and

$$[D]^* = \frac{E}{(1+\nu)(1-2\nu)}\begin{bmatrix} (1-\nu) & \nu & 0 & 0 & 0 \\ \nu & (1-\nu) & 0 & 0 & 0 \\ 0 & 0 & \frac{(1-2\nu)}{2} & 0 & 0 \\ 0 & 0 & 0 & \frac{(1-2\nu)}{2} & 0 \\ 0 & 0 & 0 & 0 & \frac{(1-2\nu)}{2} \end{bmatrix} \qquad (46)$$

In the load vector term given in equation (38), the nodal load vector, $[\psi_j]$ now represents three equivalent nodal loads (x, y and z components). The x and y components are still evaluated according to procedures set out in Section 3.3.9. The third component (P_{zj}) is evaluated as set out below.

Adopting the convention shown in Figure 3.10b, then the shear traction acting on the element edge is given by τ_z (this will be the resultant of the shear stresses τ_{yz} and τ_{zx}). Thus, the third equivalent nodal load is expressed as

$$P_{zj} = \int N_j \tau_z dS \tag{47}$$

Along the element edge shown in Figure 3.10b η is fixed and equal to -1. Thus, S, x & y along this edge are only dependent on ξ and we can write

$$\delta S = \frac{\partial S}{\partial \xi}\delta\xi, \quad \delta x = \frac{\partial x}{\partial \xi}\delta\xi \quad \text{and} \quad \delta y = \frac{\partial y}{\partial \xi}\delta\xi$$

Also from Pythagoras we have

$$\delta S = \left[\delta x^2 + \delta y^2\right]^{\frac{1}{2}}$$

$$\therefore \quad \delta S = \left[\left(\frac{\partial x}{\partial \xi}\right)^2 + \left(\frac{\partial y}{\partial \xi}\right)^2\right]^{\frac{1}{2}}\delta\xi$$

On substituting the above into (47) we get for the third equivalent nodal load

$$P_{zj} = \int N_j \tau_z \left[\left(\frac{\partial x}{\partial \xi}\right)^2 + \left(\frac{\partial y}{\partial \xi}\right)^2\right]^{\frac{1}{2}} d\xi \qquad (\eta = 1 \text{ or } -1) \tag{48}$$

Integration of equation (48) is also carried out using numerical procedures.

For cases where loaded edges are defined by $\xi = 1$ or -1, then the variables η and ξ in equation (48) are interchanged.

3.5 THE FEM IN TERMS OF POLAR COORDINATES

The relationships developed so far in this chapter have been with reference to cartesian coordinates for ease of mathematical notation. However, there are certain advantages in adopting a polar coordinate system when analysing circular excavations. For example, the shape functions can follow the wellbore geometry exactly when used in conjunction with polar coordinates, whereas they only approximate the geometry in terms of cartesian coordinates. The relevant relationships with respect to polar coordinates are only presented here. However, they can easily be derived following the same principles given earlier.

3.5.1 Strain-Displacement Relationships

The $[d]$, $[\varepsilon]^*$ vectors and the $[B]$ matrix in equation (16) are now defined as

$$[d]^T = [u_r,\ u_\theta,\ u_z]$$

where u_r, u_θ and u_z are defined in Figure 3.11

$$[\varepsilon]^{*T} = [\varepsilon_r,\ \varepsilon_\theta,\ \gamma_{r\theta},\ \gamma_{\theta z},\ \gamma_{zr}]$$

and

$$[B_i]^T = -\begin{bmatrix} \frac{\partial N_i}{\partial r} & \frac{N_i}{r} & \frac{1}{r}\frac{\partial N_i}{\partial \theta} & 0 & 0 \\ 0 & \frac{1}{r}\frac{\partial N_i}{\partial \theta} & \left(\frac{\partial N_i}{\partial r}+\frac{N_i}{r}\right) & 0 & 0 \\ 0 & 0 & 0 & \frac{\partial N_i}{\partial r} & \frac{1}{r}\frac{\partial N_i}{\partial \theta} \end{bmatrix}$$

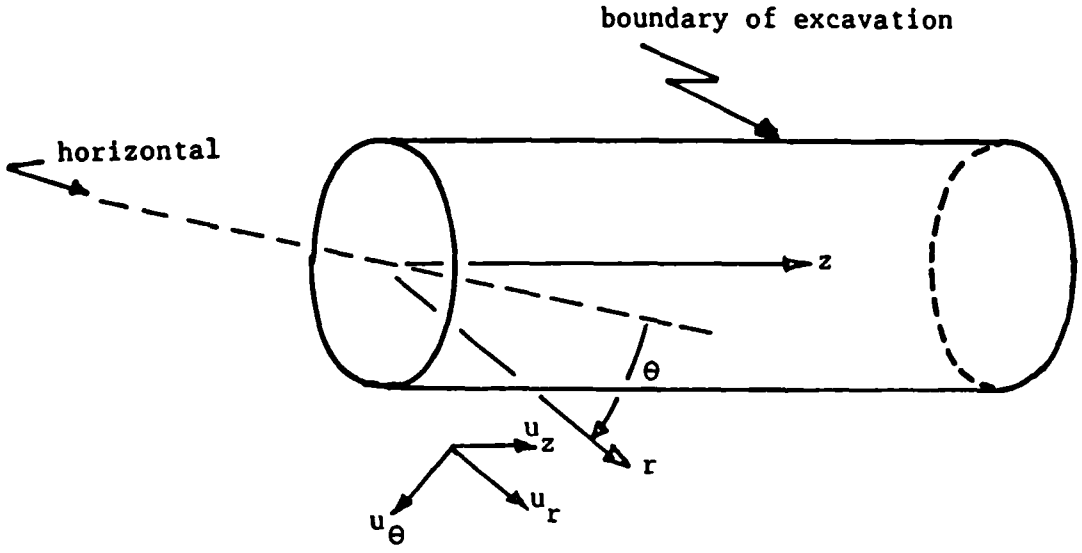


Figure 3.11 Circular excavation defined in terms of polar coordinates.

3.5.2 The Jacobian

The Jacobian matrix given by (20), which upon inversion allows determination of the terms in the [B] matrix, is now expressed as

$$[J] = \begin{bmatrix} \frac{\partial r}{\partial \xi} & \frac{\partial \theta}{\partial \xi} \\ \frac{\partial r}{\partial \eta} & \frac{\partial \theta}{\partial \eta} \end{bmatrix} = \sum_{i=1}^{8} \left\{ \begin{bmatrix} \frac{\partial N_i}{\partial \xi} \\ \frac{\partial N_i}{\partial \eta} \end{bmatrix} \begin{bmatrix} r_i & \theta_i \end{bmatrix} \right\}$$

and equation (21) becomes

$$\begin{bmatrix} \frac{\partial N_i}{\partial r} \\ \frac{\partial N_i}{\partial \theta} \end{bmatrix} = [J]^{-1} \begin{bmatrix} \frac{\partial N_i}{\partial \xi} \\ \frac{\partial N_i}{\partial \eta} \end{bmatrix}$$

where $$[J]^{-1} = \frac{1}{|J|} \begin{bmatrix} \frac{\partial \theta}{\partial \eta} & -\frac{\partial \theta}{\partial \xi} \\ -\frac{\partial r}{\partial \eta} & \frac{\partial r}{\partial \xi} \end{bmatrix}$$

3.5.3 Stress-Strain Relationship

The stress vector $[\sigma]^*$ in equation (23) is now given by

$$[\sigma]^{*T} = [\sigma_r, \sigma_\theta, \tau_{r\theta}, \tau_{\theta z}, \tau_{zr}]$$

The D matrix corresponds to the complete plane strain matrix of compliances given in (46).

3.5.4 Integration of the Strain Energy Term

In Section 3.3.8 the independent variable dA_e was converted from cartesian coordinates to intrinsic coordinates such that the element sub-matrix of stiffness coefficients, $[K_{jk}]^e$, could be expressed in terms of consistent variables as given in equation (37). For conversion from polar to intrinsic coordinates equation (37) has the same form.

However, the term $[T_{jk}]^*$ is now given by

$$[T_{jk}]^* = [B_j]^T[D]^*[B_i]r(\xi,\eta)|J^*| \qquad (49)$$

3.5.5 Surface Traction Term

As in Figures 3.8 and 3.10b it is assumed that the loaded element edge is defined by $\eta = -1$. Then the two nodal load components required for a simple plane strain analysis in polar coordinates (c.f. equations (41) and (42) in cartesian coordinates) are given by

$$P_{rj} = \int N_j \left(\sigma r \frac{\partial\theta}{\partial\xi} + \tau \frac{\partial r}{\partial\xi}\right) d\xi \qquad (\eta = -1)$$

and $$P_{\theta j} = \int N_j \left(\tau r \frac{\partial\theta}{\partial\xi} - \sigma \frac{\partial r}{\partial\xi}\right) d\xi \qquad (\eta = -1)$$

and the third nodal load required for complete plane strain analysis (c.f. equation (48) for cartesian coordinates) is given by

$$P_{zj} = \int N_j \tau_z \left[\left(\frac{\partial r}{\partial\xi}\right)^2 + (r(\xi))^2 \left(\frac{\partial\theta}{\partial\xi}\right)^2\right]^{\frac{1}{2}} d\xi \qquad (\eta = -1)$$

3.6 EQUATION SOLUTION

As given in Section 3.3.7, the unknown displacements, [u], are inter related by a set of simultaneous equations of the form

$$[K][u] = [\psi]$$

In order to find the unknowns it is necessary to solve the set of simultaneous equations. In large FEM problems the number of equations can be many thousands and therefore involve millions of computations. The equation solution routine of a FEM program can often account for the majority of the computing time required to analyse a problem.

Most FEM equation solvers are based on the Gaussian direct elimination technique involving forward reduction of the global stiffness matrix, followed by back substitution into the reduced matrix. However, there are a number of variations in solver routines which use this technique (Forsythe[65]). One of the most efficient and revolutionary of its time is the frontal solver technique, which is used in the program for this work. A full listing and description of the solver is given by its originator, Irons.[66] The computer logic and 'house keeping' used in the frontal solver is rather complex and beyond the context of this thesis. However, it is worth pointing out three of its properties.

1. All FEM solvers developed for analysis of linear elastic problems take advantage of symmetry about the leading diagonal in the global stiffness matrix, [K] (see Figure 3.6), and the frontal solver is no exception. This symmetry is as a result of symmetry of the elemental sub-matrices, $[K_{jk}]^e$, as pointed out in Section 3.3.7.

2. As explained in Section 3.3.7, large areas of the global stiffness matrix contain zero stiffness coefficients. FEM solvers take advantage of this to various degrees of efficiency, with the frontal solver as perhaps the most efficient.

3. The global node numbering defined by the user or an element generator can have considerable influence on the efficiency of an equation solver (Melosh and Bamford[67]). However, the efficiency of a frontal solver is dependent on element numbering, not node numbering, which considerably reduces the complexity of a FEM mesh generation.

In reference to Item 3 above, Irons[66] defined nodes (or variables)

as active on their first appearance when summing up element contributions to the global stiffness matrix and load vector. The active node is then eliminated when fully summed after its last appearance. Thus, using Figure 3.5 as an example, we have eight active nodes on introducing terms from element 1. Once element 1 has been accounted for, then nodes 2 and 14 can be eliminated since they do not appear in any other elements and are therefore fully summed. Thus, before element 2 is introduced there are 6 active nodes remaining (1,3,9,10,13 and 15). On introducing element 2 a further 5 nodes become active (4,5,11,16 and 17), increasing the number of active nodes to eleven. However, once element 2 has been accounted for, nodes 3,4,10,15 and 16 can be eliminated reducing the number of active nodes back to 6. It can be seen on continuing the process until all 4 elements are accounted for, that the maximum number of active nodes at any one time is eleven. The efficiency of the frontal solver is at a maximum when the maximum number of active nodes is kept to a minimum.

3.7 POST PROCESSING

Once equation solution has been performed, the displacement components at each node are known. The displacements may be of interest in many problems, but it is more common that designs are based on the predicted stresses within a structure. Thus, from the known displacements it is necessary to calculate the stresses at selected points within the structure. This can be achieved quite simply from equation (23) in Section 3.3.4. Substituting for $[\varepsilon]$ using the element strain-displacement relationship, then we have for the stress vector $[\sigma]$ at point (ξ,η)

$$[\sigma(\xi,\eta)]^* = [D]^* \sum_{i=1}^{8} [B_i][d_i]$$

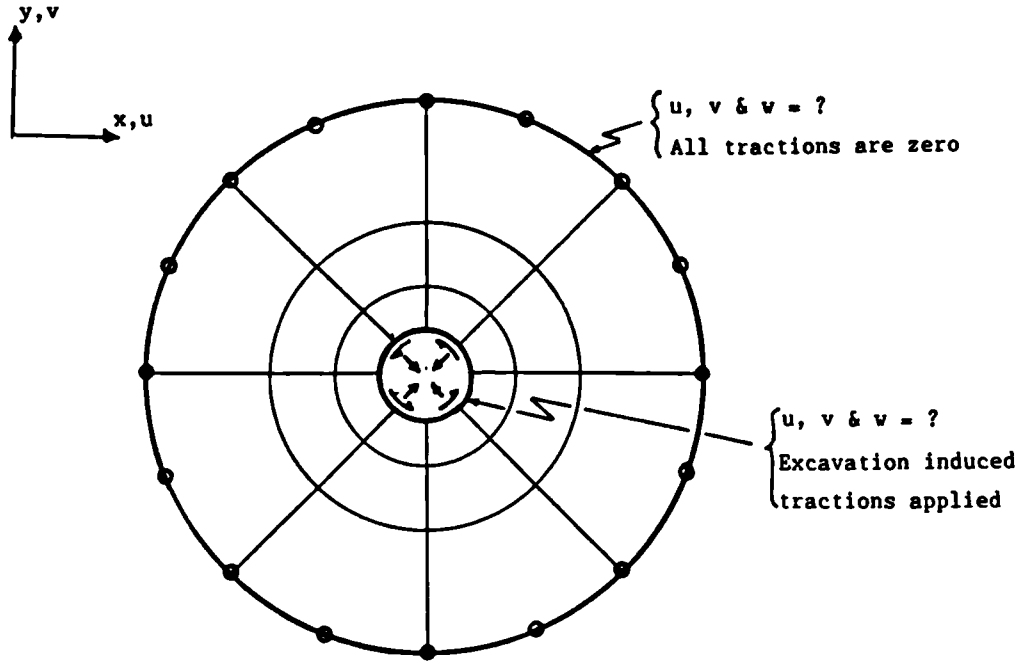
For ease of interpretation it is desirable that $[\sigma]$ is determined at nodal points (ξ_i, η_i) rather than at seemingly arbitrary Gauss points (ξ_p, η_q). However, this conflicts with the needs of the nonlinear techniques used in Chapters 5 and 6. Thus, although somewhat of a drawback, stresses are determined at Gauss points and not nodal points.

3.8 PROBLEM DEFINITION

Before a FEM program can be run the user must define the problem within certain constraints. Many programs contain element generators of varying degrees of sophistication, which will reduce the amount of input data required by the user. When defining a wellbore stress analysis problem a number of aspects must be considered, either by the user or the element generator. These are location of the outer boundary, fixed displacements on the outer boundary and symmetry conditions.

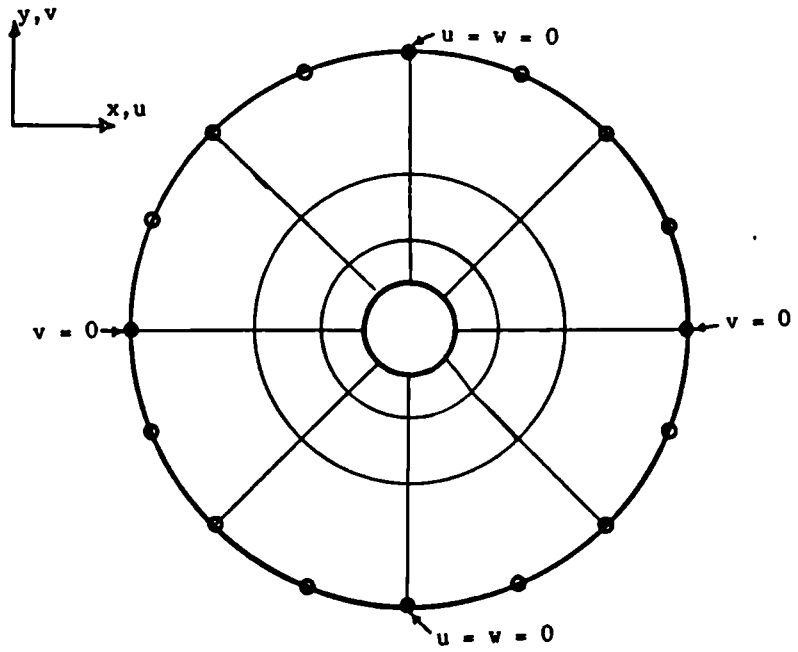
3.8.1 Location of the Outer Boundary

In closed form solutions relating to circular excavations in rock it is often assumed that the opening exists in an unbounded rock mass. Such a condition results in the induced stresses and displacements, from tractions applied to the excavation boundary, only decaying to zero at an infinite radius from the centre of the excavation. At any finite radius the induced stresses and displacements have finite values, although for large radii they could be assumed negligible. Naturally, it is impractical to extend the finite element mesh to infinity. An approximate solution to this problem is to extend the outer boundary of the mesh to a radial distance where it may be assumed that induced stresses and/or displacements are negligible and therefore zero. The



Incomplete boundary conditions (allows rigid body displacement)

(a)



Additional boundary conditions required to fix structure

(b)

Figure 3.12 Prevention of rigid body displacement.

problem for the user, or the element generator, is to decide at what distance to place the outer boundary, such that accuracy is not impaired. Also, the user is unlikely to be interested in the stress/displacement conditions beyond a relatively short distance from the excavation boundary, and many of the elements will be simply used to make up the rock mass, but of little use otherwise.

3.8.2 Rigid Body Displacement

At nodal points it is necessary to know either the applied loading or displacement conditions in each component direction. An obvious set of conditions for the FEM mesh shown in Figure 3.12a is to stipulate that the induced displacements are unknown on both the inner and outer boundaries, and the tractions on the outer boundary are zero and on the inner boundary given by the traction change as a result of introducing the opening. However, the displacements resulting from equation solution will not be unique, and in fact equation solution could not be performed. Such an expression in cartesian coordinates would have the form given below (c.f. equation (31))

$$[K][\alpha u] = [\psi]$$

where for complete plane strain we have

$$[\alpha u]^T = [\alpha_x u_1, \alpha_y v_1, \alpha_z w_1, \alpha_x u_2, \alpha_y v_2, \alpha_z w_2, \ldots\ldots, \alpha_x u_n, \alpha_y v_n, \alpha_z w_n]$$

u, v and w are the x, y and z components of displacement,

and α_x, α_y and α_z can take on values between $-\infty$ and $+\infty$.

Thus, the whole structure could be subjected to a rigid body displacement component in any of the three coordinate directions. In order to prevent this anomaly, it is necessary to fix all three displacement components at a convenient point(s) on the structure. For

the problem defined in Figure 3.12a, a solution would be to fix displacements at the exterior nodes as shown in Figure 3.12b.

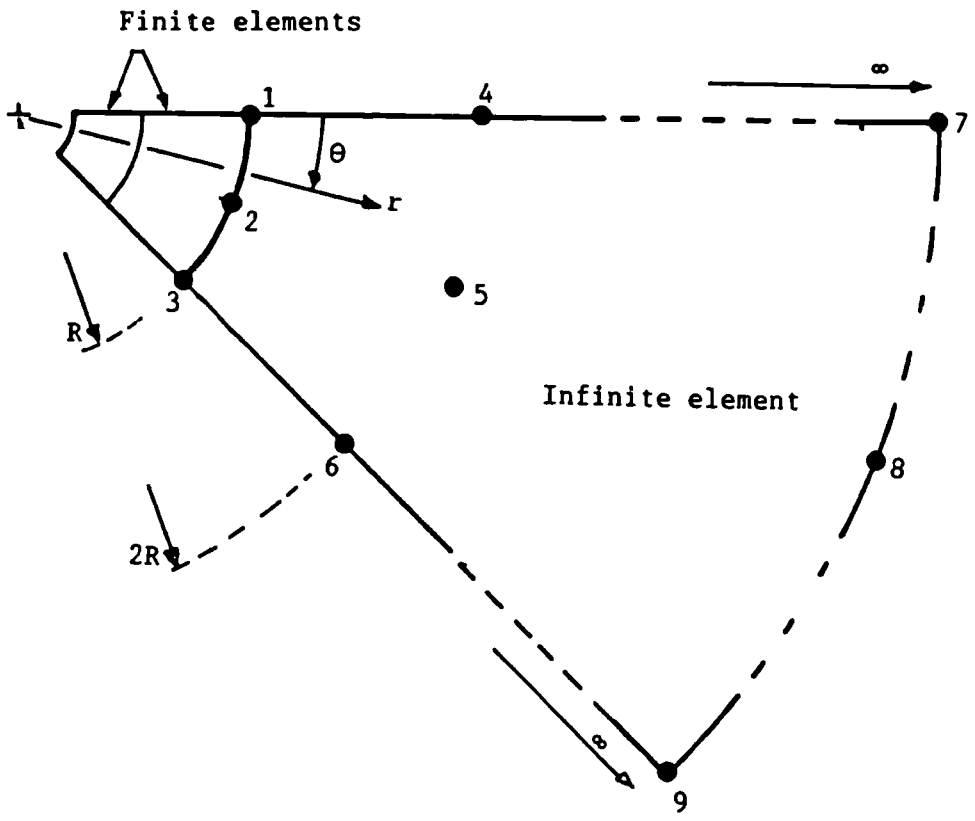
3.8.3 Infinite Elements

In addition to the method outlined in Section 3.8.1, there are a number of solutions to the problem of coping with an unbounded exterior domain. Two well documented approaches are to model the exterior domain with (i) boundary elements (e.g. Zienkiewicz et al[68]), and (ii) infinite elements (e.g. Zienkiewicz et al[69]). The preferred approach here is to use infinite elements, since coupling a finite element mesh with the boundary integral method involves a substantial increase in computer coding. A variety of infinite elements have been published (e.g. Beer (e.g. Beer and Meek,[70] Ungless[71] and Bettes[72]), but the infinite element proposed by Zienkiewicz et al[69] is used in preference to others due to the ease with which it is incorporated into this FEM computer code. The functions relating to a specific form of the 2-dimensional infinite element are given below.

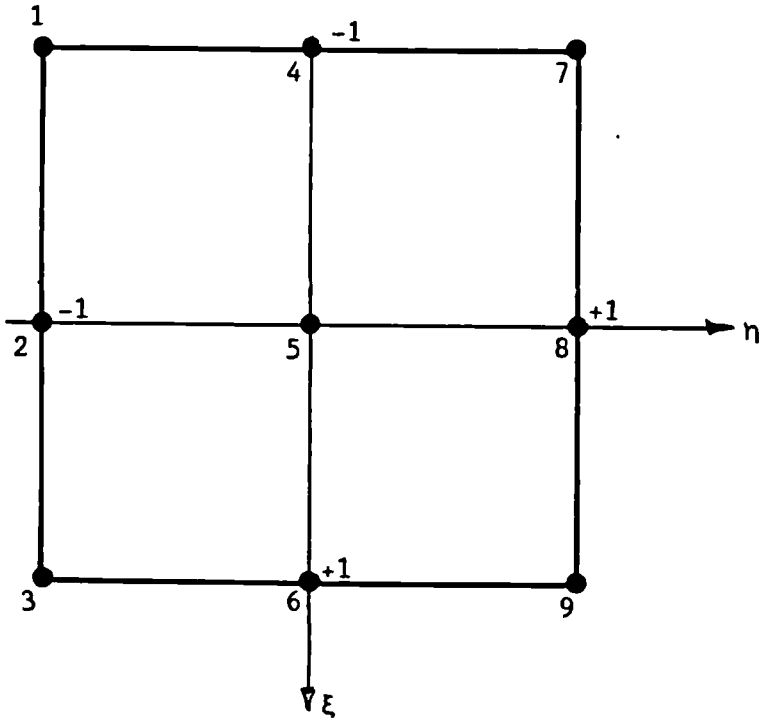
Consider the portion of a FEM mesh shown in Figure 3.13a. The exterior domain is modelled by a set of infinite elements, one of which is shown in Figure 3.13a. The infinite element is of a similar form to the 9-node Lagrangian finite element (Owen and Hinton[35]), but here three of the nodes (7, 8 and 9) are located at infinity. Nodes 4, 5 and 6 are positioned at twice the radial distance of nodes 1, 2 and 3. The infinite element is mapped onto the intrinsic coordinate system as shown in Figure 3.13b. It is assumed that in generating the infinite element the following conditions are imposed

$$\theta_7 = \theta_4 = \theta_1, \quad \theta_9 = \theta_6 = \theta_3,$$

$$\text{and} \quad \theta_8 = \theta_5 = \theta_2 = \frac{1}{2}(\theta_1 + \theta_3)$$



(a)



(b)

Figure 3.13 Mapping of infinite elements.

Using the above conditions, the mapping functions used by Zienkiewicz et al[69] can be simplified to

$$r(\xi,\eta) = \frac{2r_1}{1-\eta}$$

and $$\theta(\xi,\eta) = \frac{1}{2}[(1+\xi)\theta_3 + (1-\xi)\theta_1]$$

where r_1 is the radius at local node number 1

and θ_1 and θ_3 are the direction angles for local nodes 1 and 3 respectively.

Thus, the terms in the Jacobian matrix (see Section 3.5.2) are given by

$$\frac{\partial r}{\partial \xi} = 0 \qquad \frac{\partial \theta}{\partial \xi} = \frac{1}{2}[\theta_3 - \theta_1]$$

$$\frac{\partial r}{\partial \eta} = \frac{2r_1}{(1-\eta)^2} \qquad \frac{\partial \theta}{\partial \eta} = 0$$

[Note: To relate polar and intrinsic coordinates in this specific case, it is not necessary to sum all the nodal contributions as with the general finite element formulations given in Section 3.3.]

Lagrangian shape functions are used to describe the variation of the basic unknown, and with reference to the node numbering defined in Figure 3.13 the functions are given by

$$N_i = \frac{1}{4}(\xi^2 + \xi\xi_i)(\eta^2 + \eta\eta_i) \qquad i = 1 \text{ and } 3$$

$$N_i = \frac{1}{2}\eta_i^2(\eta^2 + \eta\eta_i)(1-\xi^2) + \frac{1}{2}\xi_i^2(\xi^2 + \xi\xi_i)(1-\eta^2) \qquad i = 2, 4 \text{ and } 6$$

$$N_i = (1-\xi^2)(1-\eta^2) \qquad i = 5$$

Since the induced displacements at infinity (nodes 7, 8 and 9) are taken to be zero the following expression is true

$$\sum_{i=1}^{6} N_i[d_i] = \sum_{i=1}^{9} N_i[d_i]$$

Thus, it is unnecessary to sum nodal contributions beyond node 6, and therefore the displacement variation functions for nodes 7, 8 and 9 are irrelevant.

The relevant [B] matrices for complete plane strain, as defined in Section 3.5.1, can now be determined using the Jacobian terms and shape functions given above.

The FEM nodal equation (30) need not be applied to nodes 7, 8 and 9 of the infinite element, since all the terms are zero, and only local nodes 1 to 6 will appear in the global stiffness matrix. As the structure is now fixed in space by specifying that displacements at infinity are zero, it is not necessary to fix the displacements of any of the nodes in the finite domain to prevent rigid body displacement, as discussed in Section 3.8.2.

3.8.4 Symmetry Conditions

For stress analysis of circular excavations in rock it is often possible to take advantage of symmetry conditions, depending on in-situ stress state and well azimuth. If symmetry can be utilized then the amount of computer time and storage space can be reduced significantly.

Investigation of symmetry conditions is achieved by inspection of the applied loading conditions with reference to the shape of the structure. The simplest problem case for a circular opening occurs when the in-situ stress field is isotropic, i.e. $\sigma_v = \sigma_H = \sigma_h$ (see Figure 2.1, Chapter 2). Under these conditions the resultant stress state around the wellbore becomes independent of θ for all wellbore azimuths (this can be seen for the linear elastic case by reference to equations (7) to (12), Section 2.2). Thus, the problem is axisymmetric

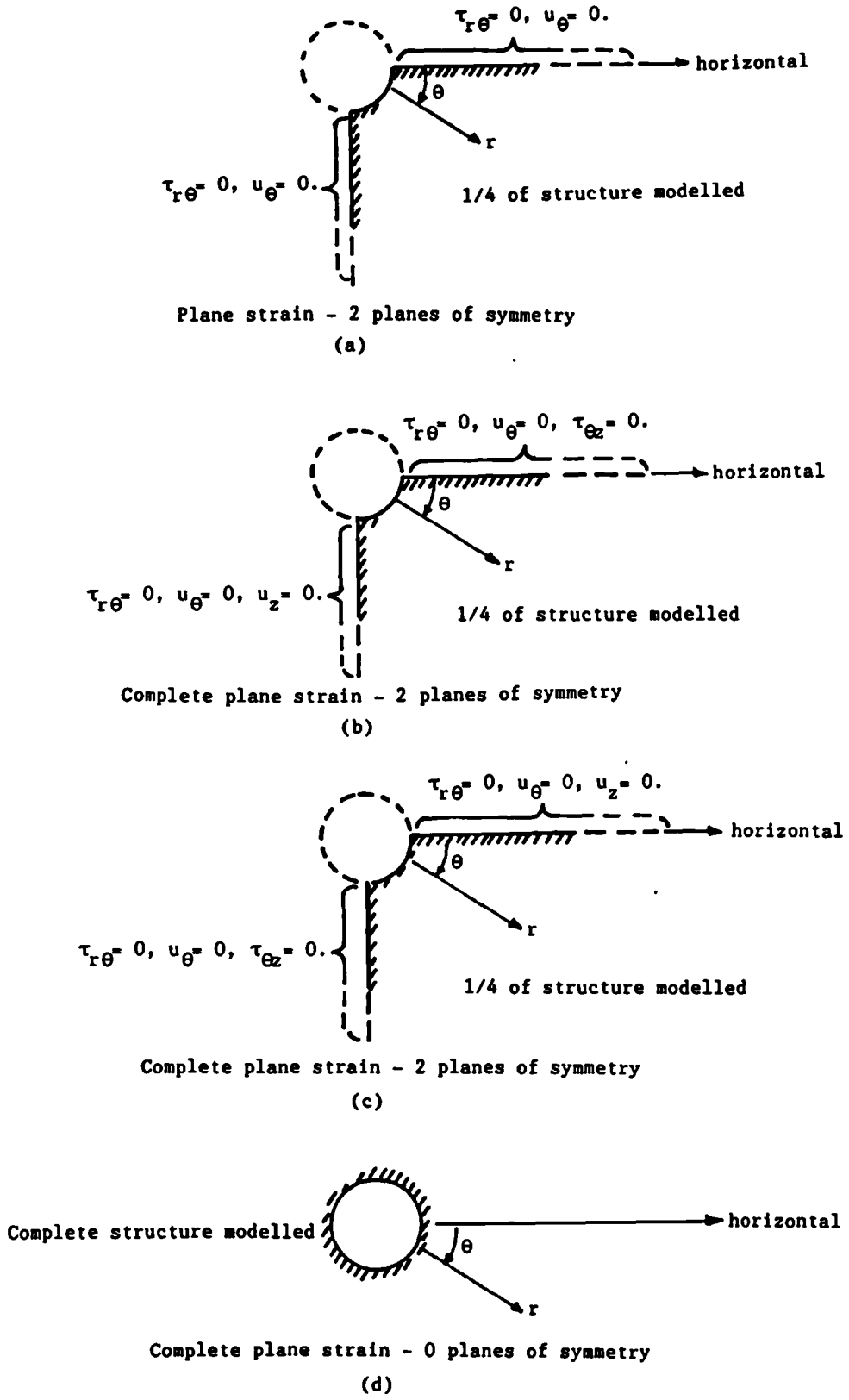


Figure 3.14 Relevant boundary conditions for utilization of symmetry.

and effectively 1-dimensional. Such a condition can be analysed by the FEM. However, even when nonlinear material behaviour is introduced, a FEM analysis is unwarranted, since much simpler numerical and analytical techniques can be adopted for analysis of the axisymmetric case (e.g. Brown et al,[49] Santarelli and Brown[51]).

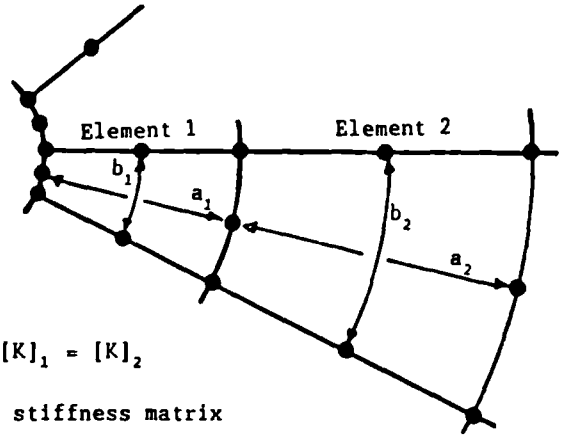
For a wellbore that parallels a principal stress direction (e.g. a vertical wellbore) the applied shear stresses τ_{xy}, τ_{yz} and τ_{zx} (given in equations (4), (5) and (6) - Section 2.2) all reduce to zero. This reduces the problem to simple plane strain and in general two orthogonal planes of symmetry exist which are parallel to the in-plane, in-situ, principal stresses. Along these planes of symmetry it can be deduced that the circumferential displacement (u_θ) and the shear traction ($\tau_{r\theta}$) are both zero (see Figure 3.14a).

For the case when the wellbore does not parallel an in-situ, principal stress the transformed stress state referenced with respect to the wellbore axis (see Figure 2.1, Chapter 2) can be considered as the sum of two stress states, i.e. (i) in-plane stresses (σ_r, σ_θ, $\tau_{r\theta}$) with two planes of symmetry and (ii) antiplane stresses ($\tau_{\theta z}$, τ_{zr}) with one true plane of symmetry. However, in general, the symmetry plane for case (ii) will not coincide with either of the two symmetry planes for case (i). Thus, when the two stress cases are combined (which is necessary for nonlinear analysis) we find that there are no symmetry planes. However, in a number of special cases coincidence of the symmetry planes for the two applied loading conditions will occur, and advantage can be taken of this (see Table 4). The true plane of symmetry for the antiplane loading is given by the axis along which the traction $\tau_{\theta z}$ is zero. At first it may be thought that only this symmetry plane can be utilized under these loading conditions. However, along the axis perpendicular to this plane it can be deduced (even for nonlinear

Stress State	Well Deviatn, α,	Well Directn, β, (see Figure 2.1)	No. of Planes of Symmetry
$\sigma_v = \sigma_H = \sigma_h$	$0 \leq \alpha \leq 90°$	$0 \leq \beta \leq 360°$	axisymmetric
$\sigma_v \neq \sigma_H = \sigma_h$	$\alpha = 0°$	(vertical well)	axisymmetric
" " "	$0 < \alpha < 90°$	$0 \leq \beta \leq 360°$	2 (Fig. 3.14c)
" " "	$\alpha = 90°$	$0 \leq \beta \leq 360°$	2 (Fig. 3.14a)
$\sigma_v = \sigma_H > \sigma_h$	$\alpha = 0°$	(vertical well)	2 (Fig. 3.14a)
" " "	$0 < \alpha \leq 90°$	$\beta = 0/180°$	2 (Fig. 3.14a)
" " "	$0 < \alpha < 90°$	$\beta = 90/270°$	2 (Fig. 3.14c)
" " "	$0 < \alpha < 90°$	$\beta \neq 0/180°$ $90/270°$	0 (Fig. 3.14d)
" " "	$\alpha = 90°$	$\beta = 90/270°$	axisymmetric
" " "	$\alpha = 90°$	$\beta \neq 0/180°$ $90/270°$	2 (Fig. 3.14b)
$\sigma_v = \sigma_h < \sigma_H$	$\alpha = 0°$	(vertical well)	2 (Fig. 3.14a)
" " "	$0 < \alpha \leq 90°$	$\beta = 90/270°$	2 (Fig. 3.14a)
" " "	$0 < \alpha < 90°$	$\beta = 0/180°$	2 (Fig. 3.14c)
" " "	$0 < \alpha < 90°$	$\beta \neq 0/180°$ $90/270°$	0 (Fig. 3.14d)
" " "	$\alpha = 90°$	$\beta = 0/180°$	axisymmetric
" " "	$\alpha = 90°$	$\beta \neq 0/180°$ $90/270°$	2 (Fig. 3.14b)
$\sigma_v \neq \sigma_H \neq \sigma_h$	$\alpha = 0°$	(vertical well)	2 (Fig. 3.14a)
" " "	$0 < \alpha < 90°$	$\beta = 0/180°$ $90/270°$	2 (Fig. 3.14c)
" " "	$0 < \alpha < 90°$	$\beta \neq 0/180°$ $90/270°$	0 (Fig. 3.14d)
" " "	$\alpha = 90°$	$\beta = 0/180°$ $90/270°$	2 (Fig. 3.14a)
" " "	$\alpha = 90°$	$\beta \neq 0/180°$ $90/180°$	2 (Fig. 3.14b)

Cases of symmetry conditions for analysis of stresses around a wellbore.

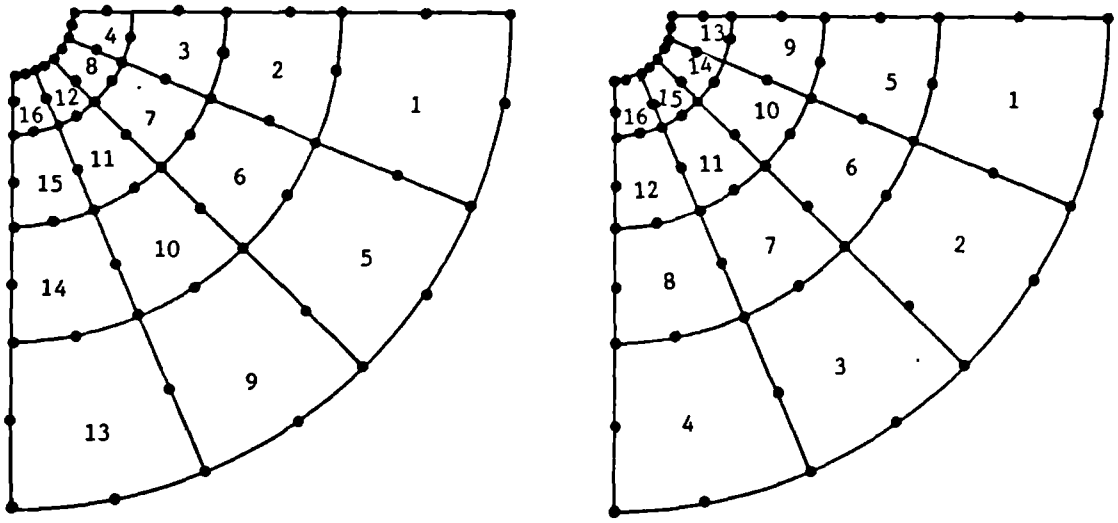
TABLE 4



$\frac{a_1}{a_2} = \frac{b_1}{b_2}$, giving $[K]_1 = [K]_2$

where [K] is the element stiffness matrix

Figure 3.15 Gradation of the element mesh.



Radial numbering

(a)

Circumferential numbering

(b)

Figure 3.16 Element numbering.

material behaviour) that the axial displacement (u_z) is zero, and for points symmetric about this plane the axial displacements are equal in absolute magnitude and opposite in direction.

Table 4 gives a complete list of loading conditions where symmetry conditions can be utilized, and Figure 3.14 shows the relevant boundary conditions for FEM analyses of these cases.

3.8.5 Mesh Generation

The element generator at the front end of the program grades elements in the radial direction according to the linear conditions shown in Figure 3.15. This gradation ensures that for linear elasticity every finite element has the same stiffness matrix when formulated with respect to polar coordinates. The number of elements required in the circumferential direction (N_c) and radial direction (N_r) are chosen by the user. However, the number of circumferential elements required should take into consideration the loading conditions. For example, in axisymmetric loading there is no variation in stress/displacement conditions in the circumferential direction, thus, only one circumferential element is necessary to monitor conditions, as shown in Figure 3.17.

For optimisation of the equation solver (Section 3.5) there are two main options for element numbering: (i) numbering in a radial direction (Figure 3.16a), and (ii) numbering in a circumferential direction (Figure 3.16b). In both cases it is irrelevant whether the element numbering is initiated from the internal or external mesh boundaries.

It can be shown from inspection that the maximum number of active

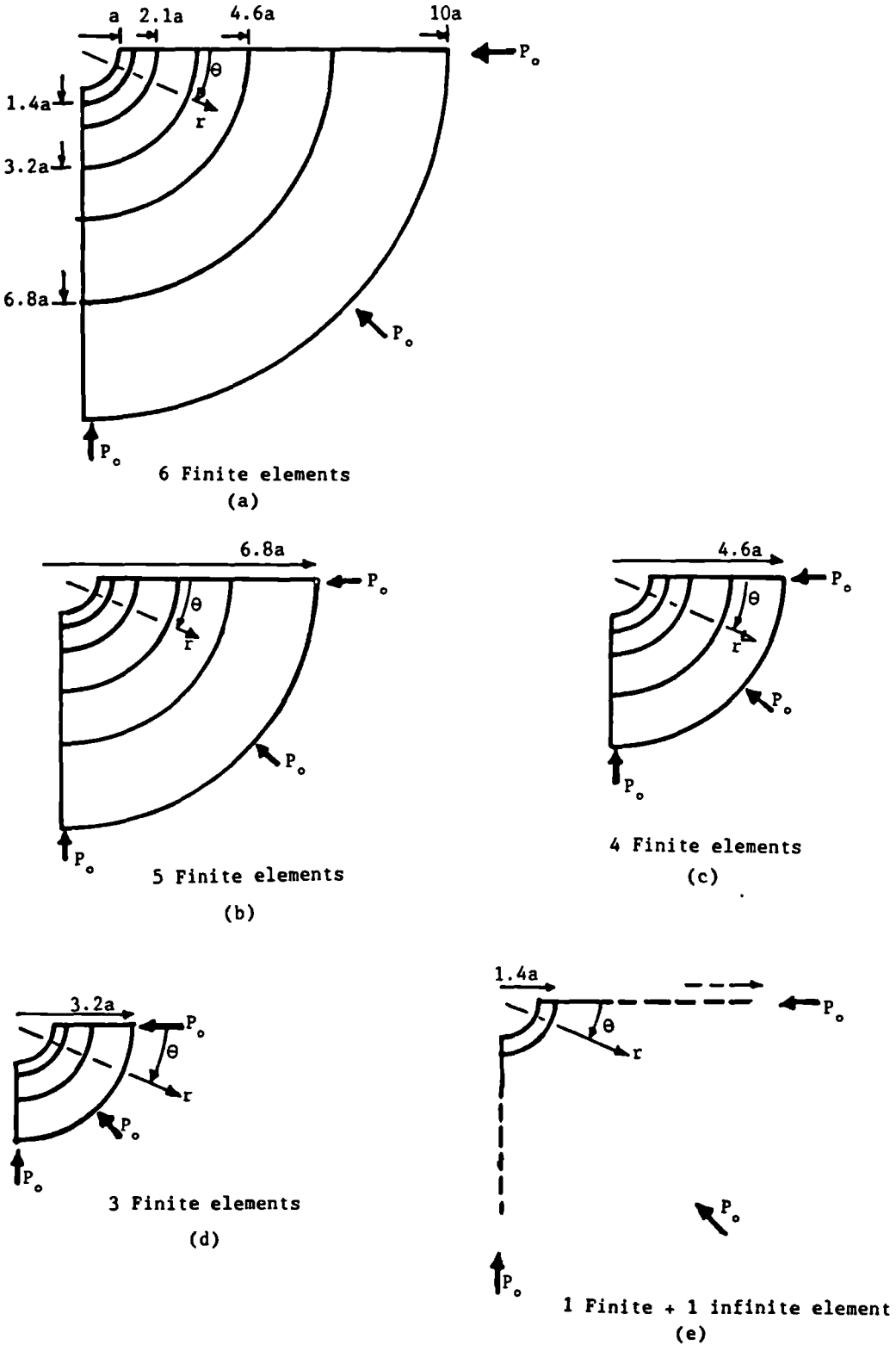


Figure 3.17 Various FEM meshes for analysis of axisymmetric loading.

nodes, A_{max} (as defined in Section 3.5), resulting from the element generations are

Two planes of symmetry

$A_{max} = 2(N_c + 3)$ circumferential numbering

$A_{max} = 2(N_r + 3)$ radial numbering

No planes of symmetry

$A_{max} = 2(N_c + 3) + 1$ circumferential numbering

$A_{max} = 2(2N_r + 3) + 1$ radial numbering

Thus, in the case of no symmetry planes, N_c would have to be greater than twice N_r before radial numbering would give the most economic equation solution. In cases where two planes of symmetry can be utilized, then for N_c greater than N_r radial numbering is preferable. In both the above cases it is felt that meshes generated are likely to favour circumferential element numbering. Only circumferential numbering is catered for in the developed program.

3.9 PROGRAMME VALIDATION FOR LINEAR ELASTIC BEHAVIOUR

To ensure that the computer coding is correct and to assess the suitability of various mesh geometries it is necessary to carry out a number of validation tests. For linear elasticity this is a relatively simple process, since the closed form solutions presented in Section 2.2 of Chapter 2 can be used to test the accuracy of the FEM solutions.

Numerical validation of the model is carried out for three different types of loading.

1. A vertical wellbore in an isotropic horizontal stress field (i.e. axisymmetric loading).

2. A vertical wellbore in an anisotropic horizontal stress field

(i.e. plane strain).

3. An inclined wellbore in an anisotropic stress field (i.e. complete plane strain).

For the first load case a number of mesh geometries are compared for an assessment of the benefits of introducing infinite elements.

3.9.1 The Axisymmetric Wellbore

For axisymmetric loading there is no variation in displacement/stress conditions in the circumferential direction (provided displacement/stresses are referenced in terms of polar coordinates). Thus, it is unnecessary to have more than one element monitoring conditions in the circumferential direction. The initial FEM grid proposed for this analysis is shown in Figure 3.17a. The outer boundary is set at 10 times the radius of the wellbore. The in-situ stress field is given by P_o, and no pressure is applied to the wellbore wall. Initially no infinite elements are used. The finite domain is split into 6 elements with radii as shown, with four Gauss points per element.

Table 5 gives the dimensionless radial and hoop stresses at an inner most Gauss point, calculated by the FEM and closed form solutions, and the corresponding error in the FEM values. It is possible to compare the FEM and closed form stress conditions at all the Gauss points. However, for clarity and conciseness only conditions at the inner most Gauss points are considered, since it is next to the wellbore wall where stress conditions are at their most critical. Also in Table 5 are the results for other mesh designs including one with an infinite element. The mesh designs are shown in Figure 3.17a,b,c,d and e. It can be seen

Mesh Type	σ_r/P_o	Error	σ_θ/P_o	Error
Closed Form Solution	0.1719	-	1.828	-
6 Elements Fig. 3.17a	0.1713	0.3%	1.849	1.1%
5 Elements Fig. 3.17b	0.1733	0.8%	1.871	2.3%
4 Elements Fig. 3.17c	0.1779	3.4%	1.920	5.0%
3 Elements Fig. 3.17d	0.1884	9.6%	2.034	11.3%
1 FE + 1 IE Fig. 3.17e	0.1696	1.3%	1.830	0.1%

Results of an elastic analysis a wellbore in a hydrostatic stress field.

TABLE 5

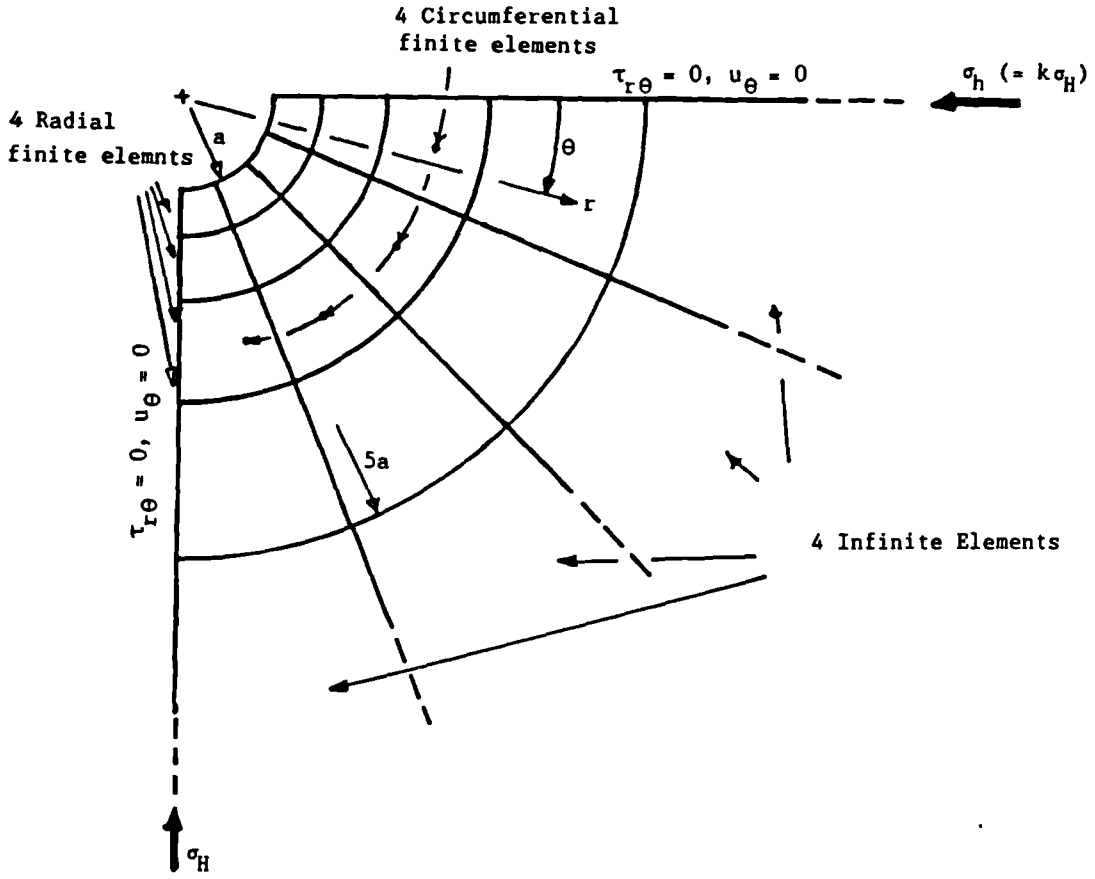


Figure 3.18 FEM mesh for validation under plane strain conditions.

that when the outer boundary of the finite element mesh is extended to between 6 and 10 times the well radius (5 and 6 element meshes), the accuracy of the resultant stresses are acceptable. When the outer boundary is reduced further the errors, particularly in the hoop stress become intolerably large, considering the simplicity of the problem. However, when an infinite element is used in conjunction with only one finite element good agreement is obtained, thus showing the economic value of introducing infinite elements.

3.9.2 Plane Strain Conditions

For the case of a vertical well in an anisotropic horizontal stress field the stress/displacement conditions will vary in both the radial and circumferential directions. Validation in plane strain conditions is performed with respect to the problem presented in Figure 3.18. The mesh is made up of 16 finite elements (4 elements in both the circumferential and radial directions) and 4 infinite elements. The radius of the finite element external boundary is 5 times the well radius, i.e. R = 5a. The degree of anisotropy, k, is taken to be 0.6, where k is given by

$$k = \frac{\sigma_h}{\sigma_H}$$

No inner pressure is applied to the wellbore wall.

The results of the FEM analysis for the radial, circumferential and shear stresses are given in Table 6 along with the exact solutions calculated from equations presented in Section 2.2 of Chapter 2. In general the agreement is good considering the coarseness of the grid. The largest errors (4 to 9%) occur in the radial and shear stresses at

Gauss point		σ_r/σ_H			σ_θ/σ_H			$\tau_{r\theta}/\sigma_H$		
r	θ	Exact	FEM	Error	Exact	FEM	Error	Exact	FEM	Error
1.105	17.7	0.1878	0.1799	4.2%	1.9463	1.9526	0.3%	0.0723	0.0672	7.1%
1.105	40.2	0.1536	0.1517	1.2%	1.5557	1.5600	0.3%	0.1231	0.1139	7.5%
1.105	62.7	0.1145	0.1181	3.1%	1.1062	1.1074	0.1%	0.1018	0.0939	8.2%
1.105	85.2	0.0938	0.0987	5.2%	0.8612	0.8600	0.2%	0.0208	0.0189	9.1%
1.652	17.7	0.5171	0.5155	0.3%	1.3219	1.3220	0.0%	0.1541	0.1515	1.7%
1.652	40.2	0.5090	0.5087	0.1%	1.1399	1.1420	0.2%	0.2623	0.2578	2.1%
1.652	62.7	0.4996	0.5003	0.1%	0.9322	0.9339	0.2%	0.2168	0.2132	1.7%
1.652	85.2	0.4945	0.4952	0.1%	0.8165	0.8196	0.4%	0.0444	0.0436	1.8%
2.470	17.7	0.5996	0.5996	0.0%	1.1073	1.1036	0.3%	0.1445	0.1423	1.5%
2.470	40.2	0.6547	0.6546	0.0%	0.9672	0.9666	0.1%	0.2460	0.2421	1.5%
2.470	62.7	0.7181	0.7177	0.1%	0.8059	0.8090	0.4%	0.2033	0.2000	1.6%
2.470	85.2	0.7527	0.7520	0.1%	0.7181	0.7232	0.7%	0.0416	0.0408	1.9%

Results of an elastic analysis of a vertical wellbore in an anisotropic stress field.

TABLE 6

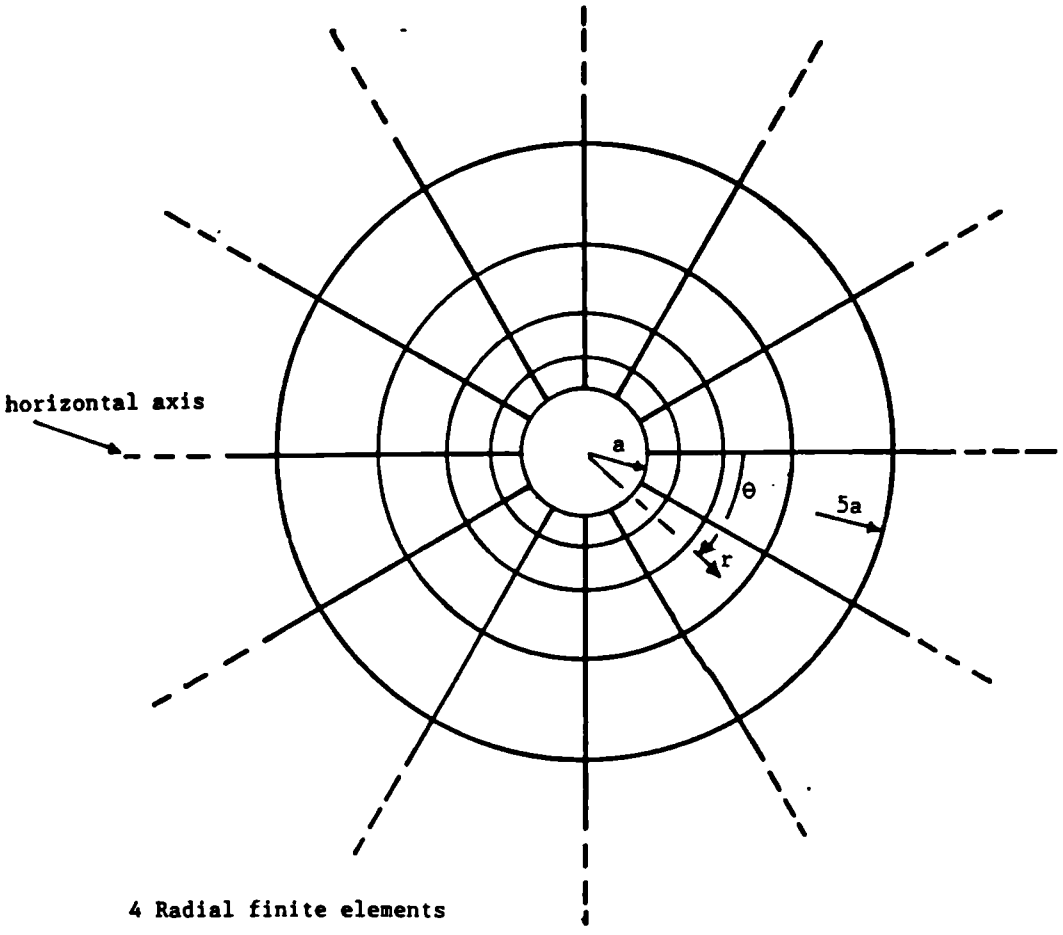


Figure 3.19 FEM mesh for validation under complete plane strain conditions.

Gauss points next to the wellbore wall. However, the absolute values of these stresses are relatively small. If these errors become unacceptable then a finer element grid would be necessary and/or an increase in the number of Gauss points per element from 4 to 9.

3.9.3 Complete Plane Strain Conditions

Complete plane strain conditions are induced when drilling a deviated well in a non-hydrostatic in-situ stress field. The problem analysed for validation is a well drilled with a deviation of 30° and a direction angle relative to the maximum horizontal stress direction, β, (see Figure 2.1, Chapter 2) of 70°. The in-situ horizontal principal stresses are considered to have fixed ratios with respect to the overburden stress and given by

$$\sigma_H = 0.8\sigma_v \quad \text{and} \quad \sigma_h = 0.5\sigma_v$$

No planes of symmetry can be utilized when viewing the total stress state around the wellbore, thus it is necessary to model the complete circumference around the well. The FEM mesh used to analyse this problem is given in Figure 3.19.

The results of the FEM analysis at a number of Gauss points are presented in Table 7. The FEM predictions are compared with the exact solutions given by equations presented in Section 2.2 of Chapter 2. These comparisons along with the computed errors in the FEM results are also given in Table 7. As with the plane strain results, good agreement can be seen throughout, with the less accurate results given by σ_r and $\tau_{r\theta}$ values near the wellbore wall. The antiplane stresses, $\tau_{\theta z}$ and τ_{zr}, are in particularly good agreement.

Gauss Point		σ_r/σ_v			σ_θ/σ_v			$\tau_{r\theta}/\sigma_v$			$\tau_{\theta z}/\sigma_v$			τ_{zr}/σ_v		
r/a	θ	Exact	FEM	Error	Exact	FEM	Error	Exact	FEM	Error	Exact	FEM	Error	Exact	FEM	Error
1.105	23.7	0.1016	0.1044	2.7%	0.9873	0.9901	0.3%	0.0092	0.0084	8.7%	0.3706	0.3706	0.0%	0.0066	0.0066	0.7%
1.105	53.7	0.1114	0.1104	0.9%	1.0994	1.0996	0.0%	-0.0494	-0.0455	7.9%	0.2875	0.2877	0.1%	0.0241	0.0238	1.2%
1.105	83.7	0.1377	0.1320	4.1%	1.4005	1.3997	0.1%	-0.0586	-0.0539	8.0%	0.1274	0.1278	0.3%	0.0352	0.0347	1.4%
1.652	23.7	0.4424	0.4426	0.0%	0.8274	0.8304	0.4%	0.0196	0.0199	1.5%	0.2784	0.2782	0.1%	0.0233	0.0232	0.4%
1.652	53.7	0.4447	0.4439	0.2%	0.8796	0.8805	0.1%	-0.1053	-0.1023	2.8%	0.2159	0.2160	0.0%	0.0847	0.0844	0.4%
1.652	83.7	0.4510	0.4490	0.4%	1.0198	1.0185	0.1%	-0.1249	-0.1222	2.1%	0.0957	0.0959	0.2%	0.1234	0.1230	0.3%
2.470	23.7	0.6345	0.6339	0.1%	0.7162	0.7194	0.5%	0.0184	0.0184	0.0%	0.2371	0.2368	0.1%	0.0307	0.0306	0.3%
2.470	53.7	0.6187	0.6180	0.1%	0.7564	0.7584	0.3%	-0.0987	-0.0964	2.3%	0.1839	0.1838	0.1%	0.1118	0.1115	0.3%
2.470	83.7	0.5762	0.5758	0.1%	0.8643	0.8635	0.1%	-0.1171	-0.1147	2.0%	0.0815	0.0816	0.1%	0.1629	0.1625	0.2%

Results of a complete plane strain elastic analysis of a deviated wellbore in an anisotropic stress field.

TABLE 7

3.10 CONCLUDING REMARKS

In this chapter the finite element method has been presented in reference to circular excavations in a homogenous, isotropic, linear elastic material. The FEM relationships and equations were presented for the analysis of plane strain conditions and subsequently extended to allow for complete plane strain. The introduction of complete plane strain is necessary to allow analysis of deviated wells without having to impose unlikely field conditions. A number of further numerical considerations were presented relating to the equation solver, symmetry conditions, and the introduction of infinite elements for modelling the exterior domain. Finally, set problems were analysed to validate the computer coding in linear elastic conditions.

The next step in the FEM development is to allow for nonlinear material behaviour. Most structural materials will behave in an elastic manner for a limited stress range, which once exceeded will initiate yield or failure. Analysis of material behaviour beyond the elastic limit is often carried out using the theory of plasticity, and this method of modelling material behaviour is covered in Chapter 4. Further extensions to plasticity theory to allow a more suitable representation of rock behaviour are also presented and discussed in Chapter 4. FEM modifications necessary to cope with plastic behaviour are then presented in Chapter 5.

CHAPTER 4

PLASTICITY AS A MEANS OF MODELLING MATERIAL BEHAVIOUR

4.1 INTRODUCTION

In Chapter 3 the FEM was presented for the analysis of linear elastic problems under plane strain and complete plane strain conditions. For a wide variety of problems the structural material may follow an elastic behaviour according to Hooke's law. However, more commonly in rock mechanics problems, only part of the structure responds elastically, and the more critically stressed areas exhibit inelastic behaviour by yielding, fracturing, or simply slipping on surfaces of weakness. Thus, although linear elasticity provides a useful assessment of structural behaviour, a better model would incorporate the inelastic (or plastic) portion of the rock's stress-strain behaviour in addition to the elastic portion.

This chapter sets out the procedures required to model rock behaviour using plasticity. Perfect plasticity, strain hardening and strain softening (Figure 4.1) are discussed with methods of implementing their behaviour into the FEM analysis. Both associated and non-associated flow are considered (discussed later in Section 4.6). In Chapter 5, additions to the FEM necessary to analyse an elasto-plastic behaviour are presented.

4.2 TYPES OF NONLINEAR PROBLEMS

There are a number of forms of nonlinearity in structural behaviour. Nonlinearity can be broadly categorized into geometric nonlinearity and material nonlinearity.

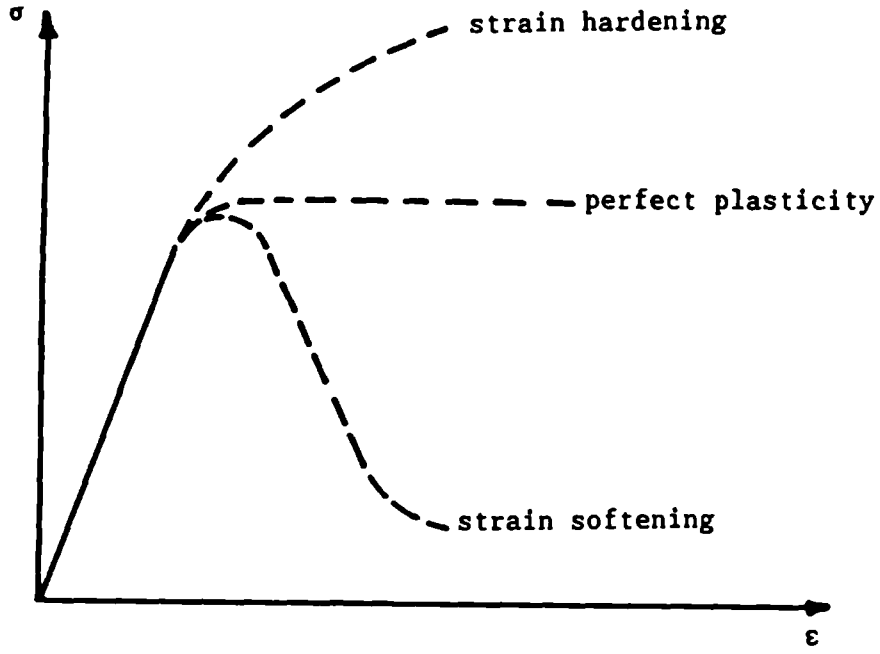


Figure 4.1 Various plastic responses to loading.

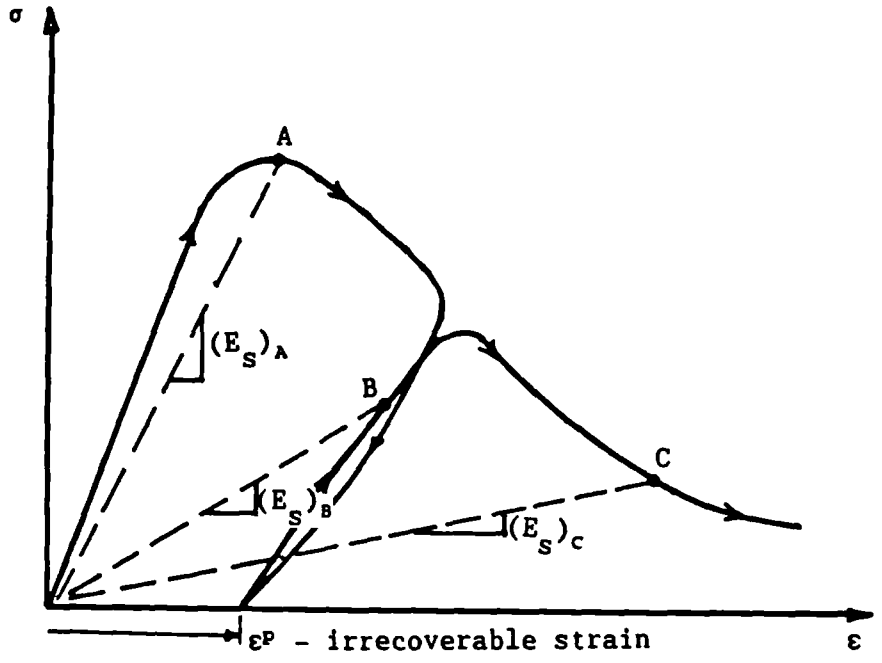


Figure 4.2 Irrecoverable strain and variation of secant stiffness.

4.2.1 Geometric Nonlinearity

Provided displacements are small, the geometry of a structure remains relatively unchanged upon application of load. However, for soft materials or materials undergoing large viscous or plastic strains, this may not hold, and the first-order infinitesimal linear strain approximations cannot be applied to the total strain undergone. In such cases an iterative procedure must be employed, part of which involves incremental loading with recalculation of the geometry of the structure at each load increment. In this research it is assumed that relative displacement magnitudes are sufficiently small such that the familiar strain-displacement relationships can be employed.

4.2.2 Material Nonlinearity

A number of material nonlinearities can be identified. With reference to wellbore studies, nonlinearity may be the result of one or a combination of the following.

1. Nonlinear elasticity.
2. Inelasticity (plasticity) as a result of a material exceeding its yield strength.
3. Viscous material behaviour (e.g. salt deformation), or viscous behaviour due to transient fluid or temperature flow/migration.
4. Rigid body movements as a result of slippage along pre-existing joints.

Item 1 above is covered in Chapter 6, and Item 2 is covered in this chapter. Items 3 and 4, although relevant in certain instances, are beyond the context of this research.

For simple elasto-plastic analysis the secant stiffness is a function of stress and stress path history. Considering the case of uniaxial loading, a typical loading/unloading/reloading stress-strain path is depicted in Figure 4.2. The secant modulus, E_s, is a function of the stress level, σ, and the amount of permanent deformation undergone, ε^p, and we can write

$$\sigma = E_s(\sigma, \varepsilon^p)\varepsilon$$

Similarly the biaxial and triaxial stress-strain relationships, given in (23) in Chapter 3, become stress path dependent and can be written as

$$[\sigma] = [D(\sigma, \varepsilon^p)][\varepsilon]$$

This results in dependence of the global stiffness matrix on stress and stress path history, and the set of simultaneous equations expressed by (31) in Chapter 3 become

$$[K(\sigma, \varepsilon^p)][u] = [\psi] \qquad (1)$$

Direct solution of equation system (1) is generally impossible and an iterative scheme must be employed. The iterative techniques used to solve such a set of simultaneous equations are given later in Section 5.1, Chapter 5.

4.3 PLASITICITY THEORY

Fundamental treatment of plasticity is dealt with in a number of texts (e.g. Hill,[74] Prager[75]). In this thesis no attempt is made at giving any physical insight into controversial aspects of plasticity theory such as associated flow. Plasticity theory is simply considered as an empirical technique to take laboratory measured material properties through to numerical and/or analytical application.

Plasticity behaviour in materials occurs when deformation induced by loading is not totally recoverable on unloading (Figure 4.2). Plasticity has been applied in the field of rock mechanics to the study of a region around a circular opening as far back as 1940 (Westergaard[34]) and has had increasing usage in this area from more recent research (e.g. Brown and Bray,[36] Gumusoglu[76]). However, it is in the field of Mechanical Engineering that plasticity has received the most attention, and it is in its application to metallic behaviour that most of the fundamentals are based. As a result of its foundation, it is often discovered that some of the accepted numerical treatments of plasticity are inappropriate when applied to rock behaviour (e.g. associated flow - Ladanyi[77]).

4.3.1 Behaviour Law Requirements

Plasticity theory involves combining a number of laws and relationships into a consistent set that can be used to uniquely define the stress-strain behaviour of a material during plastic loading/unloading. For a homogeneous, isotropic rock sample only Young's Modulus, E, and Poisson's Ratio, ν, need be specified to provide a unique description for linear elastic loading. Various empirical approaches can be used to define material inelastic behaviour. In this text the plastic behaviour of rock is uniquely defined by three governing characteristics, which are

1. The yield criterion.
2. Variation of yield envelope as a function of permanent deformation.
3. The flow rule.

These three topics are covered in detail in the following sections.

4.4 THE STRENGTH CRITERION

Materials are considered to behave elastically until the stresses imposed reach a certain limiting condition, beyond which the material behaves as an elasto-plastic material. This limiting condition is often termed the 'yield function' or 'yield criterion'. In its most general form the value of the yield function (F) can be written as

$$F = F(\sigma, K_1, K_2, \ldots K_n) \leq 0$$

where σ is the stress state,

$K_1, K_2, \ldots K_n$ are material strength paramaters determined experimentally,

and n is the number of strength parameters required (in most cases only one or two).

The strength parameters are often dependent on the stress history undergone by the rock mass or sample under consideration. More specifically, the parameter K can be related to the amount of permanent deformation suffered by the sample (i.e. ε^p). Thus, we can write

$$F = F(\sigma, K_1(\varepsilon^p), K_2(\varepsilon^p), \ldots K_n(\varepsilon^p)) \leq 0 \qquad (2)$$

Confusion may often arise in the interpretation of strength criteria. A number of different terms are used to describe these criteria, for example 'yield', 'peak strength' or 'failure' criteria, depending on their particular application. Here only the term 'yield' criteria is used, and points on a stress-strain curve that relate to initial yielding, peak strength and residual strength are taken to be particular cases of yield in a loading/unloading/reloading cycle. This application of the yield criteria is explained below in Sections 4.4.1 and 4.4.2.

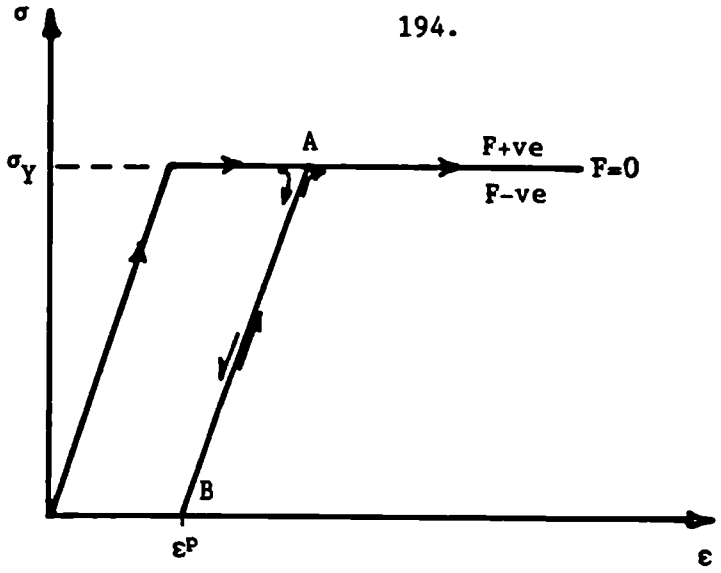
4.4.1 Uniaxial Loading

To explain the function of the yield criterion, first consider the idealized uniaxial stress-strain relationships given in Figure 4.3. In Figure 4.3a the sample is behaving in an elastic-perfectly plastic manner. Below σ_Y (which is equivalent to the uniaxial compressive strength, σ_c) the value of the yield function (F) is less than zero and the material is behaving in an elastic manner. Upon reaching σ_Y the value of F becomes zero (i.e. the limiting case) and the material may undergo permanent (plastic) deformation (e.g. to point A in Figure 4.3a). On unloading, the sample returns to an elastic response (A to B). On reloading, the sample remains elastic until the stress level reaches σ_Y again, upon which the sample will undergo further plastic deformation. Above σ_Y the value of F is positive, however, the sample will not accommodate axial loading above σ_Y, and therefore positive values relate to unachievable stress states.

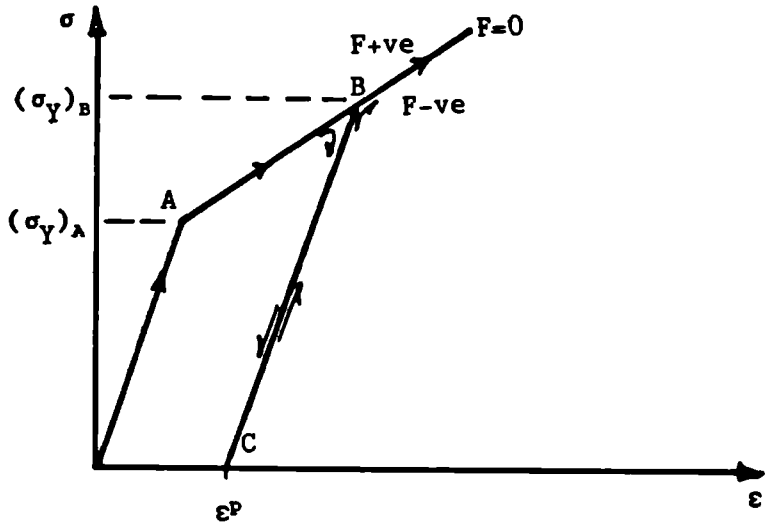
As can be seen in Figure 4.3a, the stress level at which yield occurs (σ_Y) is constant and unaffected by the amount of permanent deformation suffered. Thus, the yield criterion is independent of ε^p and the general form given in (2) simplifies to

$$F = F(\sigma, K_1, K_2, \ldots K_n) \leq 0, \qquad \text{with } \frac{\partial F}{\partial \varepsilon^p} = 0 \text{ for all } \sigma$$

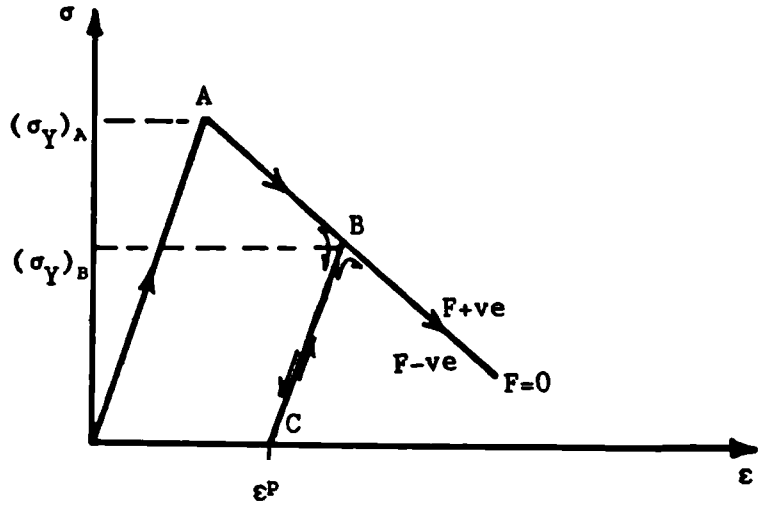
Figure 4.3b shows an idealized uniaxial stress-strain relationship for a sample that is undergoing strain hardening. On initial loading the sample is behaving elastically until reaching A, at which point yield occurs. On continuing loading to B the sample undergoes permanent deformation. Unloading from B to C is elastic. However, on reloading, the material now behaves elastically until reaching the stress level at B, i.e. the uniaxial yield strength has risen from its initial value of



(a) Perfect plasticity



(b) Strain hardening



(c) Strain softening

Figure 4.3 Variation of yield strength with deformation.

$(\sigma_Y)_A$ to a higher yield strength of $(\sigma_Y)_B$. This phenomenon is known as strain hardening, i.e. the yield strength increases as a result of having undergone permanent deformation, and the general form of the yield function given in (2) remains.

Figure 4.3c shows an idealized stress-strain relationship for a strain softening material subjected to uniaxial loading. The sample is subjected to a similar loading/unloading/reloading path as the strain hardening material in Figure 4.3b. However, now the yield strength of the sample is reduced as a result of having suffered permanent deformation, thus introducing the concept of strain softening. (In Item J, Section 1.4.1 of Chapter 1, it was noted that during strain softening there may be complications due to differences between 'true' and 'apparent' stress-strain behaviour. This problem is not considered here, and it is assumed that 'apparent' and 'true' behaviour are the same).

4.4.2 2-Dimensional Stress State

The concept of a yield function and its dependence on plastic strain (except in the case of perfect plasticity) was described with reference to uniaxial loading in Section 4.4.1. However, in general, the stress state applied will be triaxial and not simply uniaxial. To describe the yield function with respect to a triaxial stress state is conceptually complex, and it is worth referencing it to a 2-dimensional stress state before extending to a triaxial stress state.

A number of yield criteria are a function of only two of the three principal stresses, specifically the maximum and minimum principal stresses (σ_1 and σ_3 respectively), e.g. Mohr-Coulomb, Tresca, Hoek-

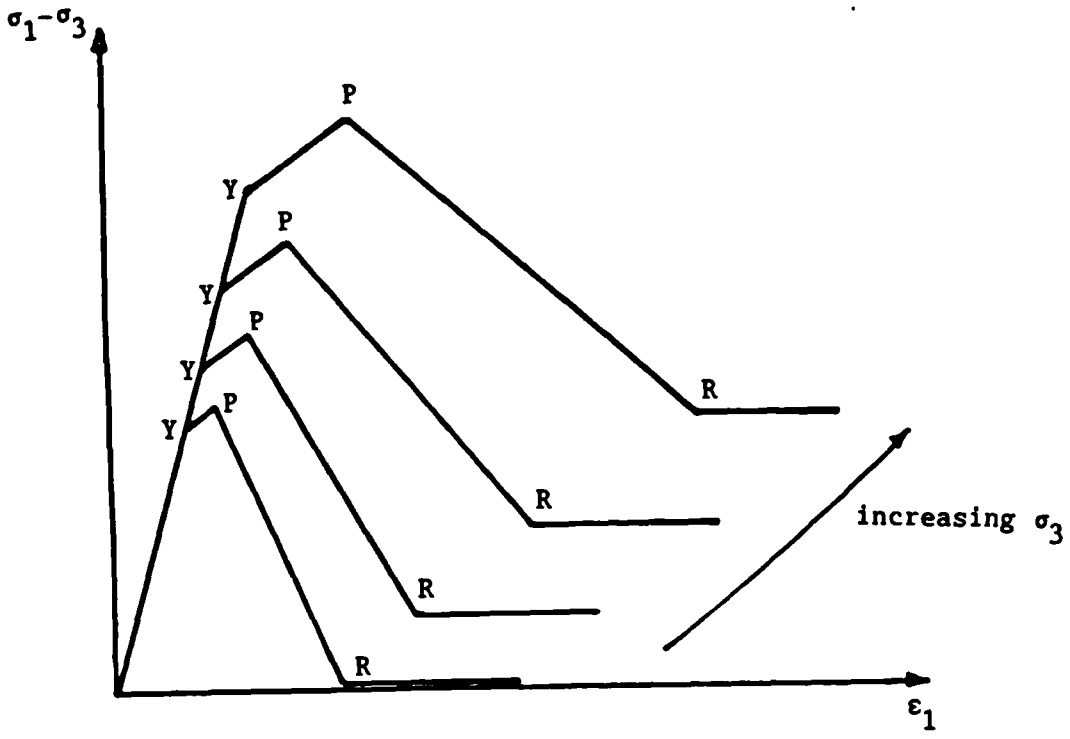
Brown.[78] These criteria can be described in a 2-dimensional plot with axes of σ_1 and σ_3. A real set of triaxial stress-strain test results on a sandstone, taken from Santarelli,[18] is given in Figure 1.16, Chapter 1. An idealized version of a set of triaxial tests is given in Figure 4.4a. The stress-strain plots cover a range of confining pressures ($\sigma_2 = \sigma_3$ = confining pressure). It can be seen that the deviatoric stress ($\sigma_1-\sigma_3$) at peak increases with increase in σ_3. Thus, it is necessary to use a yield criterion that allows for an increase in strength with increase in confinement. There are numerous criteria that can account for this material behaviour. Here it is assumed that the Mohr-Coulomb criterion is adequate at describing the material strength. The Mohr-Coulomb criterion is a function of stress state and two strength parameters; the cohesion coefficient, c, and the friction angle, ϕ. It is assumed that expansion or contraction of the yield surface, is accommodated by changes in both c and ϕ, which are functions of the plastic strain, ε^p. Thus, the Mohr-Coulomb criterion can be written as

$$F = \sigma_1 - \sigma_3 - (\sigma_1 + \sigma_3)\sin\phi - 2c\cos\phi \qquad (3)$$

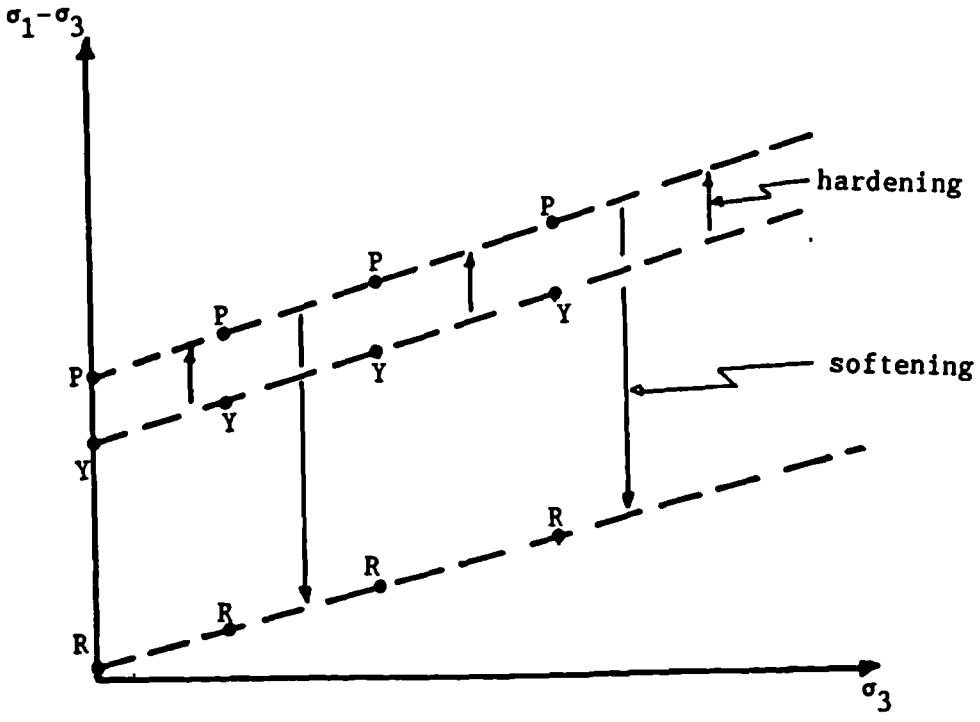
where for hardening or softening materials we have

$$c = c(\varepsilon^p), \quad \text{and} \quad \phi = \phi(\varepsilon^p)$$

In Figure 4.4b the yield criterion is plotted for the three extreme cases, which are (i) at initial yielding (points 'Y' in Figure 4.4a), (ii) at the end of the strain hardening portion, i.e. peak strength (points 'P' in Figure 4.4a) and (iii) at the end of the strain softening portion, i.e. at residual strength (points 'R' in Figure 4.4a). The points are connected to form three distinct yield surfaces. However, the yield function is continuously variable between these extremes. Thus, during strain hardening the yield surface expands from the initial yield



(a) Idealised set of triaxial tests



(b) Yield surfaces at initial yield, peak and residual strength

Figure 4.4 Mohr-Coulomb yield surfaces resulting from triaxial data.

line to the peak strength line, with intermediate positions of the yield surface dependent on the amount of plastic strain undergone. Upon reaching the yield surface describing peak strength, the surface then contracts until it reaches residual strength. Again the position of the yield surface during softening is dependent on the extent of the plastic deformation.

4.4.3 Triaxial Stress State

A geometric interpretation of the Mohr-Coulomb yield criterion in a 3-dimensional stress state is given in Figure 4.5. The axes σ_i, σ_j & σ_k are the three principal stresses. The transformation of the 2-dimensional plots given in Figure 4.4b to the 3-dimensional plot is obtained by considering all 6 possible stress combinations in reference to the yield function given in (3). The stress combinations are as follows

$$\sigma_i > \sigma_j > \sigma_k \qquad \sigma_j > \sigma_k > \sigma_i$$
$$\sigma_i > \sigma_k > \sigma_j \qquad \sigma_k > \sigma_i > \sigma_j$$
$$\sigma_j > \sigma_i > \sigma_k \qquad \sigma_k > \sigma_j > \sigma_i$$

The yield surface for the Mohr-Coulomb criterion is a conical surface whose normal to the space diagonal (defined by $\sigma_i=\sigma_j=\sigma_k$) is an irregular hexagon. For comparison, the Drucker-Prager criterion (described in a number of texts e.g. Owen and Hinton[35]) is plotted on the same diagram, which describes a circular cone.

Within the bounds of the Mohr-Coulomb yield criterion in Figure 4.5 we have $F < 0$. On reaching the yield surface $F = 0$, and plastic deformation occurs if further shear loading is applied. With continued plastic deformation the yield surface may expand, dilate or remain

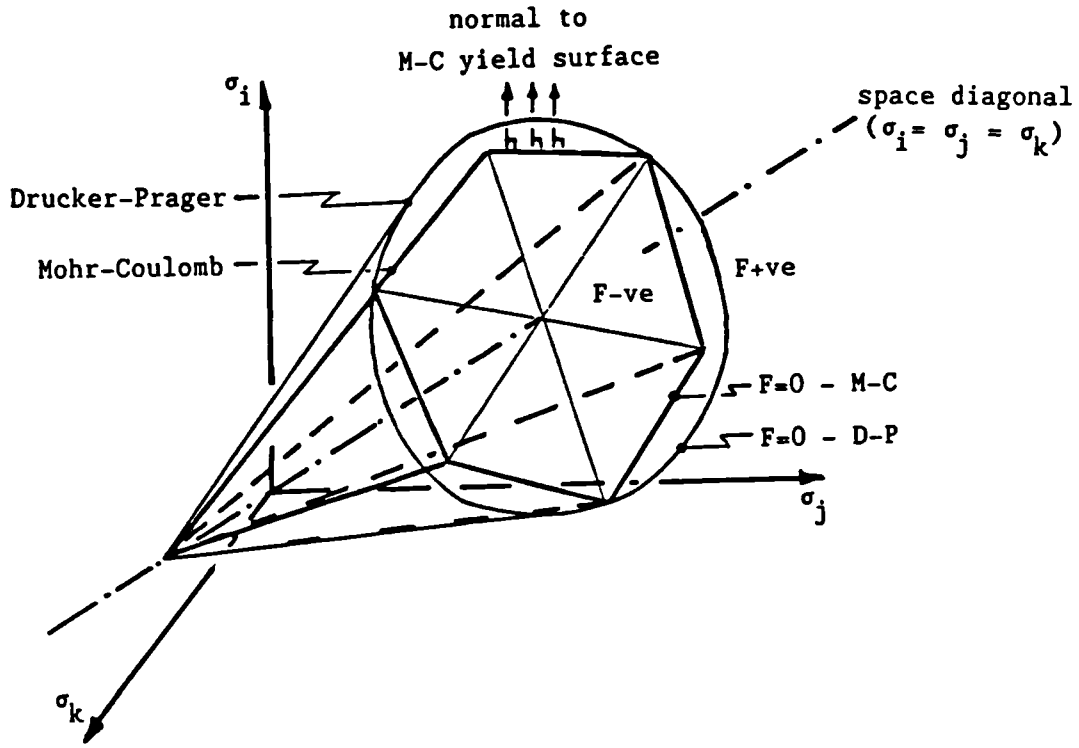


Figure 4.5 3-D interpretation of the Mohr-Coulomb and Drucker-Prager yield criteria.

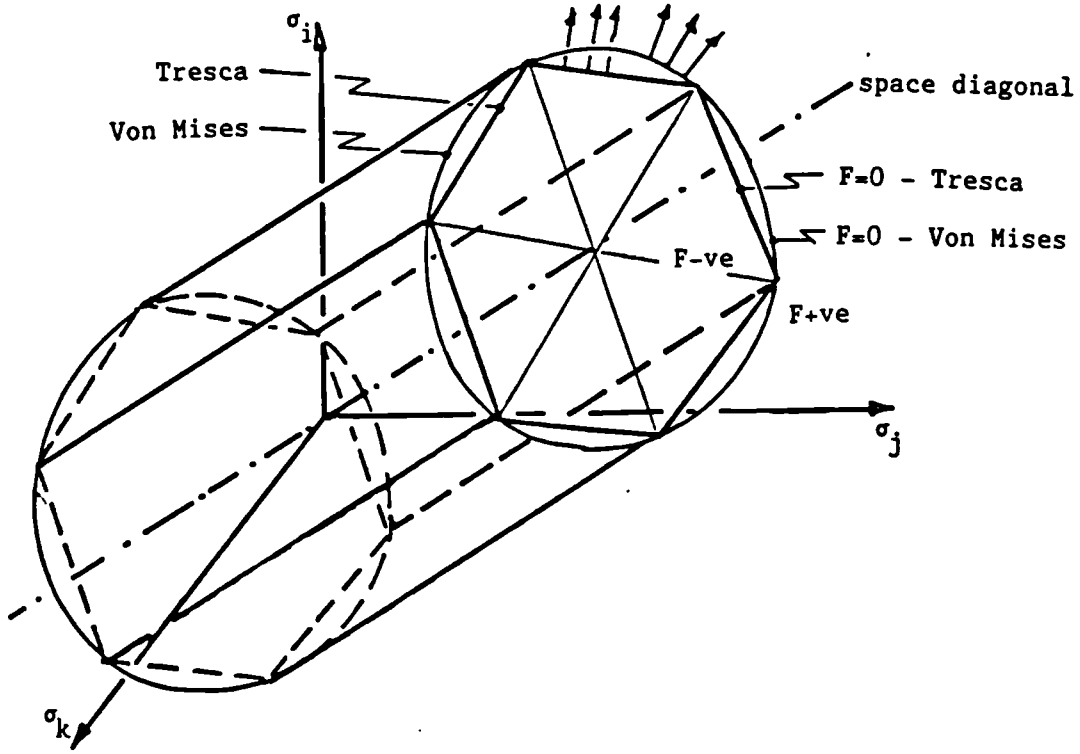


Figure 4.6 3-D interpretation of the Tresca and Von Mises yield criteria.

unchanged, depending on whether the material is undergoing strain hardening, strain softening or perfectly plastic deformation.

4.4.4 Other Yield Criteria

In addition to the Mohr-Coulomb criterion given in expression (3), the coding developed in this research allows for three other criteria, as given below.

1. Tresca

$$F = \sigma_1 - \sigma_3 - \sigma_Y \leq 0 \tag{4}$$

where $\sigma_Y = \sigma_Y(\varepsilon^p)$

2. Von Mises

$$F = \frac{1}{2}[(\sigma_1-\sigma_2)^2 + (\sigma_2-\sigma_3)^2 + (\sigma_3-\sigma_1)^2] - \sigma_Y^2 \leq 0 \tag{5}$$

where $\sigma_Y = \sigma_Y(\varepsilon^p)$

3. Hoek-Brown

$$F = (\sigma_1 - \sigma_3)^2 - m\sigma_c\sigma_3 - s\sigma_c^2 \leq 0 \tag{6}$$

where $m = m(\varepsilon^p)$, and $s = s(\varepsilon^p)$

The parameter σ_Y in expressions (4) and (5) is the uniaxial yield strength as discussed in Section 4.4.1. Geometric interpretations of the Tresca and Von Mises criteria are given in Figure 4.6. The distance from the space diagonal ($\sigma_i=\sigma_j=\sigma_k$) to the yield surface is a measure of the deviatoric or shear component of the stress state. It can be seen that as the hydrostatic portion of the loading is increased (i.e. traveling up the space diagonal) there is no change in the deviatoric stress component that the material can withstand. This results in the Tresca criterion describing an infinitely long regular hexagonal cylinder, and the Von Mises criterion describing an infinitely long circular cylinder.

These two criteria have had much application to metallic behaviour, but are inadequate at modelling rock behaviour, where it is accepted that strength increases with increase in hydrostatic loading.* However, these two criteria have been included, since other FEM codes often incorporate them and comparison with closed form solutions are available as discussed later in Section 5.5, Chapter 5.

[* Although it is accepted that rock strength increases with confinement, it is not necessarily true that the yield strength (or elastic limit) will increase with confinement. A number of rocks are reported to have undergone plastic deformation in the form of pore collapse, through the application of hydrostatic loading (e.g. Elliott[79]). However, in this research no allowance is made for yielding as a result of increased hydrostatic loading.]

A representation of the Hoek-Brown criterion is given in both 2-D and 3-D plots in Figures 4.7a and b respectively. The expression for the Hoek-Brown criterion in (6) may not be familiar, and a more common relationship is

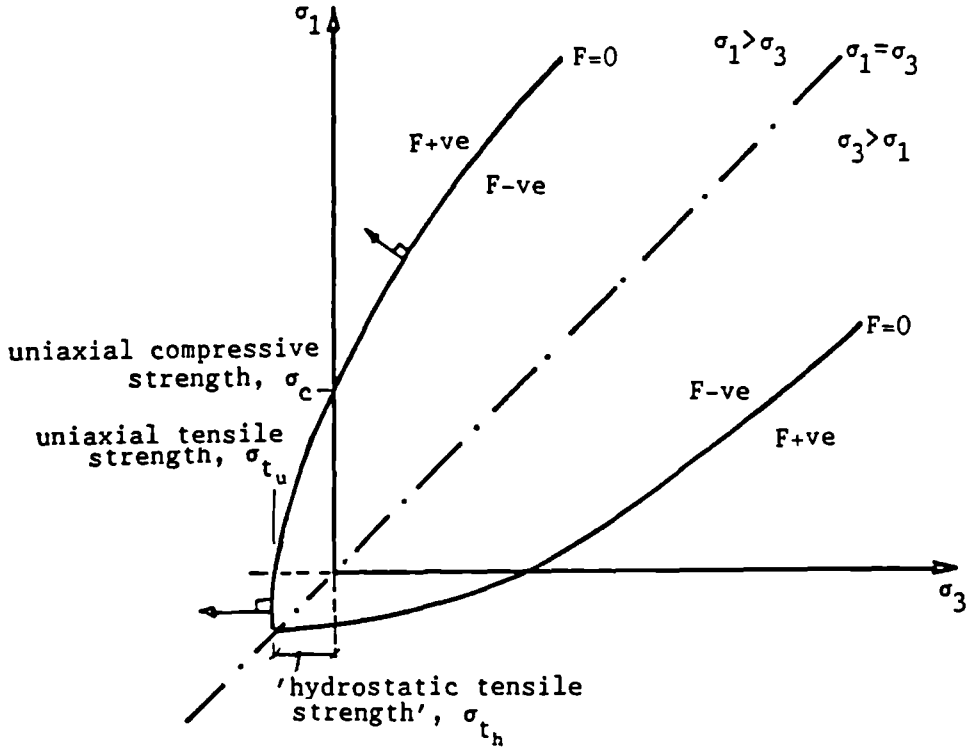
$$F = \sigma_1 - \sigma_3 - \sqrt{(m\sigma_c\sigma_3 + s\sigma_c^2)} \leq 0 \qquad (6a)$$

The form given in (6) is simply obtained by considering the limiting case where we can write

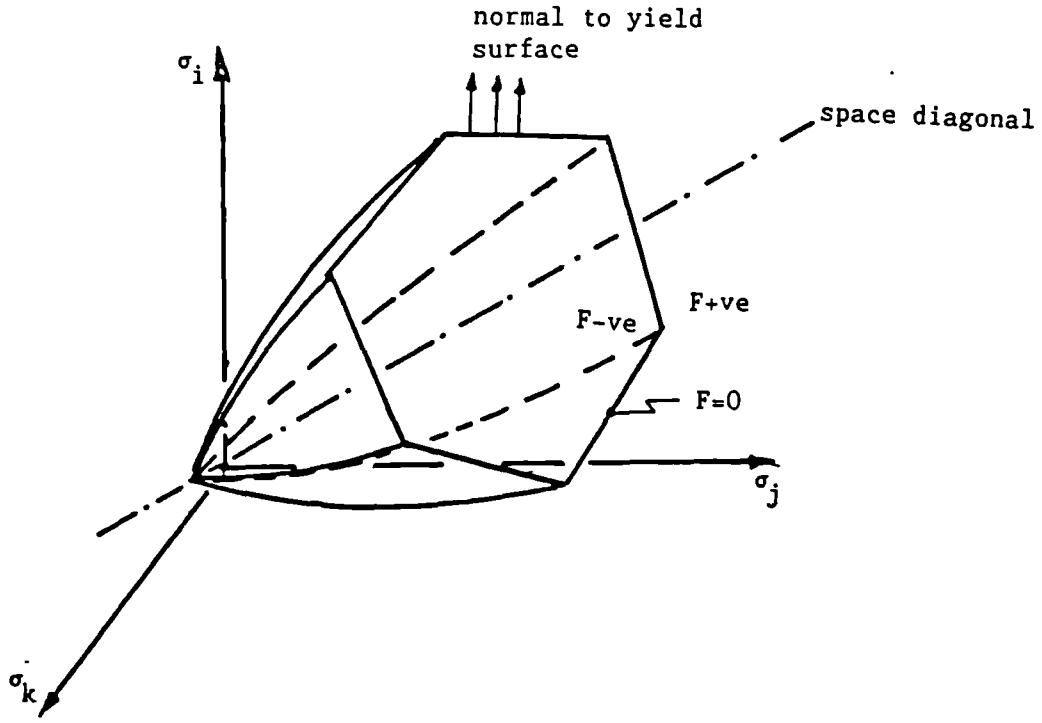
$$\sigma_1 - \sigma_3 = \sqrt{(m\sigma_c\sigma_3 + s\sigma_c^2)}$$

Thus, $$(\sigma_1 - \sigma_3)^2 = m\sigma_c\sigma_3 + s\sigma_c^2$$

From the above expression it is easy to see how equation (6) is derived. The non-zero values for F in (6) and (6a) are unequal, however, it is only the points at which F = 0 that are important, which is the same for



(a) 2-D representation of the Hoek-Brown criterion.



(b) 3-D representation of the Hoek-Brown criterion.

Figure 4.7 The Hoek-Brown criterion.

both equation (6) and (6a). There are a number of reasons for rearranging the Hoek-Brown criterion and these are explained later in Section 4.6.1 and Section 5.3.6, Chapter 5.

Of the four criteria chosen, the Hoek-Brown is the most applicable when applied to rock strength, due to its nonlinear representation of shear strength v minimum principal stress. In expression (6) 'm' and 's' are empirical strength parameters. The uniaxial compressive strength, σ_c, in (6) is for intact rock samples and is taken to be independent of ε^p. For a detailed description of the Hoek-Brown criterion and its application the reader is referred to Hoek and Brown.[78]

The remainder of this thesis concentrates on the development of the numerical formulations with respect to the criteria most suitable for modelling rock behaviour, i.e. the Mohr-Coulomb and Hoek-Brown criteria. It may be argued that these criteria are still lacking, since no account is taken of the intermediate principal stress (σ_2). However, Brown[80] carried out a set of biaxial tests and showed that, provided particular care is given to reducing end effects, the influence of σ_2 is not significant.

4.5 EXPANSION/CONTRACTION OF THE YIELD SURFACE

In Section 4.4 it was mentioned that the variation of the yield surface once the elastic limit is reached may be assumed to be a function of the plastic strain, ε^p. It may be argued equally well that the variation of the yield surface should be dependent on the minimum strain component, ε_3^p, the maximum strain component, ε_1^p, or a combination of all three components (ε_1^p, ε_2^p and ε_3^p). Here, in keeping with Brown et al,[49] it is assumed that strength variation is a function of the maximum

principal plastic strain, ε_1^p, only. Thus, the strength parameters in equations (3) to (6) can now be written as

$\sigma_Y = \sigma_Y(\varepsilon_1^p)$ - Tresca and Von Mises

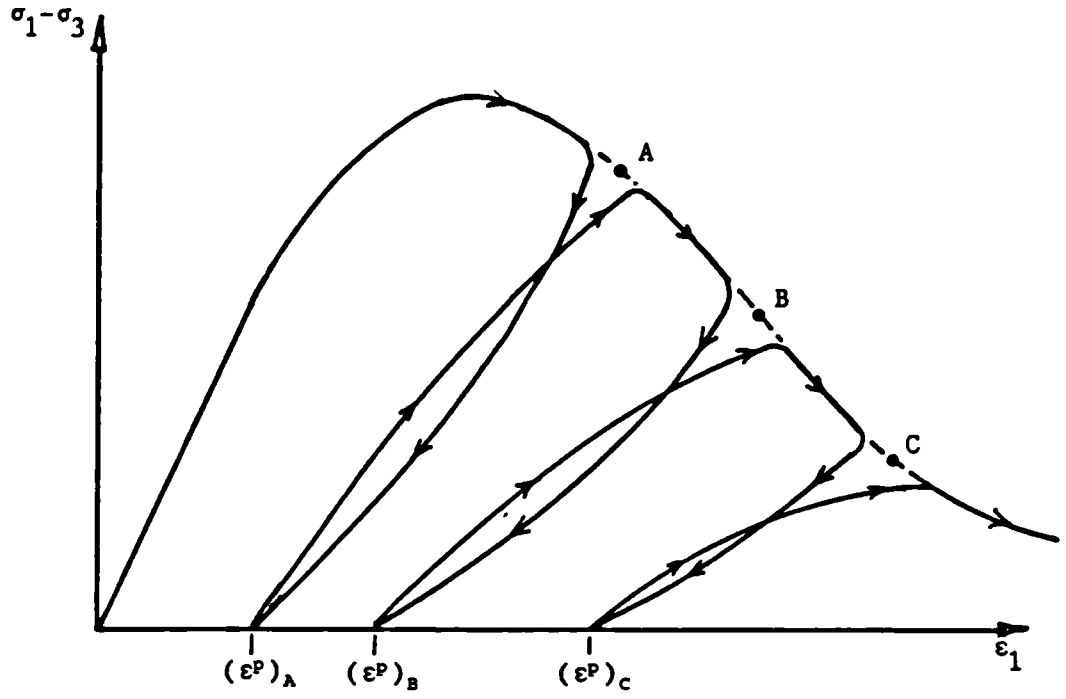
$c = c(\varepsilon_1^p)$, $\phi = \phi(\varepsilon_1^p)$ - Mohr-Coulomb

$m = m(\varepsilon_1^p)$, $s = s(\varepsilon_1^p)$ - Hoek-Brown

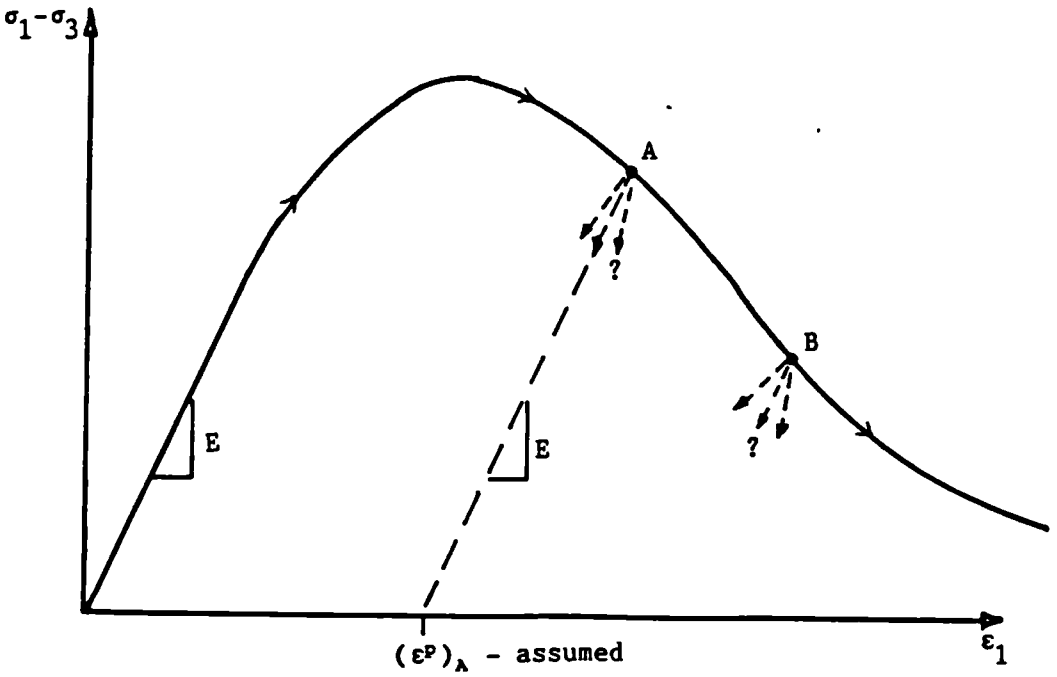
Before defining the functions relating the strength parmeters and ε_1^p, it is necessary to define the interpretation and measurement of ε_1^p as discussed in the next section.

4.5.1 Measurement of the Maximum Principal Plastic Strain

Figures 4.8a and b show typical stress-strain paths for triaxial tests carried out on a sandstone. In Figure 4.8a it can be seen that during the test a number of unloading/reloading paths have been followed. In such cases it is a simple matter of reading the irrecoverable strains directly off the stress-strain plot. However, more common is the plot shown in Figure 4.8b, where the sample is loaded up to failure on to residual strength, with no elastic unloading portions. In such cases the plastic strain incurred at a point on the stress-strain curve (e.g. point 'A', Figure 4.8b) must be inferred. Ignoring complications due to hysteresis, it can be seen that the elastic modulus of a rock reduces with continued plastic deformation (Figure 4.8a). This tendency further complicates the estimation of the plastic portion of the strain at a point on the stress-strain curve. In this analysis it is assumed that the elastic modulus is unaffected by permanent deformation, and an unloading line parallel to the initial elastic modulus can be drawn to define the plastic strain undergone (see Figure 4.8b). This



(a) Triaxial test with elastic unloading portions



(b) Triaxial test with no elastic unloading

Figure 4.8 Measurment of major principal plastic strain for triaxial data.

assumption reduces the complexity of the problem, but it may be considered as a poor assumption considering the experimental evidence to support the drop in elastic modulus with deformation (e.g. Bieniawski[81]). However, in the case of an element of rock that has yielded, and remains on the yield surface, it is unlikely this assumption will adversely effect the predicted behaviour. Thus, only when the response involves elastic unloading from a state of yield are significant errors likely to be introduced. This argument is similar to that proposed by Brown and Bray.[36] Their idealized stress-strain behaviour, given in Figure 4.9, shows allowance for a reduced elastic modulus, after suffering plastic deformation. However, they do not allow for this behaviour explicitly, but its effect is subsumed in the post peak flow behaviour. The model is applied to a rock-support interaction problem, where support originally offered by the excavated rock is partially replaced by a liner. The rock surrounding the excavation becomes increasingly critically loaded until yield occurs. On further reduction of support the yielded zone extends further into the rock mass. During this process, elements of rock that suffer yielding remain on the yield surface and do not experience elastic unloading, thus incorporation of elastic modulus variation within the flow behaviour is acceptable. However, if the problem had involved a decrease followed by an increase in support offered (i.e. loading followed unloading), then the solutions would have been dependent on β. Therefore, in cases where the surrounding rock is subjected to a monotonic reduction of support, the assumption of an unaltered elastic modulus is unlikely to adversely effect the results.

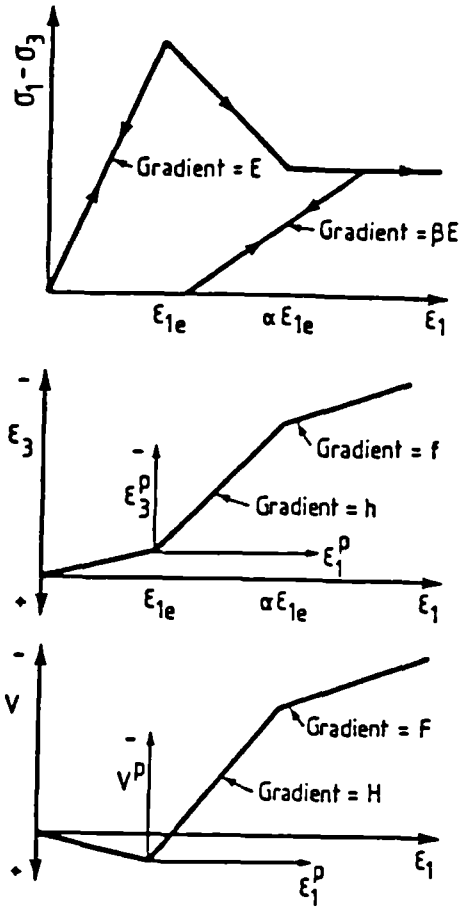


Figure 4.9 Idealised representation of rock stress-strain behaviour (after Brown and Bray[39]).

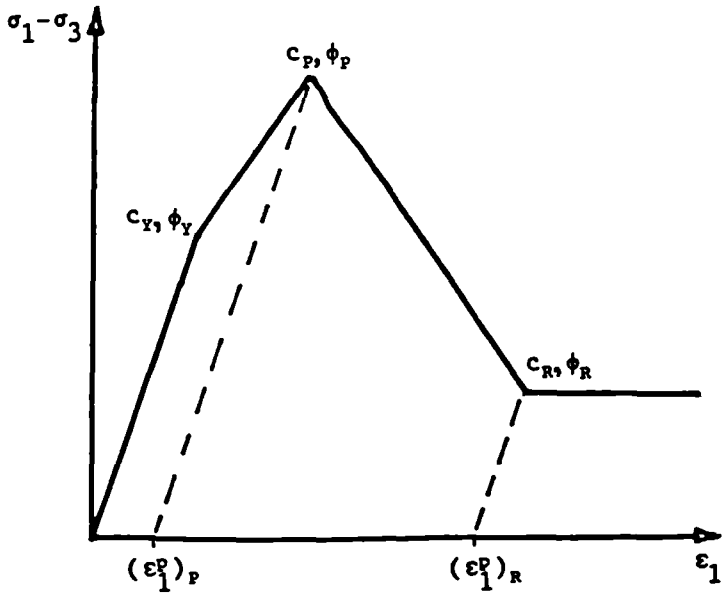


Figure 4.10 Idealised representation of a triaxial test using Mohr-Coulomb strength parameters.

4.5.2 Strength Parameter-Plastic Strain Relationships

Having decided on the interpretation of plastic strain, it is now necessary to specify the functions relating strength parameters (σ_Y, c, ϕ, m and s) and the principal plastic strain, ε_1^p. The simplest relationship is a linear one, i.e. increments in strength parameters are directly proportional to increments in ε_1^p. Therefore, in the case of the Tresca criterion we have

$$\delta\sigma_Y = \alpha\delta\varepsilon_1^p$$

where $\alpha > 0$ during hardening

$\alpha < 0$ during softening

and $\alpha = 0$ for perfect plasticity (or residual strength)

For the case of the Mohr-Coulomb criterion we have

$$\delta c = \alpha_c \delta\varepsilon_1^p \quad \text{and} \quad \delta\phi = \alpha_\phi \delta\varepsilon_1^p \tag{7}$$

For the uniaxial load case shown in Figure 4.10 the factors α_c and α_ϕ in the hardening portion are given by

$$\alpha_c = \frac{c_P - c_Y}{(\varepsilon_1^p)_P} \quad \text{and} \quad \alpha_\phi = \frac{\phi_P - \phi_Y}{(\varepsilon_1^p)_P} \tag{8}$$

and in the softening portion

$$\alpha_c = \frac{c_R - c_P}{(\varepsilon_1^p)_R - (\varepsilon_1^p)_P} \quad \text{and} \quad \alpha_\phi = \frac{\phi_R - \phi_P}{(\varepsilon_1^p)_R - (\varepsilon_1^p)_P} \tag{9}$$

where c_Y, c_P and c_R are the values of the cohesion coefficients at yield, peak and residual strength respectively,

ϕ_Y, ϕ_P and ϕ_R are the friction angle values at yield, peak and residual strength respectively,

and $(\varepsilon_1^p)_P$ and $(\varepsilon_1^p)_R$ are the principal plastic strain values at peak and residual strength respectively.

The relationship between stress and ε_1^p is now uniquely defined for the

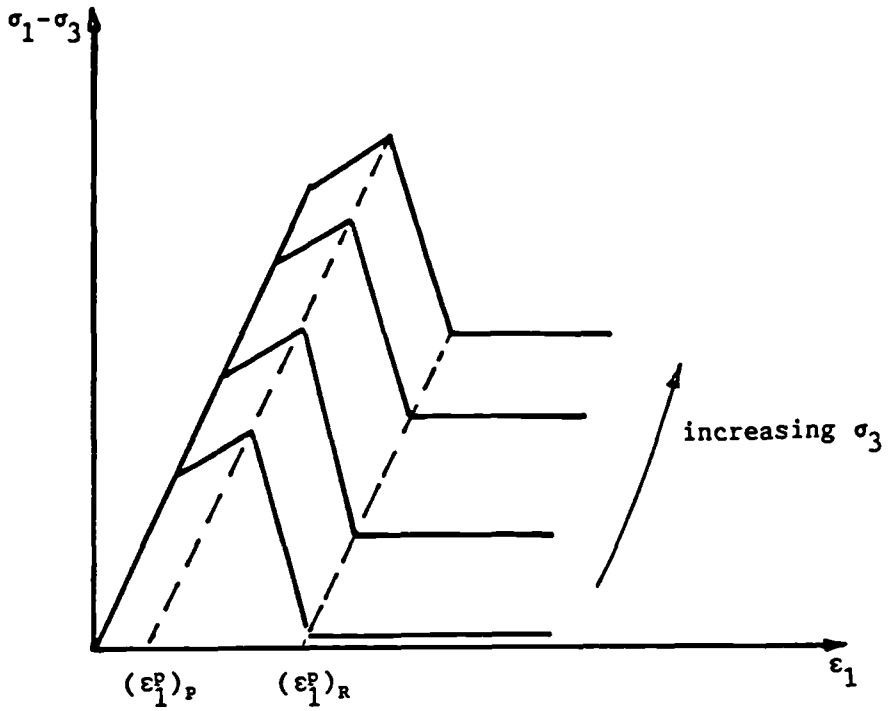


Figure 4.11 Idealised model representation of triaxial test results showing no increase in ductility with increased confining pressure.

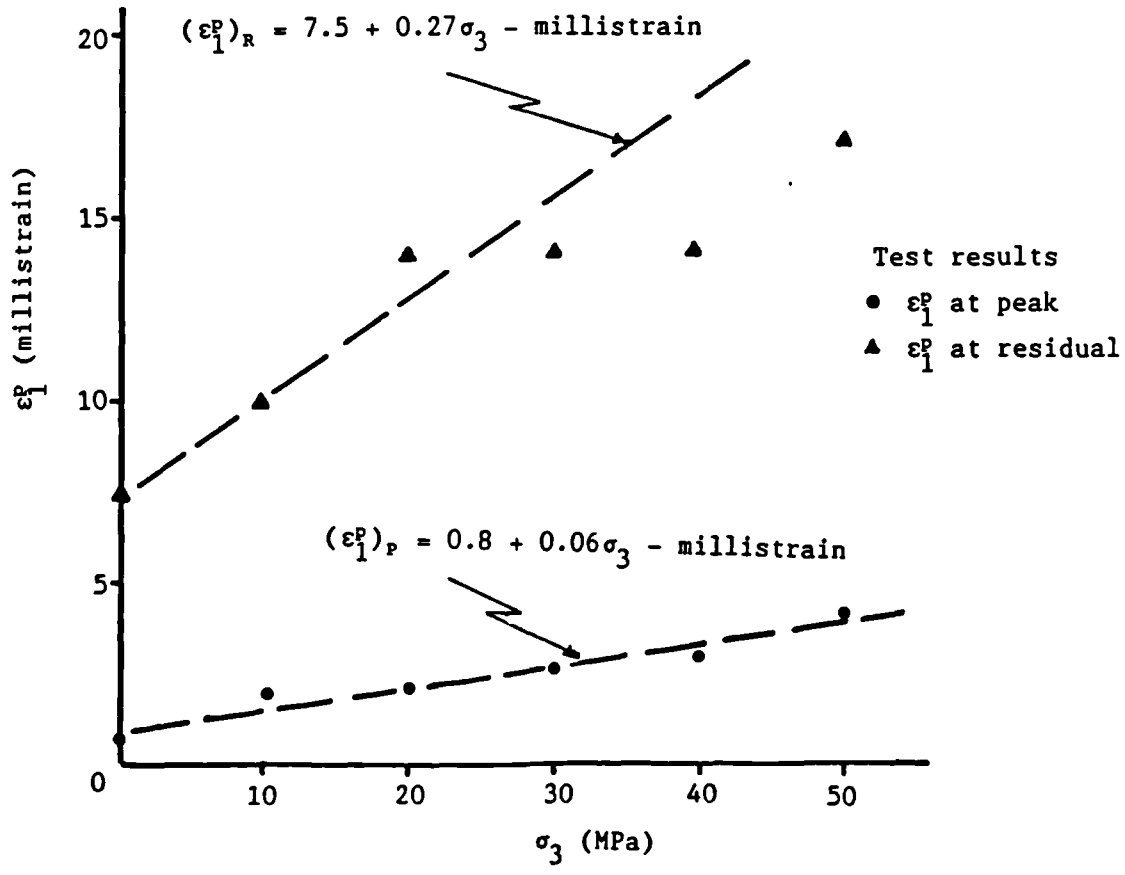


Figure 4.12 Variation of ε_1^p at peak and residual as a function of confining pressure.

case of the Mohr-Coulomb criterion using expressions (3),(7),(8) and (9). The resulting trilinear strength criterion may be adequate for describing a uniaxial test or a triaxial test at a particular confining pressure (e.g. Figure 4.10). However, when the model is applied to a set of tests carried out over a range of confining pressures, the predicted set of triaxial results proves to be unrealistic. Figure 4.11 shows the type of plots generated by using the Mohr-Coulomb model behaviour expressions. When Figure 4.11 is compared to a more realistic idealized behaviour (e.g. Figure 4.4a) it can be seen that the model is unable to predict the increase in ductility experienced by rock when subjected to higher confining pressures. The inherent defect in the model is due to the coupling of two assumptions; (i) the amount of plastic strain required to reach peak and residual strength is independent of confining pressure, and (ii) the elastic modulus is unaffected by plastic deformation. If assumption (ii) is to remain, then to provide for a more realistic model it is necessary to have the extent of the plastic strain at peak and residual strength dependent on stress state, or more specifically on the minimum principal stress (σ_3).

4.5.3 Variation of Plastic Strain with Confining Pressure

To incorporate the dependence of plastic strain on confining pressure, then additional relationships to the yield criterion expressions ((3),(7),(8) and (9) in the case of the Mohr-Coulomb criterion) must be defined, which in general terms are

$$(\varepsilon_1^p)_P = f_P(\sigma_3) \qquad \text{and} \quad (\varepsilon_1^p)_R = f_R(\sigma_3)$$

To facilitate the appreciation of the effect of confining pressure on plastic deformation, ε_1^p was determined for a set of triaxial tests on a Carboniferous sandstone (Santarelli[18]) using the principles set out in

Section 4.5.2. The stress-strain plots for these tests are shown in Figures A.1 to A.6 of Appendix A. The resulting values of $(\varepsilon_1^p)_P$ and $(\varepsilon_1^p)_R$ are plotted as a function of σ_3 in Figure 4.12. It can be seen that there is a general trend for $(\varepsilon_1^p)_P$ and $(\varepsilon_1^p)_R$ to increase with increasing confining pressure, although the trend is much more marked in the case of $(\varepsilon_1^p)_R$. For simplicity the functions f_P and f_R are assumed to be linear. Thus, we can write

$$(\varepsilon_1^p)_P = [(\varepsilon_1^p)_P]_{uniax} + A_P\sigma_3 \tag{10}$$

$$\text{and} \quad (\varepsilon_1^p)_R = [(\varepsilon_1^p)_R]_{uniax} + A_R\sigma_3 \tag{11}$$

The values of $(\varepsilon_1^p)_P$ and $(\varepsilon_1^p)_R$ for uniaxial compression can be read off directly from test results. The constants A_P and A_R can be determined graphically from a number of triaxial tests at varying confining pressures. For the particular case of the Carboniferous sandstone results used here, we have

$[(\varepsilon_1^p)_P]_{uniax}$ = 0.8 millistrain, and A_P = 0.06 millistrain/MPa

$[(\varepsilon_1^p)_R]_{uniax}$ = 7.2 millistrain, and A_R = 0.27 millistrain/MPa

4.6 THE FLOW RULE

In Sections 4.4 and 4.5 relationships were presented to uniquely define the extent of plastic strain in the principal stress direction, ε_1^p, in response to loading. In well instrumented triaxial testing the radial strain component, ε_r ($\equiv \varepsilon_3$), is monitored, in addition to the axial strain, ε_z ($\equiv \varepsilon_1$). This response is either recorded directly as radial strain, or combined with the axial strain to give the volumetric strain, ε_v. Thus,

$$\varepsilon_v = \varepsilon_z + 2\varepsilon_r \quad (= \varepsilon_1 + 2\varepsilon_3)$$

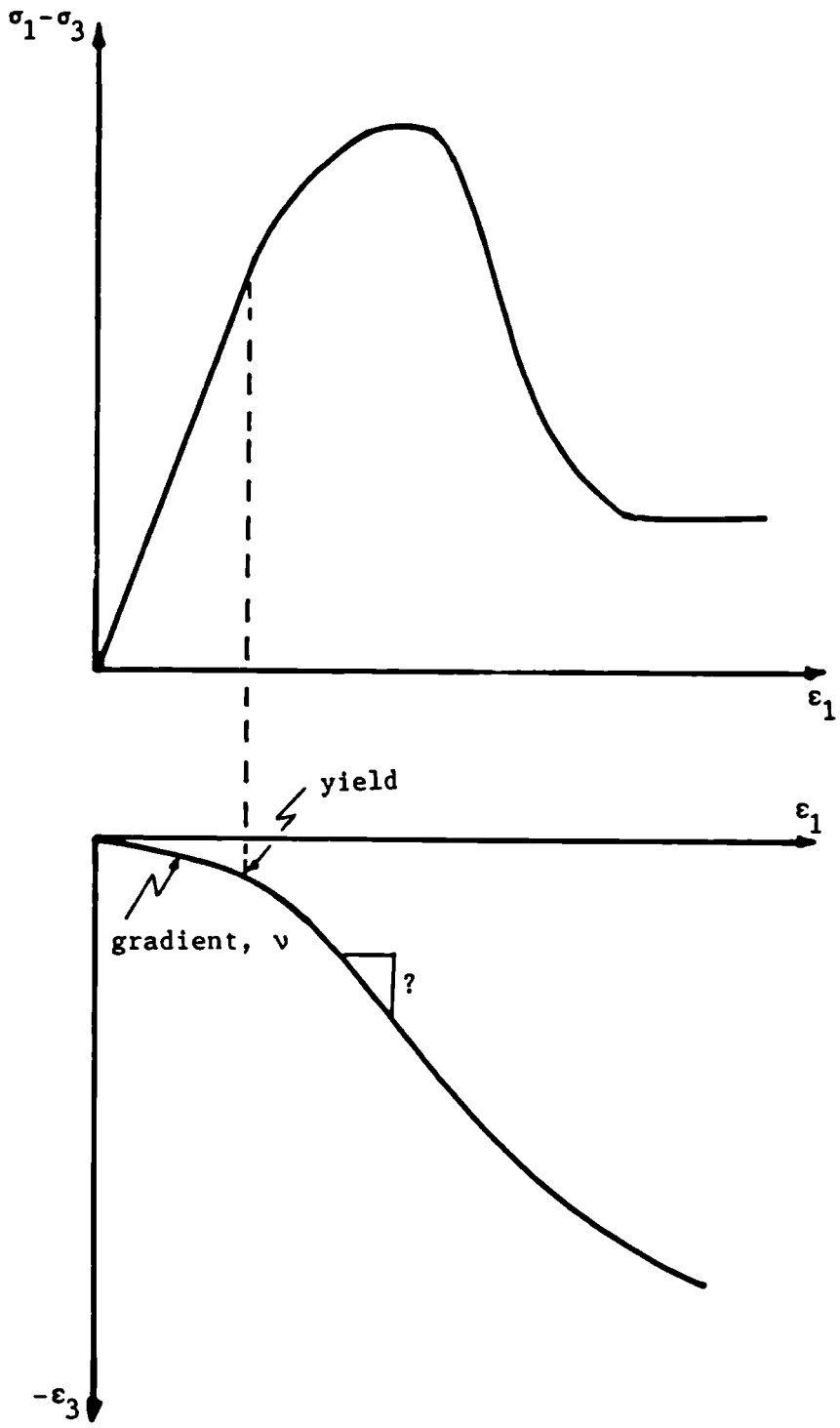


Figure 4.13 Radial response to loading in a triaxial test.

For a homogeneous, isotropic, linear elastic material tested in a triaxial cell, the radial strain relative to the axial strain can be predicted using Poisson's ratio. However, once loading exceeds the samples elastic limit, both ε_z and ε_r include a plastic component, and Poisson's ratio is no longer sufficient for defining the total radial strain (see Figure 4.13). In plasticity theory this problem is overcome by introducing the flow rule.

In terms of principal strains the plastic strain vector is given by

$$[\varepsilon^p]^T = [\varepsilon_1^p, \varepsilon_2^p, \varepsilon_3^p]$$

where ε_1^p, ε_2^p and ε_3^p are the maximum, intermediate and minimum principal plastic strains respectively.

Or in terms of plastic strain increments

$$[\delta\varepsilon^p]^T = [\delta\varepsilon_1^p, \delta\varepsilon_2^p, \delta\varepsilon_3^p] \qquad (12)$$

With the assumption that axes of principal plastic strain increments and principal stress are coincident, then the flow rule provides the direction of the incremental plastic strain vector $[\delta\varepsilon^p]$. Thus, if the magnitude of one of the increment components (e.g. $\delta\varepsilon_1^p$) is known, then the other two components ($\delta\varepsilon_2^p$ and $\delta\varepsilon_3^p$) can be determined.

4.6.1 Associated Flow

In most applications of plasticity theory it is found that the assumption of associated flow is made (e.g. Owen and Hinton[35]). Associated flow simply means that the incremental plastic strain vector, $[\delta\varepsilon^p]$, is associated with the strength criterion. Implied in associated flow is the 'normality condition'. This results in the strain vector, $[\delta\varepsilon^p]$, having a direction normal to the surface defined by the yield

criterion. Normality of $[\delta\varepsilon^p]$ to the yield surface is shown with respect to the four criteria used here (Tresca, Von Mises, Mohr-Coulomb and Hoek-Brown) in Figures 4.5, 4.6 and 4.7. Thus, by drawing the similarity with fluid flow, the yield surface can be considered as a 'potential' surface and the plastic strain components as plastic 'flow' components. Therefore, by differentiating the plastic potential with respect to the axes (σ_1, σ_2 and σ_3), the relative plastic strain components ($\delta\varepsilon_1^p$, $\delta\varepsilon_2^p$, and $\delta\varepsilon_3^p$) can be determined. Thus, expressed as partial differential equations, we have

$$\delta\varepsilon_1^p = \lambda\frac{\partial F}{\partial\sigma_1}, \qquad \delta\varepsilon_2^p = \lambda\frac{\partial F}{\partial\sigma_2} \qquad \text{and} \qquad \delta\varepsilon_3^p = \lambda\frac{\partial F}{\partial\sigma_3}$$

Or in vector notation

$$[\delta\varepsilon^p] = \lambda[a] \tag{13}$$

where λ is a scalar quantity termed the 'plastic multipier',

and $[a]$ is the differential of the yield function, which in terms of principal stress is given by

$$[a]^T = \left[\frac{\partial F}{\partial\sigma_1}, \frac{\partial F}{\partial\sigma_2}, \frac{\partial F}{\partial\sigma_3}\right]$$

Thus, if λ can be determined for a particular increment of load, then the extent of the induced plastic strain can be determined. It is not necessary to consider the determination of λ at this stage, however, it is covered later in Section 5.3.1, Chapter 5.

Of the four criteria considered it can be seen from differentiation of their respective yield functions (equations (3) to (6)) using the flow rule expression system, (13), only the Von Mises criterion has a non-zero platsic component in the intermediate principal stress direction ($\delta\varepsilon_2^p$). The other criteria (Tresca, Mohr-Coulomb and Hoek-Brown) are independent of σ_2, resulting in $\delta\varepsilon_2^p = 0$.

Taking the Mohr-Coulomb criterion as an example, at first it appears from equations (7) to (11) that the strength parameters c and ϕ are a a function of σ_3, and therefore in (13), $\frac{\partial c}{\partial \sigma_3} \neq 0$ and $\frac{\partial \phi}{\partial \sigma_3} \neq 0$. However, the values of c and ϕ are a function of stress history and not current stress level, and from the argument that a change in strength can only be accommodated by an increment in plastic strain, then we must have

$$\left(\frac{\partial c}{\partial \sigma_3}\right)_{\varepsilon_1^p=\text{const.}} = 0 \qquad \text{and} \qquad \left(\frac{\partial \phi}{\partial \sigma_3}\right)_{\varepsilon_1^p=\text{const.}} = 0$$

Table 8 shows the resultant functions for the plastic strain components for the four criteria using associated flow. The points to notice in Table 8 are the plastic volumetric strains. The Tresca and Von Mises associated flow predicts deformation at constant volume, whereas both the Mohr-Coulomb and Hoek-Brown criteria predict plastic dilation. An assessment as to the validity of associated flow when applied to a Carboniferous sandstone is given later in Section 4.7.

At this point it is worth noting the importance of rearranging the Hoek-Brown criterion as mentioned Section 4.4.4. The differentiation of equation (6a) with respect to the three principal stresses yields the following,

$$\frac{\delta\varepsilon_1^p}{\lambda} = 1.0, \qquad \frac{\delta\varepsilon_2^p}{\lambda} = 0.0, \qquad \text{and} \qquad \frac{\delta\varepsilon_3^p}{\lambda} = -\frac{m\sigma_c}{2\sqrt{(m\sigma_c\sigma_3+s\sigma_c^2)}}$$

It can be seen that as $\sigma_3 \rightarrow -s\sigma_c/m$ the demoninator of the minimum principal strain component approaches zero and $\delta\varepsilon_3^p/\lambda$ approaches infinity. The physical interpretation of this can be seen in Figure 4.7a. As the stress point approaches the $\sigma_1=\sigma_3$ diagonal the normal to the yield surface has no component in the maximum principal stress direction. Thus, $\delta\varepsilon_1^p/\lambda = 0$. Consequently the expressions derived from equation (6a) become unmanageable around this area of the yield surface. However, the expressions derived from equation (6) do not

Criterion	$\frac{\delta\varepsilon_1^p}{\lambda}$	$\frac{\delta\varepsilon_2^p}{\lambda}$	$\frac{\delta\varepsilon_3^p}{\lambda}$	$\frac{\delta\varepsilon_3^p}{\lambda}$
Tresca	1.0	0.0	-1.0	0.0
Von Mises	$2\sigma_1-\sigma_2-\sigma_3$	$2\sigma_2-\sigma_1-\sigma_3$	$2\sigma_3-\sigma_2-\sigma_1$	0.0
Mohr-Coulomb	$1-\sin\phi$	0.0	$-1-\sin\phi$	$2\sin\phi$
Hoek-Brown	$2(\sigma_1-\sigma_3)$	0.0	$2(\sigma_3-\sigma_1) - m\sigma_3$	$-m\sigma_3$

Strain ratios found from the application of the associated flow rule.

TABLE 8

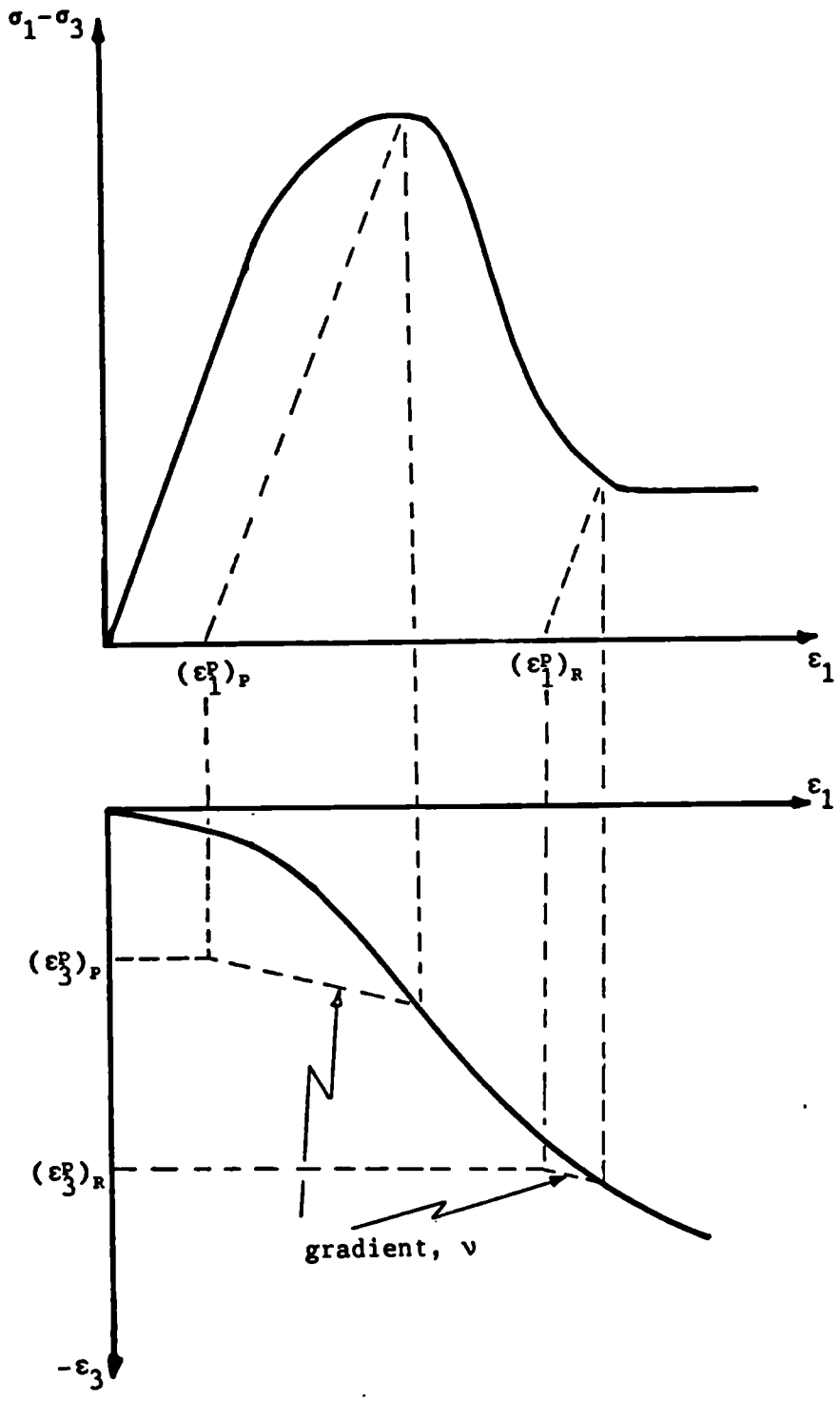


Figure 4.14 Measurement of ε_3^p from a triaxial data.

suffer from this problem and are finite for all values of σ_1 and σ_3.

4.6.2 Measurement of Plastic Flow Ratios

Before introducing non-associated flow, it is necessary to stipulate how plastic flow is determined. Figure 4.14 gives the general shape of the deviator stress-axial strain curve and mean radial strain-axial strain curve for a triaxial test. The point of yield is often considered as the point at which the stress-strain curve deviates from linearity, however, this point is often hard to define. Here yield is considered to occur when the radial strain-axial strain curve deviates from 'linearity', which is often more markedly defined. In Section 4.5.1 it was assumed that Young's modulus is unaffected by plastic deformation. To allow determination of the radial plastic strain component a further assumption is made that Poisson's ratio is constant and independent of plastic deformation. Thus, in Figure 4.14, the radial plastic strain at peak and residual strength is determined using the construction lines indicated.

A common assumption in non-associated flow rules is that plastic straining only occurs in the maximum and minimum principal stress direction (e.g. Brown et al,[49] Gumusoglu[76]). This assumption is made in the non-associated flow relationship presented in the next section. However, such an assumption is problematic when applied to triaxial test results where $\sigma_2 = \sigma_3$. This problem is dealt with further in Section 5.3.4, Chapter 5, when applied to singular points on the yield surface, but for present it is assumed that plastic straining during triaxial testing occurs in only one cartesian direction in the plane perpendicular to loading. Therefore, if the mean radial plastic strain

is given by $(\varepsilon_r^p)_{av}$, we have

$$(\varepsilon_r^p)_{av} = \frac{1}{2}(\varepsilon_2^p + \varepsilon_3^p), \qquad \text{and } \varepsilon_2^p = 0$$

$$\therefore \quad \varepsilon_3^p = 2(\varepsilon_r^p)_{av}$$

Here the flow ratio is defined as $\partial\varepsilon_3^p/\partial\varepsilon_1^p$ (note $\partial\varepsilon_2^p/\partial\varepsilon_1^p$ is assumed zero). Continuous determination of the flow ratio over the loading path is a lengthy and tedious process. Thus, the flow ratio is considered as a trilinear relationship, given by constant flow ratios between (i) yield and peak, (ii) peak and residual and (iii) residual onwards. The determination of the flow ratio between peak and residual (see Figure 4.14), for example, is given by

$$\frac{\partial\varepsilon_3^p}{\partial\varepsilon_1^p} = \frac{2[(\varepsilon_r^p)_R-(\varepsilon_r^p)_P]}{(\varepsilon_z^p)_R-(\varepsilon_z^p)_P}$$

4.6.3 Non-Associated Flow

In certain cases it is found that associated flow does not adequately describe a rock's plastic deformation (Ladanyi,[77] Brown et al[49]). A solution to this is to use a non-associated flow rule. In such cases a plastic potential surface other than the yield criterion must be specified. The advantage of a non-associated flow is that plastic strain can be better modelled. However, the non-associated flow potential function and its parameters become additional input information which must be found and specified.

The maximum principal plastic strain components for the triaxial test results performed on a Carboniferous sandstone (Figures A.1 to A.6) were determined and presented in Section 4.5.3. To determine flow ratios the corresponding minimum principal plastic strain components were found using procedures set out in Section 4.6.2. The resulting plastic flow

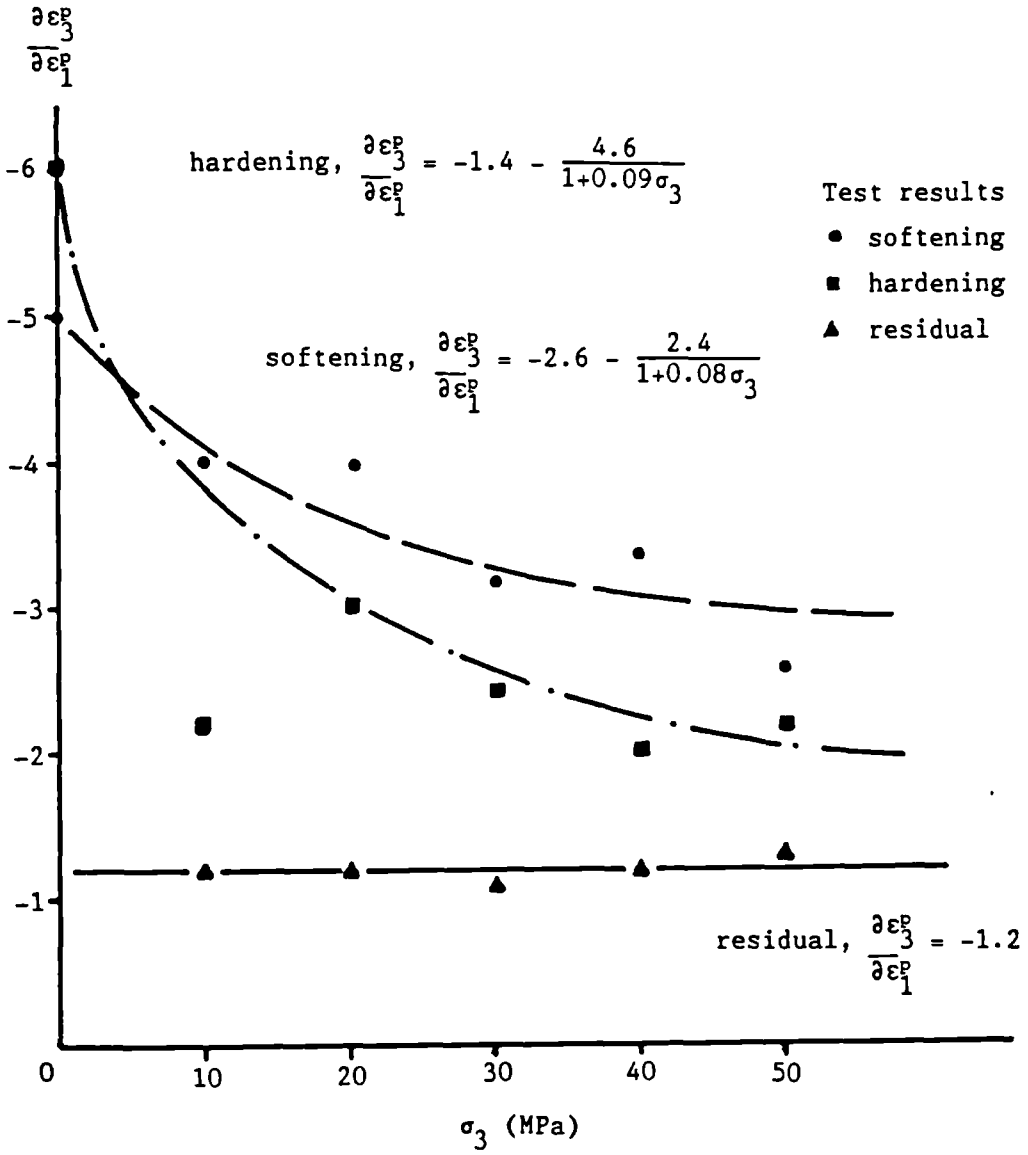


Figure 4.15 Plot of interpreted flow ratio ($\partial \varepsilon_3^p / \partial \varepsilon_1^p$) against confining pressure for a Carboniferous sandstone.

ratios are presented in Figure 4.15. As with ductility, it can be seen that the flow ratios during hardening and softening show dependency on confining pressure. In the case of continued deformation at residual strength, the flow ratio shows little or no dependence on confining pressure. Also, with a flow ratio of approximately -1.2, residual deformation is occurring at close to constant volume conditions (constant volume ≡ flow ratio = -1). Curves are fitted to the flow ratios as shown in Figure 4.15. The general form of the flow ratio relationships is

$$\frac{\partial \varepsilon_3^p}{\partial \varepsilon_1^p} = f_\infty + \frac{C}{1 + D\sigma_3} \qquad (\text{for } \sigma_3 \geq 0) \qquad (14)$$

where f_∞ is equivalent to a flow ratio at infinite confining pressure, and C and D are constants.

For the proposed trilinear plastic flow model f_∞, C and D take on values corresponding to (1) hardening, i.e. $(f_\infty)_H$, C_H and D_H,

(2) softening, i.e. $(f_\infty)_S$, C_S and D_S,

and (3) residual, i.e. $(f_\infty)_R$, C_R and D_R.

In the case of the Carboniferous sandstone analysed here, we have

$(f_\infty)_H = -2.6$, $C_H = -2.4$ and $D_H = 0.08$ MPa^{-1}

$(f_\infty)_S = -1.4$, $C_S = -4.6$ and $D_S = 0.09$ MPa^{-1}

and $(f_\infty)_R = -1.2$, $C_R = 0.0$ and D_R - irrelevant

Later in Section 5.3.3, Chapter 5, it is shown when applying the FEM to plasticity it is necessary to have the flow rule in the form of a plastic potential, which on differentiation yields the plastic flow vector (see equation (13) for associated flow). A potential function which yields the general non-associated flow ratio, given in (14), is

$$Q = \sigma_1 + f_\infty \sigma_3 + \frac{C}{D}.\ln(1+D\sigma_3) \qquad (15)$$

Thus, the flow vector in terms of principal strains is given by

$$[\delta\varepsilon^p]^T = \lambda[f] \tag{16}$$

where $[f]^T = \left[\frac{\partial Q}{\partial \sigma_1}, \frac{\partial Q}{\partial \sigma_2}, \frac{\partial Q}{\partial \sigma_3}\right]$

and λ and $[\delta\varepsilon^p]^T$ were previously defined with respect to equation (13).

4.7 APPLICATION OF MODEL TO CARBONIFEROUS SANDSTONE TRIAXIAL RESULTS

Sections 4.4 to 4.6 covered the development of plasticity modelling with respect to both associated and non-associated flow and four yield criteria, in particular the Mohr-Coulomb criterion. The combined laws and relationships provide a unique description of a material's stress-strain response when taken above its elastic limit. However, the model is complex, making it difficult to relate to its physical interpretation of rock behaviour. A good method of appreciating the physical interpretation of a behaviour model is to compare its prediction of triaxial testing to actual test results. This is carried out with respect to the Carboniferous sandstone tested by Santarelli[18] using both Mohr-Coulomb and Hoek-Brown criteria in conjunction with both associated and non-associated flow.

4.7.1 Mohr-Coulomb Criterion

From the test results given in Figures A1 to A6 the yield, peak and residual strengths where found and plotted as a function of confining pressure in Figure 4.16. A Mohr-Coulomb criterion is fitted to these points for the three limiting conditions. It can be seen that due to the nonlinear dependence of strength on confinement the Mohr-Coulomb criterion cannot adequately fit the results over the range of σ_3 used. Here the linear criterion has been used to fit the lower range of

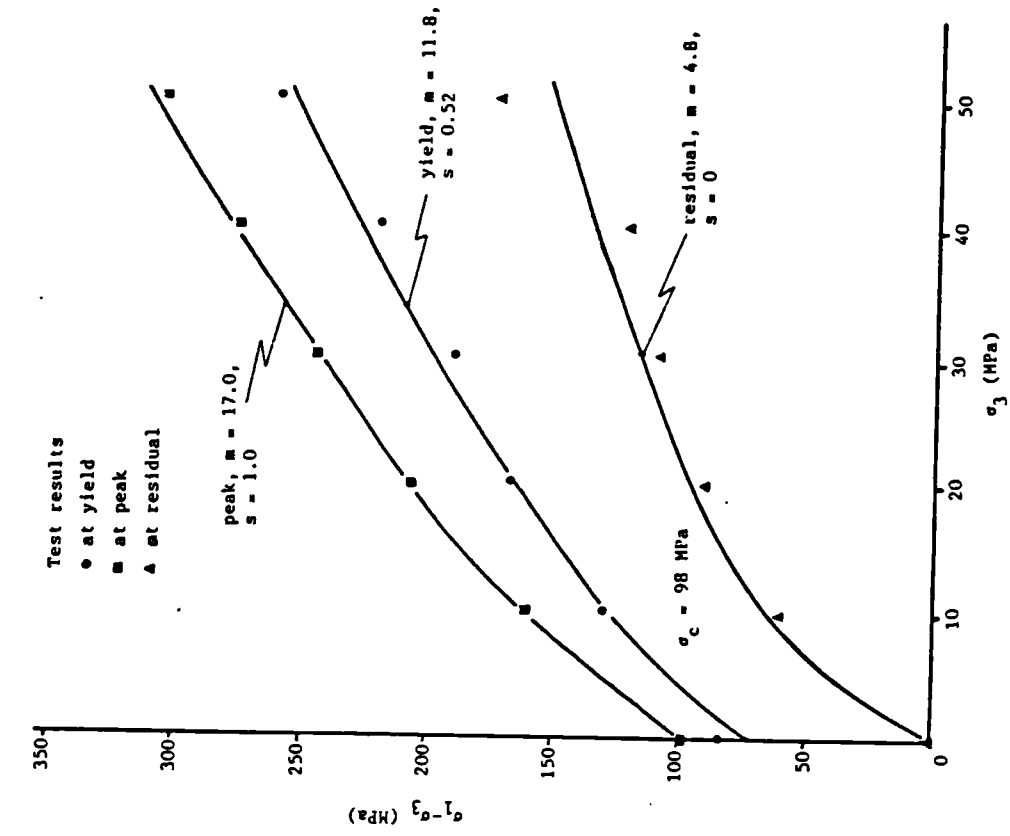


Figure 4.17 Hoek-Brown criterion fitted to yield, peak and residual strength values for a Carboniferous sandstone.

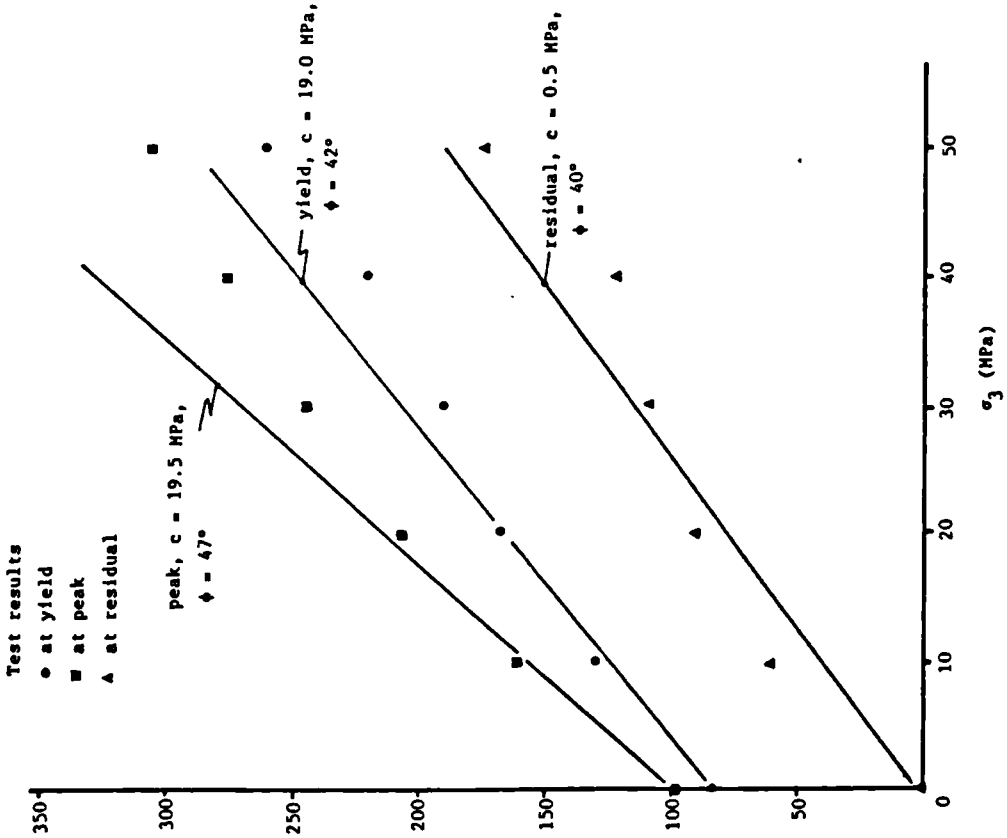


Figure 4.16 Mohr-Coulomb criterion fitted to yield, peak and residual strength values for a Carboniferous sandstone.

confining pressures, resulting in an over prediction of strength at higher values of σ_3.

As discussed, in Item I of Section 1.4.1 of Chapter 1, many rocks exhibit an increase in elastic modulus with increase in confining pressure, and the sandstone considered here is no exception. The tangent modulus at 50% of peak strength (E_{50}) ranged from around 14 GPa for uniaxial compression to around 26 GPa for a confining pressure of 50 MPa. Over the same range Santarelli[18] quotes a drop in Poisson's Ratio, ν, from 0.25 to 0.06. Since no allowance is made for variation in the elastic parameters in this model, fixed values have been chosen of $E = 19$ GPa, and $\nu = 0.20$.

Using relationships (3),(8),(9),(10) and (11) in conjunction with the values of c and ϕ taken from Figure 4.16 and the elastic constants given above, the model behaviour is plotted for associated flow in Figures A.7 to A.12, and non-associated flow in Figures A.13 to A.18. The flow rules are given in Table 8 for associated flow and equations (15) and (16) for non-associated flow. As expected the model shows a fair agreement in terms of strength with the actual behaviour only at low confining pressures for both associated and non-associated flow (strength prediction is independent of the flow rule). At the higher confining pressures of 40 MPa (Figures A.11 and A.17) and at 50 MPa (Figures A.12 and A.18) the model increasingly over predicts strength. Also, as expected, the elastic portion of the stress-strain plot is steeper than the actual response for uniaxial compression, whereas at high confining pressures (30 MPa and above) the slope is less than the actual response (again this response is independent of the flow rule).

The points at which the predicted radial strain departs sharply from the linear elastic response is a function of the strength criterion and the elastic modulus. The slope of the predicted radial strain-axial

strain plots after exceeding the yield strength is largely dominated by the flow rule. It can be seen from Figures A.7 to A.12, that apart from uniaxial loading the associated flow tends to grossly over-predict this slope after peak strength is reached. However, for the non-associated flow model the slope of radial v axial strain after exceeding peak strength is much more consistent with the actual response. Due to the assumption of a constant elastic modulus, the point at which large radial strains are initiated is under predicted at low confining pressures and over predicted for high confining pressures for both associated and non-associated flow.

4.7.2 Hoek-Brown Criterion

In Figure 4.17 the Hoek-Brown criterion is used to fit the sandstone strengths at yield, peak and residual strength. The 'm' and 's' parameters were determined using fitting techniques described by Hoek and Brown.[24] It can be seen from comparison of Figures 4.16 and 4.17, that the Hoek-Brown criterion (given by equation (6)) follows the actual strengths over the confining range far better than the linear Mohr-Coulomb criterion. The variation of the Mohr-Coulomb strength parameters with permanent deformation are given in equations (7) to (9). The corresponding relationships for the Hoek-Brown parameters (m and s) are assumed to be

$$\delta m = \alpha_m \delta \varepsilon_1^p \qquad \text{and} \quad \delta s = \alpha_s \delta \varepsilon_1^p \tag{17}$$

where, for hardening, the factors α_m and α_s are given by

$$\alpha_m = \frac{m_P - m_Y}{(\varepsilon_1^p)_P} \qquad \text{and} \quad \alpha_s = \frac{s_P - s_Y}{(\varepsilon_1^p)_P} \tag{18}$$

and during softening

$$\alpha_m = \frac{m_R - m_P}{(\varepsilon_1^p)_R - (\varepsilon_1^p)_P} \qquad \text{and} \qquad \alpha_s = \frac{s_R - s_P}{(\varepsilon_1^p)_R - (\varepsilon_1^p)_P} \tag{19}$$

and on reaching residual strength $\alpha_m = 0$ and $\alpha_s = 0$,

where m_Y, m_P and m_R are the values of 'm' at yield, peak and residual strength respectively,

and s_Y, s_P and s_R are the values of 's' at yield, peak and residual strength respectively.

$(\varepsilon_1^p)_P$ and $(\varepsilon_1^p)_R$ were previously defined in Sections 4.5.2 and 4.5.3.

The model behaviour using the Hoek-Brown criterion is now defined using equations (6),(10),(11),(17),(18) and (19). The Hoek-Brown associated flow relationship is given in Table 8, and the non-associated flow rule is again given by equations (15) and (16). The results of the Hoek-Brown model predictions are given in Figures A.19 to A.24 for associated flow and A.25 to A.30 for non-associated flow.

As expected, the Hoek-Brown prediction of strength relative to the Mohr-Coulomb model (Figures A.7 to A.18) is far better over the whole range of confining pressures. An interesting point to note is the shape of the post peak stress-strain predictions. Linear relationships between strength parameters and plastic strain are assumed for both the Mohr-Coulomb and Hoek-Brown criteria (equations (7) and (17) respectively). However, since the Hoek-Brown criterion has a power relationship between strength and strength parameters the resulting axial stress-strain plot is markedly non-linear, whereas the Mohr-Coulomb criterion is made up of approximately linear portions. (The variation of strength with strain is not exactly linear for the Mohr-Coulomb criterion since it is a trigonometric function of ϕ. However, the nonlinearity is not visible in Figures A.7 to A.18, due to the relatively small variation in ϕ). This nonlinear stress-strain prediction of the model shows an improvement on

the Mohr-Coulomb behaviour, particularly for uniaxial compression (Figures A.19 and A.25).

As with the Mohr-Coulomb model, the point at which large radial strains are predicted to occur suffers from the constant elastic modulus assumption. However, the Hoek-Brown associated flow model (Figures A.19 to A.24) shows an improvement in prediction of the slope of the radial v axial strain plot during softening when compared with the Mohr-Coulomb model (Figures A.7 to A.12). This improvement in strain rates is only sustained up to residual strength. For continued deformation at residual strength the Hoek-Brown associated flow rule deviates considerably from the actual response, with gross over predictions of sample dilation.

4.7.3 Conclusions on Model Behaviour

Of the two strength criteria chosen the Hoek-Brown gives better predictions of the sandstone strength when compared with the Mohr-Coulomb criterion over a wide range of confining pressures. However, the Mohr-Coulomb criterion may be suitable for linearizing strength over small ranges of confinement. The Hoek-Brown criterion also shows an improvement in the prediction of the post peak stress-strain relationship.

Use of an associated flow rule in conjunction with the Mohr-Coulomb criterion may result in a gross over estimation of sample dilation during plastic loading. The Hoek-Brown associated flow model may prove acceptable until residual strength is reached, after which it also over predicts sample dilation. For the best prediction of radial (or volumetric) strain over the complete loading path, a non-associated flow rule is likely to be the most suitable, however, this will require

determination of the relevant flow rule input parameters when put into practice.

The elastic and plastic model behaviour predictions suffer from the assumption of a constant elastic modulus. This is true for both Mohr-Coulomb and Hoek-Brown criteria and both associated and non-associated flow.

CHAPTER 5

THE FEM APPLIED TO ELASTO-PLASTIC MATERIAL BEHAVIOUR

This chapter sets out the requirements for using the FEM to analyse an elasto-plastic material behaviour of the form described in Chapter 4, in particular for the application of strain softening and non-associated flow. Many of the techniques used to apply the FEM to plastic behaviour are based on methods presented by Zienkiewicz[62] and Owen and Hinton.[35] Assessment of the validity of the coding is carried out in Section 5.5 using versions of analytical/numerical models developed by Galin,[73] Detournay[85] and Brown et al.[49] Finally, the chapter presents the results of a study into the effects of various parameters on the elasto-plastic regime around a wellbore.

5.1 ITERATIVE TECHNIQUES

A number of texts present the techniques required for analysis of plasticity problems using the FEM (e.g. Zienkiewicz,[62] Owen and Hinton[35]). However, for completeness, the technique used in this research program is explained below.

Three basic methods are often employed. These are

(i) Initial stiffness method.

(ii) Tangential stiffness method.

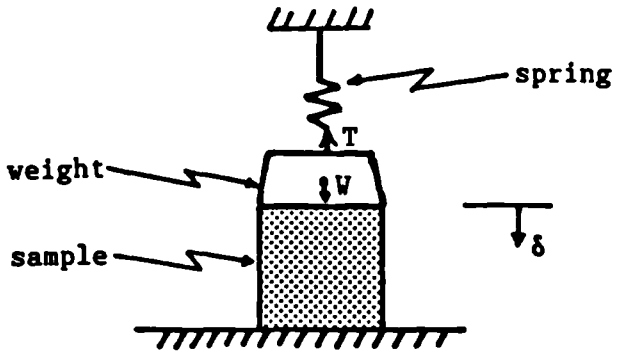
(iii) Mixed algorithm - combination of (i) and (ii).

Other methods may be used (e.g. secant stiffness - Owen and Hinton[35]). However, only the three methods given above are covered in this text.

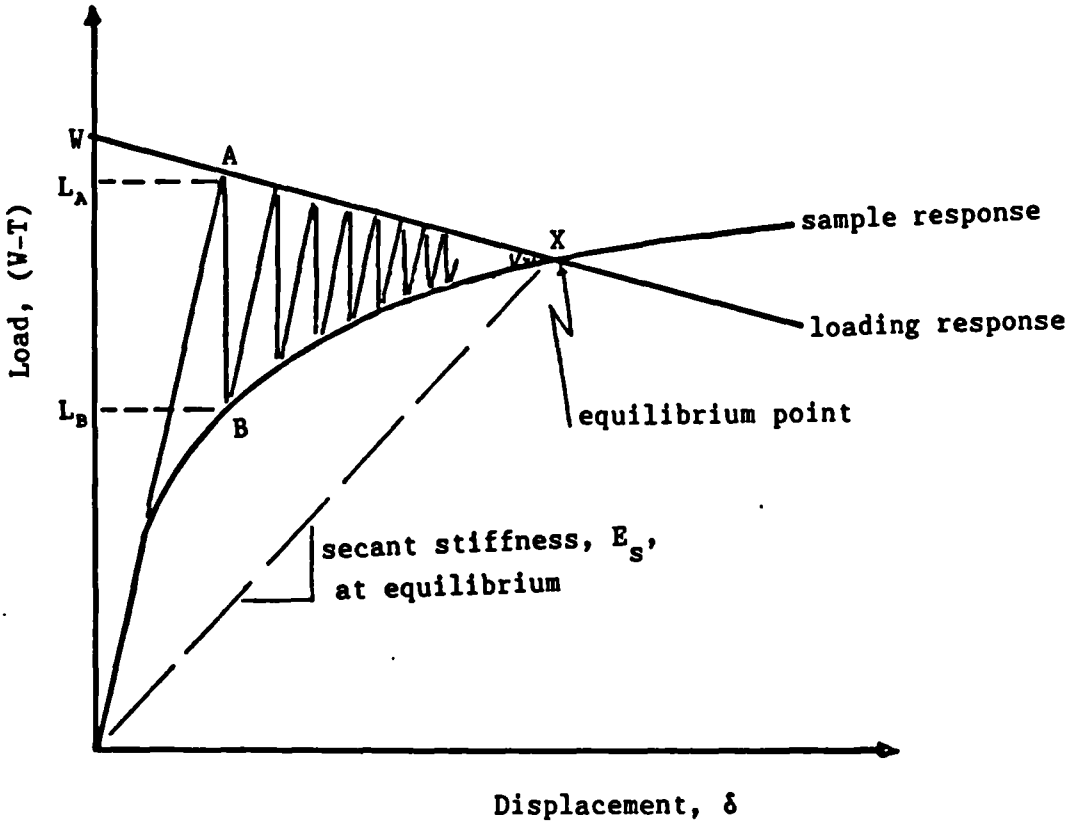
5.1.1 Initial Stiffness Method

In order to explain the initial stiffness method graphically it is necessary to refer to 1-dimensional problems. General 2-dimensional and 3-dimensional problems are too complex to represent graphically.

Consider the simple loading case given in Figure 5.1a. A cubic sample of rock is loaded uniaxially by a weight supported by a spring. The initial conditions before the load is applied is given by displacement, δ, equal to zero. It is assumed that the applied loading and end conditions are such that a homogeneous stress state develops within the sample. Both the response of the applied loading (load weight, W, less the spring tension, T) and the rock sample elastic and plastic variation are plotted as functions of displacement in Figure 5.1b. The rock behaviour used here is characteristic of a strain hardening material. (Note: The load-displacement response could easily be converted to a stress-strain plot if required.) Assuming the load is applied slowly and the kinetic energy of the system is dissipated then equilibrium is reached where the two responses intersect at X. Obviously this equilibrium point can be found quite simply graphically. However, if a FEM analysis is performed to solve this problem then we run into problems in determining the stiffness of the rock sample. The secant stiffness (see Figure 5.1b) is only known once the problem is solved. Thus, an iterative method is used. A possible approach is to use the initial linear elastic response of the rock as a first approximation. On solving the simultaneous equations, equilibrium is predicted to occur at point A. It is seen that the load at A lies above the allowable response of the rock sample. The allowable applied load for this displacement is found and given by B. However, at B the applied load and sample reaction are no longer in equilibrium by an amount given by L_A-L_B (see Figure



(a) loading conditions



(b) load and sample responses

Figure 5.1 Initial stiffness method applied to simple uniaxial loading case.

5.1b). This load imbalance (residual load) is re-applied to the system from point B. For numerical purposes the rock response is still assumed elastic, i.e. the initial stiffness is used. On solving the equations for the residual load, equilibrium is now predicted to occur at point C. Again the applied load for this displacement is found to exceed the rock strength. However, predicted equilibrium at C is closer to the actual equilibrium point than the first approximation at A. The process described above is continued until the approximate solution is considered sufficiently accurate. Convergence is usually monitored by evaluating the ratio of the residual load to the initial load applied.

Exactly the same technique can be applied to 2 or 3-dimensional structures. The set of simultaneous equations relating displacement and applied load for an FEM analysis is given by (31) in Section 3.3.7, Chapter 3. Rearranging this equation system we can write

$$[u] = [K]^{-1}[\psi]$$

where $[K]^{-1}$ is the inverse of the global stiffness matrix,

$[\psi]$ is the applied loading in terms of equivalent nodal loads,

and $[u]$ is the loading induced displacement vector.

In terms of the initial stiffness method the above relationship can be rewritten as

$$[\Delta u]_i = [K_0]^{-1}[\Delta\psi]_i$$

where $[K_0]$ is the initial (or elastic) global stiffness matrix,

$[\Delta u]_i$ is the displacement increment vector for the i^{th} iteration,

and $[\Delta\psi]_i$ is the residual load applied on the i^{th} iteration.

The cumulative displacement after iteration i is given by

$$[u]_i = \sum_{j=1}^{i} [\Delta u]_j$$

For the given set of nodal displacements, $[u]_i$, it is possible to determine the allowable stress state within elements of the structure (this process is covered later in Section 5.3.6). From this stress state the equivalent nodal loads resulting from the structure's reaction can be determined. Let the nodal load vector resulting from the allowable stress state for displacements $[u]_i$ be given by $[\psi]_i^r$, where the superscript 'r' represents allowable reaction loads. Then, assuming part or all of the structure under consideration has exceeded its elastic limit, the following inequality is generally true,

$$[\psi]_i^r \neq [\psi]$$

and the residual nodal load vector for the $i+1^{th}$ iteration is given by,

$$[\Delta\psi]_{i+1} = [\psi] - [\psi]_i^r \qquad (1)$$

5.1.2 Tangential Stiffness Method

Referring to the same problem depicted in Figure 5.1a, the number of iterations required to reach convergence can be reduced by using a tangential stiffness method instead of the initial stiffness. In this approach the stiffness of the rock sample used at each iteration is found by taking the tangent to the sample load-displacement curve at the displacement accumulated on the previous iteration. This method is depicted in Figure 5.2. In general terms for a FEM problem this is expressed as

$$[\Delta u]_i = [K]_{i-1}^{-1}[\Delta\psi]_i$$

where $[K]_{i-1}$ is the tangent stiffness at the stage when the structure has undergone a set of displacements $[u]_{i-1}$.

As seen by comparing Figures 5.1b and 5.2, this technique may reduce the

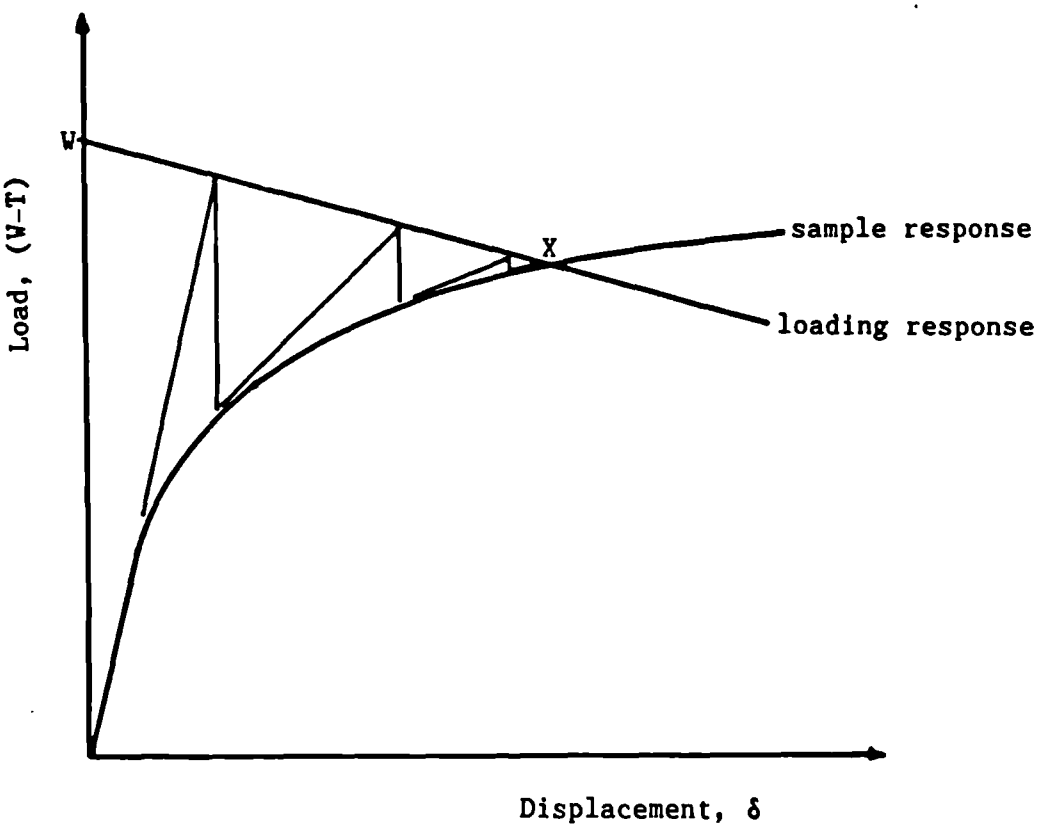


Figure 5.2 Tangent stiffness method.

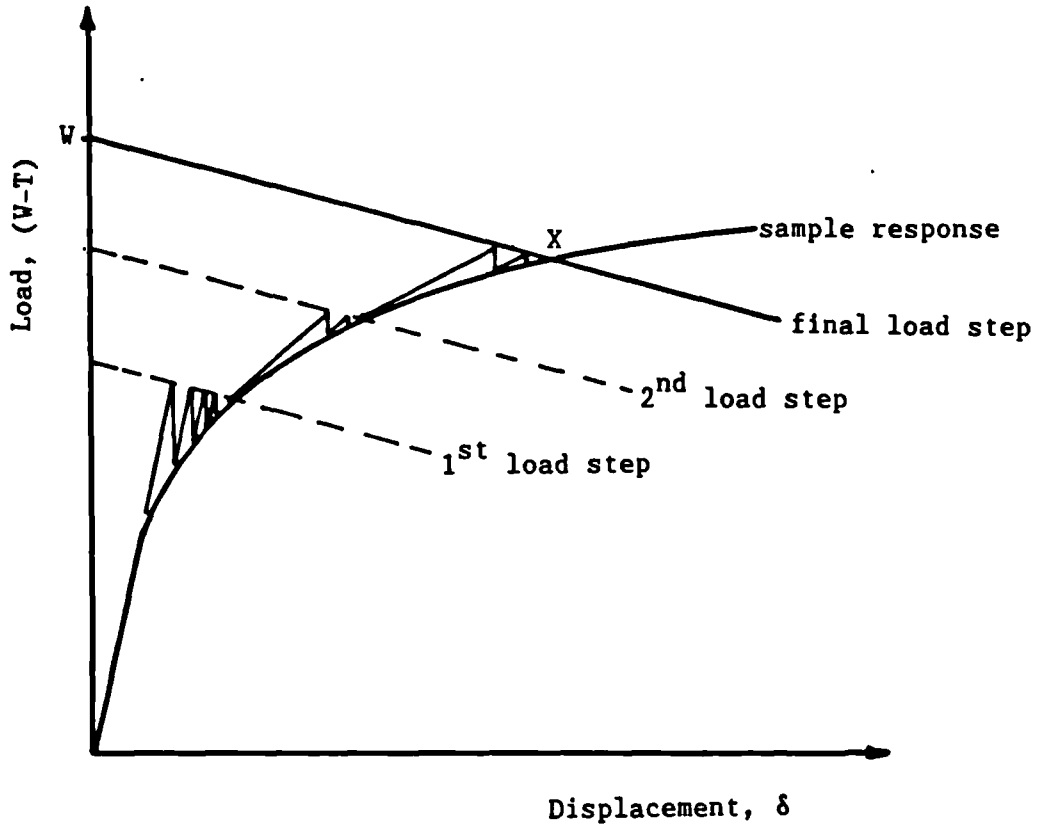


Figure 5.3 Mixed algorithm approach.

number of iterations required considerably. However, recalculation and forward reduction of the global stiffness matrix must be performed at each iteration, whereas this is only performed on the first iteration for the initial stiffness method. As discussed in Section 3.6, Chapter 3, formation and forward reduction of the global stiffness matrix accounts for a considerable percentage of the overall computer time. Thus, gains resulting from a reduced number of iterations are offset to some extent by increased time spent on equation solution.

5.1.3 Mixed Algorithm

The relative economies of the initial stiffness and tangential stiffness methods depend to a large extent on the degree of nonlinearity inherent in the problem considered. The optimum algorithm is generally provided by an amalgamation of both processes, in which the stiffnesses are changed at selected intervals (Owen and Hinton[35]).

In many analyses it is desirable to divide the applied loading into increments, either to investigate the reaction of the structure to the extent of loading, or to reduce the extent of any errors inherent in nonlinear FEM analyses. Figure 5.3 shows a mixed algorithm approach with respect to the structure defined in Figure 5.1a. Here the tangent stiffness is only recalculated at the start of each load increment. However, other criteria may be used to determine when the global stiffness matrix is reformed, such as when Gauss points or elements show marked changes in stress-strain response (e.g. upon yielding, or reaching residual strength).

5.2 STRESS INVARIANTS APPLIED TO YIELD CRITERIA

In order to determine when a point within a structure reaches its elastic limit it is necessary to apply the yield criterion. All the yield criteria given in Section 4.4, Chapter 4, are in terms of principal stresses. However, the stress at a point obtained from an FEM analysis is in terms of the general stress tensor referenced to a cartesian or polar coordinate system. Thus, in order to check for yield the stresses predicted from the FEM analysis must be converted into principal stresses, or the yield criteria must be rewritten in terms of the general stress tensor. Expressing yield criteria in terms of the general stress tensor is achieved by using stress invariants. This approach is adopted in FEM analyses since, as shown later in Sections 5.3.2 and 5.3.3, the stress invariants are also required to determine plastic flow rates.

Note: In the FEM, stresses and strains found from equation solution are those induced by the excavation (see Section 3.4.1, Chapter 3). However, in order to assess whether a Gauss point has exceeded the yield limit of the rock it is necessary to combine both the pre-existing and induced stress states. Thus, stresses, $[\sigma]$, referred to in the following derivations are taken to be the sum of both these components.

5.2.1 Principal Stresses in Terms of Stress Invariants

Many good texts covering stress analysis explain the principle of stress invariants and their derivations (e.g. Jaeger and Cook[82]). In this text only the relevant expressions are presented, and no derivations are given.

Determination of the three principal stresses is obtained from finding the three roots of the following cubic equation

$$\sigma^3 - I_1\sigma^2 - I_2\sigma - I_3 = 0 \qquad (2)$$

where σ represents the three principal stresses (i.e. σ_1, σ_2 and σ_3), and in terms of polar coordinates I_1, I_2 and I_3 are given as

$$I_1 = \sigma_r + \sigma_\theta + \sigma_z$$

$$I_2 = -(\sigma_r\sigma_\theta + \sigma_\theta\sigma_z + \sigma_z\sigma_r) + \tau_{r\theta}^2 + \tau_{\theta z}^2 + \tau_{zr}^2$$

$$I_3 = \sigma_r\sigma_\theta\sigma_z + 2\tau_{r\theta}\tau_{\theta z}\tau_{zr} - \sigma_r\tau_{\theta z}^2 - \sigma_\theta\tau_{zr}^2 - \sigma_z\tau_{r\theta}^2$$

I_1, I_2 and I_3 are termed stress invariants since they are independent of the orientation of the coordinate system chosen.

By converting the normal stresses into deviatoric components, such that

$$\sigma_r^* = \sigma_r - I_1/3, \qquad \sigma_\theta^* = \sigma_\theta - I_1/3, \qquad \sigma_z^* = \sigma_z - I_1/3$$

then equation (2) can be rearranged to give

$$\sigma^{*3} - J_1\sigma^{*2} - J_2\sigma^* - J_3 = 0 \qquad (3)$$

where $J_1 = \sigma_r^* + \sigma_\theta^* + \sigma_z^* = 0$

$$J_2 = I_2 - I_1^2/3$$

and $J_3 = \frac{2}{27}I_1^3 + I_1I_2/3 + I_3$

The deviatoric invariants J_2 and J_3 can also be expressed as

$$J_2 = \frac{1}{2}(\sigma_r^{*2} + \sigma_\theta^{*2} + \sigma_z^{*2}) + \tau_{r\theta}^2 + \tau_{\theta z}^2 + \tau_{zr}^2$$

$$J_3 = \sigma_r^*\sigma_\theta^*\sigma_z^* + 2\tau_{r\theta}\tau_{\theta z}\tau_{zr} - \sigma_r^*\tau_{\theta z}^2 - \sigma_\theta^*\tau_{zr}^2 - \sigma_z^*\tau_{r\theta}^2$$

The general form of the above relationships are required for complete plane strain analysis (see Section 3.4, Chapter 3), but for simple plane strain analysis the invariants can be simplified since $\tau_{\theta z} = \tau_{zr} = 0$.

As $J_1 = 0$, equation (3) reduces to

$$\sigma^{*3} - J_2\sigma^* - J_3 = 0 \qquad (4)$$

Comparing (4) with the trigonometric identity

$$\sin^3\theta - \frac{3}{4}\sin\theta + \frac{1}{4}\sin 3\theta = 0 \tag{5}$$

and substituting $\sigma' = r \sin\theta$ into (4) we get

$$\sin^3\theta - \frac{J_2}{r^2}\sin\theta - \frac{J_3}{r^3} = 0 \tag{6}$$

Comparing (5) and (6) gives

$$r = \frac{2\sqrt{J_2}}{\sqrt{3}}$$

$$\text{and} \quad \sin 3\theta = -\frac{3\sqrt{3}}{2}\frac{J_3}{\sqrt{(J_2{}^3)}} \tag{7}$$

The solution to (7) is found for $-\pi/6 \leq \theta \leq +\pi/6$ and the principal stresses can be written as

$$\begin{bmatrix}\sigma_1\\ \sigma_2\\ \sigma_3\end{bmatrix} = \frac{2\sqrt{J_2}}{\sqrt{3}}\begin{bmatrix}\sin(\theta+2\pi/3)\\ \sin\theta\\ \sin(\theta+4\pi/3)\end{bmatrix} + \frac{I_1}{3}\begin{bmatrix}1\\1\\1\end{bmatrix} \tag{8}$$

5.2.2 Yield Criteria Expressed in Terms of Stress Invariants

The yield criteria presented in Section 4.4, Chapter 4, can now be expressed in terms of the stress invariants using equation system (8). Only the resulting expressions for the Mohr-Coulomb and Hoek-Brown criteria are presented. Expressions for the Tresca and Von Mises criteria can be found in Owen and Hinton.[35]

Substituting for σ_1 and σ_3 in equation (3) in Chapter 4, using (8) and rearranging, the Mohr-Coulomb criterion can be expressed as

$$F = \sqrt{J_2}(\cos\theta + \frac{1}{\sqrt{3}}\sin\theta.\sin\phi) - \frac{I_1}{3}\sin\phi - c.\cos\phi \tag{9}$$

Similarly for equation (6) in Chapter 4, the Hoek-Brown criterion can be

expressed as

$$F = 4J_2\cos^2\theta - \frac{m\sigma_c}{3}\left(I_1 - \sqrt{(3J_2)}(\sin\theta+\sqrt{3}\cos\theta)\right) - s\sigma_c^2 \qquad (10)$$

5.3 RETURNING STRESS POINTS TO THE YIELD SURFACE

As described in Sections 5.1.1 and 5.1.2, part of the iterative process involves evaluating the allowable stress states the structural material can withstand for a given set of displacements. The strain increments at any point within a FEM mesh can be evaluated from the given nodal displacements using shape functions (see Section 3.3.2, Chapter 3). The process of determining increments of stress from a given set of imposed strain increments is given in this section. In order to achieve this, the plastic strain increments incurred must be found. From inspection of equation (16) in Chapter 4, it is seen that increments of plastic strain can be determined if the flow vector and the plastic multiplier are known. The determination of the plastic multiplier, λ, the associated flow vector, [a], and non-associated flow vector, [f], are given in the following sub-sections.

5.3.1 Determination of the Plastic Multiplier

Equations (13) and (16) in Chapter 4 give the relationship between plastic strain and the potential function for both associated and non-associated flow respectively. The following derivations are with respect to the more general relationship given by (16) in Chapter 4, with associated flow taken to be the particular case of [f] = [a].

In Section 4.6, Chapter 4, both [f] and [a] are referred to in terms of principal stresses. In this analysis they are redefined in

terms of the general stress tensor. Thus, for complete plane strain analysis, we now have

$$[a]^T = \left[\frac{\partial F}{\partial \sigma_r}, \frac{\partial F}{\partial \sigma_\theta}, \frac{\partial F}{\partial \tau_{r\theta}}, \frac{\partial F}{\partial \tau_{\theta z}}, \frac{\partial F}{\partial \tau_{zr}}, \frac{\partial F}{\partial \sigma_z}\right] \tag{11}$$

and $$[f]^T = \left[\frac{\partial Q}{\partial \sigma_r}, \frac{\partial Q}{\partial \sigma_\theta}, \frac{\partial Q}{\partial \tau_{r\theta}}, \frac{\partial Q}{\partial \tau_{\theta z}}, \frac{\partial Q}{\partial \tau_{zr}}, \frac{\partial Q}{\partial \sigma_z}\right] \tag{12}$$

Also, redefining the plastic strain vector from principal strains to the general strain tensor in terms of polar coordinates, we have

$$[\delta\varepsilon^p]^T = [\delta\varepsilon^p_r, \delta\varepsilon^p_\theta, \delta\gamma^p_{r\theta}, \delta\gamma^p_{\theta z}, \delta\gamma^p_{zr}, \delta\varepsilon^p_z]$$

(Note: The axial stress component is included in the strain vector above, whereas, in Chapter 3 axial components of stress and strain were not considered in the development. The need for inclusion of axial components becomes apparent in the development that follows.)

In general terms the plastic increment of strain is given by

$$[\delta\varepsilon^p] = \lambda[f]$$

where [f] is given by (12) and for associated flow the potential function Q is equivalent to the yield criterion, F.

For an element of rock that lies on the yield surface and is subjected to plastic loading the total strain increment, $[\delta\varepsilon]$, is generally made up of an elastic portion, $[\delta\varepsilon^e]$, and a plastic portion $[\delta\varepsilon^p]$. Thus,

$$[\delta\varepsilon] = [\delta\varepsilon^e] + [\delta\varepsilon^p] = [\delta\varepsilon^e] + \lambda[f]$$

Or $$[\delta\varepsilon^e] = [\delta\varepsilon] - \lambda[f] \tag{13}$$

The elastic portion of the strain, resulting from applying a stress increment $[\delta\sigma]$, where $[\delta\sigma]$ is given by

$$[\delta\sigma]^T = [\delta\sigma_r, \delta\sigma_\theta, \delta\tau_{r\theta}, \delta\tau_{\theta z}, \delta\tau_{zr}, \delta\sigma_z]$$

is determined using the set of elastic stress-strain compliances. For linear elastic, complete plane strain analysis, where it is known that

the axial strain component, $\delta\varepsilon_z$, is zero, we can use the $[D]^*$ matrix given by equation (46) in Chapter 3. For plastic, complete plane strain analysis $\delta\varepsilon_z$ is also zero. However, it is not necessarily true that the elastic portion of the axial strain, $\delta\varepsilon_z^e$, is zero if plastic flow has a component in the axial direction. In such cases we have

$$\delta\varepsilon_z = \delta\varepsilon_z^e + \delta\varepsilon_z^p = 0$$

but, under certain conditions $\delta\varepsilon_z^e = -\delta\varepsilon_z^p \neq 0$.

Thus, the linear elastic, complete plane strain matrix of compliances must must be extended to allow for $\delta\varepsilon_z^e \neq 0$. Therefore the new set of compliances, [D], is given by

$$[D] = \frac{E}{(1+\nu)(1-2\nu)}\begin{bmatrix} (1-\nu) & \nu & 0 & 0 & 0 & \nu \\ \nu & (1-\nu) & 0 & 0 & 0 & \nu \\ 0 & 0 & \frac{(1-2\nu)}{2} & 0 & 0 & 0 \\ 0 & 0 & 0 & \frac{(1-2\nu)}{2} & 0 & 0 \\ 0 & 0 & 0 & 0 & \frac{(1-2\nu)}{2} & 0 \\ \nu & \nu & 0 & 0 & 0 & (1-\nu) \end{bmatrix}$$

and the stress-elastic strain relationship is now given by

$$[\delta\sigma] = [D][\delta\varepsilon^e] \tag{14}$$

Assuming an element of rock lying on the yield surface remains on the yield surface upon application of the stress increment $[\delta\sigma]$ (i.e. the sample is not allowed to unload elastically), then the yield function value, F, remains zero. Thus, $\delta F = 0$. For the Mohr-Coulomb criterion, (9), we have

$$\delta F = \left[\frac{\partial F}{\partial \sigma}\right]^T [\delta\sigma] + \frac{\partial F}{\partial c}.\delta c + \frac{\partial F}{\partial \phi}.\delta\phi = 0$$

The vector $\left[\frac{\partial F}{\partial \sigma}\right]$ is given in (11) in reference to associated flow. Thus, the above equation can be written

$$\delta F = [a]^T[\delta\sigma] + \frac{\partial F}{\partial c}.\delta c + \frac{\partial F}{\partial \phi}.\delta\phi = 0 \tag{15}$$

From (13), (14) and (15) we arrive at

$$[a]^T[D]([\delta\varepsilon] - \lambda[f]) + \frac{\partial F}{\partial c}\delta c + \frac{\partial F}{\partial \phi}\delta\phi = 0 \qquad (16)$$

From equation (7) in Chapter 4, we have $\delta c = \alpha_c \delta\varepsilon_1^p$ and $\delta\phi = \alpha_\phi \delta\varepsilon_1^p$

The major principal plastic strain increment, $\delta\varepsilon_1^p$, can be expressed as

$$\delta\varepsilon_1^p = \lambda f_1$$

where f_1 is the major principal component of the flow vector. Thus, δc and $\delta\phi$ can now be expressed as

$$\delta c = \lambda\alpha_c f_1 \qquad \text{and} \qquad \delta\phi = \lambda\alpha_\phi f_1$$

Substituting the relationships for δc and $\delta\phi$ into (16) and rearranging we arrive at

$$\lambda = \frac{[a]^T[D][\delta\varepsilon]}{[a]^T[D][f] - \left(\frac{\partial F}{\partial c}\alpha_c f_1 + \frac{\partial F}{\partial \phi}\alpha_\phi f_1\right)} \qquad (17)$$

Similarly the relationship for λ for the Hoek-Brown criterion is given by

$$\lambda = \frac{[a]^T[D][\delta\varepsilon]}{[a]^T[D][f] - \left(\frac{\partial F}{\partial m}\alpha_m f_1 + \frac{\partial F}{\partial s}\alpha_s f_1\right)} \qquad (18)$$

(The part of the denominator in the curved brackets in both (17) and (18) is, in principle, the same as the hardening parameter, H', used by Owen and Hinton[35]).

Assume a point at a known stress level, $[\sigma]$, lies on the yield surface. Then the **instantaneous** values of $[a]$, $[f]$, f_1, $\frac{\partial F}{\partial c}$, $\frac{\partial F}{\partial \phi}$, α_c and α_ϕ can be determined from the known stress level, and previous stress history. (The equations resulting from differentiation of the yield function and flow potential function are given in the following section). Also, the $[D]$ matrix is constant and known. Therefore, if the strain increment $[\delta\varepsilon]$, imposed on the element is known, then the **instantaneous** value of the plastic multiplier, λ, can be determined from (17) for a material

obeying the Mohr-Coulomb criterion, and similarly from (18) for the Hoek-Brown criterion.

5.3.2 Determination of the Vector of Yield Function Derivatives, [a]

In general terms the Mohr-Coulomb and Hoek-Brown criteria, (9) and (10), can be expressed as

Mohr-Coulomb - $F = F(I_1, J_2, \theta, c, \phi)$

Hoek-Brown - $F = F(I_1, J_2, \theta, m, s)$

and from (7), $\theta = \theta(J_2, J_3)$

From reasoning given in Section 4.6.1, Chapter 4, we have

$$\frac{\partial c}{\partial \sigma} = 0, \quad \frac{\partial \phi}{\partial \sigma} = 0 \quad \text{and} \quad \frac{\partial m}{\partial \sigma} = 0, \quad \frac{\partial s}{\partial \sigma} = 0$$

Therefore the general form of the vector [a] (equation (11)) for both criteria is expressed as

$$[a] = \frac{\partial F}{\partial I_1}\left[\frac{\partial I_1}{\partial \sigma}\right] + \frac{\partial F}{\partial J_2}\left[\frac{\partial J_2}{\partial \sigma}\right] + \frac{\partial F}{\partial \theta}\left[\frac{\partial \theta}{\partial \sigma}\right] \tag{19}$$

where $\left[\frac{\partial \theta}{\partial \sigma}\right] = \frac{\partial \theta}{\partial J_2}\left[\frac{\partial J_2}{\partial \sigma}\right] + \frac{\partial \theta}{\partial J_3}\left[\frac{\partial J_3}{\partial \sigma}\right]$

Rearranging (19) we can write the general form of [a] as

$$[a] = C_1[a_1] + C_2[a_2] + C_3[a_3]$$

where $C_1 = \frac{\partial F}{\partial I_1}$ (20)

$$C_2 = \frac{\partial F}{\partial J_2} + \frac{\partial F}{\partial \theta}\cdot\frac{\partial \theta}{\partial J_2} \tag{21}$$

$$C_3 = \frac{\partial F}{\partial \theta}\cdot\frac{\partial \theta}{\partial J_3} \tag{22}$$

and $[a_1]^T = \left[\frac{\partial I_1}{\partial \sigma}\right]^T = \left[\frac{\partial I_1}{\partial \sigma_r}, \frac{\partial I_1}{\partial \sigma_\theta}, \frac{\partial I_1}{\partial \tau_{r\theta}}, \frac{\partial I_1}{\partial \tau_{\theta z}}, \frac{\partial I_1}{\partial \tau_{zr}}, \frac{\partial I_1}{\partial \sigma_z}\right]$

$$[a_2]^T = \left[\frac{\partial J_2}{\partial \sigma}\right]^T = \left[\frac{\partial J_2}{\partial \sigma_r}, \frac{\partial J_2}{\partial \sigma_\theta}, \frac{\partial J_2}{\partial \tau_{r\theta}}, \frac{\partial J_2}{\partial \tau_{\theta z}}, \frac{\partial J_2}{\partial \tau_{zr}}, \frac{\partial J_2}{\partial \sigma_z}\right]$$

$$[a_3]^T = \left[\frac{\partial J_3}{\partial \sigma}\right]^T = \left[\frac{\partial J_3}{\partial \sigma_r}, \frac{\partial J_3}{\partial \sigma_\theta}, \frac{\partial J_3}{\partial \tau_{r\theta}}, \frac{\partial J_3}{\partial \tau_{\theta z}}, \frac{\partial J_3}{\partial \tau_{zr}}, \frac{\partial J_3}{\partial \sigma_z}\right]$$

From differentiating the stress invariants given in Section 5.2.1 the vectors $[a_1]$, $[a_2]$ and $[a_3]$ as defined above become

$$[a_1]^T = \left[1,\ 1,\ 0,\ 0,\ 0,\ 1\right] \tag{23}$$

$$[a_2]^T = \left[\sigma'_r,\ \sigma'_\theta,\ 2\tau_{r\theta},\ 2\tau_{\theta z},\ 2\tau_{zr},\ \sigma'_z\right] \tag{24}$$

and $$[a_3]^T = \left[(\sigma'_\theta\sigma'_z - \tau^2_{\theta z} + J_2/3),\ (\sigma'_r\sigma'_z - \tau^2_{zr} + J_2/3),\right.$$
$$2(\tau_{\theta z}\tau_{zr} - \sigma'_z\tau_{r\theta}),\ 2(\tau_{r\theta}\tau_{zr} - \sigma'_z\tau_{r\theta}),$$
$$\left.2(\tau_{r\theta}\tau_{\theta z} - \sigma'_\theta\tau_{zr}),\ (\sigma'_r\sigma'_\theta - \tau^2_{r\theta} + J_2/3)\right] \tag{25}$$

where σ'_r, σ'_θ and σ'_z are defined in Section 5.2.1.

The relationships given above are suitable for complete plane strain analysis. The vectors $[a_1]$, $[a_2]$ and $[a_3]$ are simplified somewhat when applied to simple plane strain analysis, since $\tau_{r\theta} = \tau_{zr} = 0$.

The vectors $[a_1]$, $[a_2]$ and $[a_3]$ are independent of yield criteria. However, the scalars C_1, C_2 and C_3 are dependent on the criterion. The expressions for these scalars are found by differentiating the yield criterion (Mohr-Coulomb - (9), and Hoek-Brown - (10)) according to equations (20), (21) and (22) for C_1, C_2 and C_3 respectively. The resulting expressions for the Mohr-Coulomb and Hoek-Brown criteria are given below.

Mohr-Coulomb Criterion:-

$$C_1 = -\frac{\sin\phi}{3} \tag{26}$$

$$C_2 = \frac{\cos\theta}{2\sqrt{J_2}}\left[1 + \tan\theta.\tan 3\theta + \sin\phi(\tan\theta - \tan 3\theta)\right] \tag{27}$$

$$C_3 = \frac{\sqrt{3}\sin\theta - \cos\theta.\sin\phi}{2J_2\cos 3\theta} \tag{28}$$

Hoek-Brown Criterion:-

$$C_1 = -\frac{m\sigma_c}{3} \tag{29}$$

$$C_2 = \frac{\cos\theta}{\sqrt{J_2}}\left[\sqrt{3}(\cos\theta + \sin\theta.\tan 3\theta) + \frac{m\sigma_c}{2\sqrt{3}}\left(\sqrt{3}(1+\tan\theta.\tan 3\theta) + \tan\theta - \tan 3\theta\right)\right] \tag{30}$$

$$C_3 = \frac{\cos\theta}{J_2\cos 3\theta}\left[4\sqrt{(3J_2)}\sin\theta - \frac{m\sigma_c}{2}(1-\sqrt{3}\tan\theta)\right] \tag{31}$$

5.3.3 Determination of the Flow Vector, [f]

For associated flow the vector [f] is equivalent to the vector [a], and no further computations need be performed to find [f]. However, for non-associated flow similar procedures to those outlined in Section 5.3.2 are used to determine [f], with the yield function, F, replaced by the plastic potential function Q.

The general non-associated flow potential used in this work is expressed in terms of principal stresses in equation (15), Chapter 4. Using (8) to express the potential function in terms of the stress invariants we get after rearranging

$$Q = 2\sqrt{J_2}\cos\theta + (1+f_\infty)\left[I_1/3 - \sqrt{(3J_2)}(\sin\theta+\sqrt{3}\cos\theta)\right] + \frac{C}{D}\ln\left[1 + D(I_1/3 - \sqrt{(3J_2)}(\sin\theta+\sqrt{3}\cos\theta)\right] \tag{32}$$

Or in general terms

$$Q = Q(I_1, J_2, \theta)$$

Using the same process described in Section 5.3.2, then [f] can be expressed as

$$[f] = C_1[a_1] + C_2[a_2] + C_3[a_3]$$

As before the vectors $[a_1]$, $[a_2]$ and $[a_3]$ are given by (23), (24) and

(25) respectively. The scalars C_1, C_2 and C_3 for the non-associated flow potential function, Q, given in (32) are found to be

$$C_1 = \frac{1}{3}(1+f_\infty+C/T) \tag{33}$$

$$C_2 = \frac{\cos\theta}{2\sqrt{J_2}}\Big[\tan3\theta[2\tan\theta + \sqrt{3}(1-\sqrt{3}\tan\theta)(1+f_\infty+C/T)] + 2 - \sqrt{3}(\sqrt{3}+\tan\theta)(1+f_\infty+C/T)\Big] \tag{34}$$

$$C_3 = \frac{\sqrt{3}\cos\theta}{2J_2\cos3\theta}\Big[2\tan\theta + \sqrt{3}(1-\tan\theta)(1+f_\infty+C/T)\Big] \tag{35}$$

where $T = 1 + D[I_1/3 - \sqrt{(3J_2)}(\sin\theta+\sqrt{3}\cos\theta)]$ (36)

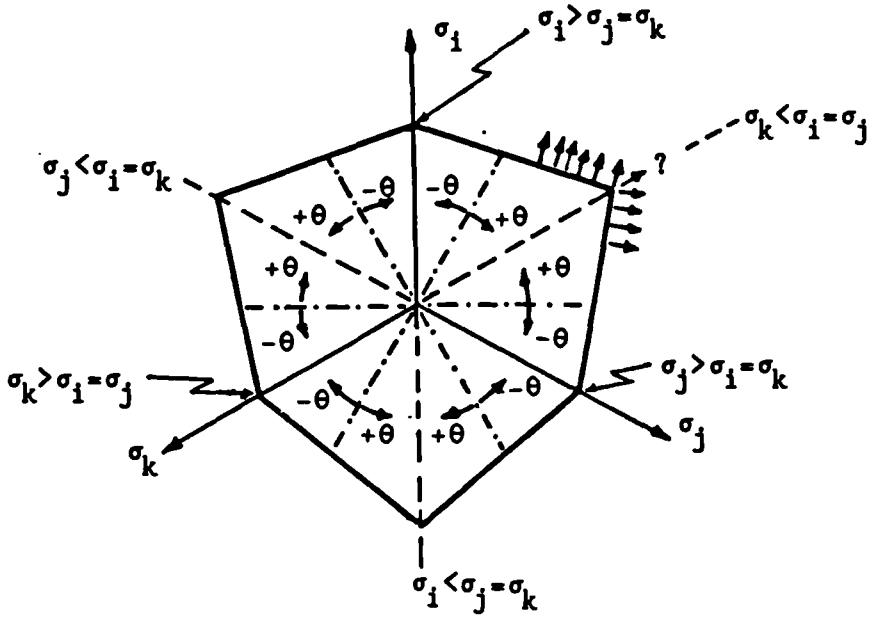
5.3.4 Singularities on the yield surface

From inspection of equation system (8) it can be seen that the following conditions hold,

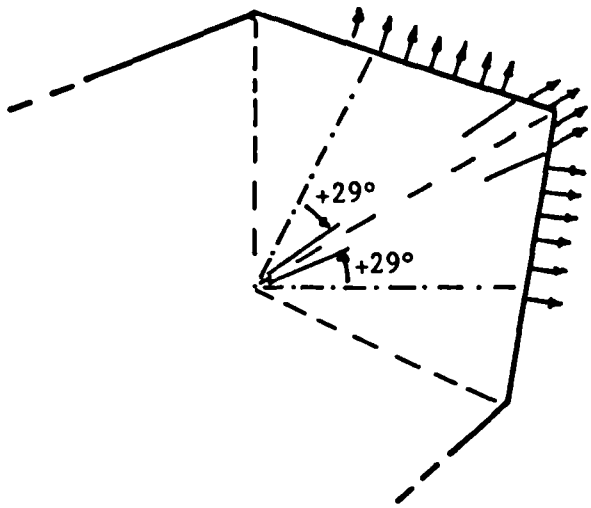
for $\theta = -\pi/6$, $\sigma_1 > \sigma_2 = \sigma_3$

and for $\theta = +\pi/6$, $\sigma_1 = \sigma_2 > \sigma_3$

The above conditions correspond to the edges of the yield criteria shown in Figures 4.5, 4.6 and 4.7, Chapter 4. Figure 5.4a shows a π-plane projection of the Mohr-Coulomb criteria. At the corners we may expect problems in determining the normal to the yield surface. This is shown to be the case on inspection of the scalars C_2 and C_3 for the Mohr-Coulomb and Hoek-Brown criteria. When $\theta \rightarrow \pm \pi/6$ in equations (27), (28), (30) and (31), then for both criteria we have $C_2 \rightarrow \infty$ and $C_3 \rightarrow \infty$. In addition, since the non-associated flow potential function, Q, is independent of σ_2 (see equation (15), Chapter 4) its section through the π-plane also describes an irregular hexagon. Thus, the non-associated



(a) π-plane projection of the Mohr-Coulomb criterion



(b) revised flow at singular points

Figure 5.4 Flow at singular points on the yield surface.

flow vector for the condition $\theta = \pm \pi/6$ is also indeterminate as seen from inspection of equations (34) and (35).

The solution to the problem of singularities on the surface of yield criteria and flow potential functions can be tackled in a number of ways, e.g. by artificially rounding off the corners of the surface. Here the method used by Owen and Hinton[35] is adopted. This consists of the following,

$$\text{for } \theta \leq -29^\circ, \quad \text{then} \quad \theta = -30^\circ$$

$$\text{and for } \theta \geq +29^\circ, \quad \text{then} \quad \theta = +30^\circ$$

When the above conditions are satisfied the explicit value of θ is used in equations (9), (10) and (32) before the yield and potential functions are differentiated with respect to the remaining variables. Therefore, since we now have $\frac{\partial F}{\partial \theta} = 0$, the general form of equations (21) and (22) reduce to

$$C_2 = \frac{\partial F}{\partial J_2}$$

$$\text{and} \quad C_3 = 0$$

Equation (20) for C_1 remains unchanged since it is independent of differentials with respect to θ. The corresponding relationships for the non-associated flow potential are found by replacing F with Q in the above. By differentiating equations (9), (10) and (32) with respect to the above, we now have for $\theta \leq -29^\circ$, or $\theta \geq 29^\circ$,

Mohr-Coulomb $C_2 = \frac{\cos\theta}{2\sqrt{J_2}}(1 + \frac{1}{\sqrt{3}}\tan\theta.\sin\phi)$, and $C_3 = 0$

Hoek-Brown $C_2 = \frac{\cos\theta}{2\sqrt{J_2}}\left[8\sqrt{J_2}\cos\theta + \frac{m\sigma_c}{\sqrt{3}}(\sqrt{3}+\tan\theta)\right]$, and $C_3 = 0$

Non-Ass. Flow $C_2 = \frac{\cos\theta}{2\sqrt{J_2}}\left[2 - \sqrt{3}(\sqrt{3}+\tan\theta)(1+f_\infty+C/T)\right]$, and $C_3 = 0$

where T is given by (36).

A physical interpretation of the flow conditions at the singular points is shown in Figure 5.4b.

5.3.5 Determination of the 'Hardening Parameter'

Drawing the similarity with the hardening parameter defined by Owen and Hinton,[35] the equations for λ, (17) and (18), can be expressed as

$$\lambda = \frac{[a]^T[D][\delta\varepsilon]}{[a]^T[D][f] + H'} \tag{37}$$

where H' is the hardening (or softening) parameter and given by

$$H' = -\frac{\partial F}{\partial c}\alpha_c f_1 - \frac{\partial F}{\partial \phi}\alpha_\phi f_1 \qquad \text{- Mohr-Coulomb criterion} \tag{38}$$

$$\text{and} \quad H' = -\frac{\partial F}{\partial m}\alpha_m f_1 - \frac{\partial F}{\partial s}\alpha_s f_1 \qquad \text{- Hoek-Brown criterion} \tag{39}$$

Expressions and methods of determining α_c, α_ϕ, α_m and α_s are given in Sections 4.5.2, 4.5.3 and 4.7.2, Chapter 4. Thus, in order to determine H' for the two criteria, all that remains is the determination of $\frac{\partial F}{\partial c}$, $\frac{\partial F}{\partial \phi}$, $\frac{\partial F}{\partial m}$, $\frac{\partial F}{\partial s}$ and f_1. Differential terms relating variation of the yield function with strength parameters are found from equations (9) and (10) which on partial differentiation yield,

Mohr-Coulomb:-

$$\frac{\partial F}{\partial c} = -\cos\phi$$

$$\text{and} \quad \frac{\partial F}{\partial \phi} = \sqrt{J_2}\cos\phi\left[\frac{1}{\sqrt{3}}\sin\theta - I_1/3 + c.\tan\phi\right]$$

Hoek-Brown:-

$$\frac{\partial F}{\partial m} = -\sigma_c\sigma_3$$

$$\text{and} \quad \frac{\partial F}{\partial s} = -\sigma_c^2$$

The major principal component of the flow vector, f_1, is given by

$$f_1 = \frac{\partial Q}{\partial \sigma_1} \left(= \frac{\delta \varepsilon_1^p}{\lambda}\right)$$

The values of f_1 for associated flow (i.e. $Q \equiv F$) are given in Table 8 (Chapter 4), and for non-associated flow, differentiation of equation (15) in Chapter 4 yields $f_1 = 1$. The values of f_1 thus obtained are true for all stress states apart from the singular point defined by $\sigma_1 = \sigma_2$ (i.e. $\theta = \pi/6$), where f_1 is half of the values shown for the Tresca, Mohr-Coulomb and Hoek-Brown associated flow rules, and the same for non-associated flow. The Von Mises criterion does not have singularities on its surface, and therefore need not be considered. Thus, for $\sigma_1 = \sigma_2$, we have

$f_1 = \frac{1}{2}$ - for the Tresca associated flow,

$f_1 = \frac{1}{2}(1-\sin\phi)$ - for the Mohr-Coulomb associated flow,

$f_1 = (\sigma_1 - \sigma_3)$ - for the Hoek-Brown associated flow,

and $f_1 = \frac{1}{2}$ - for the non-associated flow given in equation (15)

5.3.6 Returning Stress Points to the Yield Surface

Following the iterative techniques outlined in Section 5.1, then assume on iteration, i-1, a stress point exceeded its elastic limit and now lies on the yield surface with a stress state given by $[\sigma]_{i-1}$. The reaction nodal loads are compared with the applied nodal loads and found to be imbalanced, thus resulting in a residual load to be reapplied. Upon application of the residual load the stress point under consideration is found to have undergone additional straining given by $[\Delta\varepsilon]_i$. The first step in determining the new stress state, given the

additional strains, is to test whether the stress point has unloaded elastically. Thus, if the response is elastic we have

$$[\sigma^e]_i = [\sigma]_{i-1} + [\Delta\sigma]_i = [\sigma]_{i-1} + [D][\Delta\varepsilon]_i \qquad (40)$$

where $[\sigma^e]_i$ is the new stress state assuming a return to elastic behaviour. If the applied residual load results in an elastic response then the value of the yield function is now less than zero. Thus,

$$F([\sigma^e]_i) < 0$$

However, if $F > 0$, then the new stress state lies outside the yield surface and is therefore invalid. For this case the stress point must be brought back to the yield surface, such that the new stress state is compatible with the new set of strains. This procedure is explained below.

The increment of stress resulting from a small increment of total strain during plastic loading is given by eliminating $[\delta\varepsilon^e]$ from (14) using (13). Thus,

$$[\delta\sigma] = [D]([\delta\varepsilon] - \lambda[f])$$

or more correctly for finite increments of stress and strain

$$[\delta\sigma] \simeq [D]([\delta\varepsilon] - \lambda[f]) \qquad (41)$$

Expressions for λ are given in (17) and (18) depending the yield criterion. Determination of the relevant terms in (17) and (18) are covered in Sections 5.3.2 to 5.3.5. Thus, $[\delta\sigma]$ can be determined from (41) for a given increment of strain $[\delta\varepsilon]$. Equation (41) is approximate since λ and $[f]$ are dependent on the stress level. Thus, equation (41) is only suitable for small increments of stress and strain. In general, the stress increment, $[\Delta\sigma]_i$, compatible with the strain increment, $[\Delta\varepsilon]_i$, cannot be found directly from (41) without the introduction of

large errors. The standard approach to this problem is to divide $[\Delta\varepsilon]_i$ into smaller increments, $[\delta\varepsilon]_i$, the number of increments depending on the magnitude of $F([\sigma^*]_i)$ ($F > 0$, with $[\sigma^*]_i$ given by equation (40)). Thus,

$$\text{number of increments, } N \propto F([\sigma^*]_i)$$

$$\text{and } [\delta\varepsilon]_i = [\Delta\varepsilon]_i/N$$

After the application of each increment $[\delta\varepsilon]_i$, the corresponding increment in stress, $[\delta\sigma]_i$, is determined and added to the total stress vector, allowing redetermination of the flow vector, [f], and the plastic multiplier, λ. The new values of [f] and λ are used in (41) for the next increment.

As pointed out by Owen and Hinton,[35] this method only converges to the exact solution as the number of increments, N, tends to ∞, which is impractical. For a finite number of increments there is some 'drift' of the stress point away from the yield surface. Therefore, once the stress increments are accumulated to give $[\sigma]_i$, an adjustment must be made to bring the stress point back to the yield surface. A further consideration is the first time a stress point exceeds the material's elastic limit. For this case the stress point may not originate from the yield surface, and the stress path must be divided into elastic and plastic portions. This part of the numerical technique is not covered here, however, Owen and Hinton[35] give a comprehensive explanation of this procedure.

Once the stress state compatible with the imposed displacements has been calculated at each Gauss point, the nodal loads equivalent to this stress state are found. In development of equation (30) in

Chapter 3, we find that for zero body forces

$$\int N_j[t]dS = \int [B_j]^T[\sigma]^* dA$$

The term on the left hand side is the equivalent nodal load vector. Thus, the nodal load vector equivalent to the stress state after iteration 'i' is given by

$$[\psi]_I^r = \int [B_j]^T[\sigma]_i dA \qquad (42)$$

Therefore the nodal loads representing the reaction of the structure to the imposed displacements, (given by $[\psi]^r$ - see Section 5.1.1), are found from equation (42). Integration is performed numerically for each element using Gaussian integration. Gaussian integration is described with respect to forming the global stiffness matrix in Section 3.3.8, Chapter 3. The global nodal load vector resulting from the structural reaction to the imposed displacements is found by summing the element contributions. The residual load is found from equation (1) in Section 5.1.1. Note that once part of the structure has undergone nonlinear deformation, the equivalent loads at some internal nodes will no longer be zero, due to applied and reaction load imbalance.

As mentioned earlier in Section 4.4.4, Chapter 4 there are a number of reasons for rearranging the Hoek-Brown criterion as given in equation (6), Chapter 4, instead of the more common relationship given in (6a), also Chapter 4. The importance of this was shown with respect to associated flow in Section 4.6.1, and even in cases of non-associated flow it has implications in determination of λ, since λ is a function of vector [a], as given in equation (18). A further implication involves returning exterior stress points to the yield surface. Figure 5.5 shows a stress point that temporarily exists outside the yield surface, and is also in the tensile zone. In the shaded area, F determined from

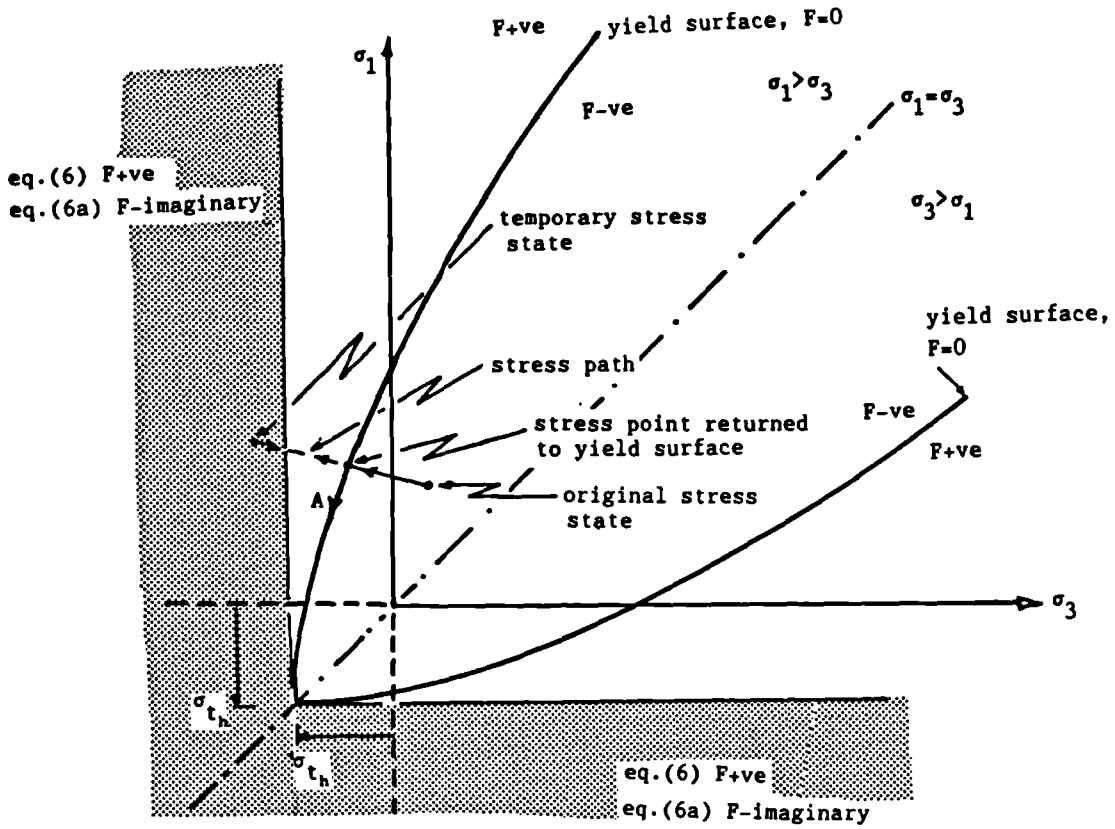


Figure 5.5 Returning stress point to yield surface with respect to the Hoek-Brown criterion.

equation (6a), Chapter 4, contains an imaginary portion, whilst for equation (6), Chapter 4, F is still real and positive. However, the shape of the yield surface is the same for both criteria. Thus, equation (6) is more robust in numerical analysis, whereas equation (6a) needs a certain degree of care in its use.

Another point worth highlighting here is the Hoek-Brown tensile cut off. Beyond the 'hydrostatic tensile strength', σ_{t_h}, shown in Figure 5.5, the yield surface does not exist, and we can write

$$F(\sigma_1, \sigma_3 > \sigma_{t_h}) > 0$$

In contrast the Mohr-Coulomb criterion, for example, is continuous for minimum principal stresses to minus infinity, although its application to the tensile region is spurious. Thus, in addition to monitoring compressive yielding, the Hoek-Brown criterion also provides a tensile failure criterion, preventing Gauss points exceeding the inferred tensile strength. This aspect of the Hoek-Brown criterion may at times also result in spurious results. If the stress point shown returning to the yield surface in Figure 5.5, moves in direction 'A' upon further application of load, it may eventually end up at the 'hydrostatic tensile strength'. Such a stress state is unlikely to occur around a wellbore in practice. Thus, if tensile stresses are generated around the well, the resultant material response and stress state must be regarded with a critical eye. The potential for anomalous results in tensile regions applies to all four criteria used here.

5.3.7 The Elasto-Plastic Stress-Strain Compliances

For a complete plane strain, tangent stiffness method of analysis the instantaneous matrix of stress-strain compliances, $[D_{ep}]^*$, is required to formulate the global stiffness matrix. Although the axial

components of the elasto-plastic compliance matrix are not required, the following derivation gives the whole matrix of compliances, i.e. $[D_{ep}]$. The complete plane strain version is obtained by ignoring the axial components in $[D_{ep}]$.

Thus, $$[\delta\sigma] = [D_{ep}][\delta\varepsilon]$$

where the total strain, $[\delta\varepsilon]$, is a combination of elastic and plastic portions.

Substituting for λ in (41) using equation (37) we get,

$$[\delta\sigma] \simeq [D]\left\{[\delta\varepsilon] - \frac{[a]^T[D][\delta\varepsilon][f]}{[a]^T[D][f] + H'}\right\} \tag{43}$$

Since, $[a]^T[D][\delta\varepsilon]$ reduces to a scalar, (43) can be rearranged to give

$$[\delta\sigma] \simeq [D]\left\{[\delta\varepsilon] - \frac{[f][a]^T[D][\delta\varepsilon]}{[a]^T[D][f] + H'}\right\}$$

which on further rearranging gives

$$[\delta\sigma] \simeq [D_{ep}][\delta\varepsilon]$$

where $$[D_{ep}] = [D] - \frac{[D][f][a]^T[D]}{[a]^T[D][f] + H'} \tag{44}$$

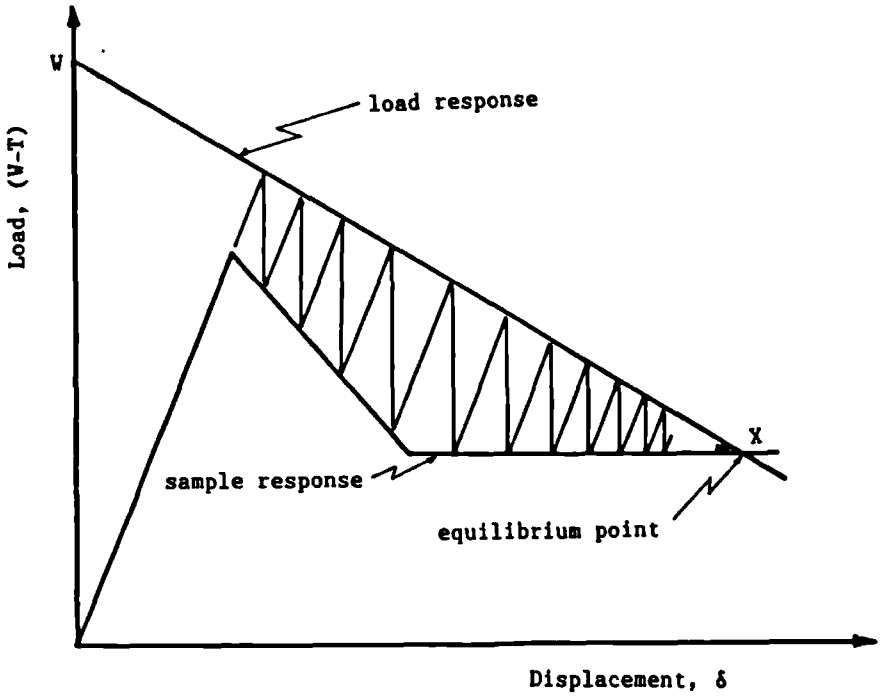
In the tangent stiffness approach the elasto-plastic stress-strain relationship for complete plane strain, $[D_{ep}]^*$, is substituted for the elastic version, $[D]^*$, in equation (49), Chapter 3, for assembly of the global stiffness matrix. The elastic matrix of compliances is symmetric about the leading diagonal. From inspection of equation (44) it can be seen that when $[f]=[a]$ (i.e. associated flow), then $[D_{ep}]$ is also symmetric. However, when $[f]\neq[a]$ (i.e. non-associated flow), then $[D_{ep}]$ is non-symmetric. Non-symmetry of the compliance matrix results in non-symmetry of the global stiffness matrix. As discussed in Section 3.6, Chapter 3, FEM equation solvers often take advantage of symmetry in the stiffness matrix to reduce the number of numerical operations, and the

original frontal solver listed in Owen and Hinton[35] is based on symmetry. Thus, to allow for non-associated flow in conjunction with a tangent stiffness approach it was necessary to modify the frontal solver to cope with a non-symmetric stiffness matrix. Although the number of numerical operations are doubled by this modification, the complexity of the solver is reduced.

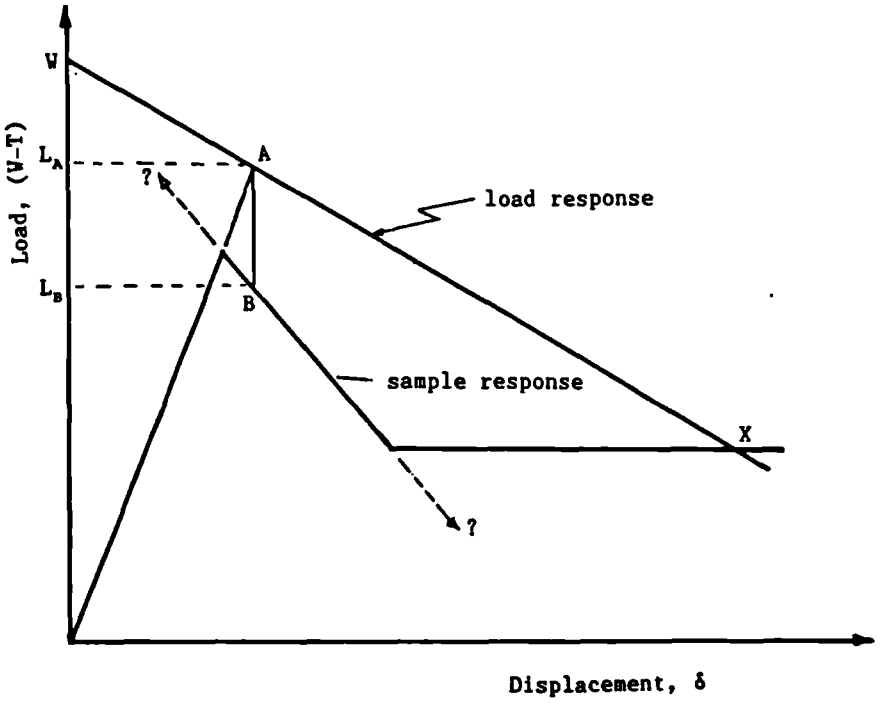
5.4 ADDITIONAL NUMERICAL REQUIREMENTS FOR ANALYSIS OF STRAIN SOFTENING

In Sections 5.1.1 to 5.1.3, iterative techniques used to analyse plasticity problems were introduced. The methods were explained with reference to a strain hardening material. However, as noted previously, rocks may exhibit a strain softening response to loading. Figure 5.6a shows the application of the initial stiffness to the problem depicted in Figure 5.1a. In this case the sample displays an initial elastic response followed by an idealized strain softening/residual strength response. Three points worth noting from Figure 5.6a are (i) the large number of iterations required to reach the equilibrium point, (ii) that for many iterations the solution appears to be diverging, (i.e. the magnitude of the residual load increases with each iteration), and (iii) despite the divergence anomaly and large number of iterations the solution finally converges to the exact solution.

Figure 5.6b shows the same problem described in the previous paragraph, but in this case the tangent stiffness approach is adopted. The initial or elastic response intersects the applied loading response at A. The allowable load for the displacement imposed is given at B. The tangent stiffness at B is found, and the residual load, (L_A-L_B), reapplied. At this point a problem occurs which ever direction the algorithm searches for a solution. In the positive displacement



(a) initial stiffness method



(b) tangent stiffness method

Figure 5.6 Iterative techniques applied to a strain softening material.

direction the tangent stiffness and load response lines diverge and no intersection point is found. In the negative displacement direction the sample rebounds also resulting in spurious predictions. The problem is that although the reduction in strength of the sample 'tails off' on reaching residual strength, the algorithm does not know that at point B.

The mechanisms involved in 2-D and 3-D problems are more complicated than those shown in Figures 5.6a and b, but the basic principles are the same.

A further problem when applying the tangent stiffness method to analysis of strain softening materials (and in some cases perfectly plastic materials) is localization of failure. Consider the sample shown in Figure 5.1a. The loading is applied until the sample exceeds its elastic limit and is now undergoing strain softening. The stress state is assumed homogenous within the sample. However, if an element within the sample is fractionally overstressed with respect to surrounding elements, then localized failure will occur in that element. As the element contracts in the axial direction, neighbouring elements will attempt to shed their loads by expanding in the axial direction. The result of this mechanism is that the whole sample attempts to relieve its load onto the element suffering localized failure. This process is depicted in Figure 5.7. As mentioned before, the stress state within the sample is assumed homogeneous, however, in practice, due to rounding off errors in numerical analyses, no two points within the sample will have exactly the same stress state, and an FEM analysis will result in localized failure or numerical instability in the equation solver. When uncontrolled localized failure of this type is encountered in an FEM analysis, the displacements predicted around the point concerned violate the assumption of small strains and often tend to $\pm\infty$.

In order to provide a physical understanding of this localized

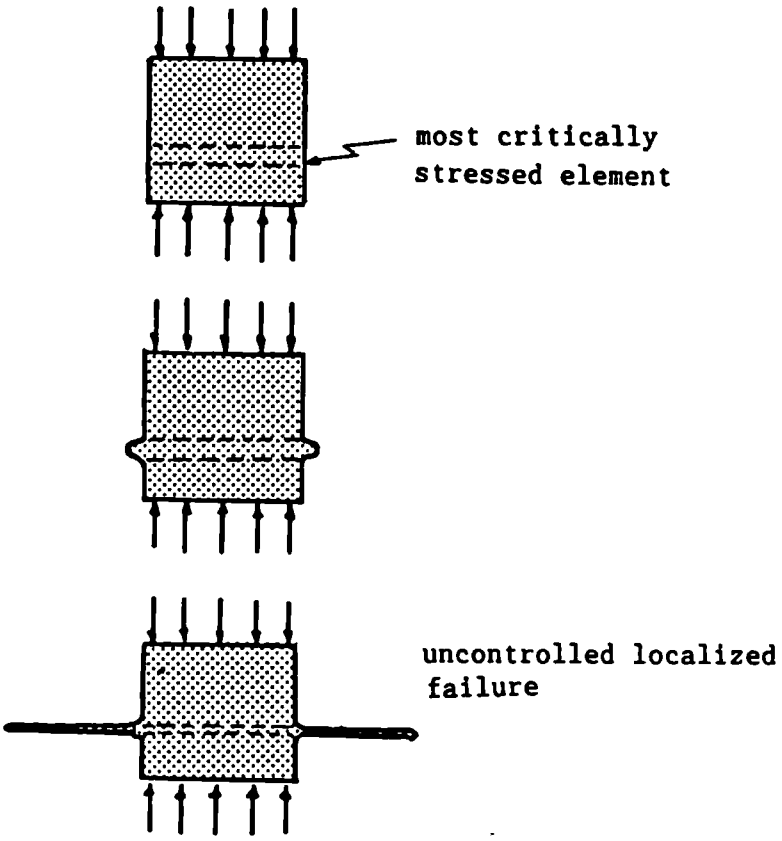


Figure 5.7 Prediction of localized failure in a uniaxially loaded sample undergoing strain softening (or perfect plasticity).

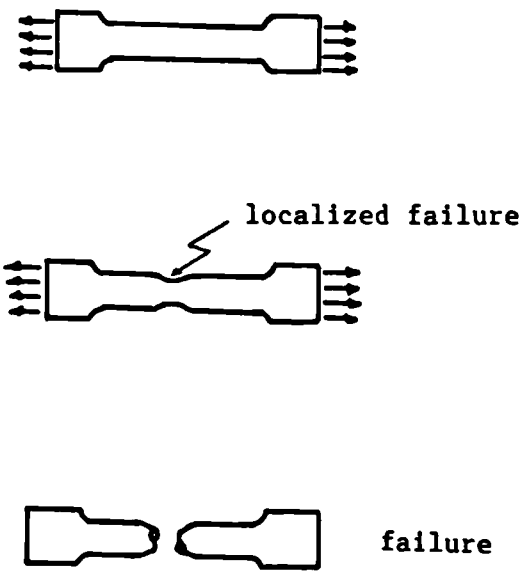


Figure 5.8 Localized failure in a steel bar loaded uniaxially.

failure we can draw a similarity between the problem discussed above and tensile loading of a steel bar. In this case when the steel reaches its elastic limit and yields, localization of failure occurs somewhere along its length depicted by a reduction in diameter followed by failure (see Figure 5.8). In this case, the steel may be undergoing perfect plasticity (or even strain hardening) with respect to its true stress state, however, it is undergoing strain softening with respect to its apparent stress (load divided by original cross sectional area). In this case the condition of small strains is also violated, and eventually the sample parts and is no longer continuous.

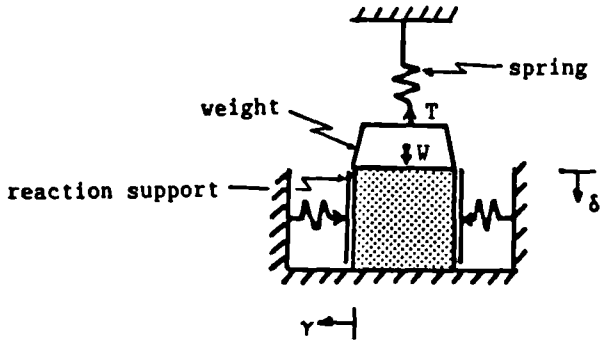
The problem of uncontrolled localized failure does not occur in the initial stiffness method, since on each load application the resultant displacements are restricted to a linear elastic response.

In conclusion, then for strain softening analysis, an initial stiffness approach is likely to converge after many iterations, although some divergence may occur at stages in the algorithm, while the tangent stiffness approach is likely to be unstable. These conclusions concur with comments made by Owen and Hinton.[35]

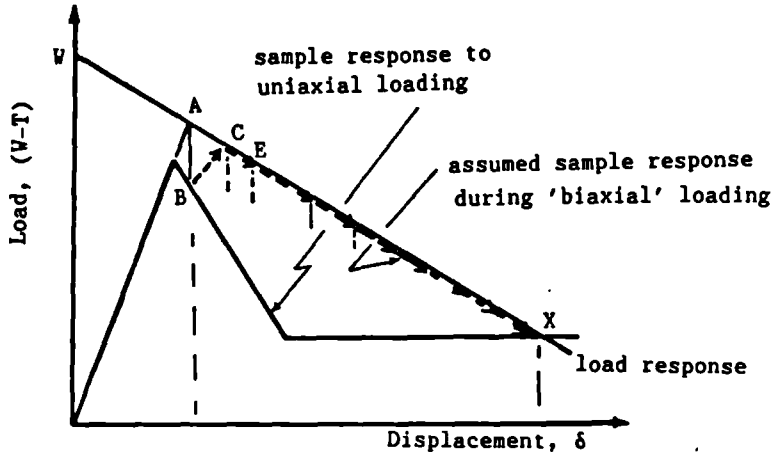
5.4.1 Adapted Algorithm for Strain Softening Materials

In order to find a compromise between the stable but tediously slow initial stiffness method and the unstable but potentially quicker tangent stiffness method, the following problem is considered.

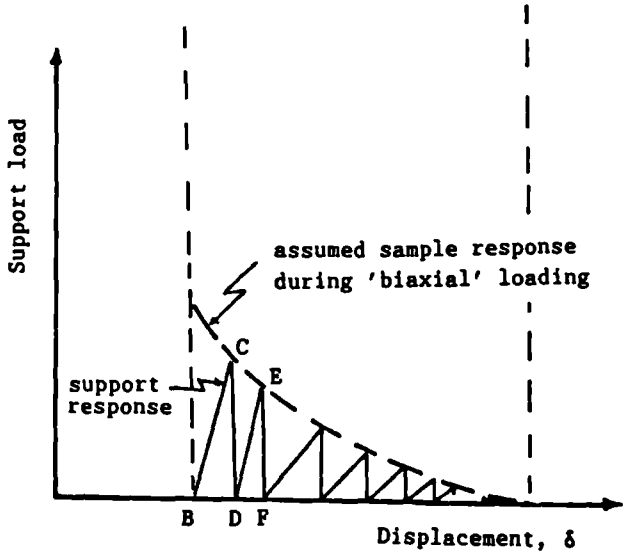
A sample exhibiting a strain softening response is again loaded vertically with the spring supported weight mechanism shown in Figure 5.9a. However, in this case it is assumed that lateral support is available as shown. The purpose of the lateral restraint is to prevent



(a) load conditions with passive lateral support



(b) axial load and sample response



(c) lateral support and sample response

Figure 5.9 Adapted algorithm for the tangent stiffness method applied to strain softening materials.

uncontrolled localized failure. Thus, if an element undergoing local failure attempts to dilate in the lateral direction a support load builds up, which increases the element's load carrying capacity in the axial direction. Provided the support stiffness is sufficient, the susceptibility to failure of the element concerned reduces relative to surrounding elements, thus preventing further localized failure. The response in the other horizontal direction is assumed irrelevant to the behaviour of the system.

For this algorithm the load is released, but initially the lateral support is not utilized, thus loading is uniaxial. Intersection with the load response is given at A in Figure 5.9b and the allowable sample reaction at B. Since it is known that the sample will now behave in a strain softening manner, the lateral support is now introduced in a passive role (i.e. lateral loading only takes place when the sample extends in that direction). Now the stiffness of the combined sample/support mechanism to axial loading is a function of the elasto-plastic behaviour of the sample and the stiffness of the lateral support. At the two extremes we have an infinitely soft support, which is equivalent to no support at all, and the other extreme an infinitely stiff support, which would not allow any lateral movement of the sample. The objective is to choose a support stiffness that allows some lateral movement, but prevents the prediction of total collapse of the sample.

From point B in Figure 5.9b, the axial residual load is reapplied to the sample, but now further residual loads include the build up of lateral load in the 'ficticious support'. Thus, the sample is now under biaxial loading (ignoring the third cartesian direction) instead of uniaxial. The first application of the axial load with the lateral support in place involves the transfer of loading from uniaxial to biaxial (B → C in Figure 5.9b). Each following application of the

residual load involves reducing the lateral support in controlled steps, until eventually the lateral support is negligible. The exact response of the sample to the combined axial and lateral loading is complex and not readily apparent, however, after the 'ficitious support' is activated, axial residual loads are likely to be small in comparison to lateral residual loads. Here it is assumed that the axial load-displacement response follows the dotted line shown in Figure 5.9b, i.e. the axial residual loads are negligible.

Figure 5.9c shows the assumed lateral load-axial displacement response for the sample. The response of the support shown in Figure 5.9c is dependent on the stiffness of the support and the ratio of the axial and lateral displacements (δ/γ). Its initial response is assumed to follow the line B-C. The iterative process can now be related to a physical system. After each load application the build up of load in the lateral support is released and reapplied to the sample as a residual load. If an acceleration of convergence is required then this can simply be achieved by reducing the stiffness of the support (e.g point F in Figure 5.c). Convergence is achieved when the support load is considered negligible.

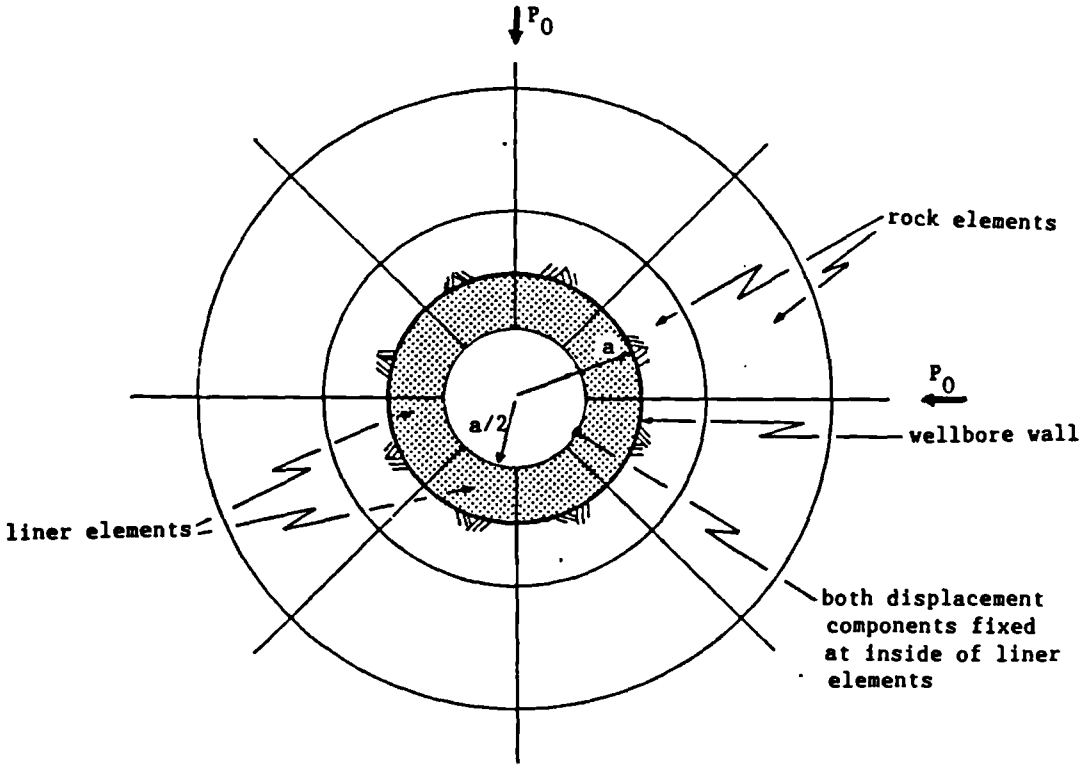
It is assumed that the equilibrium point 'X' is the same as if the uniaxial stress path of the sample had been followed. However, since the stress path followed in this algorithm is biaxial, this is not necessarily the case, and some differences may occur.

The algorithm with a 'ficticious support' is more complex than the simple initial or tangent stiffness approaches, however, it has the advantage over the initial stiffness method of allowing acceleration of convergence while reducing the potential for instability inherent in the tangent stiffness method.

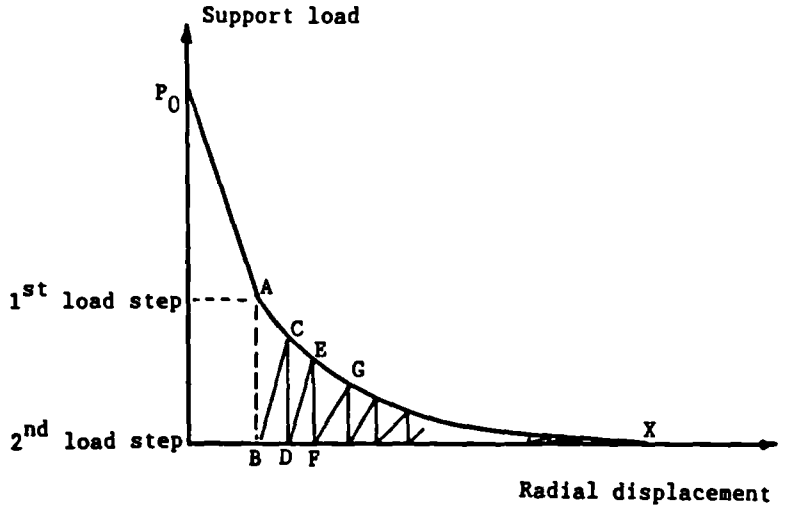
5.4.2 Fictitious Support Applied to Wellbore Analysis

Analysis of plasticity around a wellbore lends itself ideally to the algorithm described in Section 5.4.1. Take the case of axisymmetric loading conditions in a homogenous isotropic formation. The gradual excavation of the rock is assumed to take place under plane conditions. (This is a simplification, since plane conditions will only return when the drill bit has passed some distance beyond the section under consideration.) The induced displacement at the wellbore wall as a function of the reduced support is given in Figure 5.10b (similar to the rock-support interaction diagrams given by Brown et al[49]).

At point A, the rock at the wellbore wall reaches its elastic limit and undergoes strain softening. Assume the original support given by the excavated rock is reduced in 2 load steps. The first load step takes the response to the point where yielding just occurs at the wellbore wall (or the innermost Gauss point in the case of a FEM analysis). At this point a fictitious liner is placed at the boundary of the wellbore wall. The thickness and boundary conditions at the inside of the liner are given in Figure 5.10a. Initially the elastic constants of the liner are taken to be the same as the rock. The global stiffness matrix is reassembled using tangent stiffnesses and including the new support elements. The remaining load is applied and now the response at the wellbore wall includes a build up of support from the liner resulting in temporary equilibrium at C. The load built up in the liner is now released, thus moving from C to D. The residual load is now reapplied giving the response from D to E. The displacement at the wellbore wall is moving from A to C to E and converging on the exact solution, X, in controlled steps. In the next load step (F→G) the stiffness of the liner is reduced by halving the elastic modulus,



(a) FEM mesh for analysis of strain softening materials



(b) support and wellbore load-displacement responses

Figure 5.10 FEM analysis of strain softening behaviour around a wellbore using a fictitious liner.

resulting in an accelerated convergence. Convergence occurs when the residual support given by the fictitious liner is considered negligible.

A problem with introducing support elements is that generally the stress path followed by the surrounding rock is a function of the type of support system and its stiffness (as mentioned in Section 5.4.1). Only for the axisymmetric case is the stress path independent of the support stiffness. With softer supports we may expect the formation rock to have a greater tendency towards local concentrations of plastic flow. This aspect of the analysis is of some concern, since it is undesirable to have results heavily dependent on the support stiffness, which is after all, only a numerical tool and not a physical known. This problem was investigated previously (McLean[83]) by varying the elastic modulus of the support, from a value equal to the surrounding rock to a fifth of the rock's modulus, for the non-hydrostatic loading case. Over this range the effect on the final results was found to be minimal. To give the fictitious support physical significance, it may be considered as an idealized simulation of the excavation process.

5.4.3 Potential Sources of Instability in the Plastic Multiplier

The plastic multiplier, λ, is defined in equation (37). Instability in λ occurs if the denominator in (37) approaches zero. From inspection of the relevant terms in (38) and (39) it can be seen that for conditions of strain hardening, H' is positive, while for strain softening, H', is negative. The term $[a]^T[D][f]$ is always positive, therefore critical conditions for determination of λ may only occur in the case of strain softening.

To investigate possible values of the denominator in (37) the [a] and [f] vectors and [D] matrix are expressed in terms of principal stresses, and with reference to triaxial testing where $\sigma_2 = \sigma_3$.
Many linear failure criteria can be expressed in the form

$$\sigma_1 = \sigma_c + A\sigma_3$$

or $$F = \sigma_1 - \sigma_c - A\sigma_3 \ (= 0, \text{ at yield}) \qquad (45)$$

where A = 1 for the Tresca criterion, and A > 1 for the Mohr-Coulomb criterion. Values of A < 1 may apply to materials that undergo hydrostatic yielding (as mentioned in Section 4.4.4, Chapter 4), however, this behaviour is not considered here. Thus, with respect to a triaxial test the [a] vector can now be expressed as

$$[a]^T = \left[\frac{\partial F}{\partial \sigma_1}, \frac{\partial F}{\partial \sigma_2}, \frac{\partial F}{\partial \sigma_3}\right] = [1, -A/2, -A/2] \qquad (46)$$

where $A \geq 1$.

Similarly a linearised flow potential can be expressed as

$$Q = \sigma_1 - B\sigma_3$$

For the plastic deformation to result in zero plastic volumetric strain then B = 1. For some materials values of B < 1 may occur during strain hardening, but are unlikely to occur during strain softening or perfect plasticity, since this is indicative of a material that is 'imploding'. Thus, vector [f] expressed with respect to a triaxial test is given by

$$[f]^T = \left[\frac{\partial Q}{\partial \sigma_1}, \frac{\partial Q}{\partial \sigma_2}, \frac{\partial Q}{\partial \sigma_3}\right] = [1, -B/2, -B/2] \qquad (47)$$

where $B \geq 1$.

A further assumption made here is that strain softening only results in a reduction of the uniaxial strength, σ_c, and the constant, A, in (45) is independent of deformation. For a Mohr-Coulomb criterion this implies that ϕ is constant and only the cohesion coefficient, c, reduces with

permanent deformation. The particular case of the transition between a Class I and Class II response is shown in Figure 5.11. Gumusoglu[76] interprets this as the critical case where $\lambda \rightarrow \infty$, i.e. the denominator, D_n, in (37) is zero. Thus, Gumusoglu limits the use of his numerical analysis to Class I behaviour. This conclusion would also inhibit the use of elasto-plastic model behaviour using a Hoek-Brown criterion, since, as seen in Figures A.19 and A.25, part of the model stress-strain curve for the Carboniferous sandstone shows Class II behaviour.

The strain hardening parameter, H', for the criterion defined in (45) is given by

$$H' = -\frac{\partial F}{\partial \varepsilon_1^p} = \frac{\partial \sigma_c}{\partial \varepsilon_1^p} \qquad \text{(note: 'A' assumed independent of } \varepsilon_1^p\text{)}$$

For the transitional response in Figure 5.11, H' is given by

$$H' = \frac{\partial \sigma_c}{\partial \varepsilon_1^p} = -E \tag{48}$$

Thus, by substituting the relevent terms into (37) using (46), (47) and (48), we get

$$\text{Denominator, } D_n = [a]^T[D][f] + H'$$

$$= \frac{E}{(1+\nu)(1-2\nu)}\left[1 - \nu - A\nu - B\nu - \frac{A\,B}{2}\right] - E$$

Thus, for $D_n = 0$, we have after rearranging

$$-\nu A - \nu B - \frac{A\,B}{2} + 2\nu^2 = 0$$

or $$(2\nu - A)(2\nu - B) = 0$$

For drained elastic response of rocks, $\nu < 0.5$. Thus, since $A \geq 1$ and $B \geq 1$, then $D_n > 0$. Therefore, Gumusoglu's conclusion that the transition between Class I and Class II behaviour represents the case of $\lambda \rightarrow \infty$, is

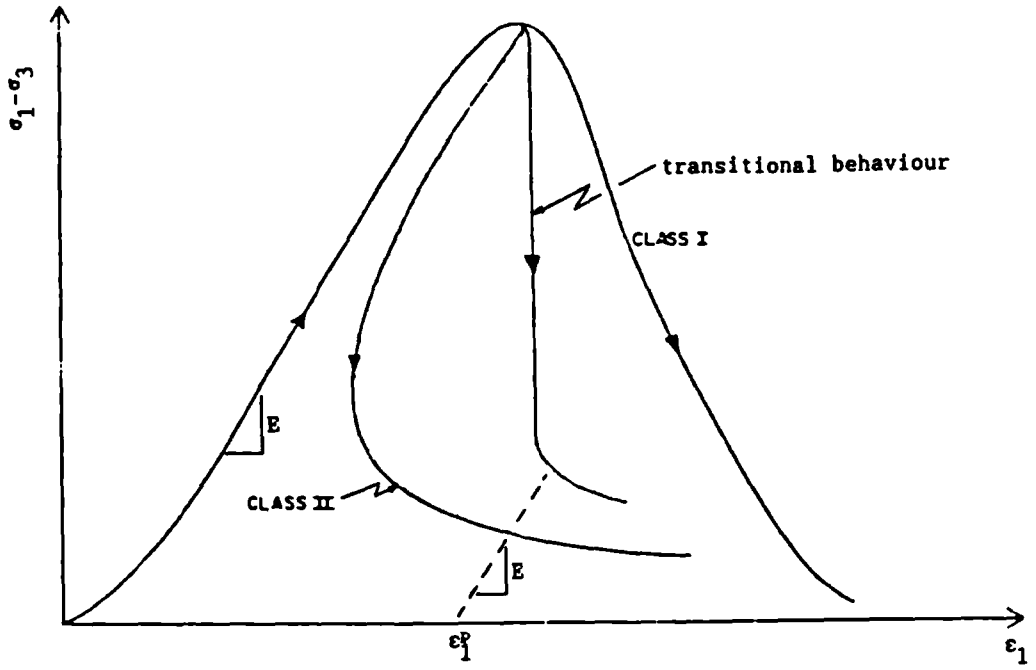


Figure 5.11 Class I, Class II and transitional material behaviour (adapted from Hudson et al[86]).

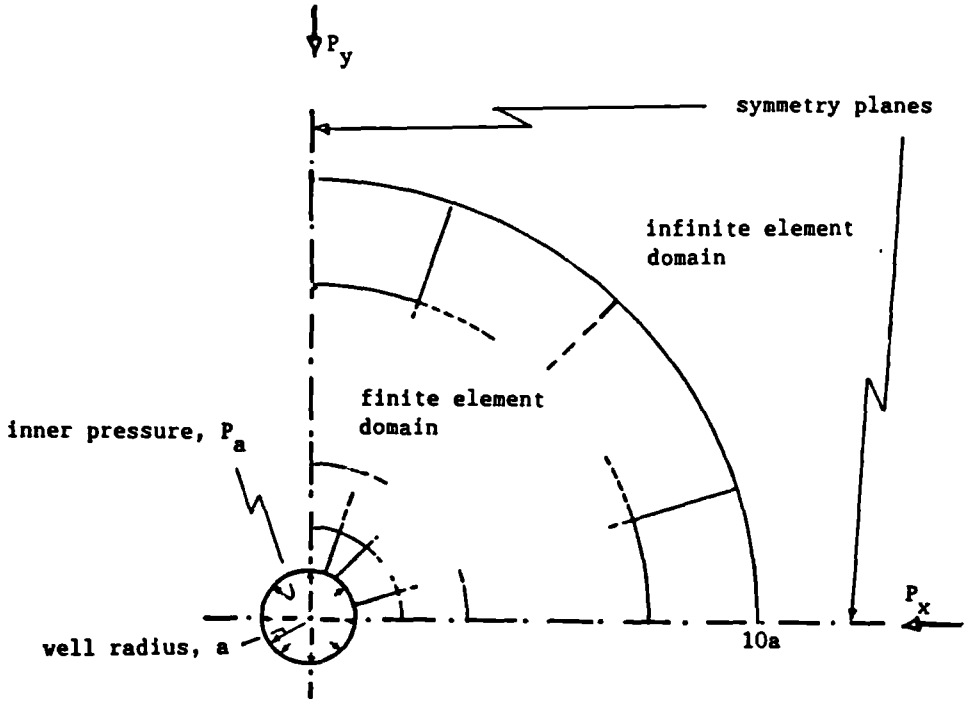


Figure 5.12 FEM mesh for analysis of a circular excavation in an anisotropic stress field under plane strain conditions.

incorrect, and certain cases of Class II behaviour are also amenable to analysis. Naturally the value of H' reduces further the more marked the Class II behaviour, until eventually $\lambda \rightarrow \infty$, and analysis can no longer be carried out. This aspect is investigated continually during program execution when strain softening behaviour is modelled. When negative or zero values of the denominator occur, program execution is stopped and the user flagged as to the reason.

5.5 VALIDATION OF THE FEM PROGRAM FOR PLASTIC BEHAVIOUR

Validation of the program for plastic behaviour is limited by the number and lack of generality of available analytical solutions. No solutions are available for general complete plane strain analysis of plasticity. However, for plane strain conditions Galin's solution[73] can be adopted provided certain conditions are met. The relevant equations and conditions required are presented in Appendix B. The main criteria are that post elastic behaviour is represented by perfect plasticity, and the yield criterion is independent of the hydrostatic portion of the stress state (i.e. Tresca and Von-Mises criteria are suitable, and Mohr-Coulomb and Hoek-Brown criteria are unsuitable). Detournay[85] extended Galin's solution to allow analysis of a frictional material. Detournay's solution is used to assess the validity of the coding using the Mohr-Coulomb criterion, but it is still restricted to perfect plasticity. For the case of hardening or softening materials no analytical solution exists for the general plane strain analysis of a circular opening in an infinite medium. However, a number of closed form and simple numerical solutions exist for the axisymmetric loading case. The FEM program is validated for the case of a strain softening material under axisymmetric

conditions, using a variation of the solution presented by Brown et al.[49]

5.5.1 Validation of FEM using Galin's Solution

The problem considered for validation is shown in Figure 5.12. The applied loading is given by

$$P_y/\sigma_Y = 1.3, \qquad P_x/\sigma_Y = 1.0 \qquad \text{and} \quad P_a/\sigma_Y = 0.1$$

where σ_Y is the uniaxial yield strength.

The elastic properties used in the FEM analysis are given by

$$E/\sigma_Y = 1000 \qquad \text{and} \quad \nu = 0.20$$

Note that all input parameters with units of stress are made dimensionless by dividing by the uniaxial yield strength. Linear dimensions are made dimensionless by dividing by the well radius, 'a'. The material strength is defined by the Tresca criterion, with the uniaxial yield strength assumed unaffected by continued plastic deformation. The stress state in both the elastic and plastic regions, given by Galin's solution in Appendix B, is independent of the flow rule. However, in the FEM analysis both associated flow (equivalent to $\partial\varepsilon_3^p/\partial\varepsilon_1^p = -1$) and a non-associated flow of $\partial\varepsilon_3^p/\partial\varepsilon_1^p = -2$, are used to check that the stress state predicted by the FEM is relatively unaffected by the flow rule.

Using symmetry conditions only a quarter of the problem need be analysed (see Figure 5.12). Boundary conditions on the symmetry planes are defined by zero applied shear tractions, and zero circumferential displacement. The finite element mesh is made up of 40 elements (10 radial and 4 circumferential). The remainder of the unbounded domain is modelled using infinite elements.

With a non-linear analysis the final results are dependent to some extent on the size and number of load steps, the convergence tolerance and the type of iterative procedure (initial stiffness, tangential stiffness or mixed algorithm). The iterative procedure is based on a mixed algorithm. Element stiffnesses are reformulated when a Gauss point undergoes one of the following changes:

1. Change from elastic to plastic behaviour, or visa versa.
2. Change from strain hardening to strain softening or residual strength.
3. Change from strain softening to residual strength.
4. A 90° rotation in principal stress axes (for example when a Gauss point having undergone plastic straining only within the r-θ plane, now undergoes plastic straining in the axial direction).

Naturally, every time an element stiffness is reformulated the global stiffness must be reformulated and undergo forward reduction.

Load application consists of applying the elastic portion of the load in one step, and the remainder of the load in five equal steps. The elastic portion is the load that just initiates yield on the most critically stressed Gauss point. This point is determined by the program. As mentioned in Section 5.1.1 convergence is monitored by checking the extent of the residual load remaining. More specifically the convergence ratio is defined as

$$\text{Convergence ratio} = \left\{ \frac{\sum_{i=1}^{Nn} \sum_{j=1}^{Nd} (P^a_{ji} - P^r_{ji})^2}{\sum_{i=1}^{Nn} \sum_{j=1}^{Nd} (P^a_{ji})^2} \right\}^{\frac{1}{2}} \times 100\% \qquad (49)$$

where Nn is the number of global nodes,

Nd is the number of degrees of freedom per node (2 for plane strain and 3 for complete plane strain),

P^a_{ji} is the applied nodal load component j at node i,

and P^r_{ji} is the reaction nodal load component j at node i.

For this problem, when the convergence ratio reaches a value of less than 0.5% then convergence is assumed to have occurred.

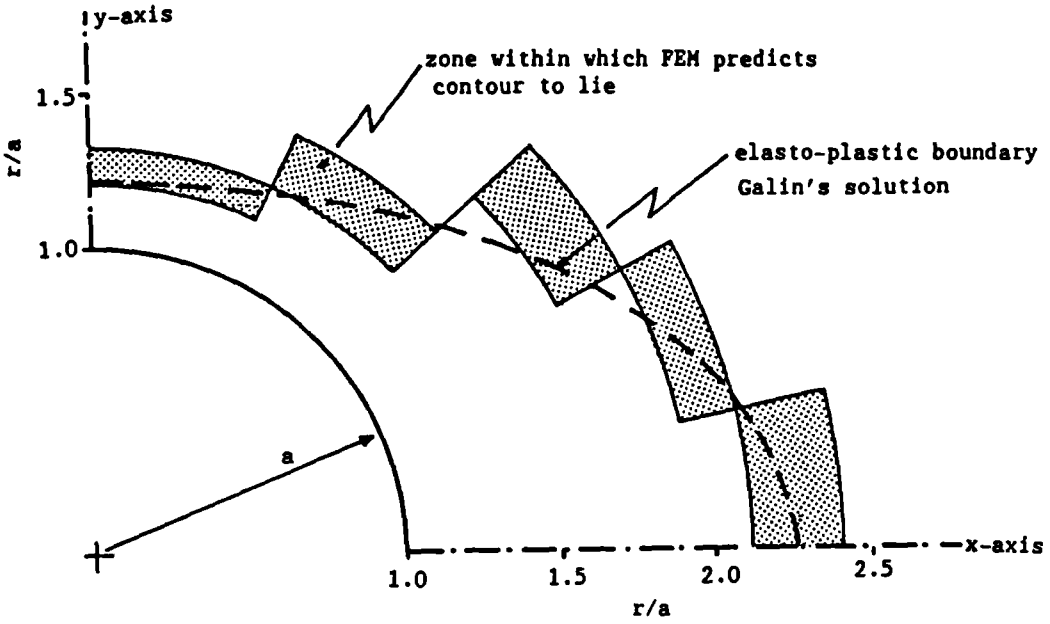
The resulting stresses from the FEM using associated flow, are shown and compared with Galin's solution in Table 9. In general, good agreement is found, particularly for the circumferential stress components. A number of the shear stress components show high percentage errors. However, when the absolute values of the shear stresses are small, the error calculation becomes sensitive to differences between the FEM and the analytical solution.

A number of the radial stress components show relatively high errors (6.8%, at r/a = 1.328 and θ = 4.8°). Often this is due to the inability of the mesh chosen to model accurately the contour separating the elastic and plastic zones. The exact position of this contour cannot be found directly from the FEM results, although it is possible to use some interpolation technique. In Figure 5.13a the shaded region denotes an area within which the contour must lie. The upper and lower boundaries are found from inspection of where Gauss points have and have not yielded. Due to the coarseness of the grid, the definition of the contour is poor. However, in Figure 5.13b a finer grid is used, where the same finite element domain is now represented by 120 elements (6 circumferential and 20 radial). Here the agreement between Galin's solution and the FEM is much better.

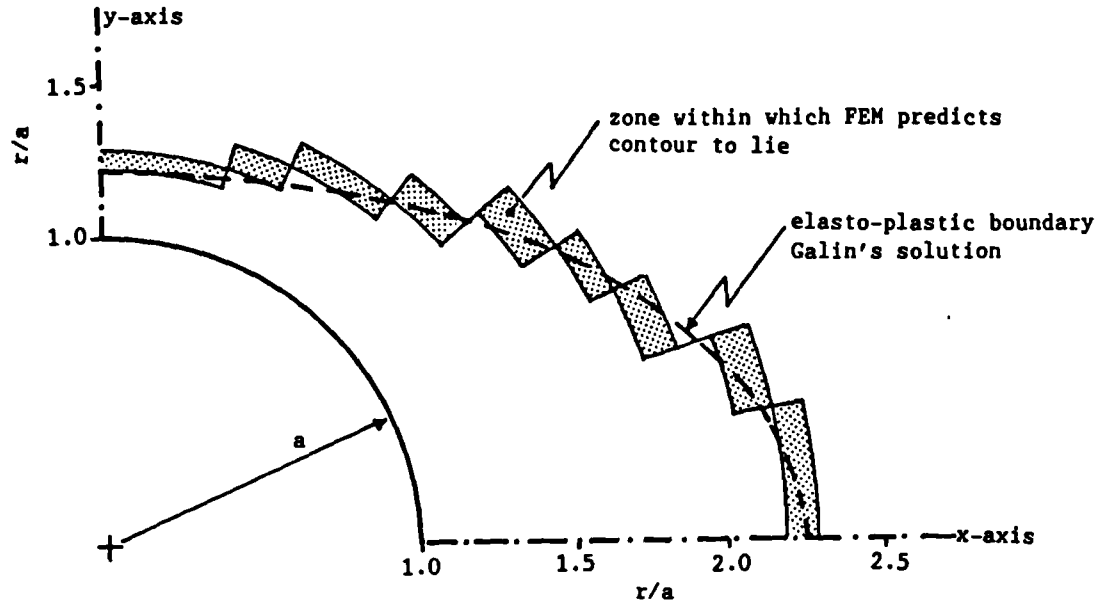
Gauss point		σ_r/σ_Y			σ_θ/σ_Y			$\tau_{r\theta}/\sigma_Y$		
r/a	θ	Exact	FEM	Error	Exact	FEM	Error	Exact	FEM	Error
1.055	4.8	0.154	0.155	0.6%	1.154	1.155	0.1%	0.000	-0.004	-
1.055	27.3	0.154	0.150	2.6%	1.154	1.150	0.3%	0.000	0.002	-
1.055	49.8	0.154	0.157	1.9%	1.154	1.157	0.3%	0.000	-0.004	-
1.055	72.3	0.154	0.143	5.8%	1.154	1.139	1.3%	0.000	0.007	-
1.328	4.8	0.384	0.379	1.3%	1.384	1.366	1.3%	0.000	0.002	-
1.328	27.3	0.384	0.400	4.2%	1.384	1.394	0.7%	0.000	-0.013	-
1.328	49.8	0.384	0.370	3.6%	1.384	1.369	1.1%	0.000	0.009	-
1.328	72.3	0.380	0.406	6.8%	1.324	1.318	0.4%	0.013	0.009	30.8%
1.672	4.8	0.614	0.620	1.0%	1.614	1.619	0.3%	0.000	-0.003	-
1.672	27.3	0.614	0.610	0.7%	1.614	1.610	0.2%	0.000	0.001	-
1.672	49.8	0.579	0.601	3.8%	1.460	1.453	0.5%	0.066	0.060	9.1%
1.672	72.3	0.586	0.579	1.2%	1.293	1.295	0.2%	0.057	0.058	1.8%
2.104	4.8	0.844	0.866	2.6%	1.844	1.866	1.2%	0.000	-0.005	-
2.104	27.3	0.780	0.792	1.5%	1.652	1.644	0.5%	0.093	0.096	3.2%
2.104	49.8	0.746	0.742	0.5%	1.407	1.409	0.2%	0.143	0.142	0.7%
2.104	72.3	0.767	0.769	0.3%	1.246	1.246	0.0%	0.087	0.088	1.1%
2.649	4.8	0.981	0.983	0.2%	1.637	1.638	0.1%	0.039	0.045	15.4%
2.649	27.3	0.902	0.897	0.6%	1.514	1.515	0.1%	0.163	0.159	2.5%
2.649	49.8	0.887	0.888	0.1%	1.333	1.333	0.0%	0.180	0.180	0.0%
2.649	72.3	0.916	0.916	0.0%	1.193	1.193	0.0%	0.102	0.102	0.0%

Results of an elastic-perfectly plastic analysis with ASSOCIATED flow of a vertical wellbore subjected to an anisotropic horizontal in-situ stress field.

TABLE 9



(a) 40 finite elements



(b) 120 finite elements

Figure 5.13 FEM definition of the elasto-plastic contour around a circular opening compared with Galin's solution.

In Table 10 the same stress state comparison is made between the FEM and Galin's solution, but in this case a non-associated flow is used with $\partial\varepsilon_3^p/\partial\varepsilon_1^p = -2$. Again agreement is good, although in general the errors are slightly greater in the case of the non-associated flow, than for associated flow. This is possibly due to greater drift from the yield surface (see Section 5.3.6) due to the higher plastic strains incurred.

Table 11 shows a comparison of the induced radial displacements for both the associated and non-associated flow rules. Here we would not expect agreement between the two models. Along the x-axis (θ=0°) the closure at the hole wall for the non-associated flow model is nearly twice that of the associated flow model. This result is to be expected since the non-associated flow ratio, $(\partial\varepsilon_3^p/\partial\varepsilon_1^p)$, used here is twice that of the associated flow ratio. On moving further along the x-axis it can be seen that the displacements for the two models converge, until around the elasto-plastic boundary the difference between the two models is only 4%. Along the y-axis (θ=90°) the difference between the two models is only slight. This is due to the relatively thin section of material that has yielded as measured along the y-axis.

NOTE: Gumusoglu[76] also uses Galin's solution for validation purposes. However, the equations he quotes for the elastic stress state are incorrect. He attributes the equations to Kachanov[87], although Kachanov does not actually quote them. The equations presented by Gumusoglu only give the correct elastic stress state for values of θ = 0/180° and 90/270° (see Figure B.1, Appendix B). This may explain why the validation work was only carried out for values of θ = 0 and 90°.

Gauss point		σ_r/σ_Y			σ_θ/σ_Y			$\tau_{r\theta}/\sigma_Y$		
r/a	θ	Exact	FEM	Error	Exact	FEM	Error	Exact	FEM	Error
1.055	4.8	0.154	0.160	3.9%	1.154	1.160	0.5%	0.000	-0.014	-
1.055	27.3	0.154	0.144	6.5%	1.154	1.143	1.0%	0.000	0.015	-
1.055	49.8	0.154	0.166	7.8%	1.154	1.165	0.8%	0.000	-0.012	-
1.055	72.3	0.154	0.144	6.5%	1.154	1.144	0.9%	0.000	0.005	-
1.328	4.8	0.384	0.371	3.4%	1.384	1.371	0.5%	0.000	0.005	-
1.328	27.3	0.384	0.391	1.8%	1.384	1.391	0.5%	0.000	-0.007	-
1.328	49.8	0.384	0.388	1.0%	1.384	1.388	0.3%	0.000	0.010	-
1.328	72.3	0.380	0.402	3.2%	1.324	1.308	1.2%	0.013	0.010	23.1%
1.672	4.8	0.614	0.609	0.8%	1.614	1.609	0.3%	0.000	-0.005	-
1.672	27.3	0.614	0.624	1.6%	1.614	1.624	0.6%	0.000	-0.006	-
1.672	49.8	0.579	0.591	2.1%	1.460	1.454	0.4%	0.066	0.062	6.1%
1.672	72.3	0.586	0.576	1.7%	1.293	1.300	0.5%	0.057	0.058	1.8%
2.104	4.8	0.844	0.881	4.4%	1.844	1.880	2.0%	0.000	-0.012	-
2.104	27.3	0.780	0.799	2.4%	1.652	1.639	0.8%	0.093	0.098	5.4%
2.104	49.8	0.746	0.741	0.7%	1.407	1.411	0.3%	0.143	0.144	0.7%
2.104	72.3	0.767	0.772	0.7%	1.246	1.247	0.1%	0.087	0.089	2.3%
2.649	4.8	0.981	0.989	0.8%	1.637	1.638	0.1%	0.039	0.049	25.6%
2.649	27.3	0.902	0.894	0.9%	1.514	1.515	0.1%	0.163	0.157	2.5%
2.649	49.8	0.887	0.889	0.2%	1.333	1.332	0.1%	0.180	0.180	0.0%
2.649	72.3	0.916	0.916	0.0%	1.193	1.193	0.0%	0.102	0.101	1.0%

Results of an elastic-perfectly plastic analysis with NON-ASSOCIATED flow for a vertical wellbore subjected to an anisotropic horizontal in-situ stress field.

TABLE 10

Radius r/a	Radial Closure, $-u_r/a$					
	$\theta = 0°$			$\theta = 90°$		
	Ass.	N-Ass.	Ratio	Ass.	N-Ass.	Ratio
1.000	2.50×10^{-3}	4.43×10^{-3}	1.772	2.46×10^{-3}	2.48×10^{-3}	1.008
1.130	2.01×10^{-3}	3.45×10^{-3}	1.716	2.30×10^{-3}	2.32×10^{-3}	1.009
1.259	1.60×10^{-3}	2.66×10^{-3}	1.663	2.15×10^{-3}	2.15×10^{-3}	1.000
1.422	1.18×10^{-3}	1.88×10^{-3}	1.593	1.99×10^{-3}	1.99×10^{-3}	1.000
1.585	8.37×10^{-4}	1.27×10^{-3}	1.517	1.86×10^{-3}	1.85×10^{-3}	0.995
1.790	5.17×10^{-4}	7.22×10^{-4}	1.397	1.71×10^{-3}	1.71×10^{-3}	1.000
1.995	3.11×10^{-4}	3.64×10^{-4}	1.170	1.58×10^{-3}	1.58×10^{-3}	1.000
2.254	1.83×10^{-4}	1.76×10^{-4}	0.962	1.44×10^{-3}	1.44×10^{-3}	1.000
2.512	1.38×10^{-4}	1.29×10^{-4}	0.935	1.32×10^{-3}	1.32×10^{-3}	1.000
2.837	1.11×10^{-4}	1.06×10^{-4}	0.955	1.19×10^{-3}	1.19×10^{-3}	1.000
3.162	9.48×10^{-5}	9.16×10^{-5}	0.966	1.09×10^{-3}	1.08×10^{-3}	0.991
3.572	8.05×10^{-5}	7.83×10^{-5}	0.973	9.76×10^{-4}	9.74×10^{-3}	0.998
3.981	6.94×10^{-5}	6.77×10^{-5}	0.976	8.85×10^{-4}	8.83×10^{-3}	0.998
4.497	6.00×10^{-5}	5.88×10^{-5}	0.980	7.91×10^{-4}	7.90×10^{-3}	0.999
5.012	5.24×10^{-5}	5.14×10^{-5}	0.981	7.15×10^{-4}	7.14×10^{-3}	0.999

Elastic | Plastic

Elastic | Plastic

Comparison of Associated and Non-associated flow models on the radial closure around a hole subjected to non-hydrostatic loading under plane strain conditions.

TABLE 11

5.5.2 Validation of the FEM using Detournay's Solution

The relevant equations and overriding assumptions in Detournay's solution[85] are given in Appendix C. The equations provide the exact state of stress in the plastic zone around a circular opening in a perfectly plastic frictional material, subjected to plane strain constraints. In addition Detournay provides an approximate solution for the contour describing the elasto-plastic interface. The approximate solution is a result of truncating an infinite series to include only the first term of the series. In order to assess the accuracy of the approximate solution, and thus its applicability for validating the FEM, the effect of including the second term of the series on computed results was investigated. Detournay tabulates the relevant constants for the first 5 terms of the series for an obliquity of 0.1 (obliquity is defined in Appendix C, and explained in more detail by Detournay[85]). In Table 12 the computed results for the approximate equations given in Appendix C (number of terms, n = 1), and results from taking n = 2 are compared. The coordinates defining the elasto-plastic contour (x_e, y_e) are normalised with respect to the equivalent hydrostatic radius, R_e (defined in Appendix C). It can be seen that the difference between the two approximations is of the order of 0.1%. For higher values of obliquity this difference will increase. However, for purposes of validating the FEM the approximate solution appears more than adequate.

The problem considered for coding validation is again represented

Mapping variable ψ^o	x_e/R_e			y_e/R_e		
	n = 1	n = 2	Diff.	n = 1	n = 2	Diff.
0	1.049	1.048	0.1%	0.000	0.000	0.0%
10	1.033	1.032	0.1%	0.165	0.166	0.3%
20	0.986	0.985	0.1%	0.325	0.325	0.1%
30	0.908	0.908	0.0%	0.474	0.474	0.0%
40	0.804	0.804	0.0%	0.610	0.611	0.1%
50	0.674	0.675	0.1%	0.727	0.727	0.0%
60	0.525	0.526	0.2%	0.822	0.821	0.1%
70	0.359	0.360	0.3%	0.892	0.891	0.1%
80	0.182	0.183	0.3%	0.935	0.933	0.2%
90	0.000	0.000	0.0%	0.949	0.947	0.2%

Variation of predicted coordinates of the elasto-plastic interface around a circular opening with number of terms taken from the truncated series used in Detournay's solution.[85] Obliquity, m = 0.1.

TABLE 12

in Figure 5.12. The applied loading is given by

$$P_y/\sigma_Y = 3.0, \qquad P_x/\sigma_Y = 2.0, \qquad P_a/\sigma_Y = 0.05$$

where $\sigma_Y = \dfrac{2c.\cos\phi}{1-\sin\phi}$.

The material behaviour is defined by

Associated flow
$E/\sigma_Y = 1000$
$\nu = 0.20$
} FEM analysis only

and $\phi = 30°$

In the FEM analysis the finite element domain (see Figure 5.12) is modelled using 120 elements (20 radial and 6 circumferential). The remainder of the unbounded domain is modelled using 6 infinite elements. The boundary tractions resulting from the hole excavation are applied in 6 increments. The first increment taking loading up until a Gauss point yields, and the remaining plastic portion of the loading applied in 5 equal increments.

Figure 5.14 shows the comparison between the elasto-plastic contour found from expressions given in Appendix C and the zone within which the FEM predicts the contour to lie. It can be seen that the two solutions are in fair agreement. However, the errors in the computed stresses in the plastic zone are relatively large. Table 13 shows the comparison between the stresses computed using the FEM and the exact solutions. With errors of up to 15% and 6% in the radial and circumferential stress components respectively, the accuracy attained using the FEM cannot be considered good. Factors which may improve accuracy that can be adjusted by the user are,

- use a finer mesh,
- increase the number of Gauss points per element,
- reduce the convergence tolerance value,

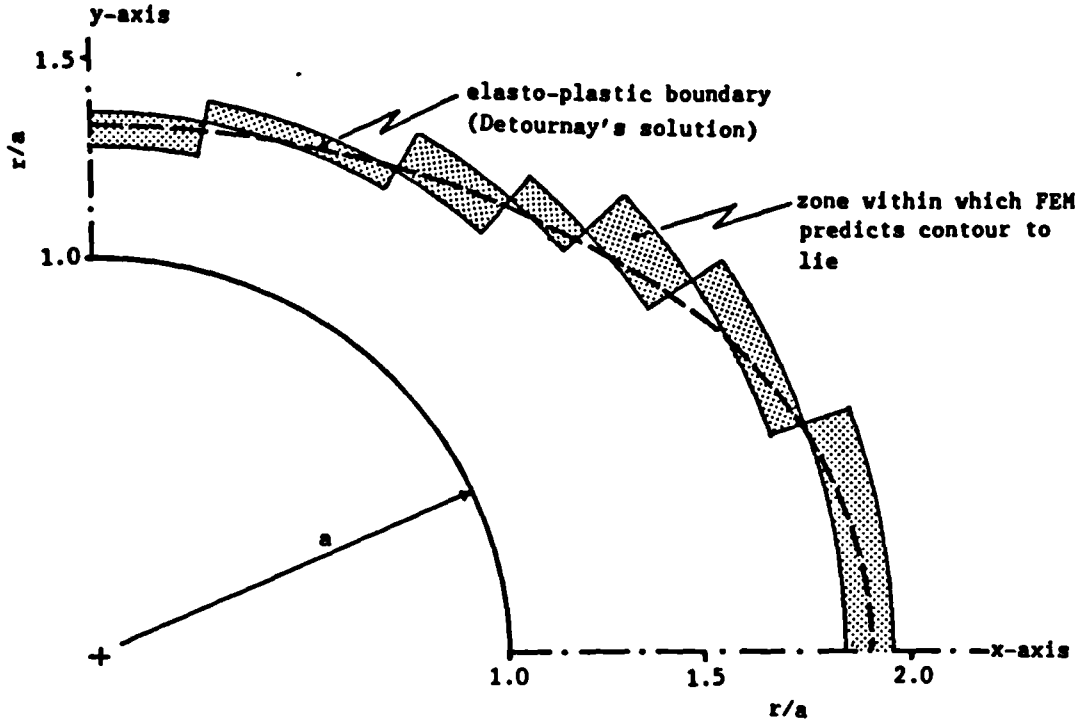


Figure 5.14 FEM definition of the elasto-plastic contour around a circular opening in a frictional material compared with Detournay's approximate solution.

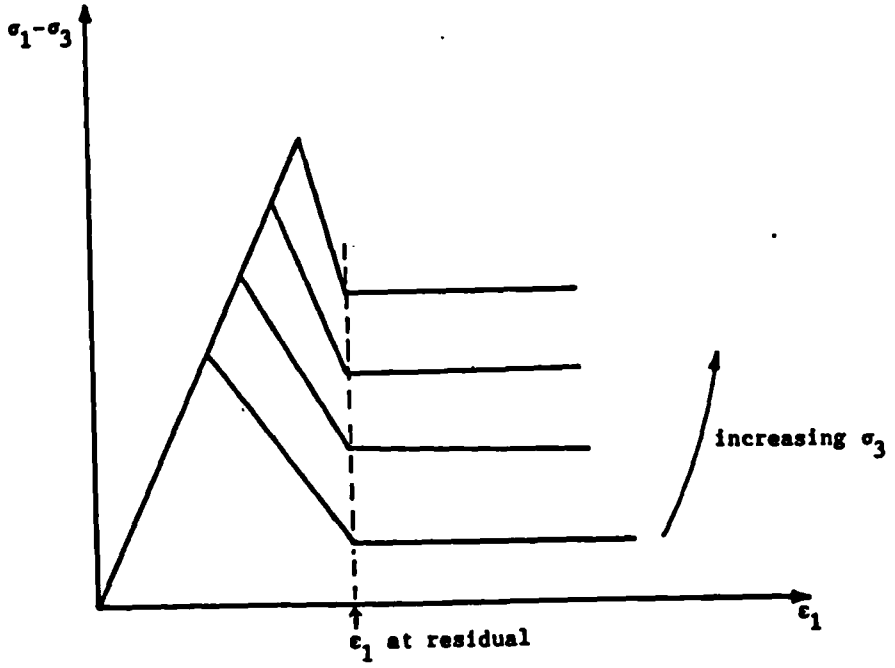


Figure 5.15 Idealized model behaviour inferred by Brown et al.[49]

Gauss point		σ_r/σ_Y			σ_θ/σ_Y			$\tau_{r\theta}/\sigma_Y$		
r/a	θ°	Exact	FEM	Error	Exact	FEM	Error	Exact	FEM	Error
1.026	11.8	0.079	0.083	5.1%	1.237	1.247	0.8%	0.000	-0.029	-
1.026	33.2	0.079	0.069	12.6%	1.237	1.206	2.5%	0.000	-0.005	-
1.026	56.8	0.079	0.073	7.6%	1.237	1.215	1.8%	0.000	0.008	-
1.026	78.2	0.079	0.073	7.6%	1.237	1.171	5.3%	0.000	0.006	-
1.151	11.8	0.229	0.194	15.3%	1.686	1.582	6.2%	0.000	0.024	-
1.151	33.2	0.229	0.246	7.4%	1.686	1.732	2.7%	0.000	-0.017	-
1.151	56.8	0.229	0.217	5.2%	1.686	1.650	2.1%	0.000	0.001	-
1.151	78.2	0.229	0.243	6.1%	1.686	1.723	2.2%	0.000	0.047	-
1.291	11.8	0.417	0.400	4.1%	2.250	2.200	2.2%	0.000	-0.006	-
1.291	33.2	0.417	0.446	6.9%	2.250	2.333	3.7%	0.000	0.046	-
1.291	56.8	0.417	0.427	2.4%	2.250	2.281	1.4%	0.000	0.029	-
1.291	78.2	0.417	0.427	2.4%	2.250	2.277	1.2%	0.000	0.015	-
1.449	11.8	0.655	0.658	0.5%	2.964	2.967	0.1%	0.000	-0.057	-
1.449	33.2	0.655	0.650	0.8%	2.964	2.950	0.5%	0.000	-0.023	-
1.449	56.8	0.655	0.631	3.7%	2.964	2.892	2.4%	0.000	-0.007	-
1.626	11.8	0.954	0.973	2.0%	3.863	3.917	0.2%	0.000	-0.029	-
1.626	33.2	0.954	0.918	3.8%	3.863	3.754	2.8%	0.000	-0.011	-
1.824	11.8	1.330	1.314	1.2%	4.990	4.941	1.0%	0.000	-0.050	-

Comparison between FEM and exact solutions for the stress state in the plastic zone around a circular excavation in an elastic-perfectly plastic Mohr-Coulomb material. Number of plastic load steps = 5.

TABLE 13

- increase the number of load steps.

An analysis of the sensitivity of the solution to the above factors is not presented here, but it is often found that increasing the number of load steps has the greatest impact on the accuracy of the FEM for analysis of plasticity. Table 14 presents results for the same problem using the same mesh, number of Gauss points and convergence tolerance, but with an increase in plastic load steps from 5 to 20. From comparison of Tables 13 and 14 it can be seen that the accuracy of the results is much improved.

5.5.3 Finite Difference Analysis of Strain Softening

In Appendix D the relevant equations and iterative techniques for analysis of strain softening behaviour for the axisymmetric wellbore are presented. The basis for these equations are taken from Brown et al,[49] although, two changes have been made to their procedure to facilitate a direct comparison between the FEM and the finite difference approach given in Appendix D. These changes are discussed in the following sub-sections.

5.5.3.1 Dependence of Strength Parameters on Plastic Strain

Brown et al simplify their model by making the assumption that once yield is initiated, increments in the Hoek-Brown strength parameters 'm' and 's' are a function of increments in the maximum principal strain. However, the model used in the FEM considers variation of strength parameters to be function of increments in plastic strain in

Gauss point		σ_r/σ_Y			σ_θ/σ_Y			$\tau_{r\theta}/\sigma_Y$		
r/a	θ°	Exact	FEM	Error	Exact	FEM	Error	Exact	FEM	Error
1.026	11.8	0.079	0.076	3.8%	1.237	1.227	0.8%	0.000	-0.003	-
1.026	33.2	0.079	0.074	6.3%	1.237	1.216	1.7%	0.000	-0.009	-
1.026	56.8	0.079	0.079	0.0%	1.237	1.236	0.1%	0.000	-0.002	-
1.026	78.2	0.079	0.083	5.1%	1.237	1.249	1.0%	0.000	0.008	-
1.151	11.8	0.229	0.232	1.3%	1.686	1.683	0.2%	0.000	0.001	-
1.151	33.2	0.229	0.238	3.9%	1.686	1.711	1.5%	0.000	-0.006	-
1.151	56.8	0.229	0.227	0.8%	1.686	1.675	0.7%	0.000	0.001	-
1.151	78.2	0.229	0.234	2.2%	1.686	1.699	0.8%	0.000	0.009	-
1.291	11.8	0.417	0.415	0.5%	2.250	2.244	0.3%	0.000	0.028	-
1.291	33.2	0.417	0.429	2.9%	2.250	2.287	1.6%	0.000	0.007	-
1.291	56.8	0.417	0.415	0.5%	2.250	2.245	0.2%	0.000	-0.009	-
1.291	78.2	0.417	0.414	0.7%	2.250	2.242	0.4%	0.000	0.002	-
1.449	11.8	0.655	0.662	1.1%	2.964	2.987	0.8%	0.000	0.008	-
1.449	33.2	0.655	0.644	1.7%	2.964	2.932	1.1%	0.000	-0.006	-
1.449	56.8	0.655	0.661	0.9%	2.964	2.984	0.7%	0.000	-0.004	-
1.626	11.8	0.954	0.948	0.6%	3.863	3.844	0.5%	0.000	-0.013	-
1.626	33.2	0.954	0.957	0.3%	3.863	3.870	0.2%	0.000	0.004	-
1.824	11.8	1.330	1.343	1.0%	4.990	5.030	0.8%	0.000	-0.002	-

Comparison between FEM and exact solutions for the stress state in the plastic zone around a circular excavation in an elastic-perfectly plastic Mohr-Coulomb material. Number of plastic load steps = 20.

TABLE 14

the maximum principal stress direction (see Section 4.5.2, Chapter 4). The assumption made by Brown et al does not lead to significant errors between the two analyses provided the plastic portion of the strain is dominant. However, in the softening zone continued deformation can lead to a large reduction in the hoop stress resulting in large elastic rebound strains. Another anomaly in the model used by Brown et al is that residual strength is reached after elements have undergone a given circumferential strain. The magnitude of this strain is assumed proportional to the circumferential strain at peak strength. This model relationship is depicted in Figure 4.9, Chapter 4. The idealized stress-strain plot shown in Figure 4.9 may be suitable for representing a triaxial test carried out at constant confining pressure. However, the stress path followed by points around a circular opening is equivalent to a triaxial test where the confining pressure is reduced during the application of the deviator stress. In effect, the model used by Brown et al infer a set of triaxial tests as represented in Figure 5.15. (Although a linear softening stress-strain plot is shown in Figure 5.15, it is recognized that the true model plot is likely to be markedly non-linear, as discussed in Section 4.7.2, Chapter 4).

From the reasoning given above it was necessary to adapt the model developed by Brown et al to allow for variation of strength parameters as a function of plastic strain. The model behaviour used in the procedures given in Appendix D assumes that residual strength is reached once the plastic strain in the major principal stress direction has reached a given value. The value of plastic strain at residual is assumed to be independent of confining pressure. Figure D.1, Appendix D, gives the triaxial interpretation of this assumed model behaviour. As noted in Section 4.5.2 this behaviour is unable to account for increased

ductility with increase in confining pressure. This anomaly in the finite difference model can be rectified by defining a function relating plastic strain at residual with confining pressure (also noted by Brown et al with respect to total strain). However, the finite difference model is only used here as a validation tool rather than a predictive tool. Thus, it is felt unwarranted to over complicate the finite difference model behaviour given in Appendix D.

5.5.3.2 Axial Plastic Strain Components

A further difference between the analysis given by Brown et al and the FEM program is in consideration given to the magnitude of the axial stress, σ_z, in relation to the other two principal stresses σ_r and σ_θ. In the model presented by Brown et al no consideration is given to the case of $\sigma_r < \sigma_\theta = \sigma_z$. This situation may arise when elements of rock undergo strain softening. Other problem cases where σ_z is the minimum principal stress or greater than σ_θ will only occur for cases of exceptional in-situ stress and/or internal pressure regimes, and need not be considered here. Occurrence of the condition $\sigma_z = \sigma_\theta > \sigma_r$ is explained below.

When the support offered to the opening is removed in the form of excavation, the radial stress at a point reduces and, in the case of an axisymmetric linear elastic analysis, the circumferential stress increases by a corresponding amount. Thus, $\Delta\sigma_r = -\Delta\sigma_\theta$, and the axial stress is unaffected, since

$$\Delta\sigma_z = \nu(\Delta\sigma_r + \Delta\sigma_\theta) = 0$$

As σ_r is progressively reduced and σ_θ increases the condition may arise where the combination of the deviator stress , $(\sigma_\theta - \sigma_r)$, and the

confining stress, σ_r, exceeds the compressive strength of the material. For perfectly plastic and strain softening materials further reduction of σ_r results in a reduction of σ_θ. This reduction in σ_θ can be particularly marked in the case of a strain softening material. As both both σ_r and σ_θ decrease so does σ_z as a result of the Poisson effect. For realistic values of Poisson's ratio, the rate of the reduction in σ_θ is much greater than the rate of reduction in σ_z, and eventually σ_θ reduces to the same magnitude as σ_z (this is shown to be the case in the validation example given later in Section 5.5.3.3). With continued reduction in σ_r both σ_θ and σ_z must now remain equal, since neither can 'out run' the other. Thus, at this stage both the circumferential and axial directions undergo compressive plastic straining. In general, the plastic strain magnitudes in the two directions are unequal. This is necessary in order to maintain equilibrium of σ_θ and σ_z.

The finite difference procedure used here allows for the possibility of axial plastic strain components. The method adopted is explained in Appendix D.

5.5.3.3 FEM Validation for Strain Softening Axisymmetric Conditions

The problem considered for validation purposes is defined below. The applied loading and Youngs Modulus are made dimensionless by dividing by the rock's uniaxial compressive strength, σ_c. The Hoek-Brown criterion is used to describe the plastic behaviour. The following input parameters are used in both the FEM and finite difference analyses:-

In-situ stress state, $P_x/\sigma_c = P_y/\sigma_c = P_z/\sigma_c = 2.0$

Elastic constants, $E/\sigma_c = 1000.0$ and $\nu = 0.2$

Initital strength paramters, $m_I = 10.0$, $s_I = 1.0$

Residual strength parameters, $m_R = 5.0$, $s_R = 0.0$

Major principal plastic strain at residual, $(\varepsilon_1^p)_R = 2\sigma_c/E$

Flow ratio during softening, $h = -1.5$

Flow ratio at residual, $f = -1.0$ ('f' and 'h' defined in Appendix D)

The FEM mesh used for this validation only models a quarter of the hole circumference, and requires only 1 element in the circumferential direction due to axisymmetric conditions. In the radial direction 10 elements are used to model the domain between $a \leq r \leq 5a$ (where 'a' is the radius of the opening). The infinite domain, defined by $r \geq 5a$ is modelled using an infinite element.

The radial, circumferential and axial stress components predicted from both the FEM and finite difference codes for the case where the inner support pressure is given by $P_a/\sigma_c = 0.1$, are shown in Figure 5.16. It can be seen that the agreement is good and little or no difference exists between the two sets of results. Radius r_A in Figure 5.16 represents the elasto-plastic interface. On moving closer to the wellbore wall the axial stress reduces due to the Poisson effect. On reaching radius r_B the axial stress becomes equal to the circumferential stress, and consequently undergoes a plastic component of strain in the axial direction, as discussed in Section 5.5.3.2. At radii less than r_B the axial and circumferential stresses remain equal.

In Figure 5.17 the prediction of the radial displacement at the wellbore wall is shown for both analyses as a function of support pressure. Again good agreement can be seen.

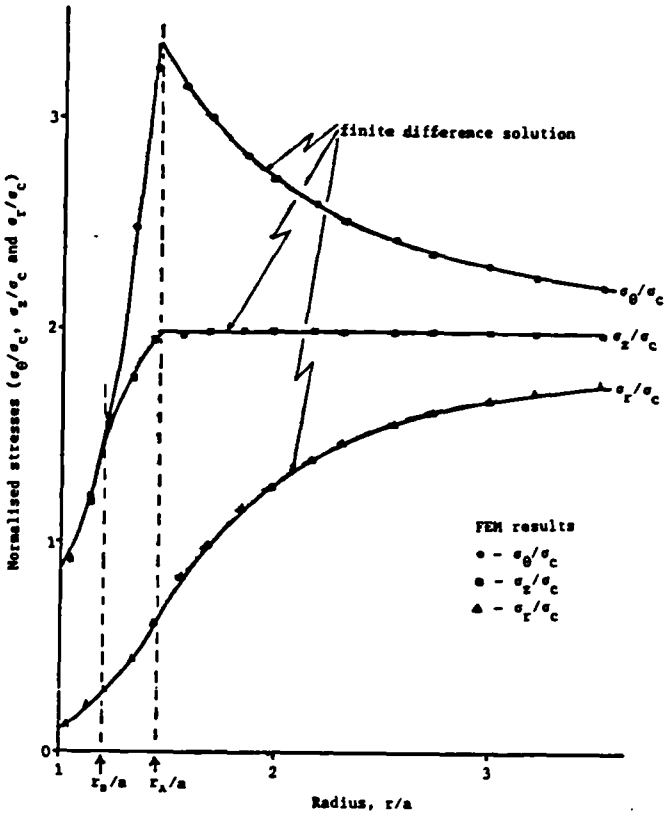


Figure 5.16 Stress state around a circular opening subjected to axi-symmetric loading and plane strain constraints.

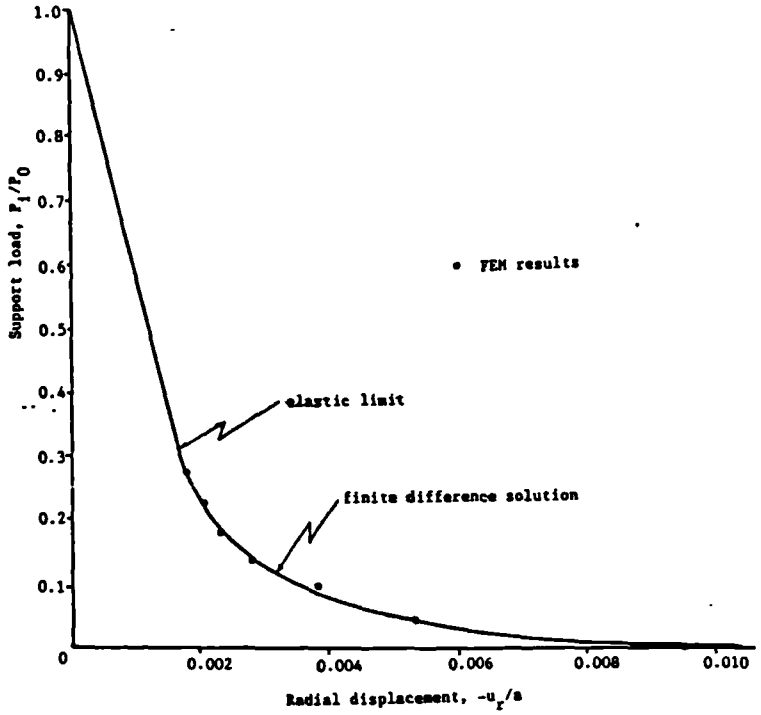


Figure 5.17 Induced dispacements at excavation boundary with reduction in support pressure.

5.5.4 Conclusions on FEM validation

From the three validations carried out using plasticity analysis it can be concluded that the FEM program is satisfactory in the following areas:

1. The iterative procedure for handling perfect plasticity in non-hydrostatic loading conditions.
2. The iterative procedure for analysis of strain softening of the axi-symmetric wellbore.
3. Use of the Tresca, Mohr-Coulomb and Hoek-Brown criteria.
4. Treatment of non-associated flow.
5. Use of associated flow for the Tresca and Mohr-Coulomb criteria.

The main restriction in program validation is in its handling of hardening or softening materials under non-hydrostatic conditions, and in particular the analysis of any plastic behaviour under complete plane strain conditions. Unfortunately there are no analytical solutions for plastic analysis of circular excavations under complete plane strain conditions, although the program has been validated for elastic complete plane strain conditions in Section 3.9.3, Chapter 3. However, despite this limitation in the validation procedures we shall proceed assuming the program is functioning correctly in these areas.

5.6 PARAMETRIC ANALYSIS

In relation to drilling operations, a number of points of interest arising from a stress analysis around a wellbore are:

1. Whether broken or partially broken rock remains in place or spalls away from the wellbore wall.

2. The extent of any radial closure.
3. The extent of any hole enlargement.
4. Dependence of the major axis of broken zones on the in-situ stress field and well azimuth.
5. Whether tensile fracturing occurs.
6. If tensile failure at the wellbore wall results in a fracture extending far into the formation (i.e. lost circulation).

Not all the points above can be determined from the FEM analysis developed in this project. Point 1 is dependent on any changes in the formation-mud cake interaction in the broken zone and the extent of erosion forces set up by circulating the drilling fluid. This is beyond the capabilities of the FEM developed here. Thus, determination of points 2 and 3 are subjective depending on whether it is felt that broken rock remains in place or spalls away. As mentioned before in Section 5.3.6, the program cannot adequately cope with tensile stresses, therefore determination of point 6 is beyond its capabilities. To cater for extension of tensile fractures the program would have to allow for discrete fractures, or at least incorporate a failure criterion specifically developed for tension (e.g. a no tension condition). However, it is possible to determine well pressures at which tension is initiated at the wellbore wall.

In the case of spalling, the program should remove elements of rock from the finite element mesh to adjust to the new wellbore geometry. This is not catered for in the FEM model, although such a procedure is likely to result in the prediction of continued uncontrolled failure.

In view of the above comments the quantitative nature of the FEM is limited in areas where tension and/or significant zones of brittle

failure are predicted. However, this should not prevent us from making an assessment of the severity of various loading conditions by viewing the extent of the broken zones. Thus, the analyses carried out in the remainder of this chapter focus on the effect various factors have on the extent of the broken zone and radial closure. Whether radial closure in broken zones is a true indication of field conditions, and in fact the rock spalls away instead, is left to engineering judgement. A further consideration covered in the parametric study is the azimuth of the major axis of the broken zone. This has important implications in assessing the in-situ stress regime (e.g. Klein and Barr[17]).

5.6.1 Material Models

Two material models are used in this parametric analysis. The first material model is based on the triaxial test results for the sandstone tested by Santarelli[18] and modelled using plasticity in Section 4.7, of Chapter 4. This model and variations of it are used to assess the implications of a number of behaviour law criteria (e.g. differences between using the Hoek-Brown and Mohr-Coulomb criteria).

The second model material is not related to any particular set of triaxial tests, and is simply developed to allow failure at more realistic wellbore depths compared with the Carboniferous sandstone model. This model is used in two studies; (i) an investigation of the effect of weak zones on the resultant plastic region around wellbores and in hollow cylinder testing, and (ii) an investigation of plastic regions around deviated wells.

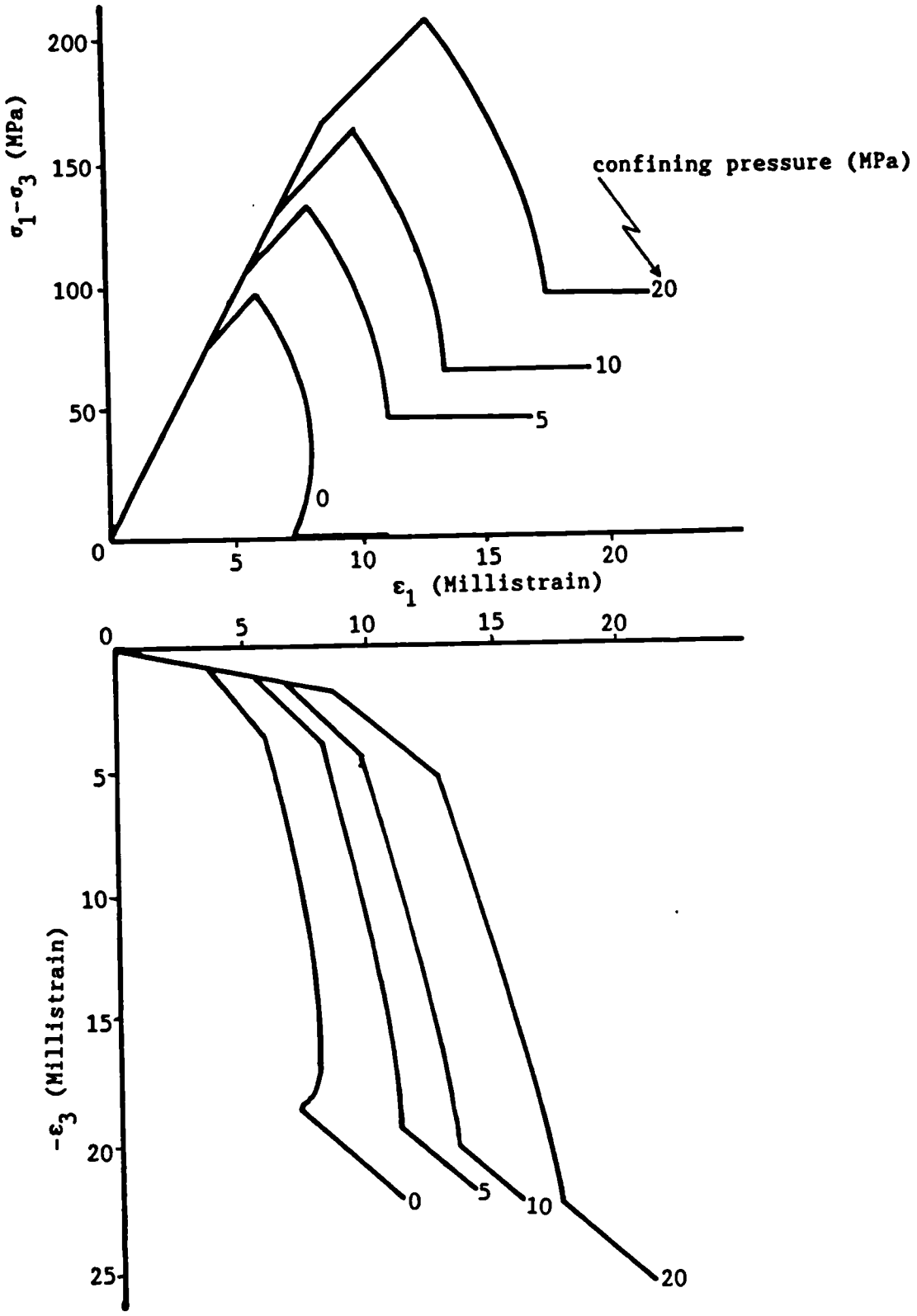


Figure 5.18 Triaxial interpretation of material Model A - 'strong sandstone formation'.

5.6.1.1 Model Material A - 'Strong Sandstone Formation'

This model is, in principle, the Hoek-Brown non-associated flow model for the Carboniferous sandstone tested by Santarelli[18]. The model is broadly described in Chapter 4, with the relevant behaviour law equations and parameters (e.g. strength parameters) defined in Section 4.7.2, Chapter 4. Plots of the triaxial response of the model behaviour are given in Figure 5.18. The material may be considered to represent a strong sandstone formation. However, with a uniaxial strength of 98 MPa (14,000 psi), this sandstone is particularly strong (published values for a U.K. onshore reservoir sandstone are around 40 MPa (6000 psi) - Klein and McLean[30]). Also the testing on the Carboniferous sandstone was carried out on dry samples (Santarelli[18]). If the samples had been saturated in formation fluid the uniaxial strength may have been reduced by as much as 50% (Broch[88]). Thus, it can be concluded that using a model based on tests performed by Santarelli may not be representative of field instability conditions.

Using realistic in-situ stress and wellbore pressure magnitudes, a linear elastic analysis would show that for typical North Sea well depths (2000m to 4000m), little or no failure occurs given this material behaviour. Thus, a parametric study performed under these conditions is of little interest. Two options are open to resolve this problem; (i) scale down the material strengths and corresponding stress-strain data, or (ii) scale up the applied loading (i.e. increase depth). The most realistic option is to scale down the material behaviour, however, this involves complications on exactly which parameters to scale and to what extent. For example if the uniaxial strength is scaled down by 50%, is the plastic strain at residual also scaled down by 50%? Thus, for this model material the simpler though less realistic option (at least for

the majority of present day drilling operations) of scaling up the loading by increasing depth is chosen.

5.6.1.2 Model Material B - 'Weak/Medium Strength Sandstone Formation'

The second model material is not based on any particular laboratory test results. The model has simply been designed to allow failure at more realistic depths and to provide a less brittle strain-softening behaviour than the model defined in Section 5.6.1.1. The model is also simplified by assuming there is no strain hardening. The parameters and equations defining the behaviour law are given below.

Elastic modulus, E = 10,000 MPa, Poisson's ratio, $\nu = 0.2$

Yield criterion - Hoek-Brown

σ_c = 25 MPa

at peak, m = 15.0 s = 1.0

at residual, m = 5.0 s = 0.01

Principal plastic strain at residual, $(\varepsilon_1^p)_R$, given by

$$(\varepsilon_1^p)_R = 3.0 + 0.4\sigma_3 \quad \text{(in millistrain)}$$

Flow is non-associated and the flow ratios are given by

$$\text{during softening,} \quad \frac{\partial \varepsilon_3^p}{\partial \varepsilon_1^p} = -2.4 - \frac{2.6}{1+0.1\sigma_3}$$

$$\text{residual strength,} \quad \frac{\partial \varepsilon_3^p}{\partial \varepsilon_1^p} = -1.2$$

Figure 5.19 gives the triaxial interpretation of the model behaviour. A shale of moderate strength may exhibit stress-strain characteristics similar to Figure 5.19 if allowed sufficient time during loading to behave in a drained fashion. However, in practice, investigation of shale instabilities without considering loading induced

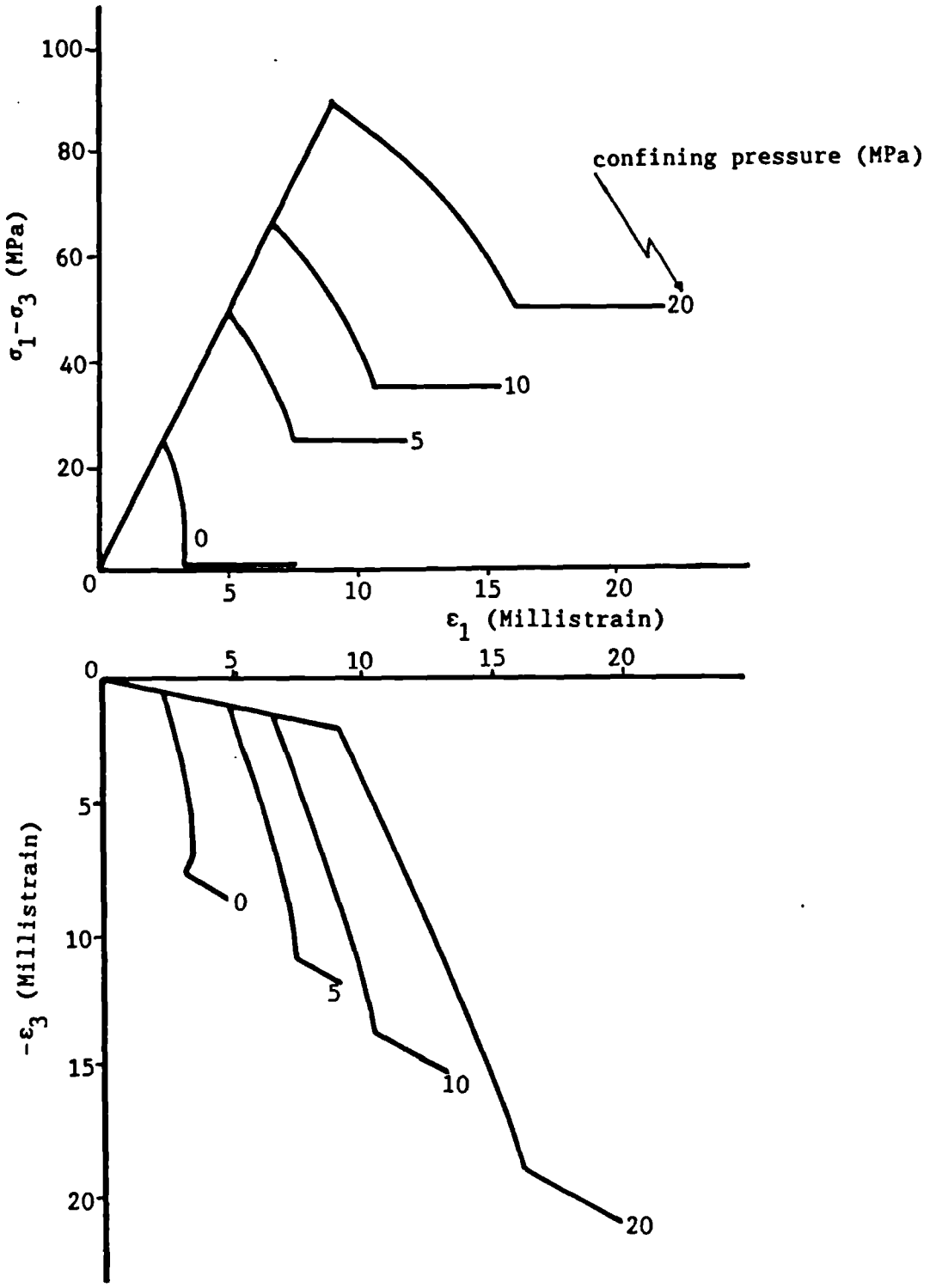


Figure 5.19 Triaxial interpretation of material Model B - 'weak-medium strength sandstone formation'.

pore pressure gradients is unlikely to be realistic. The FEM program makes no attempt at accounting for loading induced pore pressure, thus, the model material is considered to represent a weak-medium strength sandstone formation.

Both interpretative and numerical considerations were important factors in choosing this material model. From the point of interpreting the results, then a weaker material allows prediction of instability at more realistic well depths. From a numerical consideration a reduction in brittleness results in less consumption of computer time and a reduction in susceptibility to numerical instability.

5.6.2 Plastic Behaviour Law Study

This study uses the stronger sandstone material model defined in Section 5.6.1.1 to assess the significance, or otherwise, of various types of behaviour laws and criteria. The model is described as a Hoek-Brown, non-associated flow, elasto-trilinear plastic behaviour model, and shall be referred to as model A1. Three variations of this model are considered which are as follows.

Model A2 - Hoek-Brown, non-associated flow, elasto-bilinear plastic behaviour model.

Model A3 - Hoek-Brown, associated flow, elasto-trilinear plastic behaviour model.

Model A4 - Mohr-Coulomb, non-associated flow, elasto-trilinear plastic behaviour model.

In model A2 the trilinear plastic behaviour is reduced to a bilinear plastic behaviour by ignoring the strain hardening portion. Thus, the elastic limit is assumed coincident with peak strength.

Model A4 is defined using the Mohr-Coulomb strength parameters for the Carboniferous sandstone given in Figure 4.16, Chapter 4. The remaining behaviour law equations are the same as for model A1.

5.6.2.1 In-situ Stress Conditions

The in-situ stress regime taken for this parametric study is defined by the following:

Vertical stress gradient	- 0.023 MPa/m (1.00 psi/ft)
Max. horizontal stress gradient	- 0.022 MPa/m (0.95 psi/ft)
Min. horizontal stress gradient	- 0.018 MPa/m (0.80 psi/ft)
Formation pressure gradient	- 0.010 MPa/m (0.45 psi/ft)
Depth	- 8,000m (26,400ft)

Therefore the in-situ stresses at the depth given are

Vertical stress,	σ_v = 185 MPa (26,400 psi)
Max. horiz. stress,	σ_H = 176 MPa (25,100 psi)
Min. horiz. stress,	σ_h = 148 MPa (21,100 psi)
Formation pressure,	P_F = 83 MPa (11,900 psi)

5.6.2.2 Wellbore Pressure

The wellbore pressure is the simplest parameter that operations have control over, therefore the majority of the parametric study that follows considers the wellbore pressure as a variable (as with the elastic parametric study presented in Section 2.8, Chapter 2). A lower

bound limiting value for the wellbore pressure is for the case of balanced wellbore and formation pressures. Underbalance conditions are not considered, since a pore fluid pressure gradient would be initiated resulting in fluid flow into the wellbore; cases of fluid flow are not catered for in this FEM coding. In overbalance conditions it is assumed that the mud cake is effectively impermeable relative to the surrounding formation, thus preventing any mud filtrate flow into the formation.

5.6.2.3 Results

Assuming the maximum horizontal stress is coincident with the y-axis then Figure 5.20 defines the loading conditions for this problem in terms of effective stresses. The effective stress relationships assumed in the elastic analyses in Chapter 2 (see Section 2.3) are assumed to hold in the FEM coding. Thus, the effective stress loading given in Figure 5.20 is simply found by subtracting the formation pressure from the principal in-situ stresses in terms of total stress. The overbalance pressure is given by the difference between the well pressure, P_W, and the formation pressure, P_F.

The FEM mesh for this problem need only define a 1/4 of the problem shown in Figure 5.20 by utilizing the 2 symmetry planes. The domain between $a \leq r \leq 5a$ is modelled using 60 finite elements (6 circumferential, 10 radial) with 6 infinite elements modelling the unbounded domain defined by $r \geq 5a$.

The extent of the plastic zones for the 4 different material models (A1, A2, A3 and A4) are given in Figures 5.21-5.24. Material model A2 does not exhibit a strain hardening behaviour, thus no hardening zone is shown in Figure 5.22.

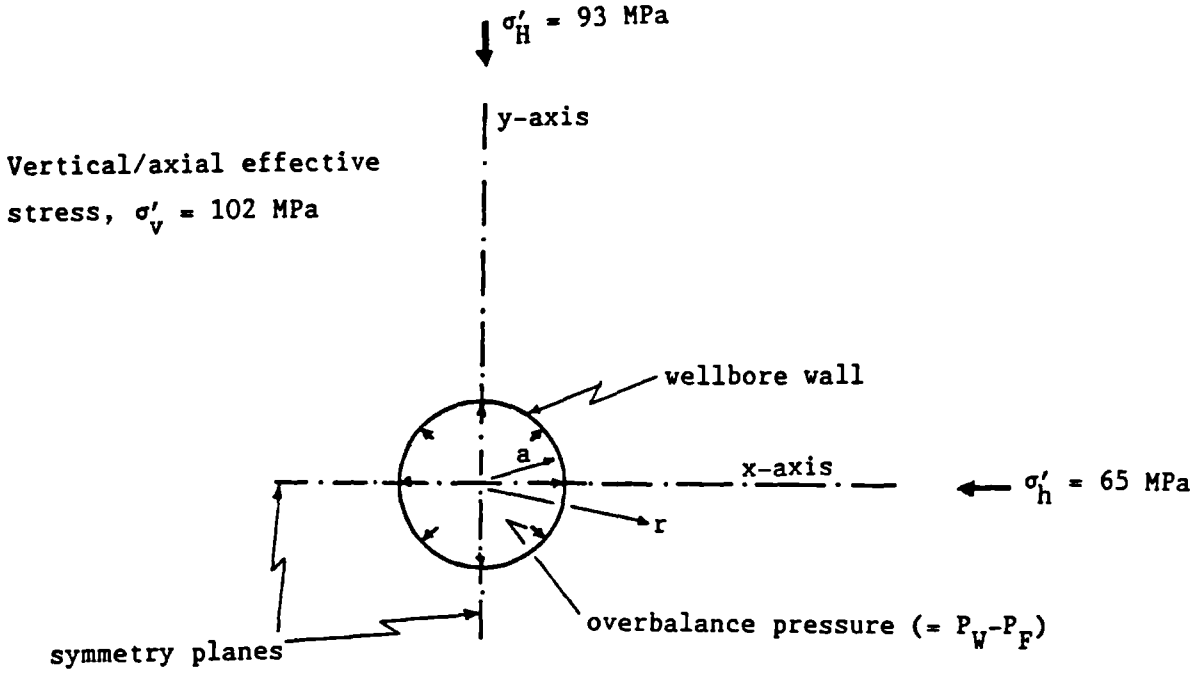


Figure 5.20 Applied loading in terms of effective stresses and overbalance pressure for material behaviour law study.

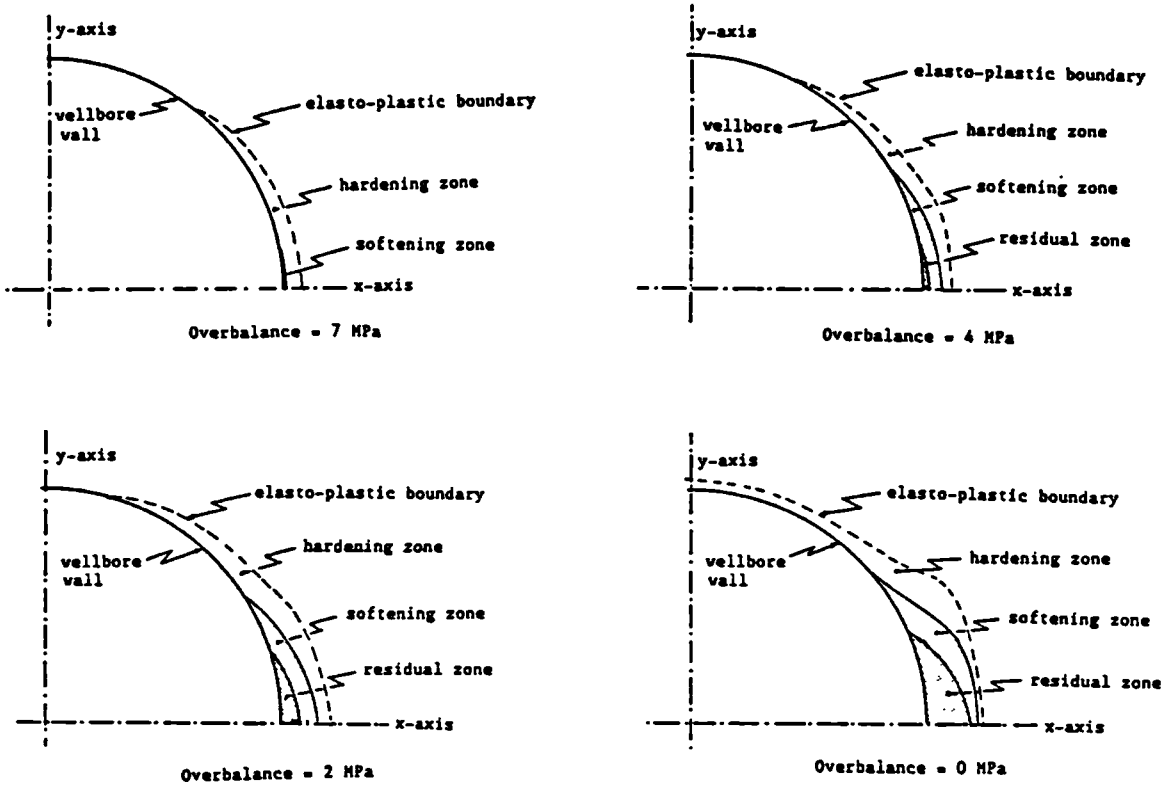


Figure 5.21 Plastic zones around a wellbore subjected to loading as per Figure 5.20, using material Model A1.

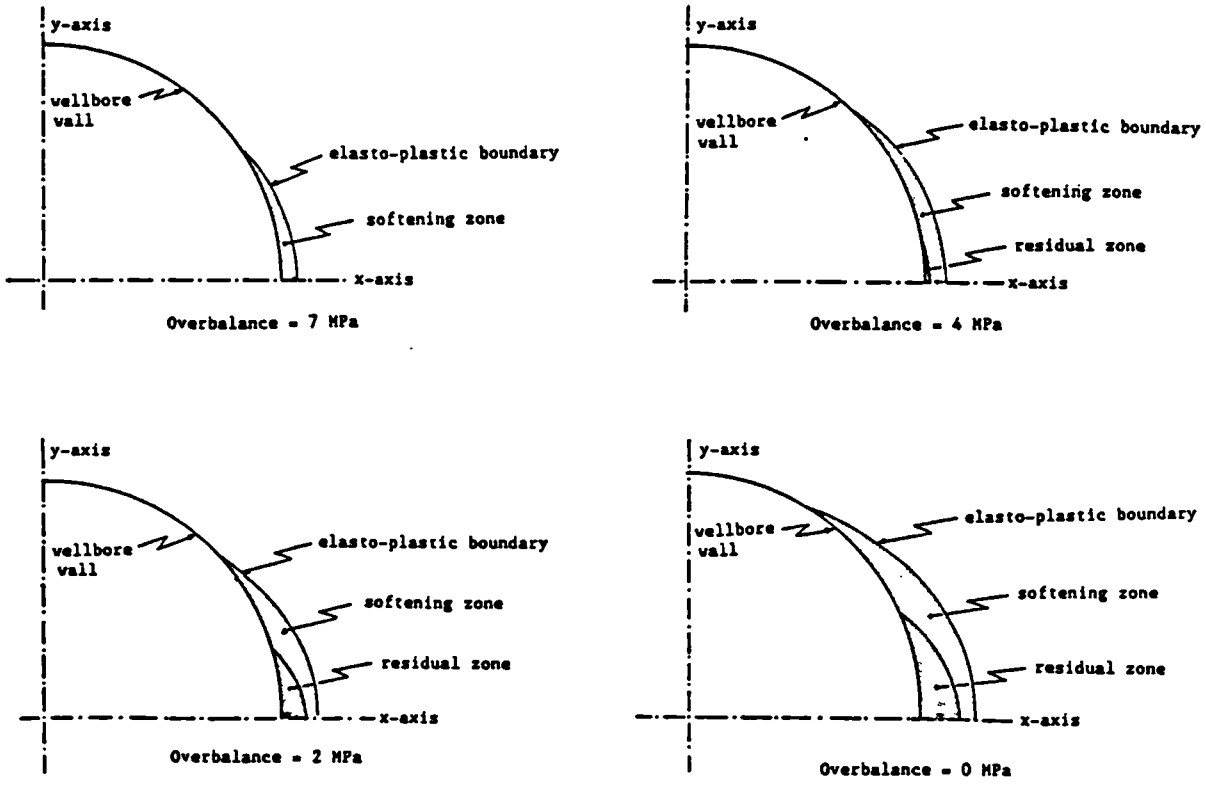


Figure 5.22 Plastic zones around a wellbore subjected to loading as per Figure 5.20, using material Model A2.

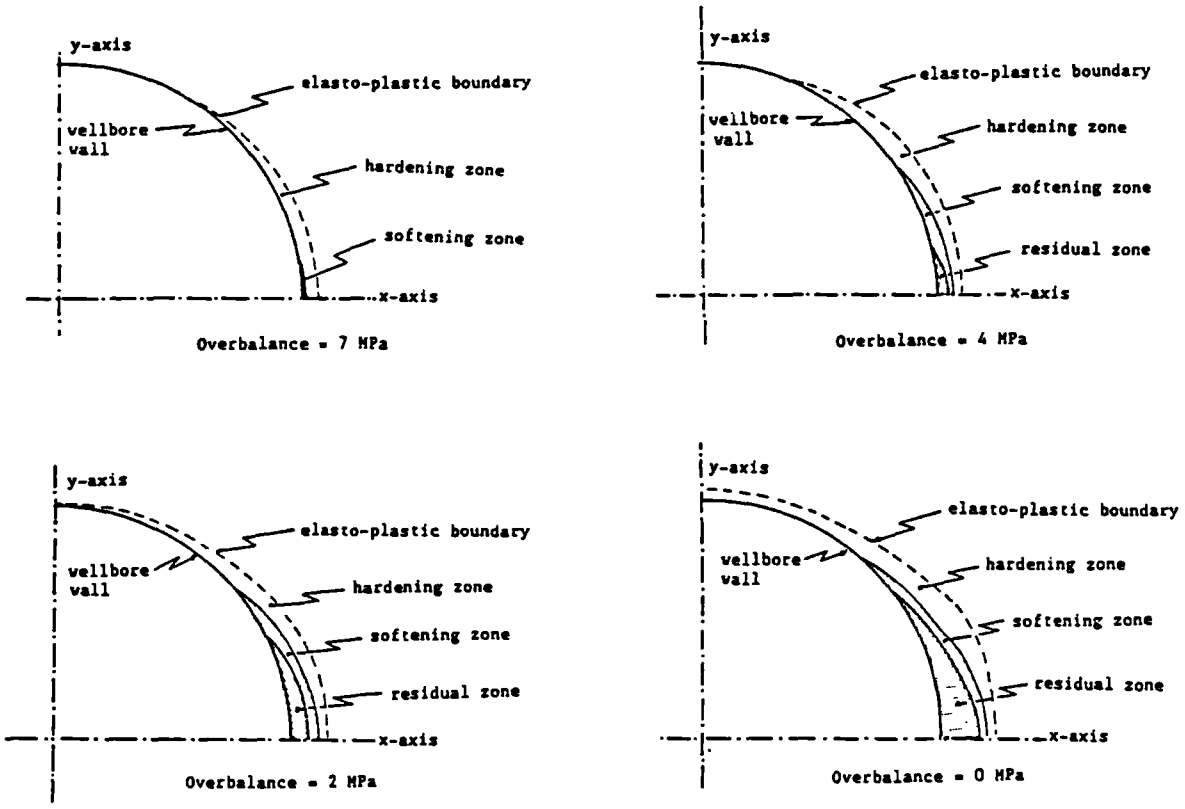


Figure 5.23 Plastic zones around a wellbore subjected to loading conditions as per Figure 5.20, using material Model A3.

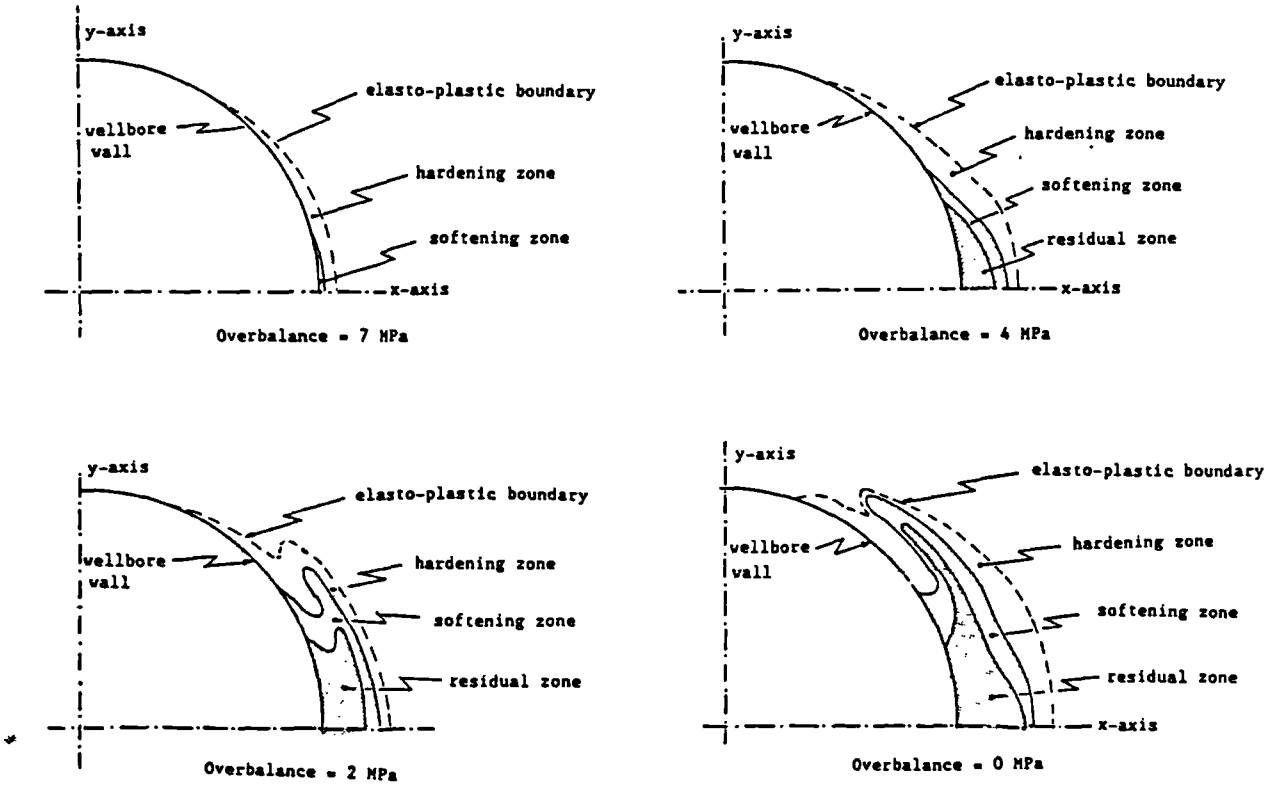


Figure 5.24 Plastic zones around a wellbore subjected to loading conditions as per Figure 5.20, using material Model A4.

Comparison between Figures 5.21 and 5.22 shows the effect of ignoring the strain hardening portion. It can be seen that model A2 (no hardening) has a larger softening zone than model A1, but there is little difference between the residual zones for the two models. If failure is considered as the point at which an element of rock exceeds its peak strength, then model A1 is only just failing at an overbalance pressure of 7 MPa, whereas model A2 shows a significant zone of failure at the same overbalance. Thus, neglecting the hardening portion effectively reduces the resistance to failure of the model, but does not considerably effect the general shape of the broken zone.

Comparison between Figures 5.21 and 5.23 shows the difference between using associated and non-associated flow rules (the non-associated flow is defined in Section 4.6.3, Chapter 4). In this case the transition from peak strength to residual strength is considerably sharper for the associated flow (Figure 5.23) resulting in a narrow softening zone. However, the strength of the models and general shape of the residual zones are similar.

The most notable changes in the model behaviour is for the Mohr-Coulomb model shown in Figure 5.24. Here the shape of the broken and partially broken zones are considerably different for model A4 for low overbalance pressures (0 and 2 MPa). For higher overbalance pressures the broken zone is closer to an 'elliptical' shape, however, the extent of the broken zone at 4 MPa overbalance is considerably greater for model A4 in comparison with the other 3 models. A further factor in using the Mohr-Coulomb material was inability to attain convergence. A convergence ratio (equation (49)) of 0.5% was specified throughout, however, after 30 iterations on the final load step it was still only possible to attain ratios of 3.1% and 1.8% for overbalances of 0 and 2

MPa respectively. In addition, anomalous tensile stresses were predicted in some regions of the residual zone.

The reason for the unusual response of the Mohr-Coulomb material can be explained by considering its ability to provide support after having lost cohesive strength. The equations presented in Appendix C for the stress state within a perfectly plastic material are equally applicable to a residual strength zone, since residual strength is a particular case of perfect plasticity. Thus, in the residual zone we have for the radial stress

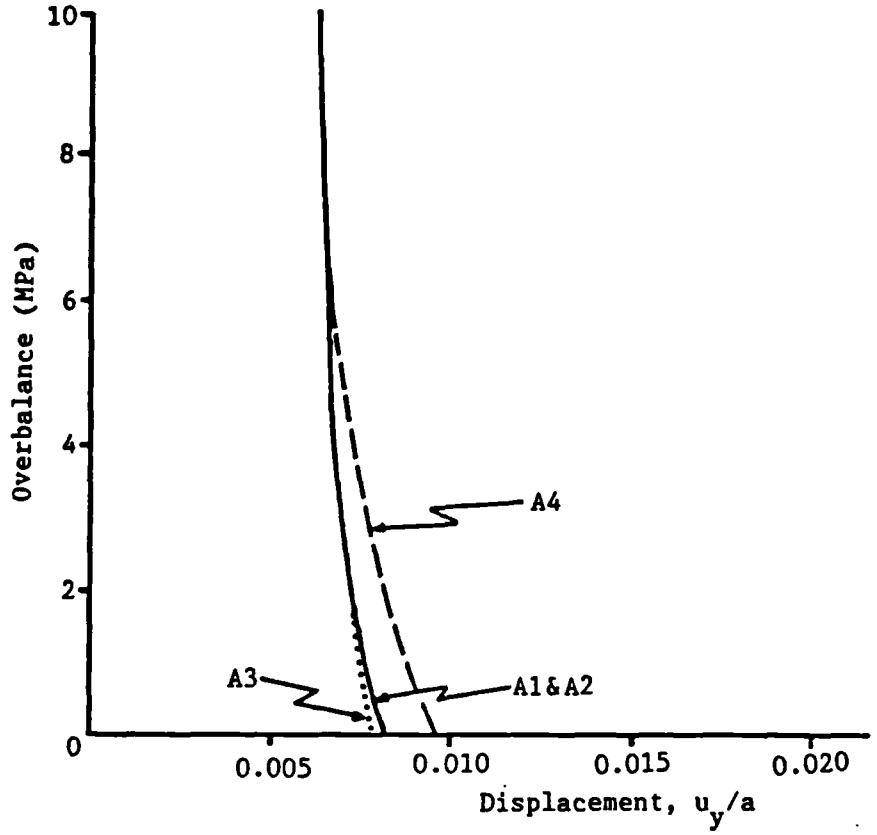
$$\sigma_r = (P_a + c.\cot\phi)\left(\frac{r}{a}\right)^{\alpha} - c.\cot\phi$$

where the relevant parameters in the above equation are defined in Appendix C.

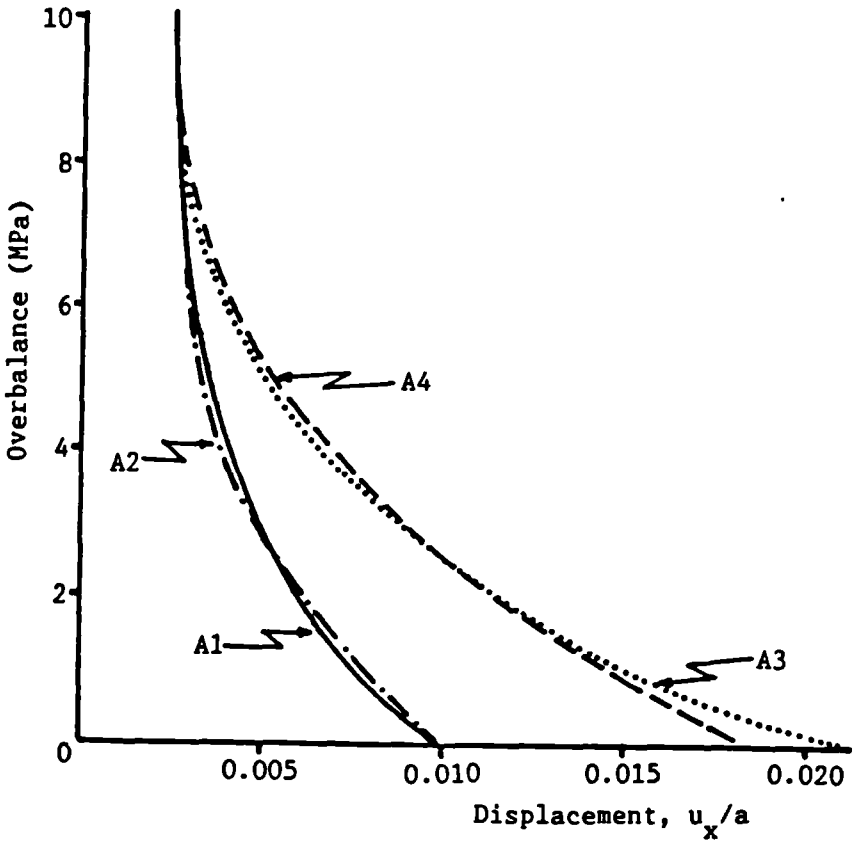
It can be seen from inspection of the expression for σ_r that as the internal pressure, P_a, and the cohesion, c, tend to zero, then σ_r tends to zero for all radii, r, and hence the material loses its ability to provide support. However, this is not the case for a Hoek-Brown material. The equivalent expression for the radial stress for a Hoek-Brown material can be shown to be (see Brown et al[49])

$$\sigma_r = P_a + \sqrt{(m\sigma_c P_a + s\sigma_c^2)}\left[\ln\left(\frac{r}{a}\right)\right] + \frac{m\sigma_c}{4}\left[\ln\left(\frac{r}{a}\right)\right]^2$$

As the cohesion (represented by 's') and P_a tend to zero then the first two terms in the above expression tend to zero. However, the last term remains positive definite. Thus, even at zero internal pressure and with no cohesive strength the Hoek-Brown material is able to provide some support around a circular opening, whereas a Mohr-Coulomb material is unable to sustain load. This difference in 'interlocking' capabilities between the two criteria explains the differences in the predicted



(a) Radial displacement along y-axis



(b) Radial displacement along x-axis

Figure 5.25 Variation of radial displacement as a function of overbalance pressure and material model type.

plastic zones shown in Figures 5.21 and 5.24.

The predicted displacements for the four model materials are shown in Figure 5.25. The radial displacements along the y-axis and x-axis (see Figure 5.20) are shown as a function of overbalance pressures in Figures 5.25a and 5.25b respectively. Apart from model A4 there is little or no difference in the radial closure along the y-axis between the other material models. The higher displacement for the Mohr-Coulomb material (A4) is a result of its inability to provide support in the residual region at low overbalance pressures.

Along the x-axis the radial closures for materials A1 and A2 are similar. At higher overbalance pressures A1 shows a slightly greater closure than A2, since model A1 yields at a lower stress level. However, as the overbalance pressure is further reduced model A2 yields and immediately undergoes strain softening while A1 is still undergoing strain hardening. Eventually as the residual zone increases with continued reduction in overbalance the difference in closure between the two models is negligible. The Hoek-Brown associated flow model and Mohr-Coulomb model (A3 and A4 respectively), both show far greater closure along the x-axis than the other two models. As discussed in Section 4.7, Chapter 4, higher strains may be anticipated when using associated flow rules. The results for model A4 are again due to its inability to provide support under these conditions.

If we assumed the nominal diameter of the wellbore to be 12 1/4 inches then the maximum radial closure would be around 0.06 inches for models A1 and A2 and 0.12 inches for models A3 and A4. Radial closures of these magnitudes are unlikely to create any problem during drilling. This result is to be expected, since the occurrences of stuck drill string resulting from hole closure in sandstones is extremely uncommon.

Sandstones, in general, do not give many instability problems during drilling. However, when stuck drill string occurs in sandstone formations it will usually be due to differential sticking (Rabia[6]) or large cavings from spalling.

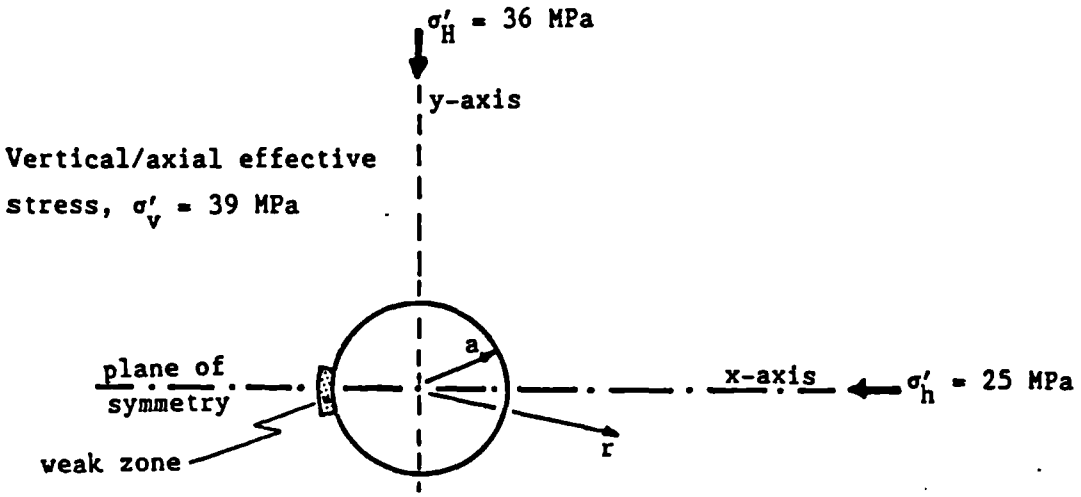
5.6.3 Keyseating or Stress Induced Failure?

This study looks at the influence of a weaker zone of material around the wellbore wall on the propagation of the plastic zone in an anisotropic stress field. The weaker rock is assumed to exist at one of the critically stressed zones (see Figure 5.26a). Without the weak zone, propagation of the plastic region would be symmetric about both the x-axis and y-axis. With the introduction of the weak zone only symmetry about the x-axis can be utilized.

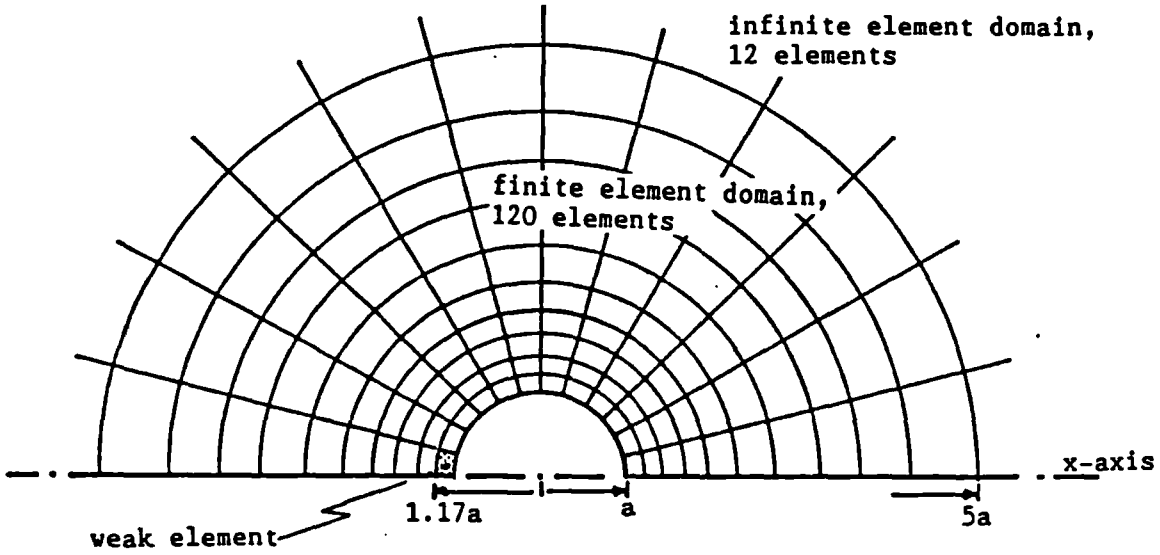
The stresses given in Figure 5.26a are equivalent to a depth of 3,000m (10,000ft) assuming the same stress gradients given in Section 5.6.2.1.

The bulk of the rock mass around the wellbore is defined by material model B given in Section 5.6.1.2 and interpreted in Figure 5.19. The weaker zone of material is assumed partially broken before excavation, such that the strength parameters are half that of the surrounding rock. The triaxial representation of the weaker material is shown in Figure 5.27.

The purpose of this problem is to determine whether the plastic region developed with a weak zone is markedly non-symmetric. If this is the case, it has implications in our ability to distinguish between stress induced instability and 'key seating' (see Figure 1.7, Chapter 1, and Klein and Barr[17]).



(a) loading conditions



(b) FEM mesh

Figure 5.26 Loading consitions and FEM mesh for analysis of the effect of a weak zone on the plastic region around a wellbore in an anisotropic stress field.

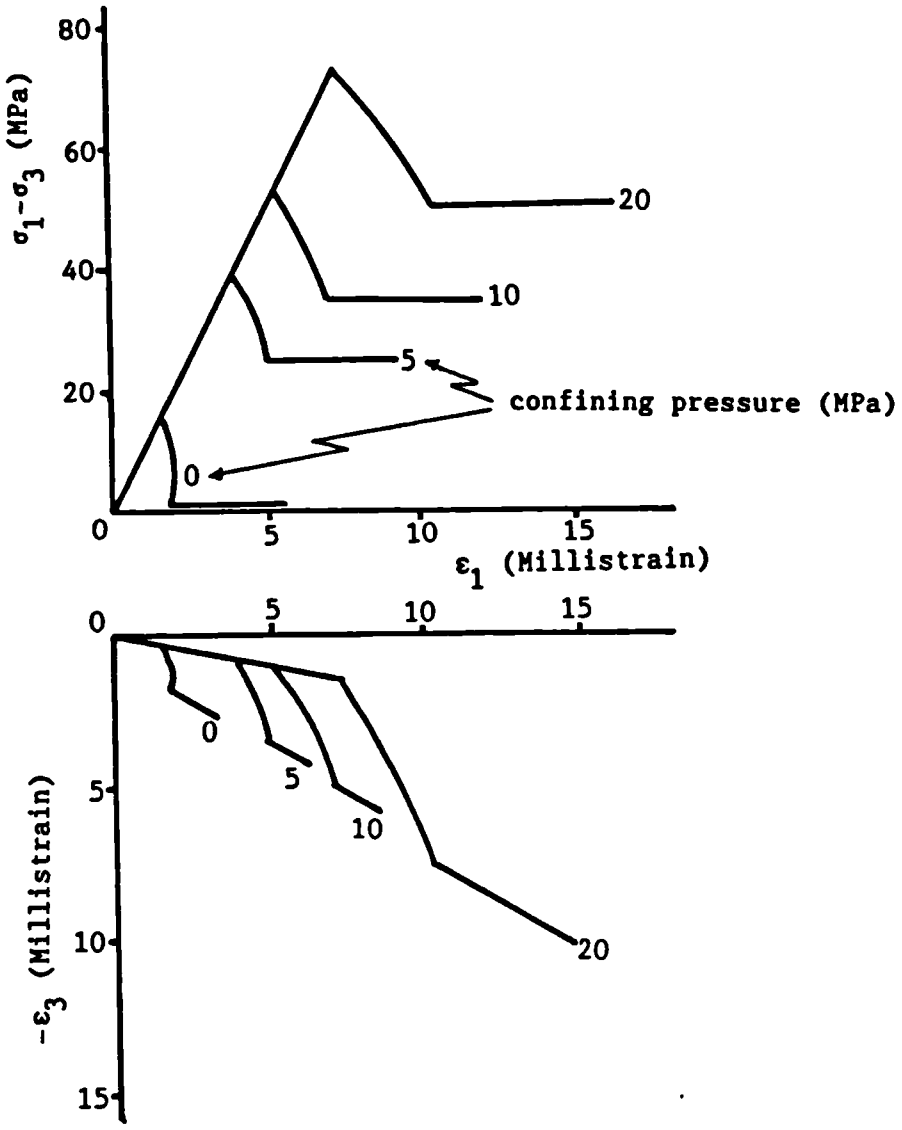
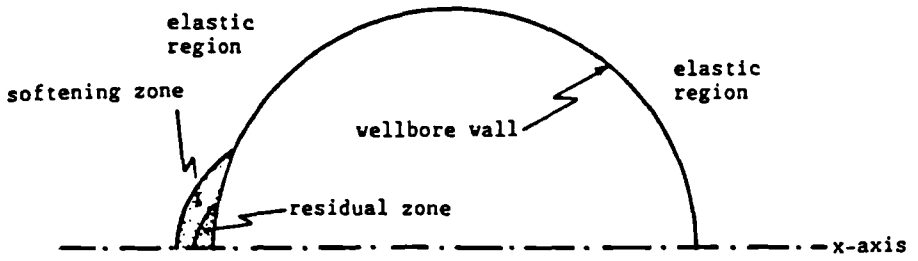
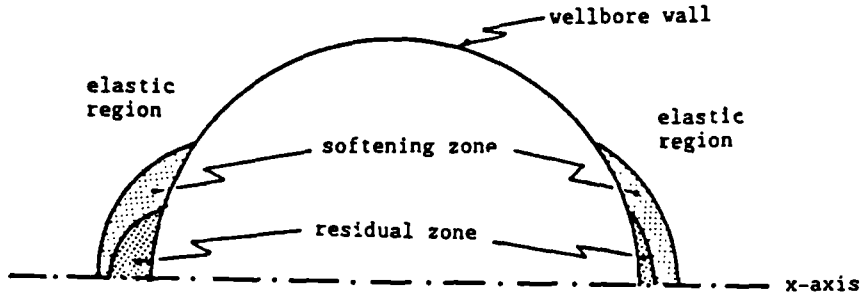


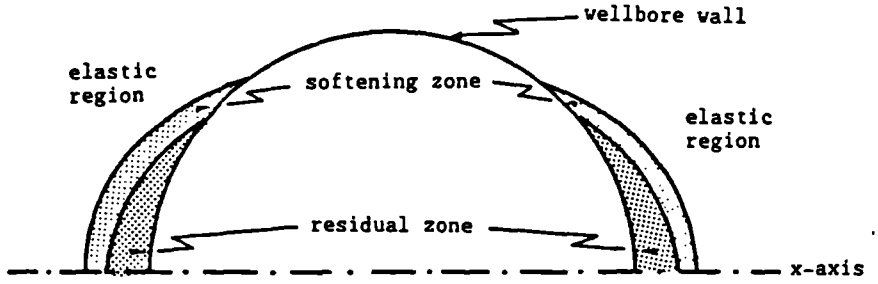
Figure 5.27 Triaxial interpretation of model material used to simulate a a weak zone at the wellbore wall.



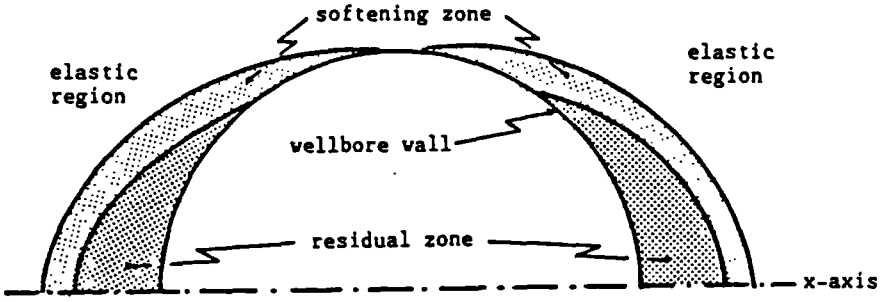
Overbalance = 7 MPa



Overbalance = 4 MPa



Overbalance = 2 MPa



Overbalance = 0 MPa

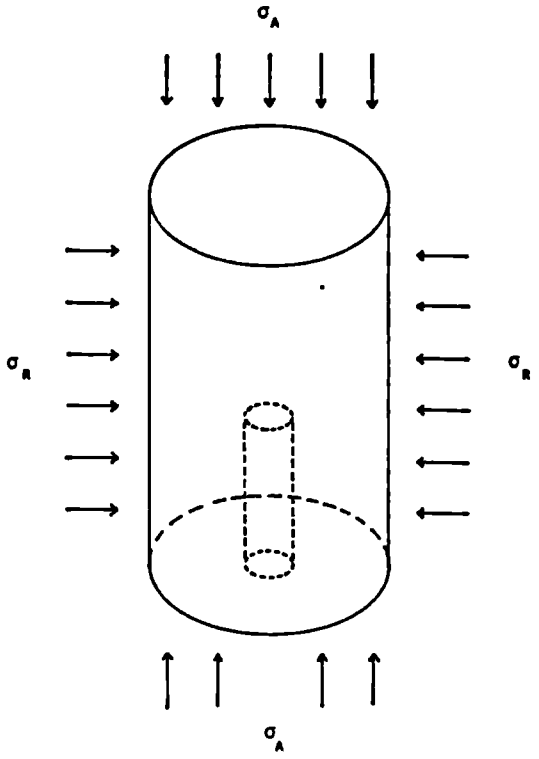
Figure 5.28 Plastic zones developed around a wellbore in an anisotropic horizontal stress field, with the presence of a weak zone.

Figure 5.28 shows the variation of the plastic zone in this study as a function of the overbalance pressure. At 7 MPa overbalance, failure has only occurred in the weaker material. At 4 MPa failure has occurred on both sides of the wellbore, although the resulting broken region is non-symmetric. At lower overbalance pressures (0 and 2 MPa) the regions of broken rock are virtually symmetric about the y-axis. Thus, as the severity of hole enlargement increases, the more likely stress induced instability will result in an 'elliptical' shaped hole irrespective of points of weakness around the wellbore wall. Conversely, in cases where large hole enlargement has occurred only on one side of the well, this is less likely to be indicative of stress induced failure.

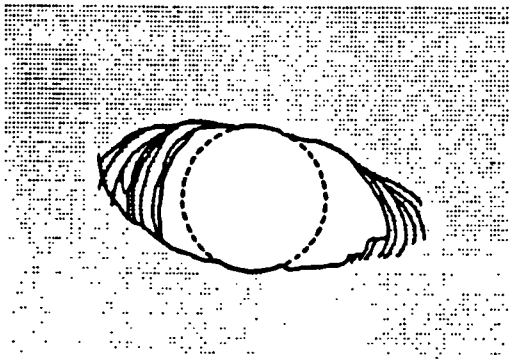
It is worth stressing that the conclusions above are for the ideal situation of a vertical wellbore in an isotropic material. The same results cannot be assumed for a deviated well, or a vertical well in a steeply dipping laminated formation.

5.6.4 Effect of a Weak Zone around a Circular Opening under Axisymmetric Loading

A number of laboratory simulations of instability around a circular opening have been published (e.g. Santarelli,[18] Barton et al[89]), the majority of which are performed on cylinders of rock with an internal bore (Santarelli[18]) or cavity (Fjaer et al[90]). For these tests the lateral stress field is axisymmetric (Figure 5.29a). However, for many of the tests the resulting failed zone around the opening is 'elliptical' (Figure 5.29b) despite the relatively homogeneous and isotropic nature of the rocks used. The purpose of this study is to see if a non-axisymmetric failed zone is developed with the presence of a



(a) applied loading conditions



(b) resultant failure around circular cavity

Figure 5.29 Elliptical failure around circular cavity in a sample of Red Wildmoor sandstone subjected to axisymmetric loading (after Fjaer et al[90]).

weak zone around (i) a vertical wellbore in an isotropic horizontal stress field, and (ii) around the bore of a hollow cylinder where the loading is applied a finite distance from the centre of the sample. In both studies model material B, defined in Section 5.6.1.2, is used.

5.6.4.1 Case of a Vertical Wellbore

The applied loading and location of the weak zone is similar to that depicted in Figure 5.26a, except in this case both the horizontal stresses (σ'_H and σ'_h) are equal and taken to be 36 MPa.

The FEM mesh is the same used in Section 5.6.3 and given in Figure 5.26b.

The resulting plastic zones developed as a function of overbalance pressure are given in Figure 5.30. At an overbalance of 7 MPa only the weak element has failed. On reducing the overbalance pressure a larger region around the weak element has failed, however, the majority of the stronger rock adjacent to the wellbore wall has also undergone failure. At zero overbalance pressure the failed region has extended all the way around the well and appears axisymmetric. At no stage during the reduction of the wellbore pressure does a failed zone diametrically opposite the weak zone appear similar to conditions shown in Figure 5.29b.

5.6.4.2 Case of a Hollow Cylinder

For the hollow cylinder example the same external loading conditions as above are assumed. However, the loads are now applied to the outer surface of the cylinder and not at infinity. In this case the sample is assumed dry, or if saturated, then under drained conditions.

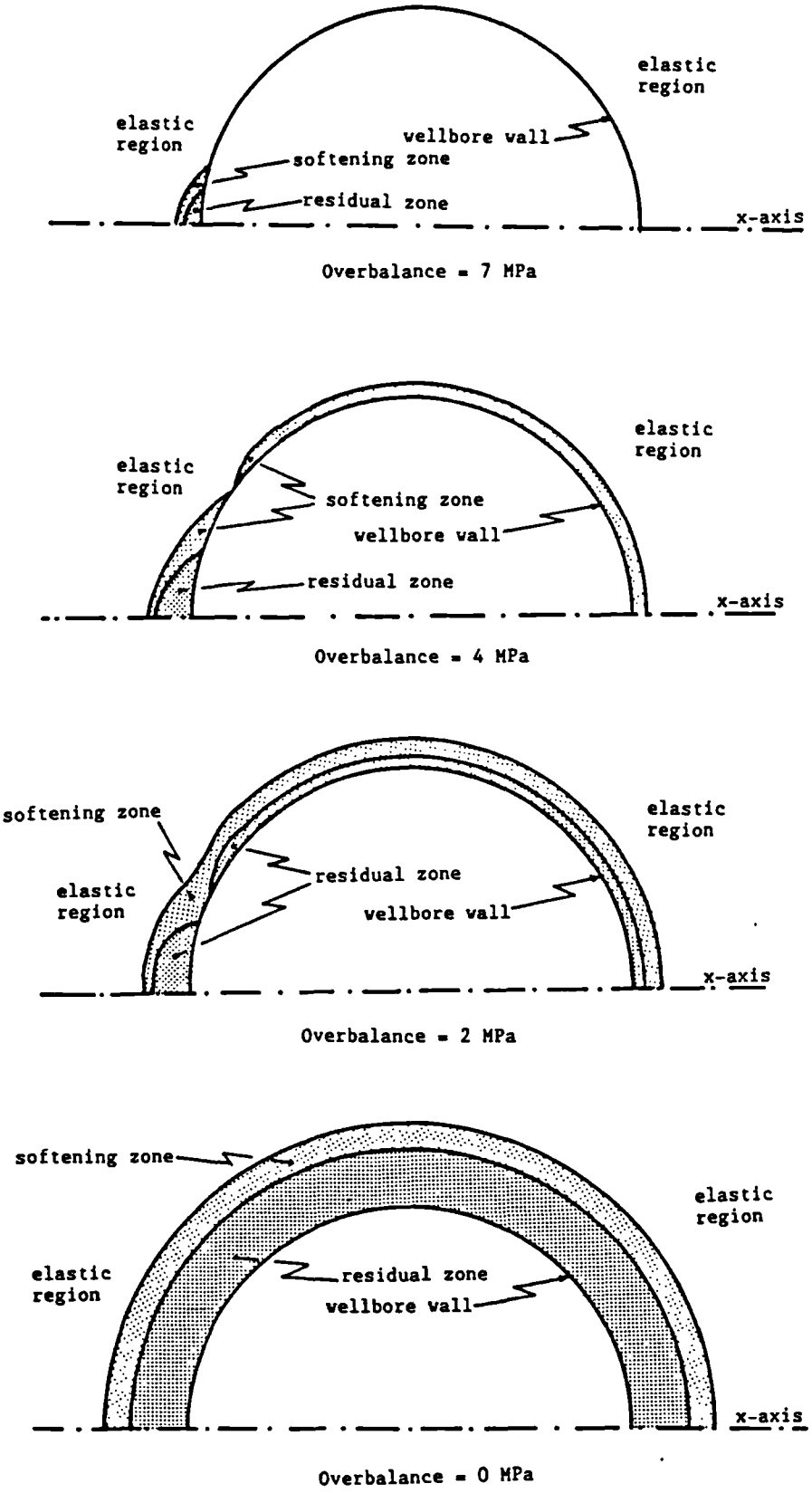


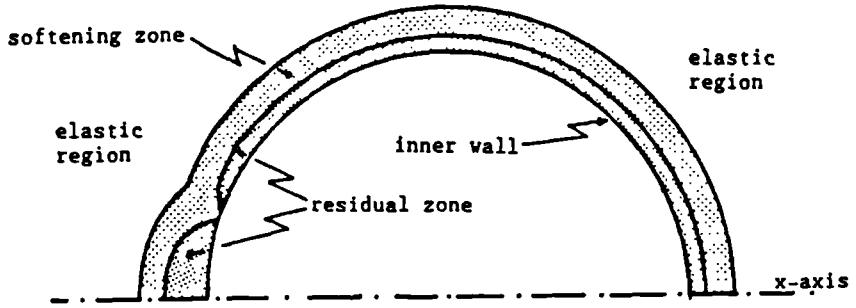
Figure 5.30 Variation of plastic zones around a vertical wellbore in an isotropic horizontal stress field with the presence of a weak zone.

Thus, the total and effective applied pressures are equivalent. The internal pressure is maintained constant at 2 MPa.

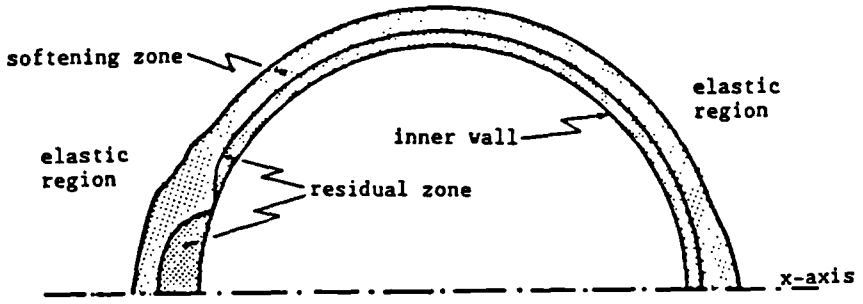
The density of elements used in this analysis is the same as before. However, infinite elements are not used and the location of the outer boundary is progressively reduced to model a reduction in the thickness of the hollow cylinder wall.

Variation of the plastic region as a function of the cylinder external and internal radii ratio (R/a) is shown in Figure 5.31. At a ratio of 4.3 the resultant plastic region is only marginally greater than that for the unbounded domain of the wellbore (Figure 5.30, overbalance = 2 MPa). As the ratio is reduced to 3.6 and 3.1 there is a slight effect on the plastic state diametrically opposite the weak zone, although still nothing like the response shown in Figure 5.29b. At a ratio of 2.6 the region of failed material is 'elliptical' indicative of laboratory findings in hollow cylinder testing. Also, the failed region at 90° to the weak zone is less than in the other 3 cases, indicating a reduced stress concentration here as a result of the increased concentration along the x-axis.

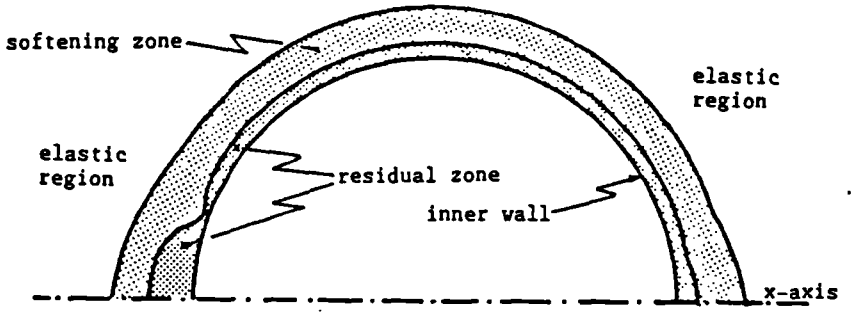
The above findings are not in agreement quantitatively with the Doddington sandstone results of Santarelli[18] where R/a was equal to 4, and the resulting failed regions were elliptical. However, a Gebdykes dolomite, also tested by Santarelli did give an axisymmetric failure. Thus, the resultant shape of the failed zone is a function of the material properties. A number of other factors may contribute to differences between a numerical prediction of failed zones and the laboratory findings. These factors are listed below. (Note: only the shape of the failed zone is considered here. The stress level at which failure occurs is considered later in Chapter 6).



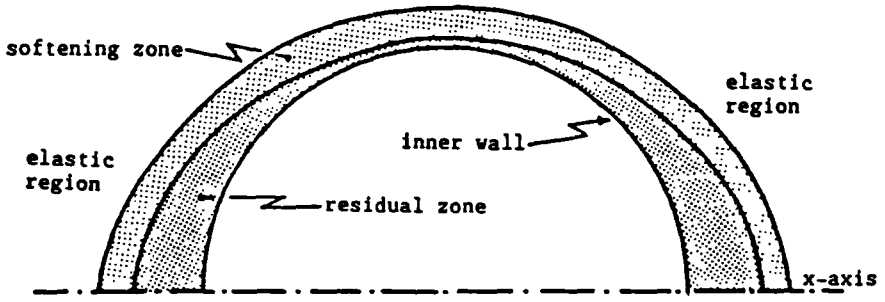
Boundary ratio, R/a = 4.3



Boundary ratio, R/a = 3.6



Boundary ratio, R/a = 3.1



Boundary ratio, R/a = 2.6

Figure 5.31 Variation of plastic zones around a hollow cylinder with the presence of a weak zone for various boundary ratios (R/a).

1. The FEM analysis does not allow for the removal of broken rock, whereas, in the laboratory studies failed rock could spall away from the wall of the sample.
2. The loading paths followed in the laboratory and in the FEM analysis are different. The paths followed are

   (i) in the laboratory no internal pressure is applied and the external pressure is increased to induce failure,

   and (ii) in the FEM the external loading is maintained at a constant pressure and the internal pressure progressively reduced to induce failure.

   If the second loading path is used in laboratory testing, then failure of the sample would occur while elements of rock at the internal wall are still under a confining pressure. This loading path would help to prevent rock spalling while undergoing failure, thus allowing some support from failed elements. A test performed under these conditions may reduce the accentuated stress concentrations resulting from removal of rock chips.
3. The FEM assumes a homogenous continuum in the failed region, and strength and flow criteria are based on triaxial test results. The actual failure around circular openings may violate these assumptions.

5.6.4.3 Conclusions

In conclusion laboratory testing of hollow cylinders subjected to axisymmetric loading often results in an elliptical failed region. These findings are likely to be due to natural variations in strength of rock elements around the internal wall. This type of failure is not predicted

by the FEM in the case of a hole in an infinite medium. In the case of hollow cylinders, prediction of elliptical failed zones is dependent on the boundary ratio (R/a). Although not conclusive, these findings may indicate that the hollow cylinder results are a function of boundary conditions and loading path, in addition to material properties.

5.6.5 Plastic Regions Developed around Deviated Wells

Hole ovality resulting from spalling of broken rock around wellbores is now increasingly used to infer maximum and minimum horizontal stress directions (e.g. Klein and Barr[17]). The application of this technique is generally restricted to vertical, or near vertical wellbores in horizontally bedded formations. As the deviation of the wellbore increases then a number factors other than horizontal stress directions may influence the resulting hole shape. Some of these factors are listed below.

1. As deviation increases then occurrences of 'keyseating' become more prevalent. However, these can often be distinguished from breakout resulting from in-situ stress redistribution as mentioned in Section 5.6.3.
2. With increased deviation in bedded formations, then the assumption of an isotropic rock mass with respect to both elastic and strength parameters becomes less realistic.
3. As deviation increases the orientation of the failed zone becomes less dependent on the horizontal stress directions and more dependent on the vertical stress.

5.6.5.1 Problem Definition

This study looks at the orientation and extent of the failed zone around a wellbore as a function of deviation for a well deviated in a particular direction. The stress state assumed is again equivalent to a depth of 3,000m (10,000ft) corresponding to the stress gradients given in Section 5.6.2.1. In addition to stress magnitudes, it is also necessary to give stress and wellbore directions when analyzing deviated wells. The following summarizes the assumed conditions.

Vertical stress, σ_v = 70 MPa (10,000 psi)

Max. horiz. stress, σ_H = 67 MPa (9,500 psi) - Direction NW-SE

Min. horiz. stress, σ_h = 56 MPa (8,000 psi) - Direction NE-SW

Formation pressure, P_F = 31 MPa (4,500 psi)

Well pressure, P_W = 33 MPa (4,800 psi)

Well direction - North

Well deviations - 0°, 20°, 40°, 60°, 80° and 90°

Subtracting the formation pressure gives in terms of effective stresses

σ'_v = 39 MPa (5,500 psi)

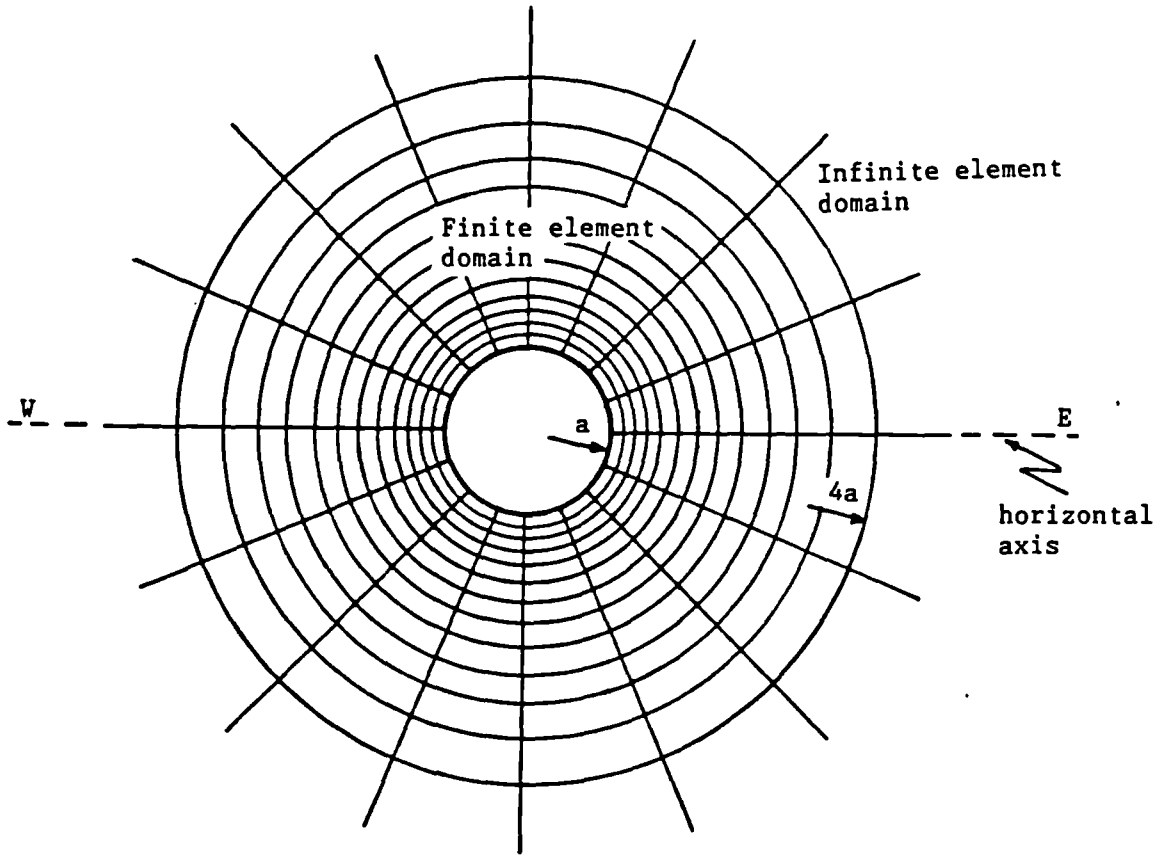
σ'_H = 36 MPa (5,000 psi)

σ'_h = 25 MPa (3,500 psi)

and an overbalance pressure of 2 MPa (300 psi)

The formation material properties are defined by model material B, given in Section 5.6.1.2.

A limitation of the study is the inability of the FEM to account for anisotropic material properties, which is necessary in the majority of formations drilled. Thus, the results of the study can only be considered to apply to isotropic materials, which discounts all shale formations.



192 Finite elements (16 circumferential, 12 radial)
16 Infinite elements

Figure 5.32 FEM mesh for analysis of plastic regions developed around deviated wellbores.

5.6.5.2 FEM Mesh and Loading Parameters

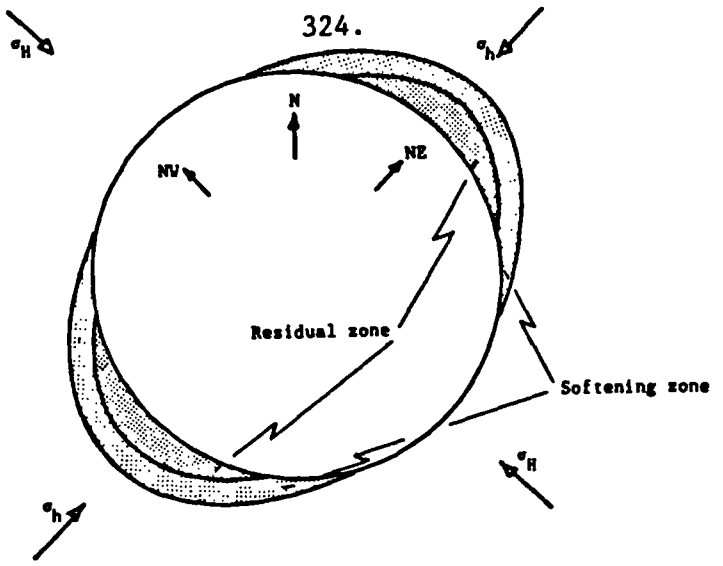
For the vertical well a plane strain analysis utilizing 2 planes of symmetry can be used. For deviated wells a complete plane strain analysis must be used, although for the horizontal well 2 planes of symmetry can again be utilized (see Table 4, Chapter 3). Thus, for the majority of the cases the complete circumference of the well must be modelled. The FEM mesh used in these analyses is given in Figure 5.32, with symmetry only utilized for deviation angles of 0 and 90°.

The loading is split up into 21 load steps. The first load step is equivalent to monotonically replacing the excavated rock with the well pressure until the most critically stressed Gauss point reaches its elastic limit. The remaining portion of the loading is applied in 20 equal load increments. The convergence tolerance ratio (equation (49)) is 0.5%. The maximum number of iterations allowed on each load step to achieve convergence is 40.

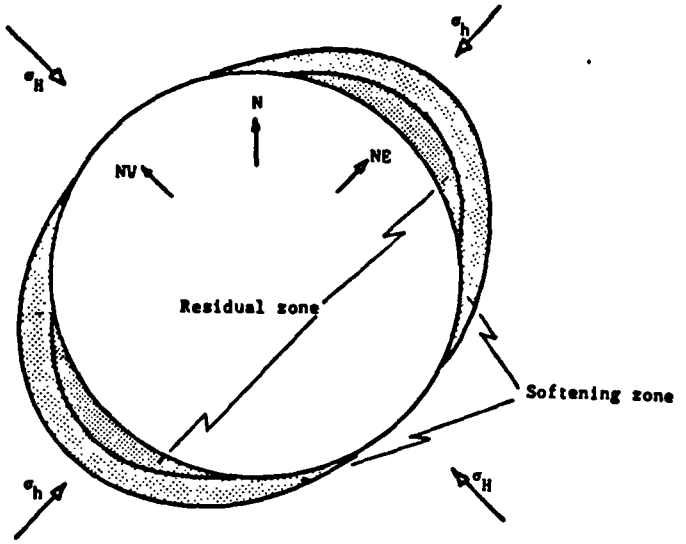
5.6.5.3 Results

Figures 5.33 and 5.34 show the extent and direction of the plastic zones around the wellbore for the deviation angles considered. The section through the wellbore is taken perpendicular to the wellbore axis. The directions of the maximum and minimum principal stresses are projected onto the inclined section as shown in Figure 3.35.

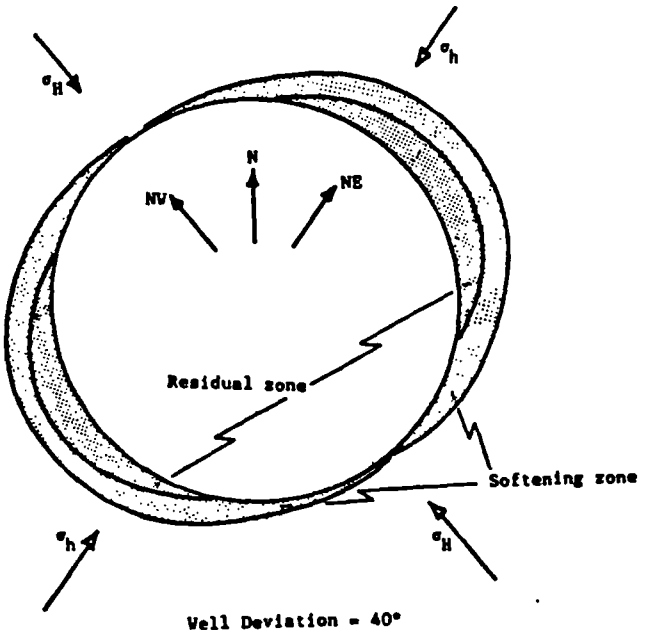
For the vertical and 20° deviated wells the maximum and minimum horizontal stresses are perpendicular and parallel to the potential elongation axis respectively. At 40° deviation the projection of the



Vertical Well



Well Deviation = 20°



Well Deviation = 40°

Figure 5.33 Plastic regions developed around a vertical well and wells deviated at angles of 20° and 30°.

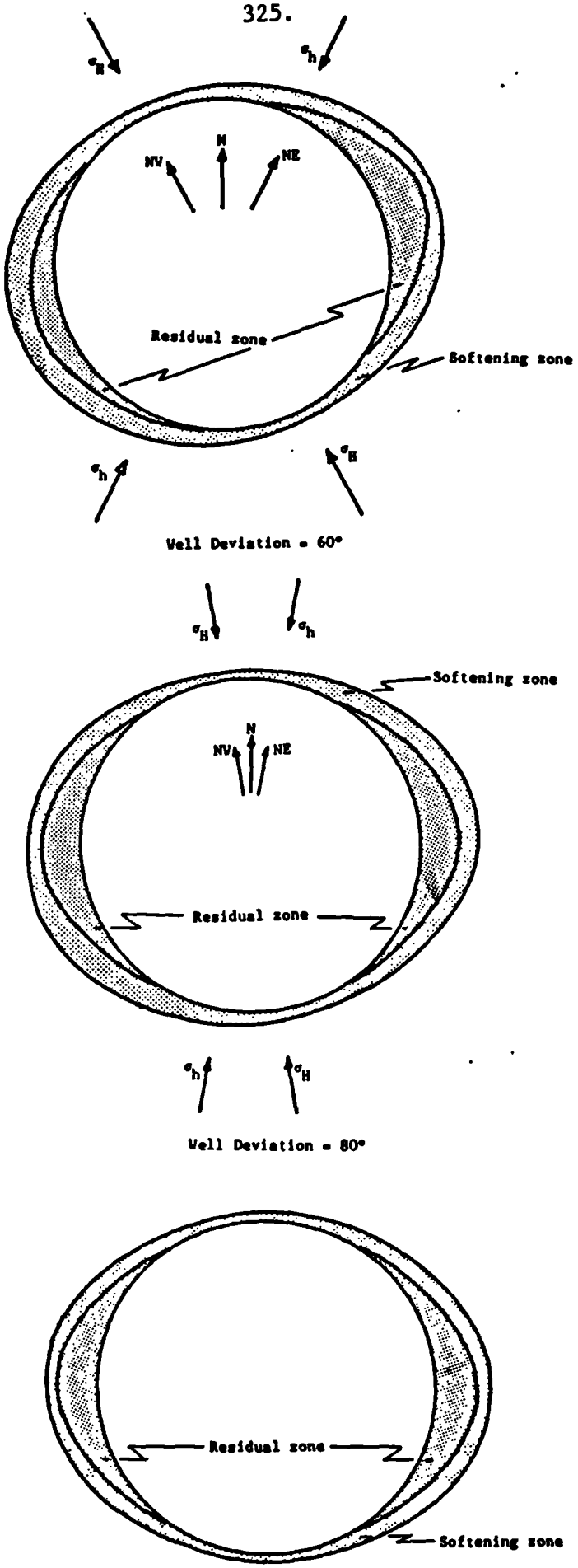
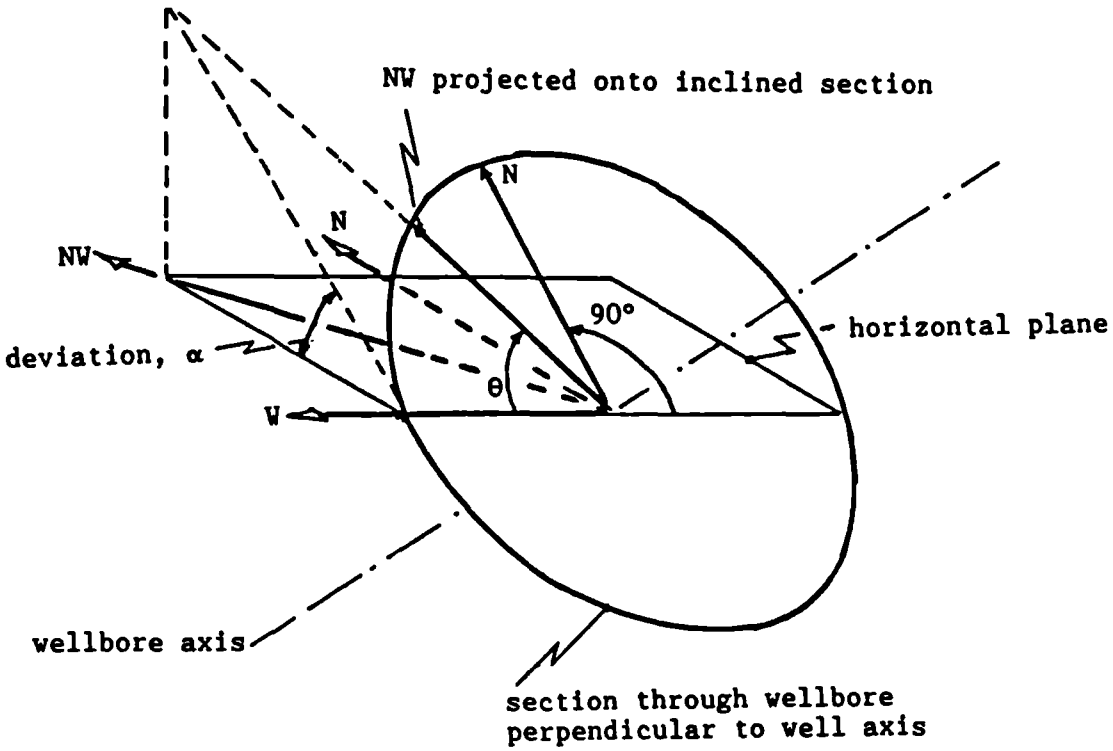


Figure 5.34 Plastic regions developed around wells deviated at angles of 60° and 80° and a horizontal well.



$$\tan\theta = \frac{1}{\cos\alpha}$$

Figure 5.35 Projection of NW onto inclined wellbore section for a well deviated in a Northerly direction.

maximum horizontal stress is still perpendicular to the elongation axis, however, the minimum is now some 20°-30° off parallel. As deviation increases, the angle subtended between the projected maximum and minimum principal stresses reduce, until for the horizontal well they no longer project onto the section. The symmetry of potential hole enlargement is fairly well maintained throughout deviation, with the least symmetry shown in the case of the well deviated at 60°.

With respect to using hole enlargement as a means of inferring the horizontal stress directions, the results indicate that the method could be used for wells deviated up to around 40°. The limiting factor in this particular case is the difficulty in relating back to stress directions from their projections onto the wellbore section. For example, is the projected minimum horizontal stress direction parallel with the elongation direction, or is the projected maximum horizontal stress direction perpendicular to elongation direction? In the case of the well deviated at 40°, the two methods would differ in inferred directions by around 20°-30°. As deviation increases so does the potential error. Thus, any limitation on deviation is likely to be restrictions caused by projection of the stress directions, rather than the increased influence of the vertical stress.

5.6.5.4 Computer Time Consumption

As yet no mention of the program run times and computer storage requirements have been made. However, at this point it is necessary to quote the extent of run times with reference to a complete plane strain analysis of strain softening behaviour. A number of factors have a major

contribution to the computer requirements of an FEM analysis. These are

- plane strain or complete plane strain analysis
- number of elements
- whether strain softening behaviour occurs
- number of load steps chosen
- maximum number of iterations allowed on each load step
- number of Gauss points per element

The case of a deviated well, where no symmetry planes can be utilized (see Table 4, Chapter 3), with strain softening behaviour gives the most demanding type of analysis with respect to computer time and storage. These analysis where carried out on a micro Vax 2000 computer. The average times for each run at a specified overbalance pressure was around 16 hours CPU. Temporary disc space used was around 3.5 Megabytes (4 bytes per real and integer for a 32 bit processor). Thus, the consumption of CPU for these analyses is extremely large and almost prohibitive. In comparison an equivalent run carried out on a vertical well with two planes of symmetry and only two degrees of freedom per node only utilizes around 15 minutes of CPU.

5.7 CONCLUDING REMARKS

The method of applying an elasto-plastic material behaviour, including strain softening behaviour, to an FEM analysis of vertical and deviated wellbores has been presented. Validation has been carried out under certain conditions, however, the extent of validation under plastic conditions is limited particularly for the case of complete plane strain.

A number of parametric studies were carried out to assess material models, the effect of weak zones and the effect of well deviation on plastic zones. A number of the notable findings are listed below.

(a) Differences between the Hoek-Brown and Mohr-Coulomb responses in broken zones at low overbalance pressures.
(b) The apparent increased strength of rock attained on allowing for pre-peak yielding.
(c) The limited influence of weak zones on the resultant plastic region in wellbores.
(d) The influence of outer to inner diameter ratio on the resultant plastic region developed in hollow cylinder testing with the presence of a weak zone.
(e) That up to deviation angles of 40° inferrence of horizontal in-situ stress directions may be possible. However, this finding is restricted to formations exhibiting isoptropic material properties.

The developed program suffers from a number of limitations, which are listed below.

1. The excessive CPU required to carry out a strain softening analysis of deviated wellbores.
2. The inability of the program to removed failed elements of rock, thus simulating spalling.
3. No allowance for anisotropy with respect to material strength and elastic properties.
4. No estimation of the program's quantitative predictive capabilities have been made here. However, it is shown later in

Chapter 6, that a simple elasto-plastic material behaviour is unable to quantitatively predict failure initiation values found in laboratory testing of hollow cylinders.

With reference to the final point above the next chapter discusses the quantitative nature of analysis of failure around a circular opening. Increased predictive powers are found by allowing for the dependence of the elastic modulus on confining pressure (see Section 4.7, Chapter 4), and Chapter 6 goes on to show how this property can be included in the FEM analysis.

CHAPTER 6

ANALYSIS USING A PRESSURE DEPENDENT STIFFNESS

This chapter introduces the concept of a pressure dependent stiffness (PDS), as defined by Santarelli,[18] and shows its relevance with respect to predicting failure around hollow cylinders. Simple solutions for the axisymmetric loading case are used to quantify the importance of allowing for PDS. Due to the strong influence of this property on hollow cylinder predictions, it is implemented into the FEM program for analysis of wellbore stability. The numerical formulations required to implement PDS into an FEM are presented, followed by the coupling of PDS with plasticity and the associated problems. A semi-closed form solution using PDS (described in Appendix E) is used to validate the FEM for the case of axisymmetric loading in Section 6.5. In Section 6.6 the programs quantitative capabilities are assessed by comparing the FEM prediction of failure against hollow cylinder test results. Finally, a parametric study using PDS is carried out in Section 6.7, followed by the chapter conclusions.

6.1 BACKGROUND AND DEFINITION OF PRESSURE DEPENDENT STIFFNESS (PDS)

6.1.1 Triaxial Testing

A set of laboratory tests on a sandstone is shown in Figure 1.16, Chapter 1. As noted in Item I, Section 1.4.1 of Chapter 1, the gradient of the axial stress-strain plots in the elastic region increases with increase in confining pressure. This behaviour is typical of many rocks

and has been noted by a number of researchers (e.g. Kulhawy,[33] Wilhelmi and Sommerton[91]). In certain cases empirical relationships are used to describe this behaviour; Santarelli[18] gives an extensive list of these these behaviour laws. However, few researchers applied this behaviour to the prediction of stresses developed within hollow cylinder samples. A notable exception to this is Santarelli.

Santarelli described the behaviour found in triaxial testing as pressure dependent stiffness (PDS), and uses two relationships to define this phenomenum. The first, originally proposed by Kulhawy,[33] is given by

$$E = E_0 \sigma_3^n \qquad (\text{for } \sigma_3 > 0) \tag{1}$$

It may be noted from equation (1) that the elastic modulus is in fact a function of the minimum principal stress, σ_3, rather than the average pressure at a stress point. Thus, the term PDS is somewhat of a misnomer. However, PDS is used throughout the remainder of this text to describe this behaviour and related expressions. Another anomaly with equation (1) occurs at low values of σ_3. It can be seen that as $\sigma_3 \rightarrow 0$, then $E \rightarrow 0$. The solution to this problem adopted by Santarelli and Brown[52] in their analysis of hollow cylinders, was to fictitiously impose a pressure of 1 MPa at the internal wall of the hollow cylinders. The advantage of equation (1) is that it allows a fully closed form solution for the stress state around a circular opening in an unbounded domain, subjected to axisymmetric conditions.

The second relationship, adopted by Santarelli in a numerical analysis of the stress state, takes the form given in equation (2)

$$E = E_0(1 + a\sigma_3^n) \qquad (\text{for } \sigma_3 > 0) \tag{2}$$

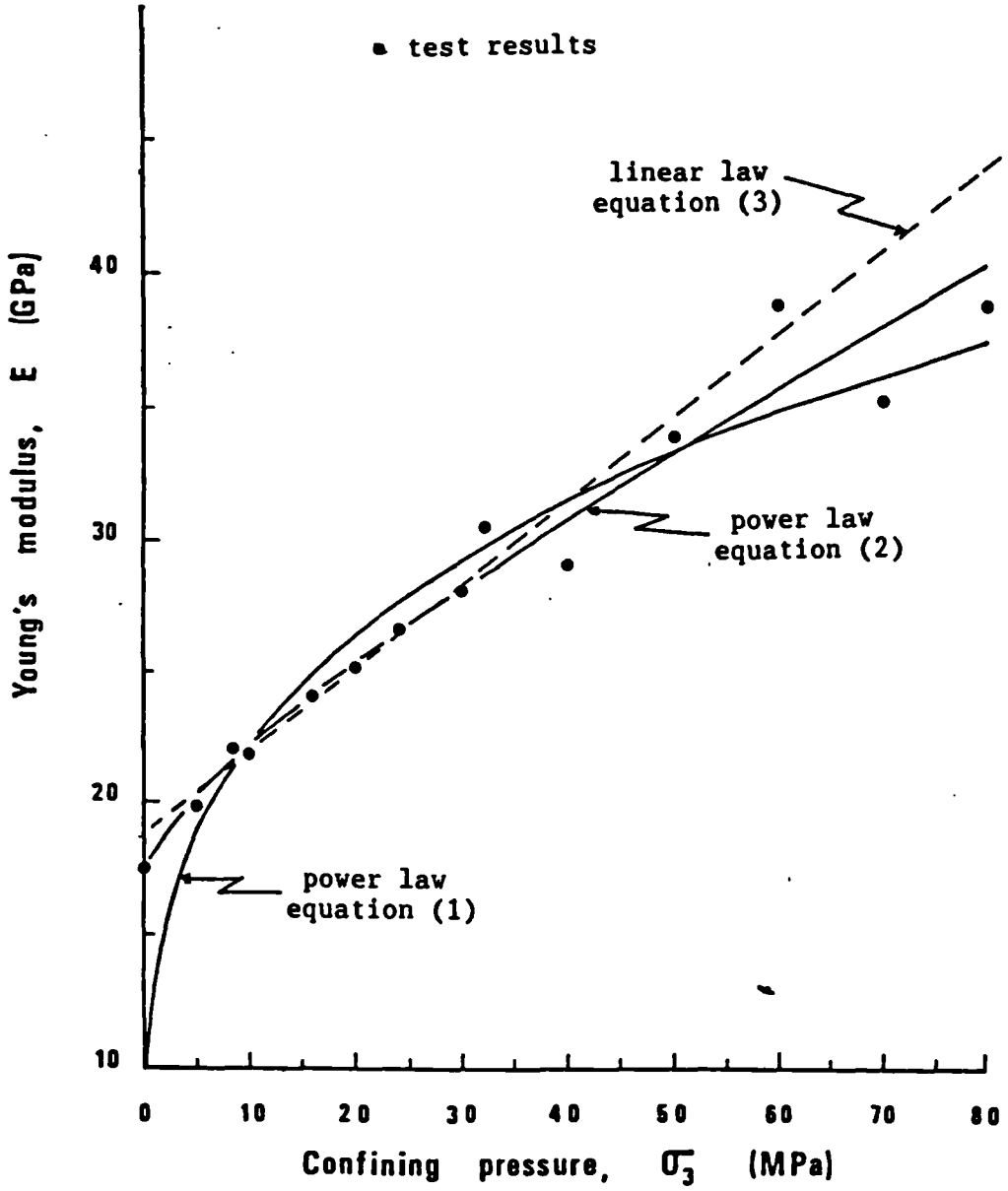


Figure 6.1 Test results and behaviour law defining the variation of Young's modulus with confining pressure for a Carboniferous sandstone (adapted from Santarelli[18]).

A comparison of the best fit line using equations (1) and (2) with actual test results for a Carboniferous sandstone is given in Figure 6.1.

6.1.2 Application to Hollow Cylinder Analysis

In addition to carrying out triaxial testing on samples of sandstone and dolomite, Santarelli performed a series of hollow cylinder tests on the same materials. He noted that the external pressure required to induce failure (see Figure 6.2) far exceed the expected pressure based on a linear elastic analysis and the uniaxial strength of the rock. (Here failure is taken to be the point at which fracturing appears at the inner surface of the cylinder). The ratio between the actual and predicted load at failure was around 2.8 for the Carboniferous sandstone. From previous literature, this apparently unnatural strength of hollow cylinders is common, and in certain cases the ratio of actual to predicted strength was as high as 8 (Hobbs[92]). Details of the other literature are not presented here. However, Santarelli[18] gives an extensive review of hollow cylinder testing.

On discovering this strength anomaly Santarelli formulated a solution for the stress state within a hollow cylinder using PDS. He found that the stress state at the internal wall, based on PDS, was significantly less severe than that predicted using linear elasticity. When the pre-peak yielding portion of the triaxial stress-strain plots was added to PDS behaviour (see Item I, Section 1.4.1, Chapter 1), the severity of the stress state was further reduced. The overall reduction in stress severity, by accounting for PDS (equation (2)) and pre-peak yielding, reduced the ratio of predicted to actual load at failure from

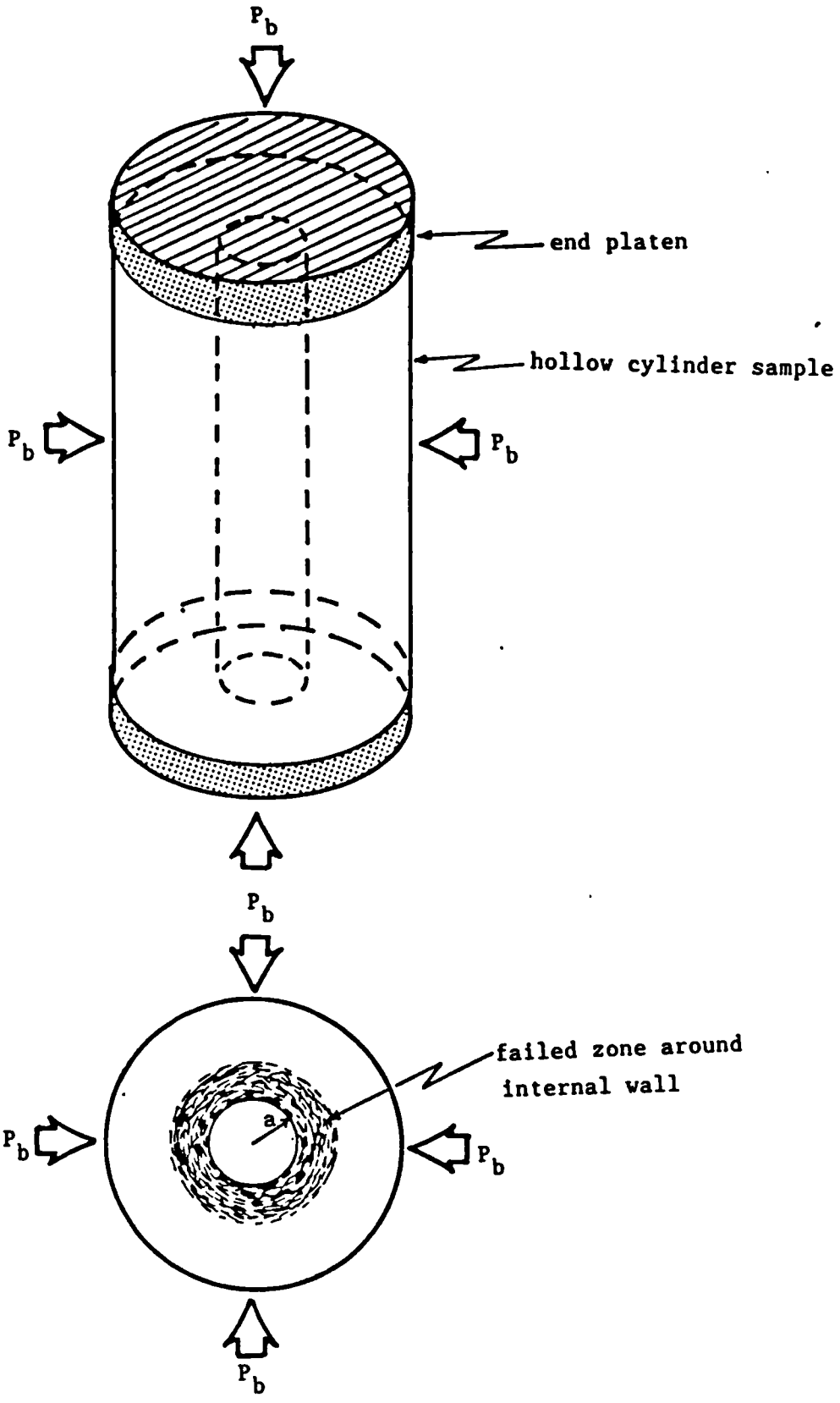


Figure 6.2 Loading conditions applied to a hollow cylinder rock sample.

a factor of 2.8 to 1.2 for the Carboniferous sandstone tested by Santarelli. (In the case of the closed form solution using expression (1), Santarelli found the factor reduced to 0.96 for the Carboniferous sandstone. However, the application of this law to tests with low or zero internal pressure is dubious.)

In conclusion, the resistance to failure of hollow cylinders may not be due to any strength enhancement relative to triaxial test results, but simply due to a more favourable stress distribution than predicted by linear elasticity. An indication of the more favourable stress state is found by allowing for PDS behaviour.

6.2 BEHAVIOUR LAWS

6.2.1 Linear Behaviour Law

As mentioned in Section 6.1.1, Santarelli chose two behaviour laws to describe PDS (equations (1) and (2)). The first has the disadvantage of anomalous predictions at low confining pressures, but allows a completely closed form solution for the stress state in the case of the unbounded domain. The second law better describes the elastic modulus variation, but requires an iterative procedure to define the complete stress state. In the treatment of PDS in this text a linear law is proposed and given by equation (3)

$$E = E_0 + E'\sigma_3 \qquad (\text{for } \sigma_3 \geq 0) \tag{3}$$

For cases where $\sigma_3 < 0$, the elastic modulus is taken to be the uniaxial value (i.e. $E = E_0$). There is no laboratory evidence for this

assumption, but it alleviates the potential for unrealistically low (or even negative) values of E for tensile stress states.

The linear law is also plotted in Figure 6.1 to allow comparison with Santarelli's laws and the test results for the Carboniferous sandstone. The parameters defining the material response for the two PDS laws are

Power law, equation (2), E_0 = 17.49 GPa, a = 0.043, n = 0.78

Linear law, equation (3), E_0 = 18.6 GPa, E' = 314.0

The linear law is unable to follow the true behaviour as well as expression (2), and tends to overpredict the elastic modulus at high confining pressures. Neither does the linear law facilitate a fully closed form solution as with expression (1). Thus, at this stage, it would appear that equation (3) has both the disadvantages suffered by (1) and (2), but none of the advantages. In fact, the reason for adopting a linear behaviour law does not become apparent until Section 6.3.4.1, where it is seen that it has a distinct advantage when applied to FEM analyses.

6.2.2 Comparison Between Behaviour Law Predictions

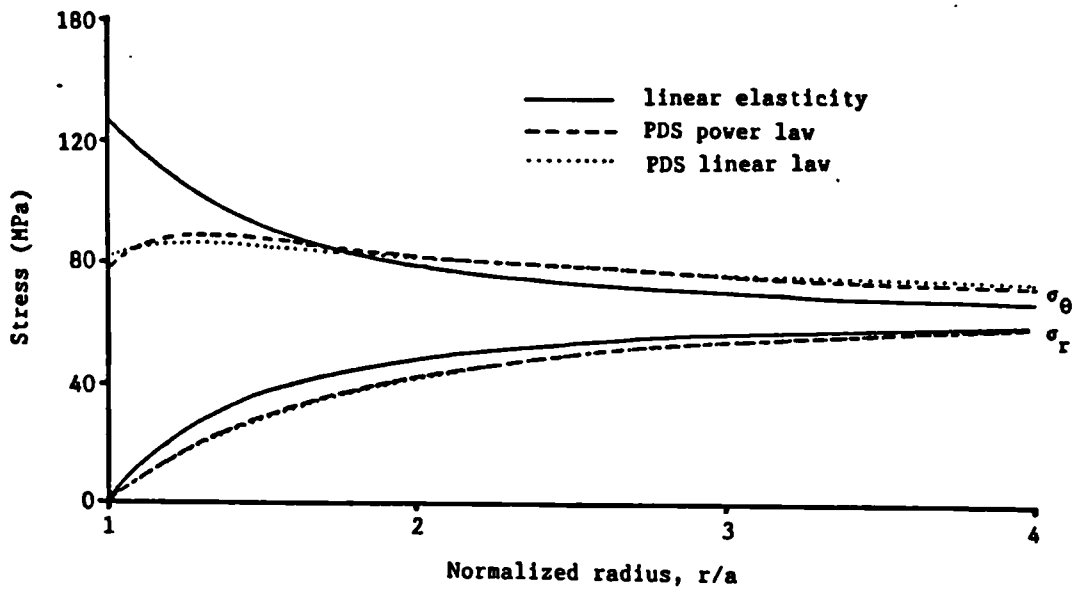
To appreciate any limitations inherent in using a linear behaviour law, it is necessary to compare the predicted stress and displacements with those using a more representative behaviour law. It is considered here that expression (2) is the best description of PDS behaviour. Therefore, the linear law results are compared with results using expression (2). A finite difference approach is necessary to find the stresses and displacements induced in a hollow cylinder using expression

(2). Santarelli developed a small program (RINPLA) for analysis using expression (2). A listing of RINPLA is given in Santarellis thesis.[18] The program accounts for both PDS elasticity and pre-peak yielding, however, only the PDS behaviour is modelled here. The equations required to calculate the stresses and displacement using expression (3) are given in Appendix E.

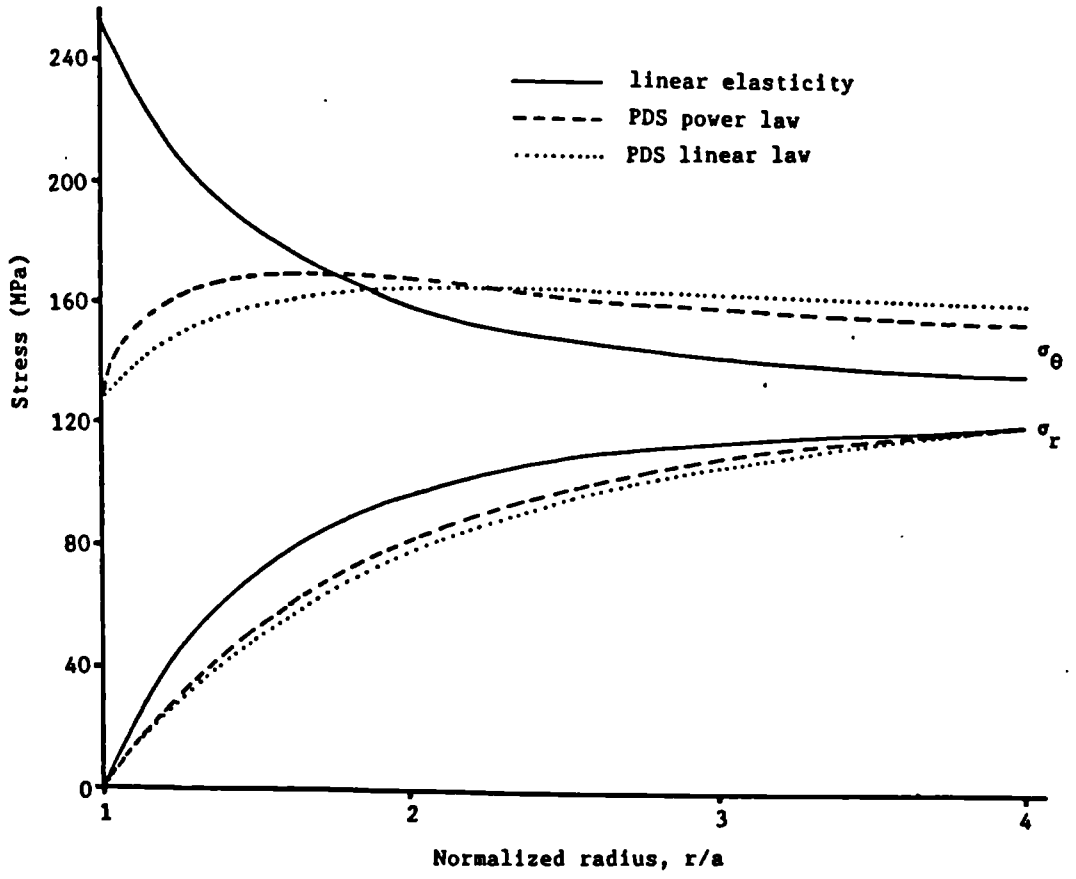
6.2.2.1 Radial and Circumferential Stress State

Figure 6.3a shows the stress state predicted for hollow cylinder samples of the Carboniferous sandstone, with an outer pressure of 60 MPa and no internal pressure. It can be seen from Figure 6.3a that expressions (2) and (3) are in good agreement, but differ considerably with respect to the linear elastic solution for the circumferential stress, σ_θ, close to the internal wall. The PDS values of σ_θ are considerably less severe than those predicted using linear elasticity, thus confirming the more favourable stress state discussed in Section 6.1.2.

In Figure 6.3b the same comparison is shown, but in this case the outer pressure is increased to 120 MPa. For this load the two behaviour laws are in less agreement. (Although the Carboniferous sandstone in question would yield under these conditions, this is not considered here). At the internal wall, the values of σ_θ for the two laws are practically the same. However, the power law predicts a far more rapid increase in σ_θ with radius near the opening than the linear law. This difference in response may lead to a less rapid development of a plastic zone when using the linear law. In certain cases the power law may lead to failure initiation at some finite distance from the opening



(a) 60 MPa external pressure



(b) 120 MPa external pressure

Figure 6.3 Comparison of predicted stress states within a hollow cylinder using linear and power PDS behaviour laws.

(Santarelli and Brown[52]) and not at the wall of the opening; prediction of this is far less likely using a linear law. The extent of the difference between the two models increases with increase in the outer pressure. The problem lies in the linear law, since at high confining pressures the true variation of the Young's modulus with confining pressure 'tails off'. However, the linear behaviour law continues to predict a uniform variation in modulus with confining pressure. Thus, a linear PDS law, as with linear strength criteria, is only suitable over a limited range of σ_3. When applied to hollow cylinder predictions, the linear law is likely to underestimate the stress severity near the wall of the opening as the outer pressure is increased beyond its applicable range.

6.2.2.2 Radial Closure

The radial closure undergone during a test is a function of the lateral pressures applied to the sample, and the axial conditions. The program RINPLA, used by Santarelli, assumes plane strain conditions prevail during loading (in fact this is incorrect as explained in Section 6.2.3). The equations adopted in Appendix E assume uniform axial strain conditions rather than plane strain. However, the hollow cylinder displacement equation ((27), Appendix E), is simply converted to plane strain by letting the axial strain, $\varepsilon_z = 0$. For this condition a direct comparison between behaviour laws (2) and (3) is possible. Table 15 shows the load-displacement response predicted by the two behaviour laws using the Carboniferous sandstone parameters given in Section 6.2.1. Good agreement is found between behaviour laws (2) and (3). As with stress prediction it is seen that with increased load the difference

Outer Pressure (MPa)	Predicted Displacement (mm)		Difference
	Power Law	Linear Law	
0	0	0	-
5	0.00053	0.00052	-1.9%
10	0.00100	0.00100	0.0%
20	0.00182	0.00183	0.5%
30	0.00253	0.00254	0.4%
40	0.00317	0.00317	0.0%
50	0.00374	0.00372	-0.5%
60	0.00428	0.00421	-1.6%
70	0.00477	0.00466	-2.3%
80	0.00522	0.00508	-2.7%
90	0.00566	0.00546	-3.5%
100	0.00606	0.00581	-4.1%
110	0.00645	0.00614	-4.8%
120	0.00682	0.00645	-5.4%

Comparison of PDS Power and Linear Behaviour Law predictions of displacement-load response for Carboniferous sandstone hollow cylinder samples.

TABLE 15

between the two models increases. At high outer pressures we may expect the linear law to under predict displacement relative to the power law.

6.2.3 Comparison Between Model Predictions and Measured Displacements

In the tests performed by Santarelli a hydrostatic pressure was applied to the outer wall and the end platens of the hollow cylinders (see Figure 6.2). The loading path consisted of increasing the hydrostatic pressure, but maintaining zero pressure at the internal wall. Thus, the average axial stress, $\bar{\sigma}_z$, within the sample is given by

$$\bar{\sigma}_z = \frac{b^2}{b^2 - a^2} \cdot P_b \qquad (4)$$

where 'a' and 'b' are the inner and outer radii of the hollow cylinder (12.7 and 50.8mm respectively for Santarellis tests),

and P_b is the external pressure applied to the sample.

The sample is continually undergoing strain in the axial direction in response to loading, therefore the axial conditions cannot be modelled assuming plane strain conditions. However, if the stiffness of the platens is much greater than the stiffness of the sample, then we may assume 'uniform axial strain' conditions. Thus, the axial strain is independent of radius. This is a better representation of axial conditions during loading than plane strain, and the solution presented in Appendix E for the linear law (equation (3)) is based on uniform axial strain. However, RINPLA (equation (2)) considers plane strain conditions throughout loading.

In Figure 6.4 the predicted closure using RINPLA (plane strain) and equation (27), Appendix E, (uniform axial strain) are compared with the actual test results of Santarelli's hollow cylinder testing of the

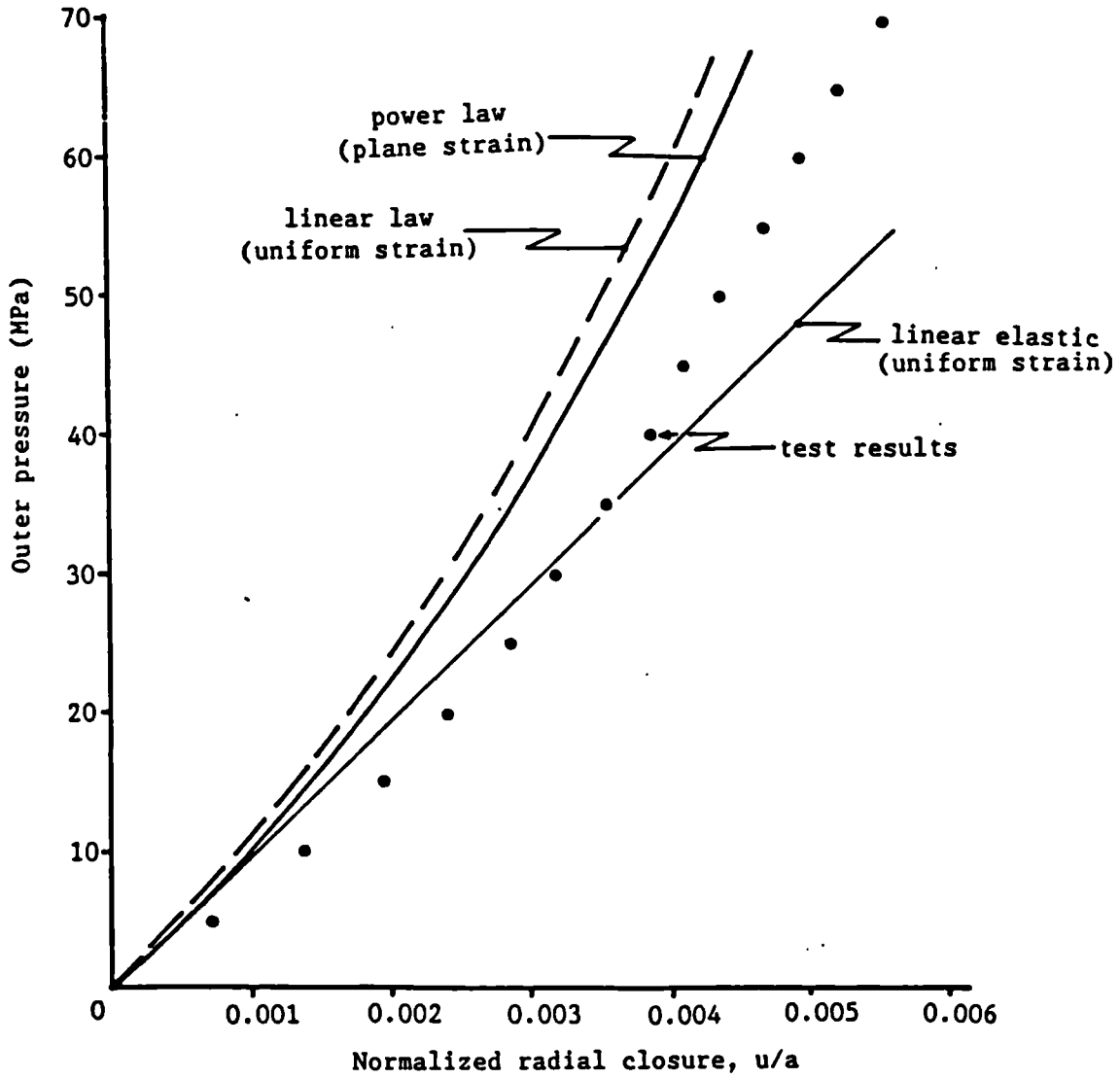


Figure 6.4 Comparison between predicted and actual radial closure for a hollow cylinder sample of the Carboniferous sandstone.

Carboniferous sandstone. Both models predict an increase in the pressure-displacement gradient with increased loading, thus agreeing with the actual test results. Whereas, the linear elastic gradient (based on a constant modulus of 19 GPa) is unable to model this trend. The difference between the two PDS solutions is mainly due to the difference in axial conditions assumed (as opposed to the different behaviour laws). The plane strain solution gives slightly better agreement with the test results than the uniform strain solution. However, this is due to the anomalous assumption rather than better modelling.

Two factors have not been considered here, which are (i) the initial 'bedding in' of the samples, and (ii) the onset of yield. The 'bedding in' will account for part of the difference between predicted and actual displacements. Yielding at the inner wall is only likely to initiate at outer pressures of around 60 MPa (as shown later in Section 6.6). Thus, its influence on the response shown in Figure 6.4 is minimal.

[Note: A possible area where displacement predictions may be improved is with respect to the values of Young's modulus quoted by Santarelli. Santarelli quotes values of E for the Carboniferous sandstone, ranging from 17.5 GPa for uniaxial compression to 33.9 GPa for a confining pressure of 50 MPa. Based on the test results shown in Figures A.1 to A.7, Appendix A, this author considers values of 14 GPa to 26 GPa over the same confining range to be more realistic. This decrease in modulus will give a better prediction of the radial displacements. However, it is not intended in this text to make reassessments of Santarelli's test results, and the values quoted in his thesis are used here.]

6.2.4 Prediction of Axial Stress State

Prediction of the axial stress state is not accounted for in the analysis presented by Santarelli. Thus, only the results from equation (25), Appendix E, and the linear elastic solution are considered.

Figure 6.5 shows the predicted axial stresses, σ_z, for the case of a hollow cylinder of Carboniferous sandstone subjected to an external pressure of 60 MPa. For linear elasticity, σ_z is constant through the sample and given by equation (4) resulting in σ_z= 64.0 MPa. For the PDS solution, σ_z varies from a minimum value of 37.3 MPa at the internal wall to a maximum of 69.3 MPa at the external wall.

Guenot[93] seperates compressive wellbore failure into three classifications (see Figure 6.6). Class B failure is induced when σ_z is the maximum principal stress and exceeds the strength of the rock. Results shown in Figure 6.5 imply that, for materials exhibiting PDS behaviour, the axial loads required to initiate Class B failure may far exceed those predicted by linear elasticity.

6.2.5 Conclusions on the Linear Behaviour Law

In conclusion, for hollow cylinder analyses of the Carboniferous sandstone, the linear law defining PDS behaviour (equation (3)) shows good agreement with the more accurate law used by Santarelli[18] (equation (2)) in prediction of σ_r and σ_θ over a limited loading range. For hollow cylinders under high external pressures, the linear law is likely to underestimate the stress severity near the internal wall of the sample.

In Appendix E the relevant equations describing the displacement

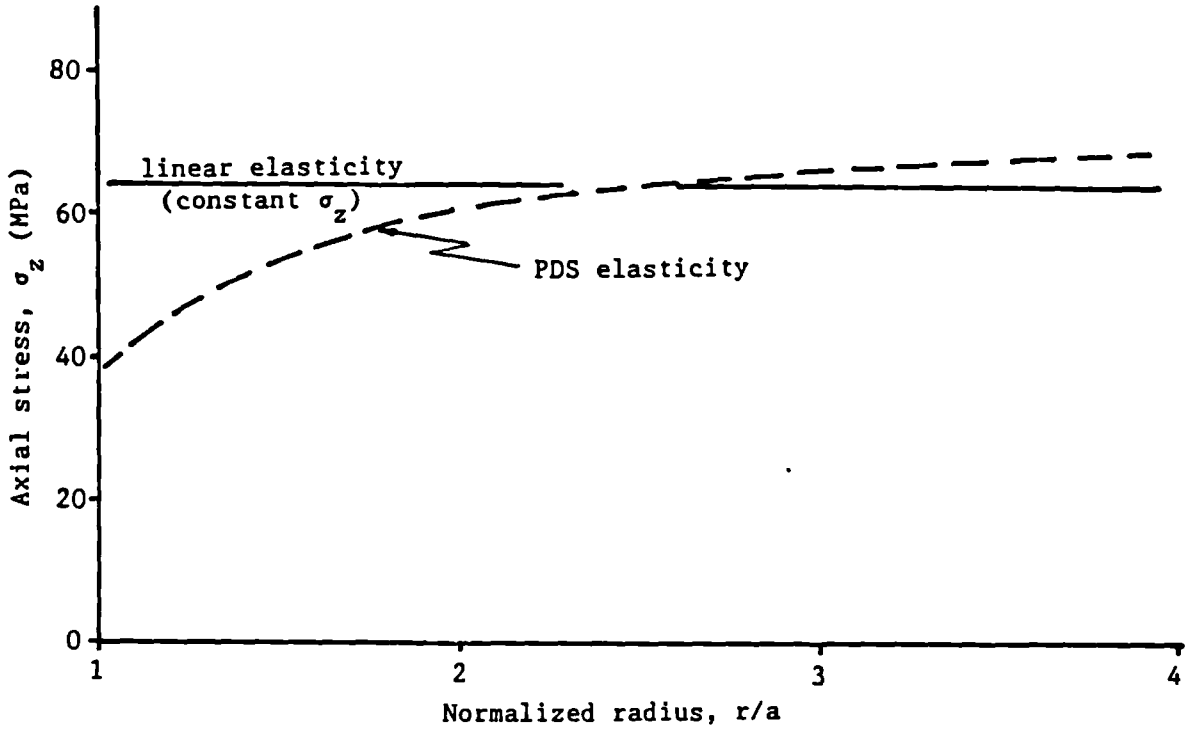


Figure 6.5 Variation of axial stress, σ_z, within a hollow cylinder sample assuming PDS elasticity and uniform strain conditions.

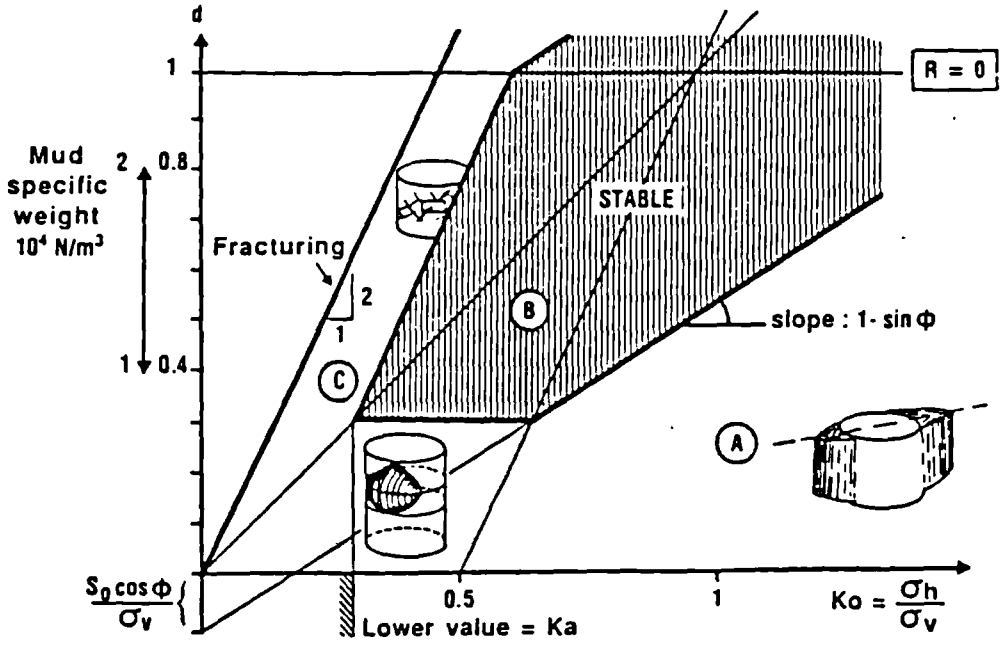


Figure 6.6 Classification of borehole failure mechanisms (after Guenot[93]).

and stress state using equation (3) are presented. Consideration of axial conditions is important for prediction of axial stresses and has an influence on the prediction of radial displacement. Equation development in Appendix E accounts for the more applicable 'uniform axial strain', rather than the plane strain solution assumed by Santarelli. With reference to the Carboniferous sandstone, the plane strain assumption overpredicts displacement by around 5% relative to the 'uniform axial strain' assumption. The predicted displacements using PDS show similar trends to the measured displacements, although PDS underpredicts the actual displacement.

The hollow cylinder stress state, resulting from using the PDS behaviour law, suggests that the sample's resistance to both axial and lateral loading may be far greater than predicted by linear elasticity. This is supported by hollow cylinder testing carried out by Santarelli and others (see Santarelli[18] for a review of previous hollow cylinder testing).

As yet, no justification has been given for the development of a solution based on a linear PDS behaviour law, however, this aspect is made clear in Section 6.3.4.1.

6.3 APPLICATION OF THE FEM TO PDS BEHAVIOUR

The introduction of PDS behaviour to the analysis of a circular opening results in a nonlinear response of the structure. Once, an element of rock has reached its elastic limit, further nonlinear response is exhibited in the form of plasticity. The purpose of the FEM formulations that follow is to facilitate the introduction of PDS behaviour, using the plasticity iterative processes already developed, thus keeping the recoding of the program to a minimum. Due to the

difference in the nature of PDS and plasticity nonlinearity, it is not always possible to apply the same techniques. Therefore, certain routines are developed specifically for the analysis of PDS behaviour. Finally, the FEM analysis combines PDS and plasticity to allow both responses to occur simultaneously.

6.3.1 PDS Nonlinearity

The linear expression (equation (3)) is used here to describe the Young's modulus variation. It is worth stressing this relates the secant modulus to minimum principal stress, and not the tangent modulus. In linear elasticity the secant and tangent moduli are one and the same. Thus, we may write

$$E = \frac{\varepsilon_1}{\sigma_1 - \nu(\sigma_2 + \sigma_3)} \qquad \text{and} \quad E = \frac{\Delta\varepsilon_1}{\Delta\sigma_1 - \nu(\Delta\sigma_2 + \Delta\sigma_3)}$$

This result allows analysis in stress and strain increments, and separate loading conditions may be combined using superposition. However, for PDS elasticity, where $E = E(\sigma_3)$, we have

$$E(\sigma_3) = \frac{\varepsilon_1}{\sigma_1 - \nu(\sigma_2 + \sigma_3)} \qquad \text{but in general,} \quad E(\sigma_3) \neq \frac{\Delta\varepsilon_1}{\Delta\sigma_1 - \nu(\Delta\sigma_2 + \Delta\sigma_3)}$$

Therefore, in the case of PDS behaviour, the stress states resulting from separate loading conditions cannot be combined by superposition. There are exceptions to this, e.g. the standard triaxial test where the confining pressure remains constant, i.e. $\Delta\sigma_2 = \Delta\sigma_3 = 0$,

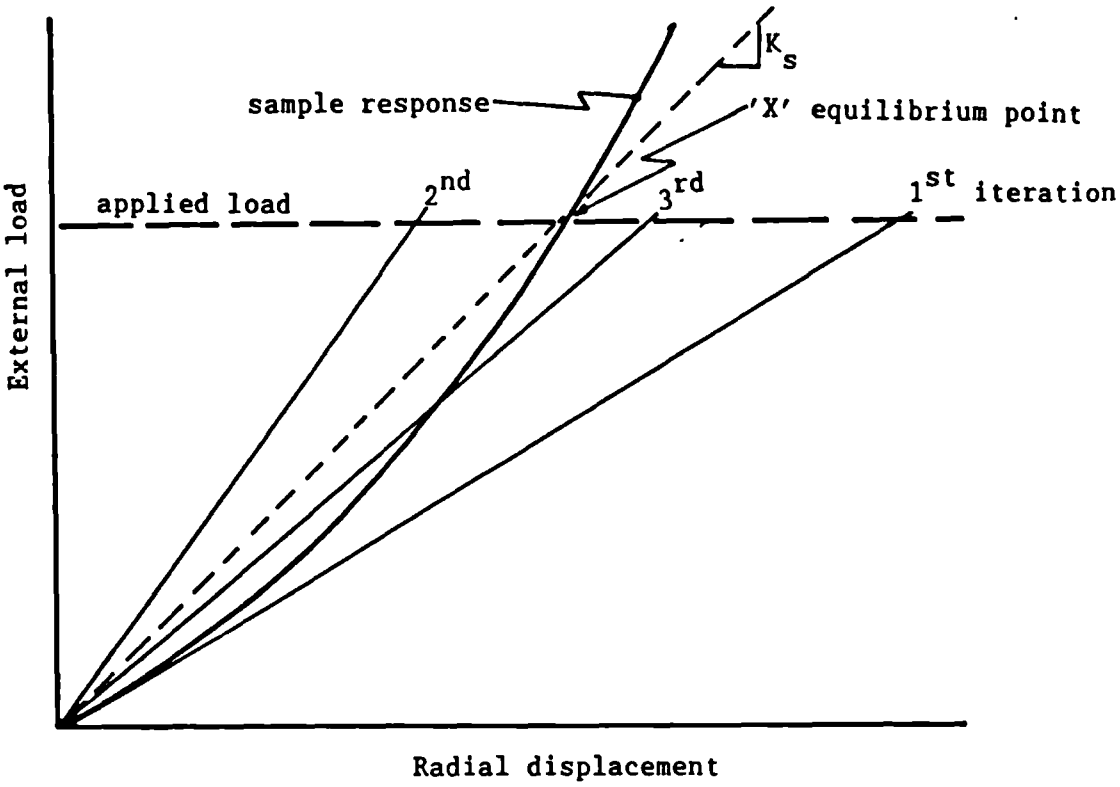
$$\therefore \quad E(\sigma_3) = \frac{\varepsilon_1}{\sigma_1 - \nu(\sigma_2 + \sigma_3)} = \frac{\Delta\varepsilon_1}{\Delta\sigma_1}$$

Thus, to introduce the concept of nonlinear PDS behaviour it is not sufficient to explain it with reference to uniaxial loading, or typical triaxial test loading, where no elastic nonlinearity is predicted. (It

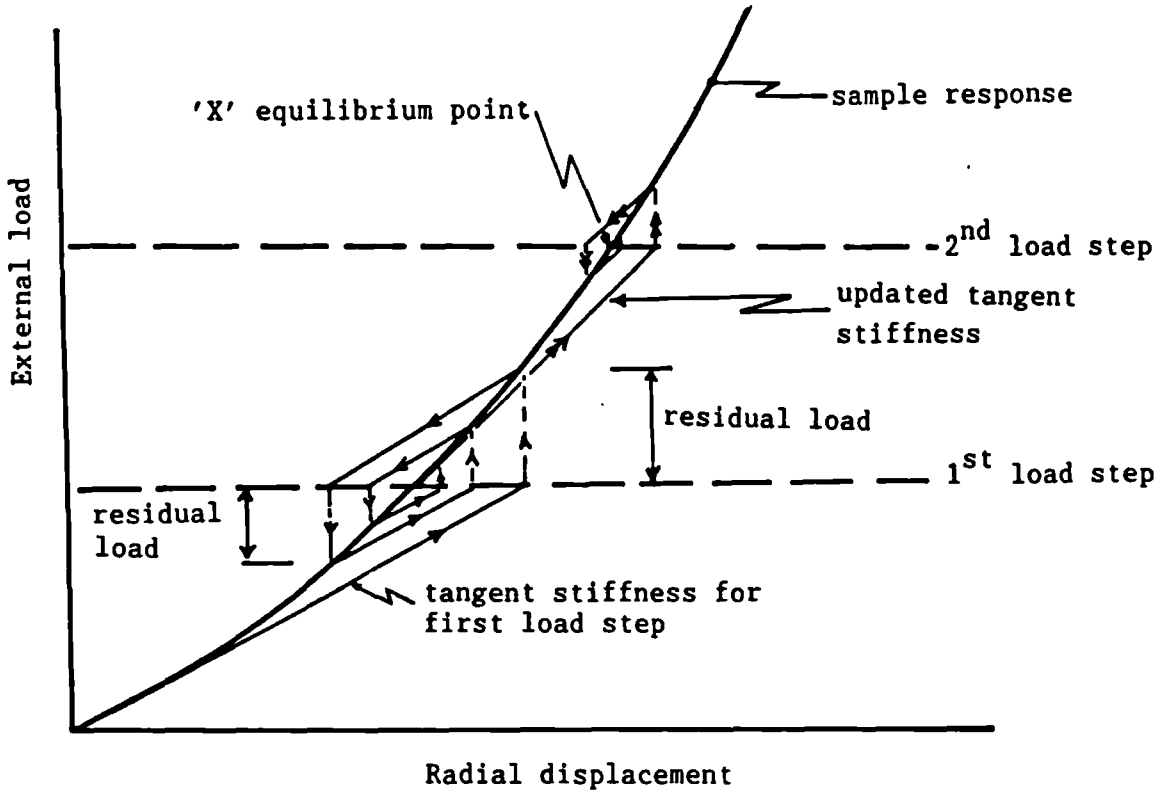
is noted that for uniaxial loading and triaxial loading at low confining pressures, nonlinearity is often present in the form of 'bedding in'. However, the PDS behaviour used here does not attempt to model this response.)

6.3.2 Iterative Method Adopted for PDS Behaviour

The hollow cylinder test provides a useful and relatively simple means of relating the iterative process used in the FEM analysis of PDS behaviour. Assume loading is applied only to the exterior of the sample as depicted in Figure 6.2 and displacement is monitored as radial closure at the inner wall of the sample. At initial conditions the cylinder is free standing and $\sigma_3 = 0$ throughout the sample. Thus, the secant modulus is equivalent to the uniaxial modulus, E_0. As loading is applied, a radial stress gradient is set up, with σ_r ranging from $\sigma_r = P_b$ at $r = b$, to $\sigma_r = 0$ at $r = a$. For the loading conditions considered, we have $\sigma_3 \equiv \sigma_r$. The elastic modulus also varies from E_0 at $r = a$, to $E(P_b)$ at $r = b$, with the average modulus across the hollow cylinder lying somewhere between the two. As P_b increases so does the modulus gradient and the average modulus. A graphical representation of this is shown in Figure 6.7. It can be seen that as P_b increases, the gradient of the pressure-displacement curve also increases. For a given value of P_b, equilibrium of the system is attained at the intersection of the loading and sample responses, given by point 'X'. The secant stiffness, K_s, is dependent on the variation of σ_r through the sample, which is not known at the outset of loading. As explained with respect to plasticity (Section 5.1.1, Chapter 5), using the FEM it is not possible to determine the equilibrium point directly, and an iterative procedure must be employed. A natural approach is to use a secant stiffness



(a) Secant stiffness



(b) Mixed algorithm

Figure 6.7 Iterative algorithms applied to analysis of a hollow cylinder sample with PDS elastic response.

method. In this method the sample stiffness is updated on successive iterations using the previous predicted values of σ_r, with the total load reapplied on each iteration. Figure 6.7a, is a graphical representation of the secant stiffness approach.

In isolation, the secant stiffness method is a suitable iterative process for analysis of PDS behaviour. However, the plasticity techniques described in Chapter 5 are based on the mixed algorithm, which is a combination of the tangent and initial stiffness methods (see Sections 5.1.1 and 5.1.2, Chapter 5). Thus, in order to maintain compatibility in the program coding, it is necessary to adopt the mixed algorithm approach to PDS behaviour. Figure 6.7b depicts the application of the mixed algorithm to PDS behaviour, where the load is applied in two equal steps. In this case loading is applied incrementally, and only residual loads are reapplied to obtain convergence at each load increment. In principle, the mixed algorithm approach adopted for PDS behaviour is the same used for plasticity analysis described in Section 5.1.3, Chapter 5. Areas where iterative techniques for the two forms of nonlinearity differ are (i) determination of tangent stiffnesses, (ii) the determination of the allowable stress state for a given set of displacements, and (iii) the points at which the tangent stiffness is redetermined. These aspects are discussed in the following sections.

6.3.3 PDS Elastic Tangent Stiffness

Determination of the tangent stiffness in relation to plastic behaviour is discussed in Section 5.3.7, Chapter 5. In order to calculate the tangent stiffness the instantaneous, elasto-plastic

stress-strain stiffness matrix, $[D_{ep}]^*$, is required. For elastic PDS behaviour the instantaneous elastic matrix of stress-strain stiffnesses, $[D']^*$, is required. The matrix $[D']^*$ is obtained by ignoring the axial components of the complete matrix of stress-strain stiffnesses, $[D']$, since the axial components are unnecessary when formulating FEM element stiffnesses (Note: The superscript '*' is used to indicate that axial components are not considered in a particular vector/matrix). The expression relating stress, strain and $[D']$, is given by

$$[\delta\sigma] = [D'][\delta\varepsilon]$$

where $[\delta\sigma]^T = [\delta\sigma_r,\ \delta\sigma_\theta,\ \delta\tau_{r\theta},\ \delta\tau_{\theta z},\ \delta\tau_{zr},\ \delta\sigma_z]$

and $[\delta\varepsilon]^T = [\delta\varepsilon_r,\ \delta\varepsilon_\theta,\ \delta\gamma_{r\theta},\ \delta\gamma_{\theta z},\ \delta\gamma_{zr},\ \delta\sigma_z]$

At this stage it is assumed that elements of rock remain elastic. Thus, $[D']$ is the instantaneous, elastic, PDS matrix of stress-strain stiffnesses. The matrix $[D']$ is not found directly, instead its inverse, the matrix of stress-strain compliances, $[S']$, is found, where $[S']$ is given by

$$[\delta\varepsilon] = [S'][\delta\sigma] \qquad (5)$$

The determination of $[S']$ is set out in the following sub-section, after which $[S']$ is inverted to yield $[D']$.

Note: The FEM calculates stresses and strains induced by the excavation (Section 3.4.1, Chapter 3). However, in the following derivations, stresses, $[\sigma]$, and strains, $[\varepsilon]$, are taken to be the sum of both induced and pre-existing components.

6.3.3.1 Determination of the Stress-Strain Stiffness Matrix, [S']

Taking the radial strain for example, then the total strain at a point for PDS behaviour is given by

$$\varepsilon_r = \frac{1}{E(\sigma_3)}[\sigma_r - \nu(\sigma_\theta + \sigma_z)] \tag{6}$$

Using equation (3) to model the PDS behaviour, then it can be shown that for small increments of stress and strain, equation (6) yields

$$\delta\varepsilon_r = \frac{1}{E(\sigma_3)}[\delta\sigma_r - \nu(\delta\sigma_\theta + \delta\sigma_z)] - \frac{E'}{E(\sigma_3)^2}[\sigma_r - \nu(\sigma_\theta + \sigma_z)].\delta\sigma_3 \tag{7}$$

where $E(\sigma_3)^2$ is taken to mean $(E_0+E'\sigma_3)^2$

Similar expressions for the circumferential and axial incremental strain-stress relationships are obtained by rotating the subscripts r, θ and z in equation (7).

The total shear strain component, $\gamma_{r\theta}$, at a point is given by

$$\gamma_{r\theta} = \frac{2(1+\nu)}{E(\sigma_3)}.\tau_{r\theta} \tag{8}$$

which for small increments of stress and strain yields

$$\delta\gamma_{r\theta} = 2(1+\nu)\frac{1}{E(\sigma_3)}\left[\delta\tau_{r\theta} - \frac{E'}{E(\sigma_3)}.\tau_{r\theta}\delta\sigma_3\right] \tag{9}$$

Expressions for the other shear components ($\gamma_{\theta r}$ and γ_{zr}) are found by rotation of subscripts.

The increment in minimum principal stress, $\delta\sigma_3$, in equations (7) and (9) is found by differentiation of the stress invariant expression for the principal stress state given in equation set (8), Chapter 5. Thus,

$$\sigma_3 = \frac{2\sqrt{J_2}}{\sqrt{3}}.\sin(\theta+4\pi/3) + I_1/3 \tag{10}$$

which in terms of stress increments yields

$$\delta\sigma_3 = \left[\frac{\partial\sigma_3}{\partial\sigma}\right][\delta\sigma] \tag{11}$$

Drawing the similarity with differentials of the yield function in Section 5.3.2, Chapter 5, we can write

$$\left[\frac{\partial\sigma_3}{\partial\sigma}\right] = C_1[a_1]^T + C_2[a_2]^T + C_3[a_3]^T \tag{12}$$

where $[a_1]$, $[a_2]$ and $[a_3]$ are given by equations (23), (24) and (25), in Chapter 5, respectively,

$$C_1 = \frac{\partial\sigma_3}{\partial I_1} = \frac{1}{3}$$

$$C_2 = \frac{\partial\sigma_3}{\partial J_2} + \frac{\partial\sigma_3}{\partial\theta}\cdot\frac{\partial\theta}{\partial J_2} = \frac{1}{\sqrt{(3J_2)}}\cdot\sin(\theta+4\pi/3) - \frac{1}{\sqrt{J_2}}\cdot\tan3\theta\cdot\cos(\theta+4\pi/3) \tag{13}$$

and $$C_3 = \frac{\partial\sigma_3}{\partial\theta}\cdot\frac{\partial\theta}{\partial J_3} = -\frac{\cos(\theta+4\pi/3)}{J_2\cos3\theta} \tag{14}$$

For ease of mathematical notation let $[s] = \left[\frac{\partial\sigma_3}{\partial\sigma}\right]$, where the components of the vector $[s]$, found from expression (12), are

$$s_r = \frac{\partial\sigma_3}{\partial\sigma_r}, \qquad s_\theta = \frac{\partial\sigma_3}{\partial\sigma_\theta}, \qquad s_{r\theta} = \frac{\partial\sigma_3}{\partial\tau_{r\theta}}, \quad \text{... etc}$$

Then, from inspection of equations (7), (9) and (11) we can formulate the matrix of stress-strain compliances, $[S']$, defined in equation (5). Thus,

$$[S'] = [S_1'] - [S_2'] \tag{15}$$

where $$[S_1'] = \frac{1}{E(\sigma_3)}\begin{bmatrix} 1 & -\nu & 0 & 0 & 0 & -\nu \\ -\nu & 1 & 0 & 0 & 0 & -\nu \\ 0 & 0 & 2(1+\nu) & 0 & 0 & 0 \\ 0 & 0 & 0 & 2(1+\nu) & 0 & 0 \\ 0 & 0 & 0 & 0 & 2(1+\nu) & 0 \\ -\nu & -\nu & 0 & 0 & 0 & 1 \end{bmatrix}$$

$$\text{and } [S_2'] = \frac{E'}{E(\sigma_3)^2}\begin{bmatrix} A_r \cdot s_r & A_r \cdot s_\theta & A_r \cdot s_{r\theta} & A_r \cdot s_{\theta z} & A_r \cdot s_{zr} & A_r \cdot s_z \\ A_\theta \cdot s_r & A_\theta \cdot s_\theta & A_\theta \cdot s_{r\theta} & A_\theta \cdot s_{\theta z} & A_\theta \cdot s_{zr} & A_\theta \cdot s_z \\ A_{r\theta} \cdot s_r & A_{r\theta} \cdot s_\theta & A_{r\theta} \cdot s_{r\theta} & A_{r\theta} \cdot s_{\theta z} & A_{r\theta} \cdot s_{zr} & A_{r\theta} \cdot s_z \\ A_{\theta z} \cdot s_r & A_{\theta z} \cdot s_\theta & A_{\theta z} \cdot s_{r\theta} & A_{\theta z} \cdot s_{\theta z} & A_{\theta z} \cdot s_{zr} & A_{\theta z} \cdot s_z \\ A_{zr} \cdot s_r & A_{zr} \cdot s_\theta & A_{zr} \cdot s_{r\theta} & A_{zr} \cdot s_{\theta z} & A_{zr} \cdot s_{zr} & A_{zr} \cdot s_z \\ A_z \cdot s_r & A_z \cdot s_\theta & A_z \cdot s_{r\theta} & A_z \cdot s_{\theta z} & A_z \cdot s_{zr} & A_z \cdot s_z \end{bmatrix}$$

The parameters A_r and $A_{r\theta}$ in the expression for $[S_2']$ are given by

$$A_r = \sigma_r - \nu(\sigma_\theta + \sigma_z) \tag{16}$$

$$\text{and } A_{r\theta} = 2(1+\nu)\tau_{r\theta} \tag{17}$$

with A_θ and A_z defined by rotation of subscripts in equation (16), and $A_{\theta z}$ and A_{zr} defined by rotating subscripts in equation (17).

6.3.3.2 Singularities in the Determination of [S']

It can be seen from equations (13) and (14) that determination of the scalars C_2 and C_3 becomes indeterminate as $\theta \to \pm 30°$. At these singular points we have $\sigma_2 = \sigma_3$ ($\theta = -30°$), or $\sigma_1 = \sigma_2$ ($\theta = +30°$). This problem is discussed with reference to plastic flow in Section 5.3.4, Chapter 5, and the same solution to the problem is adopted here. Thus, for the conditions $\theta \leq -29°$ and $\theta \geq +29°$, we have

$$C_2 = \frac{1}{\sqrt{(3J_2)}} \cdot \sin(\theta + 4\pi/3)$$

$$C_3 = 0$$

In addition to singularities resulting from $\theta = \pm 30°$, it is seen that C_2 and C_3 (equations (13) and (14)) are also indeterminate as $J_2 \to 0$. This corresponds to a hydrostatic stress state (i.e. $\sigma_1 = \sigma_2 = \sigma_3$). This problem is not relevant to the plasticity development carried out in

Section 5.3, Chapter 5, since a stress point under hydrostatic loading is in the elastic region, well below the yield surface. (Note: No consideration is given to yielding resulting from hydrostatic loading - Section 4.4.4, Chapter 4.) The solution adopted here is similar in principle to the case where only two of the three principal stresses are equal. The stress state is considered sufficiently close to hydrostatic when the following condition is met

$$\frac{J_2}{I_1} < 10^{-10} \qquad (18)$$

For this condition the explicit value of J_2 (i.e. $\simeq 0$) is used in equation (10) before differentiation. This results in both C_2 and C_3 reducing to zero, with C_1 remaining the only non-zero scalar.

Under certain conditions $I_1 \rightarrow 0$, and the hydrostatic stress state criterion (expression (18)) is indeterminate. In terms of principal stresses, I_1 is given by

$$I_1 = \sigma_1 + \sigma_2 + \sigma_3$$

Thus, for the condition $I_1=0$, then either all three principal stresses must be zero, or σ_3 is tensile. When $\sigma_3 < 0$, the PDS behaviour law does not apply (see Section 6.2.1), so the operation given by expression (18) would not be carried out. The case of a point under no stress may occur if the FEM followed the stress path adopted during hollow cylinder testing (i.e. no load at initial conditions). However, the load path adopted by the FEM is for the case of a wellbore, where initial conditions are given by the pre-existing state of stress. Thus, consideration of instability in expression (18) is unwarranted in the coding.

6.3.3.3 Inversion of [S']

The matrix [S'] defines the compliances between strain and stress, as given in equation (5). Inverting equation (5) yields

$$[\delta\sigma] = [S']^{-1}[\delta\varepsilon] = [D'][\delta\varepsilon]$$

Thus, [D'] is found by inversion of [S'], previously found from equation (15). In the FEM program this is performed using simple matrix inversion techniques found in any good Mathematics text book (e.g. Kreyszig[94]).

6.3.4 Correction of Stress State

In FEM plasticity analysis, the stress state at Gauss points that exceed the current yield strength of the material cannot be determined directly. Initially, the stress state is calculated assuming a linear elastic response, where upon it is found that the stress point lies above the yield surface (see Section 5.3.6, Chapter 5). Following this check, the numerical process determines the state of stress for the point compatible with the current set of displacements. Due to the nonlinearity inherent in PDS behaviour, it is also necessary to adjust the stress state at Gauss points to ensure compatibility with the current set of displacements. However, for linear elasto-plastic analyses only Gauss points that violate the yield criterion need be adjusted, whereas, in PDS elasticity every Gauss point undergoes some adjustment.

Assume on iteration 'i-1', the stress state at a particular Gauss point, $[\sigma]_{i-1}$, compatible with the total strain, $[\varepsilon]_{i-1}$, is determined and found to be imbalanced with the applied nodal loads, $[\psi]$. This

imbalance results in the reapplication of the residual nodal load vector $[\Delta\psi]_i$ on iteration 'i' (see Section 5.1.1). Using the shape functions, the displacements determined from equation solution lead to the strain increments, $[\Delta\varepsilon]_i$. The resulting stress increments, $[\Delta\sigma]_i$, can be estimated using the current tangent stress-strain stiffness matrix, $[D']_{i-1}$, at each Gauss point (Note: Determination of the current $[D']$ matrix is based on the stress state at the end of the previous iteration, 'i-1'). Thus,

$$[\sigma]_i = [\sigma]_{i-1} + [\Delta\sigma]_i \tag{19}$$

$$\text{where} \quad [\Delta\sigma]_i \simeq [D']_{i-1}[\Delta\varepsilon]_i \tag{20}$$

The value of $[\sigma]_i$ is an estimate of the resultant stress state, since equation (20) is nonlinear and therefore $[\Delta\sigma]_i$ is only an approximation. This operation is required when elasto-plastic analyses are carried out. However, in cases where only PDS elasticity is considered, it is unnecessary to make a first estimate of the stress state using expression (19). Instead, we go directly to the exact stress state compatible with the given set of displacements.

Assume the total strain undergone at a Gauss point prior to application of the residual load $[\Delta\psi]_i$, is $[\varepsilon]_{i-1}$. In the FEM coding, strain accumulated from previous load applications is not held in storage. Instead, the current value of the minimum principal stress at each Gauss point is stored in an array. Thus, the total strain accumulated at a Gauss point on the previous iteration can be found from

$$[\varepsilon]_{i-1} = [S_i']_{i-1}[\sigma]_{i-1} \tag{21}$$

where $[S_i']$ is defined in reference to equation (15), and calculated using the minimum principal stress, $\sigma_{3_{i-1}}$

[It is worth noting here, that strain accumulated from each load increment would not give the same result as equation (21). Displacements

(and ∴ strains) calculated by the FEM coding are those induced by the excavation (see Section 3.4.1, Chapter 3). Equation (21), however, gives the sum of both induced and pre-existing strains.]

Thus, having found $[\varepsilon]_{i-1}$ from equation (21), the total strain after iteration 'i' can now be determined from

$$[\varepsilon]_i = [\varepsilon]_{i-1} + [\Delta\varepsilon]_i$$

By converting the general strain tensor, $[\varepsilon]_i$, into strain invariants, the three principal strains (ε_{1_i}, ε_{2_i} and ε_{3_i}) can be found. This procedure is described with respect to stresses in Section 5.2.1, Chapter 5. The same equations can be applied to determine principal strains by making the following equivalences,

$$\text{normal strains } (\varepsilon_r, \varepsilon_\theta, \varepsilon_z) \equiv \text{normal stresses } (\sigma_r, \sigma_\theta, \sigma_z)$$

$$\text{shear strains } (\gamma_{r\theta}, \gamma_{\theta z}, \gamma_{zr}) \equiv \text{2xshear stresses } (2\tau_{r\theta}, 2\tau_{\theta z}, 2\tau_{zr})$$

The minimum principal stress for the given set of displacements (and ∴ strains) can now be determined, since

$$\sigma_{3_i} = \frac{E(\sigma_{3_i})}{(1+\nu)(1-2\nu)}\left[(1-\nu)\varepsilon_{3_i} + \nu(\varepsilon_{1_i} + \varepsilon_{2_i})\right] \qquad (22)$$

which for the linear behaviour law (equation (3)), yields after rearranging

$$\sigma_{3_i} = \frac{E_0[(1-\nu)\varepsilon_{3_i} + \nu(\varepsilon_{1_i} + \varepsilon_{2_i})]}{(1+\nu)(1-2\nu) - E'[(1-\nu)\varepsilon_{3_i} + \nu(\varepsilon_{1_i} + \varepsilon_{2_i})]} \qquad (23)$$

Having determined σ_{3_i}, the <u>secant</u>, elastic matrix of stress-strain stiffnesses, $[D]_i$, is determined. $[D]_i$ is found from expression (14), Chapter 5, by replacing the linear elastic modulus, E, with the PDS modulus, $E(\sigma_{3_i})$.

The exact stress state at a Gauss point on iteration 'i' is now found from

$$[\sigma]_i = [D]_i[\varepsilon]_i$$

Although $[\sigma]_i$ is the exact stress state compatible with the current set of displacements, the resulting nodal reaction loads are unlikely to balance the applied nodal loads. If the load imbalance (residual load) is negligible then convergence is deemed to have occurred, otherwise the residual load is reapplied on the next iteration, until final convergence is achieved.

6.3.4.1 Disadvantage of the PDS Power Law Behaviour

The FEM numerical formulations developed for PDS analysis are based on the linear behaviour law (equation (3)). Here we examine the drawback suffered by using the more applicable power law (equation (2)).

When the elastic modulus variation described by equation (2) is substituted into equations (6) and (8), the incremental derivatives become

$$\delta\varepsilon_r = \frac{1}{E(\sigma_3)}[\delta\sigma_r - \nu(\delta\sigma_\theta + \delta\sigma_z)] - \frac{n.a\sigma_3^{n-1}}{E_0(1+a\sigma_3^n)2}[\sigma_r - \nu(\sigma_\theta - \sigma_z)].\delta\sigma_3$$

$$\delta\gamma_{r\theta} = 2(1+\nu)\left[\frac{1}{E(\sigma_3)}.\delta\tau_{r\theta} - \frac{n.a\sigma_3^{n-1}}{E_0(1+a\sigma_3^n)2}.\tau_{r\theta}.\delta\sigma_3\right]$$

These expressions are slightly more complex than their counterparts from the linear behaviour law (equations (7) and (9)), but do not cause any particular difficulty. However, when the power law is applied to equation (22) and rearranged the resulting expression takes the form

$$\sigma_{3_i}^n + A\sigma_{3_i} + B = 0 \qquad (24)$$

where A and B are functions of E_0, a, ν, ε_{1_i}, ε_{2_i} and ε_{3_i}

Determination of σ_{3_i} from (24) cannot be performed directly, and a numerical technique must be adopted. (Note: In general, n is bounded by $0 < n < 1$). Construction of a routine to perform this operation does not create any great problem, but determination of σ_3 is carried out at every Gauss point on every iteration. Thus, this process may account for a significant portion of a program run time. Therefore, the coding has been developed using the simpler linear behaviour law.

6.3.5 Factors Effecting the Accuracy of the Results

In Section 6.3.4, it was shown how to find the stress state corresponding to a given set of displacements, when the FEM is applied to PDS behaviour. The method is not subject to any 'drift', as with plasticity analysis (Section 5.3.6, Chapter 5), and the stress state corresponds exactly to the given strain state. In addition, the final stress-strain state is independent of the stress path taken. These facts mean that the accuracy of the results are independent of the number and size of the load steps. In plasticity analysis, however, the number of load steps employed may have a strong influence on stress path and accuracy (Section 5.5.2, Chapter 5). Thus, for elastic PDS behaviour the remaining factors which still influence accuracy are

- density of element mesh
- number of Gauss points per element
- convergence tolerance (equation (49), Chapter 5)

Of the factors given, the number of Gauss points has generally the least influence on accuracy.

6.3.6 Points at which the Tangent Stiffness is Redetermined

As discussed in Section 6.3.4, the accuracy of an elastic PDS, FEM analysis is independent of the number of load steps. Thus, it is sufficient to apply the total load in one step. This approach can be adopted when it is known from the outset that the material will not yield and undergo plastic deformations. However, if plastic behaviour may occur then it is necessary to search for the proportion of load that can be applied before plastic deformations occur. For linear elastic behaviour the proportion of elastic loading can be determined relatively simply, since the induced stresses are directly proportional to the applied loading. For PDS behaviour this is not so, and a more complex approach must be adopted.

The approach adopted in the FEM to determine the elastic portion of the loading is depicted in Figure 6.8. The plot represents a hollow cylinder test, where the outer loading is sufficiently large to cause yielding at the inner wall of the sample. In this case the increase in the load-displacement curve gradient, characteristic of elastic loading, levels out after the onset of plastic behaviour and eventually the trend is reversed. Initially the loading is divided into 5 increments, i.e. 20% of the load is applied on each increment. Once convergence is achieved assuming PDS behaviour only, each Gauss point is checked to determine whether the stress state exceeds the elastic limit (Note: For linear elasticity it is only necessary to check the inner most Gauss points, since they are the most critically stressed. However, for PDS elasticity this is not necessarily the case - Santarelli and Brown[52]). Assuming no Gauss point has exceeded the yield criterion on the first load step, then the tangent stiffness is redetermined at this point and

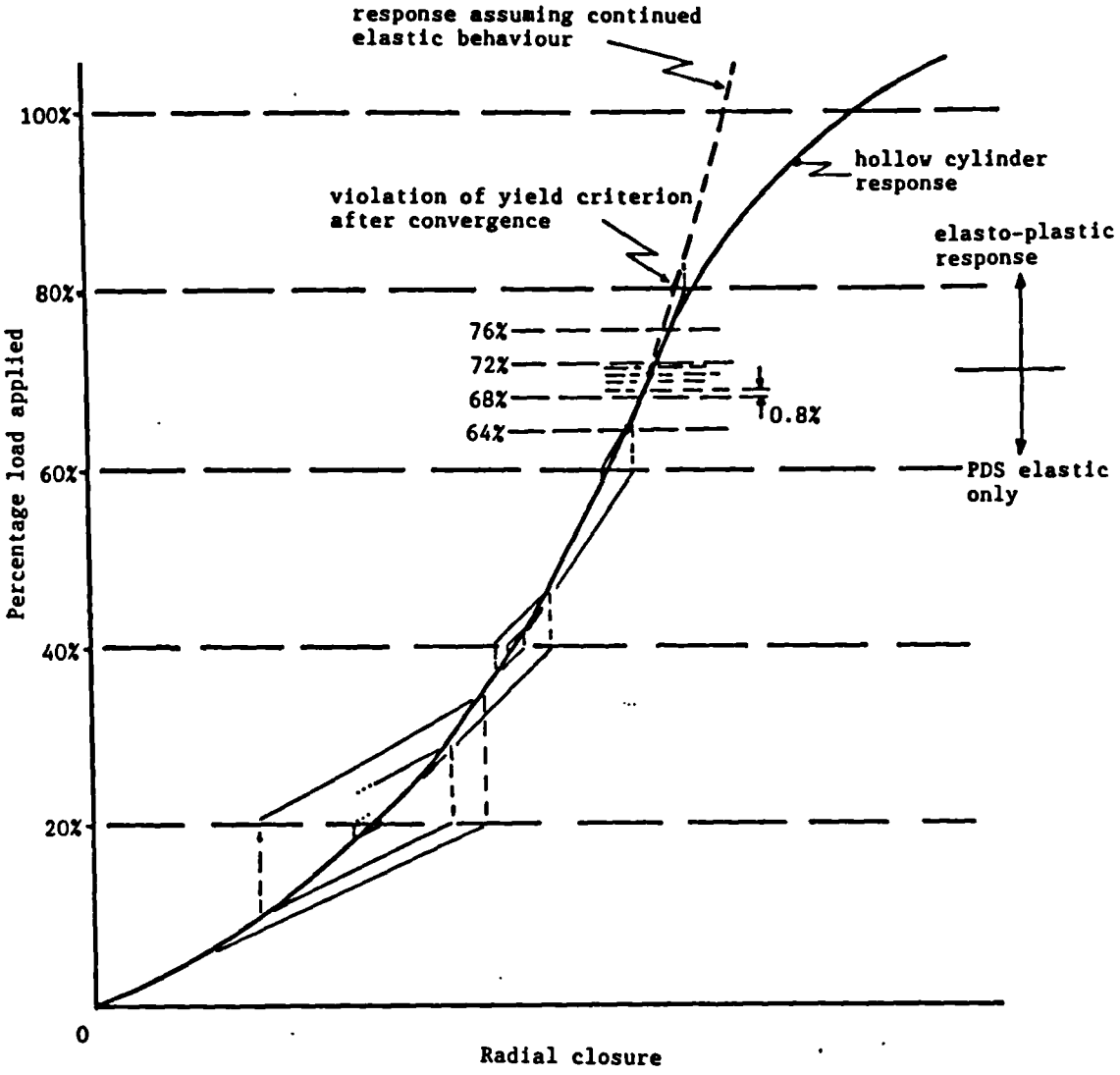


Figure 6.8 Algorithm for determining the percentage of load applied before yield occurs.

the second load increment applied. This process is repeated until the total load has been applied or yield occurs. Assume that a Gauss point(s) has yielded after convergence on the fourth load step. When this occurs the program returns to the stress state which existed after the third load increment, and the fourth load increment is sub-divided into 5 increments (i.e. now 4% load per increment). The process is then repeated to locate initial yield to within 4% of the applied load, whereupon a further sub-division is carried out to find the load to within 0.8%. Greater accuracy than this is considered unwarranted. Thus, for PDS behaviour the program goes through a process to determine the proportion of load that can be applied, to within 0.8%, before the most critically stressed Gauss point yields. The load steps required to follow the remainder of the load, i.e. the PDS-plastic portion, is specified by the user.

6.3.7 Irregularities in Material Response

Under certain stress conditions a PDS model behaviour may predict net volumetric expansions when we would expect volumetric contractions, or visa versa. Occurrence of this phenomenon is explained with the help of the following example.

Consider a triaxial sample under a confining pressure, σ_r, and axial stress, σ_z. The stress state is below the yield point, and PDS elasticity is used to describe the stress-strain response. Thus, the total radial and axial strains are given by

$$\varepsilon_r = \frac{(1-\nu)\sigma_r - \nu\sigma_z}{E_0+E'\sigma_r} \qquad \text{and} \quad \varepsilon_z = \frac{\sigma_z - 2\nu\sigma_r}{E_0+E'\sigma_r}$$

$\therefore$ the volumetric strain, ε_v, is given by

$$\varepsilon_v = \frac{(1-2\nu)(\sigma_z + 2\sigma_r)}{E_0+E'\sigma_r}$$

Differentiating ε_v with respect to σ_r gives

$$\frac{\partial\varepsilon_v}{\partial\sigma_r} = \frac{2(1-2\nu)}{E_0+E'\sigma_r} - \frac{E'(1-2\nu)(\sigma_z + 2\sigma_r)}{(E_0+E'\sigma_r)^2} \qquad (25)$$

It can be shown that when $E' > 2E_0/\sigma_z$ in equation (25) then $\partial\varepsilon_v/\partial\sigma_r < 0$. This result implies that a triaxial sample conforming to these conditions would give a volumetric expansion for an increase in confining pressure while maintaining a constant axial stress (Note: not constant deviator stress). Taking the Carboniferous sandstone as an example, where E_0 = 18.6 GPa and E' = 314, then we have

for σ_r = 10 MPa and σ_z = 100 MPa, $2E_0/\sigma_z = 371 > E'$

but for σ_r = 15 MPa and σ_z = 130 MPa, $2E_0/\sigma_z = 286 < E'$

It can be seen from Figures A2 and A3, Appendix A, that the stress levels chosen are not unreasonable, and from Figure 6.1, that the linear PDS law is a good approximation over this range of confining pressure. This author has no evidence to support or dispute this response. However, it is a fairly simple task to carry out a set of triaxial tests to check its validity.

6.4 APPLICATION OF THE FEM TO COUPLED PDS AND PLASTICITY BEHAVIOUR

After the elastic portion of the loading has been determined the remainder of the load application involves some Gauss points undergoing plastic deformation. After equation solution has been performed for a

specific load increment (or residual load application), it is necessary to test each Gauss point for yield. At this point, we adopt the first approximation to the stress state given by equation (19). Thus, assuming an elastic response we have

$$[\sigma^*]_i = [\sigma]_{i-1} + [\Delta\sigma]_i \simeq [\sigma]_{i-1} + [D'][\Delta\varepsilon]_i$$

where $[\sigma^*]_i$ is the new stress state assuming an elastic response. The yield function, F, is now applied to the approximate value of $[\sigma^*]_i$ found above. Thus, if we have

$$F([\sigma^*]_i) < 0$$

then the response is considered to be elastic and the procedures described in Section 6.3.4 are carried out to determine the exact value of $[\sigma]_i$. However, if $F > 0$, then the new stress point violates the yield criterion. For this case the stress point must be returned to the yield surface. This procedure is given below.

6.4.1 Returning Stress Points to the Yield Surface

In Section 5.3.6, Chapter 5, the process of determining the stress state for a point undergoing elasto-plastic deformation was described. This process hinges on finding the increment in stress state for iteration 'i', $[\Delta\sigma]_i$, for a given increment in strain, $[\Delta\varepsilon]_i$. The governing equation allowing this determination (equation (41), Chapter 5) is repeated below

$$[\delta\sigma] \simeq [D]([\delta\varepsilon] - \lambda[f]) \qquad (26)$$

where [f] is the plastic flow vector,

and λ is the plastic multiplier.

Determination of λ and [f] are described in Sections 5.3.1 and 5.3.3, Chapter 5, respectively. The [D] matrix is the instantaneous matrix of

elastic stress-strain stiffnesses, which for linear elasticity is the same as the secant matrix. As discussed in Section 5.3.6, Chapter 5, equation (26) above is a linear approximation applicable for small increments only. Thus, in general, $[\Delta\varepsilon]_i$ is too large to use directly in equation (26). The method adopted is to divide $[\Delta\varepsilon]_i$ into smaller increments, $[\delta\varepsilon]_i$, and sum the resultant stress increments, $[\delta\sigma]_i$, for each application of $[\delta\varepsilon]_i$ to give $[\Delta\sigma]_i$. At each application of $[\delta\varepsilon]_i$, the instantaneous values of λ and $[f]$ are determined. As the method adopted is approximate, errors can accumulate. These errors are related to the number of increments used and the size of the load steps. The larger the load step and the fewer the increments, the less accurate the results.

The elasto-plastic process used in the FEM when elasticity is described using PDS behaviour, is in principle, the same as the method outlined above. The major difference between the two is that the elastic secant and tangent moduli are no longer the same (as discussed in Section 6.3.1). Thus, $[D]$ in equation (26) is replaced by the PDS elastic, tangent stiffness matrix $[D']$. Thus, we now have

$$[\delta\sigma] \simeq [D']([\delta\varepsilon] - \lambda[f]) \tag{27}$$

where λ is now given by

$$\lambda = \frac{[a]^T[D'][\delta\varepsilon]}{[a]^T[D'][f] + H'} \tag{28}$$

It is seen from the development in Section 6.3.3, that $[D']$ is dependent on the stress state. Thus, in equation (26) λ, $[f]$ and $[D']$ are all changing with increments in stress. Thus, when determining the stress increment, $[\Delta\sigma]$, equivalent to an elasto-plastic strain increment, $[\Delta\varepsilon]$, the terms λ, $[f]$, and $[D']$ in (27) and (28) are all updated on each application of $[\delta\varepsilon]$. Determination of $[D']$ is time consuming, involving

formation and inversion of a 4x4 matrix (plane strain) or a 6x6 matrix (complete plane strain). Thus, if large areas of the structure are undergoing plastic deformation, then a significant portion of the CPU time, is spent on adjustment of stress states at Gauss points in the plastic regions.

As outlined in Section 5.3.6, Chapter 5, the elasto-plastic procedures used result in the stress point undergoing a certain degree of 'drift' from the yield surface. Thus, after summing $[\delta\sigma]$ found from equation (27) to give the total stress state, $[\sigma]$, adjustments to $[\sigma]$ are made to ensure that the stress point lies on the yield surface. This process is covered in detail by Owen and Hinton.[35]

6.4.2 The PDS Elasto-Plastic Stress-Strain Stiffness Matrix

In Section 5.3.7, Chapter 5, development procedures for determination of the linear elasto-plastic stress-strain stiffness matrix, $[D_{ep}]$, are presented. The final expression for $[D_{ep}]$ is given in equation (44), Chapter 5. This stiffness matrix is required to formulate element stiffnesses where one or more of the element Gauss points are undergoing plastic deformations. From the same procedures it can be shown that for PDS elasto-plastic analysis the stiffness matrix, $[D'_{ep}]$ is required, where $[D'_{ep}]$ is given by

$$[D'_{ep}] = [D'] - \frac{[D'][f][a]^T[D']}{[a]^T[D'][f] + H'} \qquad (29)$$

where $[D']$ is the PDS elastic instantaneous matrix of stress-strain stiffnesses,

$[f]$ is the plastic flow vector (Section 5.3.3, Chapter 5),

[a] is the yield function derivative (Section 5.3.2, Chapter 5), and H' is the hardening/softening parameter (Section 5.3.1, Chapter 5).

Note: For linear elastic analysis, [D] is symmetric about the leading diagonal, whereas, [D'] is non-symmetric. Thus, particular care must be taken to ensure columns and rows are not interchanged when carrying out the operations $[a][D']^T$ and [D'][f] in equation (29).

6.4.3 Numerical Instabilities

As mentioned in the last section the secant matrix of stress-strain compliances [D'] is not symmetric about the leading diagonal. In addition, the leading diagonal terms may not be the dominant coefficients in all rows and columns. Under certain conditions this results in a zero or negative value for the term $[a]^T[D'][f]$ in equations (28) and (29), whereas the linear elastic version, $[a]^T[D][f]$, is positive for all non-trivial flow and yield potential functions. Taking the case of a perfectly plastic material, where H'=0, then equations (28) and (29) are indeterminate when the denominator is zero. When the denominator is negative then 'reverse plasticity' is predicted, i.e. plastic compression and extension are predicted in the minor and major principal stress directions respectively. When these conditions arise in an analysis the numerical procedure is unable to continue, and the program is terminated.

Some physical insight into this numerical instability is provided in the following example.

Assume a triaxial sample having reached its elastic limit displays

perfectly plastic behaviour according to the Tresca criterion using associated flow. The material behaviour and loading are given by

$$E_0/\sigma_c = 200, \quad \nu = 0.2$$

$$\sigma_r/\sigma_c = 0.4 \quad \text{and} \quad \sigma_z/\sigma_c = 1.4$$

The associated flow rule results in a flow ratio of $\frac{\partial \varepsilon_r^p}{\partial \varepsilon_z^p} = -\frac{1}{2}$.

For a PDS modulus variation parameter, E', given by E' = 599.7, and adopting procedures set out in Section 6.3.3, it can be shown that the resultant elastic stress-strain compliances give

$$\Delta\sigma_r/\sigma_c \simeq 1343\Delta\varepsilon_r + 268\Delta\varepsilon_z$$

$$\text{and} \quad \Delta\sigma_z/\sigma_c \simeq 2809\Delta\varepsilon_r + 1001\Delta\varepsilon_z$$

If for a given set of strain increments $(\Delta\varepsilon_r, \Delta\varepsilon_z)$ we have $\Delta\sigma_r < \Delta\sigma_z$, then plastic deformation occurs. Therefore, the imposed strain increments must contain both elastic and plastic portions. Thus, the stress-strain relationships must be written as

$$\Delta\sigma_r/\sigma_c \simeq 1343(\Delta\varepsilon_r + \Delta\varepsilon_z^p/2) + 268(\Delta\varepsilon_z - \Delta\varepsilon_z^p) \tag{30}$$

$$\text{and} \quad \Delta\sigma_z/\sigma_c \simeq 2809(\Delta\varepsilon_z + \Delta\varepsilon_z^p/2) + 1001(\Delta\varepsilon_z - \Delta\varepsilon_z^p) \tag{31}$$

For the new stress point to remain on the yield surface then we must have $\Delta\sigma_z = \Delta\sigma_r$. However, when we equate (30) and (31) we find that $\Delta\varepsilon_z^p$ is indeterminate. In effect this means that the sample is unable to adjust to the strain increments imposed, either through an elastic or plastic response. This is the basic stumbling block for the FEM iterative process, which relies on stress points conforming to any given set of strain increments at each iteration. When this cannot be achieved, or spurious stress paths are predicted (i.e. 'reverse plasticity') the procedure breaks down.

Tendency towards numerical instability is dependent on a number of

factors, which are

(i) stress state

(ii) flow rule

(iii) modulus variation

(iv) Poisson's ratio

and (v) material frictional characteristics.

The worst stress state occurs when we have $\sigma_1 = \sigma_2 > \sigma_3$.

Consider the case where we have

$$E_0/\sigma_c = 200, \quad \nu = 0.2, \quad \sigma_1/\sigma_c = \sigma_2/\sigma_c = 1.4, \quad \text{and} \quad \sigma_3/\sigma_c = 0.4$$

then Figure 6.9 gives the relationship between E', 'ϕ' and 'f' for limiting case of numerical stability, where ϕ is the materials instantaneous angle of friction, and f is the flow ratio, given by

$$f = \frac{\partial \varepsilon_3^p}{\partial \varepsilon_1^p}$$

A value of $\phi = 0$ is equivalent to a Tresca material, and a value of $f = -1$, is equivalent to deformation without a net plastic volumetric change.

It can be seen from Figure 6.9 that as the friction angle increases the model behaviour is less prone to numerical stability, and for realistic values of ϕ and E' (say $\phi > 30°$ and $E' < 600.0$) no numerical instability occurs.

Note: Figure 6.9 is a guide to the effect the variable parameters have on numerical stability, and is not a unique relationship true for all material responses. The curves in Figure 6.9 are also dependent on the stress state, Poisson's ratio and the uniaxial modulus, E_0, and whether the material exhibits strain hardening, strain softening or perfect plasticity.

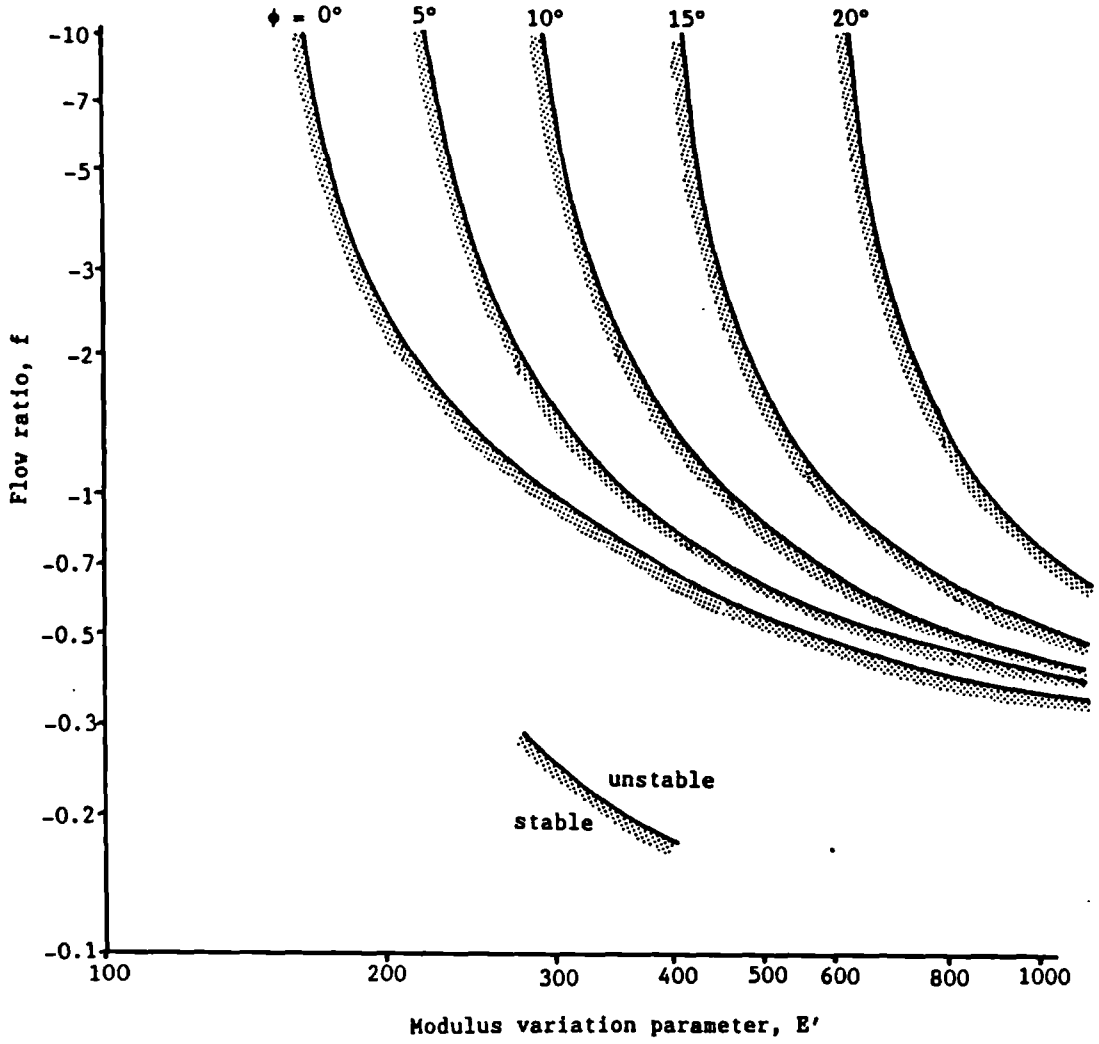


Figure 6.9 Limiting conditions for instability of the numerical algorithm for analysis of PDS elasticity coupled with perfect plasticity.

6.5 PROGRAM VALIDATION FOR PDS BEHAVIOUR

Scope for coding validation of the FEM where the material exhibits PDS elasticity and PDS elasticity coupled with plasticity is limited. At present, direct comparisons are only available for the case of axisymmetric loading of a circular opening. Three material responses are considered for comparison under axisymmetric loading.

1. PDS elasticity only (Section 6.5.1.1).
2. PDS elasticity followed by perfect plasticity (Section 6.5.1.2).
3. PDS elasticity followed by strain softening (Section 6.5.1.3).

No complete solution exists for comparison of results when the in-plane, in-situ stresses are unequal. However, it is still possible to get an indication of the coding validity under these conditions. This validation case is covered in Section 6.5.2.

6.5.1 Axisymmetric Loading

The material elastic properties used in the following validations are listed below.

$$E_0/\sigma_c = 200 \qquad (190)$$

$$E' = 300 \qquad (314)$$

$$\nu = 0.2 \qquad (0.2)$$

The Young's modulus variation parameter, E', is dimensionless. The Young's modulus value for uniaxial compression, E_0, is made dimensionless by dividing by the uniaxial compressive strength, σ_c. The figures in brackets are the equivalent values for the Carboniferous sandstone.

As the problem is axisymmetric it is only necessary to have one element modelling conditions circumferentially in the FEM analysis. In the radial direction the mesh is made up of 10 finite elements modelling the region bounded by $a \leq r \leq 5a$. One infinite element is used to model the remainder of the domain, i.e. $5a \leq r \leq \infty$.

6.5.1.1 PDS Elastic Behaviour

The validation is applied to the case of a circular opening in an unbounded domain with material properties as defined in Section 6.5.1. For the rock mass to remain elastic the imposed loading must ensure that the strength criterion is not exceeded (assuming a Tresca yield criterion in this case). Loading is taken to be hydrostatic and made dimensionless by dividing by σ_c. Here the vertical or axial in-situ stress, σ_v, and the lateral in-situ stress, σ_H ($= \sigma_h$), are taken as

$$\sigma_v/\sigma_c = \sigma_H/\sigma_c = 0.9$$

The internal pressure, P_a, applied to the opening is taken as

$$P_a/\sigma_c = 0.1$$

Appendix E gives a semi-closed form solution to this problem allowing comparison with the FEM results. Figure 6.10 shows the axial, radial and circumferential stresses predicted by both methods. It can be seen that agreement is good, thus validating the program for this condition. It may be noted that the maximum deviatoric stress, $(\sigma_\theta - \sigma_r)/\sigma_c$, is at no point greater than 1.0. thus, given a Tresca yield criterion, the material would not have reached its elastic limit.

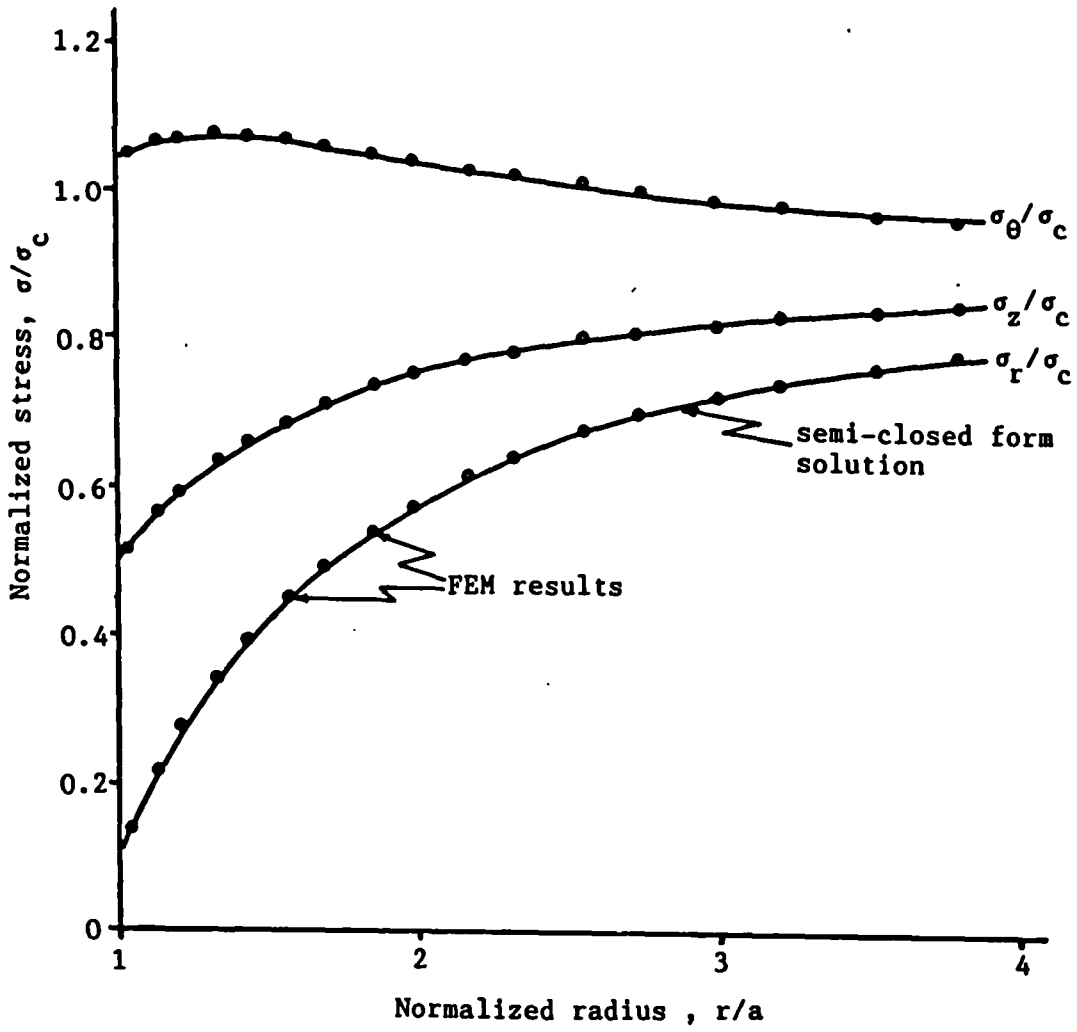


Figure 6.10 Predicted axial, radial and circumferential stresses around a circular opening in a hydrostatic stress field assuming a PDS elastic response.

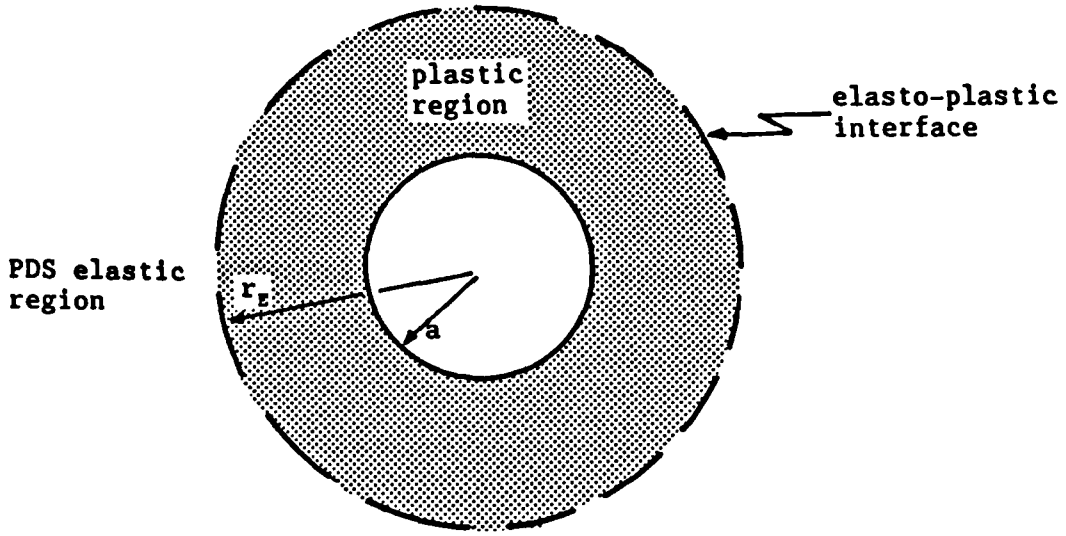


Figure 6.11 Elastic and plastic regions around a circular opening in an isotropic in-situ stress field.

6.5.1.2 PDS Elastic-Perfectly Plastic Behaviour

To attain a PDS elastic-perfectly plastic response using the FEM, the in-situ stress magnitudes used in the previous analysis are increased to induce a yielded zone around the circular opening. Once yield is initiated, the solution presented in Appendix E is no longer applicable throughout the domain. However, the problem can be solved by dividing the domain into elastic and plastic regions as shown in Figure 6.11, and making the assumption that no elastic unloading occurs in the plastic region. Assuming a Tresca yield criterion then, in the plastic region ($a \leq r \leq r_E$) we have

$$\sigma_r = P_a + \sigma_c \ln\frac{r}{a} \tag{32}$$

$$\sigma_\theta = P_a + \sigma_c\left(1 + \ln\frac{r}{a}\right) \tag{33}$$

and $$\sigma_\theta = \sigma_r + \sigma_c \tag{34}$$

Provided the lateral stress, σ_H, is bounded by $\sigma_v \geq \sigma_H \geq P_a$, then in the elastic region ($r_E \leq r \leq \infty$) from Appendix E, we have

$$\sigma_\theta = \frac{1}{1-\nu}.f(\sigma_r) + \sigma_r \tag{35}$$

where $$f(\sigma_r) = \frac{(1-2\nu)E(\sigma_r)\sigma_H}{E(\sigma_H)} - \frac{E(\sigma_r)}{E'}.\ln\left[\frac{E(\sigma_r)}{E(\sigma_H)}\right] - (1-2\nu)\sigma_r$$

At the elasto-plastic interface both equations (34) and (35) must be satisfied. Thus, solution of the two simultaneous equations gives σ_r and σ_θ at the interface, and from equation (32) the radius of the interface, r_E, can be determined. The plastic stress state and its extent is now defined. The stress state in the elastic region is found by applying the equations given in Appendix E to the region defined by $r_E \leq r \leq \infty$, where the inner pressure at the radius $r = r_E$ is given by σ_r at the interface.

The radial displacement at the interface, u_a, is determined as follows. Assuming a non-associated flow rule given by

$$\frac{d\varepsilon_3^p}{d\varepsilon_1^p} = \frac{d\varepsilon_r^p}{d\varepsilon_\theta^p} = -f = -1.2$$

then working in total (i.e. pre-existing + induced) stresses and strains, we have for the radial and circumferential strains,

$$\varepsilon_r = -\frac{du}{dr} = \varepsilon_r^e + \varepsilon_r^p = \varepsilon_r^e - f\varepsilon_\theta^p \tag{36}$$

$$\varepsilon_\theta = -\frac{u}{r} = \varepsilon_\theta^e + \varepsilon_\theta^p \tag{37}$$

where superscripts 'e' and 'p' signify elastic and plastic components respectively.

Eliminating ε_θ^p from (36) using (37) gives

$$-\frac{du}{dr} + f\frac{u}{r} = \varepsilon_r^e - f\varepsilon_\theta^e$$

which on integration between the limits $a \leq r \leq r_E$, and rearranging, gives,

$$u_a = a^{-f}\left[u_{r_E} r_E^{-f} + \int_a^{r_E} r^{-f}(\varepsilon_r^e - f\varepsilon_\theta^e)dr\right] \tag{38}$$

Integration of the right-hand side of equation (38) is performed numerically. The displacement at the elasto-plastic interface, u_{r_E}, can be determined from equation (13), Appendix E, and having found σ_r and σ_θ for various 'r' using equations (32) and (33), then ε_r^e and ε_θ^e are given by

$$\varepsilon_r^e = \frac{(1+\nu)}{E(\sigma_r)}[(1-\nu)\sigma_r - \nu\sigma_\theta] - \frac{\nu}{E(\sigma_H)}(\sigma_v - 2\nu\sigma_H)$$

$$\varepsilon_\theta^e = \frac{(1+\nu)}{E(\sigma_r)}[(1-\nu)\sigma_\theta - \nu\sigma_r] - \frac{\nu}{E(\sigma_H)}(\sigma_v - 2\nu\sigma_H)$$

Equation (38) yields the total (pre-existing + induced) displacement.

The induced displacement, Δu_a, is then found from

$$\Delta u_a = u_a + \frac{(1-\nu)\sigma_H - \nu\sigma_v}{E(\sigma_H)}.a$$

A comparison of the stress states predicted using the analysis described above and the FEM is shown in Figure 6.12. The applied loading is again hydrostatic and taken as

$$\sigma_v/\sigma_c = \sigma_H/\sigma_c = 1.5$$

In general, good agreement is found between the two solutions. At the elasto-plastic interface one of the Gauss points shows lower values of σ_θ and σ_z than the exact solution. Here the FEM predicts that the point in question has undergone elastic unloading having previously suffered some plastic deformation; this may be a result of the iterative process rather than a true response to loading.

Figure 6.13 shows the normalized induced displacements at the wall of the opening as a function of the in-situ stress magnitude (hydrostatic) when no internal pressure is applied. The initial response up to a normalized in-situ stress of around 0.9 is totally elastic. Beyond 0.9 the response of the material is elasto-plastic. Good agreement is found in both the elastic and elasto-plastic regions.

6.5.1.3 PDS Elasticity followed by Strain Softening

To facilitate the analysis of a material exhibiting a PDS elasto-plastic strain softening behaviour, it is necessary to divide the domain into elastic and plastic regions as done in the previous example. Here the elastic region is again modelled using the equations presented in

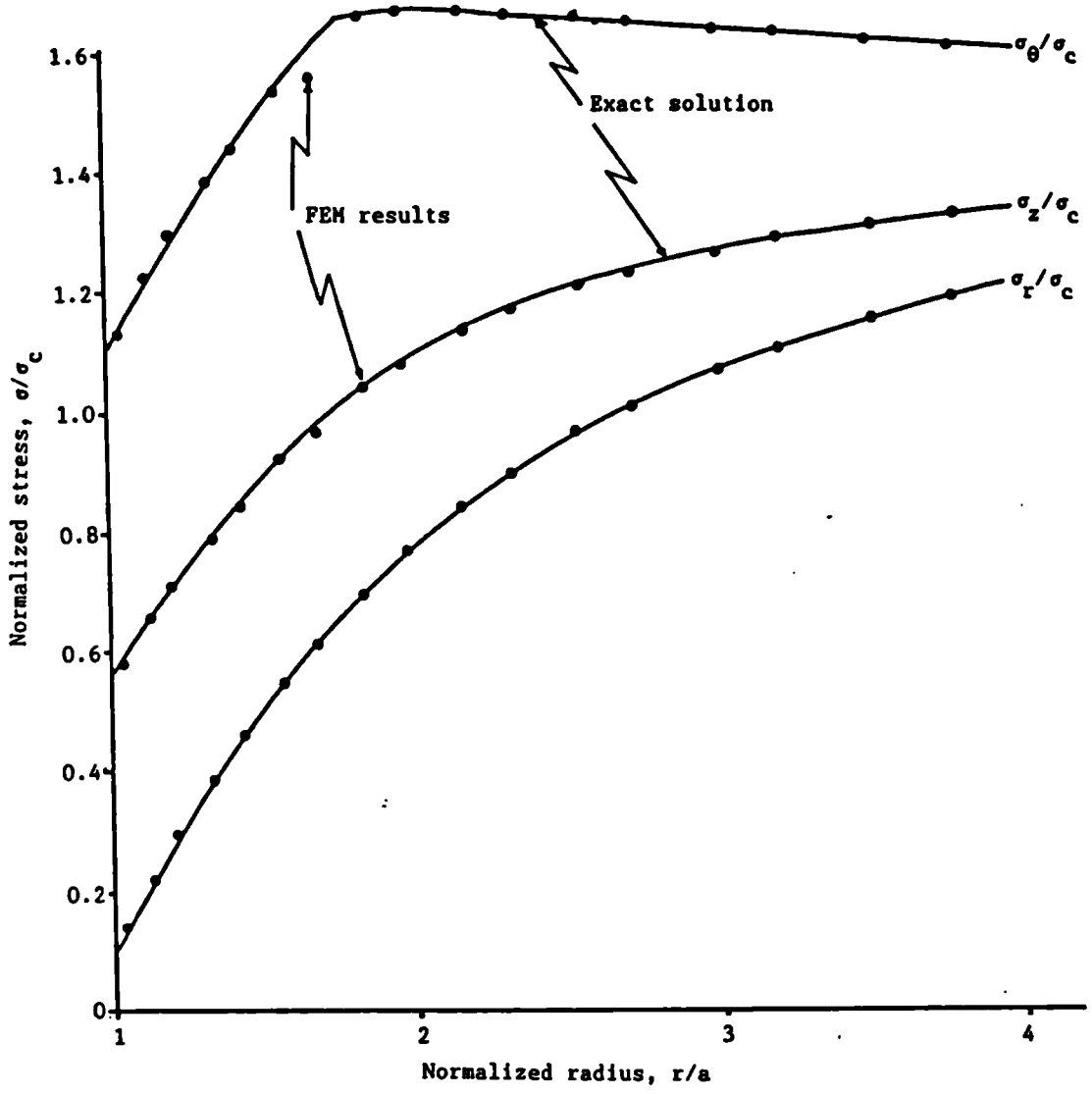


Figure 6.12 Predicted stress around a circular opening in a hydrostatic stress field, assuming a PDS elastic-perfectly plastic behaviour.

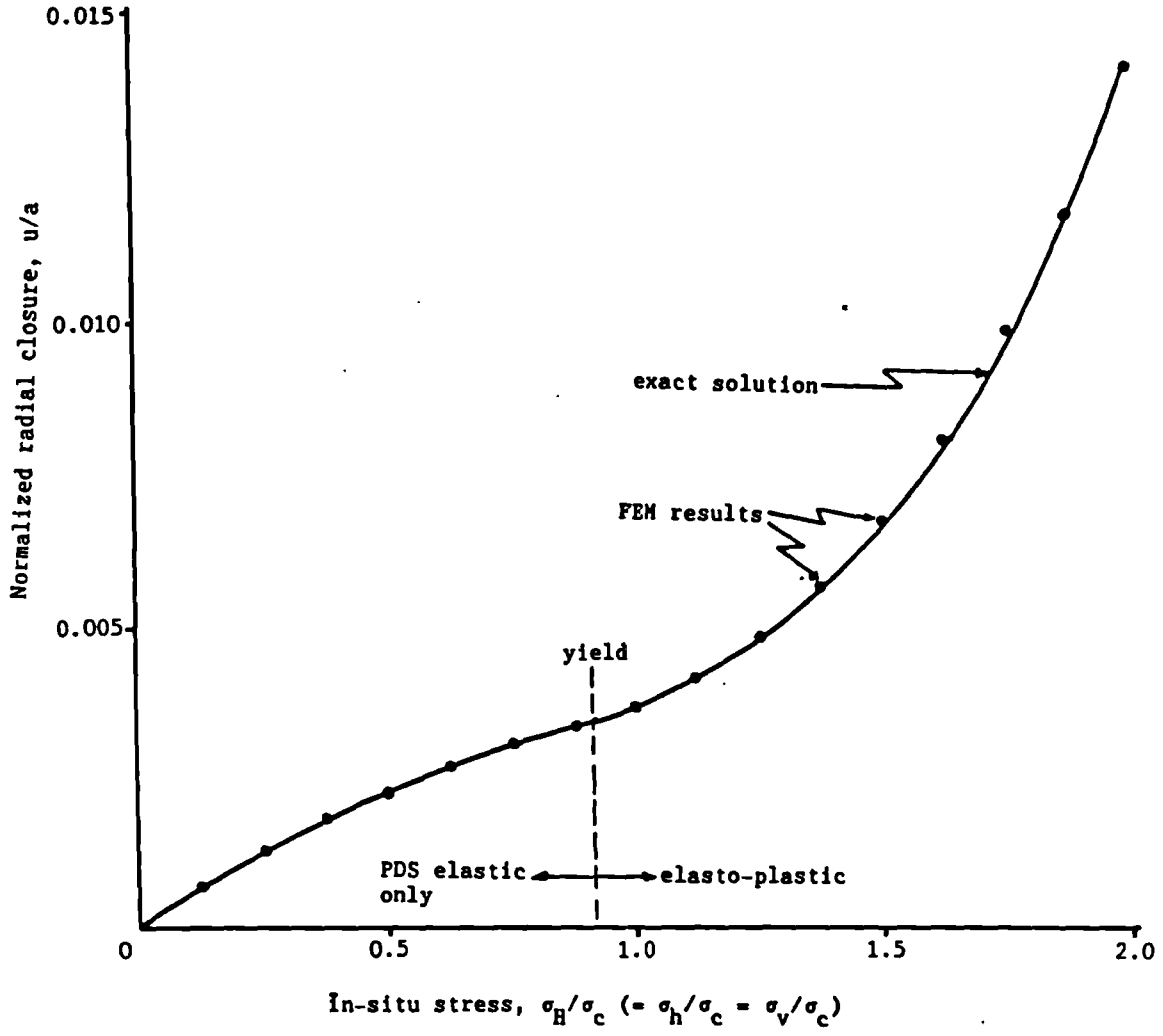


Figure 6.13 Predicted load-displacement response for a circular opening in a hydrostatic in-situ stress field, assuming a PDS elastic - perfectly plastic behaviour.

Appendix E, and the plastic region is modelled using a modified version of the procedure set out in Appendix D.

The first step to the solution is to determine the stresses at the elasto-plastic interface. In Appendix D this involves satisfying the linear elastic expression for σ_θ in terms of σ_r, and the yield criterion. For this case the radial and circumferential stresses at the interface are found by satisfying the PDS elastic stress equation (35) and the Hoek-Brown yield criterion given as

$$\sigma_\theta = \sigma_r + \sqrt{(m\sigma_c\sigma_r + s\sigma_c^2)} \qquad (39)$$

Having determined σ_r and σ_θ at the elasto-plastic interface, similar procedures to those set out in Appendix D can be used to define the radius of the interface and the stress state in the plastic region. A number of the equations in Appendix D must be adapted to a PDS elasto-plastic analysis. The following are the modifications to the equations in Appendix D for the case where the axial stress is the intermediate principal stress:

The axial stress (equation (20), Appendix D) is now calculated in operation 'h' and given by

$$\sigma_{z_j} = \nu(\sigma_{r_j} + \sigma_{\theta_j}) + \left[\frac{(1-2\nu)}{E(\sigma_H)}.\sigma_H - \varepsilon^p_{z_{j-1}}\right]E(\sigma_{r_j})$$

where $\varepsilon^p_{z_{j-1}}$ is the total plastic strain accumulated in the axial direction up to iteration 'j-1'.

The elastic radial and circumferential strains determined in operation 'h' are now given by

$$\Delta\varepsilon^e_{r_j} = [\sigma_{r_j} - \nu(\sigma_{\theta_j} + \sigma_{z_j})]/E(\sigma_{r_j}) - \varepsilon^e_{r_{j-1}}$$

$$\Delta\varepsilon^e_{\theta_j} = [\sigma_{\theta_j} - \nu(\sigma_{r_j} + \sigma_{z_j})]/E(\sigma_{r_j}) - \varepsilon^e_{r_{j-1}}$$

Similar modifications must be made to the equations defining the case when the axial stress is the maximum principal stress. With the

modifications discussed the stress state in the plastic region and its extent can be found from Appendix D. The solution presented in Appendix E is used to determine the stress state in the elastic region.

The Hoek-Brown strength parameters used in the validation (see Appendix D) are taken as

$$m_I = 10.0, \quad m_R = 5.0$$

and $$s_I = 1.0, \quad s_R = 0.0$$

The non-associated flow parameters, h and f, are taken as

$$h = -2.0 \qquad \text{and} \quad f = -1.2$$

The in-situ stress state taken for this validation is hydrostatic and given by

$$\sigma_v/\sigma_c = \sigma_H/\sigma_c = 5.0$$

The resulting stress states predicted by the finite difference solution and the FEM are given in Figure 6.14a. The stress gradients from the FEM are in good agreement with the finite difference solution. However, the FEM overpredicts the magnitude of all three stresses. The errors in stress magnitudes close to the wall of the opening are as much as 200-300%. The reason for this discrepancy is the convergence tolerance used (see equation (49), Chapter 5). The FEM results shown in Figure 6.14a are computed using a convergence tolerance of 0.2%. When strain softening is present the FEM sets up fictitious liner elements at the boundary of the opening (Section 5.4.2, Chapter 5). The liner prevents uncontrolled flow of the rock into the opening, and the iterative process takes the form of a rock-support interaction problem. Under

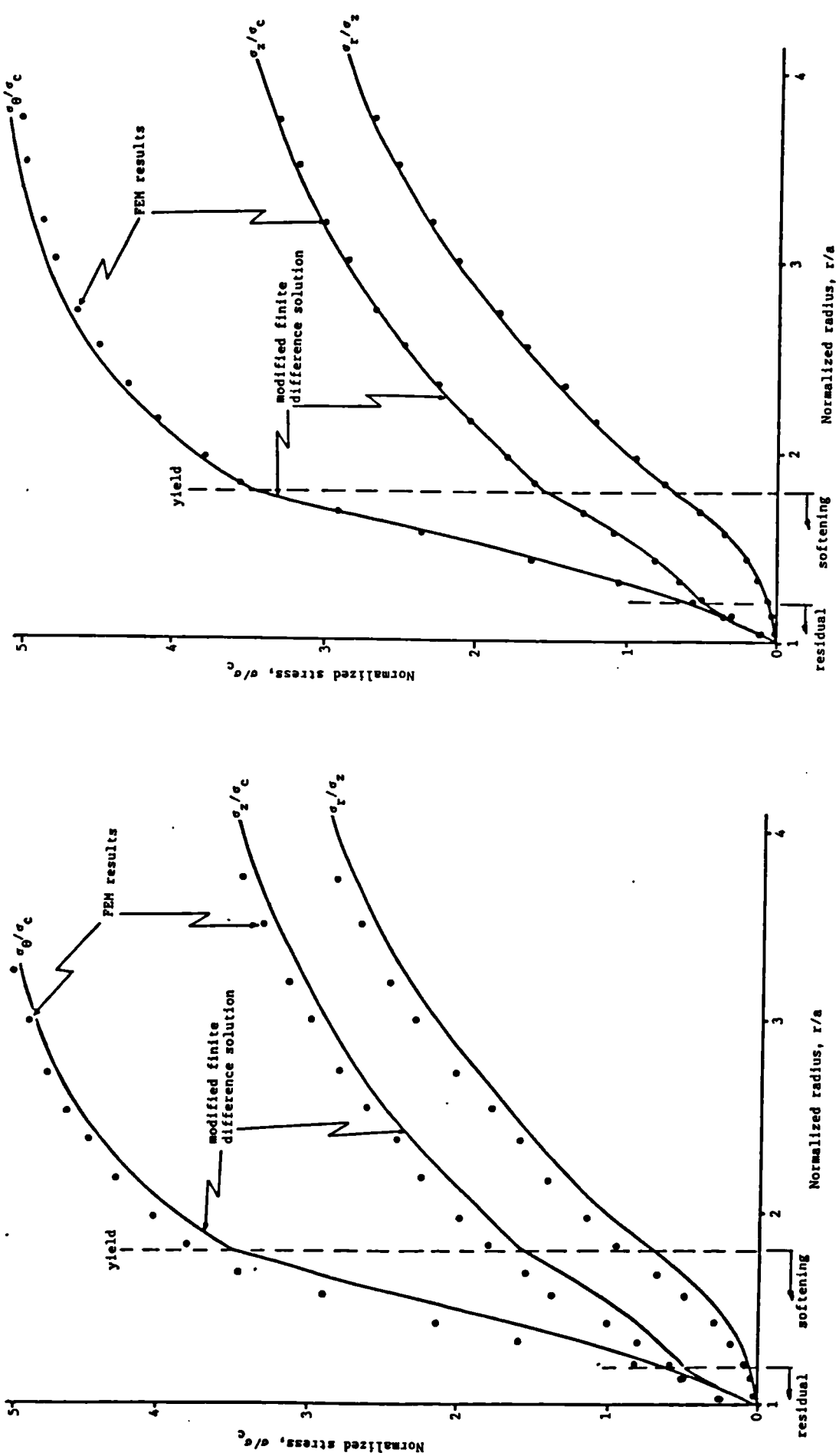


Figure 6.14 Predicted stresses around a circular opening in a hydrostatic stress field assuming a PDS elastic - strain softening plastic behaviour.

these conditions the convergence ratio is effectively a measure of the support still supplied by the fictitious liner (i.e. only when the convergence ratio reaches zero does the liner no longer provide any support). For cases of low or zero internal pressure and where the rock has lost cohesive strength (i.e. at residual), the resultant stress state is sensitive to small variations in the internal pressure. This can be seen by inspection of the equation for the radial stress in the residual zone (Brown et al[49]), which is given by

$$\sigma_r = P_a + \sqrt{(m\sigma_c P_a + s\sigma_c^2)}\left[\ln\left(\frac{r}{a}\right)\right] + \frac{m\sigma_c}{4}\left[\ln\left(\frac{r}{a}\right)\right]^2$$

If we consider a stress point at a radial distance given by $r/a = 1.2$, then with respect to the residual parameters used in this validation, it can be shown that for $P_a/\sigma_c = 0.0$, we have $\sigma_r/\sigma_c = 0.0416$. However, when we apply an internal pressure, P_a/σ_c, of only 0.005, we have $\sigma_r/\sigma_c = 0.0754$. From the Hoek-Brown yield criterion it can be shown that the corresponding values of σ_θ are given by

$$P_a/\sigma_c = 0, \qquad \sigma_\theta/\sigma_c = 0.498$$

$$\text{and} \quad P_a/\sigma_c = 0.005, \qquad \sigma_\theta/\sigma_c = 0.689$$

The internal pressure applied in the example is only equivalent to 0.1% of the traction change at the boundary wall (i.e. $\frac{1}{2}$ the convergence tolerance specified). Thus, in order to attain better results in this instance it is necessary to reduce the convergence tolerance, which is reduced here to 0.02%. (Note: In real applications of the FEM, a convergence ratio as low as 0.02% is probably unwarranted, as well as expensive in terms of CPU. However, here it is only intended to show that as the convergence tolerance is reduced, the FEM does indeed converge to the exact solution.)

Figure 6.14b gives a comparison between the FEM and the finite

difference solutions for the reduced convergence tolerance ratio, showing a much improved agreement between the two methods. Some difference is seen in the prediction of σ_θ on progressing further away from the opening. This is a result of the proximity of the outer radius of the finite element domain. Infinite elements are utilized, however, the more marked the variation of the Young's modulus, the less suitable infinite elements are for modelling the remainder of the unbounded domain.

6.5.2 Anisotropic Loading under Plane Strain Conditions

There are no solutions available allowing validation of the FEM under PDS elasticity, or PDS elasto-plastic behaviour, where the in-plane, in-situ stresses are anisotropic. However, it is still possible to gain an indication of the validity of the coding for the elasto-plastic case. For the case where PDS elasticity is followed by perfect plasticity, the stress state within the plastic zone can be determined from closed form equations, provided plastic deformation is not followed by elastic unloading. In the following validation it is assumed that the material behaviour is the same used in the validation carried out in Section 6.5.1.2.

For a perfectly plastic Tresca material the stress state in the plastic region is given by equations (32) and (33) (this is true for both the axisymmetric and general plane strain conditions - Brown and Bray[1]). Thus, although we are unable to determine the validity of the contour defining the elasto-plastic interface, we can check the validity of the stresses within the plastic region.

The loading conditions for this example are defined by

$$\sigma_v/\sigma_c = 1.0, \quad \sigma_H/\sigma_c = 1.3, \quad \text{and} \quad \sigma_h/\sigma_c = 1.0$$

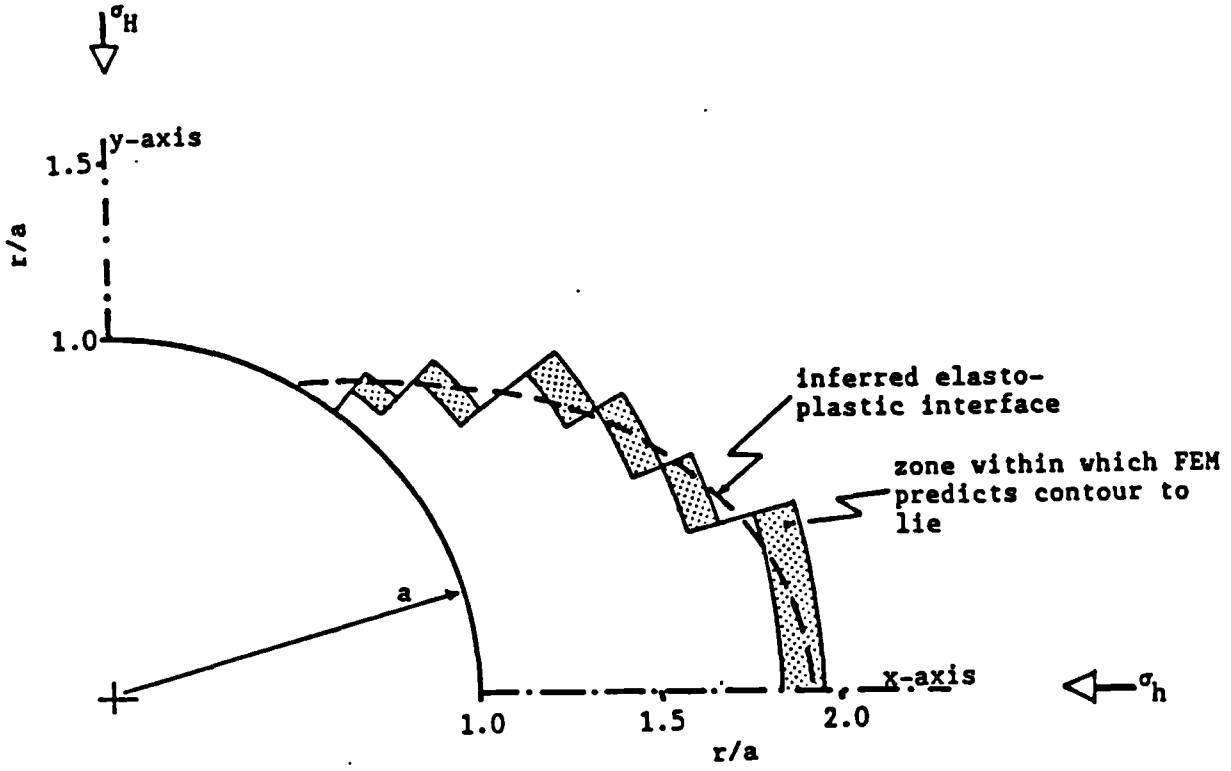
The internal pressure is taken as

$$P_a/\sigma_c = 0.1$$

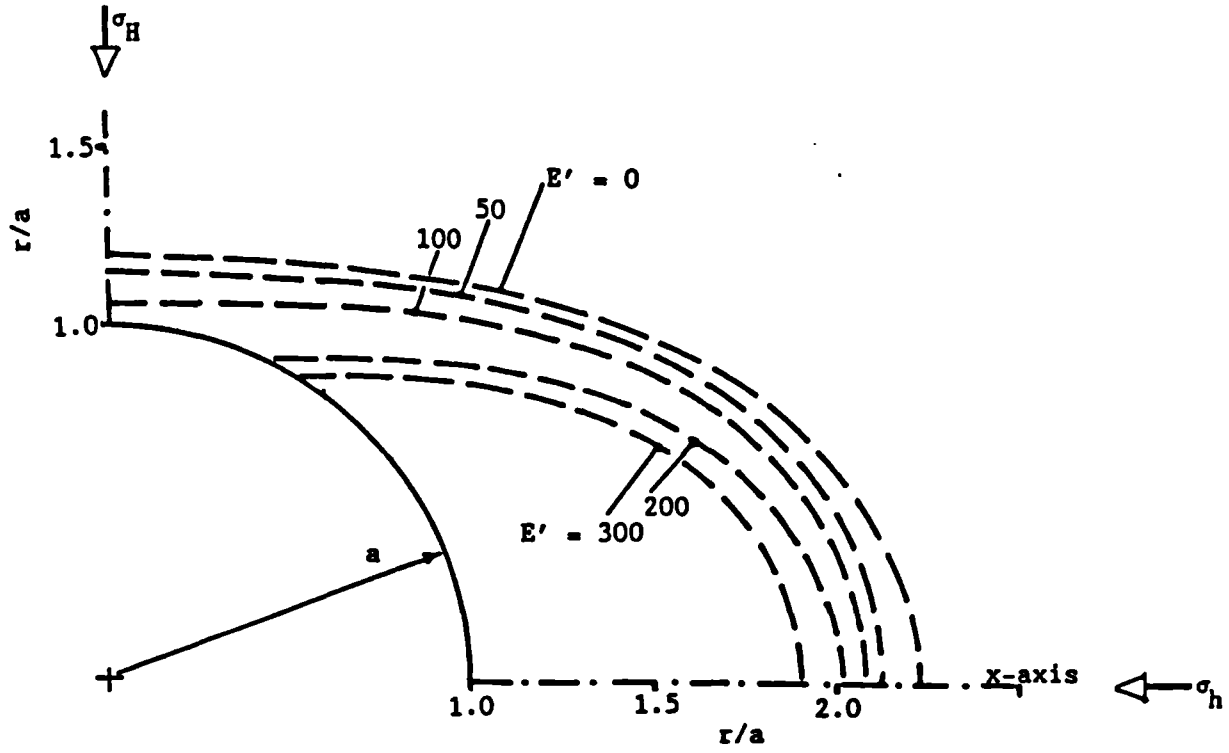
[Note: Apart from the introduction of PDS behaviour these are the same conditions used in the validation given in Section 5.5.1, using Galin's solution. The FEM mesh used is the finer one of the two used in Section 5.5.1, i.e. made up of 120 finite elements.]

The contour defining the elasto-plastic boundary determined by the FEM is given in Figure 6.15a. Table 16 gives a comparison between the FEM computed stresses and equations (32) and (33) for Gauss points lying within the plastic region. The agreement shown in Table 16 is comparable to the linear elasto-plastic validation shown in Table 9, Chapter 5. If an increase in accuracy is required, then a finer mesh and an increase in the number of load steps are likely to prove the best refinements.

In Figure 6.15b, the inferred elasto-plastic contour found from the FEM is plotted for a range of values of modulus variation parameter E'. The applied loading and strength are the same as before. The particular case of E'=0, is equivalent to a linear elastic behaviour. It can be seen from Figure 6.15b that the extent of the plastic zone reduces with increase in modulus variation, which might be expected. It was attempted to continue the analysis to include E'=400, however, the numerical instability discussed in Section 6.3.7 occurred in this case.



(a) FEM definition of contour for E′ = 300



(b) Variation of contour with E′

Figure 6.15 Elasto-plastic contour around a circular opening in an anisotropic in-plane in-situ stress field, where the material is defined by PDS elastic - perfectly plastic behaviour

Gauss point		σ_r/σ_Y			σ_θ/σ_Y			$\tau_{r\theta}/\sigma_Y$		
r/a	θ°	Exact	FEM	Error	Exact	FEM	Error	Exact	FEM	Error
1.026	3.2	0.126	0.129	2.3%	1.126	1.130	0.4%	0.000	0.009	-
1.026	18.2	0.126	0.125	0.8%	1.126	1.124	0.2%	0.000	-0.003	-
1.026	33.2	0.126	0.117	7.1%	1.126	1.116	0.9%	0.000	-0.001	-
1.026	48.2	0.126	0.127	0.8%	1.126	1.127	0.1%	0.000	-0.006	-
1.151	3.2	0.241	0.241	0.0%	1.241	1.240	0.1%	0.000	-0.009	-
1.151	18.2	0.241	0.250	3.7%	1.241	1.229	1.0%	0.000	0.016	-
1.151	33.2	0.241	0.226	6.2%	1.241	1.226	1.2%	0.000	0.007	-
1.291	3.2	0.355	0.340	4.2%	1.355	1.341	1.0%	0.000	0.005	-
1.291	18.2	0.355	0.353	0.7%	1.355	1.348	0.5%	0.000	0.019	-
1.291	33.2	0.355	0.346	2.5%	1.355	1.344	0.8%	0.000	0.013	-
1.449	3.2	0.471	0.479	1.7%	1.460	1.429	2.1%	0.000	0.009	-
1.449	18.2	0.471	0.475	0.8%	1.471	1.475	0.3%	0.000	0.010	-
1.626	3.2	0.586	0.596	1.7%	1.586	1.594	0.5%	0.000	0.004	-
1.626	18.2	0.586	0.558	4.8%	1.586	1.554	0.5%	0.000	0.011	-
1.824	3.2	0.701	0.717	2.3%	1.701	1.667	2.0%	0.000	0.001	-

Comparison of FEM and exact solution for the stress state in the plastic region for a material exibiting a PDS elastic-Tresca perfectly plastic response.

TABLE 16

6.6 QUANTITATIVE ASSESSMENT OF FAILURE PREDICTION

In this chapter and Chapters 3 and 5, comparisons have been made with other solutions to validate the program coding. In this section comparisons are made to assess the quantitative predictive capabilities of the program against the hollow cylinder tests Santarelli[18] carried out on a Carboniferous sandstone. Three behaviour models are used in this study which are:-

A. Linear elastic behaviour followed by strain softening.

B. Linear elastic behaviour followed by strain hardening to peak after which the material exhibits strain softening.

C. PDS elastic behaviour followed by strain hardening to peak after which the material exhibits strain softening.

The Hoek-Brown criterion is used for all three models to define yield. The strength parameters and flow rules for the sandstone during plastic deformation are defined in Section 4.7.2, Chapter 4. In material model A the hardening portion is simply ignored and initial yield is assumed coincident with peak strength. In model C, in addition to the plastic behaviour defined in Chapter 4, the elastic modulus of the material is assumed dependent on the minimum principal stress, defined by equation (3), where E_0 = 18.6 GPa, and E' = 314. The modulus for the linear elastic response is taken as 19 GPa.

In the laboratory tests failure initiation occurred at an external pressure of around 130 MPa and was determined from visual inspection of the internal wall of the hollow cylinders. This was the limit of the testing equipment, and therefore it was not possible to continue loading

beyond failure. In the numerical analysis we may consider that visual failure occurs when a stress point lies somewhere between peak and residual strength. Thus, a range within which failure occurs is given rather than a particular value.

The FEM used 20 radial finite elements to define the hollow cylinder. With an internal radius of 12.7 mm, the equivalent radius of the inner most Gauss point for this mesh is 12.9 mm (i.e. 0.2 mm from the wall).

Figure 6.16 shows a plot of the radial closure for the three model characterizations of the sandstone, and the actual test results, as a function of the external loading. Figure 6.16 also gives the loads at which the innermost Gauss point reaches yield, peak and residual strength for each model. The range within which the 3 models predict failure to occur are

Model A - 46 MPa → 75 MPa

Model B - 65 MPa → 80 MPa

Model C - 130 MPa → 225 MPa

Thus, model C gives the best estimate of failure load, although the range is large. For a power law PDS expression, both the range and lower and upper limits are likely to be less due to the increased stress severity predicted close to the internal wall (see Section 6.2.2.1). With respect to displacement predictions, the general shape of the curve predicted by model C is also a better representation than the other 2 models. Again, an improvement in the displacements predicted at higher values of outer pressure (> 60 MPa - see Table 15) would be found by using a power law expression for Young's modulus.

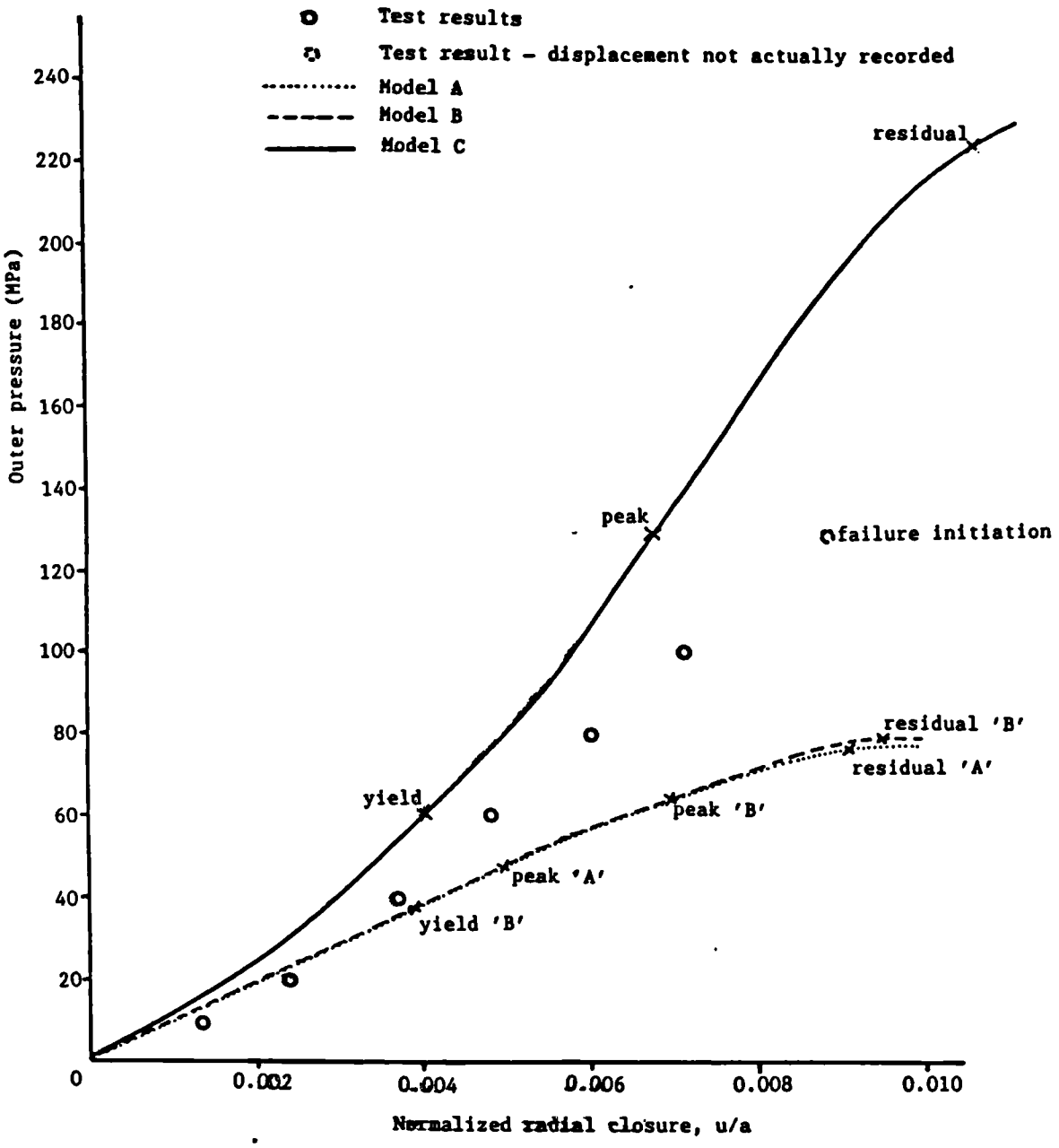


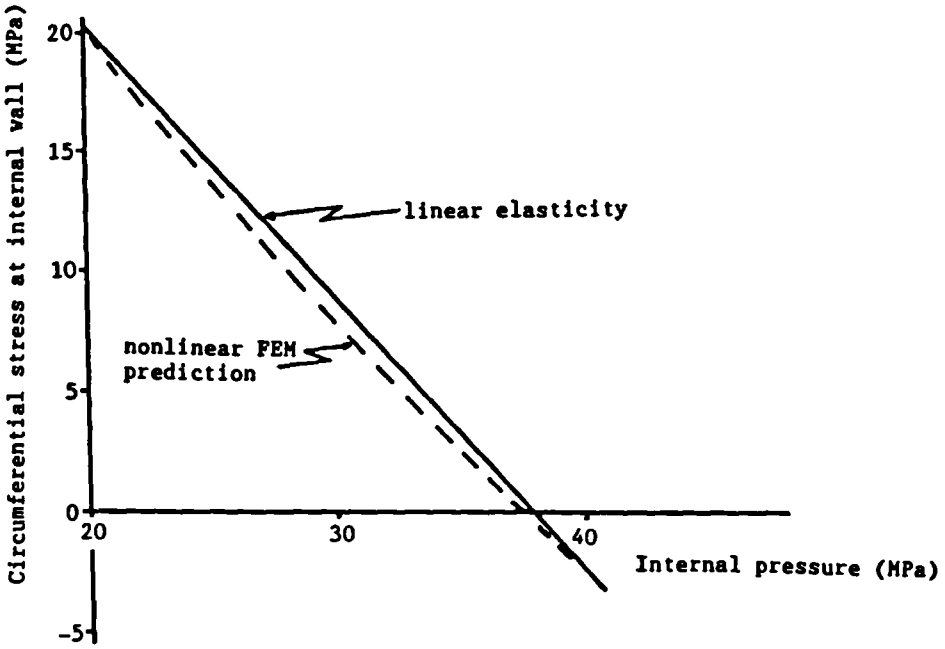
Figure 6.16 Comparison between hollow cylinder test results on a Carbonierous sandstone (Santarelli[18]) and model predictions.

In the case of model C, it is recognized that the large increase in load required to take the inner most Gauss point from peak to residual strength is to some extent a function of using a linear behaviour law. However, it may also indicate that, provided partially broken rock remains in place, a considerable increase in load is required to propagate failure over that required to initiate failure. In addition, the PDS elasto-plastic model can sustain further loading after the inner most Gauss point has reached residual strength, which is not the case for the linear elasto-plastic models (Note: Where the domain is unbounded by the introduction of an infinite element the linear elasto-plastic model is also able to sustain further loading). Laboratory support for the continued load carrying capacity after failure initiation in hollow cylinders is again found in Santarelli's results. In the case of the Gebdykes dolomite and Doddington sandstone, loading was increased after failure at the internal wall without a catastrophic failure of the whole sample.

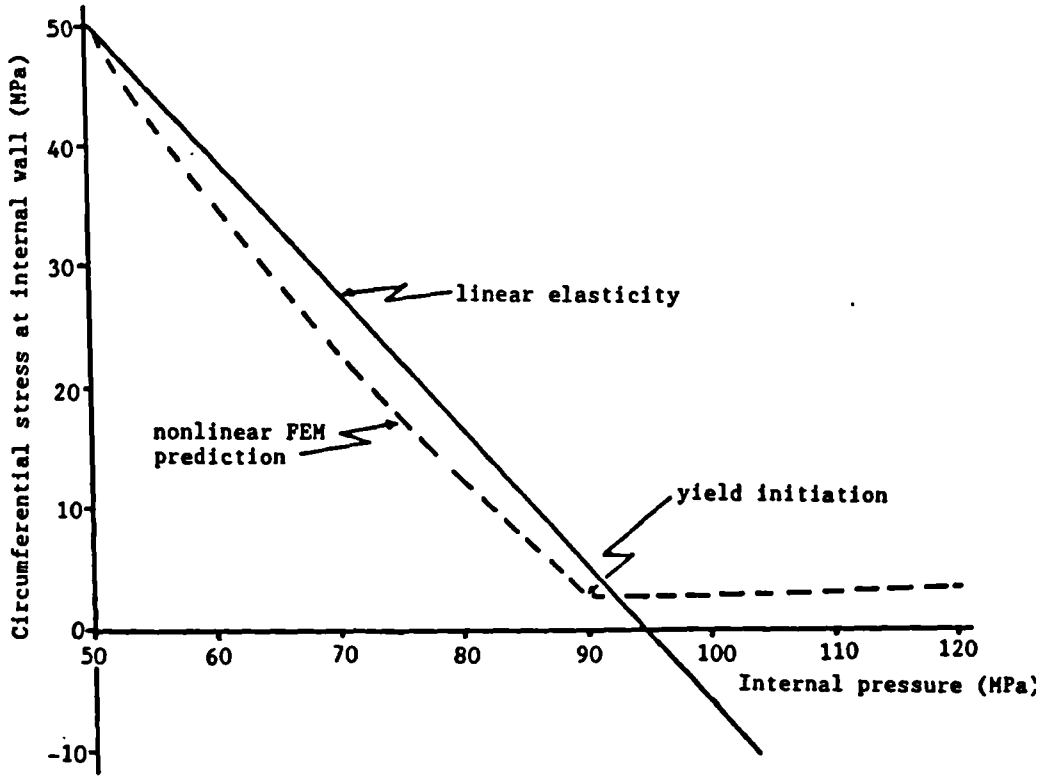
6.6.1 Tensile Failure

The tests performed by Santarelli did not investigate tensile failure in hollow cylinders induced by the application of internal pressures. However, it is worth presenting here the influence that the nonlinear behaviour laws have on the prediction of tensile failure, relative to using linear material properties.

In Figure 6.17a the predicted circumferential stress is plotted as a function of internal pressure for a simulated hollow cylinder test on the Carboniferous sandstone sample, where the outer pressure is held at 20 MPa. It is seen that the difference between the linear elastic



(a) 20 MPa External pressure



(b) 50 MPa External pressure

Figure 6.17 Predicted circumferential stress at the internal wall of a hollow cylinder of the Carboniferous sandstone with a high internal pressure.

solution and the PDS elastic solution is minimal, with PDS predicting that the pressure required to initiate tension is marginally less than the linear elastic value. At no stage during this simulation is compressive yield reached, thus the response is totally elastic.

In Figure 6.17b the results for the simulation are presented, where the outer pressure is now increased to 50 MPa. In this case compressive yield is reached before tension is initiated at the internal wall of the cylinder. Here the radial and circumferential stresses are the maximum and minimum principal stresses respectively, with yield initiated at an internal pressure of around 90 MPa. Thereafter, the stress state in the yield zone must conform to the compressive yield criterion, unless the internal pressure is reduced, whereupon elastic unloading is predicted. As the internal pressure is increased further, elements of rock within the yield zone undergo plastic extensional strain in the circumferential direction, thus allowing a build up in the circumferential stress. The result of this behaviour is that it is impossible to induce a tensile stress at the internal wall, whatever the internal pressure. Figure 6.18 shows the predicted distribution of the circumferential stress throughout the sample, for an internal pressure of 150 MPa. The minimum circumferential stress is no longer at the internal wall of the sample, but some finite distance inside. This is an interesting result, however, in practice it is likely that fluid penetration into the broken zone makes this behaviour impossible to achieve under field conditions.

As mentioned in Item 8 of Section 1.5, Chapter 1, Morita and Gray[31] carried out an analysis to predict fracture initiation pressures using a complex nonlinear behaviour law. In their analysis the nonlinear model predicted fracture initiation pressures around 17% greater than the

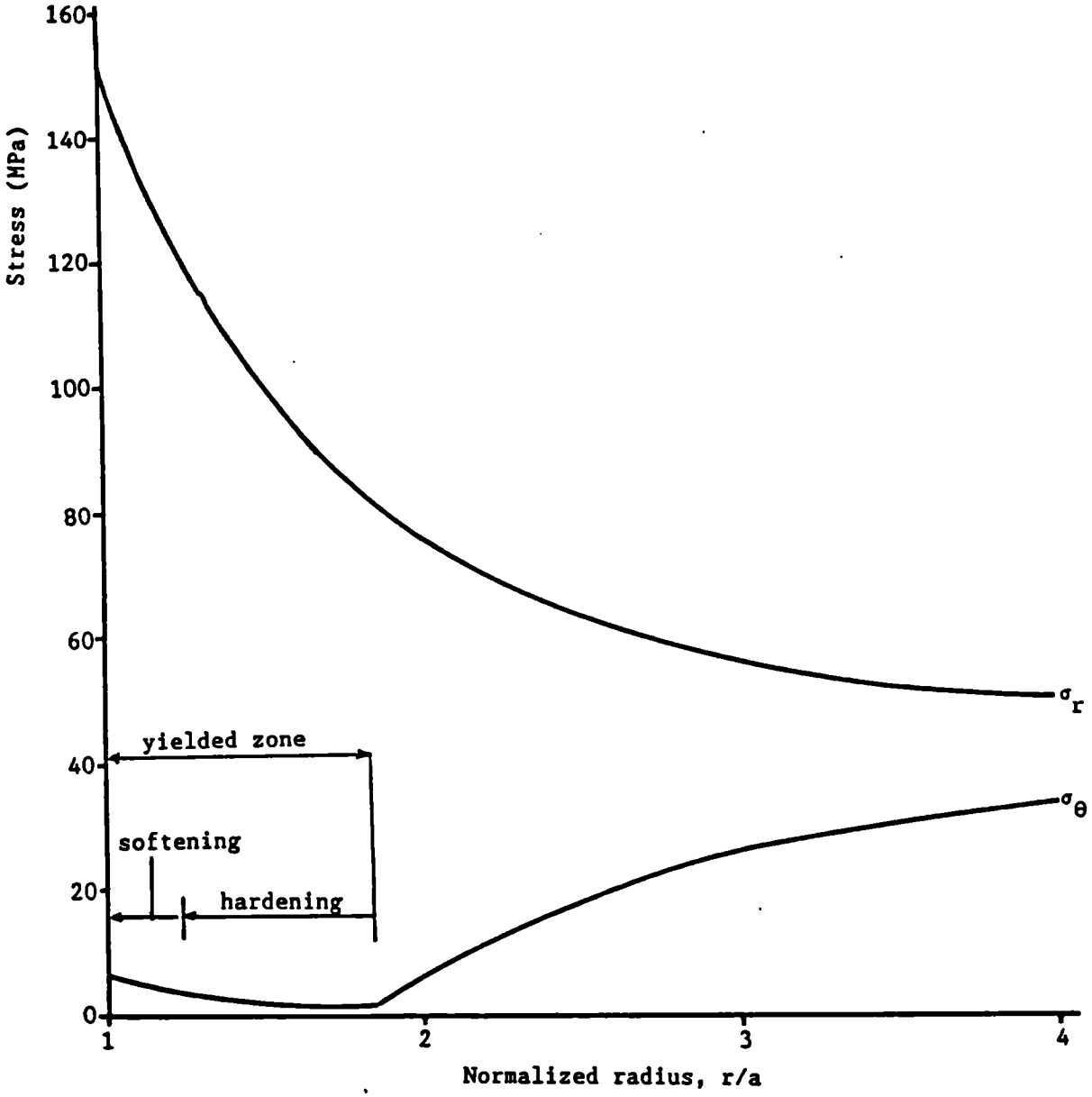


Figure 6.18 Predicted variation of radial and circumferential stress within a hollow cylinder of the Carboniferous sandstone with external and internal pressures of 50 and 150 MPa respectively.

linear elastic predictions. The majority of their simulations predict fracture initiation before the peak compressive strength of the sample is reached. However, in the simulation of a well at 15,000 ft, the stress state violates the uniaxial compressive strength of the sample, and it is surprising that this was not noted in their publication.

Although little or no published data on laboratory determined fracture initiation pressures exists, some unpublished work suggests that in certain circumstances the actual fracture initiation and propagation pressures far exceed those predicted by linear elasticity (by a factor of 5 or more). However, the key to better analysis of these results lies in attention to fluid rheology and scale effects rather than nonlinear material properties (personal communication - Professor Yew, University of Texas at Austin).

In conclusion, allowance for PDS behaviour appears to have little influence on the prediction of tensile failure induced by hydraulic fracturing. However, if compressive yield is initiated before fracture initiation pressures are reached, then tensile failure will never be predicted. It is suggested that in areas of hydraulic fracturing the difference between simple closed form analyses and laboratory data is significant. Potential for both laboratory and analytical work exists in this area.

6.7 PARAMETRIC ANALYSIS

Findings from previous sections show that allowance for PDS and pre-peak yielding behaviour can have a significant effect on the prediction of compressive failure. Tensile failure predicted by PDS elasticity is marginally less than that predicted by linear elasticity.

However, if compressive yield is initiated where the radial stress is the maximum principal stress then tensile failure will not occur.

Findings from Santarelli's hollow cylinder tests on a Carboniferous sandstone justify the nonlinear modelling of compressive failure. However, these findings are for the axisymmetric loading case only. In general, field in-situ stresses and wellbore directions do not facilitate an axisymmetric solution. Thus, the parametric analyses carried out here concentrate on the influence of PDS behaviour when we move from axisymmetric conditions to conditions of anisotropic loading.

Three parametric analyses are presented in the following sections. The first investigates the predicted stresses around a vertical wellbore under plane strain conditions as a function of stress anisotropy, σ_H/σ_h, (where σ_H and σ_h are the maximum and minimum horizontal stresses respectively), and the extent of the Young's modulus variation. The second study investigates the effect of in-situ stress anisotropy, again under plane strain conditions for the particular case of the Carboniferous sandstone, where response includes plasticity as well as PDS elasticity. The final study looks at the predicted mud weights required to prevent failure of deviated wells where response is modelled using PDS elasticity.

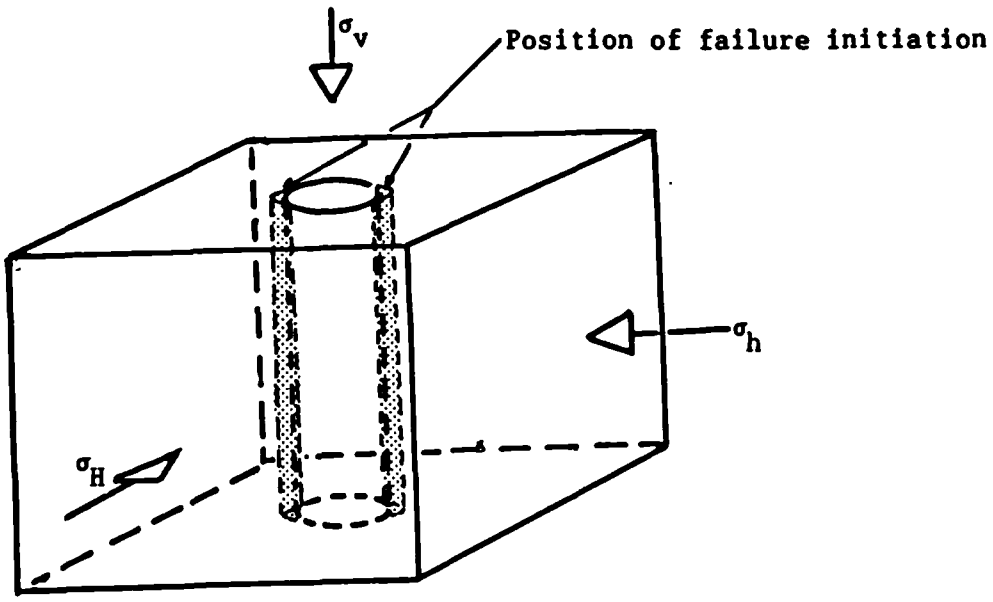
6.7.1 Influence of PDS Elasticity in Anisotropic In-Situ Stress Regimes

This study investigates the influence of PDS elasticity on predicted stresses as a function of in-situ stress anisotropy. To facilitate this study the conditions are related to a vertical well where the material response is totally elastic up to failure (i.e no

plasticity). The loading conditions and the position of failure initiation are given in Figure 6.19. Analyses were carried out to determine the value of the in-situ stress parameter σ (defined in Figure 6.19) at failure initiation. In Figures 6.20a & b the value of σ at failure using PDS elasticity, σ_{PDS}, is divided by the linear elastic value of σ at failure, σ_{LE}. The ratio σ_{PDS}/σ_{LE} is therefore a measure of the 'strength enhancement' resulting from PDS behaviour. Two values of Poisson's ratio are considered. In Figure 6.20a we have $\nu = 0.2$, and in Figure 6.20b, $\nu = 0.4$. In both figures the uniaxial modulus, E_0, is given by $E_0/\sigma_c = 200$.

It is seen from Figures 6.20a & b, that as the modulus variation parameter, E', is increased then the load carrying capacity of the opening relative to that predicted by linear elasticity is enhanced. This is true for the whole range of stress anisotropies shown in Figure 6.20. However, the ratio of PDS strength to linear elastic strength (σ_{PDS}/σ_{LE}) reduces as the anisotropic nature of the stress field increases. Thus, if we were to carry out a set of tests simulating wellbore instability on true triaxial samples (e.g. Bandis et al[89]), then we would expect the difference between load at failure and linear elastic predictions to be the most extreme in the case of hydrostatic loading. The sensitivity of the ratio, σ_{PDS}/σ_{LE}, to stress anisotropy is greatest where conditions are close to hydrostatic. These predictions lead to the requirement for a testing program on true triaxial samples to validate the model under anisotropic loading, or highlight the need for refinements in the model behaviour.

From comparison of Figures 6.20a & b it is seen that Poisson's ratio, ν, has an influence on the predicted failure loads under all the stress states considered. The sensitivity of failure prediction to the



Stress anisotropy = σ_H/σ_h

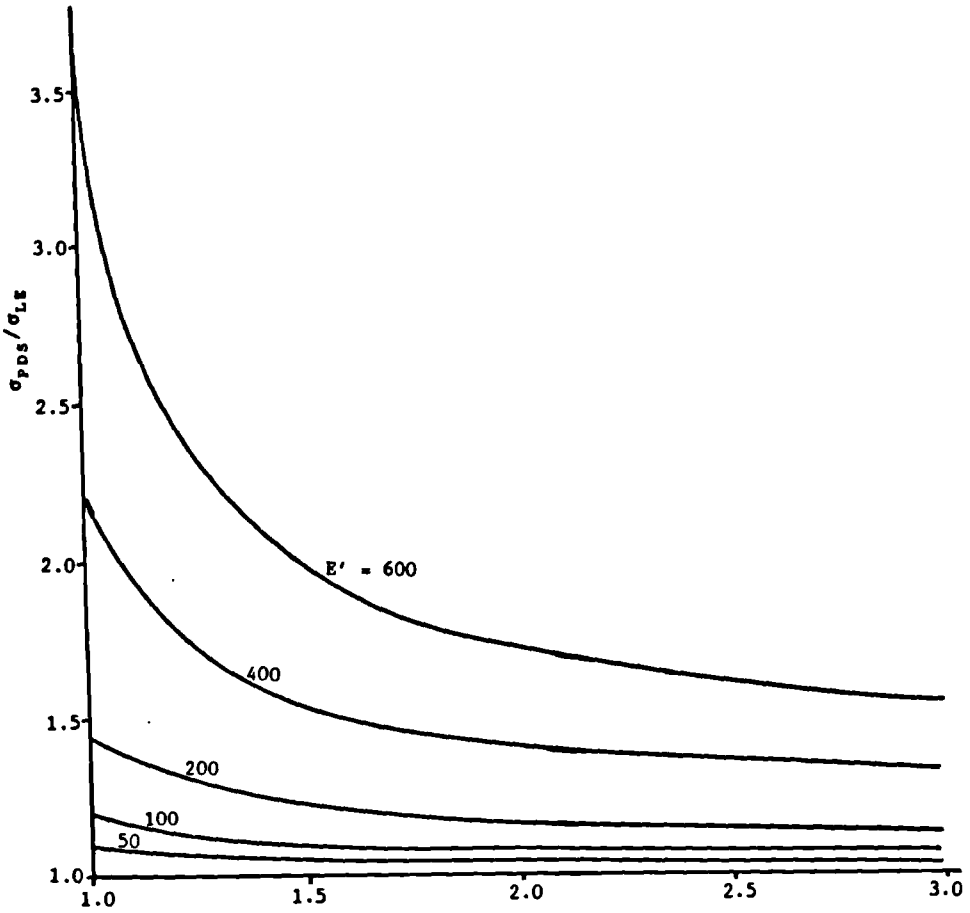
Stress state defined by $\sigma_h < \sigma_v < \sigma_H$

where $\sigma_v = \frac{1}{2}(\sigma_h + \sigma_H)$

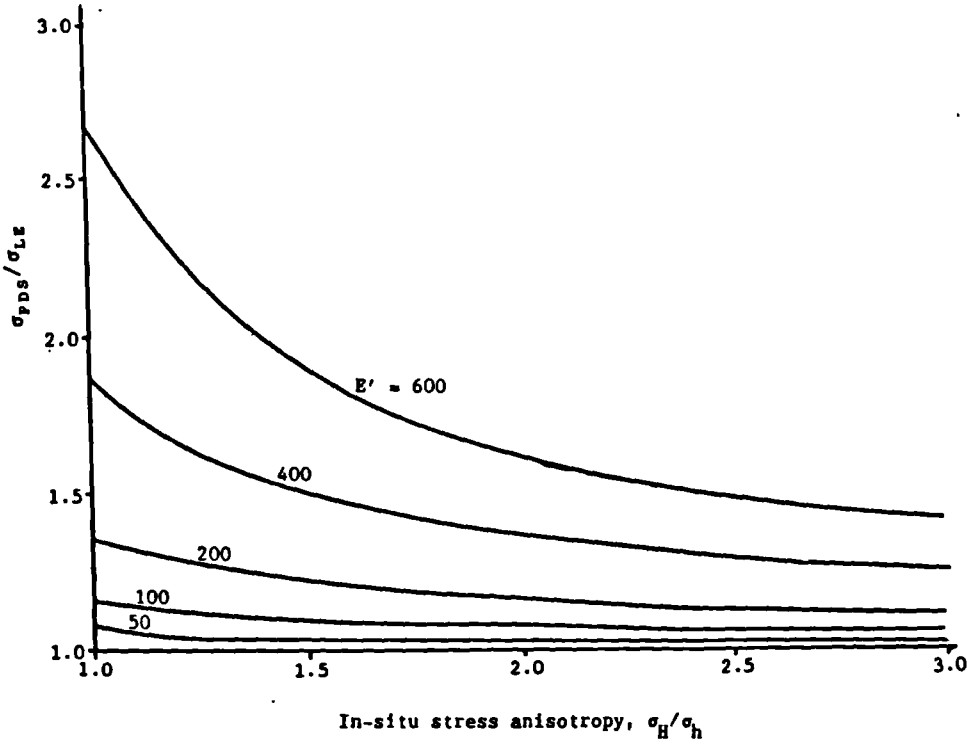
At failure initiation, σ is defined by

$$\sigma = \frac{1}{3}(\sigma_h + \sigma_v + \sigma_H)$$

Figure 6.19 Assumed loading conditions at infinity for study of PDS behaviour under anisotropic.



(a) Poisson's ratio = 0.2



(b) Poisson's ratio = 0.4

Figure 6.20 Ratio of σ_{PDS}/σ_{LE} as a function of in-situ stress anisotropy.

values of Poisson's ratio chosen is greatest under hydrostatic conditions. Taking the case where E'=400, then a reduction of ν from 0.4 to 0.2 increases the predicted failure load by 37%, for hydrostatic conditions. The influence ν on predicted failure does not decrease monotonically with increase in anisotropy, and from inspection of Figures 6.20a & b it is seen that ν appears to have the least influence when $\sigma_H/\sigma_h \simeq 1.5$. In linear elastic analyses both Young's modulus and Poisson's ratio have no influence on the stress state around a circular opening when the material is homogenous and isotropic. However, if PDS elastic behaviour is prevalent then ν can be an important parameter and careful determination of its value may be required.

6.7.2 Failure of the Carboniferous Sandstone under Anisotropic Loading

In the previous section the effect of in-situ stress anisotropy on PDS elastic predictions was investigated. Here the influence of stress anisotropy is investigated where the material is modelled using PDS elastic coupled with plastic behaviour. The vast number of parameters that can now be varied makes a complete parametric analysis unreasonable, therefore the study is restricted to the Carboniferous sandstone behaviour already characterized.

Loading is again represented in Figure 6.19. Failure initiation is taken to be the point where the most critically stressed Gauss point reaches its peak strength. Thus, stress points only undergo pre-peak yielding and the strain softening portion is irrelevant. The value of σ (see Figure 6.19) at failure for the PDS elastic-plastic response, σ_{NL} (subscript 'NL' ≡ nonlinear), is divided by σ_{LE} (the in-situ stress at failure assuming a linear elastic response) and plotted in Figure 6.21

as a function of in-situ stress anisotropy. In addition, the ratio σ_{PDS}/σ_{LE}, where σ_{PDS} is the failure stress when only the PDS behaviour is considered, is plotted in Figure 6.21.

From Figure 6.21 it can be seen that both the PDS elastic and pre-peak plastic behaviour help to enhance the stability of the opening over the whole of the stress anisotropy range chosen. The significance of including pre-peak yielding, relative to the PDS elastic behaviour only, appears to increase with the degree of in-situ stress anisotropy. For example, under hydrostatic conditions inclusion of pre-peak yielding increases strength enhancement relative to linear elasticity from 2.14 to 2.90, whereas, for a stress anisotropy of 2.5 the increase is from 1.34 to 1.64. Thus, although in absolute terms the significance of including the plastic portion decreases with stress anisotropy, in relative terms (i.e. with respect to PDS only) the significance increases.

6.7.3 Mud Weights Required for Deviated Wells

In this study the influence of PDS elasticity on required mud weights in deviated wells is investigated using the FEM program. Ideally, the analysis should investigate mud weights for a rock characterized in the laboratory, where both the PDS elastic and plastic portions from triaxial stress-strain curves can be included. However, the only material characterized here is the Carboniferous sandstone, which is particularly strong relative to problem formations encountered in practice. As mentioned in Section 5.6.1.1, Chapter 5, the strength of the Carboniferous sandstone does not facilitate failure at realistic drilling depths. At the depths required to induce failure in this rock

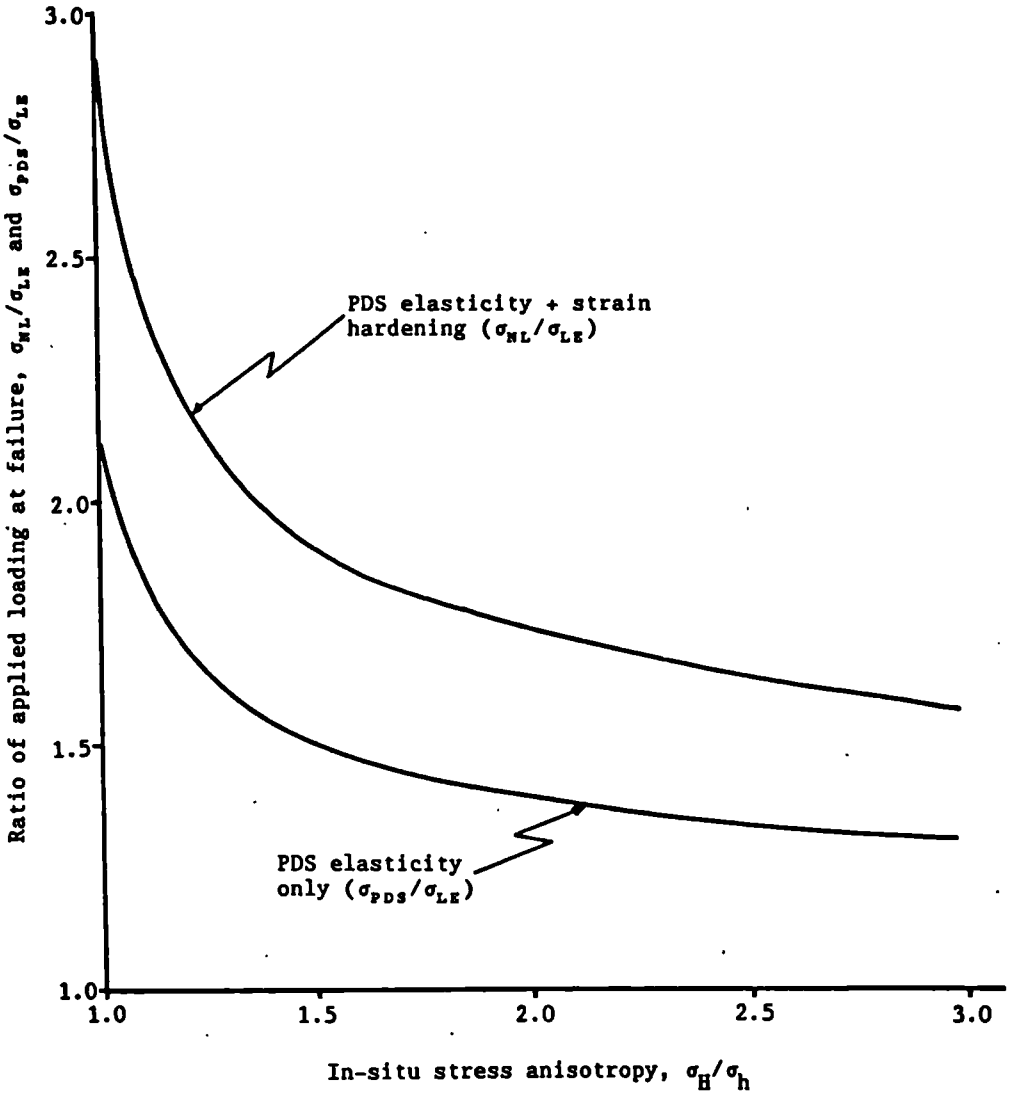


Figure 6.21 Variation of FEM predicted failure loads relative to linear elastic failure loads as a function of in-situ stress anisotropy for the Carboniferous sandstone.

the overbalance (support) pressure would be highly sensitive to variations in mud weight, and the resulting analysis could not be related to current drilling experiences. Thus, although not entirely satisfactory, a model material has been chosen.

The model material strength parameters, depth and in-situ stress gradients are taken as that used in the linear elastic analysis carried out in Section 2.8, Chapter 2. For sake of clarity the whole problem is defined below.

Yield criterion: Mohr-Coulomb

strength parameters at peak: $c = 4.8$ MPa (700 psi)

$\phi = 30°$

$\therefore \sigma_c = 16.6$ MPa (2420 psi)

Uniaxial modulus, $E_0 = 4000$ MPa (5.8×10^{-5}psi), $\therefore E_0/\sigma_c = 240$,

modulus variation parameter, $E' = 200$, 400 and 600

Poisson's ratio = 0.25

In-situ stress gradients: vertical = 0.023 MPa/m (1.0 psi/ft)

max. horizontal = 0.019 MPa/m (0.85 psi/ft)

min. horizontal = 0.016 MPa/m (0.70 psi/ft)

Formation pressure gradient = 0.011 MPa/m (0.45 psi/ft)

Depth = 1820 m (6000 ft)

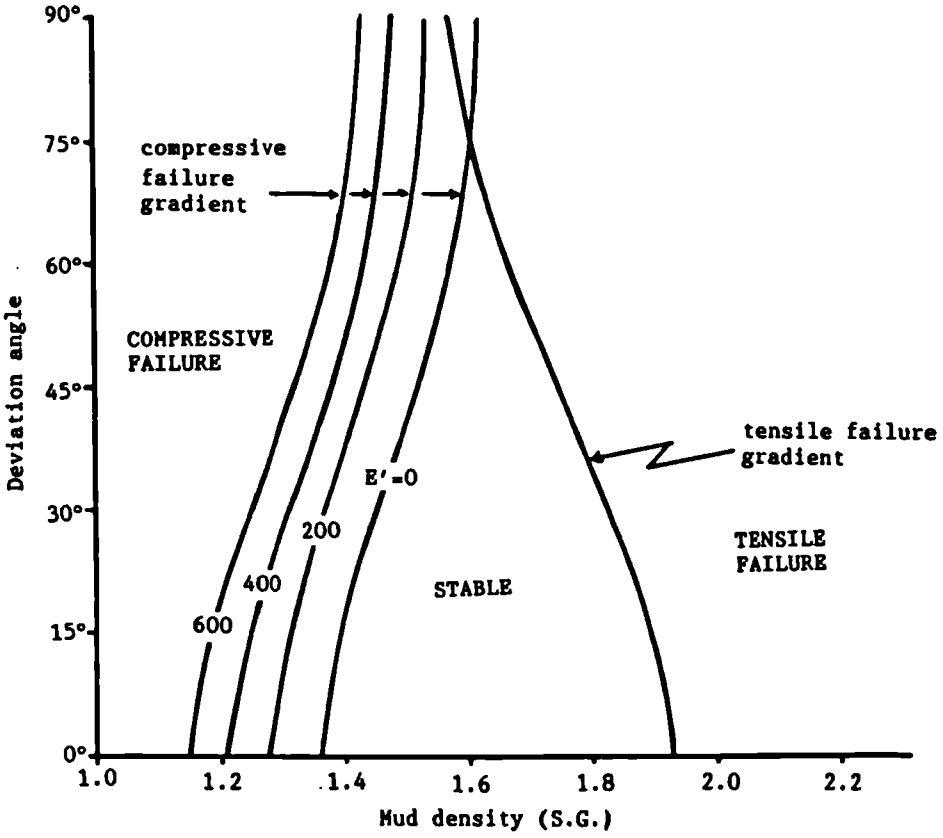
Temperature effects are not considered.

In Figures 6.22a & b the mud weights required to prevent compressive failure (as determined by the FEM) are plotted for wells deviated in the direction of the maximum and minimum horizontal stress respectively. Tensile failure is deemed to be the point where tension is is initiated (i.e. the rock has zero tensile strength). The tensile failure plot has been determined for linear elasticity only, since PDS elastic behaviour

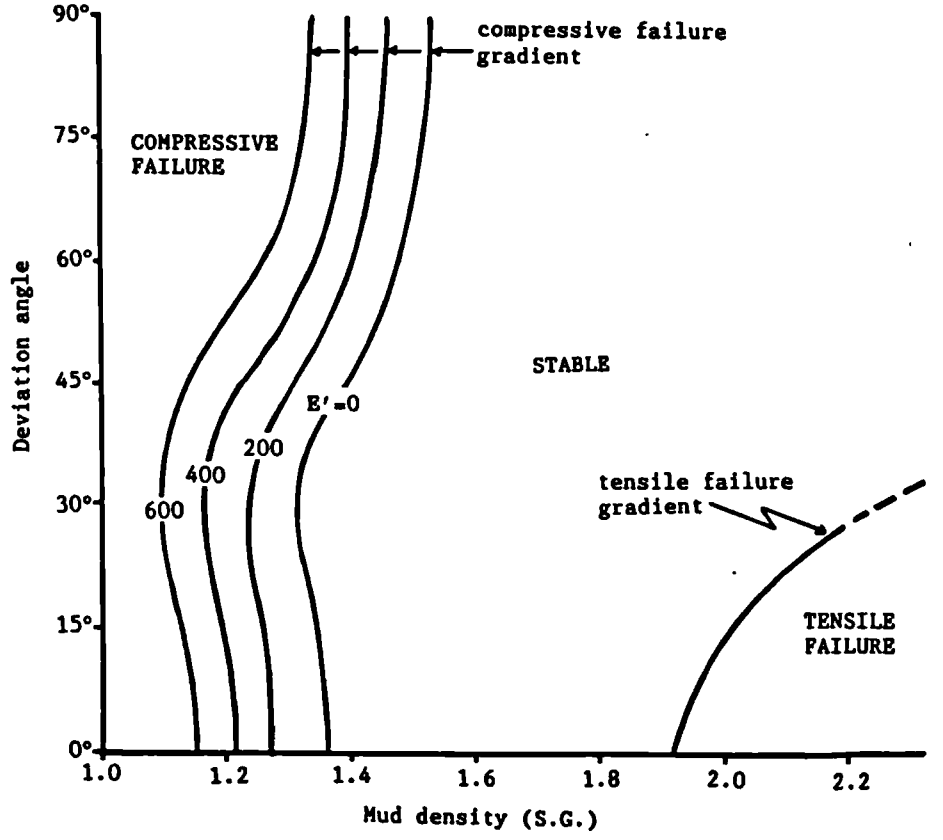
appears to have little influence on tensile failure (Section 6.6.1), and to generate the mud weights for the various values of E′ and deviation angles is a lengthy process. Generation of the compressive failure plots in Figures 22a & b, required around 150 runs of the program at approximately 30 minutes real time per run.

For a well of given azimuth, σ_θ at the wall is dependent on both the support pressure, P_a, and the PDS behaviour. The more marked the PDS response the less severe the maximum predicted value of σ_θ at the wall. However, failure for rocks with realistic friction angles is more sensititive to variations in the minimum principal stress, σ_r (= P_a at the wellbore wall), than the maximum principal stress, σ_θ. The variation of σ_r at the wall of the opening is independent of PDS behaviour. Thus, we may expect the influence of PDS behaviour to be less marked here than in Section 6.7.1, where the predicted far field stresses at failure for constant (zero) support pressure was investigated.

The above conclusions regarding the sensitivity of PDS behaviour on mud weights are born out in Figures 6.22a & b. For the vertical well, where the anisotropy of the effective horizontal far field stresses is around 1.6, the mud weight varies from 1.36 to 1.15 over the range of the range of E′ values chosen. Comparing with Figure 6.20 then, the far stresses required to induce failure at a similar stress anisotropy, vary from a factor of 1.0 to 1.9 (ν = 0.2) and 1.0 to 1.8 (ν = 0.4). However, in practical drilling terms, where changes in mud density of only 0.1 is considered notable, a reduction in mud weight from 1.36 to 1.15 is extremely significant. Lower mud weights reduce the possibility of fracturing the formation and differential sticking and increase the



(a) Well deviated // to σ_H



(b) Well deviated // to σ_h

Figure 6.22 Variation of mud weight requirements for prevention of compressive failure as a function of well deviation and PDS elasticity parameter E′.

rate of penetration (ROP). This reduction in mud weight with increased PDS behaviour is true for all well azimuths considered.

Note: A direct comparison between Figures 2.9 and 2.10, Chapter 2, and Figures 6.22a & b is not possible, since in Figures 2.9 and 2.10, temperature effects are considered and the mud cake is not fully effective.

6.8 CONCLUDING REMARKS

To summarize, the concept of PDS elasticity as defined by Santarelli[18] has been introduced. The necessity for introducing this behaviour, as opposed to linear elasticity, has been born out by experimental and analytical work on hollow cylinders of sandstone. It's introduction allows for better quantitative analysis of circular openings in rock.

A linear law defining PDS elasticity has been introduced and shown to have good correlation with the more applicable power law. However, at high stress levels agreement between the two reduces. The linear law has advantages over the power law in respect to numerical considerations in the FEM.

The process of implementing PDS elasticity and coupling it with plastic behaviour has been explained and a number of coding validations performed to give confidence in the numerical procedure.

With respect to compressive failure, PDS elasticity can have a significant effect on the predicted load required to induce failure of a circular opening under axisymmetric loading. In the case of the Carboniferous sandstone this load is around twice that predicted by

linear elasticity. Inclusion of pre-peak yielding further increases the predicted failure load.

Parametric studies show that as anisotropy in the far field stresses increases, the influence of PDS behaviour (relative to linear elasticity) on failure loads decreases. However, for all in-situ stress anisotropies covered, PDS elasticity predicts higher failure loads than predicted by linear elasticity. The parametric studies also show that Poisson's ratio can have a significant influence on predicted failure loads when using PDS elasticity.

A further parametric study showed that predicted mud weights required to support deviated wells at typical depths are also significantly influenced by the introduction of PDS behaviour.

CHAPTER 7

SUMMARY OF WORK AND FUTURE RESEARCH REQUIREMENTS

7.1 SUMMARY OF WORK PRESENTED

The purpose of this research was to develop a wellbore stability analysis that may eventually be used by The British Petroleum Company as a practical diagnostic and predictive tool for field instability studies.

In Chapter 1 of this thesis wellbore instability is defined and put into the context of the drilling operation. A review of previous wellbore instability case histories and analytical/numerical models is presented. The literature reveals a notable lack of case histories, whereas publications of theoretical analyses on wellbore stability are in relative abundance.

In the opinion of this author, apart from the model presented by Santarelli,[18] the models based on linear elasticity are the most useful to practicing engineers. Complex numerical analyses are only useful if they (a) allow an assessment of the influence of various parameters on the stability of a structure too complex to analyse using simple models, or (b) allow a quantitative assessment of stability where simple models may only provide a qualitative assessment. No laboratory or field data has been presented to show that any of the complex models (e.g. Morita and Gray[31]) give any significant improvement in predictions than can be attained from a simple linear elastic analysis. The exception to this is the laboratory and analytical work carried out by Sanatrelli,[18] where he shows that much improved quantitative predictions can be

attained by close attention to material behaviour found from triaxial tests. However, Santarelli's analyses were for the simple case of axisymmetric loading of hollow cylinders, and is therefore unsuitable for vertical wells in anisotropic horizontal stress fields or deviated wells. Nor does Santarelli consider variation of pore pressure and temperature gradients which occur in practice.

On drawing the conclusion that linear elasticity still provides a useful medium for analysis of wellbore stability, Chapter 2 was devoted to presenting, and in certain cases developing, equations based on linear elasticity. These solutions allow assessment of the influence of a wide variety of parameters on wellbore stability. The parameters which may be studied include temperature, time, well deviation, mud cake effectiveness, both under and overbalance conditions, long term and short term stability in low permeability formations and rock mechanical properties. It is recognized that linear elasticity is unlikely to provide a quantitative assessment of stability. However, a qualitative assessment alone is still of great use to the engineer.

The remainder of the thesis was devoted to the application of the FEM to analysis of stability around a circular opening. The original objectives for this research were to develop a program capable of analyzing deviated wells and allow for strain softening behaviour and pore pressure gradients. Chapter 4 described the process of using plasticity to define both strain hardening and strain softening behaviour. Techniques for implementing this behaviour into the FEM were presented in Chapter 5.

In parallel with this work Santarelli[18] carried out a laboratory study of failure induced in hollow cylinders. The results from Santarelli's tests showed that neither linear elastic nor standard

elasto-plastic analyses (including strain softening) were able to adequately predict sample response. An elasto-plastic analysis of a circular opening in a homogenous material, if not quantitative in its predictions, provides little additional information to the engineer that cannot already be attained from a linear elastic analysis. This being the case, a FEM program based on a linear elastic - strain softening plastic material response is pointless. Incorporation of pore pressure gradients into such a model would only add to the folly of the program.

Santarelli showed by incorporating an elastic modulus dependent on stress state (as identified in triaxial testing) much improved predictions of hollow cylinder behaviour were attained. Thus, it was decided that this work should concentrate on incorporating PDS elasticity into the already developed elasto-plastic FEM coding. To achieve this within the allotted work program, inclusion of pore pressure gradients was dispensed with. Chapter 6 presents the techniques required to implement PDS elasticity into the program and couple it with plastic behaviour. Numerical instability may occur in the algorithm, however for realistic rock behaviour this is unlikely. Limited coding validation for coupled PDS-plastic behaviour in Chapter 6 and quantitative comparisons are made with Santarelli's hollow cylinder test results. Finally, the facilities of the program are fully utilized by providing predictions of failure relative to linear elasticity for various in-situ stress anisotropies and well deviations.

Throughout the thesis various parametric studies have been carried out. These concentrate on studying the effect of real physical parameters on stability, rather than numerical parameters such as mesh sizes, number of Gauss points, number of load steps and CPU time. The numerical parameters, although important, are of less interest to the

engineer. However, within the coding validations some examples are given to provide insight into the effect of these numerical considerations.

7.2 MAIN CONCLUSIONS

The main conclusions of the thesis are itemized below.

1. Mechanical wellbore instability exists and can cost the Petroleum Industry large sums of money each year. To the knowledge of this author, the extent of this cost has not been published by any of the operators.

2. The foundation for improved knowledge and understanding of wellbore instability are case histories. However, published examples are scarce.

3. Numerous theoretical approaches to wellbore instability have been published, yet only one (Santarelli[18]) appears to be validated under controlled conditions. Thus, little credibility can be assigned to the others.

4. In the absence of other proven theories, linear elasticity still provides one of the best approaches for understanding wellbore instability.

5. A vertical well may not always be the most stable (Section 2.8.3.1).

6. Temperature gradients set up between the formation and the drilling fluid may have a significant influence on the short term stability

in low permeability formations. In the long term, or in permeable formations, its influence (or lack of) is strongly dependent on the stiffness and thermal expansion properties of the rock (Section 2.8.3.2).

7. An effective mud cake has a significant role in providing stability (Section 2.8.3.4).

8. Attention to pore pressure redistribution maybe necessary when interpreting leak off test results (Section 2.8.3.5).

9. Time may be one of the most important parameters when analyzing stability in low permeability formations (Section 2.9).

10. Failure maybe induced through tensile effective radial stresses in underbalance conditions in low permeable formations (Section 2.9.3).

11. Plasticity maybe used to describe the post yield behaviour of rocks through to residual strength.

12. Use of associated flow with a Mohr-Coulomb criterion may grossly overestimate sample dilation. With a Hoek-Brown criterion associated flow may prove acceptable until residual strength is reached, after which an overestimation of dilation is again predicted (Section 4.7.3).

13. When drilling close to balanced conditions in materials with low cohesive strength, considerable differences in failure may be found between using a Mohr-Coulomb and Hoek-Brown yield criterion (Section 5.6.2.3).

14. The ratio of the outer to inner diameter of a hollow cylinder sample and the loading path adopted may influence the resulting failure pattern (Section 5.6.4.2).

15. In a homogeneous, isotropic material, breakout analyses may be used for wells deviated up to as much as 40°. However, cases where these conditions would be met are likely to be scarce (Section 5.6.5.3).

16. Introducing PDS elasticity and coupling it with plasticity may transform a qualitative analysis of wellbore stability into a quantitative analysis.

17. Use of a linear relationship between Young's modulus and confining pressure is acceptable over a limited confining range. For cases of high in-situ stress states the linear law may underpredict displacement and overpredict strength (Section 6.2.5).

18. The application of strain softening is not without criticism, however, when coupled with PDS elasticity, it helps to explain the continued load carrying capacity of hollow cylinders after initiation of failure (Section 6.6).

19. If compressive yield is initiated before circumferential tension when pressurizing up a circular opening, then no hydraulic fracturing is predicted to occur, provided no fluid penetration takes place (Section 6.6.1).

20. PDS elasticity greatly increases the predicted loads required to initiate failure of a circular opening relative to linear elasticity. However, this strength enhancement reduces with increased in-situ stress anisotropy (Section 6.7.1).

21. When using PDS elasticity, Poisson's ratio can have a significant influence on the prediction of failure initiation (Section 6.7.1).

7.3 RESTRICTIONS AND POTENTIAL AREAS FOR IMPROVEMENT

The purpose of this section is (i) to highlight the short comings of this work to try and ensure that anomalous interpretations do not result from its application, and (ii) allow the interested researcher to follow on with extensions, modifications or validations of this work. To facilitate the possibility of further work, specific topics are highlighted.

7.3.1 Restrictions of this Research

Throughout this text the main assumptions are stated and reiterated. However, a number of these assumptions, their implications plus other limitations are itemized below.

1. In all the analyses carried out formations are assumed to be homogeneous and isotropic, although some heterogeneity is facilitated by the introduction of elastic and plastic regions. For a wellbore, the size of the hole is likely to be small relative to formation thicknesses and discontinuity frequency. Thus, the assumption of homogeneity does not really present any significant draw backs when applied to wellbore stability. However, the assumption of material isotropy is a significant restriction when drilling through shale formations, where both strength and elastic

parameters may only conform to transverse isotropy within the plane of bedding. Thus, in shale formations, the only case where the assumption is acceptable is when drilling a vertical well in a horizontally bedded formation. For deviated wells or dipping formations, the assumption is poor.

2. In the study of the effect of time on the stability of low permeability formations (Section 2.9) the analysis is restricted to a vertical well in an isotropic horizontal stress field.

3. Throughout the text, material strength is assumed to be uniquely defined by the strength parameters and the effective stress state. The strength parameters are taken as functions of plastic deformation. In formations such as shale and mudstone, strength may also deteriorate with increased pore water content and/or pore pressure. No allowance for this has been made.

4. When plasticity is initiated the FEM makes no allowance for removal of broken rock, which would reduce stability. Rock removal is likely to be dependent on a number of factors, in particular the drilling fluid-formation interaction (e.g. overbalance, erosion forces, mud cake).

5. The FEM makes no attempt to properly model tensile failure. Allowance for this would necessitate the introduction of discrete fractures or at least a failure criterion specifically developed for cases of tensile stress (e.g. a no tension criterion). The program flags the user when tension is predicted, whereupon the final

results should be regarded with a critical eye. This restriction makes the program less viable in highly anisotropic stress fields.

6. The program is only validated against hollow cylinder samples of a Carboniferous sandstone, although other hollow cylinder tests carried out by Santarelli[18] suggest that the behaviour laws on which the nonlinear analysis is founded are also applicable for the Gebdykes dolomite and Doddington sandstone tested. However, the majority of field instability problems occur in shale formations, for which no laboratory validations have been performed.

7. In addition to the restriction on material types, the laboratory tests with which this program has been validated are carried out under axisymmetric loading conditions. No data is presented to indicate that the predictions hold in an anisotropic in-situ stress field.

8. Only limited validation is presented for the coding where material is modelled using plasticity and PDS elasticity. The most notable short coming in respect to coding validation is for the case of deviated wells.

9. The FEM makes no allowance for pore pressure gradients. This restricts its use to overbalance conditions with a fully effective mud cake, and formations of sufficient permeability to allow 'instantaneous' fully drained conditions.

10. Analysis of strain softening materials is within the capabilities of the program, however the algorithm can be expensive in terms of CPU usage.

11. The boundary traction change followed by the FEM assumes plane strain conditions prevail. The path followed assumes a monotonic change from the in-situ stress state to the wellbore pressure. The true path followed is more complex than this and requires a truly 3D analysis.

12. The linear PDS behaviour law becomes unrealistic with increased in-situ stress magnitudes. The reason for using a linear law is related to the significant increase in CPU anticipated from using a power law (see Section 6.3.4.1). On reflection, however, this caution is probably unwarranted due to the computational power and relative economy of current computers.

13. Obtaining reliable in-situ stress data is a major draw back in any wellbore stability analysis. This is a research area in its own right, however future advances in modelling of wellbore behaviour may facilitate back analysis studies to better define the in-situ stress state. This approach would be particularly suited to development areas where many wells are drilled in one field.

7.3.2 Scope for Improvement

Scope for improvement in analysis of wellbore stability and confidence in its application is immense. To take the work to its ultimate conclusion, an ideal analysis would be capable of predicting,

with confidence, stability within any sedimentary formation for all well deviations, well pressures and mud types, incorporating temperature, time and erosion forces. Realistically, such an analysis cannot be envisaged for some time to come. However, many aspects can be significantly improved upon within the scope of a limited research program. Areas where constructive work could be directed are categorized into practical (laboratory or field work) and numerical research.

7.3.2.1 Practical Research Areas

* As discussed before there is a lack of well documented case histories with which to gain understanding and compare numerical techniques. The value of a compilation of case histories from various companies is immense. However, such a study program may be considered tedious, and would rely heavily on cooperation from oil companies.

* The largest proportion of wellbore instability problems (both Chemical and Mechanical) occur in shale formations. With regard to mechanical instability, there is little documentation on requirements and procedures necessary for characterizing these rock types in order to assess there stability. To determine which material properties are important from laboratory simulations of wellbore instability is an immense task in itself. Thus, characterizations should be based on what is believed to be the important properties (e.g. elastic and strength anisotropy, permeability, short and long term loading, water content). An excellent program of research could compile and/or design procedures for characterization of shale mechanical properties, and carry out these procedures on a number of different shales. Soil

Mechanics research into clay testing and characterization may provide a useful basis for such a program.

* There is tremendous scope for continued hollow cylinder simulations of wellbore instability. In addition to different formations of interest (e.g. salt, sandstone, shale, mudstone, limestone, unconsolidated sand), there is scope for improvement of the simulated conditions. One of the most important weapons available for combating wellbore instability is the overbalance pressure applied, and future laboratory simulations should incorporate internal pressure in the hollow cylinder tests.

* An area where hollow cylinders cannot validate numerical wellbore stability models is in regard to a truly triaxial in-situ stress state. For the case of deviated wells or a vertical well in an unequal horizontal stress field, true triaxial testing is required. Bandis et al[89] have already carried out some true triaxial testing specifically directed at wellbore stability. However, the scaling laws, stress levels and rock simulants appear totally inappropriate.

* When performing hollow cylinder tests or true triaxial tests to simulate wellbore instability there is likely to be some form of scaling involved. To date, little or no work has been carried out to validate the various scaling laws in existence with laboratory evidence in respect to wellbore behaviour. The theory of bifurcation (Vardoulakis[95]) may provide the theoretical foundation on which scaling is based. However, validation through laboratory simulations on various hole sizes is still required.

* The influence of the intermediate stress on failure has been a controversial point in Rock Mechanics for many years. The proliferation of publications which both include and ignore the intermediate stress in yield criteria, indicates that there is still no consensus of opinion in this area. In regard to wellbore behaviour, tests on hollow cylinders at constant outer pressure but with varying axial stress should provide a good indication on the influence of the intermediate stress on failure. (Note: In general, realistic loading conditions should ensure that the axial stress is the intermediate stress at the internal wall.)

7.3.2.2 Numerical Research Areas

* Allowance for pore pressure gradients in an elasto-plastic FEM program can be relatively simple or extremely complex depending to what extent this phenomenon is modelled. Pore pressure gradients can be loading or temperature induced (in shales for example) or induced by fluid flow/migration due to imbalance between the mud and formation pressures. To realistically model loading and temperature induced pore pressure gradients a transient solution must be developed, thus introducing time as a variable. To couple this with a FEM program also incorporating nonlinear material properties is an immense task, and probably beyond the scope of even a 3 year Phd study. However, there is much that can still be achieved in this area using linear elastic material properties. The transient solution presented in Section 2.7 is relatively simple, but extremely restrictive in its application, and there is much scope for further development either analytically and/or numerically.

* In cases where pseudo steady state conditions are acceptable with respect to fluid flow (see Section 2.4), its incorporation into a nonlinear FEM program can be relatively simple. If it is required to have permeability as a function of stress state or plastic deformation then the analysis becomes more complex. The case of radial flow is the simplest condition. Assuming Terzaghi's effective stress law and the effective stress-strain equations given in Section 2.3, Chapter 2, then it is possible to rearrange the FEM relationship (equation (38), Chapter 3) to give

$$\int [B_j]^T \left([D]^* [\varepsilon]^* - [L]^* \Delta p_f \right) dA = \int N_j [t] dS$$

$$\text{or} \quad \int [B_j]^T [D]^* [\varepsilon]^* dA = \int N_j [t] dS + \int [B_j] [L]^* \Delta p_f dA$$

where Δp_f is the pore pressure change relative to the formation pressure,

and $[L]^{*T} = [1, 1, 0, 0, 0]$ for complete plane strain

and $[L]^{*T} = [1, 1, 0]$ for plane strain

Therefore, for steady state radial flow the pore pressure change can be determined from equation (64), Chapter 2, and the pore pressure term in the FEM expression summed into the load vector before equation solution. Where radial flow is not appropriate (e.g. a horizontal well) then a numerical procedure (e.g. the FEM) must be used to determine the pore pressure state before determining the stress analysis load vector. Where permeability is a function of stress or deformation, then the two solutions are interdependent and an iterative procedure must be used to determine the pore pressure distribution corresponding to the stress/strain state and boundary conditions.

* Finally, one of the most biggest draw backs of both the linear elastic solutions and the FEM program is the assumption of isotropic material properties. Significant work in providing solutions for wellbore analysis using anisotropic material properties has already been carried out by Aadnoy.[96] However, utilization of Aadnoy's work has only been limited to date (e.g. Aadnoy and Chenevert[50]), and there is much scope for further analysis.

REFERENCES

1. Brown, E.T. and Bray, J.W. (1983). Wellbore Stability Analysis. First Annual Report to The British Petroleum Company p.l.c., Imperial College of Science and Technology, London.

2. Kock, R.D. (1976). Forties drilling involves high angles, gumbo. Oil & Gas J., Dec. 13, pp.70-78.

3. Holder, B.J. (1982). Drilling fluids for highly deviated wells in North Sea petroleum drilling. J. Petrol. Tech., April, pp.703-712.

4. Hardman, P. (1986). Beckingham 36 horizontal well. SPE European Petrol. Conf., London, Oct. SPE Paper 15895.

5. Eckel, J.R. (1958). Effect of pressure on rock drillability. Petrol. Trans., AIME, Vol. 213, pp.1-6.

6. Rabia, H. (1985). Oilwell Drilling Engineering - Principles and Practice. Graham and Trotman, London.

7. Moore, P.L. (1974). Drilling Practices Manual. Penn Well Books, Tulsa.

8. Kelly, J., Wells, P., Perry, G.W. and Wilkie, S.K. (1980). How using oil mud solved North Sea drilling problems. J. Petrol. Tech. June, pp.931-940.

9. Chenevert, M.E. (1970). Shale alteration by water adsorption. J. Petrol. Tech. Sept., pp.1141-1148.

10. Johancsik, C.A. and Grieve, W.R. (1987). Oil-based mud reduces borehole problems. Oil & Gas J., Apr. 27. pp.46-58.

11. Bradley, W.B. (1979). Mathematical concept-stress cloud - can predict borehole failure. Oil & Gas J., Vol. 77, No.8, Feb.19, pp.92-102.

12. Gaylord, E.W. (1983). A laboratory study of the effects of hydraulics on hole erosion. 58th Annual Tech. Conf. and Exhibition, San Francisco, CA, Oct. SPE Paper 12118.

13. Kalof, F. and El Shennawy, H.M. (1979). Drilling of Gulf of Suez evaporites. Middle East Oil Tech. Conf. of SPE, Manama, Bahrain, March. SPE Paper 7749.

14. Infante, E.F. and Chenevert, M.E. (1986). Stability of boreholes drilled through salt displaying plastic behaviour. 61st Annual Tech. Conf. and Exhibition of SPE, New Orleans, LA, Oct. SPE Paper 15513.

15. Maury, V. and Sauzay, J.M. (1987). Borehole instability: case histories, Rock Mechanics approach and results. SPE/IDAC Drilling Conf., New Orleans, LA, March.

16. Hottman, C.E., Smith, J.H. and Purcell, W.R. (1978). Relationship among earth stresses, pore pressures, and drilling problems, offshore Gulf of Alaska. 53rd Annual Tech. Conf. and Exhibition of SPE of AIME, Houston, Oct. SPE Paper 7051.

17. Klein, R.J. and Barr, M.V. (1986). Regional state of stress in Western Europe. Proc. of Int. Symp. on Rock Stress and Rock Stress Measurements, Stockholm, Sept., pp.33-44.

18. Santarelli, F.J. (1987). Theroetical and experimental investigation of the stability of the axisymmetric wellbore. Ph.D. Thesis, London Unviversity.

19. Gay, N.C. (1973). Fracture growth around openings in thick-walled cylinders of rock subjected to hydrostatic compression. Int. J. Rock Mech. Min. Sci. & Geomech. Abstr., Vol.10, pp.209-233.

20. Darley, H.C. (1969). A laboratory study of borehole stability. J. Petrol. Tech., July, pp.883-892.

21. Horsrud, P., Risnes, R. and Bratli, R.K. (1982). Fracture initiation pressures in permeable poorly consolidated sands. Int. J. Rock Mech. Min. Sci., Vol.19, No.6, Dec., pp.255-266.

22. Medlin, W.L. and Masse, L. (1982) Plasticity effects in hydraulic fracturing. 57th Annual Fall Tech. Conf. and Exhibition of SPE of AIME. New Orleans, LA, Sept. SPE Paper 11068.

23. Kojic, M. and Cheatham, J.B. (1974). Theory of plasticity of porous media with fluid flow. Soc. Petrol. Engrs J., June, pp.263-269.

24. Hoek, E. and Brown, E.T. (1980). Underground Excavations in Rock. The Inst. of Min. and Met., London.

25. Detournay, E., McLennan, J.D. and Roegiers, J.-C. (1986). Poroelastic concepts explain some of the hydraulic fracturing mechanisms. Unconventional Gas Tech. Symp. of SPE, Louisville, KY, May. pp.629-638. SPE Paper 15262.

26. Terzaghi, K. and Peck, R.B. (1967). Soil Mechanics in Engineering Practice. John Willey and Sons, New York.

27. Clegg, J.D. (1971). Casing failure study - Cedar Creek anticline. J. Petrol. Tech., June, pp.676-684.

28. Bratli, R.K. and Risnes, R. (1981). Stability and failure of sand arches. Soc. Petrol. Engrs J., Vol.21, No.3, April, pp.236-248.

29. Paslay, P.R. and Cheatham, J.B. (1963). Rock stresses induced by flow of fluids into boreholes. Soc. Petrol. Engrs. J., Vol.3, No.1, March, pp.85-91.

30. Klein, R.J. and McLean, M.R. (1988). Application of wellbore stability to a horizontal UK land well. Conf. on Applied Rock Engng., Newcastle, Jan., pp.117-126.

31. Morita, N. and Gray, K.E. (1980). A constitutive equation for non linear stress-strain curves in rocks and its application to stress analysis around a borehole during drilling. 55th Annual Fall Tech. Conf. and Exhibition of SPE of AIME, Dallas, Sept. SPE Paper 9328.

32. King, M.S. (1969). Static and dynamic elastic moduli of rocks under pressure. Rock mechanics - theory and practice, 11th Symp. on Rock Mech., W.H.Somerton (ed), Soc. Min. Engrs. AIME, New York, pp.329-351.

33. Kulhavy, F.H. (1975). Stress deformation properties of rock and rock discontinuities. Eng. Geology, Vol.9, pp.327-350.

34. Westergaard, H.M. (1940). Plastic state of stress around a deep well. J. Boston Soc. Civil Engng., Jan. Vol.27, pp.1-5.

35. Owen, D.R.J. and Hinton, E. (1980). Finite Elements in Plasticity: Theory and Practice. Pineridge Press, Swansea.

36. Brown, E.T. and Bray, J.W. (1982). Rock support interaction calculations for pressure shafts and tunnels. Rock Mechanics: Caverns and Prssure Shafts, W.Wittke (ed.), Vol.2, pp.555-565, A.A.Balkema, Rotterdam.

37. Bray, J.W. (1967). The teaching of Rock Mechanics to mining engineers. Trans. Instn. Min. Engr., Vol.126, pp.483-488.

38. Read, H.E. and Hegemier, G.A. (1984). Strain softening of rock, soil and concrete - a review article. Mechanics of Materials, Vol.3, pp.271-294.

39. Pariseau, W.G. (1979). A finite element approach to strain softening and size effects in rock mechanics. Proc. 3rd Int. Conf. on Numerical Methods in Geomech., A.A. Balkkema, Rotterdam, pp.545-558.

40. Bradley, W.B. (1978). Borehole failure near salt domes. 53rd Annual Tech. Conf. and Exibition of SPE of AIME, Houston, Oct. SPE Paper 7503.

41. Bradley, W.B. (1979). Failure of inclined wellbores. J. Energy Resources Tech., Dec. pp.233-239.

42. Eaton, B.A. (1969). Fracture gradient prediction and its application in oilfield operations. J. Petrol. Tech., Oct. pp.1353-1360.

43. Daines, S.R. (1982). Prediction of fracture pressures for wildcat wells. J. Petrol. Tech., April, pp.863-872.

44. Unger, K.W. and Howard, D.C. (1984). Unique drilling techniques improve drilling and casing deep overthrust belt salt. 59th Annual Tech. Conf. and Exhibition, Houston, Sept. SPE Paper 13108.

45. Fairhurst, C. (1964). Measurements of in situ rock stress, with particular reference to hydraulic fracturing. Felsmechanik and Ingenieurgeologie, Vol.2, pp.129-43.

46. Brady, B.H.G. and Bray, J.W. (1978). The boundary element method for determining stresses and displacements around long openings in a triaxial stress field. Int. J. Rock Mech. Min. Sci., Vol.15, No.1, Feb., pp.21-28.

47. Deily, F.H. and Owens, T.C. (1969). Stress around a wellbore. 44th Annual Fall Meeting of SPE of AIME, Denver, Sept. 28 - Oct. 1. SPE Paper 2557.

48. Kirsch, G. (1898). Die theorie der elastizitat und die bedurfnisse der festigkeitslehre. Verein Deutsher Ingenieure, Vol. 42, No.28, pp.797-807.

49. Brown, E.T., Bray, J.W., Ladanyi, B. and Hoek, E. (1983). Characteristic line calculations for rock tunnels. J. Geotech. Engng, ASCE, Vol. 109, No.1, Jan., pp.15-39.

50. Aadnoy, B.S. and Chenevert, M.E. (1987). Stability of Inclined Boreholes. SPE/IADC Drilling Conf., New Orleans, LA, March, pp.25-41. SPE/IADC Paper 16052.

51. Perkins, T.K. and Gonzalez, J.A. (1984). Changes in earth stresses around a wellbore caused by radially symmetrical pressure and temperature gradients. Soc. Petrol. Eng. J., April, pp.129-140.

52. Santarelli, F.J. and Brown, E.T. (1987). Performance of deep wellbores in rocks with a confining pressure dependent elastic modulus. Proc. 6th Congr. Int. Soc. Rock Mech., Vol.2, pp.1217-1222, A.A.Balkema, Rotterdam.

53. Biot, M.A. (1941). General theory of three-dimensional consolidation. J. Appl. Phys., Vol.12, pp.155-164.

54. Terzaghi, K. (1936). Simple tests determine hydrostatic uplift. Engineering News Record, June 18, Vol.116, pp.872-875.

55. Timosenko, S.P. and Goodier, J.N. (1982). Theory of Elasticity. (3rd Edition), McGraw-Hill International Book Company, New York.

56. Dake, L.P. (1978). Fundamentals of Reservoir Engineering, Elesvier Scientific Publishing Company, Amsterdam.

57. Carslaw, H.S. and Jaeger, J.C. (1959). Conduction of Heat in Solids. Oxford University Press, London.

58. Jaeger, J.C. (1956). Numerical values for the temperature in radial heat flow, J. Math. Phys., Vol.34, pp.316-321.

59. Chenevert, M.E. and McClure, L.J. (1978) How to run casing and open-hole pressure tests. Oil & Gas J., March 6, Vol.76, No.10, pp.66-76.

60. Hubbert, M.K. and Willis, D.G. (1957). Mechanics of hydraulic fracturing. Trans. A.I.M.E., Vol.210, pp.153-168.

61. Haldorsen, H.H. and Lake, L.W. (1984). A new approach to shale management in field-scale models. Soc. Petrol. Engrs. J., Aug., Vol.24, No.4, pp.447-457.

62. Zienkiewicz, O.C. (1977). The Finite Element Method, McGraw-Hill International Book Company, London.

63. Hinton, E. and Owen, D.R.J. (1979). An Introduction to Finite Element Computations, Pineridge Press, Swansea.

64. Naylor, D.J., Pange, G.N., Simpson, B. and Tabb, R. (1981). Finite Elements in Geotechnical Engineering, Pineridge Press, Swansea.

65. Cantin, G. (1971). An equation solver of very large capacity. Int. J. Num. Meth. Engng., Vol.3, No.3, pp.379-388.

66. Irons, B.M. (1970). A frontal solution programme for finite element analysis. Int. J. Num. Meth. Engng., Vol.2, pp.5-32.

67. Melosh, R.J. and Bamford, R.M. (1969). Efficient solution of load-deflection equations. J. ASCE (Struct. Div.), Paper No. 6510, pp.661-676.

68. Zienkiewicz, O.C., Kelly, D.W. and Bettess, P. (1977). The coupling of the finite element and boundary solution procedures. Int. J. Num. Meth. Engng., Vol.11, pp.355-375.

69. Zienkiewicz, O.C., Emson, C. and Bettess, P. (1982). A novel boundary infinite element. Int. J. Num. Meth. Engng., Vol.19, pp.393-404.

70. Beer, G. and Meek, J.L. (1981). Infinite domain elements. Int. J. Num. Meth. Engng., Vol.17, pp.43-52.

71. Ungless, R.L. (1973). An Infinite Finite Element. M.Sc. Thesis, Univ. of British Columbia.

72. Bettess, P. (1977). Infinite elements. Int. J. Num. Meth. Engng., Vol.11, pp.53-64.

73. Galin, L.A. (1946). The plane elastic-plastic problem. Prikl. Math. Mekh., Vol.10, No.3.

74. Hill, R. (1950). The Mathematical Theory of Plasticity. Clarendon Press, Oxford.

75. Prager, W. (1959). An Introduction of Plasticity. Addison-Wesley Publ. Co., Amsterdam and London.

76. Gumusoglu, C. (1986). Analysis of Underground Excavations in Strain Softening Rock Masses. PhD thesis, University of London.

77. Ladanyi, B. (1974). Use of the long-term strength concept in the determination of ground pressure on tunnel linings. Advances in Rock Mechanics; Proc. of the 3rd Cong. of the ISRM, Denver, Vol.2, part B, pp.1150-1156.

78. Hoek, E. and Brown, E.T. (1980). Empirical strength criterion for rock masses. J. Geotech. Engng. Div., ASCE, Vol.106, No.9, pp.1013-1035.

79. Elliott, G.M. (1982). An Investigation of a Yield Criterion for Porous Rock. PhD Thesis, University of London.

80. Brown, E.T. (1974). Fracture of rock under uniform biaxial compression. Advances in Rock Mechanics: Caverns and Pressure Shafts, (W.Wittke, ed), Vol.2, Balkema, Rotterdam, pp.555-565.

81. Bieniawski, Z.T. (1969). Deformation behaviour of fractured rock under multiaxial compression. Proc. of the Civil Engng. Materials Conf., Southampton, Vol.2, pp.589-598.

82. Jaeger, J.C. and Cook, N.C. (1979). Fundamentals of Rock Mechanics. 3rd Ed., Chapman and Hall, London.

83. McLean, M.R. (1985). Wellbore Stability Analysis. Third Annual Report to the British Petroleum Company p.l.c., Imperial College, London.

84. Savin, G.N. (1961). Stress concentrations around holes. Translation Ed. W.Johnson, Pergamon Press, London.

85. Detournay, E. (1986). An approximate statical solution for the elastoplastic interface for the problem of Galin with cohesive-frictional material. Int. J. Solids Structures, Vol.22, No.12, pp.1435-1454.

86. Hudson, J.A., Crouch, S.L. and Fairhurst, C. (1972). Soft, stiff and servo controlled testing machines: a review with reference to rock failure. Engng. Geol., Vol.6, pp.155-189.

87. Kachanov, L.M. (1971). Foundations of the Theory of Plasticity. Translation Eds. H.A.Lauwerier and W.T.Koiter, North-Holland Pub. Comp. Amsterdam.

88. Broch, E. (1974). The influence of water on some rock properties. Advances in Rock Mechanics, Proc. 3rd Congr., Int. Soc. Rock Mech., Denver, Vol.2, Part A, pp.33-38.

89. Bandis, S.C., Lindman, J. and Barton, N. (1987). Three-dimensional stress state and fracturing around cavities in overstressed weak rock.

Proc. 6th Int. Congress on Rock Mech., Vol.2, pp.769-775, A.A.Balkema, Rotterdam.

90. Fjaer, E., Bratli, R.K., Malmo, J.T., Lokberg, O.J. and Holt, R.M. (1987). Optical studies of cavity failure in weak sedimentary rocks. Proc. 6th Int. Congress on Rock Mech., Vol.2, pp.887-891, A.A.Balekma, Rotterdam.

91. Wilhemi, B. and Sommerton, W.H. (1967). Simlutaneous measurement of pore and elastic properties of rocks under triaxial stress conditions. Soc. Petrol. Engrs. J., Vol.7, pp.283-294.

92. Hobbs, D.W. (1962). The strength of coal under biaxial compression. Colliery Engnr., Vol.39, pp.285-290.

93. Guenot, A. (1987). Contraintes et ruptures autour des forages petroliers. Proc. 6th ISRM Congr. (G.Herget & S.Vongpaisal, eds.), pp.109-118, Rotterdam, A.A.Balkema.

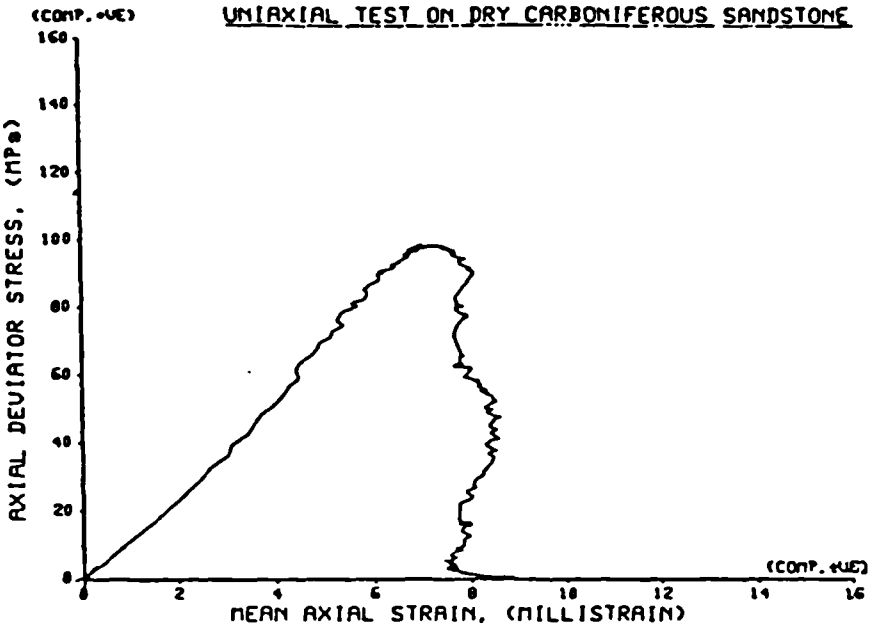
94. Kreyszig, E. (1979). Advanced Engineering Mathematics. (4th ed.), John Wiley & Sons, New York.

95. Vardoulakis, I.G. (1984). Rock bursting as a surface instability phenomenon. Int. J. Rock Mech. Min. Sci., Vol.21, No.3, pp.137-144.

96. Aadnoy, B.S. (1987). Continuum mechanics analysis of the stability of inclined boreholes in anisotropic rock formations. Ph.D Thesis, Norwegian Institute of Technology, University of Trondheim.

APPENDIX A

COMPARISON OF VARIOUS MODEL ROCK BEHAVIOUR LAWS WITH A SET OF TRIAXIAL TESTS CARRIED OUT ON A CARBONIFEROUS SANDSTONE



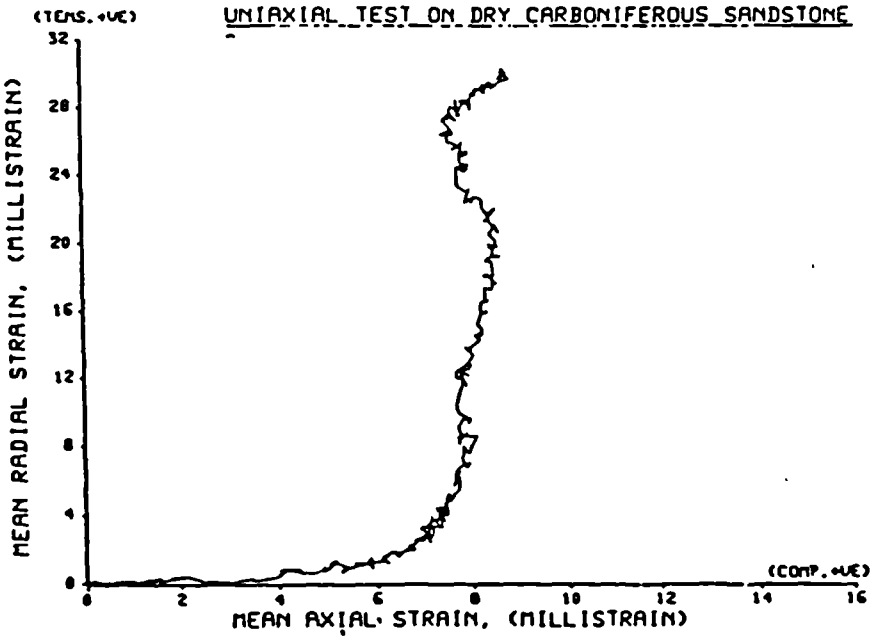


Figure A.1 Uniaxial test carried out on a Carboniferous sandstone (after Santarelli[18]).

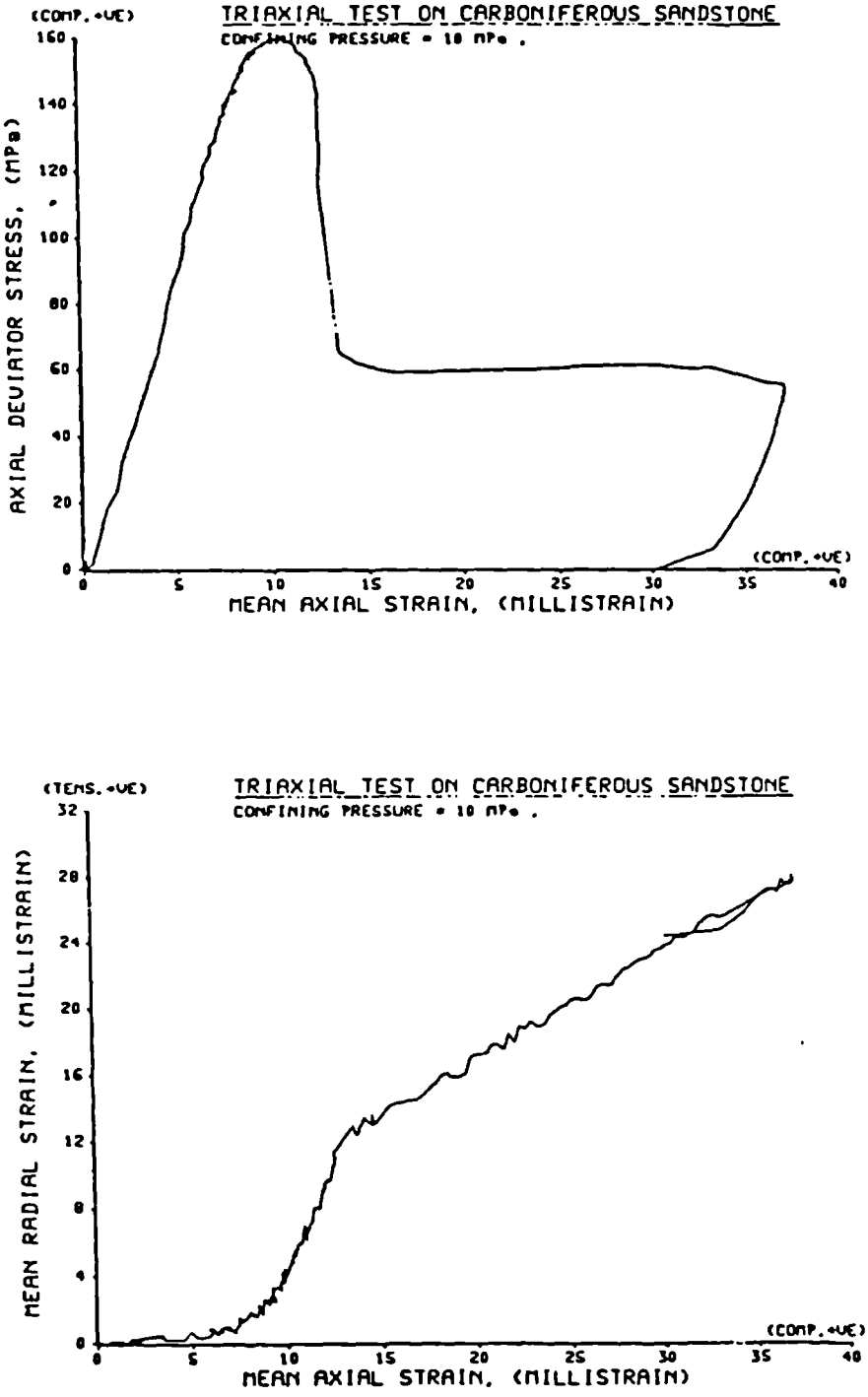


Figure A.2 Triaxial test (σ_3 = 10 MPa) carried out on a Carboniferous sandstone (after Santarelli[18]).

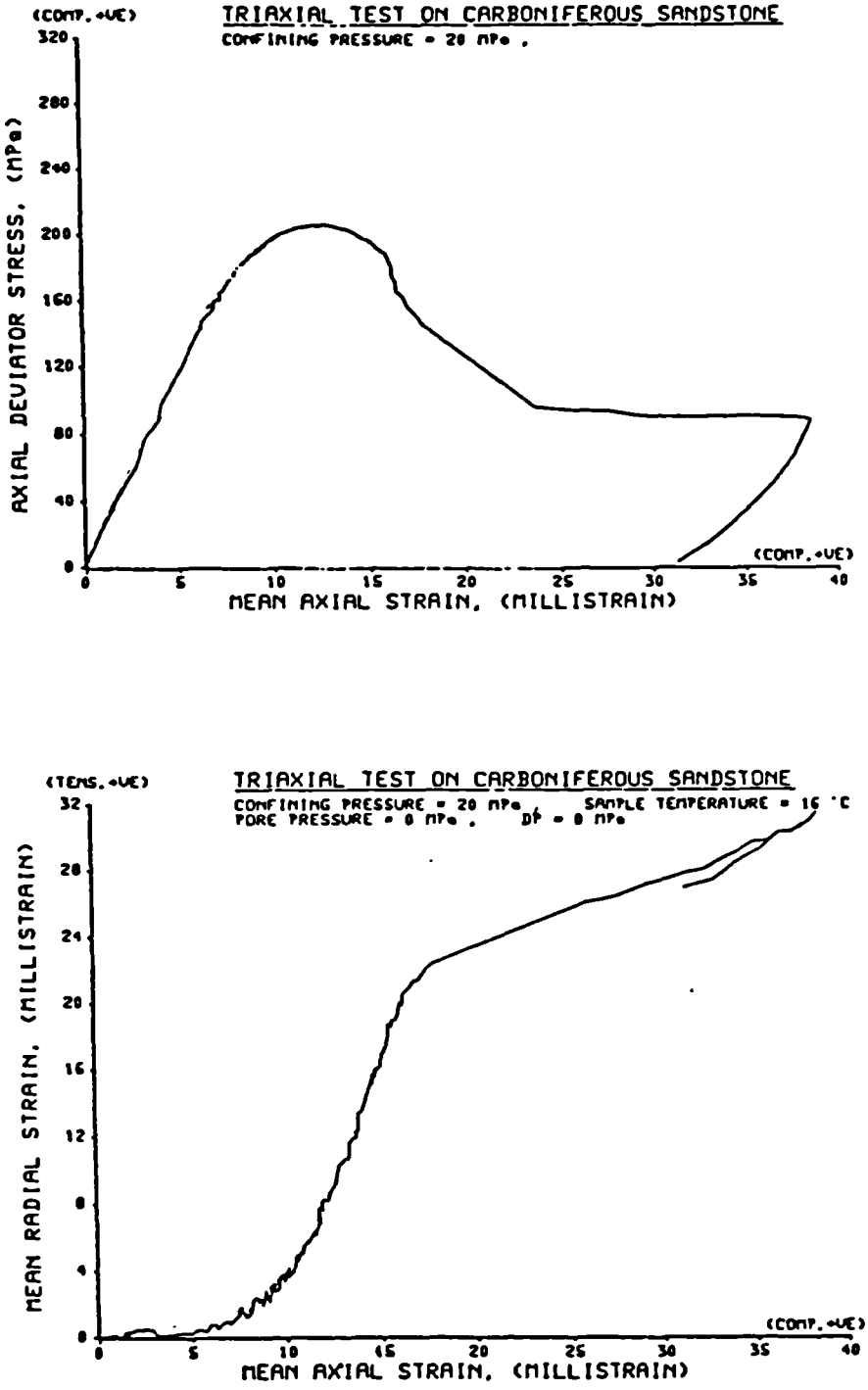
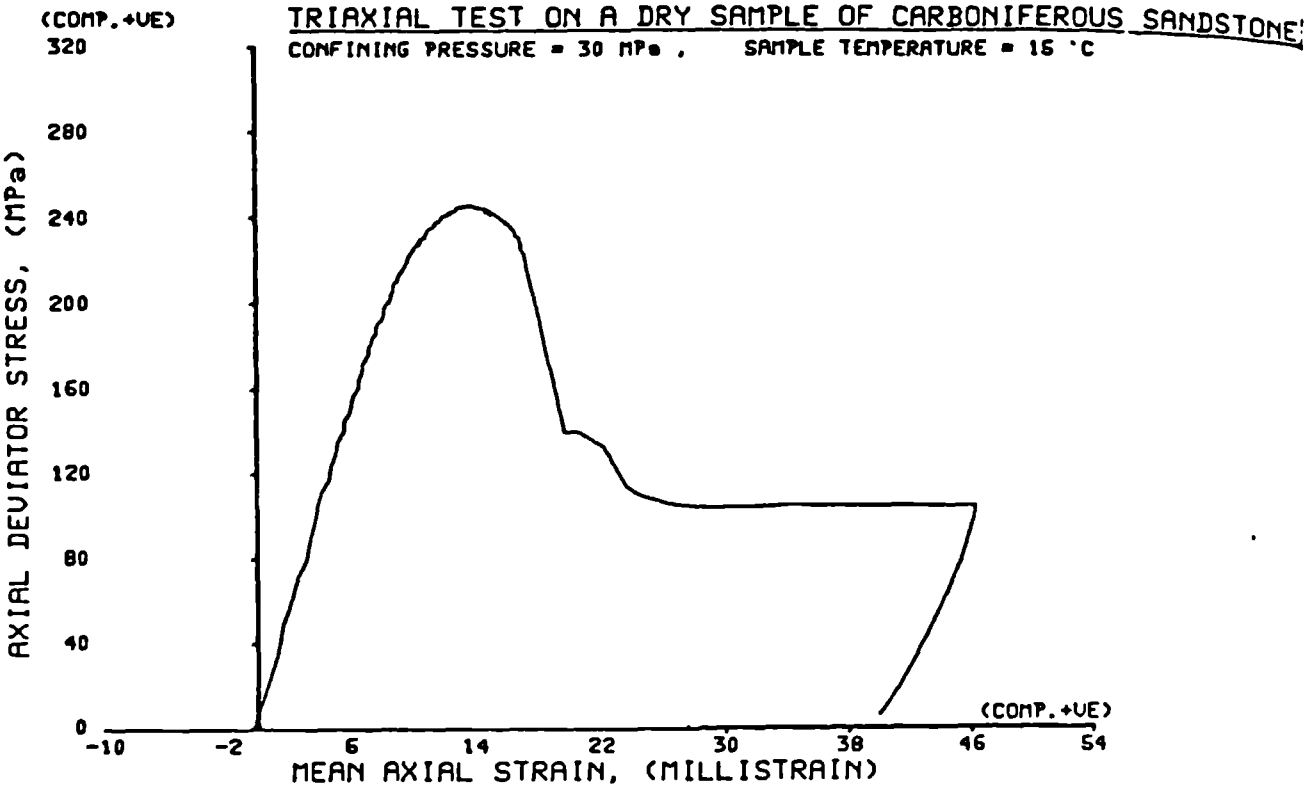


Figure A.3 Triaxial test (σ_3 = 20 MPa) carried out on a Carboniferous sandstone (after Santarelli[18]).



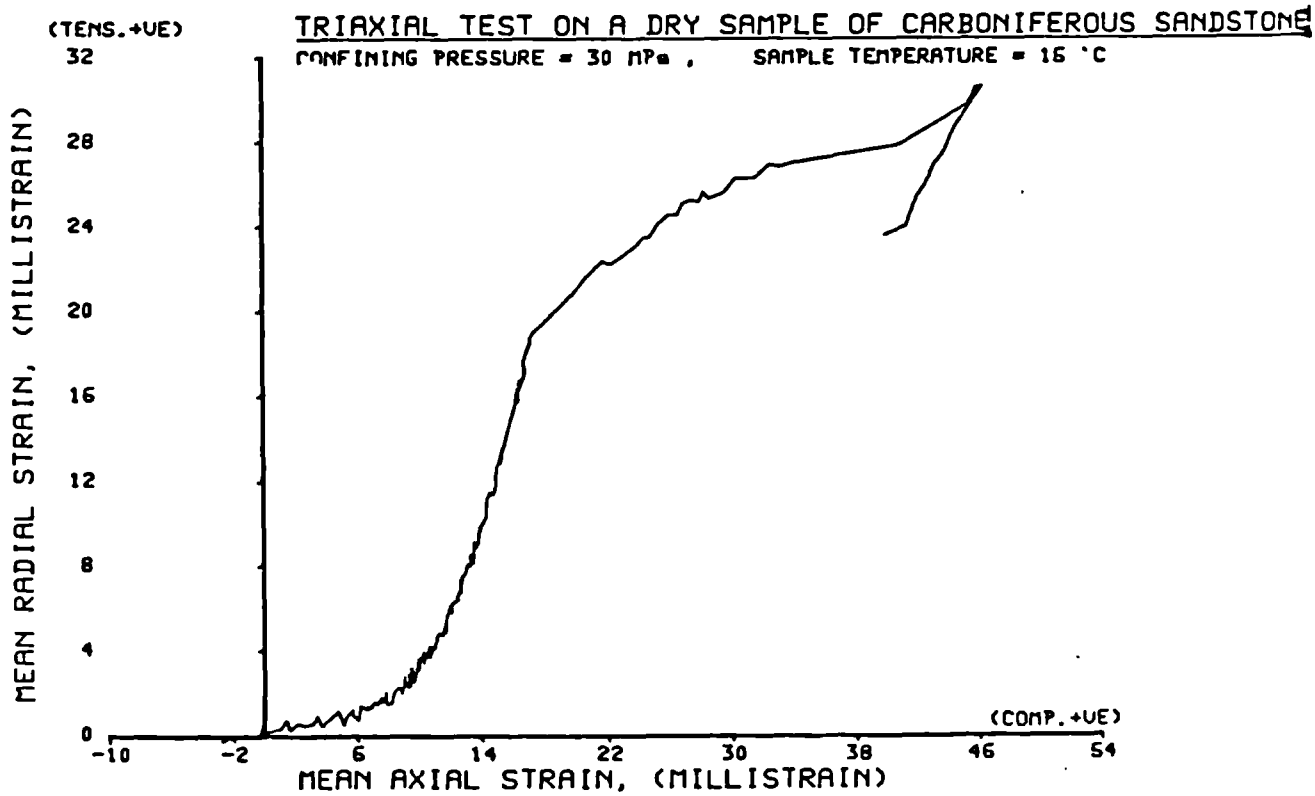
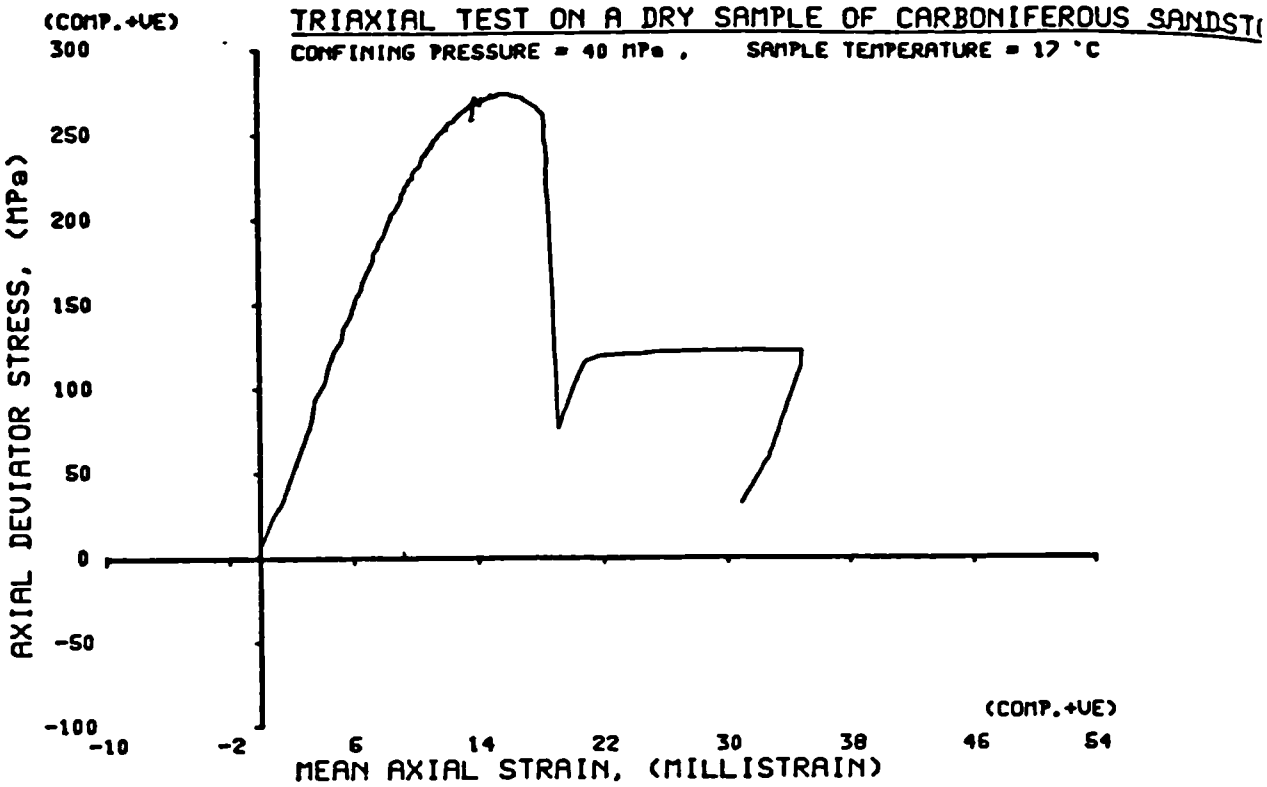


Figure A.4 Triaxial test (σ_3 = 30 MPa) carried out on a Carboniferous sandstone (after Sanatrelli[18]).



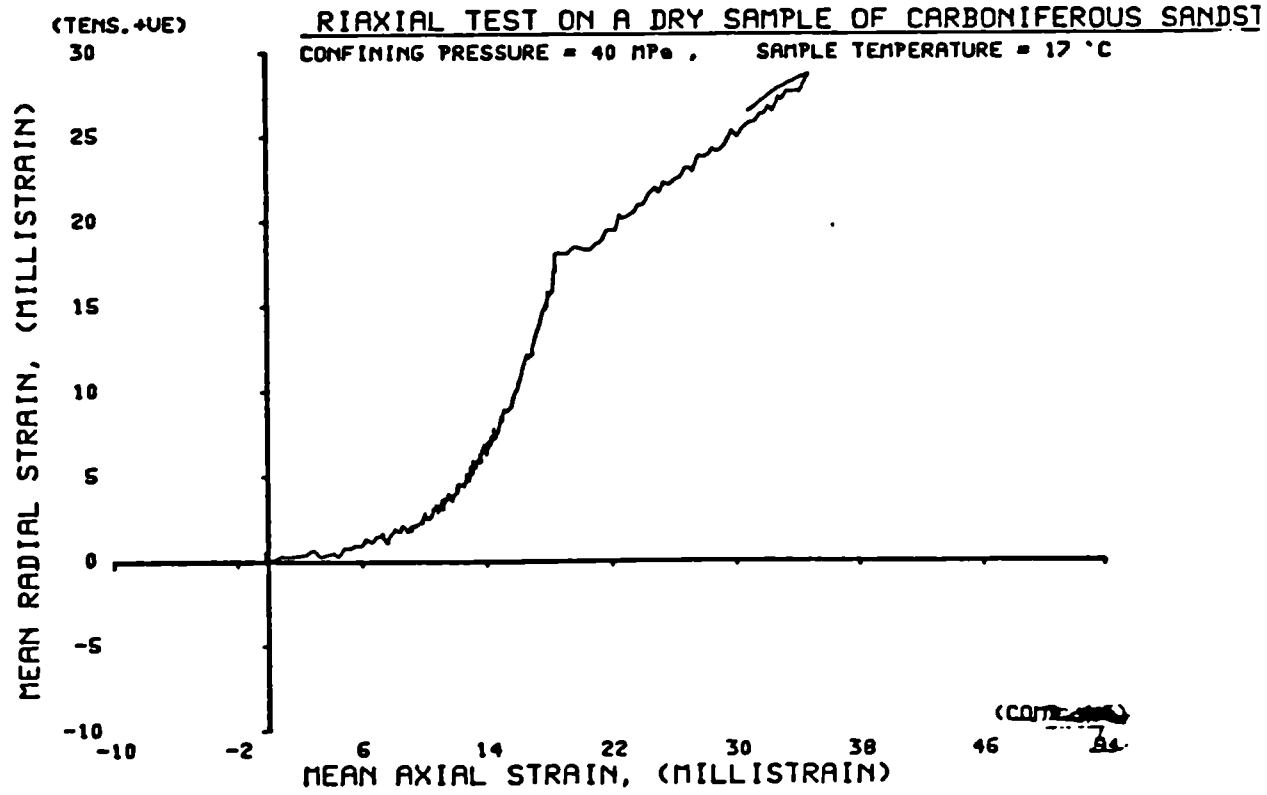


Figure A.5 Triaxial test (σ_3 = 40 MPa) carried out on a Carboniferous sandstone (after Santarelli[18]).

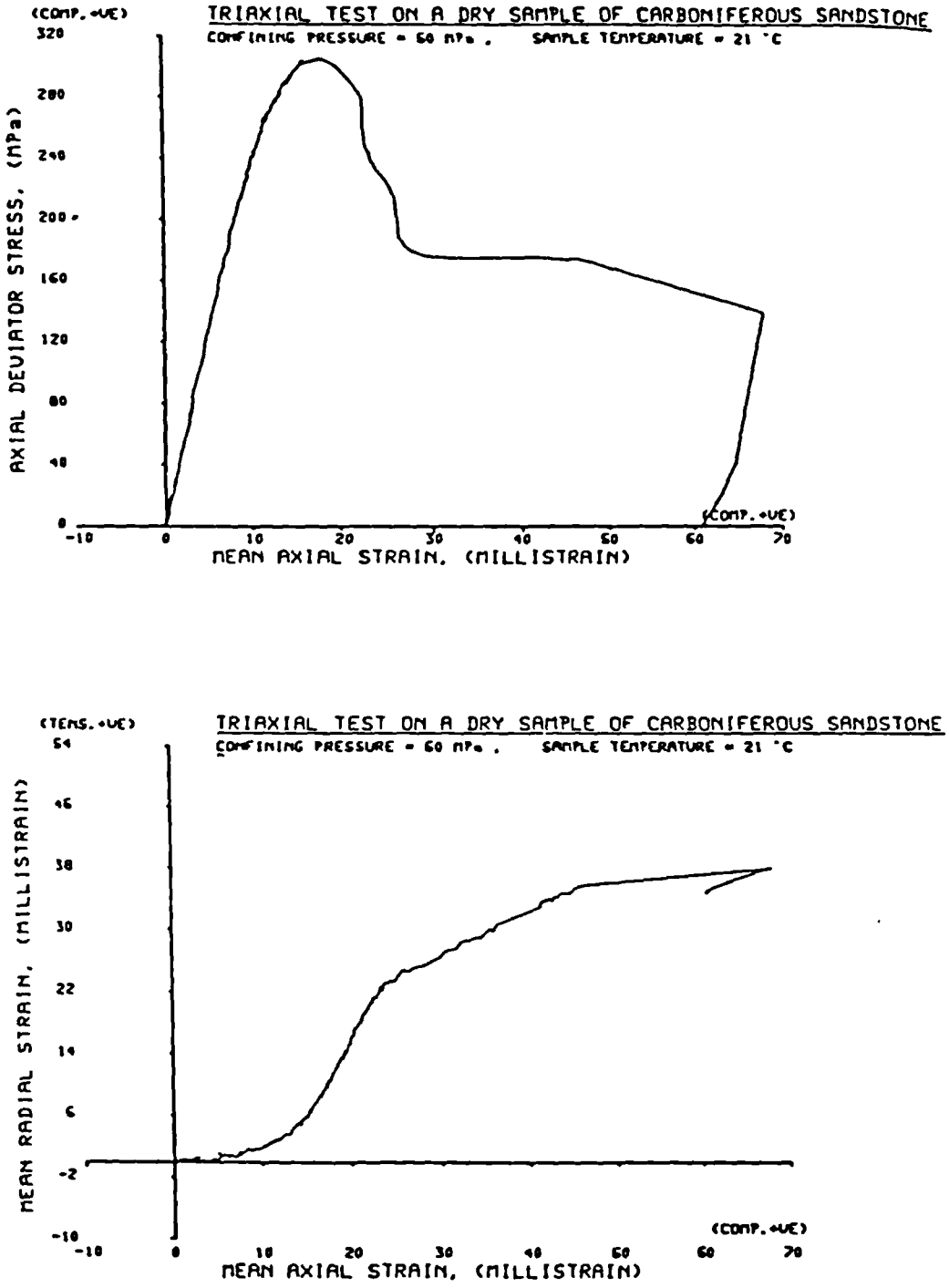
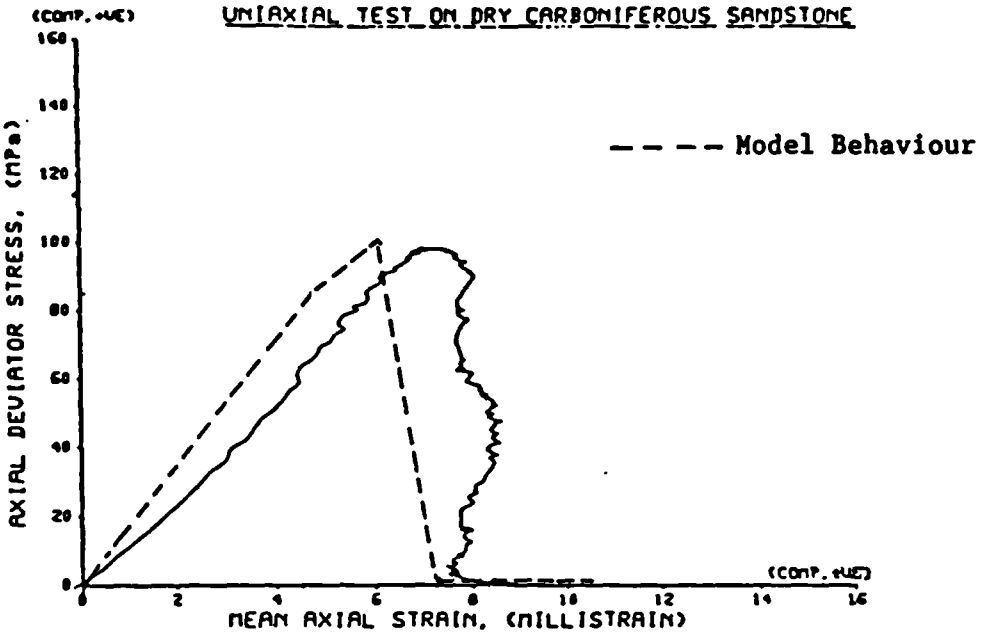


Figure A.6 Triaxial test (σ_3 = 50 MPa) carried out on a Carboniferous sandstone (after Santarelli[18]).



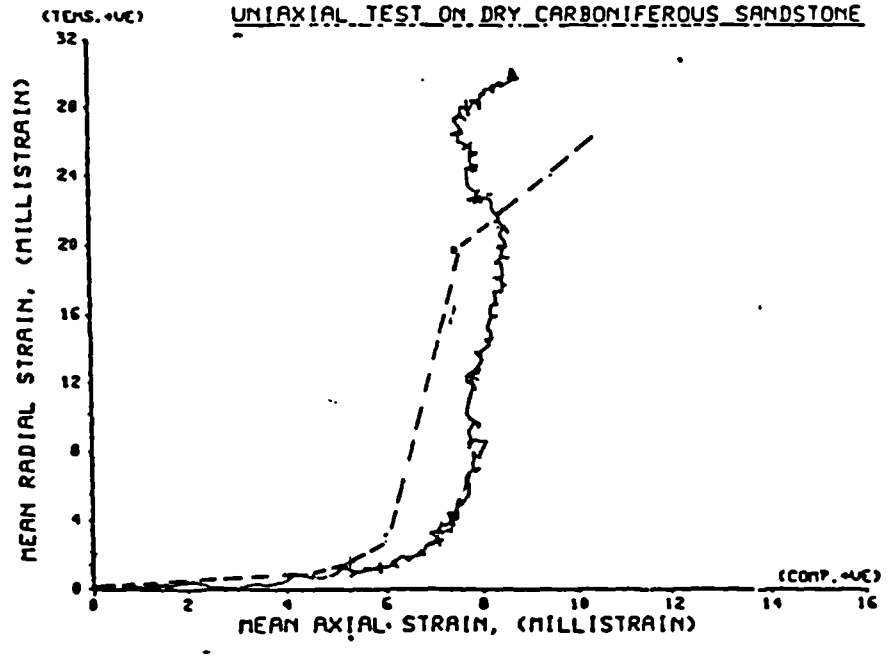


Figure A.7 Comparison of Mohr-Coulomb, associated flow model with test results (uniaxial loading).

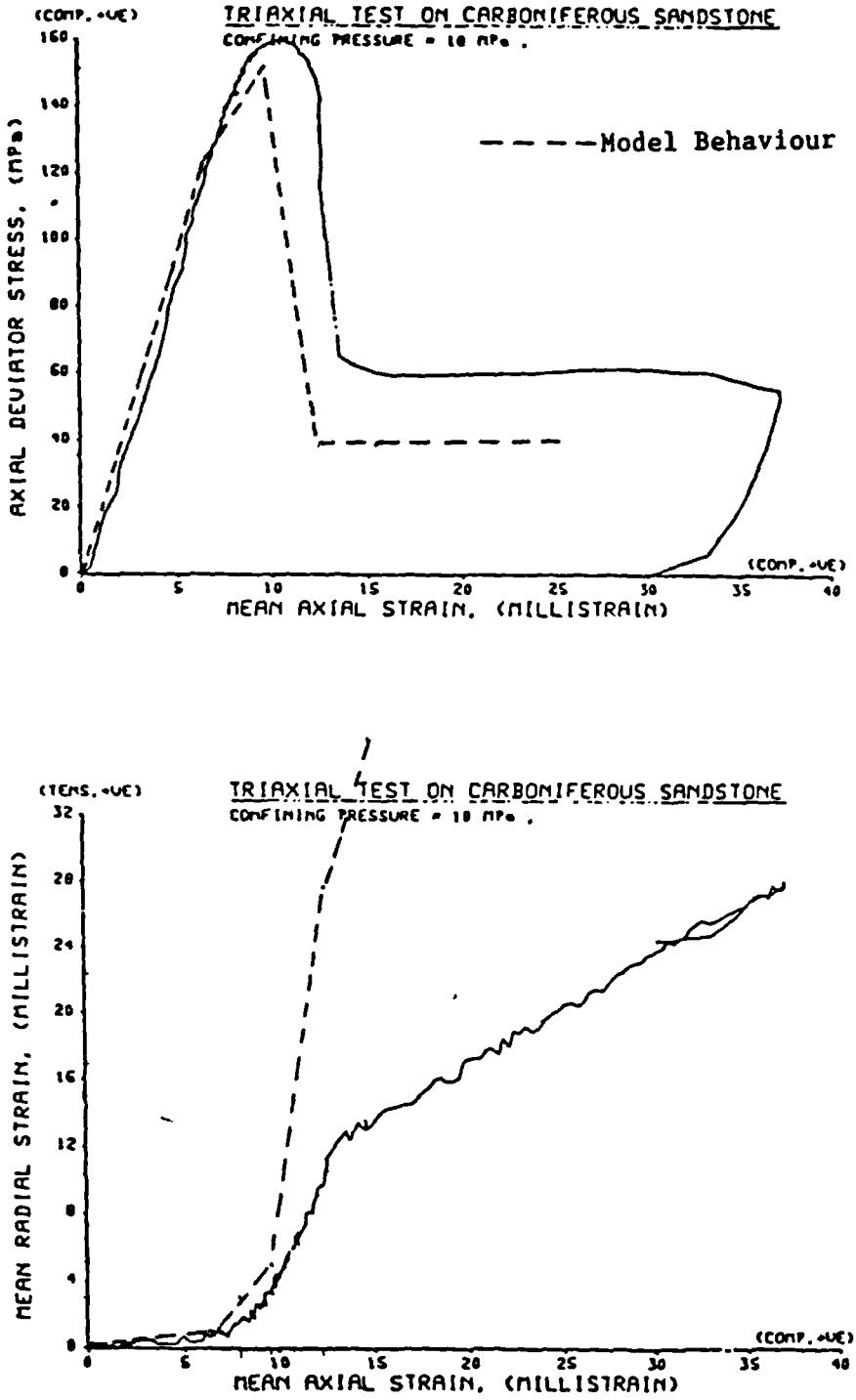


Figure A.8 Comparison of Mohr-Coulomb, associated flow model with test results (σ_3 = 10 MPa).

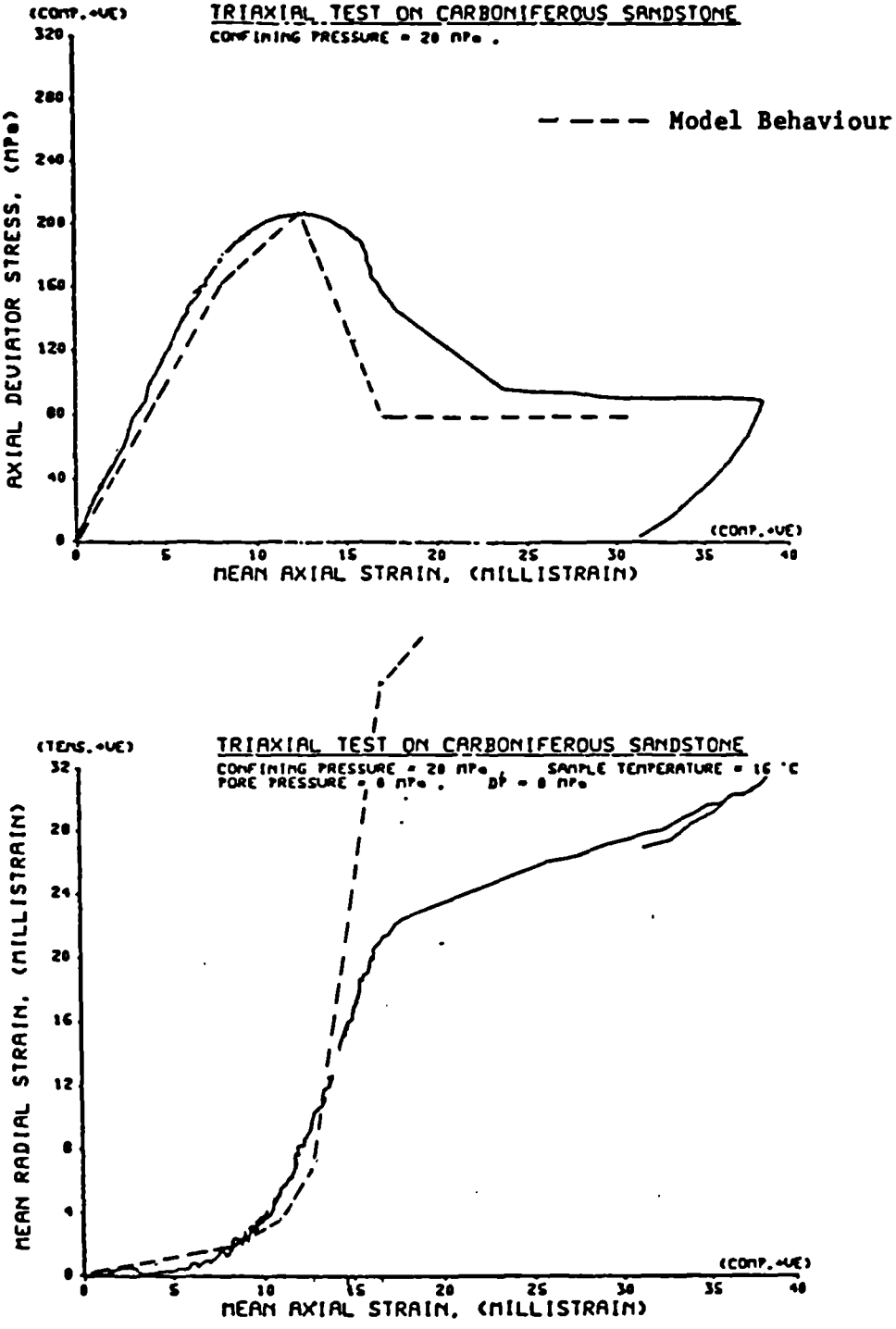


Figure A.9 Comparison of Mohr-Coulomb, associated flow model with test results (σ_3 = 20 MPa).

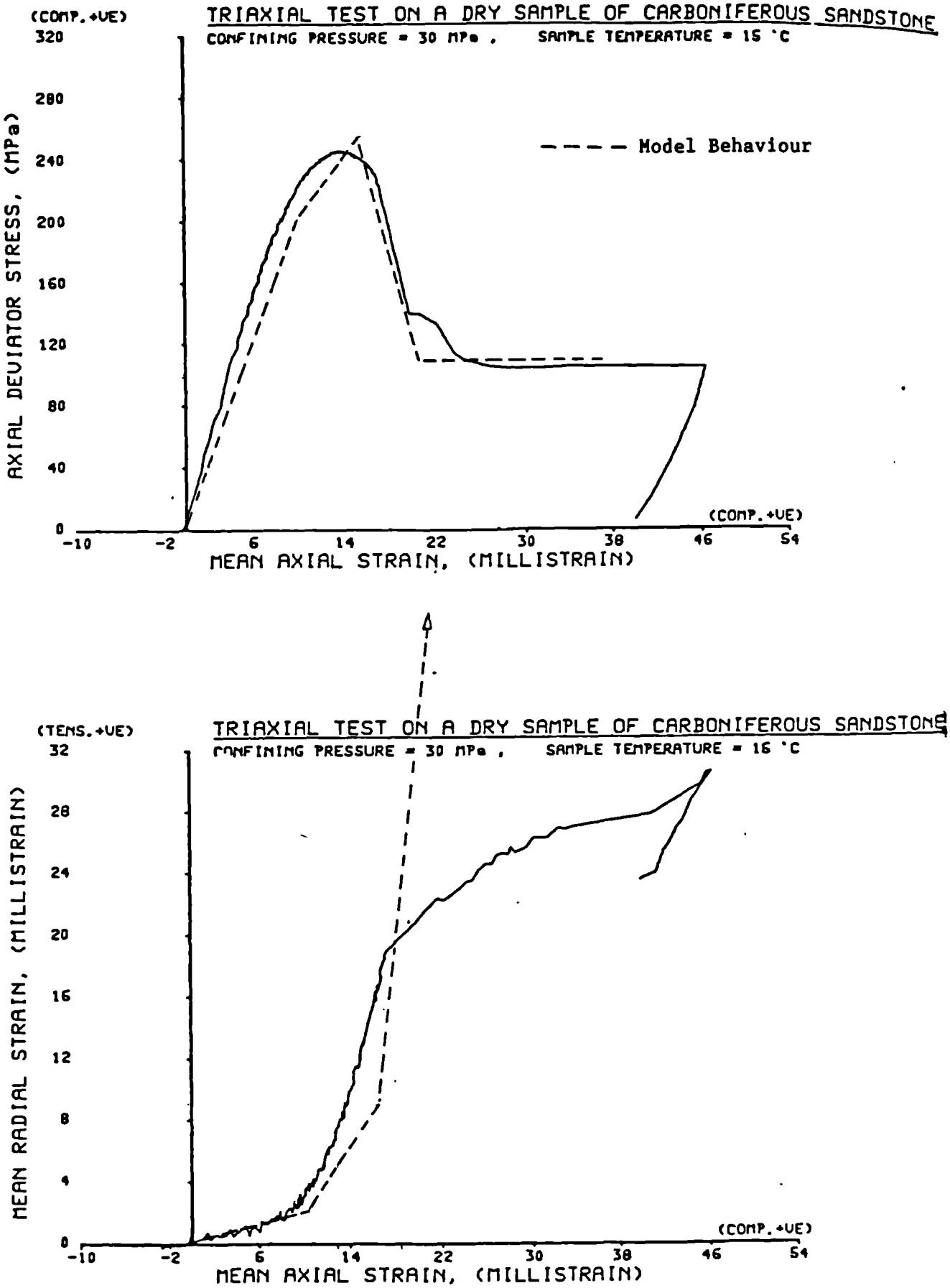
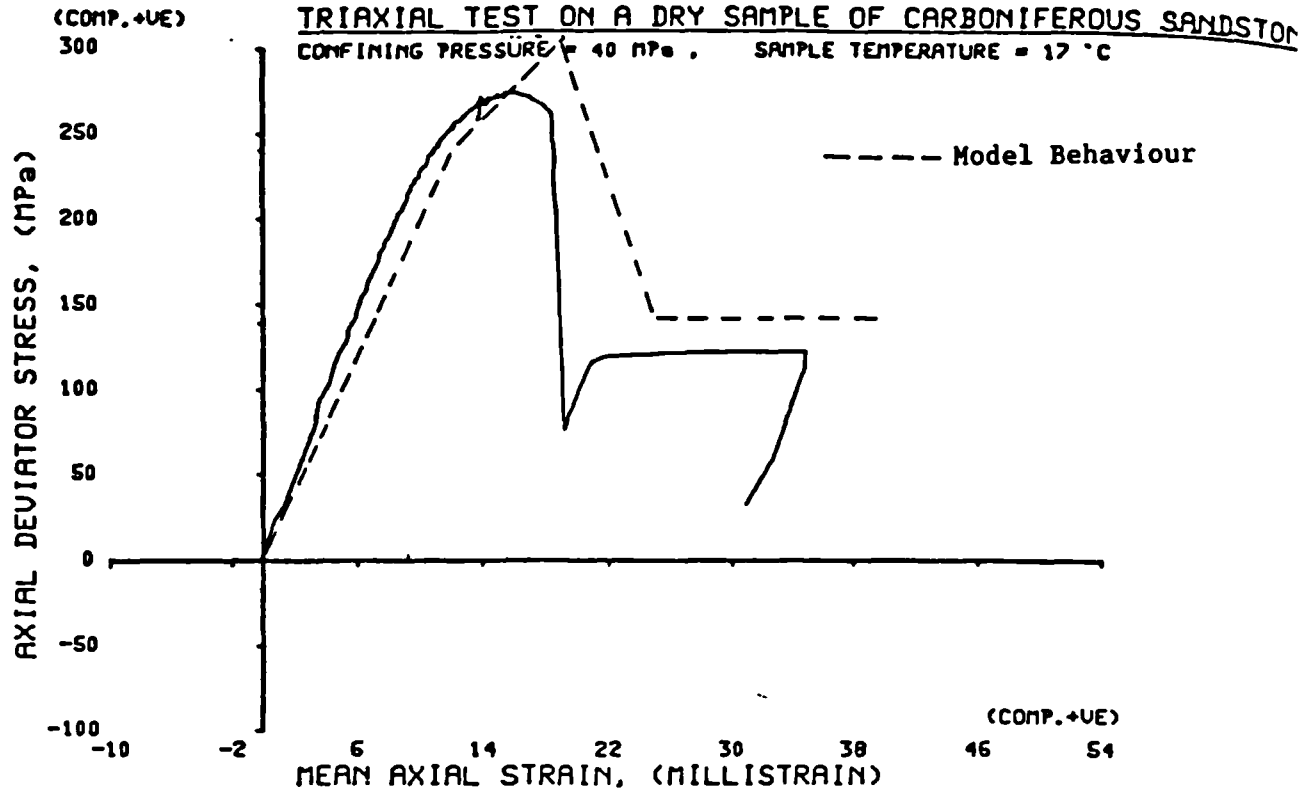


Figure A.10 Comparison of Mohr-Coulomb, associated flow model with test results (σ_3 = 30 MPa).



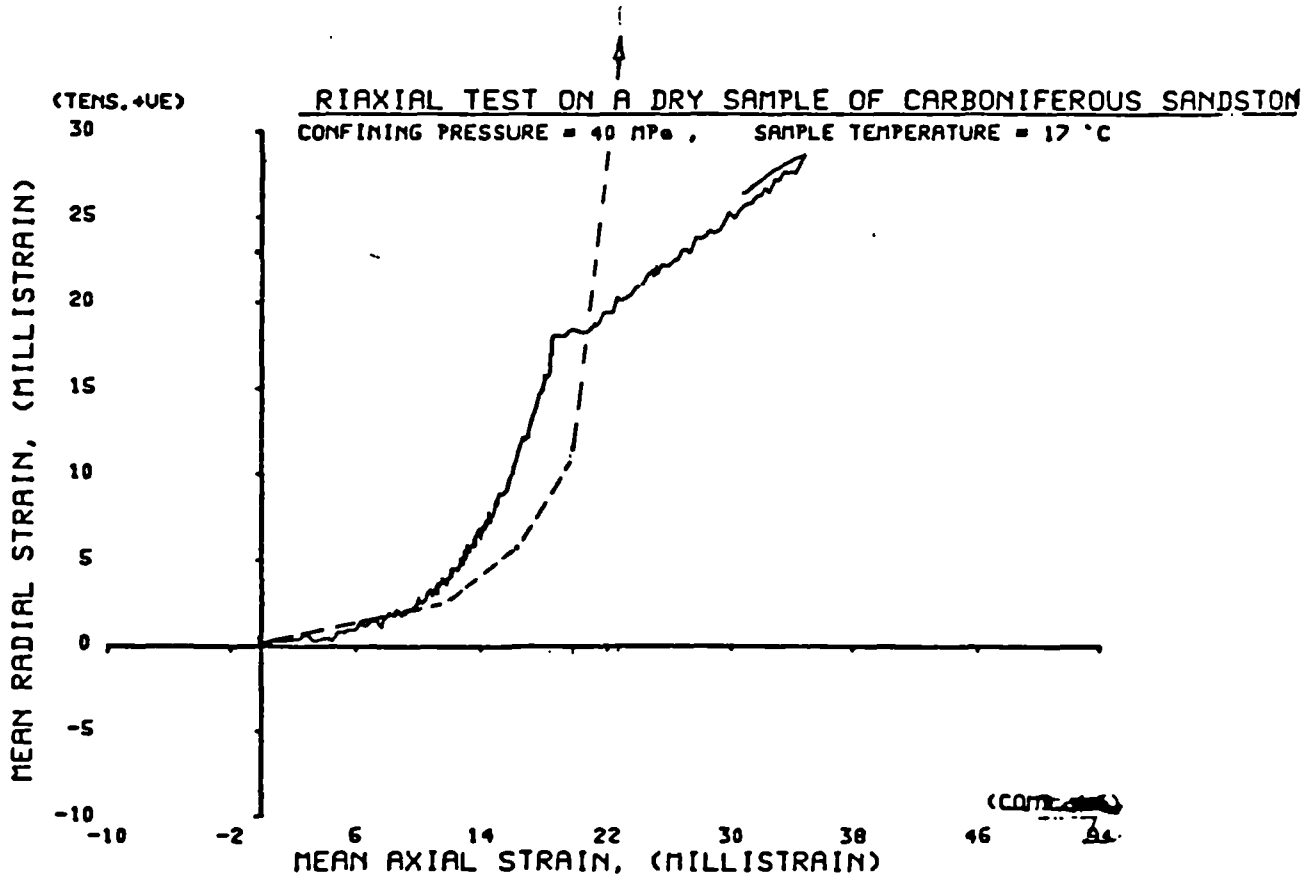


Figure A.11 Comparison of Mohr-Coulomb, associated flow model with te: results (σ_3 = 40 MPa).

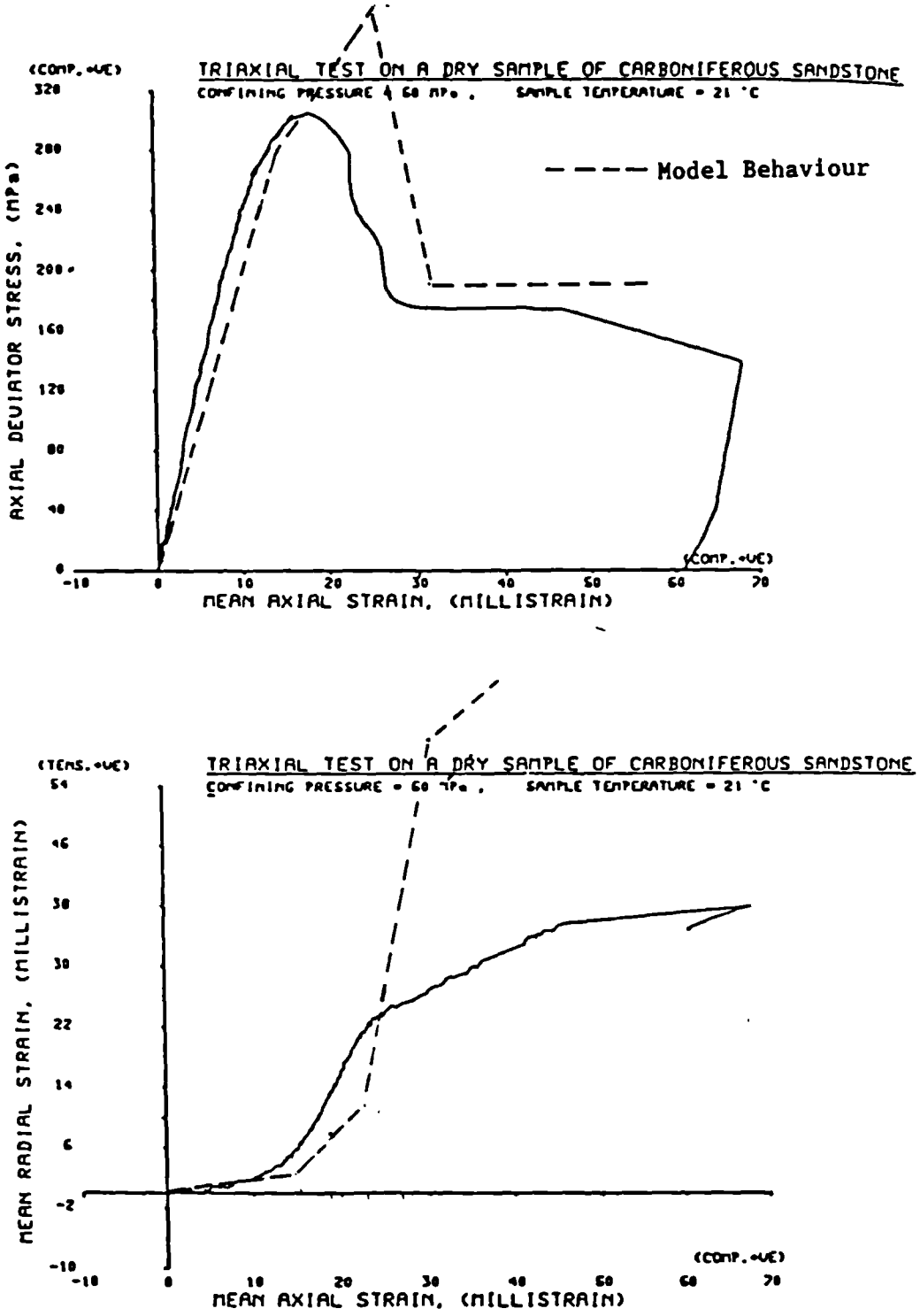


Figure A.12 Comparison of Mohr-Coulomb, associated flow model with test results (σ_3 = 50 MPa).

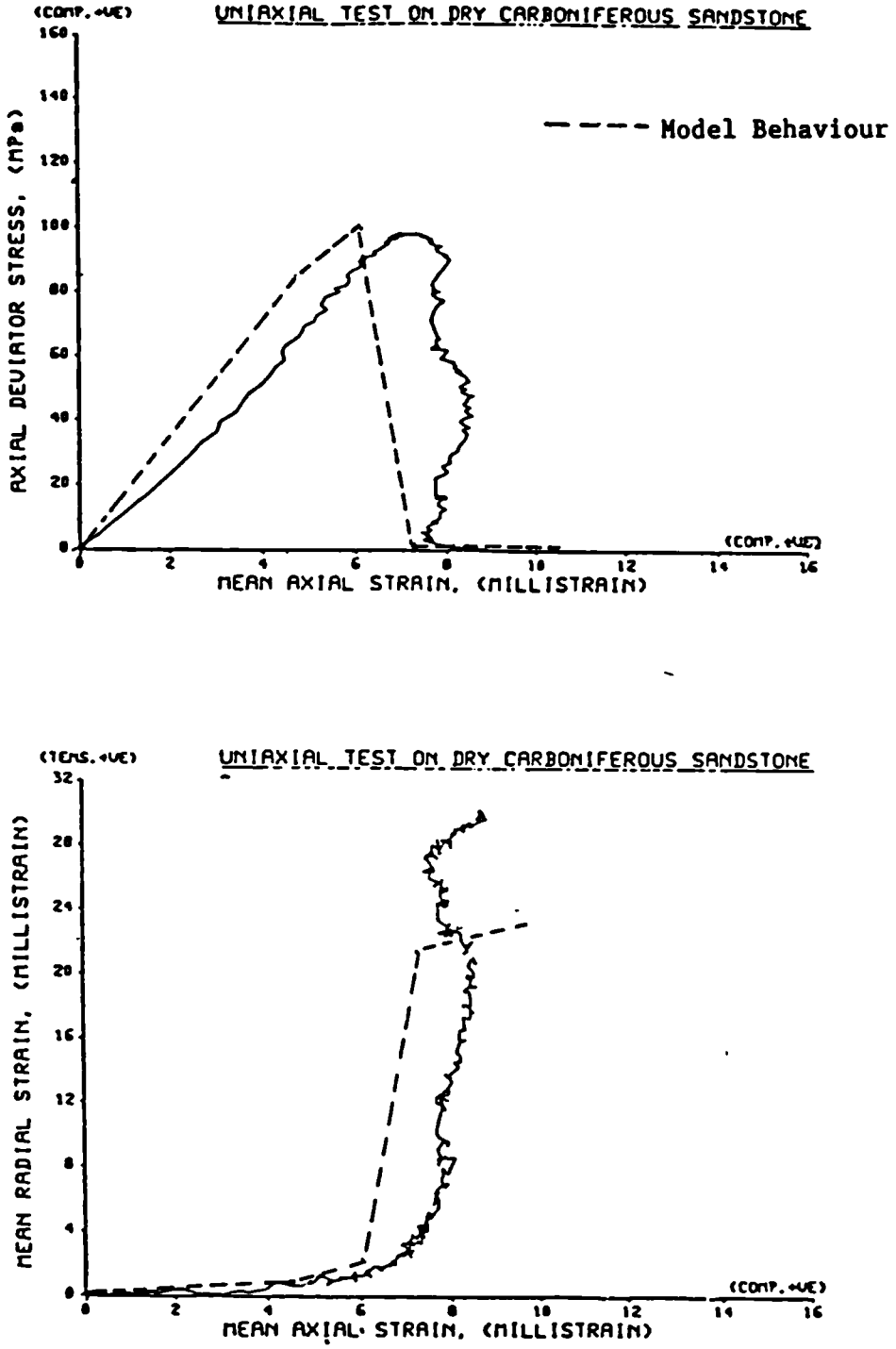


Figure A.13 Comparison of Mohr-Coulomb, non-associated flow model with test results (uniaxial loading).

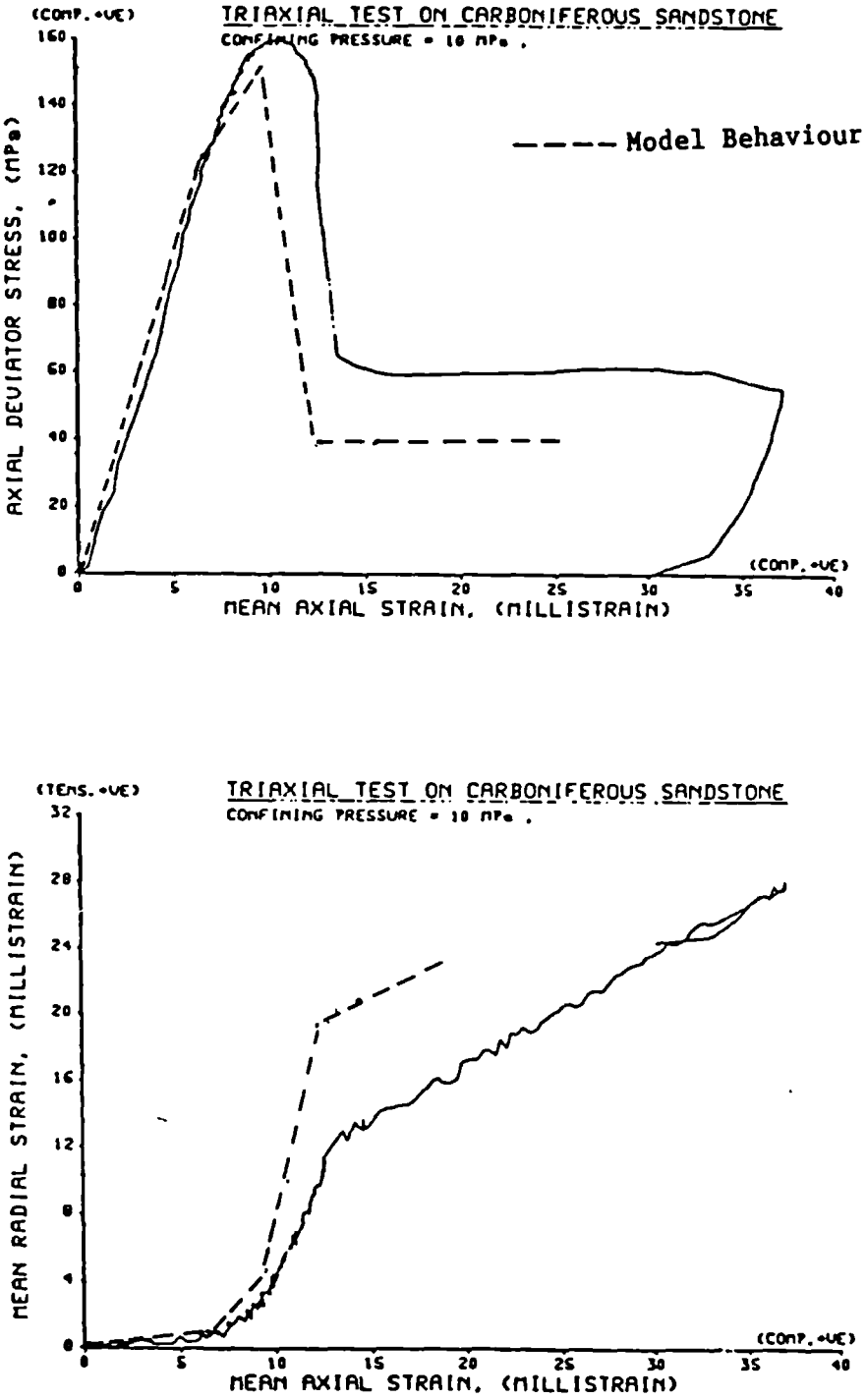
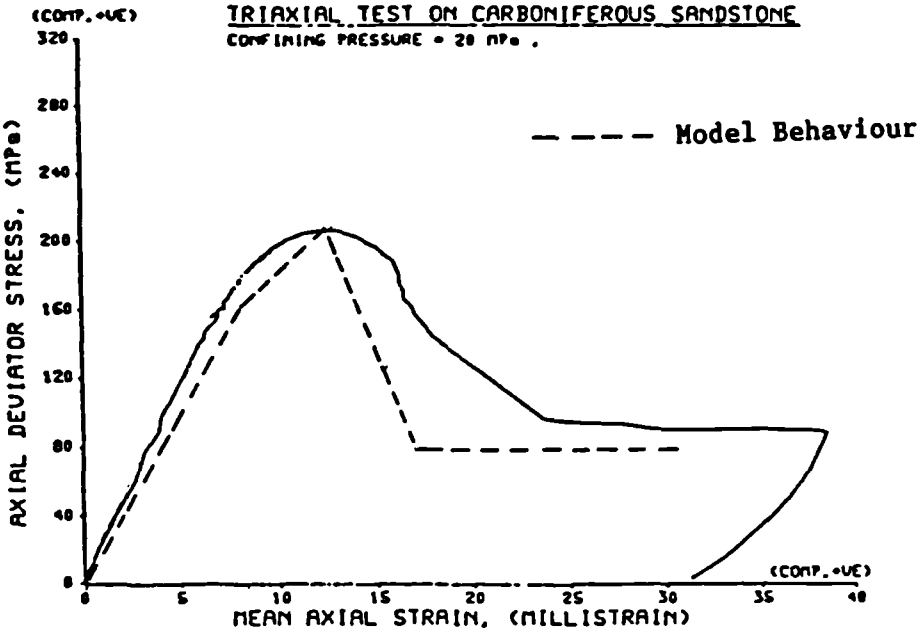


Figure A.14 Comparison of Mohr-Coulomb, non-associated flow model with test results (σ_3 = 10 MPa).



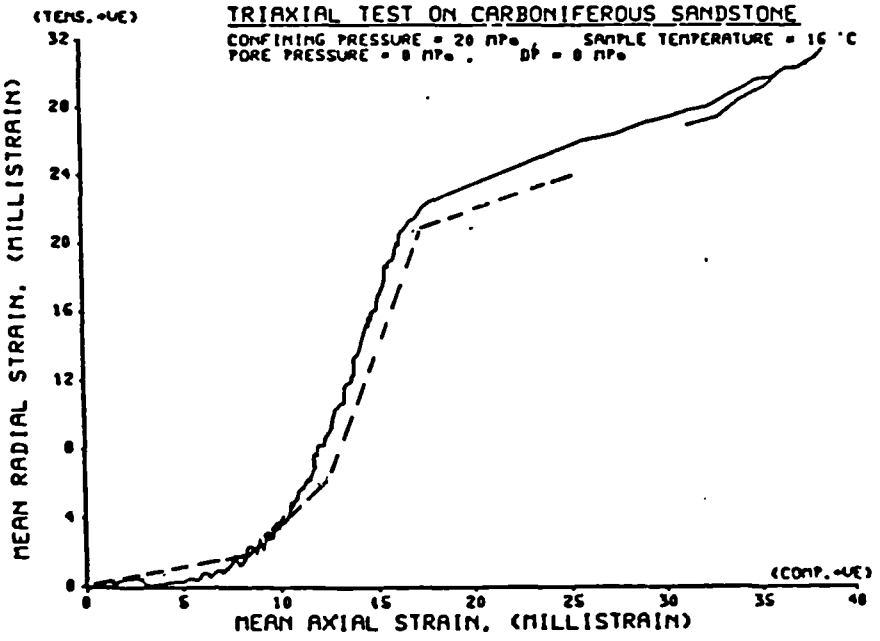
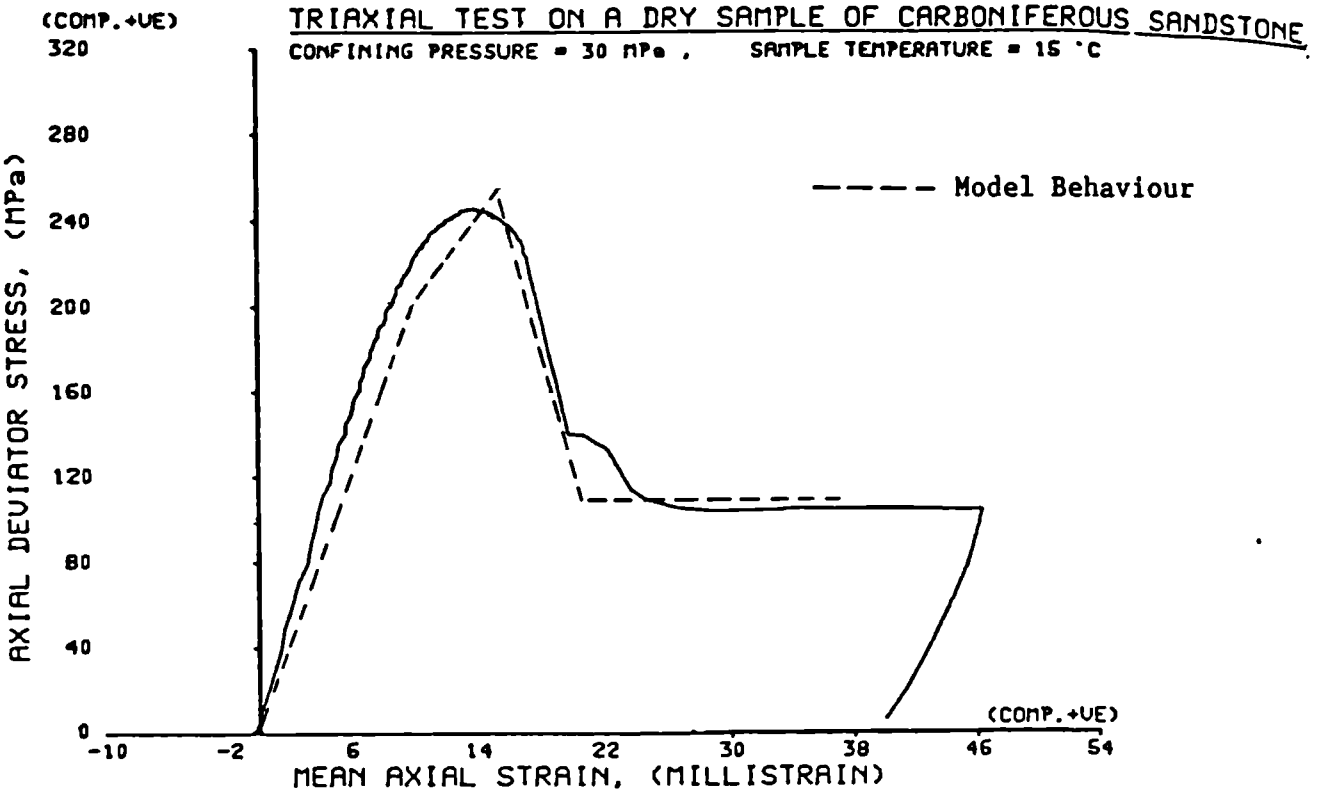


Figure A.15 Comparison of Mohr-Coulomb, non-associated flow model with test results (σ_3 = 20 MPa).



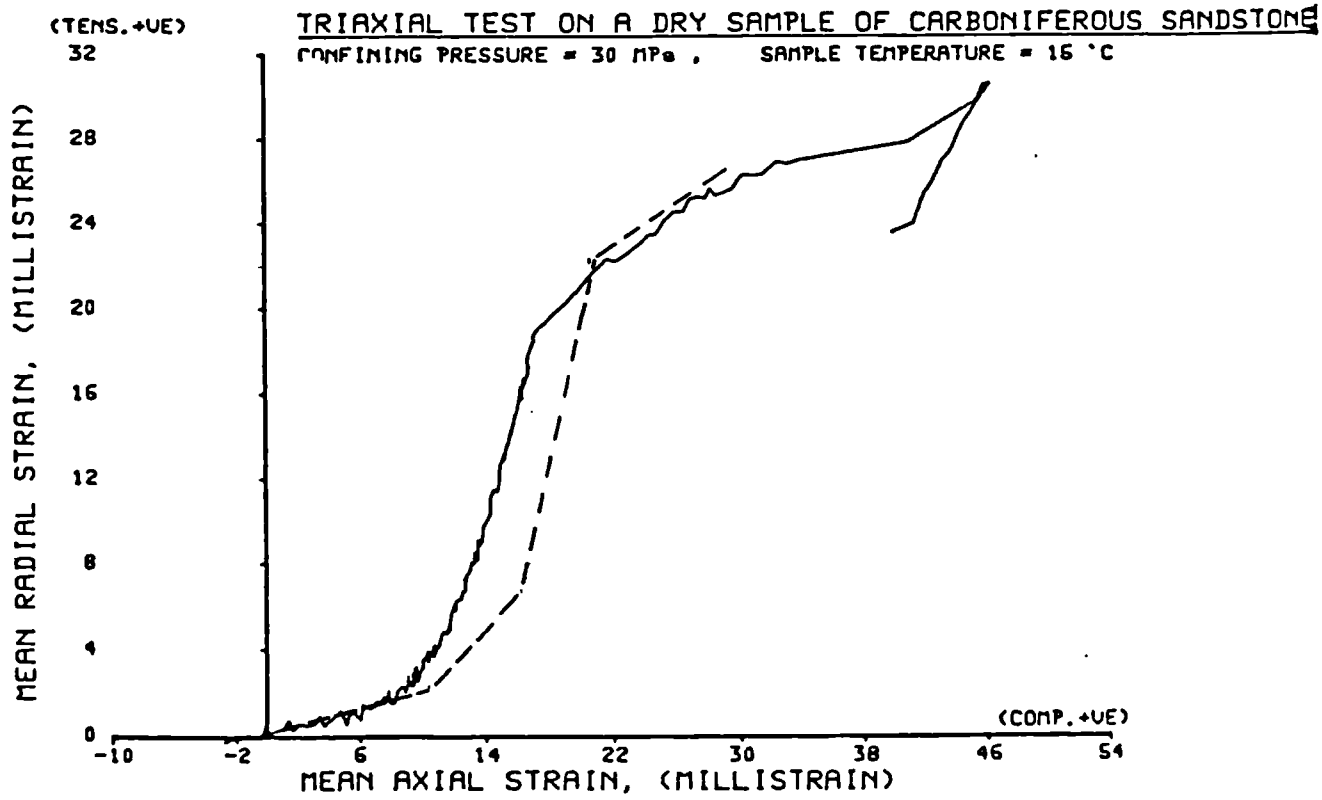
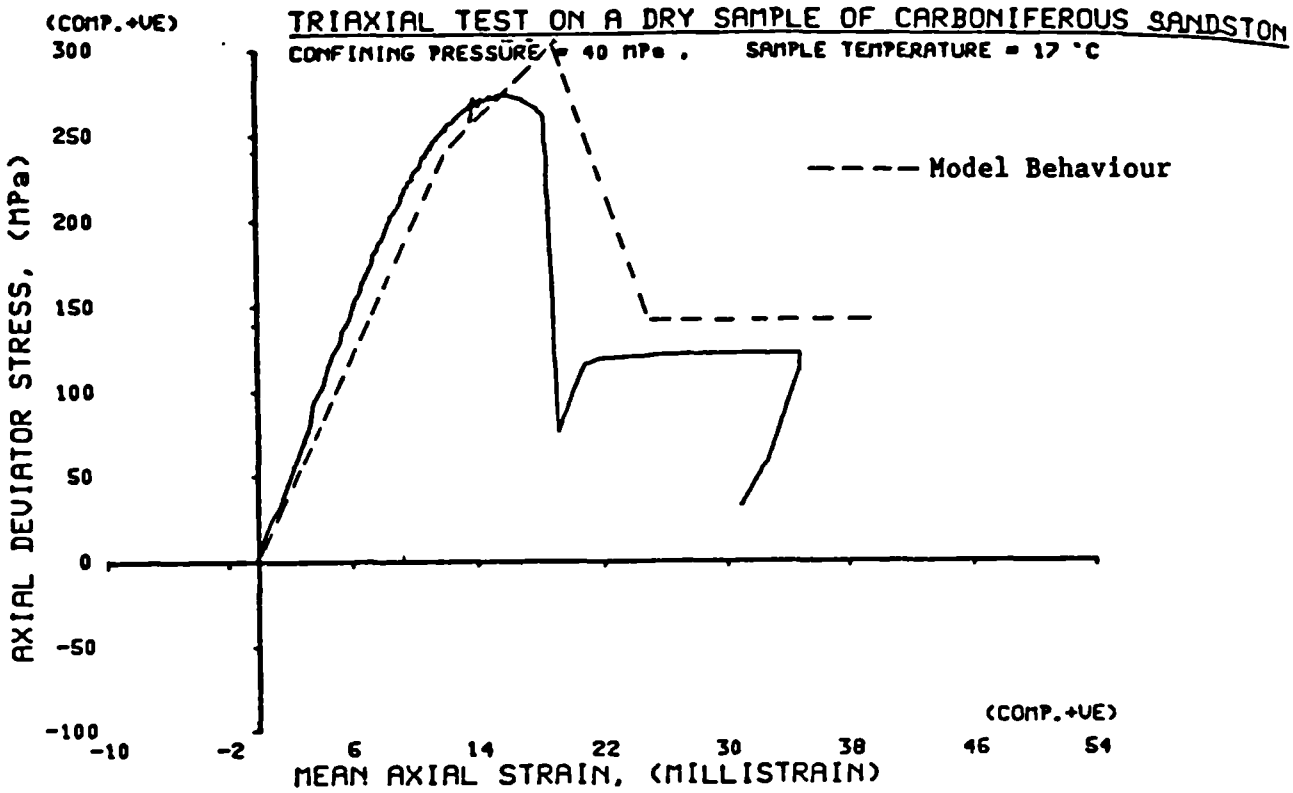


Figure A.16 Comparison of Mohr-Coulomb, non-associated flow model



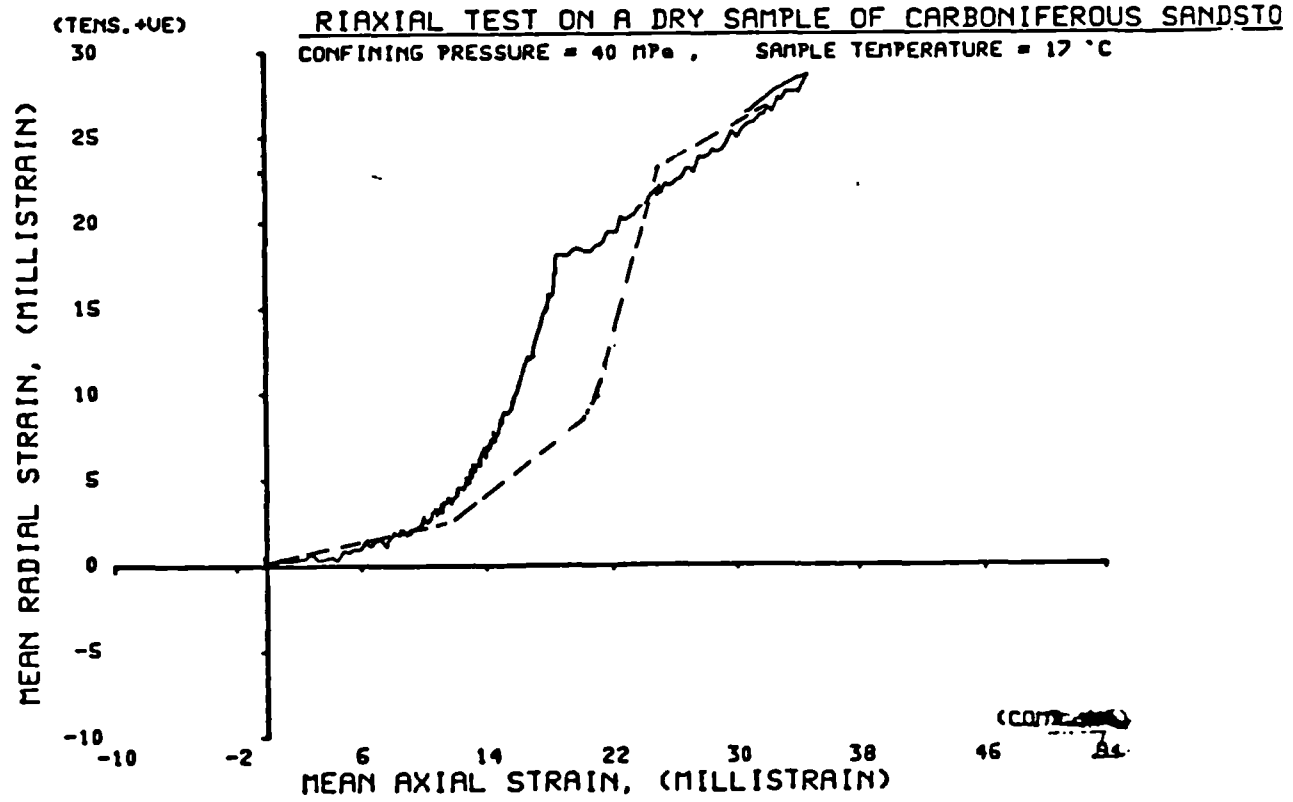
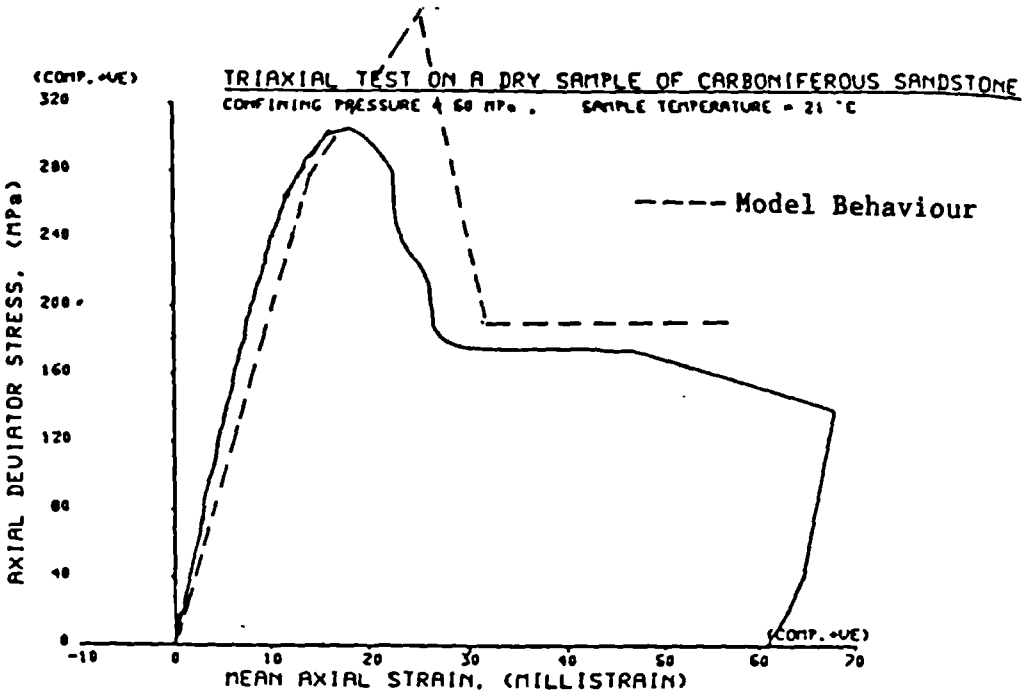


Figure A.17 Comparison of Mohr-Coulomb, non-associated flow model with test results (σ_3 = 40 MPa).



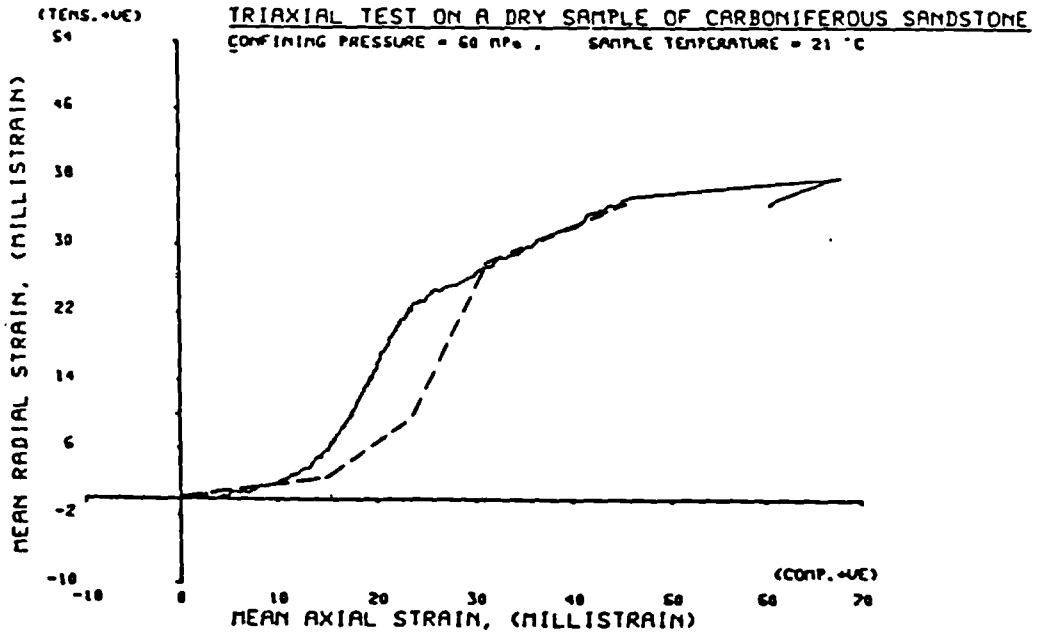


Figure A.18 Comparison of Mohr-Coulomb, non-associated flow model with test results (σ_3 = 50 MPa).

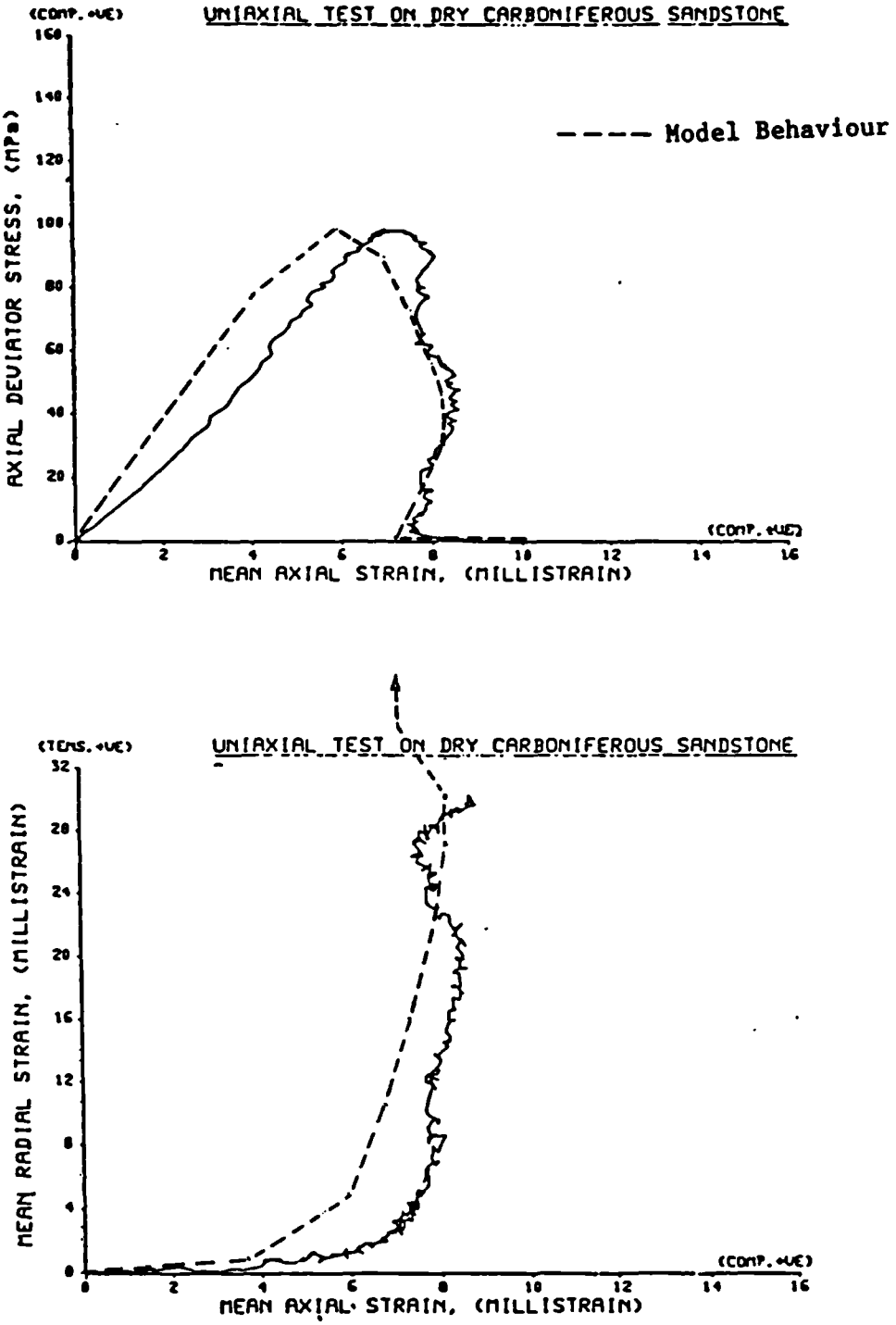
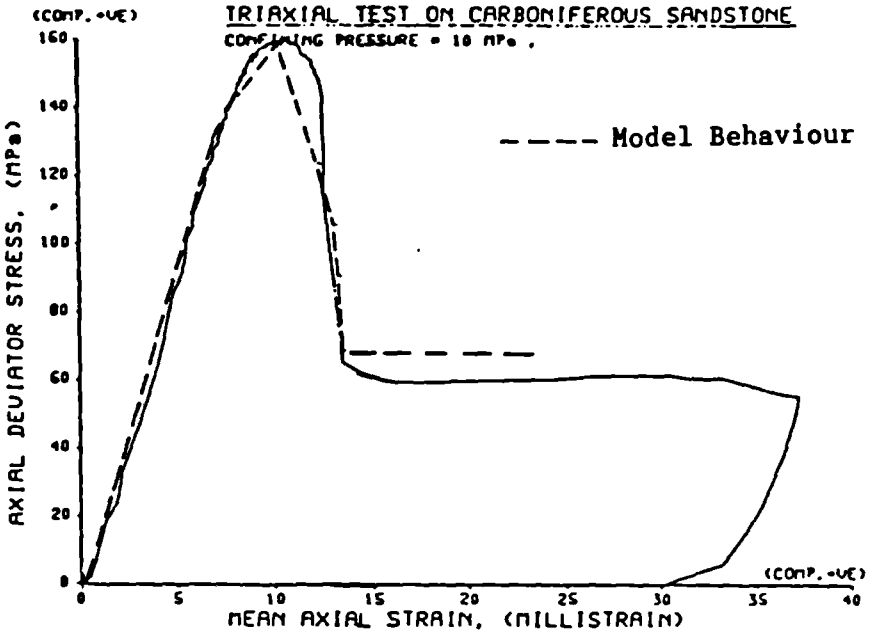


Figure A.19 Comparison of Hoek-Brown, associated flow model with test results (uniaxial loading).



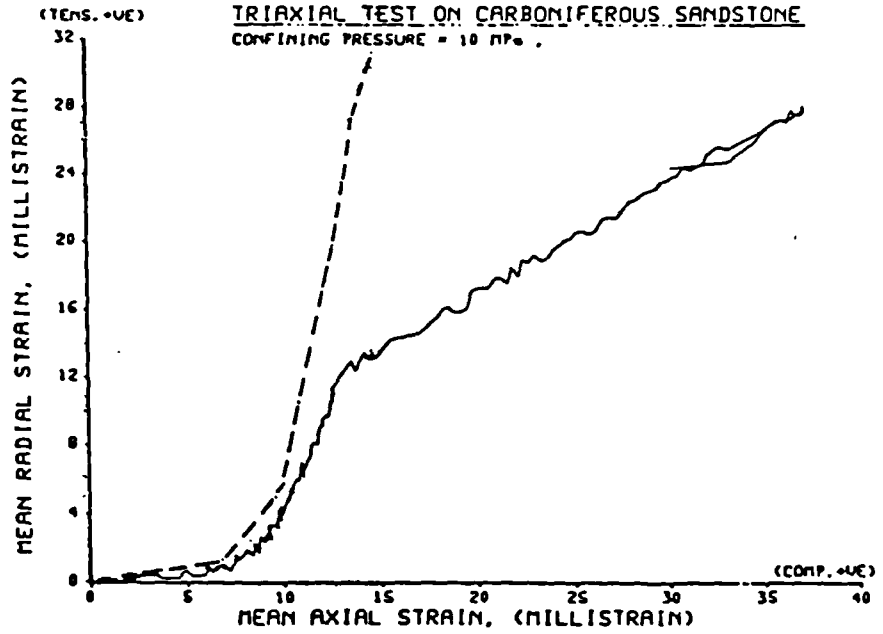
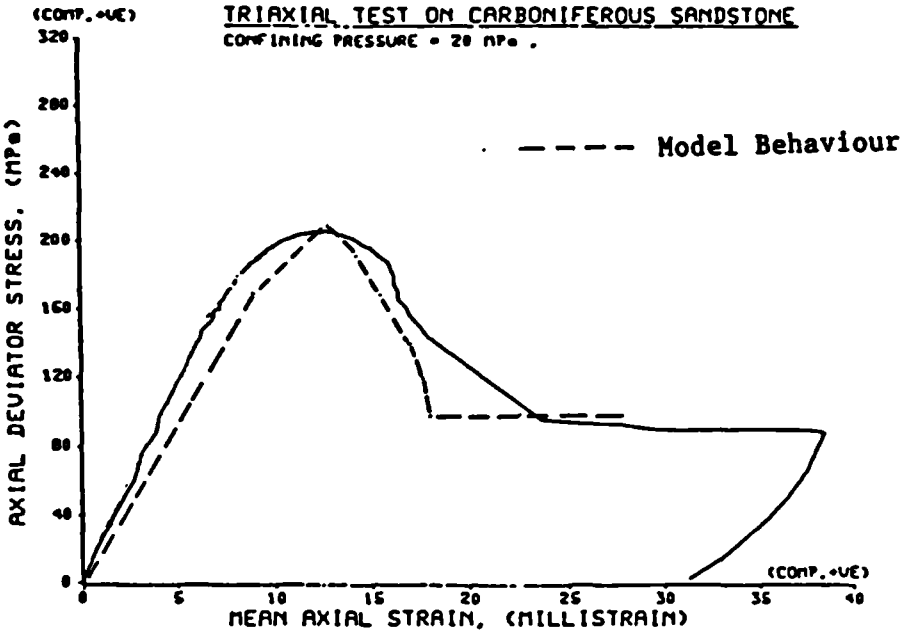


Figure A.20 Comparison of Hoek-Brown, associated flow model with test results (σ_3 = 10 MPa).



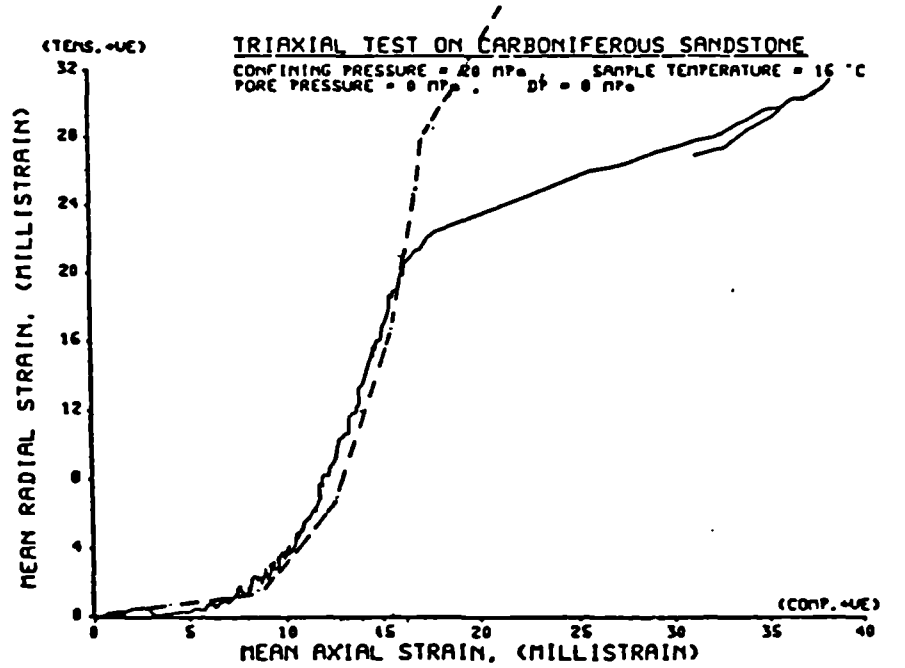
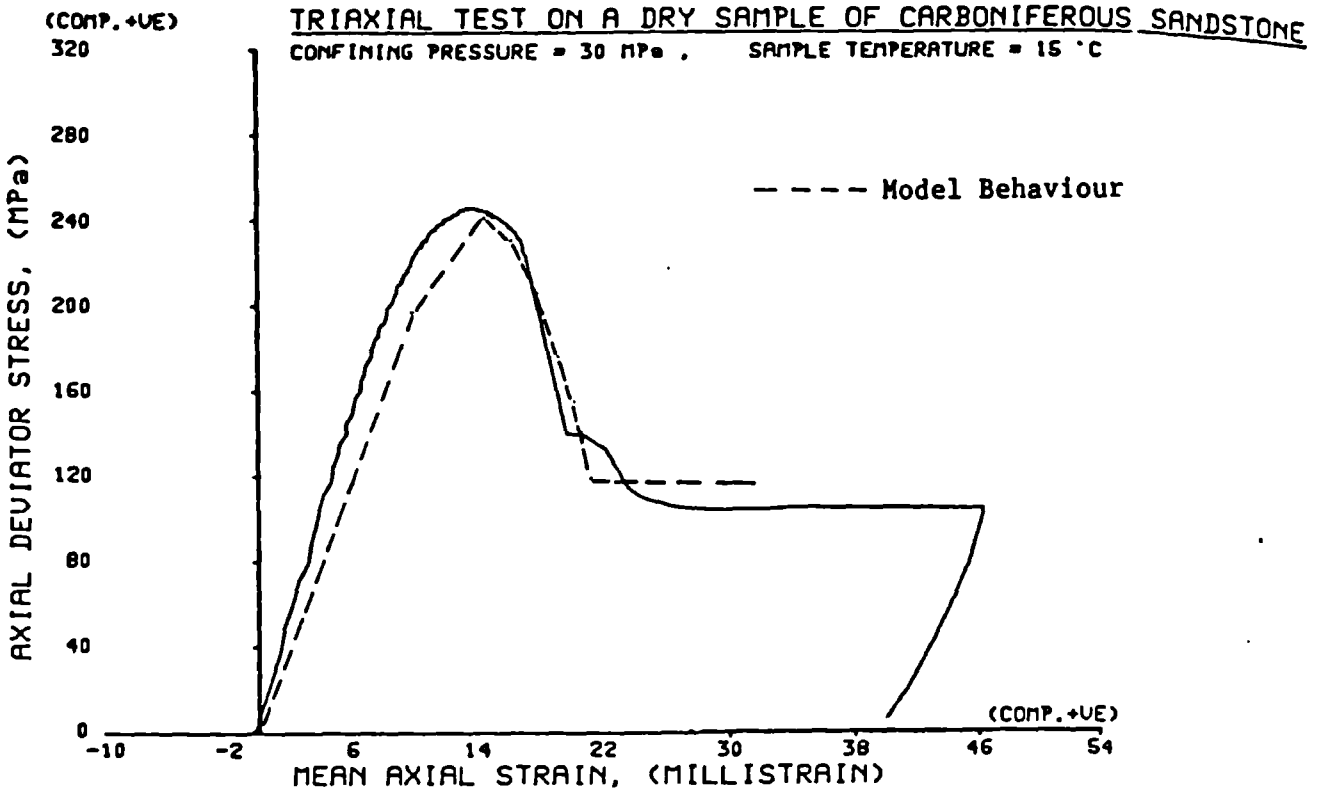


Figure A.21 Comparison of Hoek-Brown, associated flow model with test results (σ_3 = 20 MPa).



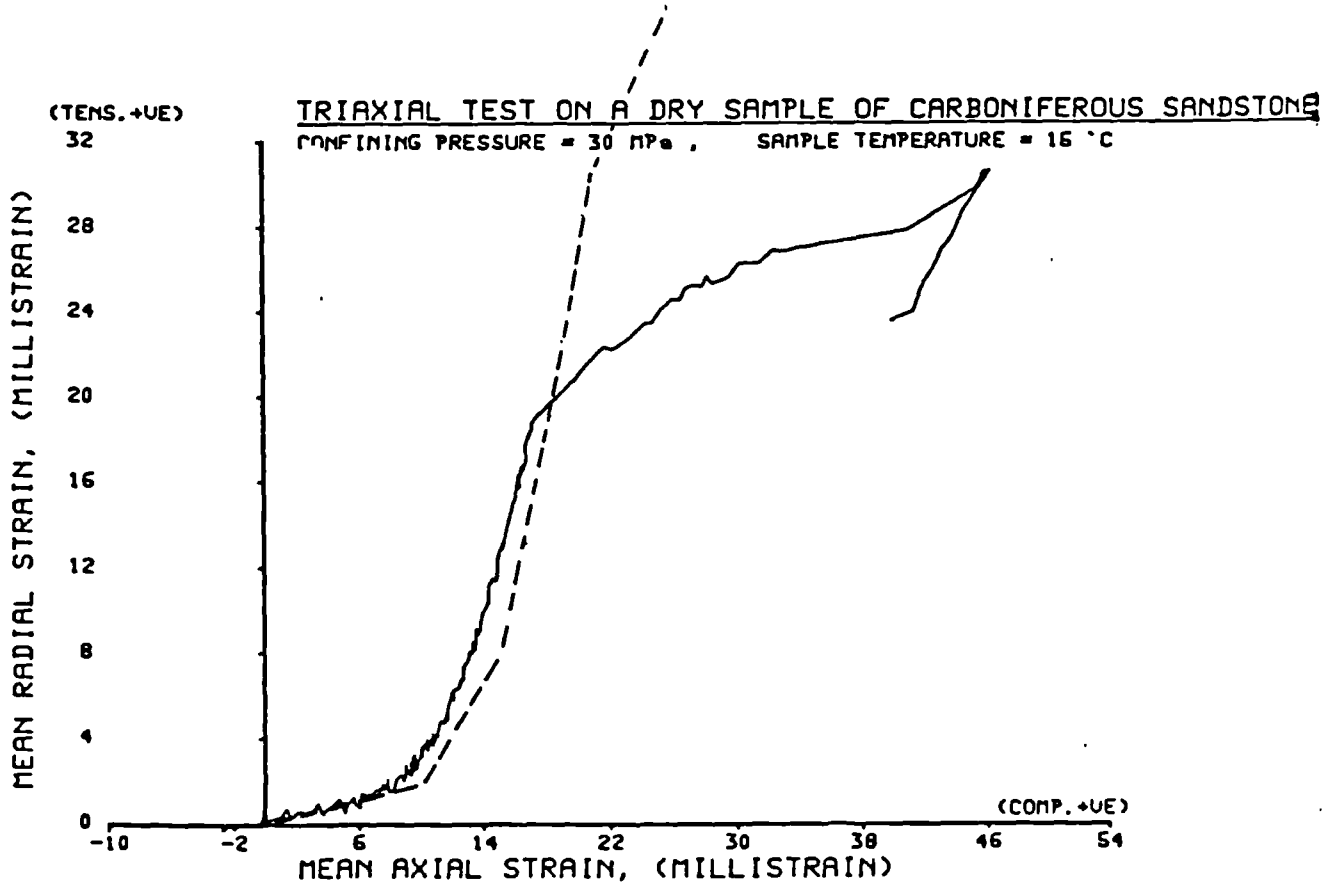
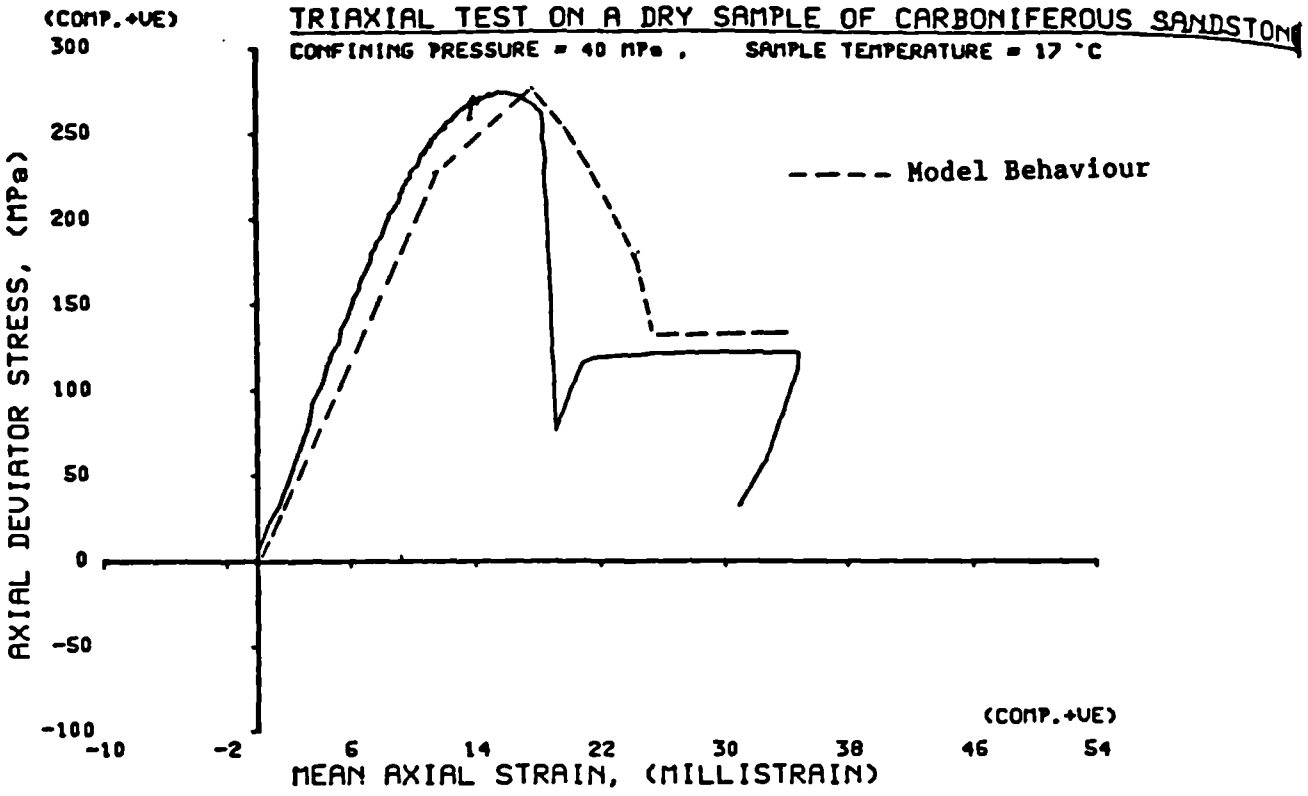


Figure A.22 Comparison of Hoek-Brown, associated flow model with test results (σ_3 = 30 MPa).



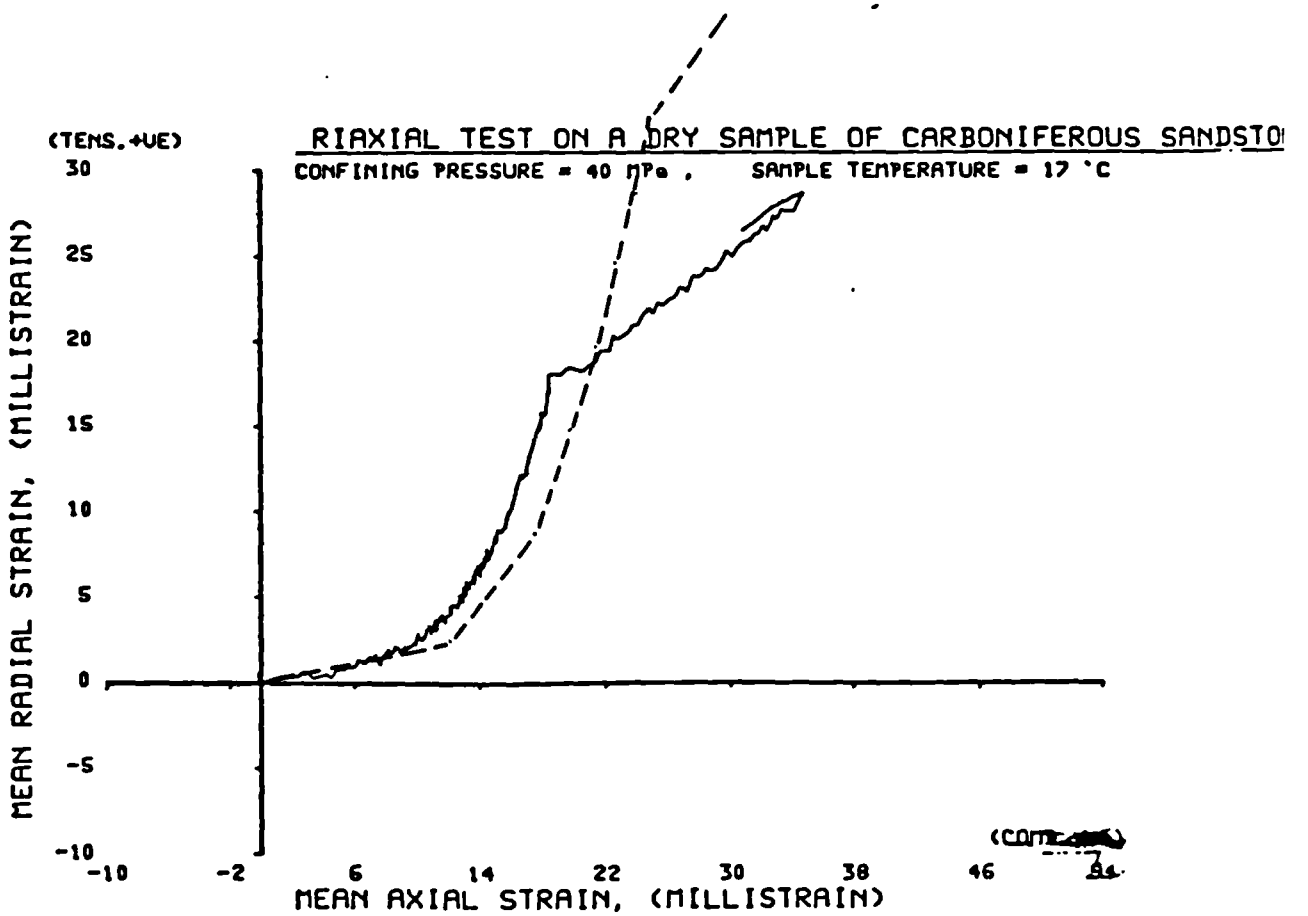


Figure A.23 Comparison of Hoek-Brown, associated flow model with test results (σ_3 = 40 MPa).

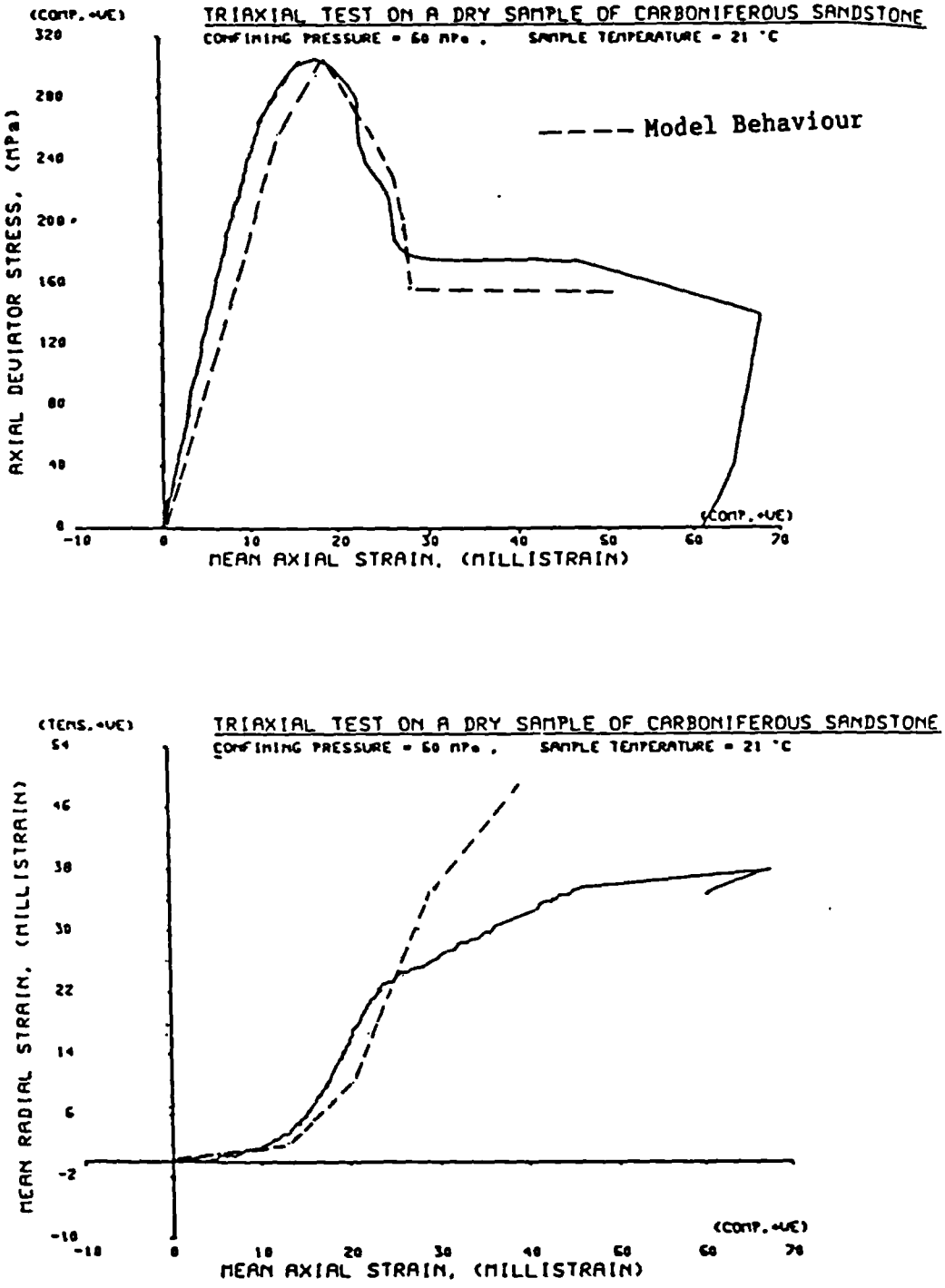
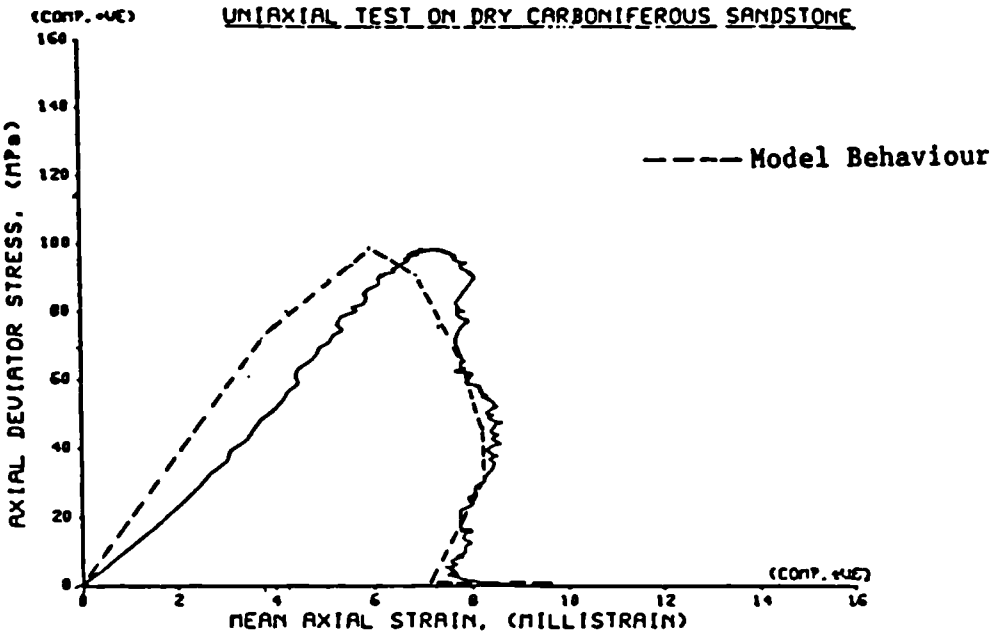


Figure A.24 Comparison of Hoek-Brown, associated flow model with test results (σ_3 = 50 MPa).



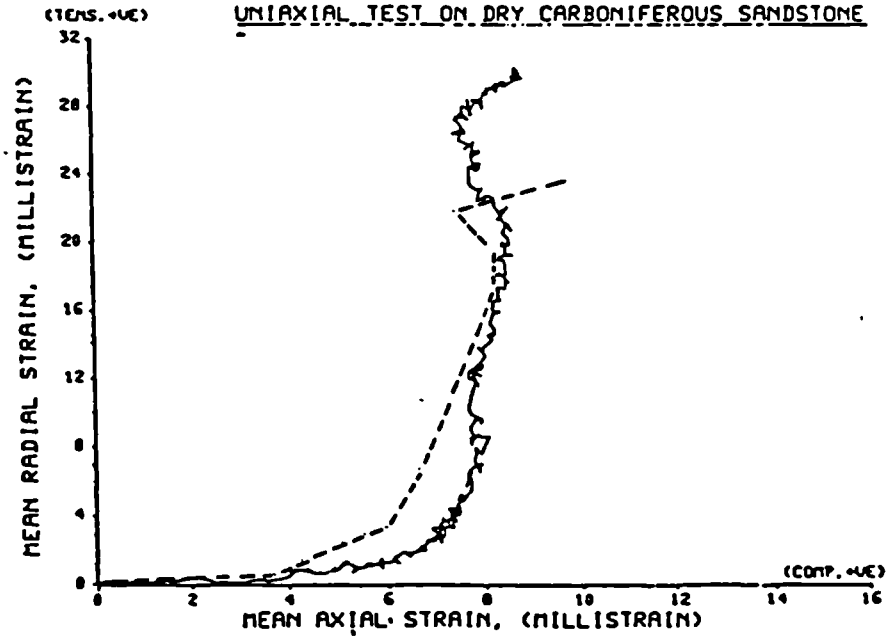
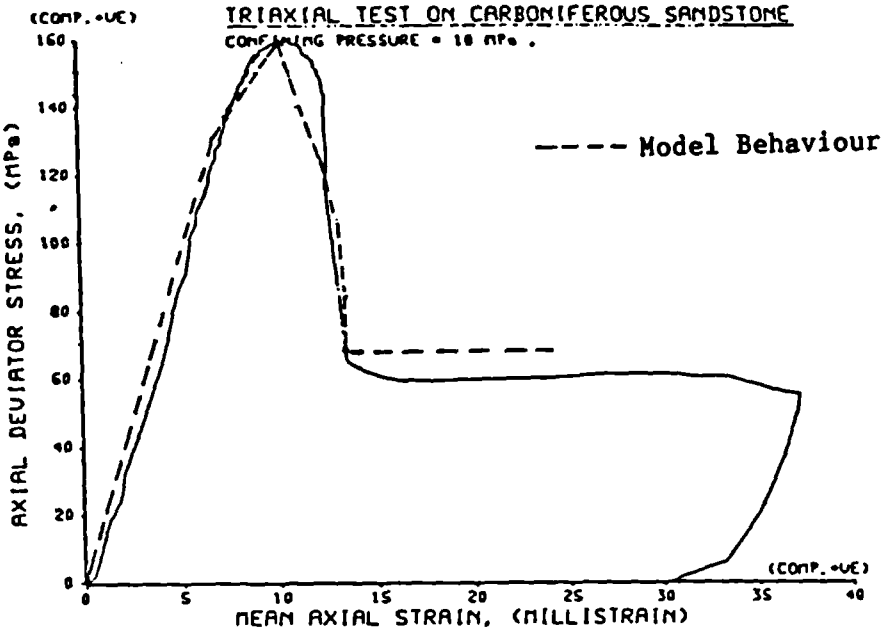


Figure A.25 Comparison of Hoek-Brown, non-associated flow model with test results (uniaxial loading).



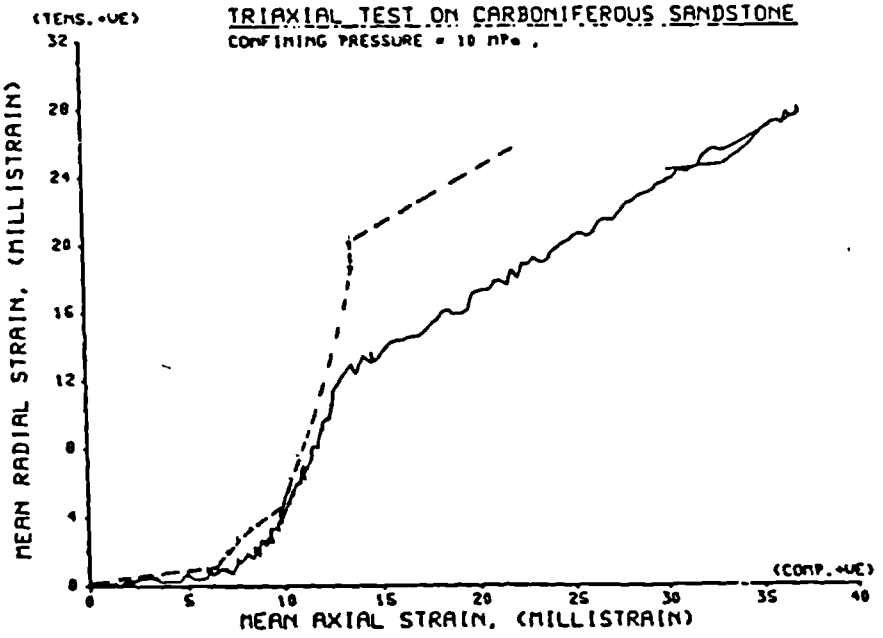


Figure A.26 Comparison of Hoek-Brown, non-associated flow model with test results (σ_3 = 10 MPa).

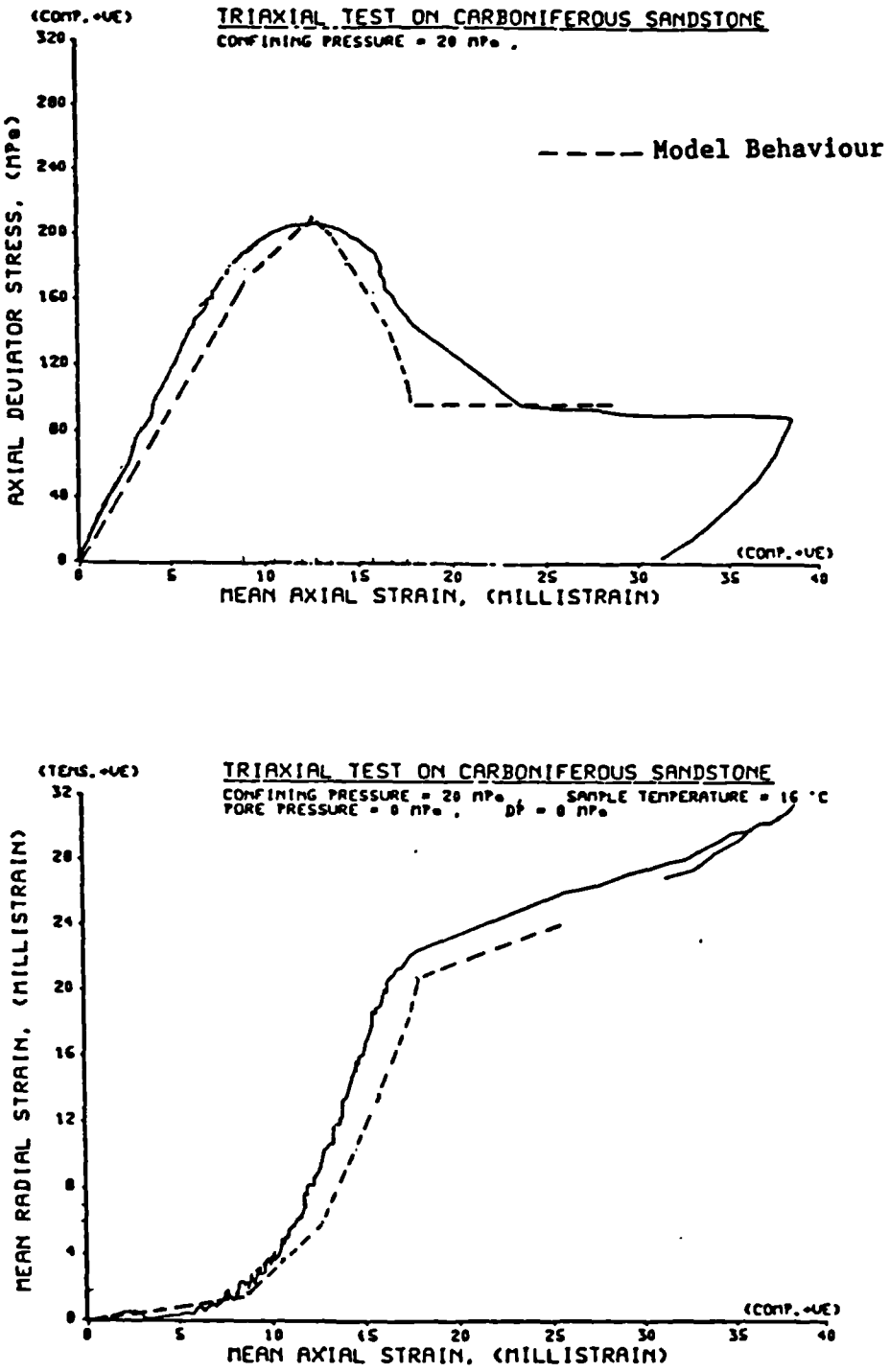
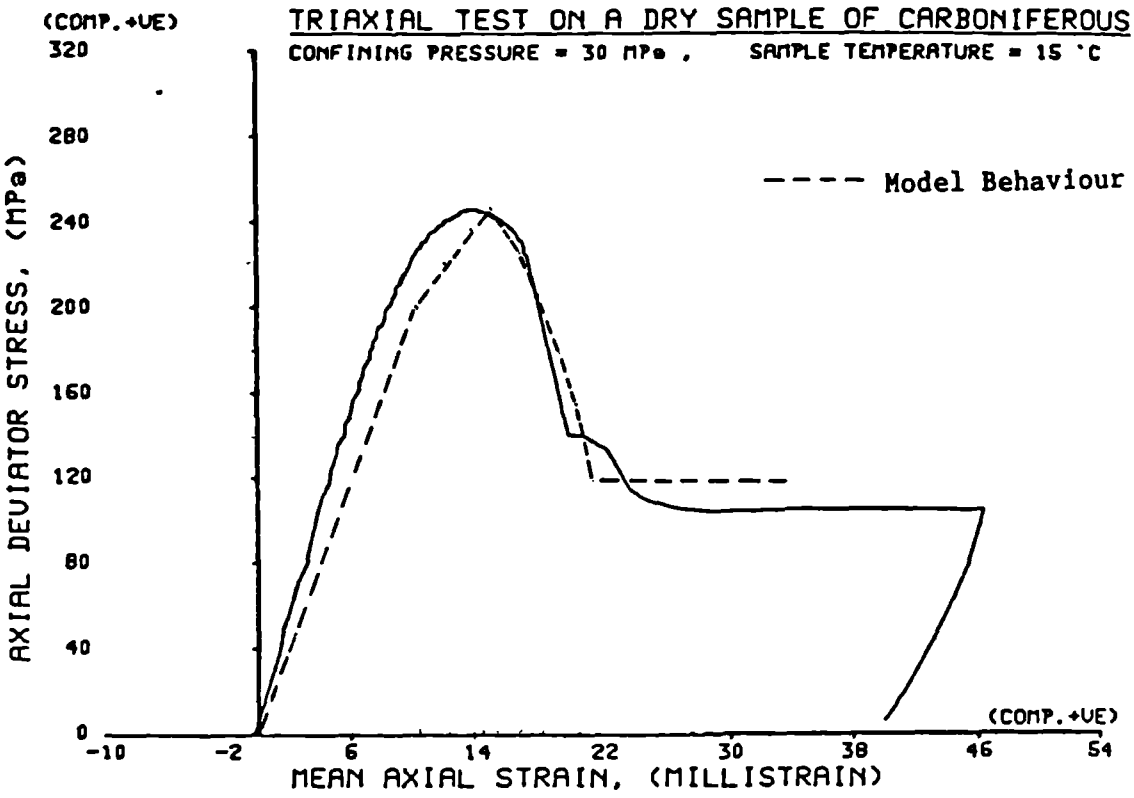


Figure A.27 Comparison of Hoek-Brown, non-associated flow model with test results (σ_3 = 20 MPa).



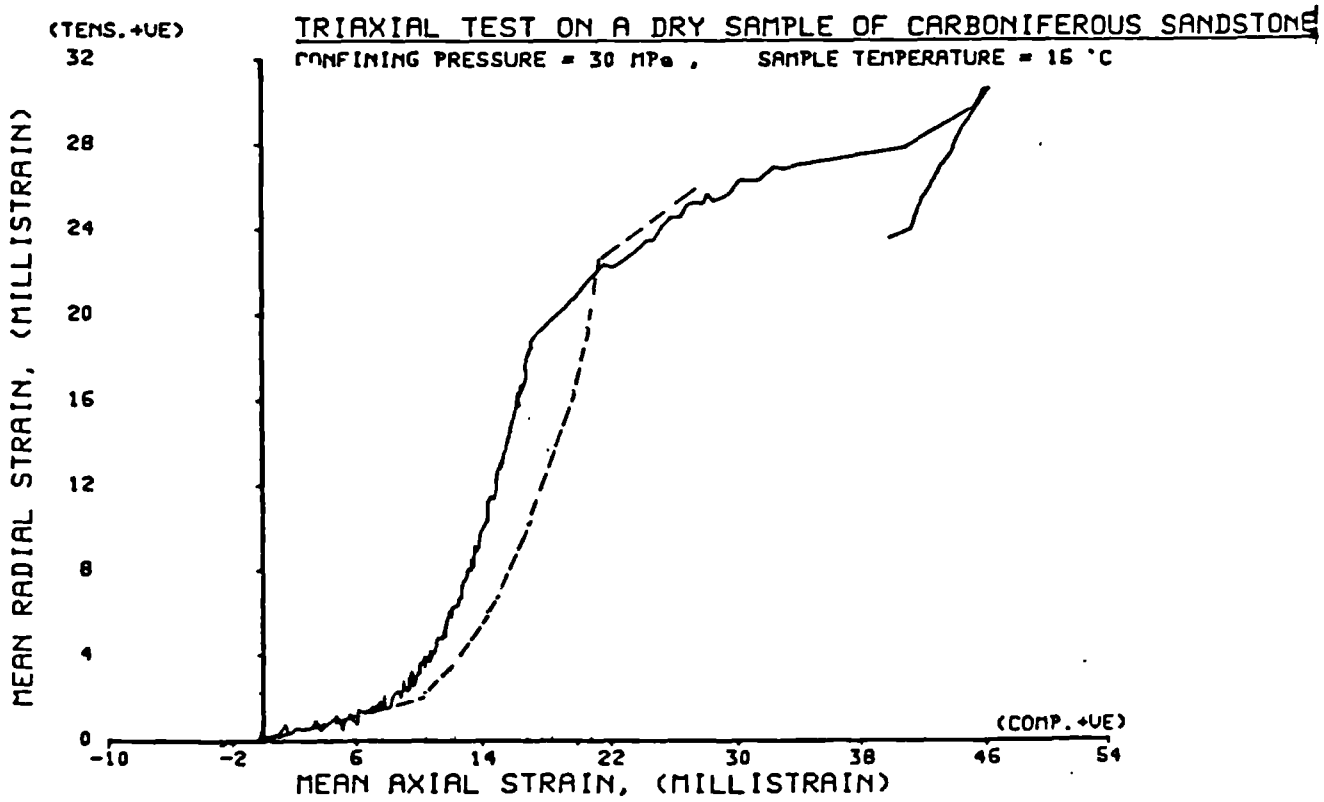
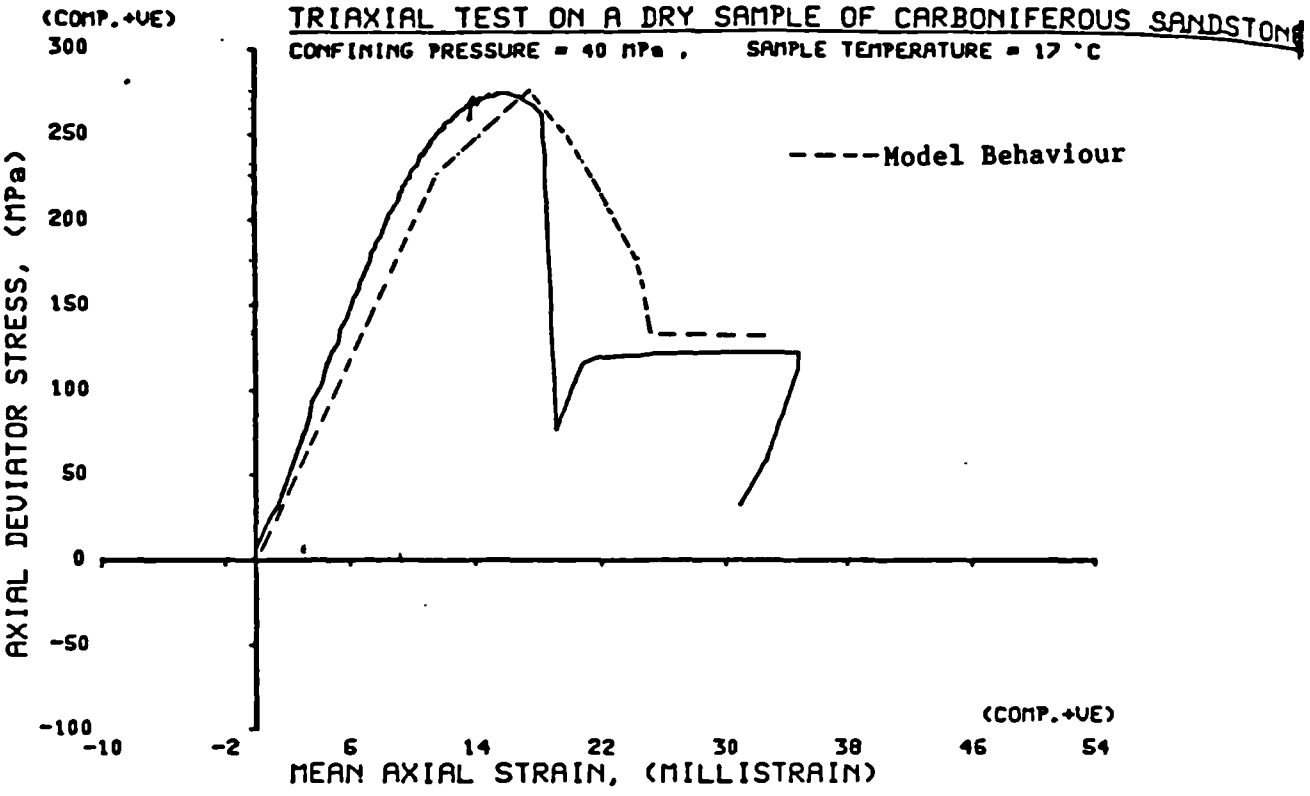


Figure A.28 Comparison of Hoek-Brown, non-associated flow model with test results (σ_3 = 30 MPa).



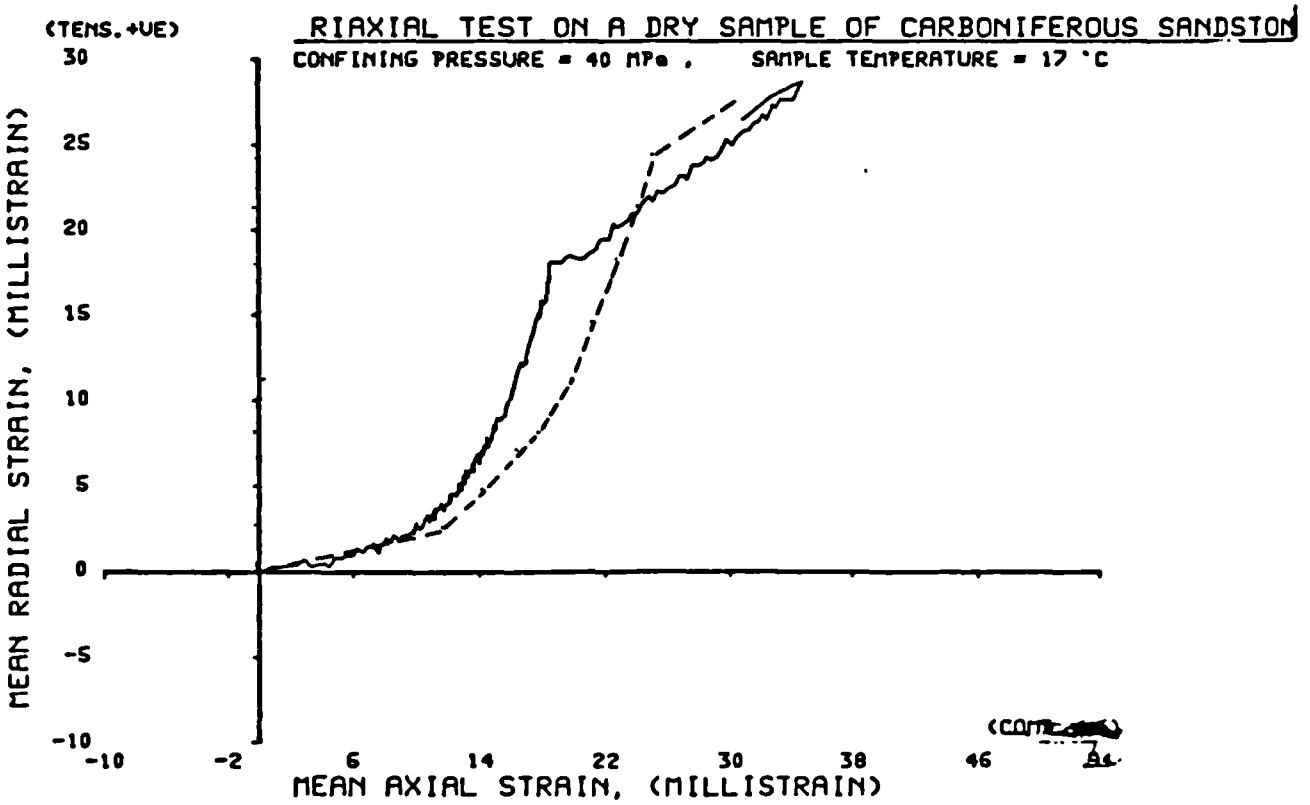


Figure A.29 Comparison of Hoek-Brown, non-associated flow model with test results (σ_3 = 40 MPa).

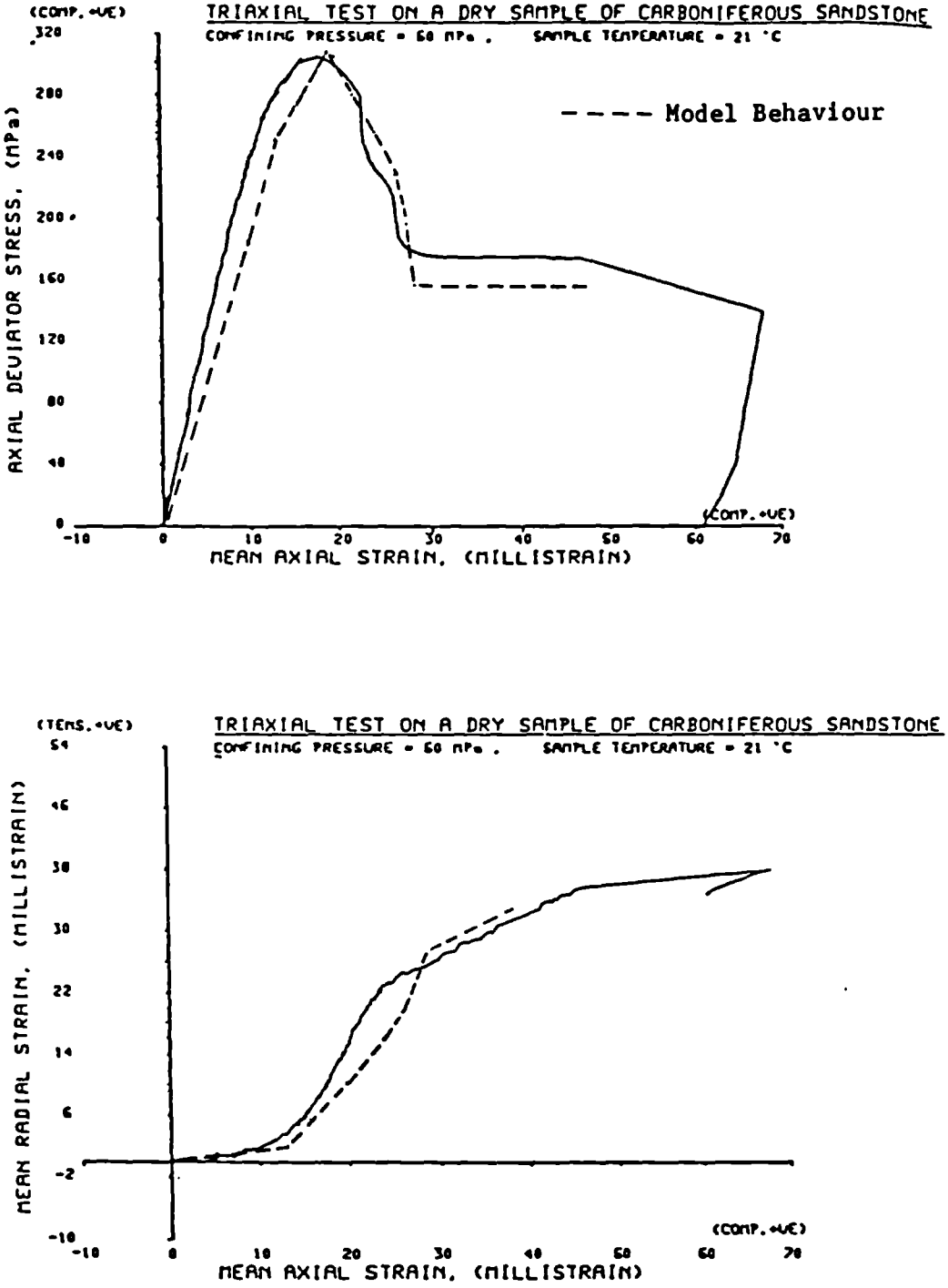


Figure A.30 Comparison of Hoek-Brown, non-associated flow model with test results (σ_3 = 50 MPa).

APPENDIX B

GALIN'S SOLUTION FOR THE ELASTO-PLASTIC STRESS DISTRIBUTION AROUND A CIRCULAR OPENING IN A MATERIAL OBEYING THE TRESCA YIELD CRITERION

The equations given in this appendix give the states of stress in the plastic and elastic regions around a circular opening conforming to the conditions specified below.

1. Plane strain conditions apply.
2. In the elastic region the material is homogeneous, isotropic and linear elastic.
3. In the plastic region the material conforms to perfect plasticity and the Tresca yield criterion.
4. The plastic region completely encompasses the hole as shown in Figure B.1.
5. The axial stress remains the intermediate stress throughout.
6. Body forces are negligible.

The solution to this problem was first presented by Galin.[73] The following equations are derived from expressions presented by Savin[84] relating to the same problem. The expressions given by Savin are in the form of complex variables and are not readily usable. Thus, some manipulation of Savin's results is required in order to arrive at some of the expressions given here. The solutions are based on mapping the x-y cartesian coordinates (Figure B.1) on to a new coordinate system defined by the ξ-η coordinates. Before proceeding let c and β be defined as

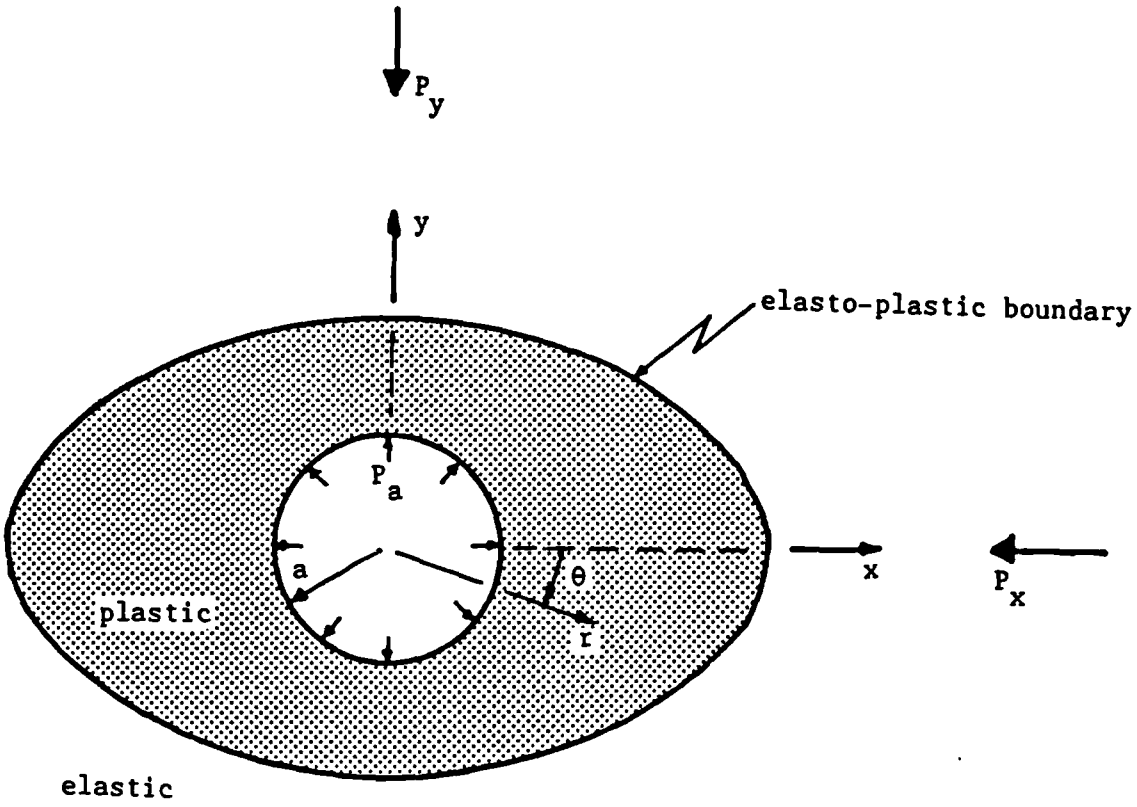


Figure B.1 Elliptical shaped plastic zone surrounding a circular excavation subjected to an anisotropic stress field.

$$c = ae^{\alpha} \qquad \text{where} \quad \alpha = \frac{1}{2\sigma_Y}\left((1+k)P_y - 2P_a - \sigma_Y\right)$$

and $$\beta = \frac{(1-k)}{2} P_y$$

where P_y and P_x are the in-situ stress magnitudes (see Figure B.1),

k is the stress anisotropy ratio P_x/P_y,

P_a is the pressure applied to the inside of the hole,

σ_Y is the uniaxial yield strength of the material (which is the same as the uniaxial peak strength, σ_c, for perfect plasticity),

and a is the hole radius.

The mapping functions can now be expressed as

$$x = c\xi(1 + \beta/\gamma^2) = c(\gamma + \beta/\gamma)\cos\psi \qquad (1)$$

$$y = c\eta(1 - \beta/\gamma^2) = c(\gamma - \beta/\gamma)\sin\psi \qquad (2)$$

where $\tan\psi = \frac{\eta}{\xi}$

and $\gamma = + \sqrt{(\xi^2 + \eta^2)}$

The contour defining the boundary between the plastic and elastic zones can now be described by putting $\gamma = 1$ in equations (1) and (2), and points defined by $\gamma > 1$ lie in the elastic region.

The stress state in the plastic zone is axisymmetric and in terms of polar coordinates (see Figure B.1) given by

$$\sigma_r = P_a + \sigma_Y \ln\frac{r}{a} \qquad (3)$$

$$\sigma_\theta = P_a + \sigma_Y\left(1 + \ln\frac{r}{a}\right) \qquad (4)$$

In the elastic zone the stress state with respect to the x-y coordinate

system is found from the following expressions (note $\gamma \geq 1$)

$$D = \sigma_x + \sigma_y = 2P_a + \sigma_Y\left\{1 + \ln\left(\frac{x^2+y^2}{a^2\gamma^2}\right)\right\} \tag{5}$$

$$E = \sigma_y - \sigma_x = \sigma_Y\left\{\frac{2\beta + [\gamma^2+(\beta/\gamma)^2]\cos 2\psi}{\gamma^2 + 2\beta\cos 2\psi + (\beta/\gamma)^2} + \frac{\beta(\gamma^2 - 1/\gamma^2) + [1+(\beta/\gamma)^2](1-\gamma^2)\cos 2\psi}{\gamma^2 - 2\beta\cos 2\psi + (\beta/\gamma)^2}\right\} \tag{6}$$

Thus, σ_x and σ_y can be found from the following

$$\sigma_x = \tfrac{1}{2}(D-E) \qquad \text{and } \sigma_y = \tfrac{1}{2}(D+E)$$

The shear component τ_{xy} is given by

$$\tau_{xy} = \frac{\sigma_Y}{2}\left\{\frac{(\beta/\gamma)^2 - \gamma^2}{\gamma^2 + 2\beta\cos 2\psi + (\beta/\gamma)^2} + \frac{(\gamma^2-1)[1-(\beta/\gamma)^2]}{\gamma^2 - 2\beta\cos 2\psi + (\beta/\gamma)^2}\right\}\sin 2\psi \tag{7}$$

The polar stress components are found from stress transformation. Thus, from (5), (6) and (7) the polar stress components in the elastic region are expressed as

$$\sigma_r = \tfrac{1}{2}(D-E)\cos^2\theta + \tfrac{1}{2}(D+E)\sin^2\theta + 2\tau_{xy}\cos\theta.\sin\theta$$

$$\sigma_\theta = \tfrac{1}{2}(D-E)\sin^2\theta + \tfrac{1}{2}(D+E)\cos^2\theta - 2\tau_{xy}\cos\theta.\sin\theta$$

and $\tau_{r\theta} = E.\cos\theta.\sin\theta + \tau_{xy}(\cos^2\theta - \sin^2\theta)$

where $\theta = \tan^{-1}\left(\frac{x}{y}\right)$

Detournay[85] quotes a limiting value on the stress anisotropy for which Galin's solution is admissable due to considerations of statical

determinacy. Adapting Detournay's result, we have a limiting value for the stress anisotropy ratio, k, of

$$[1 - \sigma_Y(\sqrt{2}-1)/P_y] \leq k \leq 1$$

(NOTE: The equations defining the elasto-plastic contour only apply when the plastic zone completely encompasses the circular opening.)

APPENDIX C

APPROXIMATE SOLUTION FOR THE CONTOUR DEFINING THE ELASTIC-PLASTIC BOUNDARY AROUND A CIRCULAR OPENING IN A PERFECTLY PLASTIC MOHR-COULOMB MATERIAL SUBJECTED TO A NON-HYDROSTATIC STRESS FIELD IN PLANE STRAIN

The equations that follow are adapted from work published by Detournay.[85] The solution described provides the exact stress state in the plastic zone and an approximate solution for the elasto-plastic boundary. Detournay considers yielding in both active ($\sigma_r > \sigma_\theta$) and passive ($\sigma_r < \sigma_\theta$) modes. In this text only the more relevant passive mode is considered. As with Galin's solution presented in Appendix B, the solution assumes the plastic zone completely encompasses the wellbore (see Figure B.1, Appendix B). The other assumptions set out in Appendix B apply here apart from the third assumption. This solution assumes a Mohr-Coulomb criterion, however, when the friction angle, ϕ, reduces to zero, the general equations presented by Detournay reduce to the Tresca criterion equations given in Appendix B. Thus, Detournay's solution is of a more general form than Galin's.

Stress state in the plastic region

The equations of stress in the plastic region are exact and are found as follows:

Assuming no elastic unloading within the plastic zone, then the yield function, F, equals zero. Also, providing no shear tractions are applied

to the wellbore wall, the stress state within a perfectly plastic material is axisymmetric (Brown and Bray[1]). Thus, σ_r and σ_θ are principal stresses, and since F=0, we have

$$\sigma_\theta = \frac{1+\sin\phi}{1-\sin\phi}\,\sigma_r + \frac{2c.\cos\phi}{1-\sin\phi} \qquad (1)$$

where c is the cohesion,

and ϕ is the angle of friction.

The axisymmetric equation for equilibrium is given by

$$\frac{d\sigma_r}{dr} = \frac{\sigma_\theta - \sigma_r}{r} \qquad (2)$$

Combining (1) and (2) to eliminate σ_θ gives

$$\frac{d\sigma_r}{dr} = \frac{2\sin\phi}{(1-\sin\phi)r}\,\sigma_r + \frac{2c.\cos\phi}{(1-\sin\phi)r}$$

which on intergration and applying the boundary condition that $\sigma_r = P_a$ at r = a (where P_a is the inner support pressure and 'a' is the hole radius), yields

$$\sigma_r = (P_a + c.\cot\phi)\left(\frac{r}{a}\right)^{\alpha} - c.\cot\phi \qquad (3)$$

where $\alpha = \frac{2\sin\phi}{1-\sin\phi}$ (4)

and on eliminating σ_r from (1) and (3) we have

$$\sigma_\theta = \frac{1+\sin\phi}{1-\sin\phi}(P_a + c.\cot\phi)\left(\frac{r}{a}\right)^{\alpha} - c.\cot\phi \qquad (5)$$

Elasto-plastic contour

The elasto-plastic boundary is now defined using the following equations, a number of which are approximate, as a result of truncating

an infinite series (see Detournay[85]). First let the parameters, k, R_e and m be defined as,

k is the stress anisotropy factor, given by

$$k = \frac{P_x}{P_y}, \qquad \text{where } P_y > P_x$$

R_e is the equivalent hydrostatic elasto-plastic boundary radius, given by

$$R_e = a\left[\frac{(1-\sin\phi)[(1+k)P_y + 2c.\cot\phi]}{2(P_a + c.\cot\phi)}\right]^{\frac{1}{\alpha}}$$

where α is defined in equation (4),

(Note: In Detournay's analysis[85] he uses the notation R_0 which is equivalent to R_e normalised with respect to the wellbore radius, 'a'),

m is the stress obliquity at infinity (see Detournay[85]), given by

$$m = \frac{(1-k)P_y}{(1+k)P_y\sin\phi + 2c.\cos\phi} \tag{6}$$

The solution for the elasto-plastic contour defined in terms of the x-y plane can now be expressed as

$$x_e \simeq \lambda R_e \cos\psi(1 + m_2) \tag{7}$$

$$y_e \simeq \lambda R_e \sin\psi(1 - m_2) \tag{8}$$

where ψ is a polar mapping variable and takes on values of 0 to 360°,

x_e and y_e the coordinate set defining the elasto-plastic interface,

and λ and m_2 are defined as

$$\lambda \simeq \left[1 + m^2\sin^2\phi\right]^{-\frac{1}{\alpha}} \qquad (\alpha \text{ defined previously in (4)})$$

$$m_2 \simeq (1-\sin\phi)m$$

As with Galin's solution Detournay quotes limiting values for the stress

obliquity for various friction angles. The reader is referred to Detournay's publication for accurate limiting values of the stress obliquity. However, for most cases values of 'm' bounded by $0 \leq m \leq 0.38$ should ensure statical determinacy.

(NOTE: The equations describing the elasto-plastic contour only apply when the plastic zone completely encompasses the circular opening.)

APPENDIX D

FINITE DIFFERENCE ANALYSIS OF STRAIN SOFTENING BEHAVIOUR AROUND A CIRCULAR OPENING IN A HYDROSTATIC IN-SITU STRESS FIELD

The majority of the following is based on work presented by Brown et al.[49] Two major areas where the analysis presented here differs from that given Brown et al are the treatment of strength parameter variation with respect to strain, and the influence of the the axial stress, σ_z. These variations are discussed in some detail in Sections 5.5.2.1 and 5.5.2.2, Chapter 5.

The analysis that follows is limited by the following assumptions:

1. Hydrostatic in-situ stress state, i.e. $P_x = P_y = P_z = P_0$.
2. Homogeneous, isotropic linear elastic behaviour up until peak strength.
3. Body forces are negligible in comparison to the in-situ stress field.
4. The Hoek-Brown yield criterion, given by

$$\sigma_1 = \sigma_3 + \sqrt{(m\sigma_c\sigma_3 + s\sigma_c^2)} \qquad (1)$$

5. A bilinear plastic behaviour as depicted in Figures D.1 and D.2. (The strain softening portion of the stress-strain plots is shown in dashed lines, since it is not truly linear. This is a result of choosing linear relationships between the strength parameters 'm' and 's' and plastic strain, and the true model stress-strain plot is described in Section 4.7.2, Chapter 4).

Figure D.3 shows the development of plastic zones around a circular opening, in a hydrostatic in-situ stress field, using the model behaviour given in Figures D.1 to D.2. Figure D.3 shows an annulus of rock next to the excavation wall at residual strength. However, this is

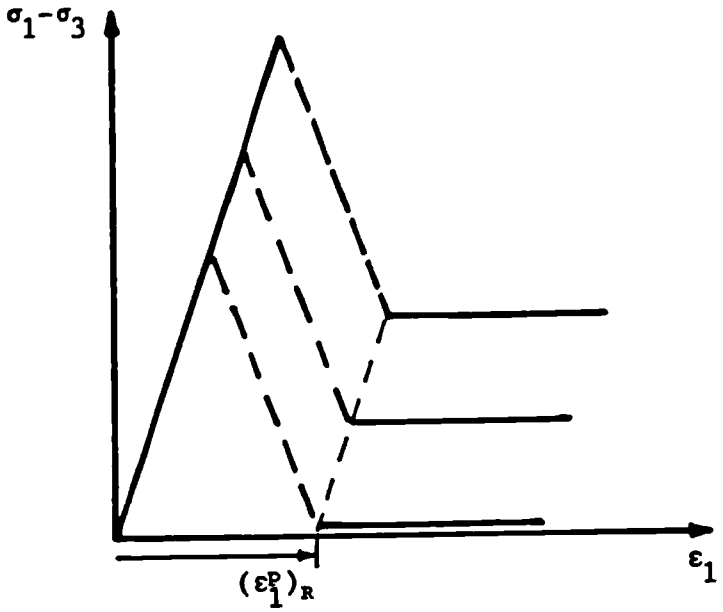


Figure D.1 Model representation of triaxial stress-strain data.

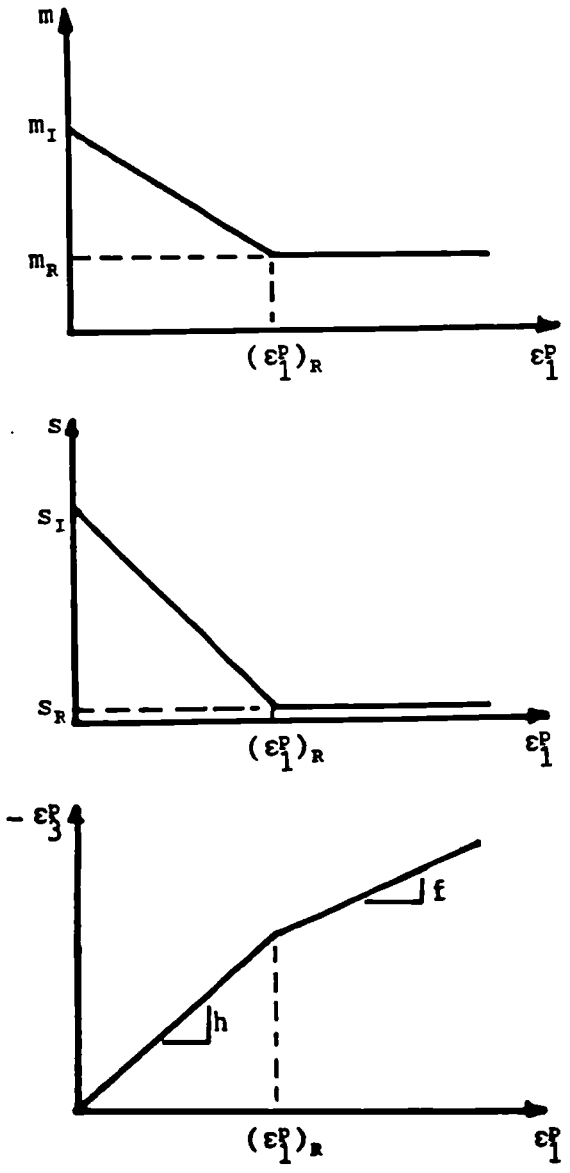


Figure D.2 Variation of strength parameters (m and s) and flow ratio with plastic deformation

not a precondition of the analysis, and the solution allows for only elastic and strain softening zones. Thus, depending on the applied loading and material behaviour three distinct material response zones may develop:

1. For $r \geq r_E$ - elastic region
2. For $r_R \leq r \leq r_E$ - strain softening region
3. For $a \leq r \leq r_R$ - residual strength region

where r_E is the radius defining the elasto-plastic interface,

r_R is the radius defining the softening-residual strength interface,

and a is the hole radius.

The finite difference solution that follows focuses on the stress-strain response of an annulus defined by an inner radius r_j. This ring exists somewhere in the plastic zone (either the softening or residual strength zone).

Elasto-plastic boundary

At $r = r_E$ the material is just on the point of yielding and for the condition where the inner pressure, P_a, $< P_0$ it can be shown that at r_E

$$\sigma_{r_E} < \sigma_{z_E} < \sigma_{\theta_E}$$

where σ_{r_E}, σ_{θ_E} and σ_{z_E} are the radial, circumferential and axial stresses at the elasto-plastic interface.

Then from Brown et al[49] we have

$$\sigma_{r_E} = P_0 - M\sigma_c \qquad (2)$$

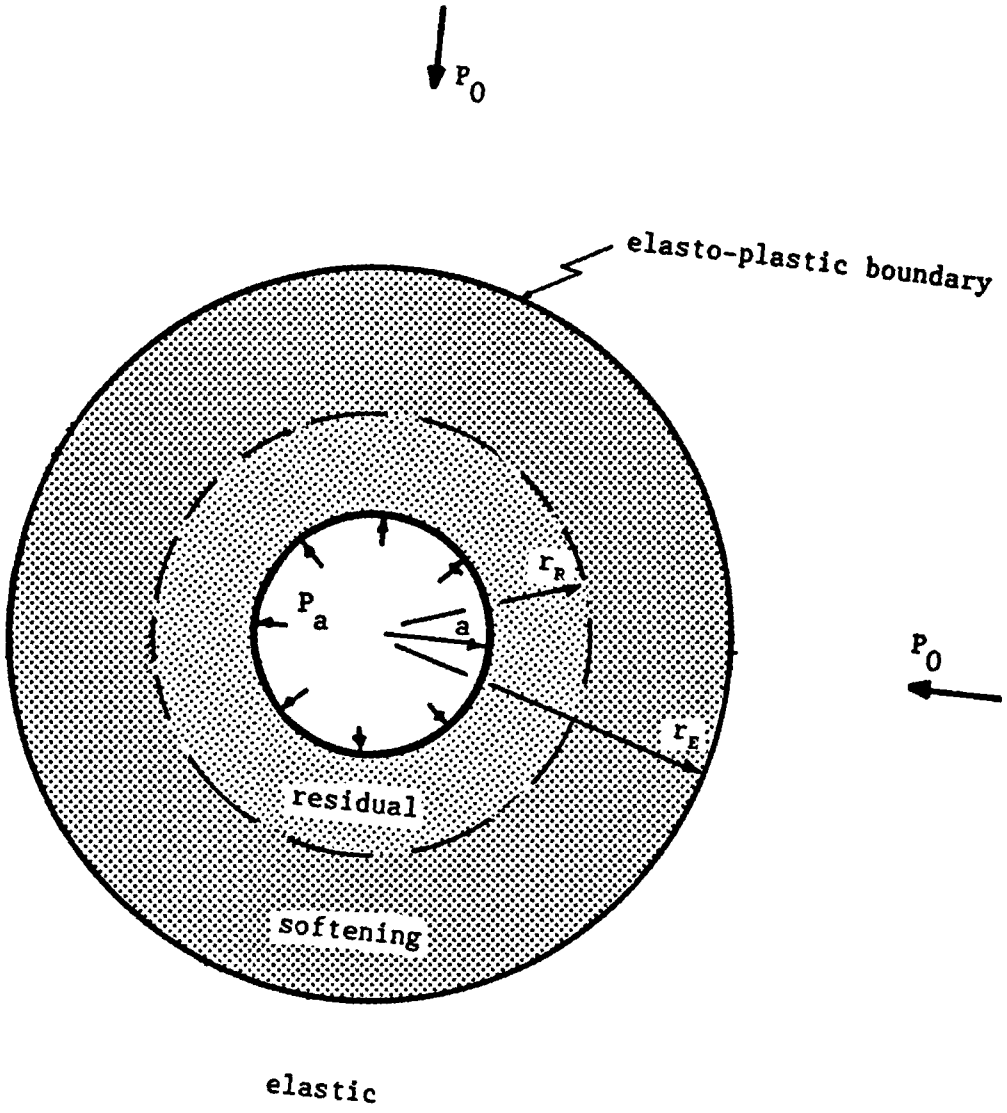


Figure D.3 Plastic zones developed around a circular opening in a hydrostatic in-situ stress field.

and $\sigma_{\theta_E} = P_0 + M\sigma_c$ (3)

where $M = \frac{1}{2}\left[(m_I/4)^2 + m_I P_0/\sigma_c + s_I\right]^{\frac{1}{2}} - m/8$

m_I and s_I are the initial values of the Hoek-Brown strength parameters.

The net Poisson effect in the axial direction is zero, resulting in no change in the axial stress in the elastic zone. Thus,

$$\sigma_{z_E} = P_0$$

The induced strains at the elasto-plastic interface are given by

$$\varepsilon_{r_E} = -\frac{M\sigma_c}{2G}, \qquad \varepsilon_{\theta_E} = +\frac{M\sigma_c}{2G} \quad \text{and} \quad \varepsilon_{z_E} = 0 \tag{4}$$

where G is the shear modulus, given by

$$G = \frac{E}{2(1+\nu)}$$

Strain-displacement relations

From Brown et al the finite difference equation relating the radius and strain for the j^{th} ring is given by

$$\frac{r_j}{r_{j-1}} = \frac{2\varepsilon_{\theta_{j-1}} - \varepsilon_{r_{j-1}} - \varepsilon_{r_j}}{2\varepsilon_{\theta_j} - \varepsilon_{r_{j-1}} - \varepsilon_{r_j}}$$

or $$\lambda_j = \frac{2\varepsilon_{\theta_{j-1}} - \varepsilon_{r_{j-1}} - \varepsilon_{r_j}}{2\varepsilon_{\theta_j} - \varepsilon_{r_{j-1}} - \varepsilon_{r_j}} . \lambda_{j-1} \tag{5}$$

where λ is the radius normalised with respect to the radius at the elasto-plastic interface, i.e., $\lambda_j = r_j/r_E$

Stress Condition A – $\sigma_{r_{j-1}} < \sigma_{z_{j-1}} \leq \sigma_{\theta_{j-1}}$

a) Assume λ_{j-1}, $\varepsilon_{r_{j-1}}$ and $\varepsilon_{\theta_{j-1}}$ are known, and ε_{θ_j} is taken to be a function of $\varepsilon_{\theta_{j-1}}$, given by

$$\varepsilon_{\theta_j} = (1+\Omega)\varepsilon_{\theta_{j-1}} \tag{6}$$

where Ω is +ve and small (e.g. Brown et al,[49] $\Omega = 0.01$)

Then on determining the radial strain component, ε_{r_j}, consistent with compatibility and the stress state, λ_j can be determined from (5).

b) For Stress Condition A it is assumed that there is no increment of plastic strain in the axial direction for ring 'j'. However, in the radial and circumferential directions the increment of strain is made up of elastic and plastic portions. Thus, in the circumferential direction we have for ring 'j',

$$\varepsilon_{\theta_j} = \varepsilon_{\theta_{j-1}} + \Delta\varepsilon_{\theta_j} = \varepsilon_{\theta_{j-1}} + \Omega\varepsilon_{\theta_{j-1}} \tag{7}$$

$$\text{where } \Delta\varepsilon_{\theta_j} = \Delta\varepsilon^e_{\theta_j} + \Delta\varepsilon^p_{\theta_j} = \Omega\varepsilon_{\theta_{j-1}} \tag{8}$$

The superscripts 'e' and 'p' denote elastic and plastic components of strain respectively.

c) The radial and circumferential plastic components of strain are related via the flow rule. Thus, if the ring is in the softening zone, we have

$$\Delta\varepsilon^p_{r_j} = -h\Delta\varepsilon^p_{\theta_j} \tag{9}$$

and in the residual zone

$$\Delta\varepsilon^p_{r_j} = -f\Delta\varepsilon^p_{\theta_j} \tag{10}$$

where f and h are defined in Figure D.2.

d) Having determined the plastic portion of the radial strain increment, the total radial strain for ring 'j' is given by

$$\varepsilon_{r_j} = \varepsilon_{r_{j-1}} + \Delta\varepsilon_{r_j} \tag{11}$$

where $\Delta\varepsilon_{r_j} = \Delta\varepsilon^{e}_{r_j} + \Delta\varepsilon^{p}_{r_j}$

e) The variation of the strength parameters in the softening zone is a function of the strength parameters, given by

$$m_j = m_{j-1} - \frac{m_I - m_R}{(\varepsilon_1^p)_R}.\Delta\varepsilon^p_{\theta_j} \tag{12}$$

$$\text{and} \quad s_j = s_{j-1} - \frac{s_I - s_R}{(\varepsilon_1^p)_R}.\Delta\varepsilon^p_{\theta_j} \tag{13}$$

where m_R and s_R are the values of the strength parameters at residual,

and $(\varepsilon_1^p)_R$ is defined in Figures D.1 and D.2.

If the ring exists in the residual zone then m_j and s_j are simply given by

$$m_j = m_R \qquad \text{and} \quad s_j = s_R \tag{14}$$

f) The finite difference form of the axisymmetric equilibrium equation used here is a modification of that given by Brown et al.[49] The modification allows simpler expressions for the radial stress at ring 'j', and is given by

$$\frac{\sigma_{r_{j-1}} - \sigma_{r_j}}{r_{j-1} - r_j} = \frac{\sigma_{\theta_{j-1}} - \sigma_{r_{j-1}}}{r_{j-1}}$$

which on rearranging gives,

$$\sigma_{r_j} = \sigma_{r_{j-1}} - \frac{\lambda_{j-1} - \lambda_j}{\lambda_{j-1}} (\sigma_{\theta_{j-1}} - \sigma_{r_{j-1}}) \tag{15}$$

where λ_j is found from equation (5).

g) The circumferential stress can be found from the yield criterion (1) and the computed value of the radial stress. Thus,

$$\sigma_{\theta_j} = \sigma_{r_j} + \sqrt{(m_j \sigma_c \sigma_{r_j} + s_j \sigma_c^2)} \tag{16}$$

h) Once the stress state is found the increments in the elastic strain components can be computed. Thus,

$$\Delta\varepsilon^{e}_{r_j} = [(1-\nu^2)(\sigma_{r_j} - \sigma_{r_{j-1}}) + \nu(1-\nu)(\sigma_{\theta_j} - \sigma_{\theta_{j-1}})]/E \tag{17}$$

and

$$\Delta\varepsilon^{e}_{\theta_j} = [(1-\nu^2)(\sigma_{\theta_j} - \sigma_{\theta_{j-1}}) + \nu(1-\nu)(\sigma_{r_j} - \sigma_{r_{j-1}})]/E \tag{18}$$

i) From (8) and (18) $\Delta\varepsilon^{p}_{\theta_j}$ is given by

$$\Delta\varepsilon^{p}_{\theta_j} = \Delta\varepsilon_{\theta_j} - \Delta\varepsilon^{e}_{\theta_j} \tag{19}$$

Solution of the sequence of operations b) to h) cannot be solved directly since they are dependent on the unknown values of $\Delta\varepsilon^{e}_{r_j}$ and $\Delta\varepsilon^{p}_{\theta_j}$. Here solution is found by making an initial guess at the values (e.g. $\Delta\varepsilon^{e}_{r_j} = 0$ and $\Delta\varepsilon^{p}_{\theta_j} = \Delta\varepsilon_{\theta_j}$). The calculation sequence defined by operations a) to h) is thus performed using the initial values of $\Delta\varepsilon^{e}_{r_j}$ and $\Delta\varepsilon^{p}_{\theta_j}$, and operations b) to h) repeated using the updated values of $\Delta\varepsilon^{e}_{r_j}$ and $\Delta\varepsilon^{p}_{\theta_j}$ found from (17) and (19). The process is continued until the values of $\Delta\varepsilon^{e}_{r_j}$ found from successive iterations are approximately equal. (Note: When calculating σ_{r_j} in operation e), λ_j, must be reformulated on each iteration to comply with the current estimates of $\Delta\varepsilon^{e}_{r_j}$ and $\Delta\varepsilon^{p}_{\theta_j}$.)

j) Once convergence is achieved the axial stress, σ_{z_j}, is determined from plane strain considerations. Thus

$$\sigma_{z_j} = \sigma_{z_{j-1}} + \nu(\Delta\sigma_{r_j} + \Delta\sigma_{\theta_j}) \tag{20}$$

Stress Condition B - $\sigma_{r_{j-1}} < \sigma_{\theta_{j-1}} < \sigma_{z_{j-1}}$

k) In this case it is assumed that plastic flow increments for ring 'j' take place in the radial and axial directions only and $\Delta\varepsilon^p_{\theta_j} = 0$. The radius of the ring is now determined by assuming a value for the plastic axial strain increment, $\Delta\varepsilon^p_{z_j}$, instead of the circumferential strain increment, $\Delta\varepsilon_{\theta_j}$. Thus, for Stress Condition B we have

$$\Delta\varepsilon^p_{z_j} = -\Delta\varepsilon^e_{z_j} = \varrho\varepsilon_{\theta_{j-1}} \tag{21}$$

l) The values of the radial plastic strain in the softening zone are given by

$$\Delta\varepsilon^p_{r_j} = -h\Delta\varepsilon^p_{z_j} \tag{22}$$

and in the residual zone

$$\Delta\varepsilon^p_{r_j} = -f\Delta\varepsilon^p_{z_j} \tag{23}$$

The total radial strain is again given by equation (11).

m) The strength parameters in the softening zone are given by

$$m_j = m_{j-1} - \frac{m_I - m_R}{(\varepsilon^p_1)_R}.\Delta\varepsilon^p_{z_j} \tag{24}$$

$$\text{and} \quad s_j = s_{j-1} - \frac{s_I - s_R}{(\varepsilon^p_1)_R}.\Delta\varepsilon^p_{z_j} \tag{25}$$

and in the residual zone the strength parameters are given by equation set (14).

n) The radial stress, σ_{r_j}, is again given by equation (15), with λ_j found from equation (5), but the axial and the circumferential stresses are now given by

$$\sigma_{z_j} = \sigma_{r_j} + \sqrt{(m_j\sigma_c\sigma_{r_j} + s_j\sigma_c^2)} \tag{26}$$

$$\sigma_{\theta_j} = \sigma_{\theta_{j-1}} + \Delta\varepsilon_{\theta_j}E + \nu(\sigma_{z_j} - \sigma_{z_{j-1}} + \sigma_{r_j} - \sigma_{r_{j-1}}) \tag{27}$$

o) The increments in total circumferential strain and elastic radial strain are given by

$$\Delta\varepsilon^{e}_{r_j} = [\sigma_{r_j} - \sigma_{r_{j-1}} - \nu(\sigma_{\theta_j} - \sigma_{\theta_{j-1}} + \sigma_{z_j} - \sigma_{z_{j-1}})]/E \qquad (28)$$

and $$\Delta\varepsilon_{\theta_j} = [\sigma_{\theta_j} - \sigma_{\theta_{j-1}} - \nu(\sigma_{r_j} - \sigma_{r_{j-1}} + \sigma_{z_j} - \sigma_{z_{j-1}})]/E \qquad (29)$$

p) The total circumferential strain can now be determined using the value of $\Delta\varepsilon_{\theta_j}$ determined from (29). Thus,

$$\varepsilon_{\theta_j} = \varepsilon_{\theta_{j-1}} + \Delta\varepsilon_{\theta_j} \qquad (30)$$

For Stress Condition B the sequence of operations m) to p) cannot be performed directly since they are dependent on the unknowns $\Delta\varepsilon^{e}_{r_j}$ and $\Delta\varepsilon_{\theta_j}$. Thus, initial estimates must be made and an iterative procedure adopted similar to the method described for Stress Condition A. In this case suitable initial values are $\Delta\varepsilon^{e}_{r_j} = 0$ and $\Delta\varepsilon_{\theta_j} = 0$. The sequence of operations i) to p) is carried out, and the values of $\Delta\varepsilon^{e}_{r_j}$, $\Delta\varepsilon_{\theta_j}$ and ε_{θ_j} updated from equations (28), (29) and (30) respectively. Operations m) to p) are then repeated until convergence is deemed to have occured. Convergence is found to be rapid, and often no more than 5 iterations are required to obtain $\Delta\varepsilon^{e}_{r_j}$ to 0.1% accuracy. (Note: As with Stress Condition A, λ_j must be updated to comply with current estimates of $\Delta\varepsilon^{e}_{r_j}$ and $\Delta\varepsilon_{\theta_j}$, before evaluating σ_{r_j} in each iteration.)

Calculation of the complete stress state in the plastic zone

The complete algorithm is now given as follows:

1. The radius of ring j = 1 is taken to be r_E. Thus,

$\sigma_{r_1} = \sigma_{r_E}$ and $\sigma_{\theta_1} = \sigma_{\theta_E}$ - computed from (2) and (3) respectively

$\sigma_{z_1} = \sigma_{z_E} = P_0$

$\varepsilon_{r_1} = \varepsilon_{r_E}$, $\varepsilon_{\theta_1} = \varepsilon_{\theta_E}$ and $\varepsilon_{z_1} = 0$ - computed from equation set (4)

$\lambda_1 = r_1/r_E = 1$

$m_1 = m_I$ and $s_1 = s_I$

2. The ring counter j is incremented by 1. If $\sigma_{z_{j-1}} \leq \sigma_{\theta_{j-1}}$ then the sequence of operations given in Stress Condition A apply, otherwise the sequence given in Stress Condition B is carried out. Convergence for both stress conditions occurs when

$$(\Delta\varepsilon^{\bullet}_{r_j})_i - (\Delta\varepsilon^{\bullet}_{r_j})_{i-1} \simeq 0$$

where i is the iteration counter for the iterative processes described for the two stress conditions.

Determination of whether a ring is in the softening or residual zone can be acheived by checking whether $s_{j-1} = s_R$ and/or $m_{j-1} = m_R$.

3. If $\sigma_{r_j} > P_a$, then step 2 above is repeated, otherwise $\sigma_{r_j} \simeq P_a$ (provided Q is small enough), and radius $r_j = a$ (the tunnel radius). The radius of the elasto-plastic interface can now be found from $r_E = a/\lambda_j$, which in turn allows determination of the radius of all the rings, using $r_j = \lambda_j r_E$. Values of radial displacement, at each ring can be found from the circumferential strain, i.e. $u_j = r_j \varepsilon_{\theta_j}$.

APPENDIX E

SEMI-CLOSED FORM SOLUTION FOR THE ANALYSIS OF STRESSES AROUND A CIRCULAR OPENING SUBJECTED TO AXISYMMETRIC LOADING ASSUMING A PRESSURE DEPENDENT STIFFNESS (PDS)

The following equations give the stress state around a circular opening in both an unbounded domain (e.g. a wellbore) or bounded domain (hollow cylinder), assuming a pressure dependent stiffness as defined by Santarelli.[18] Here it is assumed that the elastic modulus, E, is a function the minimum principal stress, σ_3, and the Poisson's ratio, ν, is constant and independent of σ_3. The basis of these assumptions stems from the work carried out by Santarelli, and discussed in Section 6.1, Chapter 6.

The assumptions made in the development are given below.

1. Plane strain conditions apply.
2. Total and effective stresses are equivalent.
3. The applied loading is axisymmetric and given by a vertical stress, σ_v, and an isotropic horizontal stress state defined by σ_H (= σ_h). The relative magnitudes of the stresses conform to the inequality, $\sigma_v \geq \sigma_H$.
4. Body forces are negligible.
5. The material is homogeneous, isotropic and remains elastic.
6. The variation of the secant Youngs modulus, E, is described by a relationship of the form

$$E = E(\sigma_3) = E_0 + E'\sigma_3 \qquad (1)$$

where E_0 is the Youngs modulus obtained from uniaxial testing, and E' is the gradient shown in Figure E.1

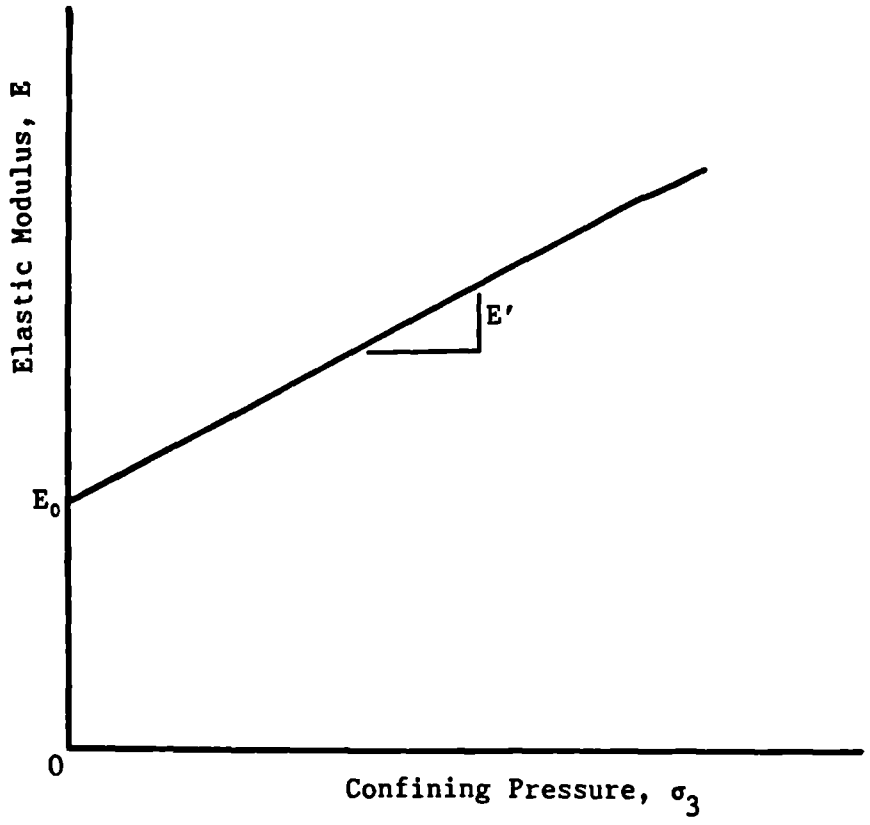


Figure E.1 Linear relationship between Young's modulus and the minimum principal stress.

Stress State around a Circular Opening in an Unbounded Domain

For a wellbore under plane strain constraints, the strain in the axial direction, ε_z, remains unaffected by the creation of the circular opening. Thus, the axial strain is given by

$$\varepsilon_z = \text{constant} = \frac{\sigma_v - 2\nu\sigma_H}{E(\sigma_H)} = \frac{\sigma_z - \nu(\sigma_r + \sigma_\theta)}{E(\sigma_r)} \tag{2}$$

where σ_r, σ_θ and σ_z are respectively the radial, circumferential and axial stresses around the opening after excavation.

Note: It is assumed in equation (2), and the majority of the following expressions, that σ_r is the minimum principal stress. This is true throughout the domain when the internal pressure at the wall of the opening, P_a, is less than σ_H. For cases where $P_a > \sigma_H$, then σ_θ becomes the minimum principal stress and $E = E(\sigma_\theta)$ after excavation.

Rearranging (2) gives

$$\sigma_z = \nu(\sigma_r + \sigma_\theta) + \frac{(\sigma_v - 2\nu\sigma_H)E(\sigma_r)}{E(\sigma_H)} \tag{3}$$

The radial strain, ε_r, is given by

$$\varepsilon_r = \frac{\sigma_r - \nu(\sigma_\theta + \sigma_z)}{E(\sigma_r)}$$

Thus, $$\sigma_r = \nu(\sigma_\theta + \sigma_z) + E(\sigma_r)\varepsilon_r \tag{4}$$

similarly, $$\sigma_\theta = \nu(\sigma_r + \sigma_z) + E(\sigma_r)\varepsilon_\theta \tag{5}$$

Subtracting (4) from (5) and rearranging gives

$$\sigma_\theta - \sigma_r = \frac{E(\sigma_r)}{1+\nu}(\varepsilon_\theta - \varepsilon_r) \tag{6}$$

From the equilibrium equation and equation (6) we arrive at

$$\frac{d\sigma_r}{dr} = \frac{\sigma_\theta - \sigma_r}{r} = \frac{E(\sigma_r)}{(1+\nu)r}(\varepsilon_\theta - \varepsilon_r)$$

and expressing strains in terms of displacement gives

$$\frac{d\sigma_r}{E(\sigma_r)} = \frac{1}{(1+\nu)r}\left[\frac{du}{dr} - \frac{u}{r}\right]dr \tag{7}$$

where u is the radial displacement.

Since $E(\sigma_r) = E_0 + E'\sigma_r$, integration of (7) gives

$$\frac{1+\nu}{E'}.\ln\left[E(\sigma_r)\right] = \frac{u}{r} + C \tag{8}$$

where C is a constant of integration.

Rearranging (8) gives

$$u = \frac{1+\nu}{E'}.r.\ln\left[E(\sigma_r)\right] - C.r \tag{9}$$

Inserting (9) into the strain-displacement relationship for ε_θ gives

$$\varepsilon_\theta = -\frac{u}{r} = -\frac{1+\nu}{E'}.\ln\left[E(\sigma_r)\right] + C \tag{10}$$

From (5) and (10) we get

$$\sigma_\theta = \nu(\sigma_r + \sigma_z) - \frac{1+\nu}{E'}.E(\sigma_r).\ln\left[E(\sigma_r)\right] + E(\sigma_r).C \tag{11}$$

As $r \to \infty$ then $\sigma_r = \sigma_\theta = \sigma_H$, and $\sigma_z = \sigma_v$. Thus, from (11) we have

$$C = \frac{(1-\nu)\sigma_H - \nu\sigma_v}{E(\sigma_H)} + \frac{1+\nu}{E'}.\ln\left[E(\sigma_H)\right] \tag{12}$$

Using (12) to eliminate C from (9) gives

$$u = \frac{1+\nu}{E'}.r.\ln\left[\frac{E(\sigma_r)}{E(\sigma_H)}\right] - \frac{(1-\nu)\sigma_H - \nu\sigma_v}{E(\sigma_H)}.r \tag{13}$$

$$\therefore \quad \varepsilon_r = -\frac{du}{dr} = -\frac{1+\nu}{E'}.\ln\left[\frac{E(\sigma_r)}{E(\sigma_H)}\right] - \frac{(1+\nu)r}{E(\sigma_r)}.\frac{d\sigma_r}{dr} + \frac{(1-\nu)\sigma_H - \nu\sigma_v}{E(\sigma_H)} \tag{14}$$

$$\text{and} \quad \varepsilon_\theta = -\frac{u}{r} = -\frac{1+\nu}{E'}.\ln\left[\frac{E(\sigma_r)}{E(\sigma_H)}\right] + \frac{(1-\nu)\sigma_H - \nu\sigma_v}{E(\sigma_H)} \tag{15}$$

The last term in equations (13), (14) and (15) relates to the pre-existing displacement and strains within the formation before excavation. Thus, the induced displacement resulting from excavation, Δu, is given by

$$\Delta u = \frac{1+\nu}{E'}.r.\ln\left[\frac{E(\sigma_r)}{E(\sigma_H)}\right] \tag{16}$$

Eliminating σ_z from (4) using (3) gives

$$\sigma_r = \frac{\nu}{1-\nu}.\sigma_\theta + \frac{\nu(\sigma_v - 2\nu\sigma_H)E(\sigma_r)}{(1-\nu^2)E(\sigma_H)} + \frac{E(\sigma_r)\varepsilon_r}{1-\nu^2} \tag{17}$$

Similarly from (5) and (3) we get

$$\sigma_\theta = \frac{\nu}{1-\nu}.\sigma_r + \frac{\nu(\sigma_v - 2\nu\sigma_H)E(\sigma_r)}{(1-\nu^2)E(\sigma_H)} + \frac{E(\sigma_r)\varepsilon_\theta}{1-\nu^2} \tag{18}$$

Using (18) to eliminate σ_θ in equation (17) gives after rearranging

$$\sigma_r = \frac{E(\sigma_r)}{(1+\nu)(1-2\nu)}\left[\frac{\nu(\sigma_v - 2\nu\sigma_H)}{E(\sigma_H)} + (1-\nu)\varepsilon_r + \nu\varepsilon_\theta\right] \tag{19}$$

From (14) and (15) we have

$$(1-\nu)\varepsilon_r + \nu\varepsilon_\theta = -\frac{1+\nu}{E'}.\ln\left[\frac{E(\sigma_r)}{E(\sigma_H)}\right] - \frac{(1+\nu)(1-\nu)r}{E(\sigma_r)}.\frac{d\sigma_r}{dr} + \frac{(1-\nu)\sigma_H - \nu\sigma_v}{E(\sigma_H)}$$

Thus, by substituting for the strain terms in (19) using the expression above, we get

$$\sigma_r = \frac{E(\sigma_r)}{(1+\nu)(1-2\nu)}\left\{\frac{(1+\nu)(1-2\nu)}{E(\sigma_H)}.\sigma_H - \frac{1+\nu}{E'}.\ln\left[\frac{E(\sigma_r)}{E(\sigma_H)}\right] - \frac{(1+\nu)(1-\nu)r}{E(\sigma_r)}.\frac{d\sigma_r}{dr}\right\}$$

which on rearranging gives

$$\frac{dr}{(1-\nu)r} = \frac{1}{f(\sigma_r)}.d\sigma_r \tag{20}$$

$$\text{where } f(\sigma_r) = \frac{(1-2\nu)E(\sigma_r)\sigma_H}{E(\sigma_H)} - \frac{E(\sigma_r)}{E'}.\ln\left[\frac{E(\sigma_r)}{E(\sigma_H)}\right] - (1-2\nu)\sigma_r \qquad (21)$$

Integrating (20) gives

$$\frac{1}{1-\nu}.\ln\left(\frac{r}{a}\right) = \int_{P_a}^{\sigma_r} \frac{1}{f(\sigma_r)}.d\sigma_r \qquad (22)$$

Integration of the right hand side of equation (22) must be performed numerically. Thus, by using the radial stress as the space parameter, the radius, r, equivalent to a radial stress σ_r, can be determined from equation (22) by integrating between the pressure applied to the wall of the opening, P_a, and σ_r.

Rearranging equation (20) and utilizing the equilibrium equation gives

$$\frac{d\sigma_r}{dr} = \frac{1}{(1-\nu)r}.f(\sigma_r) = \frac{\sigma_\theta - \sigma_r}{r}$$

$$\text{Thus,} \quad \sigma_\theta = \frac{1}{(1-\nu)}.f(\sigma_r) + \sigma_r \qquad (23)$$

Therefore the circumferential stress, σ_θ, for a given value of σ_r is determined directly from equation (23). The axial stress, σ_z, is then found from equation (3). Finally, the radial closure, Δu, of the opening is found from equation (16) by substituting $\sigma_r = P_a$ and $r = a$.

At this point it is worth checking that the above relationships reduce to the linear elastic equations when the variable term, E′, in equation (1) tends to zero. Thus, rearranging the logarithmic term which appears in equations (16) and (21), we get

$$\ln\left[\frac{E(\sigma_r)}{E(\sigma_H)}\right] = \ln\left(1 + \frac{E'}{E_0}.\sigma_r\right) - \ln\left(1 + \frac{E'}{E_0}.\sigma_H\right) \qquad (24)$$

For small E′, then $\left|\frac{E'}{E_0}.\sigma_r\right| < 1$, and $\left|\frac{E'}{E_0}.\sigma_H\right| < 1$, therefore the series

expansion of (24) is

$$\ln\left[\frac{E(\sigma_r)}{E(\sigma_H)}\right] = \frac{E'}{E_0}(\sigma_r - \sigma_H) - \frac{1}{2}\left(\frac{E'}{E_0}\right)^2(\sigma_r^2 - \sigma_H^2) + \frac{1}{3}\left(\frac{E'}{E_0}\right)^3(\sigma_r^3 - \sigma_H^3) - \ldots + \ldots$$

On substituting the series expansion into (21) and letting $E' \to 0$, then only the first term of the series remains, and we arrive at

$$f(\sigma_r) = 2(1-\nu)(\sigma_H - \sigma_r)$$

Substituting the above expression into (22) allows closed form integration giving

$$\frac{1}{1-\nu}.\ln\left(\frac{r}{a}\right) = -\frac{1}{2(1-\nu)}\ln\left[\frac{\sigma_H - \sigma_r}{\sigma_H - P_a}\right]$$

which on rearranging gives

$$\sigma_r = \sigma_H - (\sigma_H - P_a)\left(\frac{a}{r}\right)^2$$

This is the correct linear elastic expression relating radial stress to radial distance. Similarly, it can be shown that equations (16) and (23) reduce to the correct linear elastic expressions as $E' \to 0$.

Stress State around a Hollow Cylinder

In this case loading is applied at the outer surface of the hollow cylinder and not at infinity. Let the conditions defining the problem be given by a pressure P_a at the internal radius, r=a, and a pressure P_b at the external radius, r=b. Given the conditions at r=a, the first step is to use equation (22) to determine the horizontal stress at infinity which results in a radial stress of $\sigma_r = P_b$ at r=b in the case of the unbounded domain. Having determined this, then the hollow cylinder is simply treated as part of the unbounded domain defined by $a \leq r \leq b$.

Thus, σ_H in equation (21) is chosen to satisfy the following expression

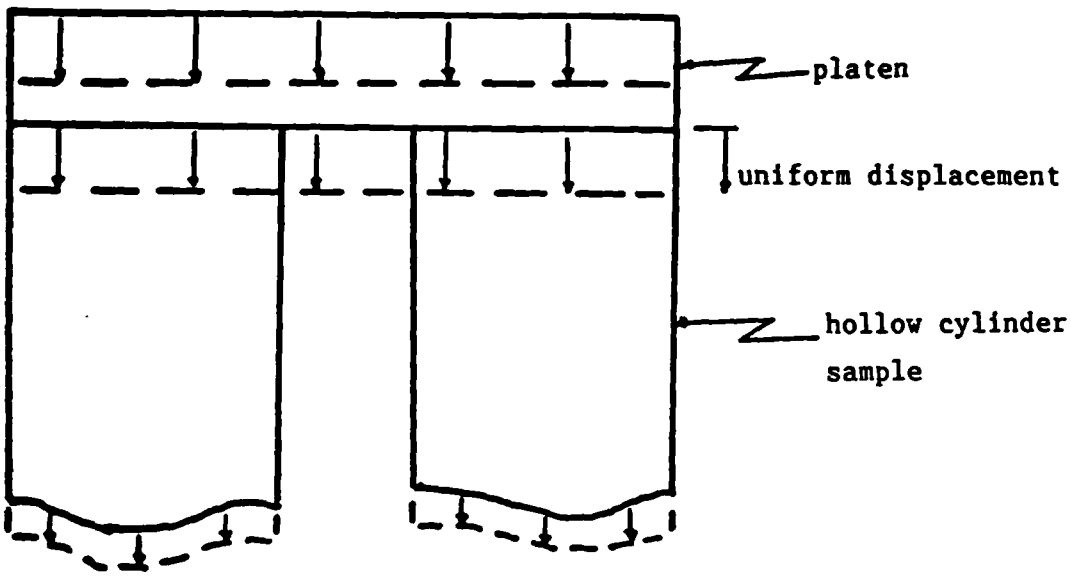
$$\frac{1}{1-\nu}.\ln\left(\frac{b}{a}\right) = \int_{P_a}^{P_b} \frac{1}{f(\sigma_r)}.d\sigma_r$$

An iterative procedure must be used to determine the value of σ_H that satisfies the above condition. Having determined the equivalent horizontal stress at infinity, then 'r' and σ_θ can be determined for values of the space parameter σ_r, bounded by $P_a \leq \sigma_r \leq P_b$. In order to determined the axial stress, σ_z, further assumptions regarding axial conditions are necessary. In general, the axial condition applied during hollow cylinder testing conforms to neither plane strain nor plane stress. However, if we assume that the stiffness of the platens far exceeds that of the rock, then the axial strain is uniform throughout the sample (see Figure E.2a). Thus, from equation (2) we have for the axial stress

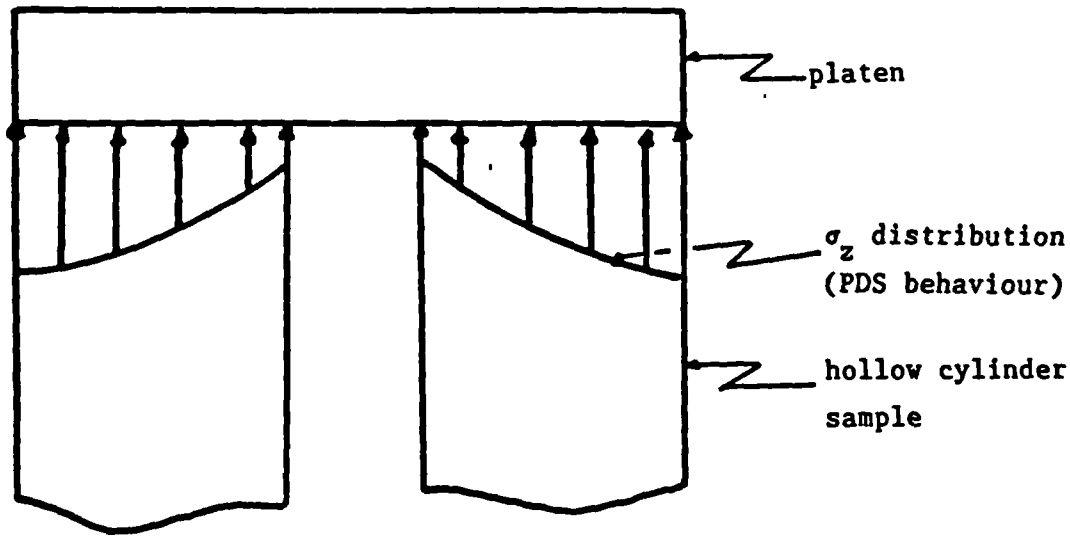
$$\sigma_z = \varepsilon_z E(\sigma_r) + \nu(\sigma_r + \sigma_\theta) \qquad (25)$$

Values of σ_r and σ_θ can be calculated throughout the cylinder as explained above, but we do not yet know ε_z. For a particular test we may specify the applied axial load, L_z. However, for a material that exhibits PDS it is incorrect to divide L_z by the X-sectional area, A, to give the axial stress. For PDS behaviour σ_z varies radially (see Figure E.2b). To find the axial strain, such that σ_z can be determined from equation (25), it is necessary to sum σ_z over the X-sectional area and equate it with the axial load, L_z. Thus,

$$L_z = \int_a^b 2\pi r\sigma_z dr = 2\pi\int_a^b r\left[\varepsilon_z E(\sigma_r) + \nu(\sigma_r + \sigma_\theta)\right]dr$$



(a) Uniform displacement assumption



(b) Axial stress variation for PDS behaviour

Figure E.2 Axial conditions during a hollow cylinder test for a material displaying PDS behaviour.

which on rearranging gives

$$\varepsilon_z = \frac{\frac{L_z}{2\pi} - \nu\int_a^b r(\sigma_r + \sigma_\theta)dr}{\int_a^b rE(\sigma_r)dr} \qquad (26)$$

Integration of the terms on the right hand side of equation (26) must be performed numerically, having already determined 'r' and σ_θ from equations (22) and (23) corresponding to values of σ_r. Once ε_z is determined, then σ_z is found from equation (25).

The expression required for the radial displacement at the inner wall of the cylinder depends on the initial and final loading applied to the sample. For example, the radial closure measured at the inner wall of the cylinder will be different for the three load paths given below.

1. At initial conditions the sample is under an axial load. Measurement of radial closure is now monitored as the external pressure on the sample is increased from zero, while the axial load remains constant.

2. At initial conditions the sample is subjected to axial loading and equal external and internal pressures. Measurement of radial closure is now monitored as the internal pressure is reduced, while the axial and external loads remain constant.

3. At initial conditions the sample is under zero radial and axial load. Measurement of radial closure is now monitored as both the axial load and external pressure are increased, while the internal pressure remains zero.

In the hollow cylinder tests performed by Santarelli[18] the third load path was adopted.* Therefore, the displacement measured at the internal wall must contain a component relating to the application of 'far field' stresses, unlike the case of a wellbore, where only the induced displacements are of interest. Thus, the displacement, u, is given by equation (13). Using equation (2) to eliminate σ_v from (13) we arrive at

$$u = \left\{\frac{1+\nu}{E'}\ln\left[\frac{E(\sigma_r)}{E(\sigma_H)}\right] - \frac{(1+\nu)(1-2\nu)}{E(\sigma_H)}\sigma_H + \nu\varepsilon_z\right\}.r \qquad (27)$$

where σ_H is the equivalent horizontal stress state at infinity, which must be found iteratively as discussed before,

and ε_z is the axial strain undergone by the sample at a particular stage of the loading and given by equation (26).

[* Note: The true load path undergone during drilling of a vertical well in an isotropic horizontal stress field is complicated by the progression of the drill bit through the formation. However, of the three stress paths given above, the second is the most representative, but it can still be improved upon. A better stress path would maintain plane strain conditions, while reducing the internal pressure, rather than maintaining constant axial load, as in the second example.]

APPENDIX F

INPUT, OUTPUT AND PROGRAM OPERATION

This appendix describes the operation of the program, the preparation of the input data and the form of the output data.

Program Operation

The FEM program is written in the FORTRAN language suitable for compilation using a FORTRAN77 compiler and runs on a VAX main frame computer. The program has also run on a micro vax 2000 computer, and is likely to be suitable for most main frame FORTRAN77 compilers.

The coding is divided into two separate programs. Program PREPRO.EXE reads the input file, INPUT.DAT, and provided no errors are found, creates a new data file, REVIN.DAT, which is subsequently read by the main execution program, EXECUTE.EXE. During the preprocessing of the data, program PREPRO.EXE checks for errors and gives warning messages to flag the user of possible mistakes in the input file (e.g. when symmetry could be utilized, but has not been requested by the user). Any error and/or warning messages plus a formatted display of the data are written to a newly created file CHECK.DAT.

The program dynamically dimensions variables as far as the FORTRAN language allows. However, it is not possible to make the program completely independent of problem size. In addition to error checking, the program PREPRO.EXE advises the user as to scratch file space

requirements and minimum dimension size needed for the COMMON array A(...) at the head of the main execution source file EXECUTE.FOR. The author has found that a dimension size of A(30000) is sufficient for most problems, but for very large problems this may have to be increased and EXECUTE.FOR recompiled. For all problems this is the only array which the user may be required to change.

During the running of the main execution program, EXECUTE.EXE, the program creates a number of scratch files for temporary storage of data. The size of these scratch files are dependent on problem size. For very large problems it is possible that the user does not have sufficient storage space to accommodate these scratch files. The extent of the scratch file space required is calculated by PREPRO.EXE and written to CHECK.DAT. Before running EXECUTE.EXE the user is advised to check this and ensure that sufficient space is available. For most problems a temporary storage space of around 4 Megabytes is sufficient (assuming 4 bytes per integer and real for a 32 bit processor).

Once PREPRO.EXE has been successfully run and the user has checked the formatted display of the input data, any warning messages and the extent of the problem size, then EXECUTE.EXE is run. EXECUTE.EXE reads the revised unformatted data file, REVIN.DAT, created by PREPRO.EXE. From the limited information required by the user, EXECUTE.EXE generates all nodes, elements and Gauss point coordinates and writes them to the output file, OUTPUT.DAT. The program calculates the nodal loads equivalent to the traction change at the wellbore wall, given the in-situ stress magnitudes and directions, well direction, formation pressure and well pressure. The traction change is then applied until

initial yield occurs (or 100% of the load applied). After yield is initiated the program applies the remainder of the load in steps defined by the user.

Preparation of File INPUT.DAT

The extent of the information required by the user is kept to a minimum by incorporporating a simple but efficient element generator. The program PREPRO.EXE will read any data without crashing, and preperation of input data can often be achieved by instruction from error messages in CHECK.DAT.

Input is split into twelve data types. The first four characters of an input line define the data type (e.g. ELAS for the material elastic properties). The data types are grouped into two classes. The first class of data are compulsory for every problem case, and the data types in the second class may or may not appear depending on the problem.

Compulsory Data:

Compulsory data make up the first nine lines of the input and consist of the following (not necessarily in the order given):

1. TITL - The problem title from columns 11 to 70 (alphanumeric).

2. MESH - Reads variables XSYMY, YSYMY, IEL, JEL, INFEL, NGP (Format 6I5, from columns 11 to 40).

Where XSYMY = symmetry request about x-axis (1 - Yes, 0 - No),
YSYMY = symmetry request about y-axis (1 - Yes, 0 - No),
IEL = number of circumferential elements (+ve integer),
JEL = number of radial elements (+ve integer),
INFEL = infinite element request (1 - Yes, 0 - No).
NGP = Gauss point rule (2 - 2x2, 3 - 3x3),

3. GEOM - Defines boundary geometry RADIUS, PERDIS (Format 2F10.*, from columns 11 to 30).

Where RADIUS = well radius (+ve real, assumed to be in metres),
PERDIS = outer boundary of FEM mesh (+ve real, assumed to be metres).

4. LDSP - Reads NINCR, MITER, IPRIN, NRDSP, CONVR (Format 4I5, F10.*, from columns 11 to 40).

Where NINCR = number of plastic load steps (+ve integer),
MITER = maximum iterations per load step (+ve integer),
IPRIN = print indicator (1 - stresses and displacements for each load step, 0 - final load step only),
NRDSP = number of reductions of fictitious liner stiffness allowed when softening behaviour occurs (+ve integer),
CONVR = convergence tolerance (+ve real, see equation (49), Chapter 5).

Note: Every time the program considers convergence is too slow during strain softening, it reduces the fictitious liner stiffness by half. After convergence, the stiffness is returned to its original value before the next load step is applied. Occasionally instability can occur

when the liner becomes very 'soft'. Thus, the user is given the opportunity to limit the number of reductions in liner stiffness, NRDSP.

5. ELAS - Reads EO, EVAR, PNU (Format 3F10.*, from columns 11 to 40).
Where EO = uniaxial modulus, E_0 (+ve real, assumed to be in MPa),
EVAR = modulus variation parameter, E' (+ve real),
PNU = Poisson's ratio, ν (+ve real).

6. PLAS - Reads IASSC, IHARD, ISOFT, NCRIT (Format 4I5, from columns 11 to 30).
Where IASSC = flow rule indicator (1 - associated, 0 - nonassociated),
IHARD = hardening indicator (1 - hardening, 0 - no hardening),
ISOFT = softening indicator (1 - softening, 0 - no softening),
NCRIT = yield criterion (0 - no plasticity, 1 - Tresca, 2 - Von Mises, 3 - Mohr-Coulomb, 4 - Hoek-Brown).

7. MDPR - Reads FORMP, WELLP (Format 2F10.*, from columns 11 to 30).
Where FORMP = formation pressure (+ve real, assumed to be in MPa),
WELLP = well pressure (+ve real, assumed to be in MPa).

8. WBDR - Reads BHDIR, BHDEV (Format 2F10.*, from columns 11 to 30).
Where BHDIR = well direction (+ve real, in degrees),
BHDEV = well deviation (+ve real, in degrees).

9. LODS - Reads SHMAX, SHMIN, SVERT, DIRMX (Format 4F10.*, from columns 11 to 50).
Where SHMAX = maximum horizontal stress (+ve real, assumed to be in MPa),

SHMIN = minimum horizontal stress (+ve real, assumed to be in MPa),

SVERT = vertical stress (+ve real, assumed to be in MPa),

DIRMX = direction of the maximum horizontal stress (+ve real, in degrees).

Problem Dependent Data:

Four data types make up the problem dependent data. Inclusion of this data dependents on the information given in the compulsory data (e.g. if NCRIT = 0, in the PLAS data, then there is no need to input the STPR data given below).

10. STPR - Reads STPRL(array) - one line each for yield, peak and residual strength as required, depending on hardening and softening indicators in PLAS data type.

Where for (i) Tresca and Von Mises criterion (Format F10.*, columns 11 to 20),

STPRL(1) = uniaxial strength (+ve real, assumed to be in MPa),

for (ii) Mohr-Coulomb criterion (Format 2F10.*, columns 11 to 30),

STPML(1) = cohesion (+ve real, assumed to be in MPa),

STPML(2) = friction angle (+ve real, in degrees),

for (iii) Hoek-Brown criterion (Format 3F10.*, columns 11 to 40),

STPML(1) = uniaxial strength (+ve real, assumed to be in MPa),

STPML(2) = 'm' parameter (+ve real),

STPML(3) = 's' parameter (+ve real).

11. FLPR - Reads FLWNN(array) for definition of non-associated flow - one line each for hardening, softening and residual flow parameters, depending on hardening and softening indicators in PLAS data type (Format 3F10.*, from columns 11 to 40). The flow parameters are defined in Section 4.6.3, Chapter 4.

Where FLWNN(1) = parameter 'f_∞' (-ve real),

FLWNN(2) = parameter 'C' (-ve real),

FLWNN(3) = parameter 'D' (+ve real, in MPa^{-1}).

12. PLST - Reads PPSPM(array) for definition of the principal plastic strain at which peak and residual strength is reached (Format f10.*, from columns 11 to 50). The principal plastic strain parameters are defined in Section 4.5.3, Chapter 4.

Where PPSPM(1) = $[(\varepsilon_1^p)_P]_{uniax}$ (+ve real, in millistrain)

PPSPM(2) = A_P (+ve real, in millistrain/MPa)

PPSPM(3) = $[(\varepsilon_1^p)_R]_{uniax}$ (+ve real, in millistrain)

PPSPM(4) = A_R (+ve real, in millistrain/MPa)

An example of data set up in the file INPUT.DAT is given in Figure F.1.

Data Written to OUTPUT.DAT

The output file, OUTPUT.DAT contains a formatted display of the following:

1. The input data.
2. The polar coordinates for each node.
3. Element numbers and associated nodes.
4. Gauss point coordinates for each element.

5. The convergence ratio for each iteration.

6. Each time the fictitious liner stiffness is reduced during softening response.

7. The percentage traction change at the end of elastic loading and each plastic load increment.

8. Displacements at each node, and polar stress tensor at each Gauss point (effective stress not total stress) after the final load step.

9. Plasticity indicator at each Gauss point after the final load step. The plasticity indicator takes on values of -1.0 if elastic, 0.0 at peak strength and +1.0 at residual strength, and intermediate values when undergoing hardening (-1.0 → 0.0) or softening (0.0 → 1.0).

10. Items 8 and 9 after each load increment, if requested.

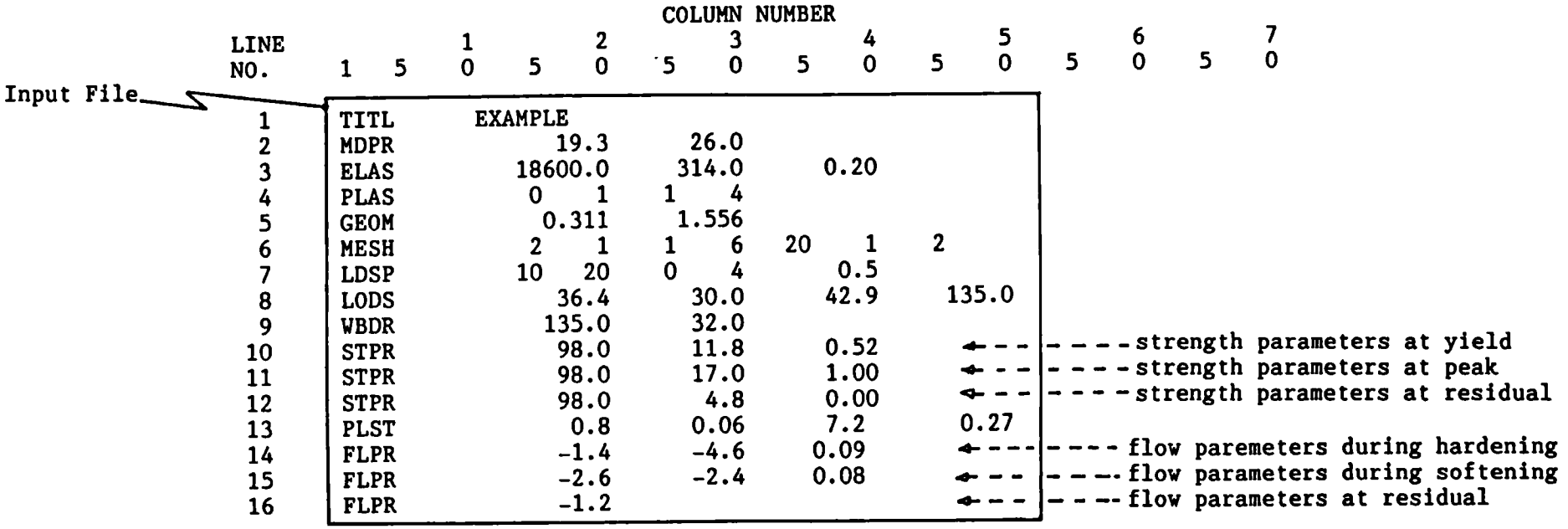


Figure F.1 Example of data layout in file INPUT.DAT.